WIND FLOW AND STRUCTURE OVER GEBBIES PASS, NEW ZEALAND: A COMPARISON BETWEEN A WIND TUNNEL SIMULATION AND FIELD MEASUREMENTS.

A thesis presented for the Degree

of

Doctor of Philosophy in Mechanical Engineering

at the

University of Canterbury

Christchurch

New Zealand.

by

D. Neal. B.E.,N.Z.C.E.(Mech.).

University of Canterbury. **December, 1979.**

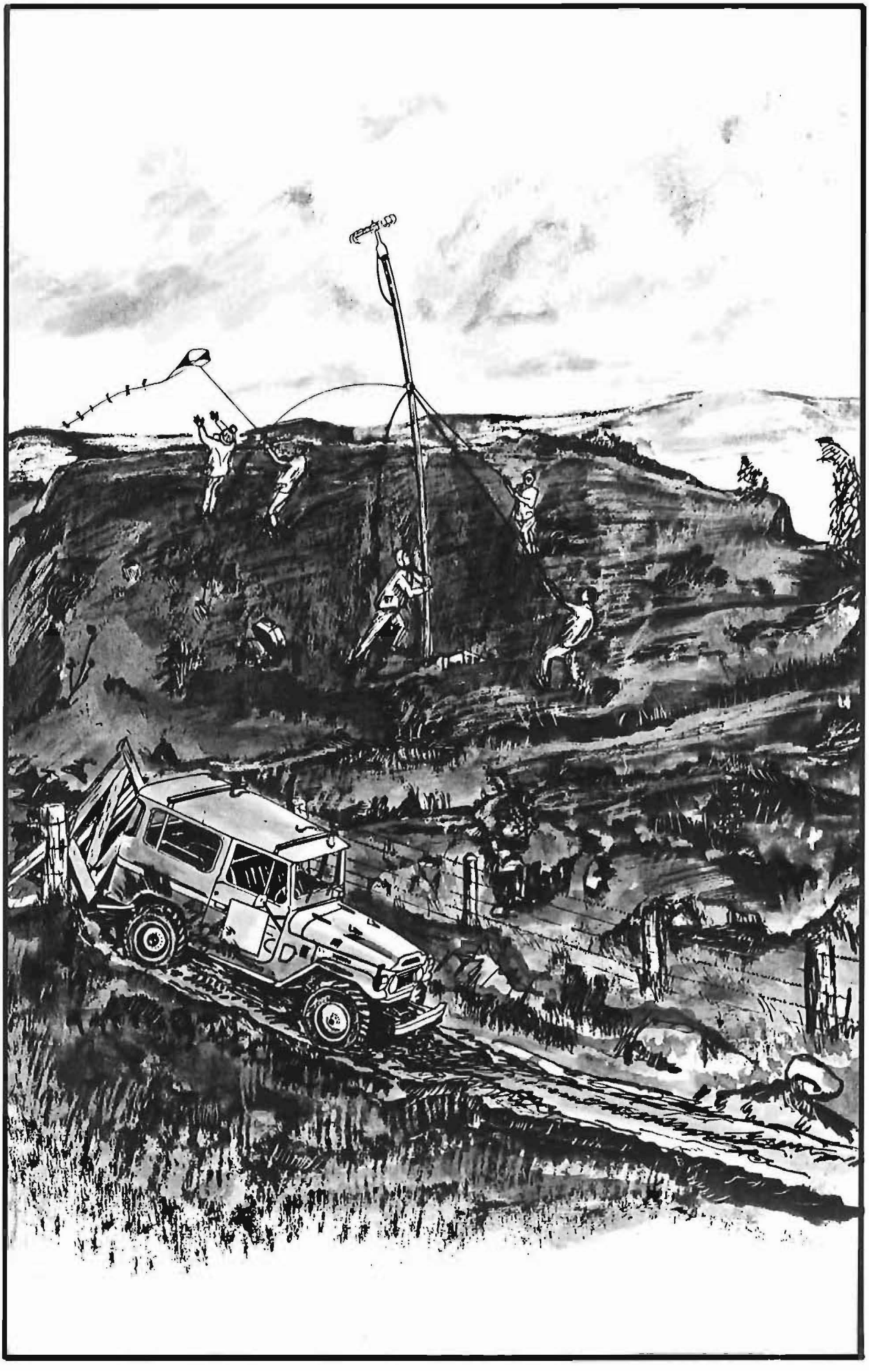

To my Mother,

in appreciation of her

interest in my future

ABSTRACT

This thesis presents the result of a study to show the validity of using wind tunnel modelling to predict the wind flow over a complex terrain situation.

A wind tunnel traversing system which is particularly suitable for flow measurements over topographical models, is described.

A 1:4000 undistorted geometric scale model of Gebbies Pass in the South Island of New Zealand was prepared. The required approach flow boundary layer was simulated in the boundary layer wind tunnel in the Department of Mechanical Engineering. This was confirmed by field measurements on the approach terrain with the Department's instrumented 20m tower and TALA kite equipment.

The model was tested in three forms of construction; terraced, contoured (terraces filled with Polyfiller), and with shelterbelts and scrub areas added. The results of the wind tunnel tests are presented in the form of isotach and isoturb contours for lateral and longitudinal cross sections through the models. The longitudinal component of the energy spectrum, autocorrelation function, $\rho\overline{uw}$ Reynolds stress profiles and integral length scales L_{u_x} were also measured. They are presented and compared, where possible, with measured and theoretical values.

The results for the various forms of construction are correlated and show that the terraced form of construction differs significantly from the other forms.

On six days when strong south-west wind events prevailed, teams of investigators surveyed field sites in the area, measuring wind speeds at a height of 10m. The results for this part of the field programme are presented and correlated with the results obtained from the models.

Detailed wind structure measurements of the velocity, turbulence intensity and $\rho\overline{uw}$ Reynolds stress profiles, autocorrelation function and the u, v and w components of the energy spectrum were made at two field sites up to a height of 20m. One site was on the level approach terrain to the region and the other was on top of the Gebbies Pass saddle. The results are presented and compared with the wind tunnel results and theoretical predictions, where possible, and show good agreement.

ACKNOWLEDGEMENTS

I would like to thank Professor D.C. Stevenson for his conscientious and enthusiastic supervision of this research. His time, effort and interest have been an invaluable source of encouragement. My thanks are also due to Dr D. Lindley, who initiated and guided the study at its inception. His encouragement and interest were greatly appreciated. I would also like to thank Dr A.J. Bowen for his useful comments, discussion and advice.

The extensive field data collection programme was assisted by the technical staff of the Department of Mechanical Engineering, and their efforts are greatly appreciated.

The care and skill of Miss J.M. Shelton in handling the photographic work and tracing the numerous diagrams is much appreciated. My thanks also go to Miss A. Scott and Mr T. Bird for their diligence and skill in the preparation of many of the diagrams.

My sincere thanks go also to Mrs P. Dowell for her enthusiasm and diligence in typing this thesis; and to Michele for her comments and help in spending hours proof reading.

I would also like to thank the workshop staff, directed by Mr E.D. Retallick, who assisted in the building of a new wind tunnel traversing system.

Finally, the co-operation and information offered by all the farmers in the Gebbies Pass region is gratefully acknowledged, and in particular, Mr M. Gebbie , who allowed the field equipment to be erected on his land.

LIST OF CONTENTS

LIST OF FIGURES

Photograph reference numbers given at bottom left-hand corner

LIST OF TABLES

LIST OF SYMBOLS

a	arbitrary constant
A_z	amplification factor defined as the mean wind speed at a height z above level ground divided by the reference mean wind speed which is measured at the same height above local ground level but in the undisturbed flow over flat ground, upstream of the hill
b	arbitrary constant
C	compression ratio
c	arbitrary constant
$C_{ii}(\tau)$	autocovariance function, $\overline{i(t).i(t+\tau)}$
d_a	characteristic dimension of prototype
d_m	characteristic dimension of model
$\frac{d_m}{d_a}$	linear scaling of an atmospheric boundary layer simulation
D	deformation ratio
e	fluctuating component of anemometer output voltage
E	eccentricity
E	linearised anemometer output voltage
f	$\frac{nz}{\bar{U}}$
f_m	$\left.\left(\frac{nz}{\bar{U}}\right)_p\right\}$ dimensionless spectral frequencies
G	gain of the DISA dual summing unit
G	Griggs-Putnam type deformation rating
k	$\frac{n}{\bar{U}}$, spectrum wave number
k_p	spectral peak wave number
k_{p_u}	spectral peak wave number of the u velocity component
k_{p_v}	spectral peak wave number of the v velocity component

k_{p_w}	spectral peak wave number of the w velocity component
k_3	hot wire anemometer calibration constant, relating the linearised anemometer voltage to the air velocity
k	surface drag coefficient
l	Prandtl mixing length
$L_{u_x} = x_{L_u}$	integral length scale of turbulence of streamwise velocity component in the streamwise direction
L_{v_x}	integral length scale of turbulence of the lateral velocity component in the streamwise direction
L_{w_x}	integral length scale of the turbulence of the vertical velocity component in the streamwise direction
L	scaling length in the model atmospheric spectra
n	frequency
n_p	spectral peak frequency
N	reel count for line out on TALA kite
p	subscript referring to a spectral peak value
r	sample correlation coefficient
s	sample standard deviation
s_x	sample standard deviation for the independent variable
s_y	sample standard deviation for the dependent variable
$s_{x/y}$	standard error of estimate
s_b	standard error of regression coefficient
$s_{ii(n)}$	power spectral density function
S	shape index
ΔS	fractional speedup ratio, the increase in wind speed at a given height to the undisturbed wind speed at the same displacement above the surface
t	time
T	time interval over which a record was obtained
T_E	Eulerian time scale of turbulence

$\bar{U},\bar{V},\bar{W}$ streamwise, lateral and vertical mean velocities respectively

u,v,w fluctuating component of streamwise, lateral and vertical velocity respectively

U,V,W instantaneous velocity in streamwise, lateral and vertical directions respectively

u',v',w' streamwise, lateral and vertical rms velocity fluctuations respectively

$\bar{U}_{\delta}$ mean streamwise velocity at $z = \delta$

$\bar{U}_{ref}$ mean flow velocity at a reference height in the wind tunnel

$\bar{U}_{\infty}$ mean streamwise velocity at $z = \delta$

$\bar{U}_z$, $\bar{u}_z$ mean velocity at a height z above the surface

u_* friction velocity, $\sqrt{\frac{\tau_o}{\rho}}$

x,y,z a system of rectangular cartesian coordinates with the x axis defined in the streamwise direction, the y axis in the lateral direction and the z axis in the vertical direction over a model hill the z distance is always measured above the hill surface

x_1 $\frac{nL}{\bar{U}_{10}}$ as in Harris spectrum

Z_p height above prototype

z height above model

Z_o roughness length

α exponent of the mean velocity profile power law

δ boundary layer thickness

ε eddy viscosity

λ actual roughness element height on model

κ von Karman constant

ν kinematic voscosity

ρ density of air

$\rho_{ii}(\tau)$ autocorrelation function

θ	angle of inclination of TALA kite
ϕ	cross-wire probe wire angle
σ_i	standard deviation of U, V or W velocity component
ψ	stream function
τ	shear stress
τ	incremental time lag
τ_o	surface shear stress

SUBSCRIPTS

a	full scale values from the atmosphere
i,j	refers to u, v or w velocity component
m	model values
o	reference quantity
p	spectral peak value
U,V,W	streamwise, lateral and vertical velocity components
z	height above ground

A bar (-) denotes a value averaged over time

Two vertical bars ($|\ |$) denote the absolute value of a quantity

CHAPTER 1

INTRODUCTION

1.1 GENERAL STATEMENT OF PROBLEM

New Zealand, like the rest of the world, faces the problem of increasing energy demands and costs. Also like many other countries, New Zealand would like to work towards energy self-sufficiency. An energy economy that is self-sufficient is likely to utilise a mix of several energy technologies. The technologies themselves will, of course, depend on the indigenous fossil and renewable resource base, as well as indigenous technological expertise. In New Zealand the energy conversion technologies that appear to have promise are:

1. Solar - for low grade heat and power.
2. Biomass - for liquid fuels and power.
3. Wind - for power and hydrogen production (by electrolysis).
4. Geothermal - for low grade heat and power.
5. Hydro-electricity - for power and hydrogen production.
6. Natural gas - for liquid fuels and heat.
7. Coal - for liquid fuels and heat.

The present work concerns itself with wind energy conversion.

The output of a windmill is, naturally, dependent on the wind régime at the site; the power available being proportional to the cube of the wind speed. Lindley, Isaacs, Tollerton, Studt, Bar and Lamb (1978) suggest that a 65m diameter machine, rated at 1 MW, would give an output of approximately 4.5×10^6 kWh/year at a site with an annual mean wind speed of 7.0 m/s. It is estimated that there are sufficient sites in New Zealand with annual mean windspeeds greater than 7.0 m/s to accommodate at least 5000 such machines. They also suggest that 450 of these machines would generate 7.2 PJ/year, (2000 GWh/year) or approximately 10% of the present annual electricity generation. In the final analysis, sites for such machines must be identified and measurements of the wind régime made in some detail prior to any decision to locate a Wind Energy Conversion System (WECS).

At the present time it is not possible to determine the wind régime of a particular site without making long term meteorological measurements. Small errors in the measurements or "estimation" of wind speed can produce large errors in the predicted amount of wind energy available. A further complicating factor is the large difference that occurs in the wind régime

AUTHOR	METHOD	SHAPE RAMP OR HILL	$\frac{h}{L}$	STABILITY	α	$\frac{z_o}{h}$	$\frac{u_o^*}{u_o(L)}$	MEASUREMENTS REPORTED p	u	u'	τ	w'	$E_u(k)$	$-C_{p_{max}}$	ΔS	S
[Δ]Field & Warden (1929-1930)	wind tunnel	Gibraltar	~1.10	N	~0	--	--			x		x		--	--	--
	field		~1.10	N						x		x		--	--	--
[Δ]Putnam (1948) (Pettersen, 1961)	field	Pond	1.27	--	.3	.05	--		x					--	--	0.84
		Glastenberg	--	--	.3	--	--		x					--	--	1.04
		Mt. Washington	.61	--	.3	.05	--		x					--	--	1.47
	wind tunnel	Pond	1.27	N	~0				x					--	--	1.29
		Glastenberg	--	N	~0				x					--	--	1.44
		Mt. Washington	.61	N	~0				x					--	--	1.30
Golding (1955)	field	Costa, Orkney U.K.	0.3-0.6	--	--	--	--		x					--	--	--
		Vestra Fiold, U.K.	0.2	--	--	--	--		x					--	--	--
Frenkiel (1961)	field	Mreiba Ridge, Israel	0.25	N,S	0.15	1.4×10^{-4}	--		x	x				--	--	--
		Givat Hamere Hill, Israel	~0.57	N,S	0.15	9×10^{-5}	--		x	x				--	--	--
[Δ]Halitsky et al. (1962-1963)	wind tunnel	Bear Mtn., NY	~0.46	N	--	--	--		x	x	x			--	--	--
Chang (1966)		→	1.0	N	.15		.036	x	x	x	x			.33	.27	1.0
Plate & Lin (1965)	wind tunnel		1.0	US*	.19	1.5×10^{-4}	.033		x		x			--	.24	1.15
			2.0	N	.15		.036	x	x	x	x			.33	.35	1.1
			0.5	N	.15		.036	x	x	x	x			.33	.35	1.0
		$\frac{1}{2}$ sine	0.8	N	.15	1.5×10^{-4}	.035	x	x	x	x		x	.55	.76	1.38
				US**	.19		.032		x		x			--	--	--
[Δ]Cermak & Peterka (1966)	wind tunnel	Pt. Arguello, CA	0.11	N	0.25	--	--		x					--	--	--
			0.11	S[ΔΔ]	0.25	--	--		x					--	>3.0	1.25
[Δ]Meroney & Cermak (1967)	wind tunnel	San Nicolas Is., CA	0.12	N	0.14	1.2×10^{-2}	.032		x	x		x		--	--	--
			0.12	S[ΔΔ]	0.20	--	--		x					--	--	--
Lin & Binder (1967)	wind tunnel		0.67	S					x					--	--	1.2
		$f(\frac{x}{L})$	1.33	S		Lee Waves			x					--	--	2.6
Garrison & Cermak (1968)	wind tunnel	San Bruno Mtn., CA	~0.43	S	0.16	2.5×10^{-3}	.125		x					--	0.5	1.07
[Δ]Hsi et al. (1968)	wind tunnel	Green River, UT	-.09	N	0.14	2×10^{-4}	--		x					--	--	1.14
[Δ]Beryland et al. (1968)	field		0.1	N	--	--	--		x					--	0.25	--
Zrajevsky, Doroshenko & Chepik (1968)	wind tunnel	"	"	N	~0	--	--		x					--	0.1	1.1
[Δ]Kitabayashi et al. (1971)	wind tunnel	Elk Mtn., WY	0.35	N	0.21	7×10^{-3}	0.149		x	x				--	0.37	1.04
				S***	0.32	--	--		x						0.29	1.29

TABLE 1·1 EXPERIMENTAL PROGRAMMES OF FLOW OVER HILLS, RIDGES AND ESCARPMENTS
(after Meroney et al 1976)

AUTHOR	METHOD	SHAPE RAMP OR HILL	$\frac{h}{L}$	STABILITY	α	$\frac{z_o}{h}$	$\frac{u_o^*}{u_o(L)}$	MEASUREMENTS REPORTED p	u	u'	τ	w'	$E_u(k)$	$-C_{p_{max}}$	ΔS	S
Ellseev (1971)	field	Razdan Valley, USSR	0.61	N	--				x					--	0.35	--
[Δ]Orgill & Cermak (1971)	wind tunnel	Climax, CO	.10	N	0.25	3.0×10^{-4}	--	x	x	x	x	x		--	1.86	1.18
			.10	S[ΔΔΔ]					x					--	0.67	1.00
			.10	N	0.57	--	--		x	x		x		--	1.20	0.75
de Bray (1973)	wind tunnel	20°	0.72	N	0.14	--	--		x					--	0.41	1.13
		sine	0.5	N	0.14	--	--		x					--	0.34	1.07
		source	--	N	0.14	--	--		x					--	0.30	1.04
				N	0.11	--	--									
Freeston (1974)	wind tunnel	20°	0.72	N	0.14	--	--	x	x					0.40	0.38	1.10
		40°	1.67	N	0.14	--	--	x	x					0.90	0.45	1.16
		60°	3.46	N	0.14	--	--	x	x					1.00	0.18	0.94
		sine	0.5	N	0.14	--	--	x	x					0.50	0.34	1.07
		source	--	N	0.14	--	--	x	x					0.40	0.30	1.04
[Δ]Bowen & Lindley (1974)	field	26°	0.98	N	0.1	5×10^{-5}	0.102		x					--	0.39	1.06
	New Zealand		∞	US	0.45	1×10^{-2}	--		x					--	1.13	1.16
	wind tunnel	26°	0.98	N	0.18	4×10^{-3}	0.160		x					--	0.40	1.12
			∞	N	0.18	5.3×10^{-3}	0.160		x					--	0.47	1.10
Meroney et al. (1976)	wind tunnel		1.0	N	0.14	9×10^{-5}	.032	x	x	x	x	x	x	0.25	0.71	1.07
			0.67	N	0.14	"	"	x	x	x				.26	0.79	1.15
			0.50	N	0.14	"	"	x	x	x				0.93	1.41	1.53
			0.33	N	0.14	"	"	x	x	x	x	x	x	0.77	1.11	1.35
			0.10	N	0.14	"	"	x	x	x	x	x	x	0.15	.40	0.90

$$C_{p_{max}} = \frac{\Delta p}{\frac{1}{2}\rho\, u_o(\delta)^2}\ ,\quad \Delta S = u(z)/u_o(z)\ ,\quad S = \frac{u(z)}{u_o(z+hf/L)}$$

*$Ri_{\delta h} = -.016$

**$Ri_{4h} = -.019$

***$Ri_{\delta} = 1.70$

[Δ]Field comparisons available

[ΔΔ]$Ri_{\delta} = 0.30$

[ΔΔΔ]$Ri_{h} = 6.0$

TABLE 1-1 (cont.) EXPERIMENTAL PROGRAMMES OF FLOW OVER HILLS, RIDGES AND ESCARPMENTS. (after Meroney et al 1976)

over small differences in the terrain; this effect is noted by Meroney, Bowen, Lindley and Pearse (1978). It is quite possible, therefore, for sites to be selected and measurements taken which are quite unrepresentative of the area as a whole. There remains, therefore, the perplexing problem of how to identify and accurately measure the resource at these sites without having to cover the country with a network of some hundreds, or possibly thousands, of anemometers.

Terrain features such as ridges, escarpments, bell-shaped hills, gorges and valleys can increase the windspeed, and thus the wind energy available, by a very significant amount. It has been shown by other researchers that hills and ridges can increase the local "ground-level" wind speed by up to 80-120%. Unfortunately much of the work done so far on this problem has been restricted to the flow over two-dimensional, triangular and sinusoidal cross section hills, escarpments and simple geometric shapes as given in Table 1.1, after Meroney, Sandborn, Bouwmeester and Rider (1976). Idealised physical models have been chosen for experiment so that the necessary boundary conditions could be satisfied by analytical models and so that by iteration between theory and experiment a better understanding of the flow mechanisms could be attained.

Unfortunately for the wind energy site prospector, however, these idealised experiments and flow models bear no resemblance to the complex terrain provided by nature. It is therefore extremely difficult, if not impossible, to apply existing experiments or theory to predict the wind régime at a site in complex terrain, much less to identify the best sites within that terrain.

Such prospectors as Golding (1949), Putnam (1948) and Prandtl (1932) had in the past, been left to synthesise meteorological records, local knowledge (power linesmen, lighthouse keepers, farmers, folklore etc) and his own experience, to identify promising wind energy sites. Such an approach can often be misleading. The Rakaia Gorge area of the Southern Alps of New Zealand had, for example, its own "folklore". An experiment that combined wind tunnel measurements with field measurements, conducted by Meroney *et al* (1978), indicated that the areas of highest windspeed were not those predicted by "folklore".

Unfortunately, it is often the most inaccessible regions that have the greatest potential for wind power.

Given that the available meteorological data for a country, or area of that country, suggests that high winds (> 7.0 m/s) exist, thus making wind energy conversion viable, there are several approaches that can be made to identify the best sites:

1. From satellite or aerial photography identify topographical or vegetation features that suggest high winds. (e.g., wind-swept trees, sand dune movements, blowholes, errosion patterns etc.).
2. Cover the area with wind velocity and direction recording instruments. (This could involve laser or other remote sensing of wind fields.)
3. Attempt a solution of the complex equations governing the flow over the terrain using meteorological data at the terrain boundaries as boundary conditions.
4. Conduct a wind tunnel survey of a scale model of the area concerned.
5. Synthesise local knowledge to identify areas of high winds.

Utilisation of the best sites could still be subject to problems such as land ownership, legal implications such as by-laws, or environmental objections such as the aesthetics of a WECS.

At present a solution to the WECS site selection problem is likely to be provided by a combination of the above techniques. Probably one of the most serious limitations for most of these methodologies is their expense. To place 1000 anemometers in the field at a cost of approximately $2000 per installation and to wait a year for data in the hope of finding 50 (or more) suitable sites, is somewhat unsatisfactory. Detailed wind structure analysis of these sites would also be required prior to installation of any WECS.

At the present time computer solutions to the equations governing flow over complex terrain are costly and still in a preliminary state of development. The development of these solutions is somewhat inhibited by the lack of experimental field data with which the computer model can be tested. Thus a requirement still exists for a method by which a 'mesoscale' area can be surveyed quickly and inexpensively to identify suitable sites for wind turbines. To some extent the problem is somewhat analogous to that of determining the wind régime in a city area like New York, or Wellington (New Zealand), where wind loads on new buildings need to be predicted at the design stage or the wind environment at street level determined. For many years such problems have been approached with success by using atmospheric boundary layer wind tunnels in which the physical situation is modelled.

The present work therefore, seeks to extend the work of Meroney *et al* (1978) in investigating the validity of using a wind tunnel modelling procedure to identify areas of high winds over complex terrain.

This tool, if proved valid, is likely to fit into an overall prospecting systems procedure in the following way:

1. Using aerial or satellite photography, local knowledge and existing meteorological data, identify mesoscale regions of the country which seem likely to have wind régimes with annual mean wind speeds greater than 7.0 m/s.
2. Complete wind tunnel model surveys of these mesoscale areas to identify in detail the high wind velocity sites within the area. Investigate turbulence structure at these sites so that detailed information of the wind structure is available to ensure compatability with wind turbine design.
3. Use this data in conjunction with numerical mesoscale models (if developed) to extrapolate tunnel data to sites where meteorological data is available; this can be used as a calibration. As confidence grows in the numerical models, it may be possible to eliminate the wind tunnel modelling stage altogether.
4. Install wind speed and direction recording equipment at the sites selected from 1 to 3 to collect longer term data which can be used to correlate with the results from 2 and 3, thus producing an iterative process which will generally enhance the understanding of wind flow analysis over complex terrain.

1.2 OBJECTIVES OF THE RESEARCH

The overall purpose of this research is to develop laboratory physical models as a tool for modelling the atmospheric planetary boundary layer over complex terrain as a means to predict Wind Energy Conversion Systems' performance on terrain enhanced sites. Wind tunnel studies which are combined with field measurements of the modelled area will contribute to the general understanding of flow over complex terrain in several ways.

i) Produce confidence (or otherwise) in model studies.
ii) Refine modelling techniques - model construction, surface finish, e.g. significance of adding surface roughness etc.
iii) Provide information unable to be obtained quickly in the field.
iv) Thermal effects will become evident.

However, it must be noted that this will not produce a general solution for complex terrain. The results of this study only apply to Gebbies Pass but as the number of such studies increase, the results will, to a greater extent, be generally applicable. One other limitation is that the wind tunnel measurements will be taken to the scaled gradient height but the field measurements, due to the limitation of the equipment, will only be taken to a height of 10m.

However, several sites will, with the aid of special equipment, be measured to 20m and others to 240m. Therefore, it is hoped that the flow in the bottom 10m produces a good correlation with the wind tunnel measurements, thus allowing confident prediction of the flow régime at heights greater than this. Using specialised equipment, tests will be made at several sites to greater heights to support or disclaim these predictions.

Architects and engineers encounter the same modelling problem when designing new buildings (particularly multi-storey) to be erected in a city. Their major problem is the lack of suitable information about the nature and structure of the wind within an urban canopy. This situation makes it very difficult to predict the wind velocities and forces to which the buildings will be subjected. If the city is situated in complex terrain, like Wellington in New Zealand, the problem is compounded by the terrain which can locally modify the wind to a significant degree.

One approach to this problem is to model the building in question; generally, buildings in close proximity are included since they can modify the local flow régime significantly, thus causing areas of exceptional turbulence or high velocity. An example of such a model and its prototype is given in Figs. 1.1 and 1.2 respectively, after Penwarden and Wise (1975). This type of analysis provides information about the building's wind loading and the wind environment around it, which have to be considered for the comfort and safety of the public. This approach is widely used throughout the world and will probably continue to be used for many years. However, with better understanding of the effects of complex terrain, whether in a city or on naturally complex terrain, this method can be developed as a more reliable tool for the design of buildings.

The use of building codes is another approach available to the designer; two such codes covering this topic are BSCP 3 (1972) and in New Zealand, NZS 4203 (1976). Major parameters such as basic wind speeds, design wind speeds, pressures and forces relevant to the building design can be calculated from these codes.

In the NZS 4203 (1976) building code, buildings are given one of three classifications. This classification, as given in Table 1.2, determines the return period for the maximum basic wind speed as given in Table 1.3 For areas not covered in Table 1.3, the value for the basic wind speed is interpolated from the map of New Zealand given in Fig.1.3. This value is then multiplied by a correction factor as given in Table 1.4. For mountainous areas, special study in consultation with the Meteorological

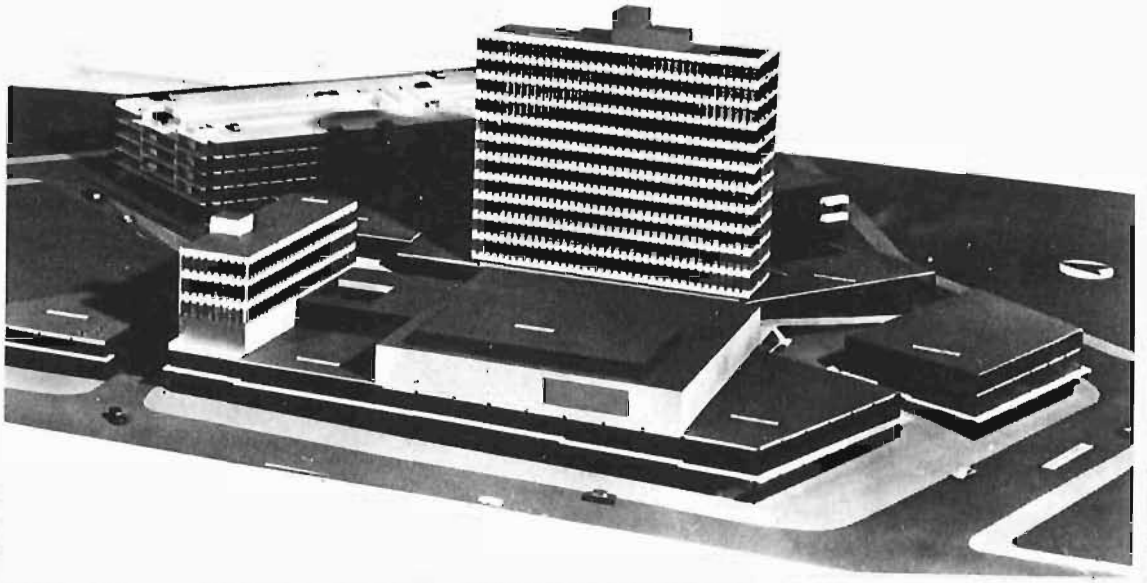

589/35

FIG 1·1 1/192 SCALE MODEL (AFTER PENWARDEN AND WISE 1975)

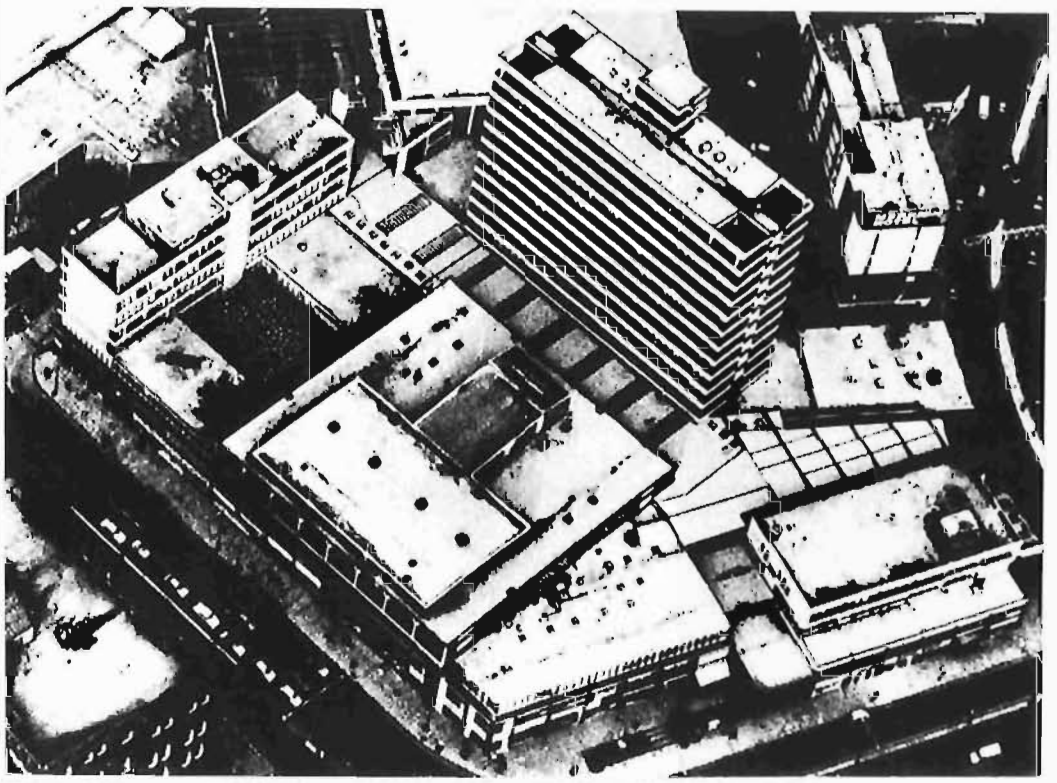

589/36

FIG 1·2 AERIAL VIEW OF THE PROTOTYPE. (AFTER PENWARDEN AND WISE 1975)

RETURN PERIOD

Nature of Building	Return Period (Years)
Structures used only during construction operations such as formwork and falsework	5
Buildings representing a low degree of hazard to life and property in the event of failure, such as isolated towers in wooded areas and farm buildings other than residential buildings or residential accessory buildings	25
All other buildings	50

TABLE 1.2: BUILDING CLASSIFICATIONS AND MAXIMUM BASIC WIND SPEED RETURN PERIODS

BASIC WIND SPEEDS FOR SOME CITIES AND TOWNS

City or Town	V (m/s) for return period of:		
	5 Years	25 Years	50 Years
Auckland	28	31	33
Blenheim	28	31	33
Christchurch	33	38	40
Dunedin	32	36	38
Gisborne	29	33	35
Hokitika	31	35	37
Invercargill	36	40	42
Kaitaia	36	44	48
Napier	31	35	37
Nelson	29	35	37
New Plymouth	34	39	41
Palmerston North	31	35	36
Rotorua	28	32	34
Tauranga	27	30	32
Timaru	31	37	39
Wanganui	36	43	46
Wellington	40	47	50
Westport	30	34	36
Whangarei	32	41	44

TABLE 1.3: BASIC WIND SPEEDS FOR SOME CITIES AND TOWNS IN NEW ZEALAND

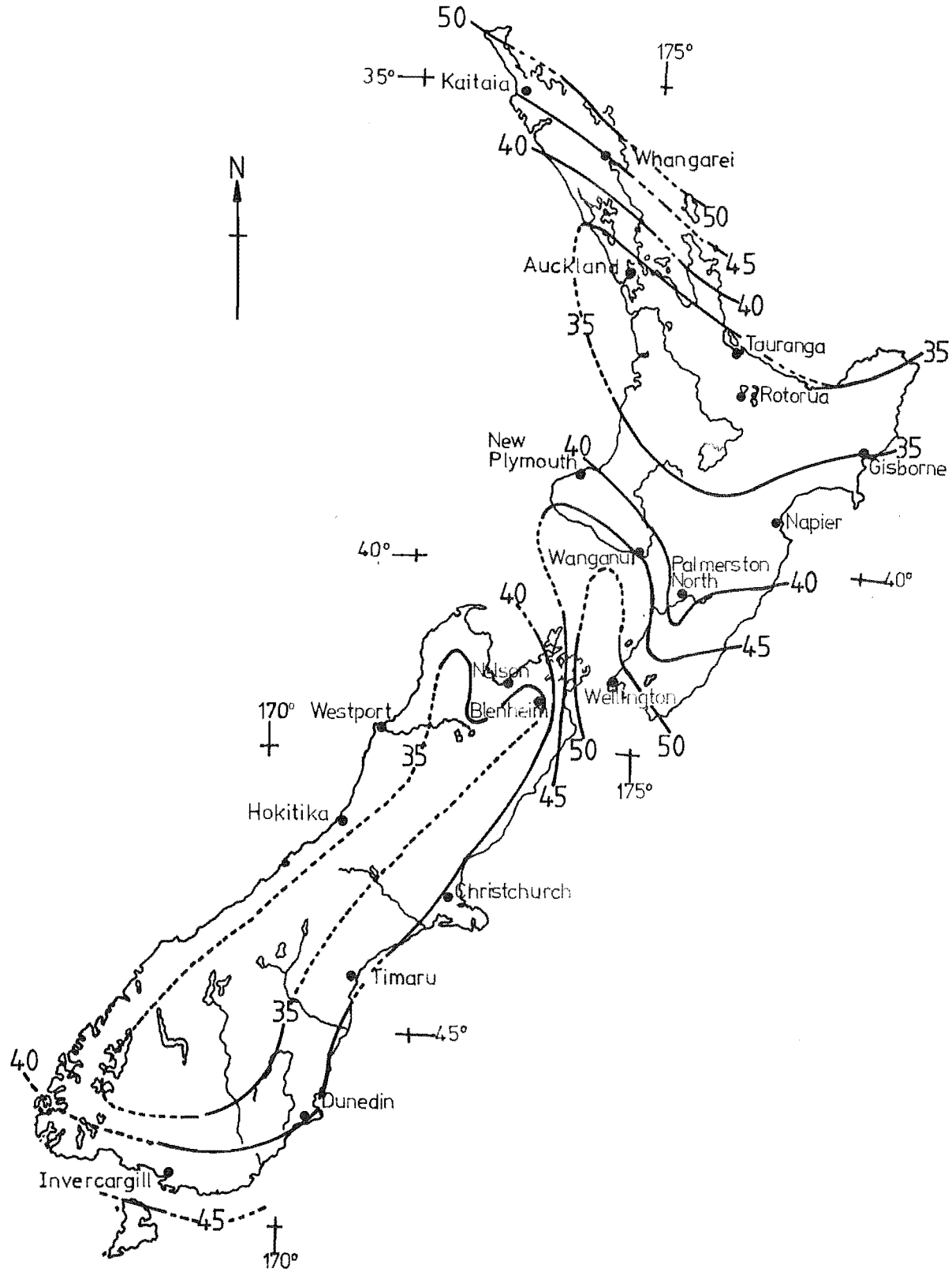

FIG. 1.3 BASIC WIND SPEED CONTOURS (m/s)

(These are maximum 3 second gust speeds with return period of 50 years.)

Service is recommended. A topography factor, s_1, is determined from Table 1.5 and a ground roughness, building size and height above ground factor, s_2, is determined from Table 1.6. Having obtained these factors, the design wind speed is calculated from the formula

$$V_s = v \times s_1 \times s_2$$

where s_1 = topography factor

s_2 = ground roughness, building size and height above ground factor

v = basic wind speed

v_s = design wind speed.

The design wind speed is the one used in all calculations relevant to the building design. This code is typical of other national building codes and highlights the uncertainty and lack of information and guidance that is available where complex terrain is a factor.

Generally the designer does not use one approach but will use a combination of building codes and modelling tests to achieve a safe and environmentally acceptable building.

It is hoped that this research will enhance the understanding of the effect complex terrain has on the structure of the wind. This information will be of great assistance to engineers involved in the design of buildings situated on complex terrain, or in the design of wind turbines which could be sited in areas where wind velocities undergo terrain enhancement, e.g. valleys, ridges etc.

1.3 PROCEDURES FOR COMPLETING OBJECTIVES

An area of complex terrain which involved wind flow over a pass was selected. A 1:4000 scale model of the Gebbies Pass area in the South Island of New Zealand was built.

To facilitate accurate measurements over the model in the wind tunnel, a new traversing system was designed and commissioned. Measurements of velocity profiles, turbulence profiles, auto-correlation coefficients and energy spectra were made at pre-selected sites.

A 20m fully instrumented tower was used to measure velocity profiles, turbulence profiles, energy spectra and auto-correlations in the field on level terrain upwind of the region to be investigated so that these conditions could be simulated correctly in the wind tunnel for the modelling phase of the work.

The region being investigated was divided into three separate models

Location	Correction Factor
(a) For locations listed in Table 1.3. As given by Table 1.3 for the appropriate return period:	N/A
(b) For other locations except mountainous areas: The wind speed given by interpolation from Fig. 6 multiplied by:	
Return period 50 years, all locations:	1.0
Return period 25 years. all locations:	0.94
Return period 5 years:	
Locations in North Auckland north or Warkworth:	0.76
All other locations:	0.82
(c) For mountainous areas: As determined by a special study in consultation with the Meteorological Service.	N/A

TABLE 1.4: CORRECTION FACTORS FOR BASIC WIND SPEEDS

Topography	S_1
Valleys and gorges shaped to produce funnelling of the wind; exposed hillsides, peaks and ridges where acceleration of the wind is known to occur; especially abnormal sites.	1.1 to 1.2 or higher
All other	1.0

TABLE 1.5: TOPOGRAPHY FACTORS

Height above Ground (m)	Ground roughness								
	1			2			3		
	Building class			Building class			Building class		
	A	B	C	A	B	C	A	B	C
3 or less	0.83	0.07	0.73	0.72	0.67	0.63	0.64	0.60	0.55
5	0.88	0.83	0.78	0.79	0.74	0.70	0.70	0.65	0.60
10	1.00	0.95	0.90	0.93	0.88	0.83	0.78	0.74	0.69
15	1.03	0.99	0.94	1.00	0.95	0.91	0.88	0.83	0.78
20	1.06	1.01	0.96	1.03	0.98	0.94	0.95	0.90	0.85
30	1.09	1.05	1.00	1.07	0.03	1.98	0.10	0.97	0.92
40	1.12	1.08	1.03	1.10	1.06	1.01	1.05	1.01	0.96
50	1.14	1.10	1.06	1.12	1.08	1.04	1.08	1.04	1.00
60	1.15	1.12	1.08	1.14	1.10	1.06	1.10	1.06	1.02
80	1.18	1.15	1.11	1.17	1.13	1.09	1.13	1.10	1.06
100	1.20	1.17	1.13	1.19	1.16	1.12	1.16	1.12	1.09
120	1.22	1.19	1.15	1.21	1.18	1.14	1.18	1.15	1.11
140	1.24	1.20	1.17	1.22	1.19	1.16	1.20	1.17	1.13
160	1.25	1.22	1.19	1.24	1.21	1.18	1.21	1.18	1.15
180	1.26	1.23	1.20	1.25	1.22	1.19	1.23	1.20	1.17
200	1.27	1.24	1.21	1.26	1.24	1.21	1.24	1.21	1.18

Definition of Terms:

GROUND ROUGHNESS 1: Open fetches of level or nearly level country with no shelter. Examples are flat coastal fringes, airfields, and swamps.

GROUND ROUGHNESS 2: Flat or undulating country with obstructions such as hedges or walls around fields, scattered windbreaks, and occasional buildings. Examples are wasteland and most agricultural land that is not well wooded.

GROUND ROUGHNESS 3: Surfaces covered with numerous large obstructions. Examples are well wooded farmland and forest areas, towns and cities.

BUILDING SIZE: The building size class shall be whichever of the following applies to the building (or part of a building) under consideration:

CLASS A: All units of cladding, glazing and roofing and their immediate fixings; individual members of unclad structures.

CLASS B: All buildings for which neither the greatest horizontal nor the greatest vertical dimension exceeds 50m.

CLASS C All buildings for which either the greatest horizontal or the greatest vertical dimension (or both) exceeds 50m.

TABLE 1.6: GROUND ROUGHNESS, BUILDING SIZE AND HEIGHT ABOVE GROUND FACTOR S_2

which were analysed for their predominant wind directions. The tests were carried out with the models in different states of construction; these being terraced, contoured and with roughness added.

The field phase of the research involved four major areas:

1. Use of Tethered Aerodynamically Lifting Anemometer (TALA) kites to obtain wind velocity profiles up to 300m.
2. Use of data loggers to record mean wind speeds over longer periods (18 months).
3. The use of a 20m portable, fully instrumented tower to give detailed analysis of the wind structure at selected sites.
4. One day duration field measuring trips were used. These involved the use of 10m portable towers which were instrumented with a 3-cup Rimco anemometer. Teams then covered the area of interest in a period of 5-6 hours, taking measurements of the mean wind speed. Details of this procedure are given later in Chapter 6.

1.4 ORGANISATION OF THIS THESIS

Chapter 2 presents a review of the literature related to modelling of atmospheric boundary layers. It divides the literature into conventional analysis methods and unconventional analysis methods, the latter being a more novel approach to the determination of high wind velocity areas.

The geology, meteorology and micro-meteorology of the Gebbies Pass region of New Zealand are discussed in Chapter 3. The assumptions, equations and similitude parameters which govern the air flow over complex terrain are established in Chapter 4 by examining and reducing the basic equations governing the atmosphere in the planetary boundary layer.

The equipment used and procedures followed during the laboratory work are described in Chapter 5. This also includes the design and commissioning of a new wind tunnel traversing system.

Chapter 6 presents the area studied and describes the equipment used and procedures followed during the collection of the field data.

Chapters 7, 8 and 9 present the results of the wind tunnel tests over models A, B and C respectively. These Chapters present some preliminary correlations for the results with the models in the various states of construction. Chapter 9 also contains the conclusions for the wind tunnel

measurement programme.

The various types of field data collected during the research programme are presented in Chapter 10.

A statistical analysis of the field and wind tunnel data is presented in Chapter 11. The analysis includes correlations, prediction of field results from the model, and null hypothesis tests. Chapter 12 presents the summary of conclusions and recommendations for further work.

CHAPTER 2

REVIEW OF LITERATURE

2.1 CONVENTIONAL ANALYSIS METHODS

The author defines conventional wind analysis methods as being those which involve either measuring the wind in the field or simulating the wind either physically in a wind tunnel or numerically with the aid of a computer. This is the type of approach that has generally been adopted to date; however, there are methodologies that investigate the effects of the wind rather than the wind itself. These have been classified by the author as unconventional analysis techniques and will be discussed in Section 2.2.

2.1.1 Early Studies

A preliminary report by E.W. Golding (1949) was presented to outline the direction of research being initiated by the Electrical Research Association (ERA). A wind power generating committee was set up in January 1948, the terms of reference for this Committee being:

"To study the technical and economic problems of large scale areodynamic generation in Great Britain; including the collection of all available information and evidence, the principles of the selection of sites and the wind energy derivable therefrom, the co-ordination of wind-driven generators and the design problems which remain to be solved."

The inital study was split into two sections to be worked concurrently, these being:

1) Wind régimes and site selection.
2) Economics, types of aerogenerators, and their design details.

The approach adopted was similar to that used earlier by Putnam (1948), involving the use of meteorological office data to selected likely windy sites. Putnam suggested that smooth hills were ideal for producing speed-up ratios of 1.2 or greater. Using this approach, Golding analysed maps of regions, in particular the Orkney Islands, to locate sites which fitted this requirement.

To record data of wind speed and direction, the ERA developed its own

recording apparatus which was used in conjunction with cup anemometers on towers at heights of 3m and 10m.

Juul (1949) was also working on wind power generation but he, like the Russian researchers of the time, was applying his effort to the design and production of aerogenerators. Their approach appeared to be orientated towards siting the turbines in known windy sites, probably based on local knowlege, without the back-up of extensive field surveys. From this paper it was not clear what their policy was on field data collection or consideration of the effects of terrain on the flow.

One of the most notable pieces of research of this time was by Golding and Stodhart (1952). In this report they outlined the need for detailed surveys of sites before contemplation of aerogenerator erection. They realised that although a hill can have a large speed-up effect on the flow, it could be that too much emphasis was being placed on this point and not enough on the prevailing wind direction. They also mentioned features which were later to be developed into a methodology in itself, later known as Eolian geomorphology. This topic will be discussed in more detail in Section 2.2.1.

One of the most significant points to emerge from this study was the development of a methodology for analysis of areas for wind power generation. This involved analysis of meteorological records to find potential regions followed by detailed studies of maps to locate topographical features suitable to produce high wind speeds. Some of the features considered at this stage were hills, passes, valleys, saddles and conical hills with close proximity to each other. After this stage, some emphasis was placed on personal inspection of selected areas, and as was pointed out, there are many detailed items not shown on maps such as new buildings, slips, planted forests or scrub, that can produce significant localised effects.

The methodology used today is not greatly different from this, the major addition to this probably being aerial photography and mesoscale numerical modelling.

Golding and Stodhart also suggested the use of laboratory tests to model flow over topography. This may have been one of the first moves to use wind tunnel techniques to predict flow patterns over complex topography for wind power generation.

The one feature that is common to all of the ERA research outlined here is that the researchers were basically looking at mean wind velocities, annual and seasonal variations, and potential output from an aerogenerator.

Wax (1956) carried out some important research when he investigated the structure of the wind using field data. In particular, he investigated gusts, their size and effect, and this was to have far-reaching effects on the design of structures, particularly aerogenerators.

Much of the theoretical analysis of the structure of the atmosphere boundary layer, particularly the generation and characteristics of turbulence, had previously been covered by Richardson (1920), Prandtl (1932), Bjerkness, V., Bjerkness, J., Solbert, Bergeron (1933) and others.

Similar work was carried out experimentally to varying degrees by Taylor (1927), Sutton (1949), Sheppard (1951) and others.

The earlier wind power generation studies can be compared with some of the more recent work of which a good deal has been funded by the United States Energy Research and Development Administration (ERDA).

2.1.2 Energy Research and Development Administration Programme

The Energy Research and Development Administration (ERDA) controls a very large programme investigating wind power generation and related areas of research. The general objective of the ERDA programme is ...."advance the technology and accelerate the development and utilisation of reliable and economically viable wind energy systems". ERDA's organisation of this research is shown in Fig. 2.1.

One specific element of the ERDA programme is the investigation of innovative wind energy concepts which might provide a significant reduction in energy cost compared with more conventional wind energy systems.

Several of the research programmes in Fig.2.1 will be expanded in this section including large horizontal axis systems and vertical axis systems. Less conventional methodologies such as Eolian geomorphology and biological analysis methods will be given in Sections 2.2.1 and 2.2.2 respectively.

Large Horizontal Axis Turbines

NASA Lewis Research Center (LeRC) has the ERDA contract for developing horizontal axis turbine technology in America. They were contracted by ERDA to design, build and test a 100 kW wind turbine at the NASA Plum Brook Station near Sundusky, Ohio. The purpose of this wind turbine was to provide early operations and performance data of a large wind turbine, in various

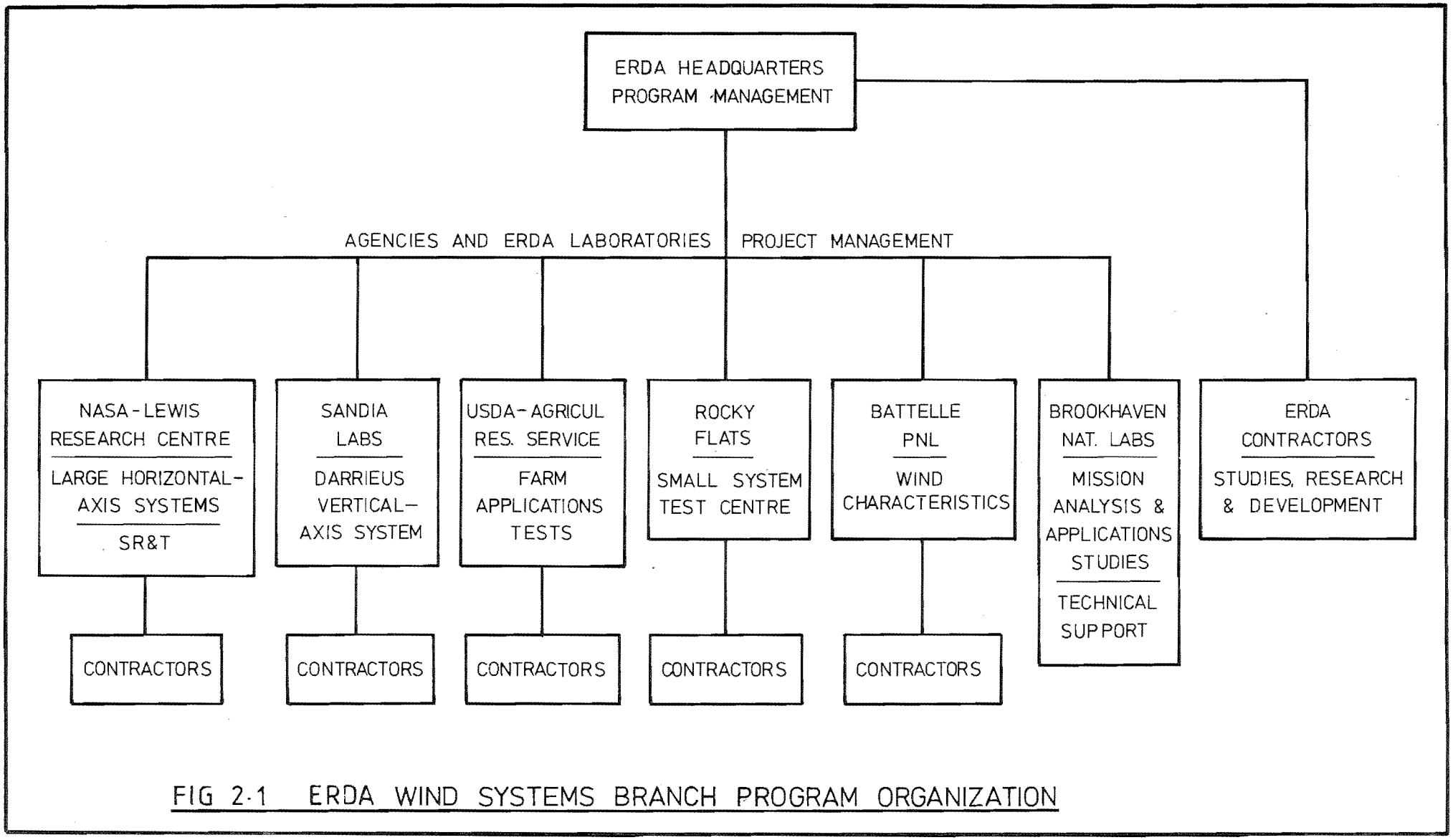

FIG 2·1 ERDA WIND SYSTEMS BRANCH PROGRAM ORGANIZATION

configurations, to aid in the design of follow-on large wind turbines. The MOD-0, 100 kW turbine shown in Fig.2.2 was designed, built and assembled in eighteen months and became operational in September 1975.

A series of these turbines have been or are being designed and will culminate in a multi-megawatt turbine. The series envisaged at this stage 1976, was

MOD - 0 (100 kW)
MOD - 0A (200 kW)
MOD - 1 (1.5 MW)
MO2 - 2 (2.5 MW).

Fig.2.3 gives a perspective of the sizes involved with these proposals.

Vertical Axis Systems

The current effort at Sandia Laboratories has been directed towards the design and fabrication of a 17m diameter, 60 kW rated Darrieus turbine, and is again funded by ERDA.

A larger 24m diameter, 200 kW rated turbine has been constructed by the National Research Council of Canada (NCR) on Magdalen Island in the Gulf of St Lawrence.

The 17m Darrieus was chosen because it represented a reasonable extrapolation from the technology available from a number of 5m turbine designs and thus was not expected to be a high risk design.

The objectives of this research are to develop the Darrieus wind turbine in three major areas:

1) Collection of performance data by continued operation of the prototype 5m Darrieus system in phase with the local utility.
2) Fabrication and testing of the 17m unit.
3) Performance of system trade-off studies to allow performance and cost optimization of the Darrieus.

It is hoped that the results of this research will give a firm engineering and economic data base for the Darrieus concept and allow assessment of its potential as an alternative to conventional systems.

2.1.3 Mesoscale Modelling

The three modelling scales to be considered for wind tunnel modelling are:

52412

FIG 2·2 ERDA / NASA MOD-0 WIND TURBINE

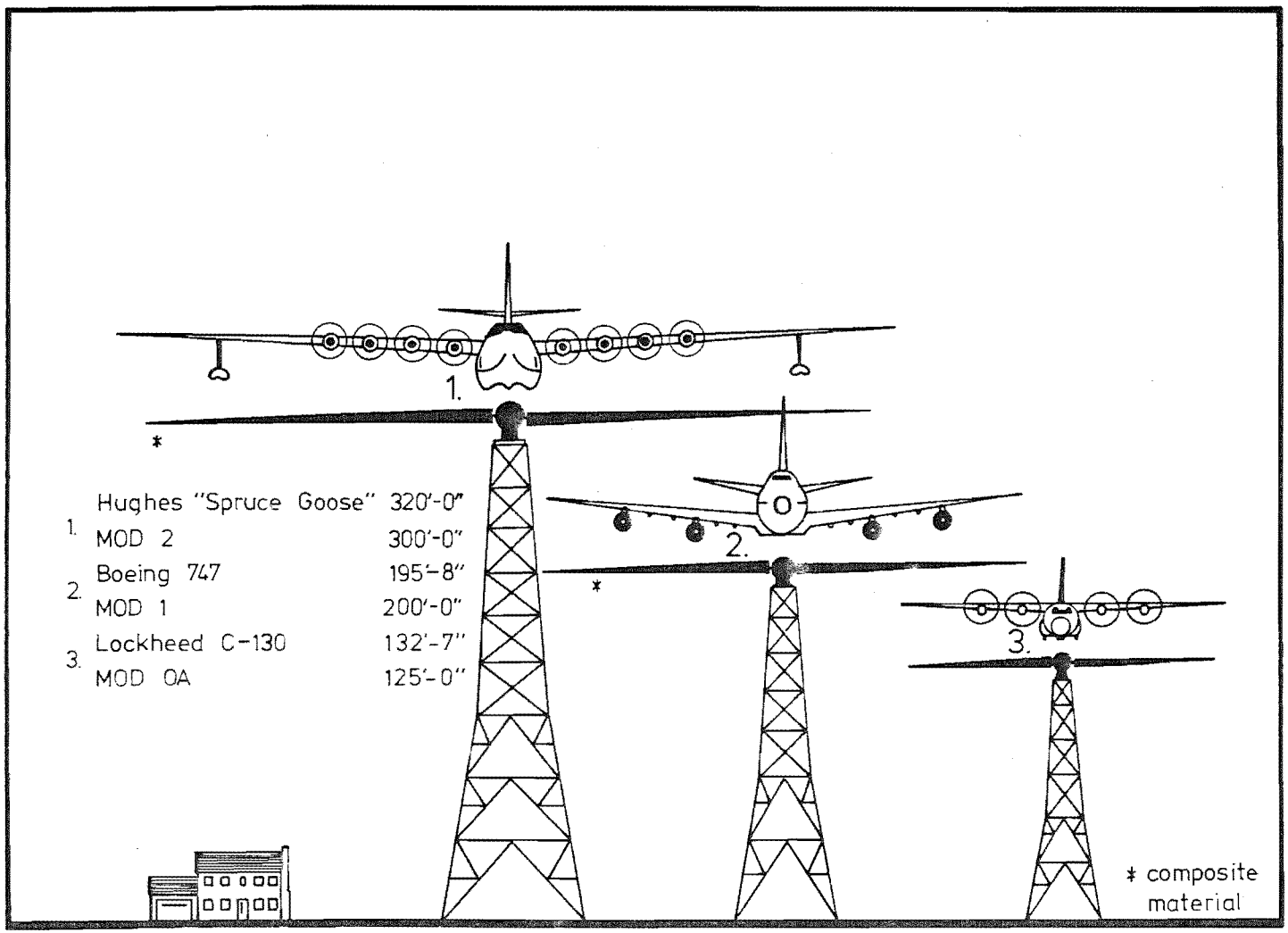

FIG. 2·3 WIND TURBINE SIZE COMPARISON

i) Mesoscale - blocking and channelling of mountain ranges are taken into account.

ii) Toposcale - this is smaller than mesoscale and its compatible with individual mountains and valleys within a mountain range.

iii) Microscale - this is at the level of individual windmill sites in complex terrain.

The description of Mesoscale modelling given above is a general one and can be further sub-divided as shown by Orlanski (1975), his interpretation being shown in Table 2.1. Based on this, the research to be undertaken for the Gebbies Pass region would be classified as Mesoscale (γ) type modelling.

Changery (1975) suggests that there are several areas that require immediate in-depth investigations, two of these being:

a) The need for two and three dimensional numerical modelling techniques which can be realistically modified to achieve the programme's objectives.

b) Wind tunnel modelling techniques and results for flow over mountains and isolated hills in flat terrain.

Research programmes are being conducted at several institutions, including Colorado State University, U.S.A. and Canterbury University, New Zealand. These involve the wind tunnel modelling and analysis for flows over symmetrical hills and complex terrain. If the methodology proves to be suitable for predicting the flow, a great deal of time and expense can be saved in the location of WECS and the development of a suitable building code for these areas will be possible.

2.1.4 Meteorological Statistics

The British Meteorological Office was established as a department of the Board of Trade in 1854 and began issuing daily weather reports with gale warnings for shipping in 1860. A similar system has operated from Paris since 1863 and the latter half of the century saw the gradual extension of the initially small network of stations. A classification of stations, based on the schedules of observations taken, was agreed upon at the International Congress of Meteorologists in Vienna in 1873 and by the end of the century, a world-wide network was in existence.

Many countries have extensive long-term meteorological data, much of which is recorded in populated areas. This is convenient for recording but not necessarily for the determination of WECS sites, remembering of course, that this was not the intention at that time.

m Hs	Km² As		Ts	MONTH	DAY	HOUR	MINUTE	SECOND
		macroscale α	global mountain area	Subtropical, it streams global wind patterns long wave ridges and troughs				
	10^8	macroscale β	continental mountain area	monsoons	storm tracks cyclones & anticyclones			
	10^6	(synoptic) mesoscale α	regional mountain area		airmasses fronts cyclogenesis			
3000	10^4	mesoscale β	mountain - valley (plain) basin island		thermo-tidal winds lee waves slope-valley wind valley plain wind channelling wake effects			
	10^2	mesoscale γ	hills ridges gorge canyon		blocking airflow speedup wake effects channelling canyon wind			
300	1	microscale α	cliffs mesas terraces gaps			airflow separations & wakes channelling		
200	10^{-2}	microscale β	cliffs, large roughness roughness trees			airflow separation vertical wind profiles turbulence		
30	10^{-4}	microscale γ	trees vegetation small roughness			vertical wind profiles	turbulence	
		Orlanski classification	general landform or roughness	climatological scale	synoptic and planetary scale	meso scale	microscale	

TABLE 2·1 A CLASSIFICATION OF THE EFFECTS OF TERRAIN ON ATMOSPHERIC MOTIONS, AFTER ORLANSKI.

A robust and accurate instrument for measuring wind velocity was required, and as early as 1846, Ramsey Robinson had developed a reliable cup-type anemometer. The most commonly used cup anemometers today are the three or four cup types, three cups being preferred in more recent times due to their superior characteristics of linearity with wind speed. Gill (1966) describes the theory and development of wind measuring systems and makes comparisons between the performance characteristics of the various systems available.

The New Zealand Meteorological Service uses either the Hall Effect switch type or the permanent magnet generator type of anemometer, which are particula: robust instruments, well suited for the job they perform.

The cup anemometer does have one restriction with regard to accurate recording, and that is the effect of pitch angle of the approaching flow. If this angle is approximately > ±10°, incorrect velocity readings of 2-4% can easily occur, and this effect can be influenced very strongly by the siting of the anemometer.

The New Zealand Meteorological network, which follows the practice of recording at areas of population settlement, is shown in Figs 2.4 and 2.5. Table 2.2 gives heights, recording history and record collection frequency, and these factors are important when the data is being analysed. If they are not taken into account, they can lead to false indications of wind energy flux (WEF) available, wind speeds, and wind speed frequency distributions. Research is continuing in New Zealand, under the guidance of the New Zealand Wind Energy Task Force, to investigate the wind energy available for power generation. The progress of this research is reported by Cherry (1976), who outlines the factors to be analaysed and the theory used for analysis.

Hennessey (1977) considers some of the problems associated with wind power statistics and describes the relationship between mean wind speed and the mean of the cube of the wind speed, which leads to the formulation of a Weibull model for the distribution of the cube of the wind speed.

New Zealand is not the only country using this approach for WECS site location. Reed (1974) shows in Fig. 2.6 the annual average wind energy flux distribution over the United States of America and the seasonal variation of wind energy flux (WEF) is shown in Fig. 2.7 for several locations within the U.S.A. Ward, Kadivar and Broughton (1974) have produced similar information for Southern Quebec, shown in Fig. 2.8.

2.1.5 Field Studies

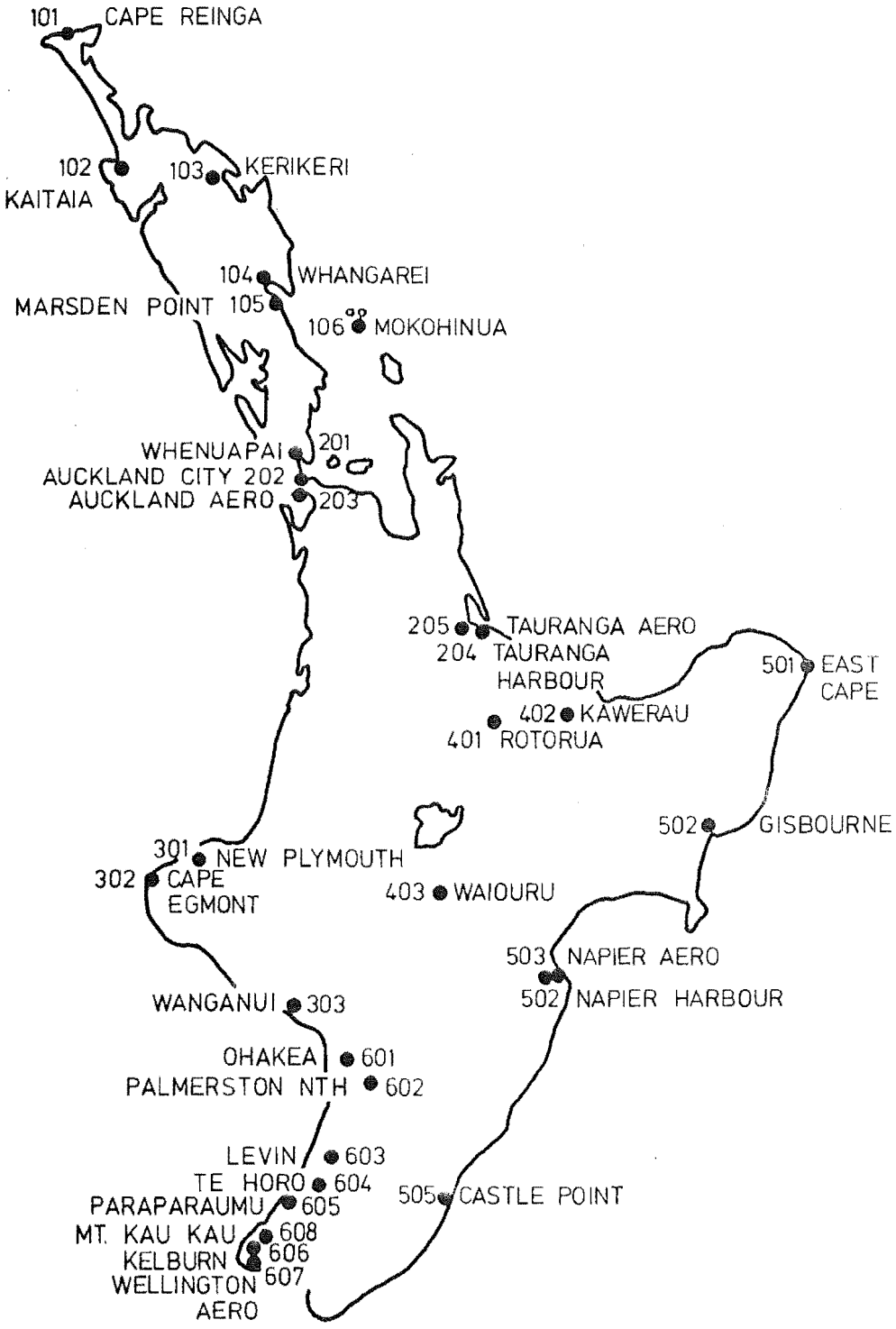

FIG. 2·4 THE NEW ZEALAND METEOROLOGICAL SERVICE ANEMOGRAPH NETWORK, WITH THE PROJECT STATION IDENTIFICATION NUMBERS, FOR THE NORTH ISLAND.
(After Cherry)

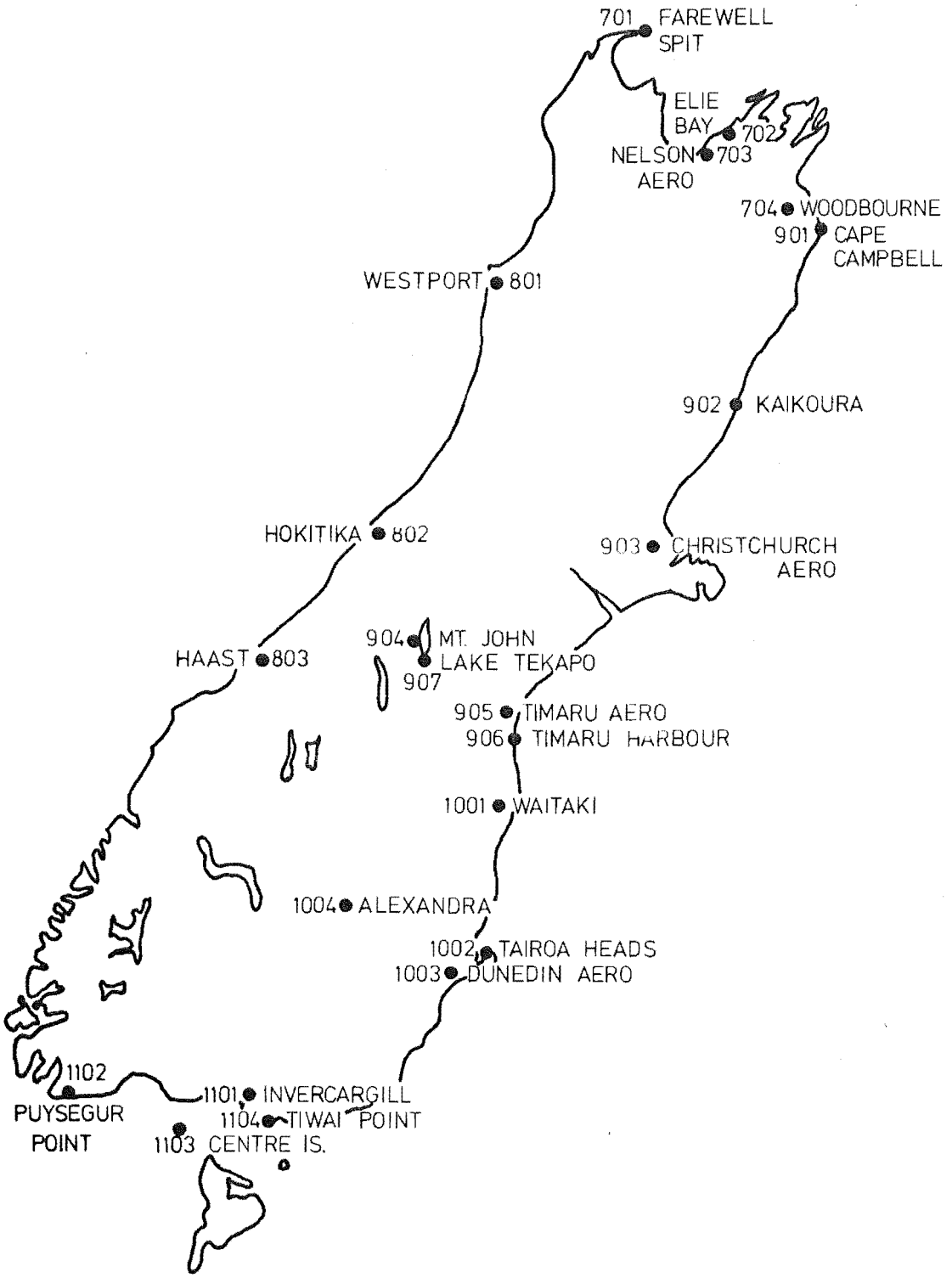

FIG. 2·5 THE NEW ZEALAND METEOROLOGICAL SERVICE ANEMOGRAPH NETWORK, WITH THE PROJECT STATION IDENTIFICATION NUMBERS, FOR THE SOUTH ISLAND.
(After Cherry)

Site	Location	H_s(m)	H(m)	Yrs	Period	Data Type
101	Cape Reinga	109.9	10.0	13	4/61–	6-hourly
102	Kaitaia Aero	80.3	10.0	12	2/62–	all
103	Kerikeri	149.0	10.3	2	8/64-7/66	all
104	Whangarei Aero	36.5	10.6	5	8/58-7/63	all
105	Marsden Point	3.0	10.0	5	1/64-8/73	all
106	Mokohunau	102.0	23.0	13	4/61–	6-hourly
201	Whenuapai	25.8	10.6	14	1/60–	all
202	Auckland City	44.4	31.3	12	2/62–	all
203	Auckland Aero	7.6	10.0	8	11/65–	all
204	Tauranga Harbour	3.0	27.4	10	7/67–	00
205	Taurange Aero	4.0	10.0	13	7/67–	06. 12. 18.
301	New Plymouth Aero	27.4	10.0	5	6/68–	all
302	Cape Egmont	8.2	10.0	3	6/70–	all
303	Wanganui	8.5	12.8	5	1/65-12/69	daylight
401	Rotorua Aero	285.8	10.0	10	4/64	all
402	Kawerau			9	1/62-12/70	03. 06. 09. 12. 15
403	Waiouru	831.0	10.0	5	12/69-9/74	all
501	East Cape	17.0	10.0	13	4/61–	06. 18.
502	Gisborne Aero	4.0	18.2	12	2/62–	all
503	Napier Aero	1.8	10.0	12	4/61–	06. 12. 18.
504	Napier Harbour	4.6	10.0	13	4/61–	00
505	Castle Point	30.4	10.0	9	1/62-12/70	06. 09. 12. 18. 21.
601	Ohakea	47.1	17.0	14	1/60–	all
602	Palmerston North	34.7	10.0	5	1/65-12/69	07. 23.
603	Levin Res, Centre	45.6	13.1	6	1/68-9/73	all
604	Te Horo	4.6	10.0	3	1/71–	all
605	Paraparaumum Aero	11.5	12.8	12	2/62–	all
606	Kelburn	124.6	21.3	12	2/62–	all
607	Wellington Aero	6.1	14.3	14	1/60–	all
608	Mt Kau Kau	443.5	121.6	6	1/69-2/75	all
701	Farewell Spit	3.6	6.1	13	4/61	6-hourly
702	Elie Bay	10.0	6.1	1	2/73-2/74	all
703	Nelson Aero	1.5	14.3	12	2/62–	all
704	Woodborne Aero	26.4	28.3	5	1/46-12/50	all
801	Wesport	1.8	12.8	13	4/61–	6-hourly
802	Hokitika	38.6	10.0	10	11/63–	all
803	Haast Aero	10.0	10.0	13	4/61–	06. 12. 18.
901	Cape Campbell	1.5	6.1	13	4/61–	06. 12. 18.
902	Kaikoura	99.1	6.7	10	1/60–	all
903	Christchurch Aero	30.1	14.0	14	1/60–	all
904	Mt John	1023.6	5.5	5	5/67-12/71	all
905	Timaru Aero	22.8	10.0	5	1/58-12/62	all
906	Timaru Harbour	16.0	14.0	3	3/71–	
907	Lake Tekapo			5	5/69–	00. 03. 06. 12. 18.
1001	Waitaki Aero	30.1	6.1	6	2/60-1/66	07.–18 incl.
1002	Tairoa Heads	75.4	15.2	13	4/61–	6-hourly
1003	Dunedin Aero	1.3	10.0	11	11/62–	all
1004	Alexandra Aero	228.0	9.1	2	4/48-3/50	all
1101	Invercargill Aero	0.3	9.1	14	1/60–	all
1102	Puysegur Point	43.0	6.0	13	4/61–	6-hourly
1103	Centre Island	70.0	6.0	5	5/68-4/73	06. 09. 12. 18.
1104	Tiwai Point	4.0	14.0	4	2/71-3/75	all
1201	Chatham Island	57.0	10.0	10	4/61-2/71	6-hourly
1202	Chatham Island Radio Station	80.0	12.0	6	2/67-12/72	00. 06.

TABLE 2·2 STATIONS OF THE NEW ZEALAND METEOROLOGICAL SERVICE ANEMOGRAPH NETWORK (after Cherry)

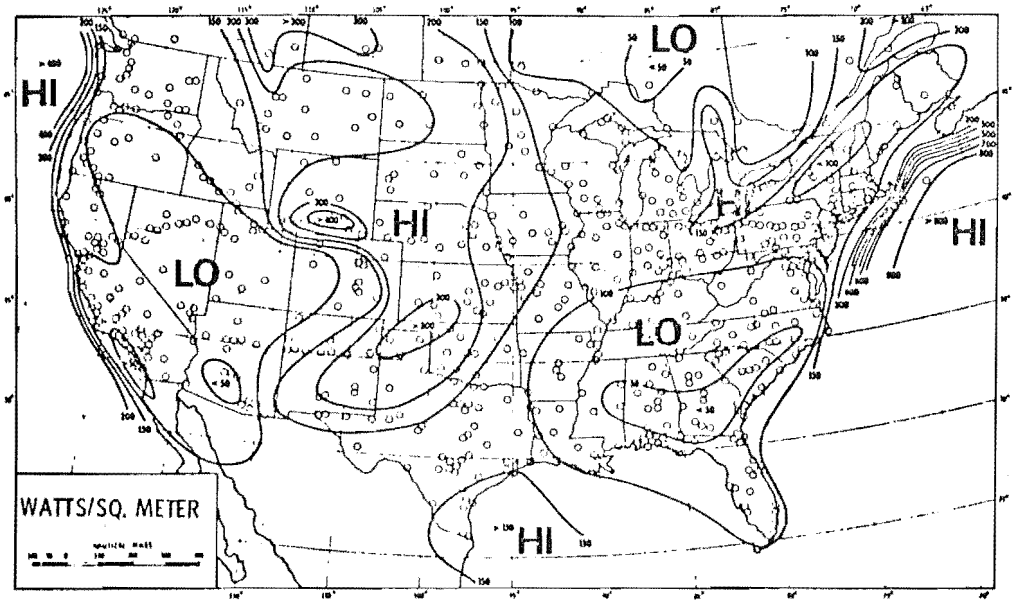

FIG. 2·6 ANNUAL MEAN WIND ENERGY FLUX OVER THE UNITED STATES, AFTER REED (1974)

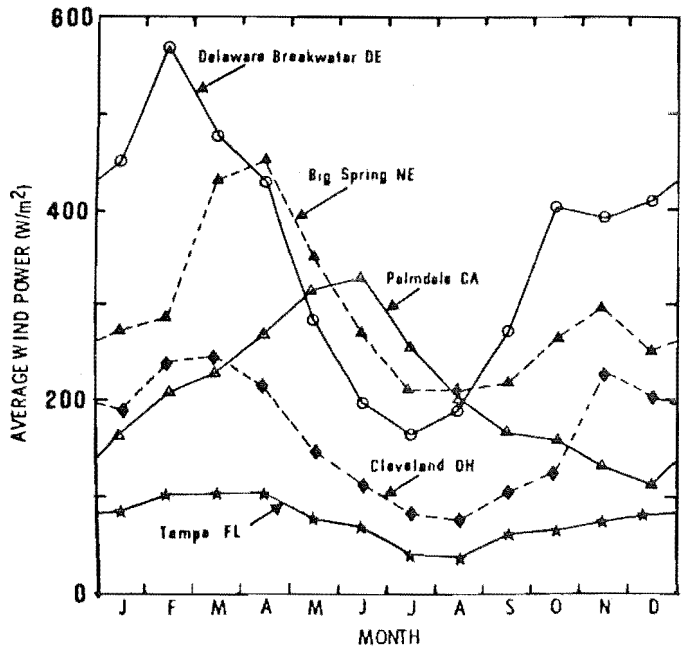

FIG. 2·7 MEAN SEASONAL VARIATION IN THE WEF AT SEVERAL U.S. LOCATIONS, REED (1974)

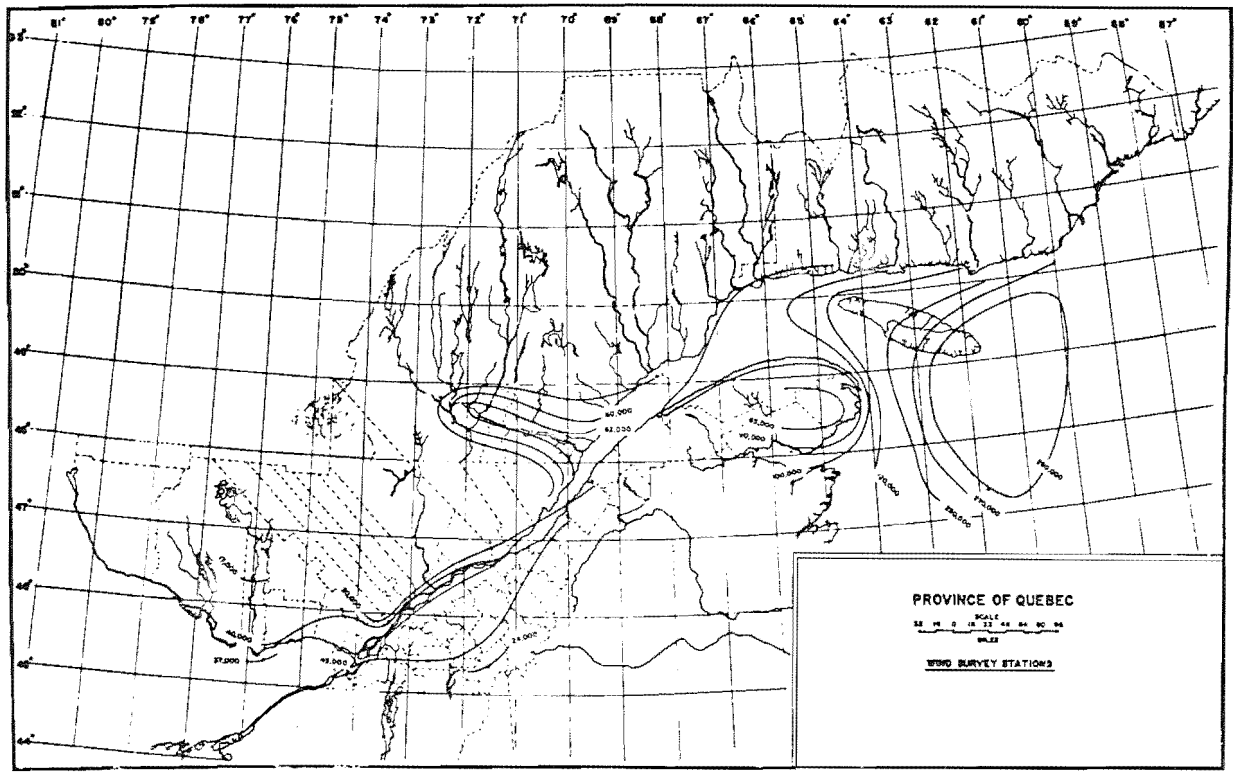

FIG. 2·8 CONTOUR LINES OF THE ANNUAL MEAN ENERGY AVAILABLE FROM A 32FT. DIAMETER BRACE AIRSCREW WIND-MILL IN THE PROVINCE OF QUEBEC, IN UNITS OF HP.HRS PER ANNUM. FROM WARD, KADIVAR AND BROUGHTON (1974).

diverse a range of terrains as possible. The information derived from this type of work is invaluable for the comparison with wind tunnel model data and theoretical predictions of flow and wind structure over different terrain. This lack of information is accentuated when one considers complex terrain because very few people have gathered detailed measurements of the wind and its structure in this situation.

Much of the early field data was of a very basic nature, mean wind speed and direction, and was used for statistical prediction of the weather for shipping. This meant that recording sites were often in coastal regions. With the advent of flight, it was necessary to have wind recording equipment at airports to provide the pilots with the necessary information.

In 1952, Golding suggested that field measurements of sites suitable for wind power generation should be made. At that time he was evaluating the speed-up effects of hills and ridges.

Since then, a great deal of research has been carried out involving analysis of the structure of the wind and this has required the development of sophisticated anemometry, recording equipment and computer analysis of the raw data.

Some of the relevant characteristics of the wind structure will be discussed here. This section will be based on measurements made in the field by several researchers.

Velocity Profile

This is the variation of longitudinal velocity with height, and the first consideration given here is for a profile of the form

$$\bar{u} = f(z) \quad \ldots\ldots\ldots\

Type of terrain	Power law exponent α	Gradient height z_g (m)	Surface drag coefficient k
(A) Open terrain with very few obstacles e.g. open grass or farmland with few trees, hedgrows and other barriers etc.; prairie, tundra shores and low islands of inland lakes; deserts.	0·16	300	0·005
(B) Terrain uniformly covered with obstacles 10 to 15 m (33 to 49ft) in height; e.g. residential suburbs; small towns; woodland and shrub. Small fields with bushes, trees and hedges.	0·28	430	0·015
(C) Terrain with large and irregular objects; e.g. centres of large cities, very broken country with many wind - breaks of tall trees etc.	0·40	560	0·050

TABLE 2·3 POWER LAW EXPONENT, GRADIENT HEIGHT AND SURFACE DRAG COEFFICIENTS FOR VARIOUS TERRAIN TYPES (After Davenport)

types (A) and (B) have been substantiated by many other workers and are classed as being reliable. However, the class (C) type terrain, which covers urban areas and complex terrain, has not been verified sufficiently to make it reliable. Therefore, sites of this class have to be considered individually. There is some debate as to whether one should use the power law with a large value for the index, as suggested by Davenport, or to have a zero plane displacement of the average height of the obstructions. This method is discussed by Harris (1970), but as he points out, neither of these approaches gives a very satisfactory treatment for the mean speed within the obstruction height. It is common knowledge that in many urban environments, areas of high wind are a function of the immediate buildings, which are effectively the roughness elements and therefore no general equation for wind structure in these conditions is possible. These two proposals are shown as profiles in Fig.2.9.

The power law is of the form

$$\frac{\bar{u}(z_1)}{\bar{u}(z_2)} = \left(\frac{z_1}{z_2}\right)^{\alpha}$$

where z_1 and z_2 are the heights at which measurements are taken.

It is common to use a reference height; typically the Meteorological Office uses 10m. Therefore, the expression becones

$$\frac{\bar{u}(z_1)}{\bar{u}_{10}} = \left(\frac{z}{10}\right)^{\alpha} \quad \ldots\ldots\ldots\ldots\ldots\ldots\ldots\ldots\ldots\ldots \quad (2.3)$$

z has to be measured in metres.

Another method of representing the profile is to use the log law. Yamomoto and Shimanuki (1964) and Lappe (1965) suggest that the log law could be used up to a height of about 140m and that it was more applicable as the roughness increased.

The turbulent shear stress ($\tilde{\tau}$) or Reynolds stress is represented by the expression

$$\tilde{\tau} = \rho\overline{uw} \quad \ldots\ldots\ldots\ldots\ldots\ldots\ldots\ldots\ldots\ldots\ldots\ldots\ldots\ldots (2.4)$$

where u is the fluctuating component of the velocity in the longitudinal direction

w is the fluctuating component of the velocity in the vertical direction.

At this stage mixing length theory has to be introduced; this is a very involved and complex topic in its own right and will not be discussed here. Suffice to say that using Prandtl's mixing length theory, see Hinze (1959) equation 2 can be written in the following form

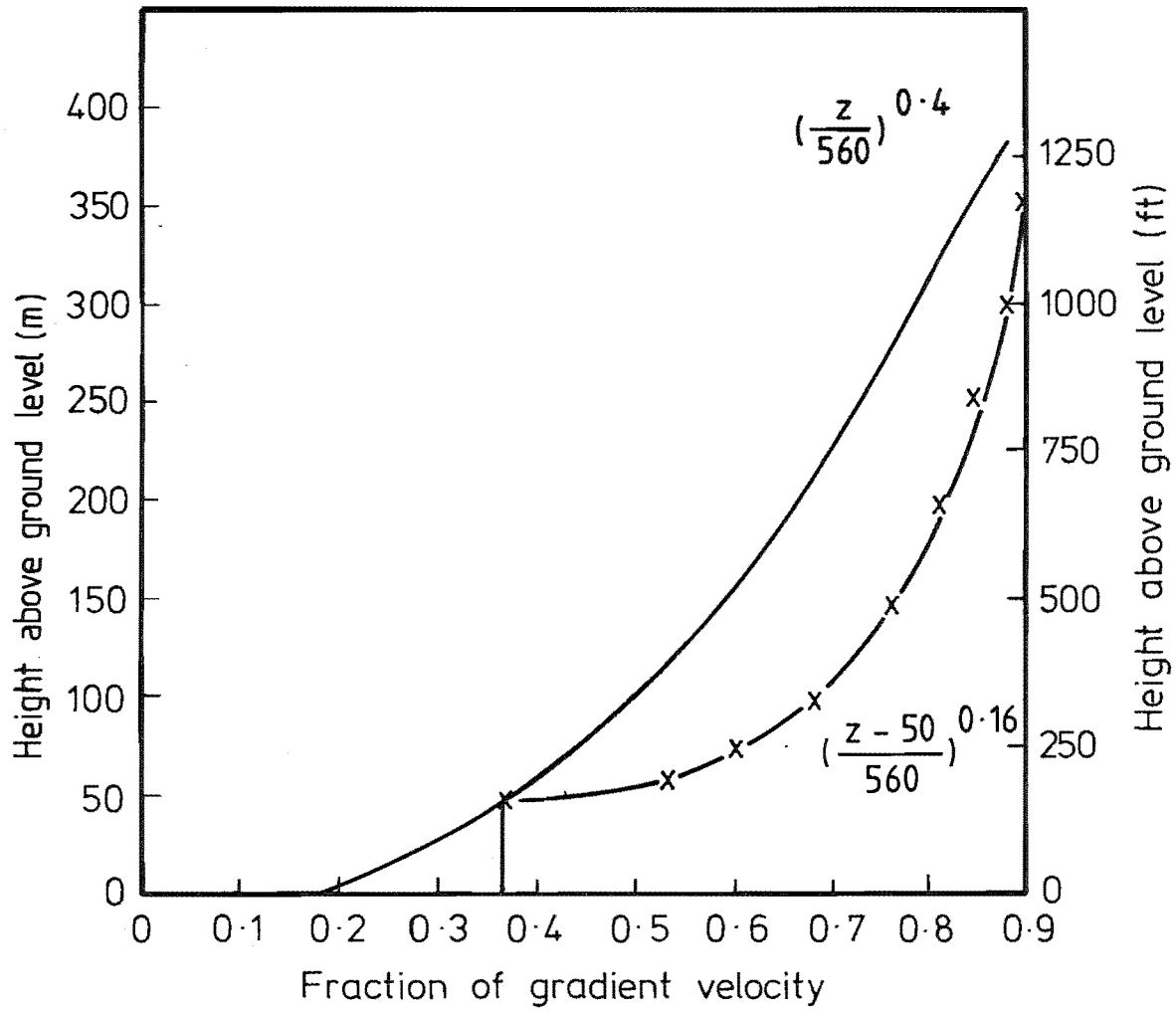

FIG. 2·9 ALTERNATIVES FOR URBAN PROFILES OF MEAN WIND VELOCITY.

$$\tau = \rho \ell \left(\frac{\partial u}{\partial z}\right)^2 \quad \ldots\ldots\ldots\ldots\ldots\ldots\ldots\ldots\ldots\ldots \quad (2.5)$$

where ℓ is the Prandtl mixing length

and $\left(\frac{\partial u}{\partial z}\right)$ is the velocity gradient.

Prandtl assumes that ℓ is proportional to z, i.e. $\ell = kz$.

Therefore, equation (2.5) becomes

$$\frac{\partial u}{\partial z} = \frac{1}{kz} \sqrt{\tau/\rho} \quad \ldots\ldots\ldots\ldots\ldots\ldots\ldots\ldots\ldots\ldots \quad (2.6)$$

Integrating this yields

$$u = \frac{1}{k} \sqrt{\tau/\rho} \ln z + \text{constant} \quad \ldots\ldots\ldots\ldots\ldots\ldots \quad (2.7)$$

However, by definition the friction velocity is given by

$$u_* = \sqrt{\tau/\rho}.$$

Hence, the logarithmic velocity profile is commonly expressed as

$$u = \frac{u_*}{\kappa} \ln \left(\frac{z}{z_o}\right) \quad \ldots\ldots\ldots\ldots\ldots\ldots\ldots\ldots\ldots\ldots \quad (2.8)$$

Von Karman's value of 0.4 is usually accepted for the value of κ, and z_o is the roughness length which is characteristic of the terrain.

Teunissen (1970) points out that the log law is valid strictly speaking only for neutral conditions, and then discusses this in more detail and suggests a modification that should be applied for non-neutral conditions, this being

$$\bar{u} = \frac{u_*}{\kappa} \left[\ln \left(\frac{z}{z_o}\right) - \psi \left(\frac{z}{L'}\right)\right] \quad \ldots\ldots\ldots\ldots\ldots \quad (2.9)$$

where L' is a temperature dependent scaling length, and ψ is a universal function of z/L' and since it can be shown that the Richardson number is a unique function of z/L', the preceding equation can be used to obtain mean velocities in non-neutral stabilities. Carruthers and Houghton (1976) suggest that the log law is only valid for approximately 20% of the total

boundary layer thickness and this agrees with the earlier work of Yamomoto and Shimanuki and also that of Lappe.

Jones, Delarringa and Wilson (1971) attempted to measure an urban velocity profile; they took measurements up to 330m and found a wide variation to the predicted power law. Their argument was based on the lapse rate at the sites in question.

Counihan (1975) has collated power index (α) measurements dating back to 1935, which he presents in a graphical form given in Fig. 2.10.. He has proposed a curve, based on the roughness length z_o, which is seen to fit the data well, noting that curves proposed by other researchers, particularly Panofsky *et al* (1960) and Davenport (1963, 1967) have consistently over-estimated the index α, particularly for roughness lengths in the terrain type 4 region.

This type of graph can be quite misleading because many of the data points in the terrain type 4 region have been collected in urban areas such as Tokyo, Copenhagen, Washington etc., where the heat island effects can have a significant bearing on the measured results.

Turbulence Intensity

This is defined as the r.m.s. value of the velocity, i.e., the fluctuating component, divided by the mean velocity. (Prime denotes rms value).

$$I = \frac{u'}{\bar{u}} \quad \ldots\ldots\ldots\ldots\ldots\ldots\ldots\ldots\ldots \quad (2.10)$$

Counihan (1975) provides similar data as previously, Fig. 2.11, for turbulence intensities normalised at 30m high. Note the lack of data for terrain type 4 where estimates (E) are used.

The value of $\frac{u'}{\bar{u}}$ usually decreases with height, mainly due to the increase of mean wind speed rather than a reduction in the r.m.s. gust speed. Teunissen (1970) and Harris (1968) have shown with field measurements that the r.m.s. value, in fact, has very little change in value with height. This effect is shown in Fig.2.12 and the variation of turbulence intensity with height is shown in Fig. 2.13.

Values of turbulence intensities over various terrains have been recorded by many researchers and are catalogued in graphical form by the Engineering Sciences Data Unit (ESDU), and this will be discussed in Section 2.1.6.

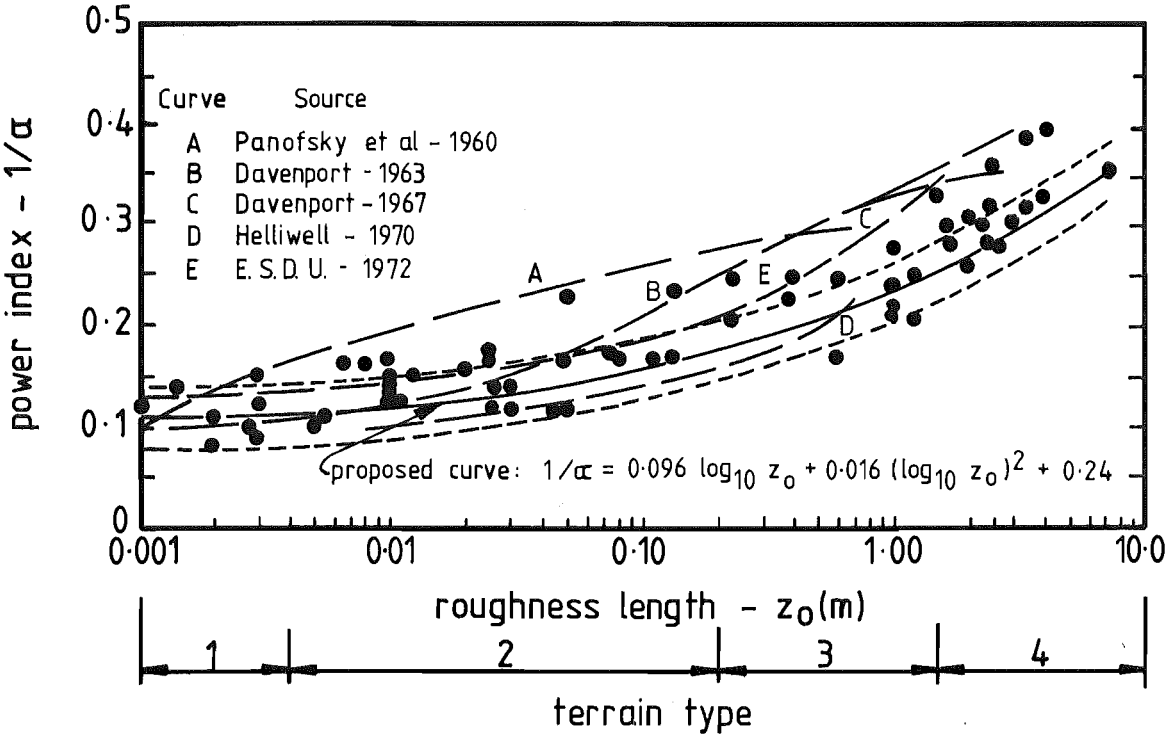

FIG 2·10 VARIATION OF THE POWER INDEX WITH ROUGHNESS LENGTH (after Counihan)

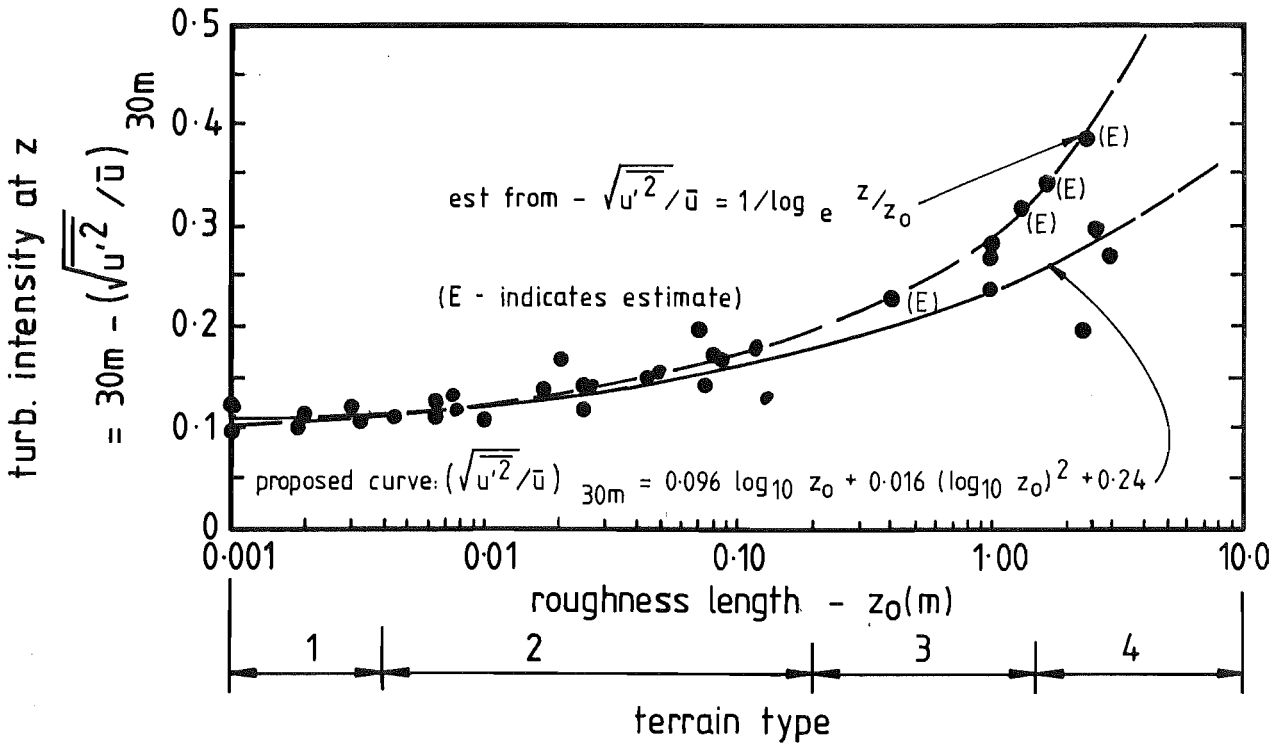

FIG 2·11 VARIATION OF TURBULENCE INTENSITY WITH ROUGHNESS LENGTH (after Counihan)

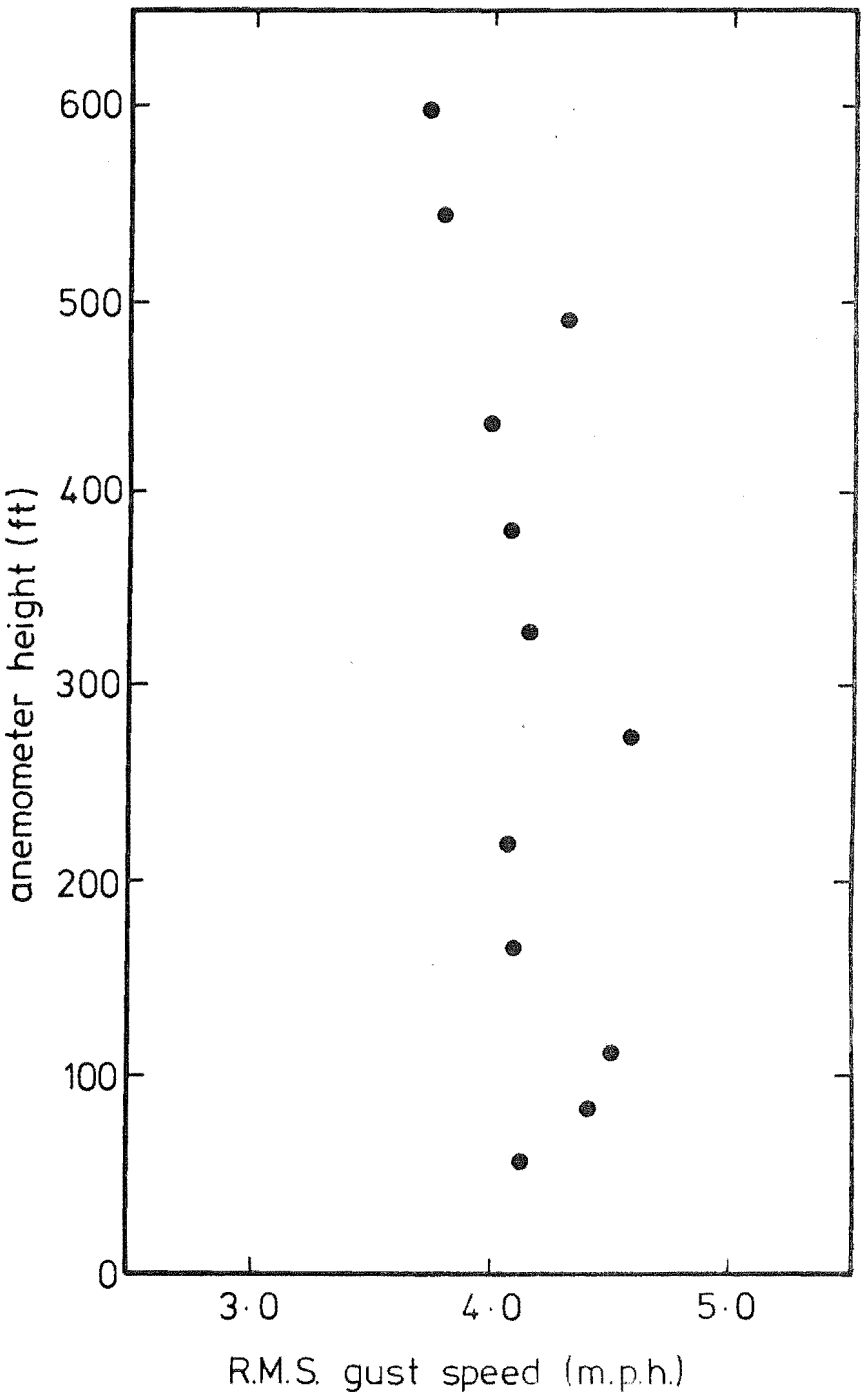

FIG 2·12 VARIATION OF R.M.S GUST SPEED WITH HEIGHT (After Harris)

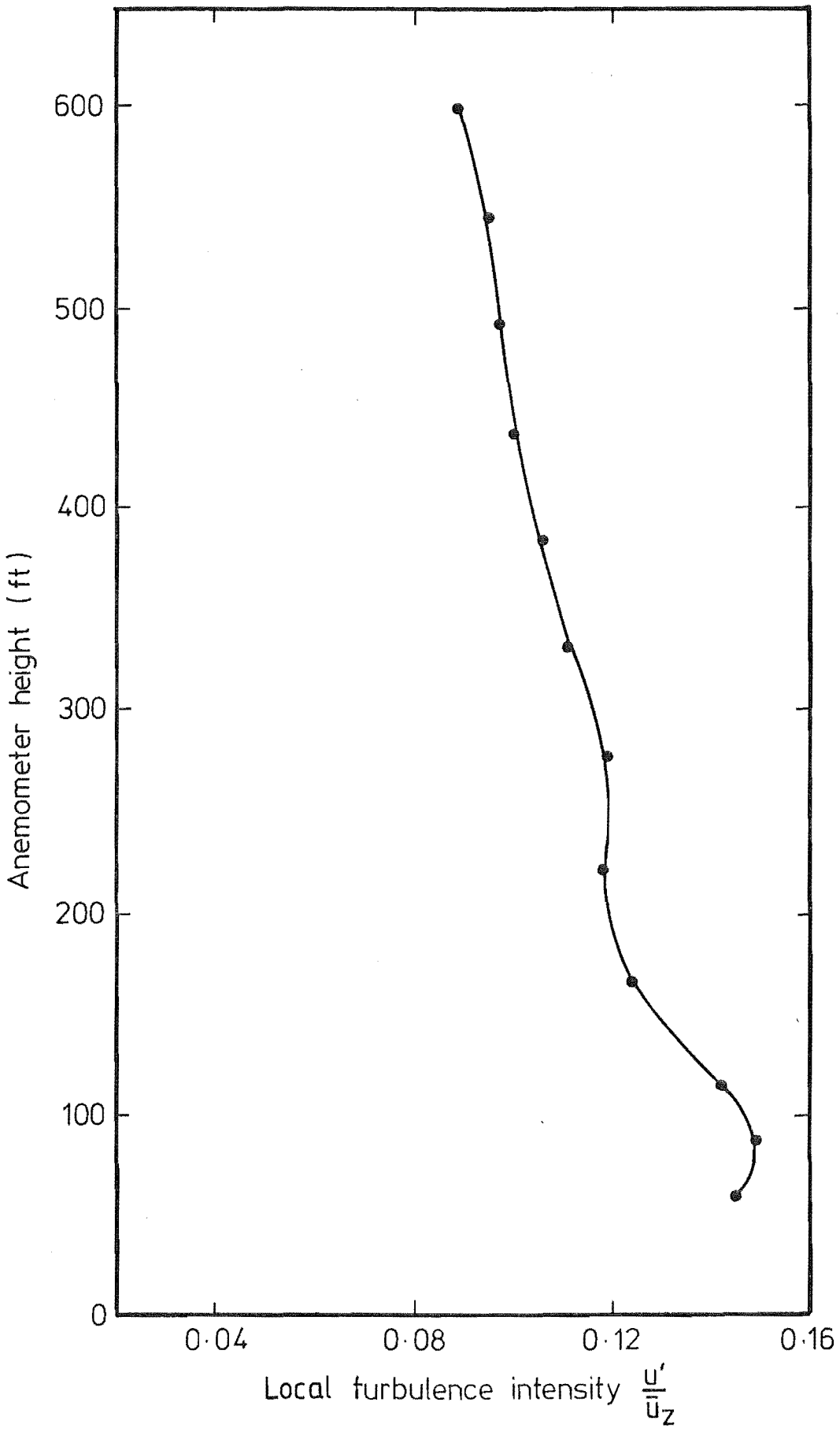

FIG 2·13 VARIATION OF TURBULENCE INTENSITY WITH HEIGHT (After Harris)

Gradient Height

This is usually expressed by z_G and is the height at which there is no further increase in wind velocity due to an increase in height.

Values for z_G for open flat country have been well established but as the terrain becomes more of a complex nature, i.e., hills, urban areas etc., z_G values are less reliable. Davenport (1963) has produced a graph which gives z_G for different terrains, and this is presented in Fig. 2.14.

Reynolds Stresses

The most significant Reynolds stress term is given by $-\overline{uw}/\bar{u}_o^2$ where u and w are the fluctuating contribution of the wind velocity and the bar (- denotes averaged with respect to time. In this form, Counihan (1975) assumes $\bar{u}_o$ at a height of 600m. Calder (1939) suggests Reynolds stress to be constant (within about 6%) up to a height of 50m. Summarising work by Pasquill (1950) Rider (1954), Ellison (1956) and Deacon (1957) a suggested value of Reynolds stress for rural terrain should be in the range

$$0.0020 < -\overline{u\,w}/\bar{u}_o^2 < 0.0030 \quad \ldots\ldots\ldots\ldots\ldots\ldots \quad (2.11)$$

at or near ground level.

Later work by Pasquill (1970) and Smith (1970) modified these values slightly and added values for sea areas

$$0.0002 < -\overline{u\,w}/\bar{u}_o^2 < 0.0008$$

and for rural areas

$$0.0020 < -\overline{u\,w}/\bar{u}_o^2 < 0.0025$$

where $\bar{u}_o$ is assumed to occur at 600m.

One interesting point noted by Counihan (1975) was that for rough terrain, the data of Davenport (1964), based on the free-stream velocity, indicated that the Reynolds stress decreased with increase of the roughness appropriate to an urban terrain. As yet, no satisfactory explan put forward for this. A plot of Reynolds stress against roughness length is given in Fig. 2.15. Note the major difference between Counihan and Davenport for class 4 terrain.

Energy Spectrum

Longitudinal Component; The shape of the longitudinal component of the power spectral density was defined by Von Karman (1948), his definition being in a form which has not changed greatly.

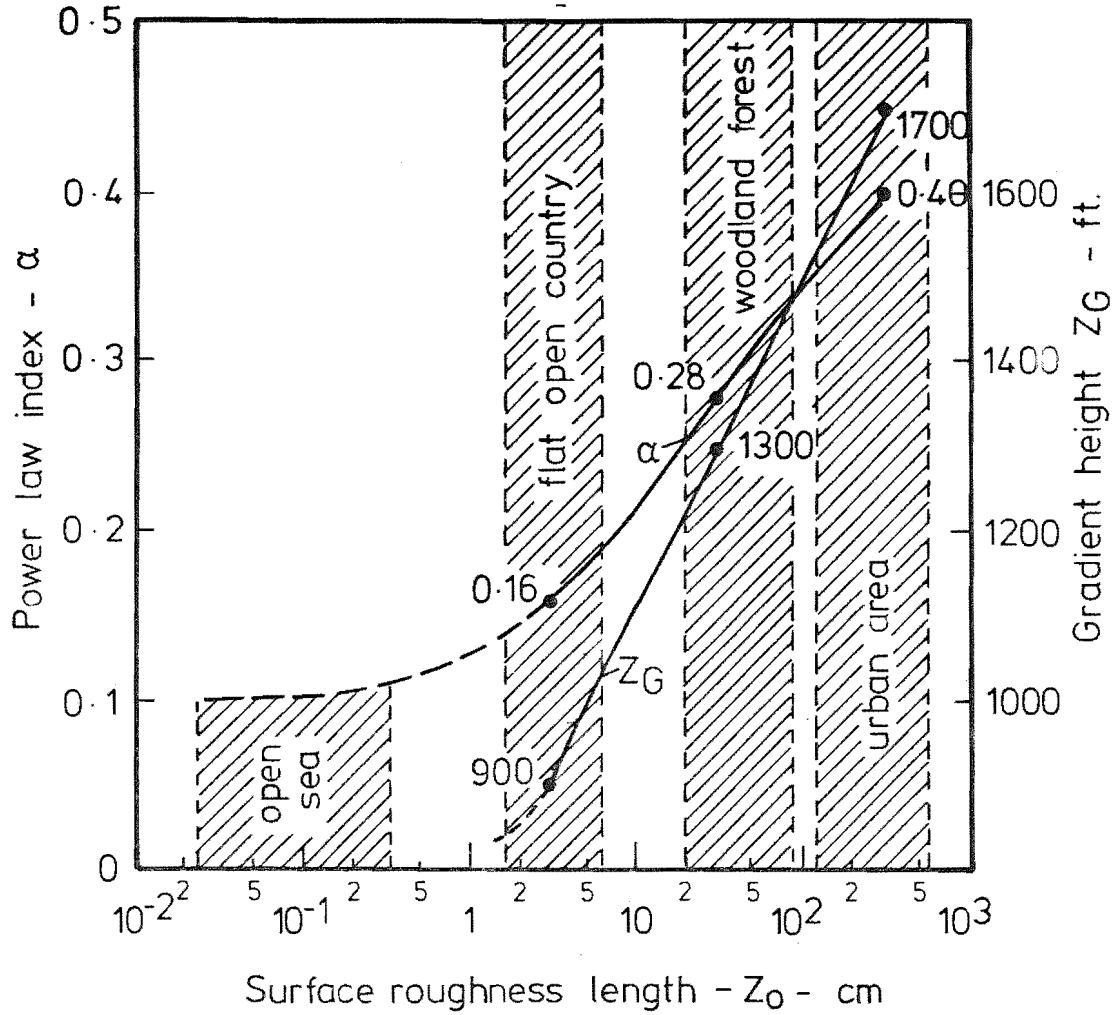

FIG. 2·14 PARAMETERS OF THE POWER LAW FOR MEAN WIND VELOCITY.

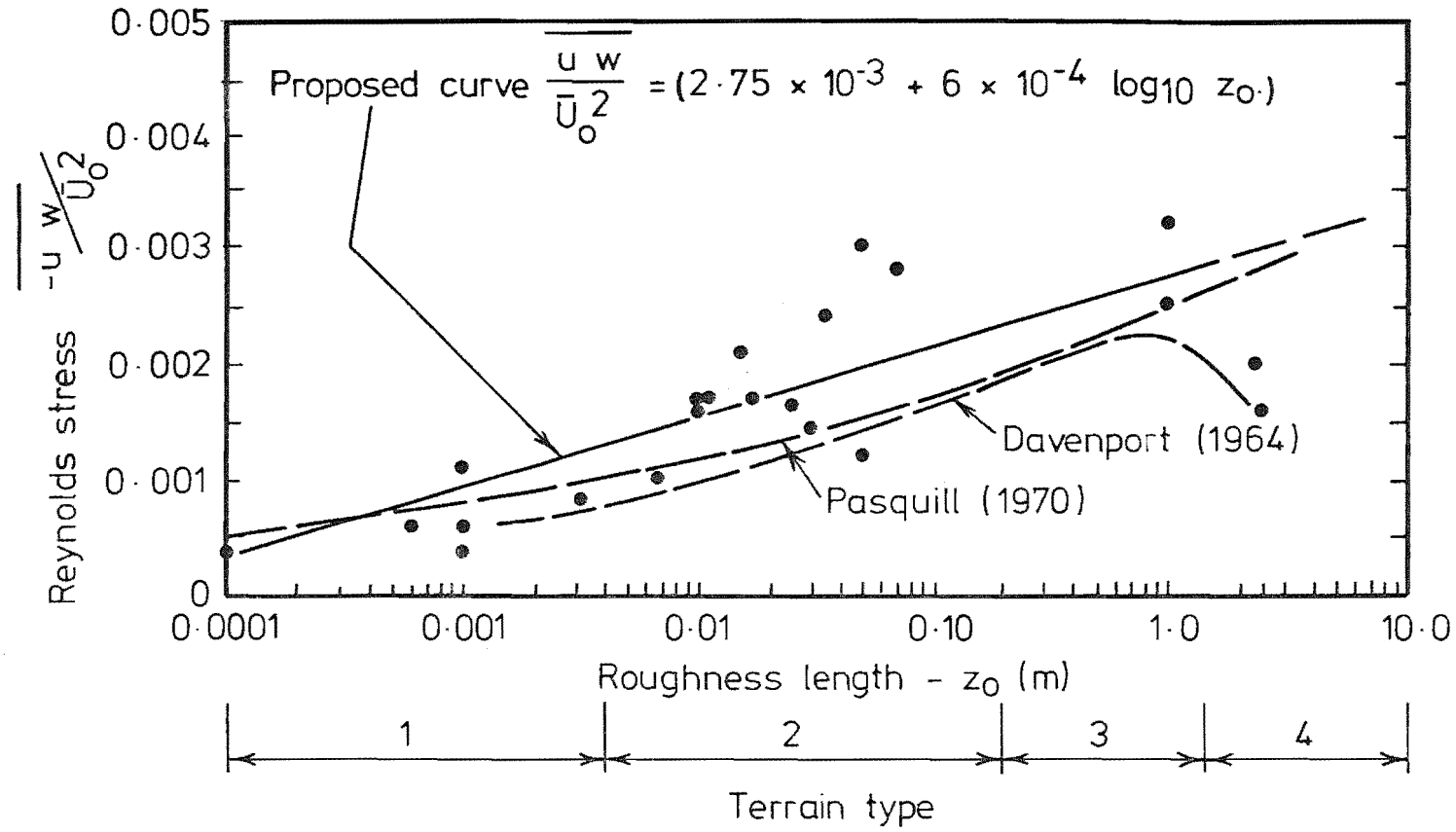

FIG. 2·15 VARIATION OF REYNOLDS STRESS WITH ROUGHNESS LENGTH

$$S\left(\frac{K}{K_o}\right) \alpha \frac{1}{\left[1 + \left(K/K_o\right)^2\right]^{5/6}} \quad \ldots\ldots\ldots\ldots\ldots\ldots \quad (2.12)$$

where $K = \frac{2\pi n}{\bar{u}}$.

The existence of a "spectral gap" which conveniently separated the mean and turbulent motions of the micrometeorological or gust range of frequencies was initially shown by Panofsky and Van der Hoven (1955). The complete spectrum of the longitudinal velocity was presented by Van der Hoven (1957) and is given in Fig. 2.16.

It was suggested that the spectral gap occurred at higher frequencies in flow over rougher terrain, and this implies a reduction in the length scales or turbulence with increase in terrain roughness.

A revised form for the longitudinal spectrum was suggested by Davenport (1961a, 1961b),

$$n\, S_u(n) \alpha \frac{1}{(1 + x^2)^{4/3}} \quad \ldots\ldots\ldots\ldots\ldots\ldots \quad (2.13)$$

where $x = \frac{nL}{\bar{u}_{10}}$

$L = 1200m.$

Counihan (1975) suggests that this form underestimates the energy in the low frequency range. A further modification of the spectrum was made by Harris (1968) who suggests

$$S_u(n) \alpha \frac{x}{(2 + x^2)^{5/6}} \quad \ldots\ldots\ldots\ldots\ldots\ldots \quad (2.14)$$

where $x = \frac{nL}{\bar{u}_{10}}$

$L = 1800m.$

For turbulence energy to be extracted from a mean flow, there must be a high velocity gradient; flow close to the ground in the atmospheric boundary layer provides such a situation. Therefore, eddies characteristic of turbulence generation are anisotropic. The turbulence energy is transferred to higher wave numbers and the smaller eddies, by inertial interaction, and is finally dissipated into molecular kinetic energy in the smallest eddies at very high wave numbers.

Hinze (1959) shows that a one dimensional energy spectrum consists of several sub-regions. However, it will suffice here to generalise these into

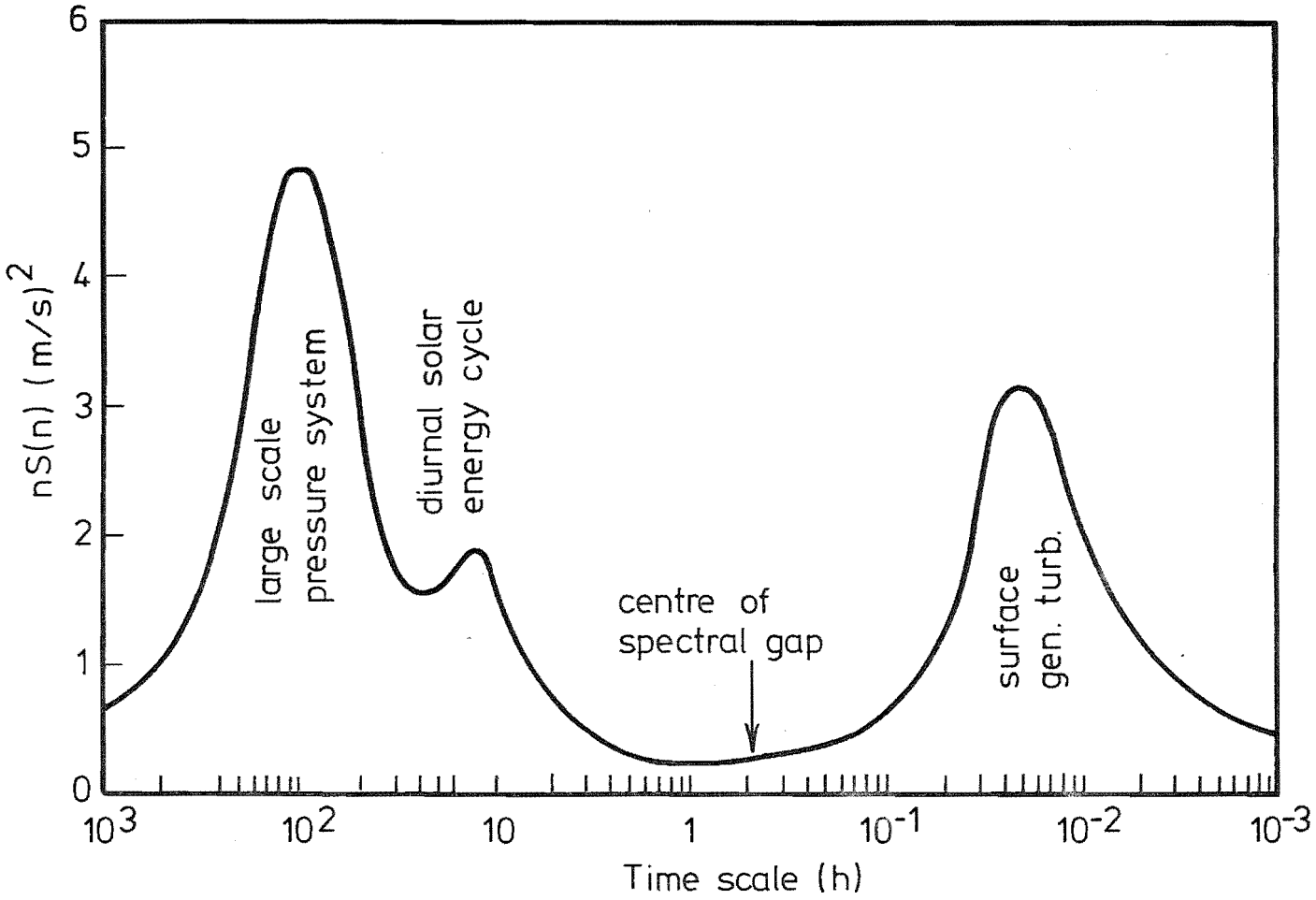

FIG 2·16 VAN DER HOVEN'S GUST SPECTRUM

three major categories:

1) A low frequency region where energy is transferred into turbulent motion from the mean flow due to high velocity gradients. As previously mentioned, this form of turbulence has the characteristic of anistropy.
2) A middle region which has the energy containing eddies. This region usually contains the spectral peak of the energy spectrum.
3) A high frequency region, Kolmogoroff, Universal equilibrium range, where viscous dissipation becomes increasingly important as frequency increases

Kolmogoroff, in his second hypothesis, proposed that at very high turbul Reynolds numbers, there existed a subrange where inertial transfer of energy was the dominating factor. This subrange is situated at the low frequency end of the universal equilibrium range which is also the upper end of the range of energy containing eddies. This subrange was, for obvious reasons, called the "inertial subrange". In this range no production or dissipation or turbulence energy occurs, only inertial transfer of energy from larger anisotropic eddies to smaller, high frequency eddies. In this subrange local isotropy is considered to exist and the spectral density is proportional to the -5/3 power of frequency.

$$S_{u_i}(k) \propto \varepsilon^{2/3} k^{-5/3} \qquad \text{.....(2.15)}$$

where ε is the dissipation by turbulence per unit of mass.

If the spectral distribution of energy is constant so that ε = constant, then a log/log plot of $S_{u_i}(k)$ vs k will exhibit a -5/3 slope in the inertial subrange. Batchelor (1953) gives the criterion for the existence of the inertial subrange as

$$Re_{l_e}^{3/8} >>> 1 \qquad \text{.....(2.16)}$$

and $$Re_{l_e} = \left\{ \frac{u' l_e}{\nu} \right\} \qquad \text{.....(2.17)}$$

where $l_e = \frac{1}{k_p}$

and k_p is the wave number corresponding to the peak of the energy spectrum. Hinze (1959) shows that the frequency dependence of $S_{u_i}(k)$ is roughly as k^0 in the low frequency region, $k^{-5/3}$ in the inertial subrange, and k^{-7} in the high frequency viscous dissipation range.

Pasquill (1970) recommended the use of a much simpler spectrum which woul apply mainly to the inertial subrange and for heights up to about 100m and suggested

$$\frac{n S_u(n)}{u_*^2} \simeq 0.26 \left(\frac{nz}{\bar{u}} \right)^{-2/3} \qquad \text{.....(2.18)}$$

where u_* is the friction velocity.

Lateral Components of Spectra

There is not a great deal of data available on this component of spectra. One of the major reasons for this is that for structural problems this is not a significant parameter.

Elderkin (1967) showed that the -5/3 law could be applied in the inertial subrange and work by Busch and Panofsky (1968), Teunissen (1970), and Kaimal (1973) discuss the topic. Kaimal *et al* (1972) suggested that this component of the spectra could be described by the following:

$$\frac{n\,S_v(n)}{u_*^2} = \frac{17f}{(1 + 9.5f)^{5/3}} \quad \ldots\ldots\ldots\ldots\ldots\ldots \quad (2.19)$$

where $f = \frac{nz}{\bar{u}_z}$

and $\sigma_v = 1.876\ u_*$.

Vertical Component of Spectra

Work on this topic is included in papers by Teunissen (1970), Busch and Panofsky (1968) and Kaimal (1973).

Busch and Panofsky suggested a modified form for the spectrum

$$\frac{n\,S_w(n)}{u_*^2} = \frac{1.075\ f/f_m}{1 + 1.5\ (f/f_m)^{5/3}} \quad \ldots\ldots\ldots\ldots\ldots \quad (2.20)$$

where $f_m = 0.32$ for adiabatic conditions

$$f = \left(\frac{nz}{\bar{u}}\right).$$

Counihan suggests that this form of vertical spectrum is the one most often used. Examples of longitudinal, lateral and vertical spectrum, as produced by Flay (1978) from field measurements on open flat rural terrain are given in Fig. 2.17.

Auto-correlation Function

The autocovariance function is formed by the mean product of a fluctuating velocity component measured at the same point but at time t and $(t + \tau)$

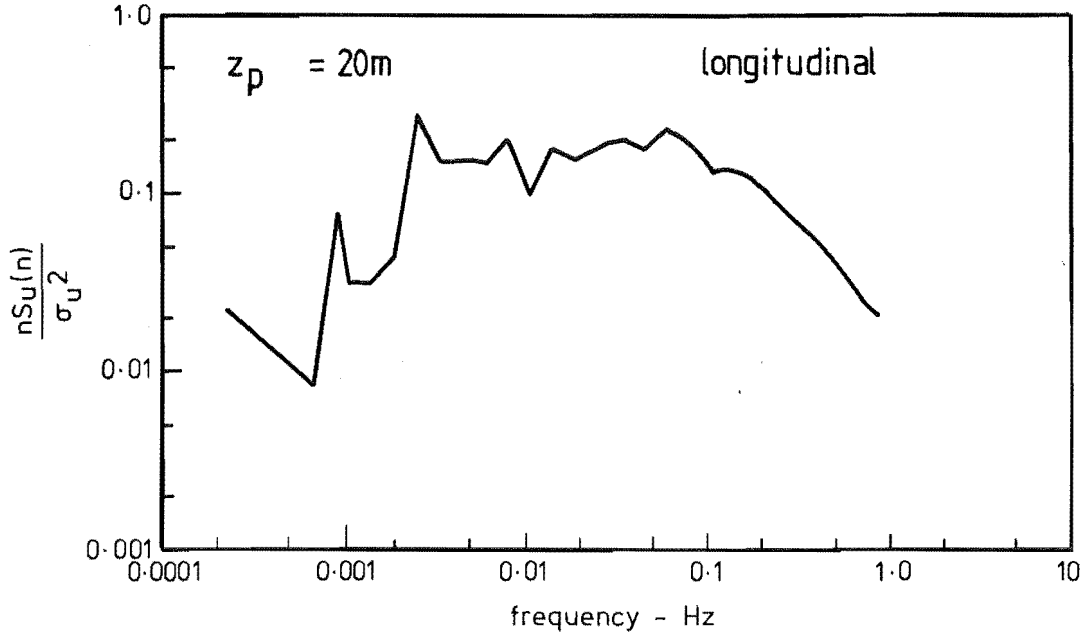

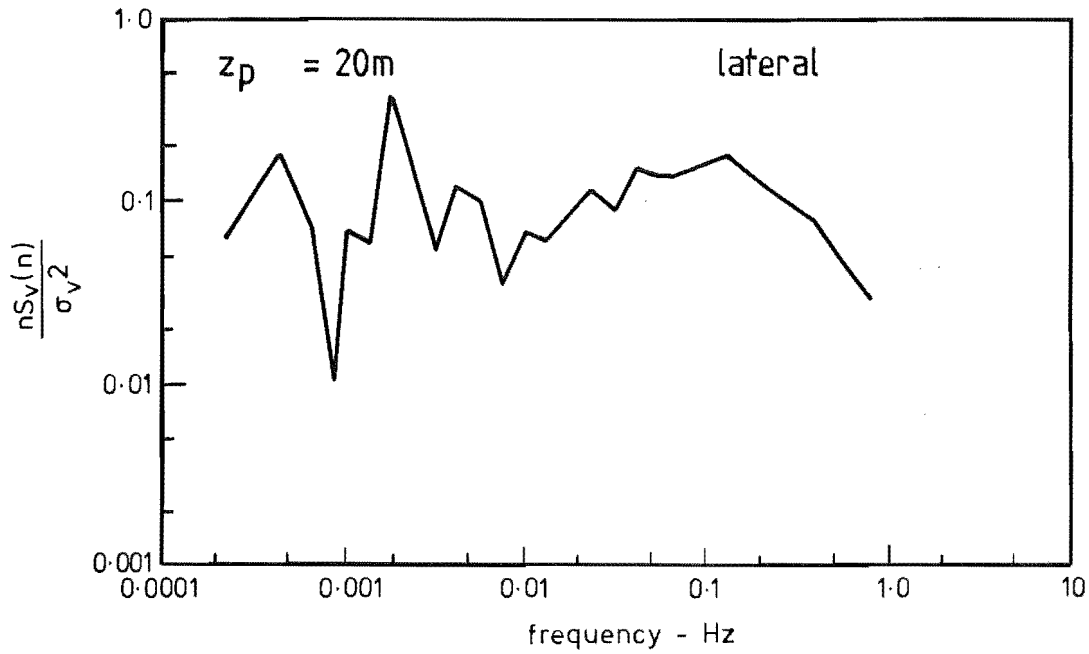

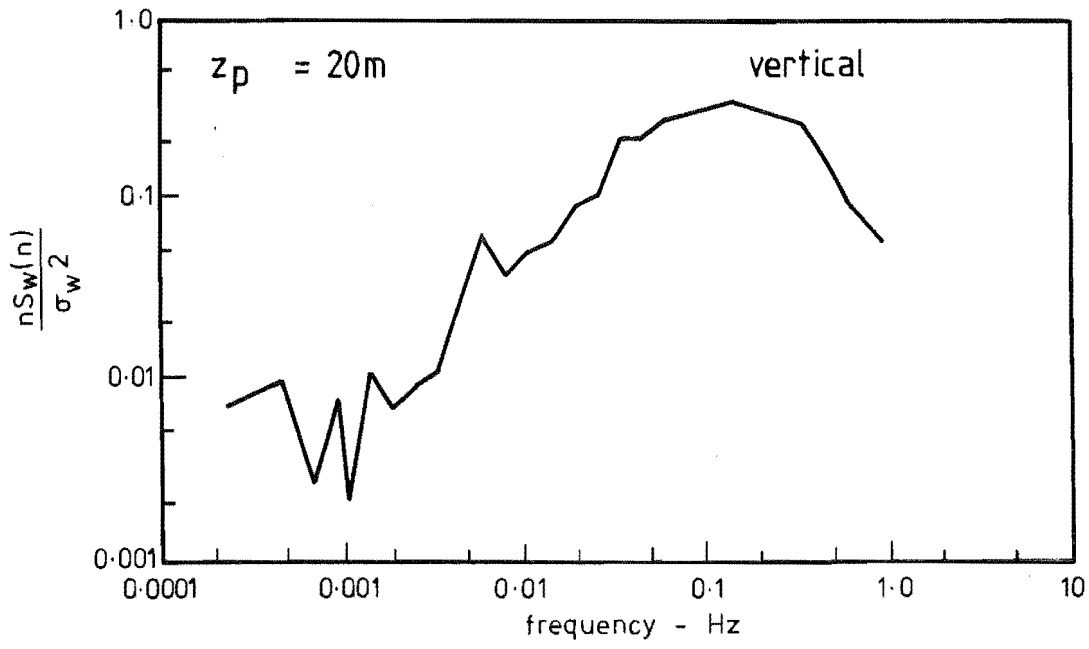

FIG 2·17 EXAMPLES OF U, V AND W ENERGY SPECTRA MEASURED ON FLAT RURAL TERRAIN (After Flay)

$$\text{i.e. } C_{ii}(\tau) = \overline{i(t).i(t+\tau)} = \lim_{T \to \infty} \frac{1}{T} \int_0^T i(t).i(t+\tau)\, dt \quad \ldots\ldots\ldots (2.21)$$

where i = u, v, w are the fluctuating components of wind speed along the x, y, z axes respectively. x,y,z axes are a system of rectangular cartesian coordinates with the x axis defined in the direction of the mean wind.

When the time lag τ is zero, then the autocovariance function reduces to the variances σ_u^2, σ_v^2, σ_w^2. It is usual to normalise the autocovariance function by dividing by the appropriate standard deviation of the constituent velocity component, thus forming the autocorrelation function

$$\rho_{ii}(\tau) = \frac{C_{ii}(\tau)}{(\sigma_i)^2} \quad \ldots\ldots\ldots\ldots\ldots\ldots\ldots\ldots\ldots\ldots (2.22)$$

It becomes apparent that when $\tau = 0$, $\rho_{ii} = 1$, the range of ρ_{ii} is, in fact ± 1 and a plot of this function against time describes the dependence of values at any point in a time history on those at any other point in the time history.

Taylor's Hypothesis is useful because it can be used to transform a time delay (τ) to an equivalent spatial separation. This involves the calculation of an integral time scale T, which is defined as the area under the autocorrelation function

$$T_i = \int_0^\infty \rho_{ii}(\tau)\, d\tau \quad \ldots\ldots\ldots\ldots\ldots\ldots\ldots\ldots\ldots (2.23)$$

where i = u, v, w.

Taylor's Hypothesis states that provided $\bar{u}$ at the height being considered (z) is much greater than u(t), the fluctuating component, the turbulence field can be considered to be frozen in space and convected past a point with velocity $\bar{u}_z$. Thus the variation of u(t) with time when the turbulence field is viewed from a stationary point, is the same as the variation observed from the point moving with velocity $\bar{u}_z$ across the "frozen" field of turbulence in the x direction. Thus Taylor's Hypothesis can be used to convert the integral time scales T_i, i = u, v, w, calculated from the autocorrelation functions to equivalent integral length scales thus:

$$^{x}L_i = \bar{u}_z \int_0^\infty \rho_{ii}(\tau)\, d\tau \quad \ldots\ldots\ldots\ldots\ldots\ldots\ldots\ldots\ldots (2.24)$$

where i = u, v, w.

Examples of autocorrelation function plots from data recorded at Rugby in England by Harris (1968) are given in Fig. 2.18. The plots are for measurements at several heights and are compared with a theoretical curve.

Length Scales

The integral length scale of turbulence is a measure of the longest correlation distance between the velocities at two points in the flow field.

There are three methods commonly employed to evaluate this parameter, but only the ones to be used in this research will be reported here.

1. The integral scale length can be estimated using the Eulerian time scale, which has been discussed in the previous section. The difficulty in using this method is the determination of the value of T_E, the Eulerian time scale which is used in the formula

$$^{x}L_u = \bar{u}T_E \quad \ldots\ldots\ldots\ldots\ldots\ldots\ldots\ldots\ldots\ldots\ldots\ldots \quad (2.25)$$

for the longitudinal component of turbulence.

At the low frequency end of the autocorrelation when τ is large, the use of finite averaging times results in oscillations of $\rho_{uu}(\tau)$ about its zero axis. To reduce this effect, it has been suggested that T_E be given the value of τ at which $\rho_{uu}(\tau)$ has reduced by a value of $1/e$; however, the error in this is that it assumes that $\rho_{uu}(\tau)$ decreases exponentially, which is not necessarily the case. This point is clearly shown in the data of Harris (1968) in Fig. 2.18.

2. The integral scale length can be obtained from the one-dimensional power spectra. In all the model spectra, there is a free scale parameter which locates the curve on the frequency axis. For the Von Karman model, this parameter is the true integral scale $^{x}L_u$. For any particular model, this scale parameter can be related to the value k_p^i frequency at which the non-dimensionalised spectrum has its maximum value. If the Von Karman spectrum is considered

$$\frac{n\,S_u(n)}{\bar{u}^2} = \frac{4\,k\,^{x}L_u}{\left[1 + 70.7\,(^{x}L_u k)^2\right]^{5/6}} \quad \ldots\ldots\ldots\ldots \quad (2.26)$$

where $k = \frac{n}{\bar{u}}$.

It is obvious that there is no minimum turning point by observation of

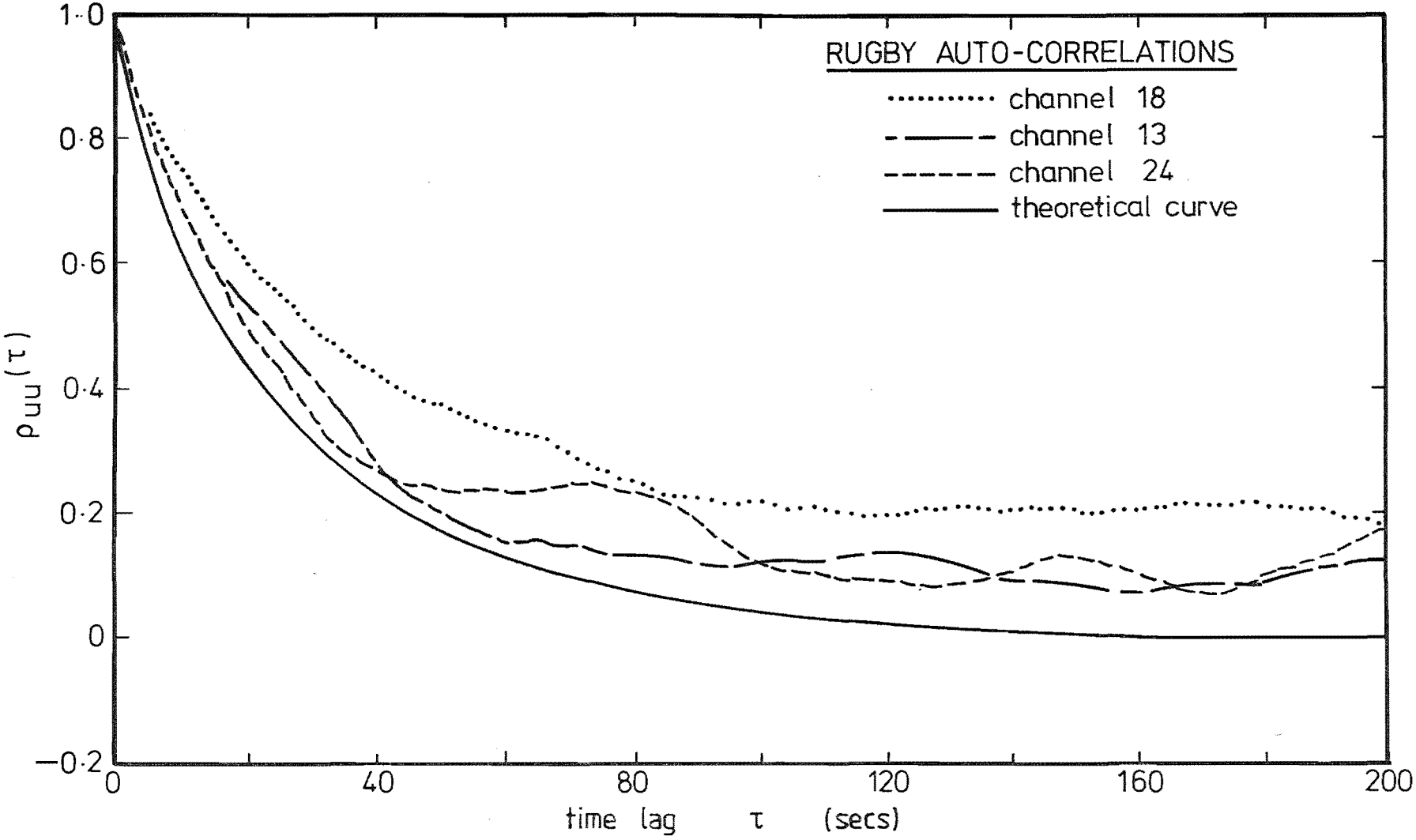

FIG 2·18 FIELD RESULTS OF AUTOCORRELATION CURVES (After Harris)

the spectrum, and therefore the differential will produce the maximum value for k_p^i. This is explained in full by Raine (1974) and Teunissen (1970) and is shown to yield

$$x_{L_u} = \frac{0.146}{k_p^u} \quad \ldots\ldots\ldots\ldots\ldots\ldots\ldots\ldots\ldots\ldots \quad (2.27)$$

and likewise for the vertical component

$$x_{L_w} = \frac{0.106}{k_p^w} \quad \ldots\ldots\ldots\ldots\ldots\ldots\ldots\ldots\ldots\ldots \quad (2.28)$$

Raine (1974) suggests that typically

$$x_{L_u} = 2^x L_v = 2^x L_w \ldots\ldots\ldots\ldots\ldots\ldots\ldots\ldots\ldots\ldots \quad (2.29)$$

There are two major problems incurred by evaluating integral length scales with this method:

i) The peak of the experimental data is not always clearly defined, particularly for the longitudinal and lateral components, making good estimates of k_p^i difficult.

ii) The peak is generally located at the low frequency end of the spectrum, data here not being as reliable as at high frequencies.

Counihan (1975) gives a plot of collected data which requires a knowledge of height, z, in metres and roughness length, z_o, to estimate length scale L_{u_x}. This plot is shown in Fig. 2.19 - note it is applicable for $10 < z(m) < 240$. Counihan also points out the need for information on terrains 3 and 4, i.e., rough and complex terrains.

These represent the major parameters that have been evaluated by researchers in the field. Some of the more general observations made by researchers involving flow over complex terrain will now be discussed.

The World Meteorological Organisation (WMO) prepared a report in 1964 aimed at evaluating WECS site selection. One point of interest in this report was the effort made to consider terrain configurations more closely, particularly the complex type that could produce higher flux levels from a speed-up effect. Probably the most significant aspect of this report is the lack of information presented that is relevant to wind flows and structure over this type of terrain.

A diurnal valley wind system could prevail in the Gebbies Pass

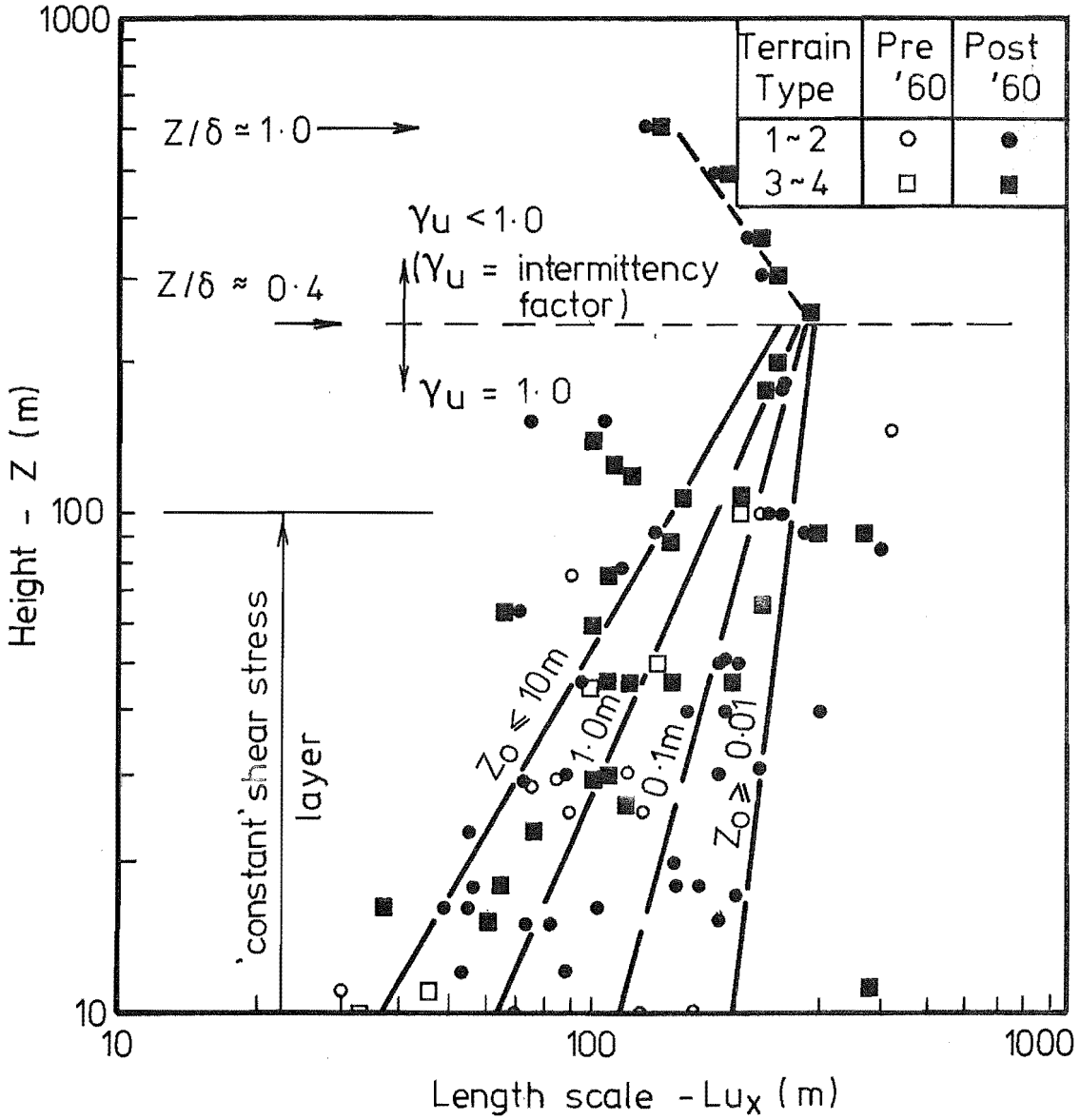

For $10 \leq Z(m) \leq 240$

Gradient height δ taken at 600m

FIG. 2·19 VARIATION OF LENGTH SCALE WITH HEIGHT AND ROUGHNESS LENGTH.

research area. This system is due essentially to the horizontal temperature difference between the air over the valley and the air over the plain into which the valley empties. A wind directed from valley to plain begins to blow around sunset and continues until several hours after sunrise, at which time the wind reverses direction and blows from the plain in the up-valley direction. Superimposed on these purely local wind circulations is the effect of the prevailing flow at the ridge line height. If the prevailing flow is strong, the diurnal local winds may be completely obscured. In these cases the geometry of the valley with respect to the prevailing flow becomes the decisive factor which determines the kind of wind régime to be found in any particular valley.

On mountain tops, speed-up effects as well as speed-down effects are suggested to be observed. This, as explained in the report, is dependent on the orography, the slope of the mountain, the surface roughness and several other features. A great deal of work has and still is being conducted involving the modelling of simple mountain shapes. Bouwmeester, Meroney, Sandborn and Rider (1977) have evaluated triangular hills, Bowen (197 has evaluated bluffs and escarpments, and Meroney *et al* (1978) have conducted a study of the flow régime over the Rakaia Gorge in New Zealand.

Some measurements and observations have been made for flows in rough and inhomogeneous terrain. Slade (1969) evaluated measurements on a tower up to a height of 270m, measuring velocity and turbulence profiles. He concluded that concepts usually applied to the atmosphere's surface boundary layer over smooth and regular terrain seem also applicable in a deep layer over quite rough and irregular terrain. Remembering that he only evaluated velocity and turbulence profiles, his conclusions are still questionable in the light of reports by Jones *et al* (1971), Harris (1968) and ESDU, who suggest otherwise.

Tyson and Preston-Whyte (1972) made observations of topographically-induced wind systems in Natal, India. They concluded that the wind régime was basically produced by the diurnal cycle of insolation, and that the possib consequences of this type of flow on the local régime could be very significar A similar conclusion was arrived at by Steel (1976) in his analysis of a valley system in Wales.

A significant feature which has prevailed throughout section 2.1.5 is the almost total lack of detailed information of the wind structure over complex terrain.

There are several reasons for this:

(1) Measurements have been needed mostly in urban or city areas to predict wind loadings on buildings. With the presence of tall towers in most cities, e.g. Rugby (Harris), T.V. Tower (Slade), measurements have been most conveniently made where there has been the most need.

(2) Crop protection requires the knowledge of wind flow and structure across various types of rural terrain (often flat). Knowledge of urban and rural wind structures is useful for aircraft dynamics, measurements usually being taken at the runway approaches.

This is a partial reason for the profusion of urban and rural measurement There are several reasons for the lack of wind structure data for flow over complex terrain, and some of these have been alluded to earlier in this Chapter and in Chapter 1.

2.1.6 Engineering Sciences Data Unit (ESDU)

The most authoritative, concise presentation of the theory of wind structure is presented by ESDU.

The results of much valuable work, both theoretical and practical, have for various reasons, not been available in a form that is readily usable ESDU's presentation of the theory of wind structure is supplemented, graphical with the inter-relationships of the main parameters. Much of the data used by ESDU has been collected in the field. However, theoretical models are also proposed for comparison. The ESDU series is being continually updated; those used in this research are:

ESDU 1972 (72026)
ESDU 1974 (74030, 74031)
ESDU 1975 (75001)

2.2 UNCONVENTIONAL ANALYSIS METHODS

This section considers two methods of evaluating WECS sites without actually measuring the wind. Instead, one makes an analysis of the effects of the wind in terms of geological and biological factors. These systems are not expected to provide a full analysis but are expected to act as a guide to locating sites which will then undergo conventional analysis techniques.

2.2.1 Eolian Geomorphology

Where possible, people avoid living in windy areas. This often results in that land having a low opportunity cost, thus making it ideal for power generation.

Unfortunately, due to the isolation it also means a lack of meteorological data for these areas. The problem that arises from this is how to obtain representative data on a long term basis. The obvious solution is to erect towers and recording equipment throughout these areas and record wind speeds. This solution is not feasible for several reasons:

(i) Areas to be covered are extensive and by their definition, isolated.
(ii) Maintenance of equipment would be a major problem.
(iii) Data needs to be collected for a long period.

The last reason is, in itself, condemning because we cannot afford to wait 5-15 years for long term data for specific sites.

The methodology outlined here overcomes the physical problems and allows an assessment of winds for the past 10-20 years.

Satellite imagery is now widely accepted as a tool for earth resource applications. Repetitive coverage and a broad perspective make satellite imagery particularly effective for regional studies. If resolution is a limiting factor, aerial photography can provide supplementary details.

Most Eolian landforms can be identified and mapped from aerial photography Large Eolian features and groups of features are readily identified from landsa imagery.

However, before this technique can be used, extensive experience in analysis of this data is required. R.Marrs and J. Marwitz of the University of Wyoming are conducting research in this methodology. Marrs and Marwitz (1977) have chosen a site in central Wyoming as a test site, where they propose to analyse this area from aerial photography and check their conclusions by conducting a programme of field measurements. The process will initially be iterative, culminating in correct predictions of wind flows and relative strengths. This gaining of experience will obviously take some time, but in the long term, will certainly be quicker, less expensive and far more general than any field programme could ever be. It is not intended to take the place of field testing, as there is obviously a place for both methods of WECS site selection. It is proposed that the Eolian geomorphology will be used as an initial site selection method, following which detailed site measurements would be made leading to the selection of a suitable site.

Research is still needed to improve the quantitative estimates of wind characteristics from Eolian features, and give a better understanding of many

of the wind landform interactions. Sand dunes are a feature used by Marrs and Marwitz (1977) in their Eolian landform analysis. Wind performs two kinds of erosional work; loose particles might be lifted in the air or rolled along the ground (Deflation), or the wind hurls particles against exposed surfaces (Abrasion). A landform produced by deflation is a shallow depression called a 'blowout'. These can be anything from a few metres to several kilometres in diameter and are usually only a metre or so deep. The formation of a 'blowout' is sketched in Fig. 2.20. The shape of sand dunes can also be used to demonstrate high wind speed areas, and naturally, as the sand dunes develop in windy areas, they become elongated in the along-wind direction, as shown in Fig. 2.21.

There are several other features which can be used to infer wind characteristics. Snow drifts and snow accumulations behind barriers form in response to winter wind patterns; soil moisture patterns often record wind flow patterns in individual storm systems. Vegetation patterns, i.e,, wind swept trees, often reflect the effects of wind either as indirect indicators of soil moisture or as vegetation communities where species and conformation of plants is controlled by the wind.

2.2.2 Biological Wind Prospecting

The term 'prospecting' as used in this heading, could be misleading in that a large element of chance is usually associated with this word. In this methodology, there may exist a small amount of chance, to be explained later, but basically it employs a scientific approach.

The objective of this new methodology is to develop techniques for selecting sites for utilisation of wind energy. Five different indices of wind effects on trees have been developed and are being calibrated in terms of various wind characteristics. The five indices are:

1) Eccentricity (E): An indicator of the departure from circularity of the trunk of a tree. The calculation of this is shown in Fig. 2.22.
2) Shape Index (S): A measure of the relative influence of wind on the radial and apical trunk growth. The ratio is calculated by dividing the circumference of the tree at 1.5m by its height.
3) Griggs-Putnam Type Deformation Rating (G): A subjective rating scale similar to that developed by Putnam (1948) and Yoshino (1973). Each tree is given a rating based on the characteristics of its wind deformation, as shown in Fig. 2.23. Class F is pure mechanical damage.
4) Deformation ration (D): An indicator of the degree of wind induced flagging of a tree. A ratio of angle α (the angle between the crown and

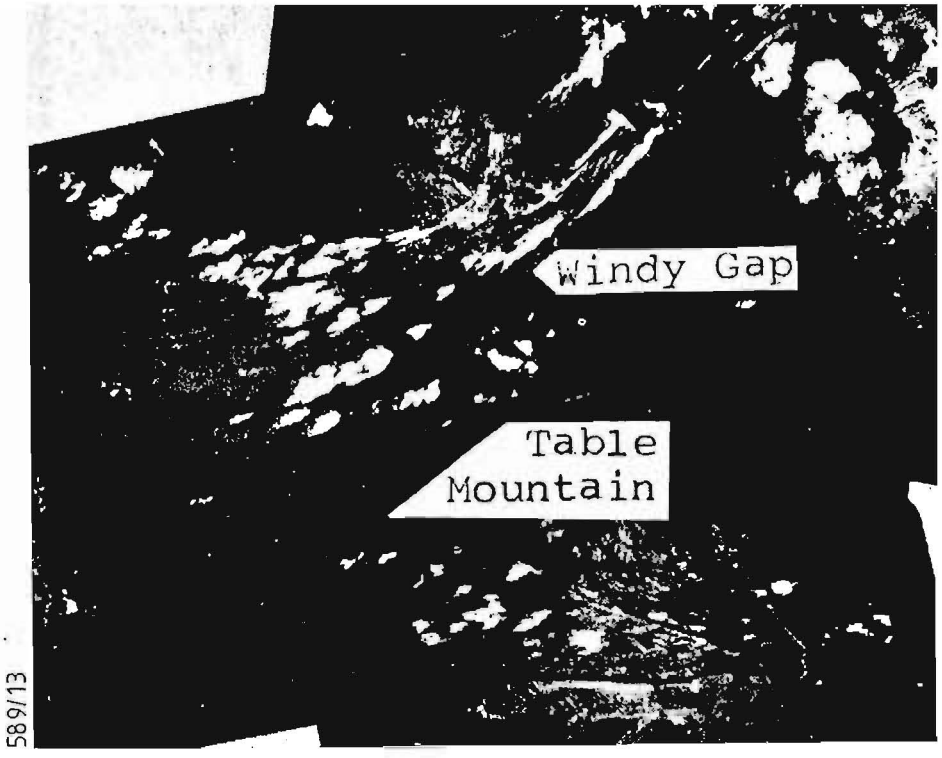

FIG 2·21 WIND FLOW ANALYSIS FROM SAND DUNE PATTERNS

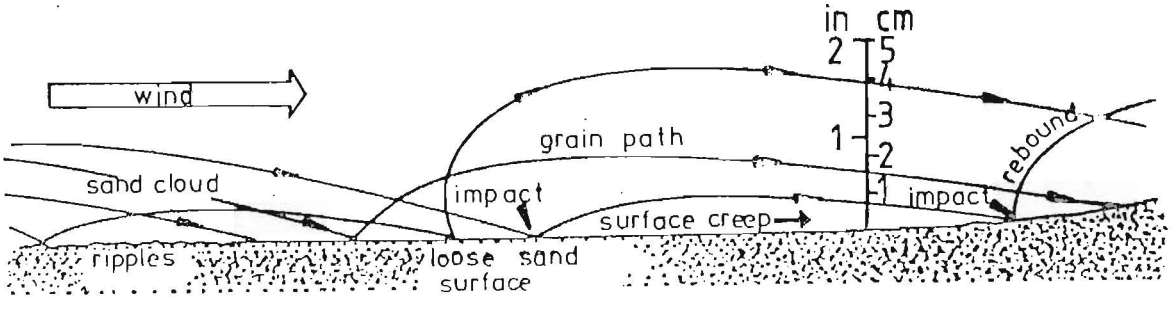

FIG 2·20 FORMATION OF PLAYAS (BLOWOUTS)

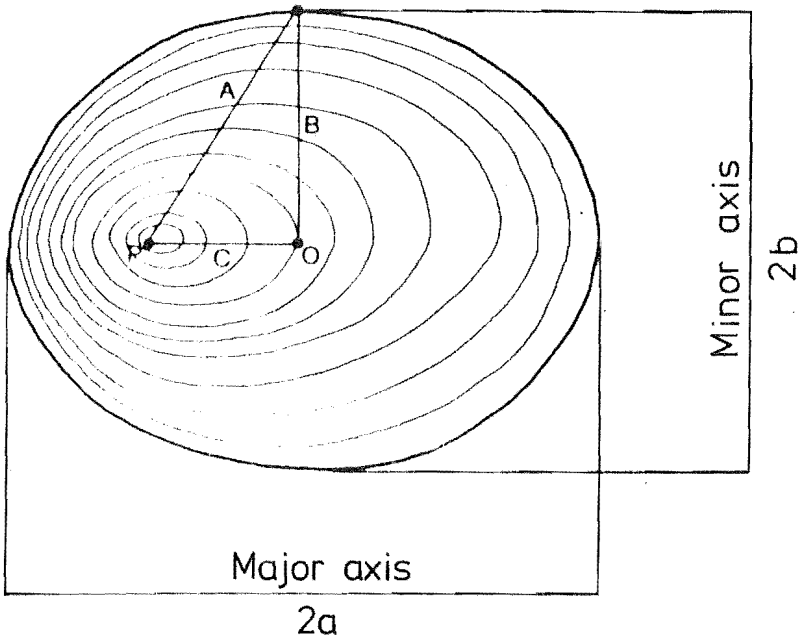

P = pith or core
0 = centre

$$E = \frac{C}{A} \quad C^2 = A^2 - B^2$$

$$E = (A^2 - B^2)^{1/2}/A$$

FIG 2·22 THE METHOD OF DETERMINING THE ECCENTRICITY OF THE TRUNK OF TREE FROM THE OUTSIDE INVOLVES MEASURING THE LENGTH OF THE MAJOR AND THE MINOR AXES WITH TREE CALIPERS.

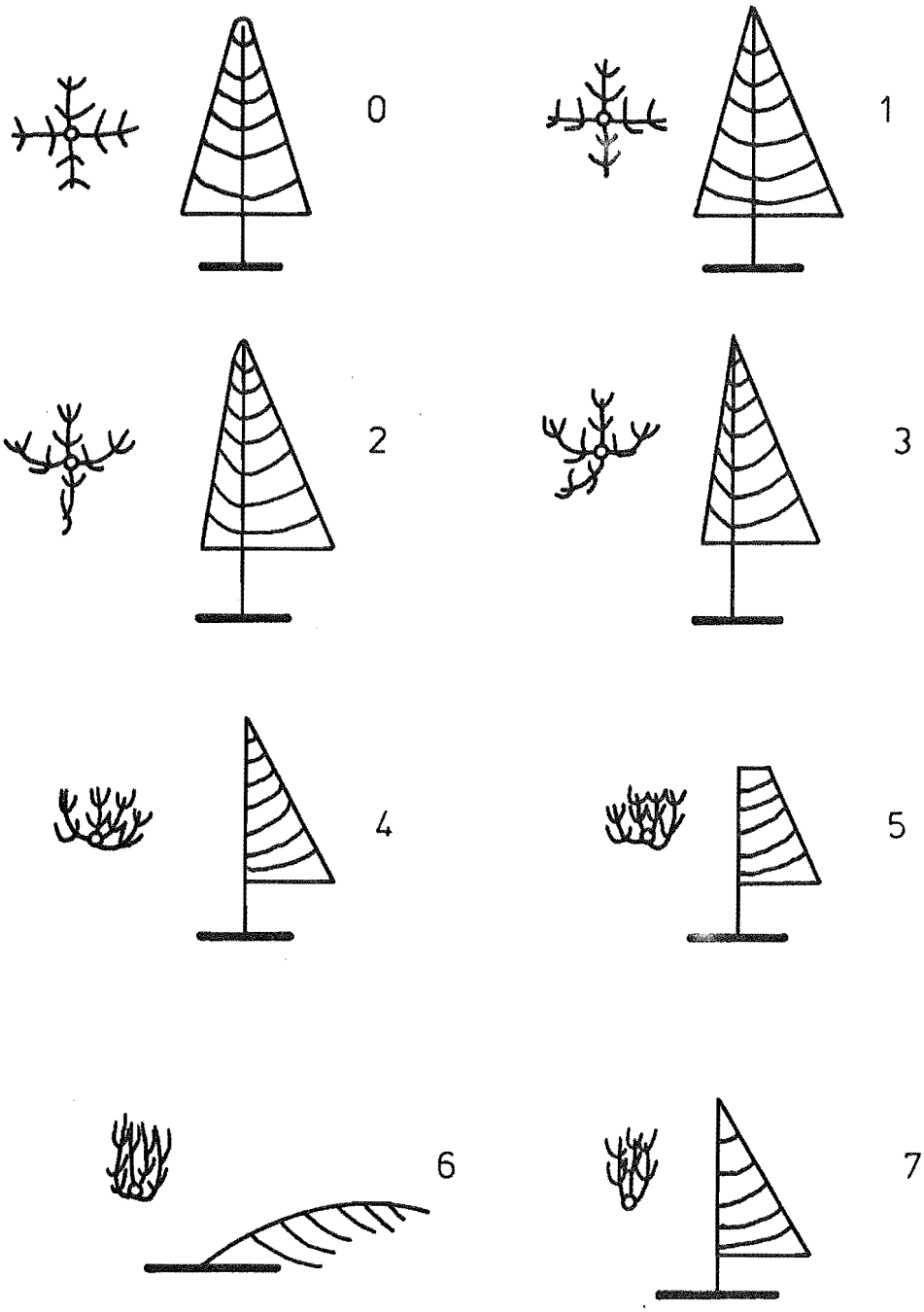

FIG 2·23 A REPRESENTATION OF THE RATING SCALE BASED ON THE SHAPE OF THE CROWN AND DEGREE OF BENDING OF TWIGS, BRANCHES AND THE TRUNK. CLASS 7 IS PURE MECHANICAL DAMAGE.

the trunk on the leeward side of the tree) and β (the angle between the crown and the trunk on the windward site of the tree) is calculated.

$$D = \frac{\alpha}{\beta}$$

This is shown in Fig. 2.24.

5) Compression ratio (C): An indication of the influence of the wind on the formation of reaction wood. This effect is shown diagramatically in Fig. 2.25. The ratio of leeward to windward growth is the compression ratio. It is a simple matter to plot the compression ratio against time to determine the steadiness of the wind over long periods, a typical plot is given in Fig. 2.26.

At several of the test sites, wind velocities are being recorded continuously so that correlations can be made between wind speeds and the facto outlined. It is obvious that a reasonable period of time will be required for experience and a sufficient amount of data to be collected before accurate predictions of wind velocities can be made.

Developments are under way to use vegetation other than trees for analysis. This has to be considered because of one very simple fact - not all areas of interest are "blessed" with trees.

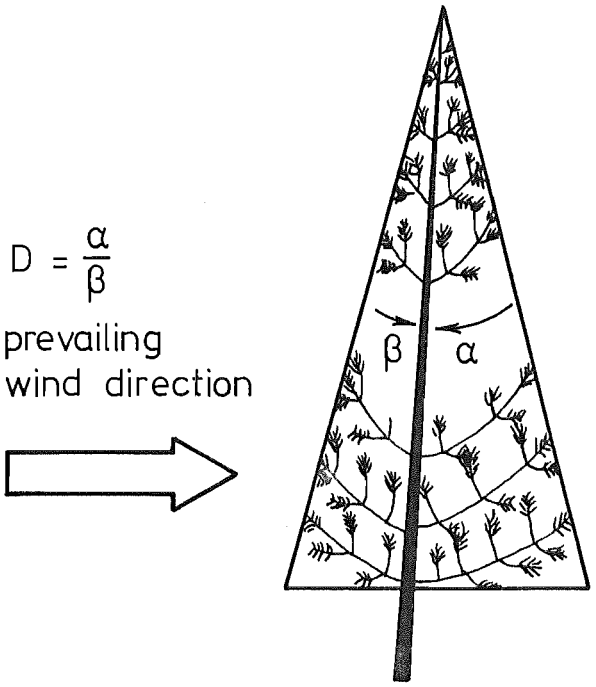

FIG 2·24 THE DEFORMATION RATIO IS BASED ON THE DEGREE OF FLAGGING OF THE CROWN.

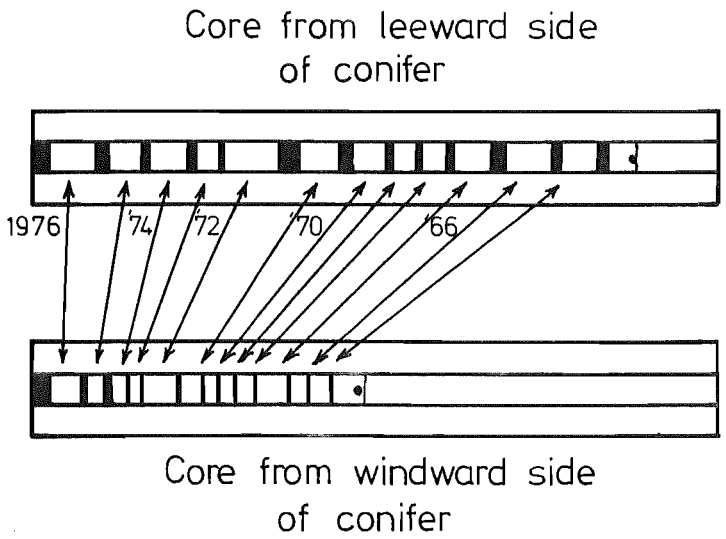

FIG. 2·25 CORES FROM EACH SIDE OF THE TREE ARE CAREFULLY CHECK– AND CROSS DATED.

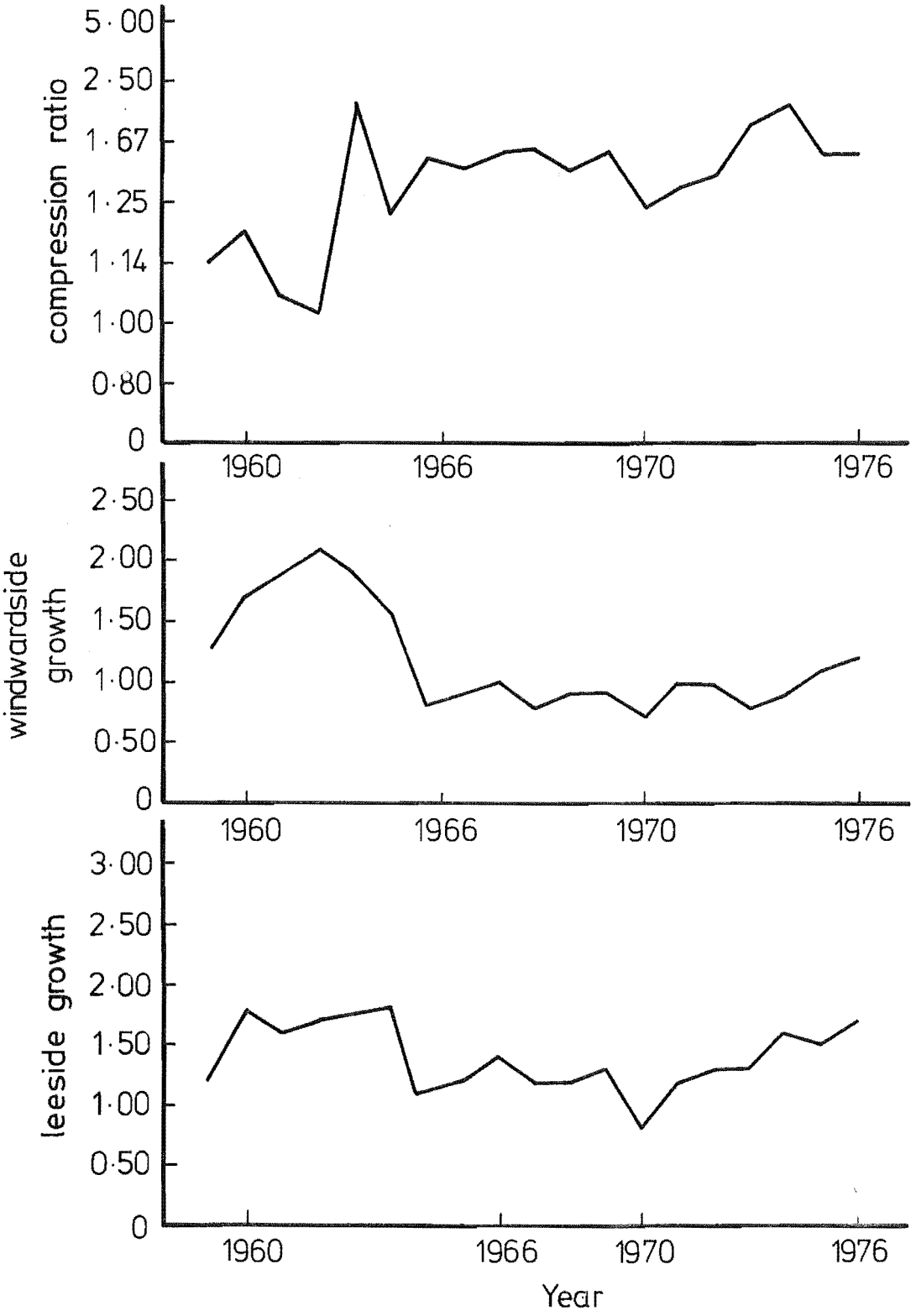

FIG. 2·26 THE COMPRESSION RATIO IS CALCULATED BY DIVIDING THE GROWTH ON THE LEEWARD SIDE OF THE TREE BY THAT ON THE WINDWARD SIDE FOR EACH YEAR. THIS RATIO CAN LATER BE COMPARED TO AVERAGE WIND SPEED FOR EACH YEAR.

CHAPTER 3

TERRAIN AND WIND CHARACTERISTICS OF THE GEBBIES PASS REGION OF NEW ZEALAND

3.1 GEOLOGY

A brief description of the geological history of the Banks Peninsula region will be given, as this provides a partial explanation for the rough nature of the terrain in the region.

In terms of the international geological time scale, New Zealand is a "young" country. It has rocks dating back 700 million years which is almost insignificant in comparison with some countries where rocks dating back as far as 3000-4000 million years have been found. The period of interest for the Banks Peninsula dates back approximately 75 million years; this is referred to as the Cenozoic era, as shown in Table 3.1.

The geological history of New Zealand is basically made up of a series of depositional phases and orogenies. This results in a changing pattern of land and sea; suggested stages leading up to today's coastline, given in Wards (1976) are shown in Fig.3.1.

During the Miocene era, Figs 1(c) and 1(d) on Fig.3.1, the land started to rise and the sea began to retreat as a result of preliminary earth movements of the Kaikoura orogeny. Volcanism became widespread in the North Island but was isolated to the volcanic centres of the Otago and Banks Peninsulas in the South Island.

Near Christchurch, eruptions of rhyolite followed by andesite started the Banks Peninsula volcanic complex, the development of which was mainly completed by the end of the Miocene era.

In the Pliocene era, the final eruptions on Banks Peninsula took place; these were of andesite and basalt. This brings us to the Quaternary period, which can, in the geological scale of time, be considered as present day. No major geological changes on the Banks Peninsula have taken place during this period; today's formations are the result of the interaction of weather and terrain during the last one million years.

A map of Banks Peninsula is given in Fig.3.2; Gebbies Pass is on the western side of the Peninsula and its axis is along a North-East/South-West line. To the North-East (NE) the area opens on to the Lyttelton Harbour inlet, which provides a fetch of 5 km in a NE direction and is 4-5 km wide.

MILLIONS OF YEARS	ERA	PERIOD	EPOCH	N.Z. EVENT
0	CENOZOIC	QUATERNARY	HOLOCENE	KAIKOURA OROGENY
			PLEISTOCENE	
		TERTIARY	PLIOCENE	
			MIOCENE	
			OLIGOCENE	DEPOSITIONAL PHASE
50			EOCENE	
			PALEOCENE	
	MESOZOIC	CRETACEOUS	UPPER	
100			LOWER	RANGITATA OROGENY
150		JURASSIC	UPPER	DEPOSITION IN NEW ZEALAND GEOSYNCLINE
			MIDDLE	
			LOWER	
		TRIASSIC	UPPER	
200			MIDDLE	
			LOWER	
250	PALEOZOIC	PERMIAN	UPPER	
			LOWER	
300		CARBONIFEROUS		TUHUA OROGENY
350		DEVONIAN	UPPER	DEPOSITIONAL PHASE
			MIDDLE	
400			LOWER	
		SILURIAN		
		ORDOVICIAN	UPPER	
450			MIDDLE	
			LOWER	
500		CAMBRIAN	UPPER	
			MIDDLE	
550			LOWER	
600	PRECAMBRIAN			?

TABLE 3·1 INTERNATIONAL GEOLOGICAL TIME SCALE

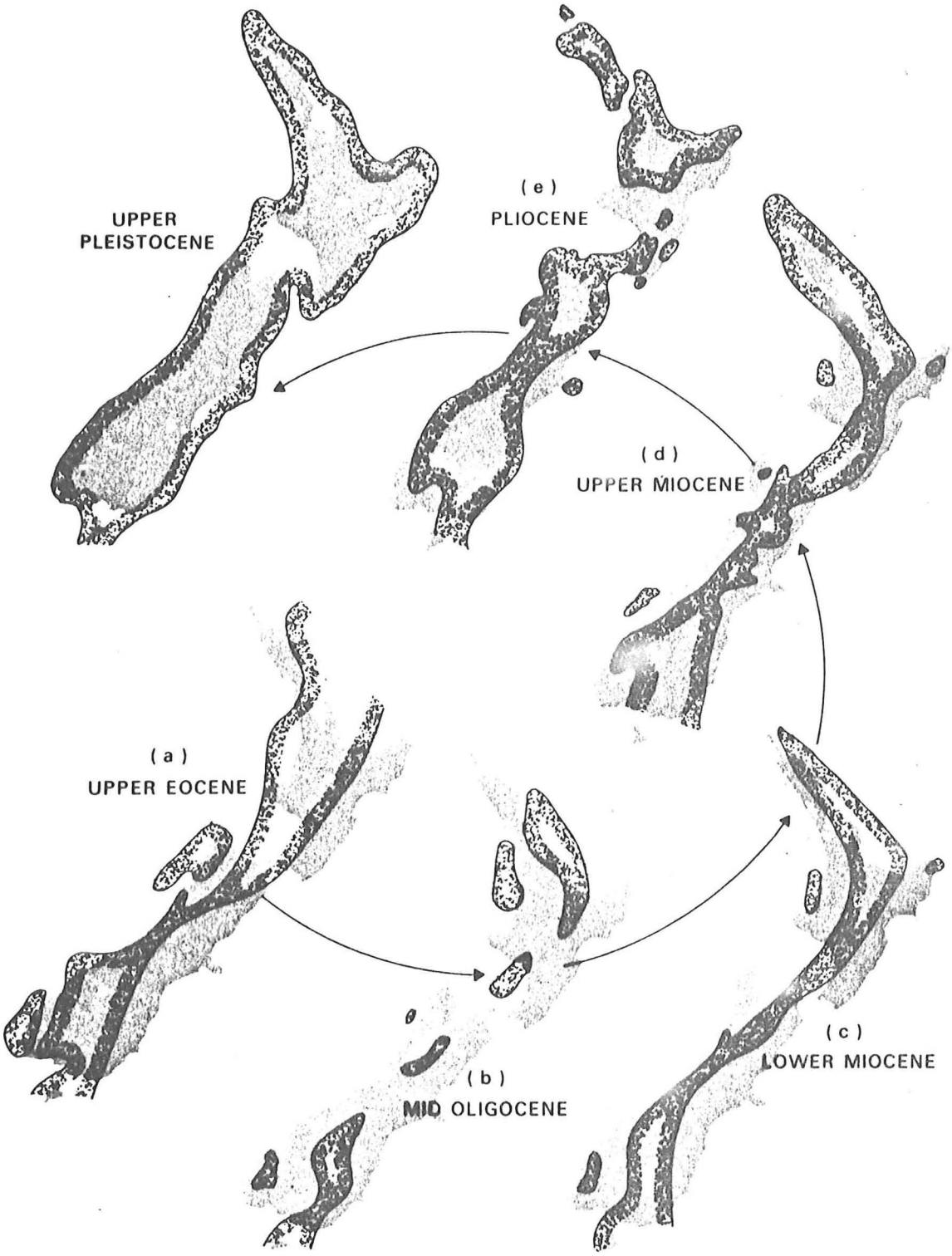

FIG 3·1 THE DEVELOPMENT OF NEW ZEALAND'S COASTLINE.
(after Wards)

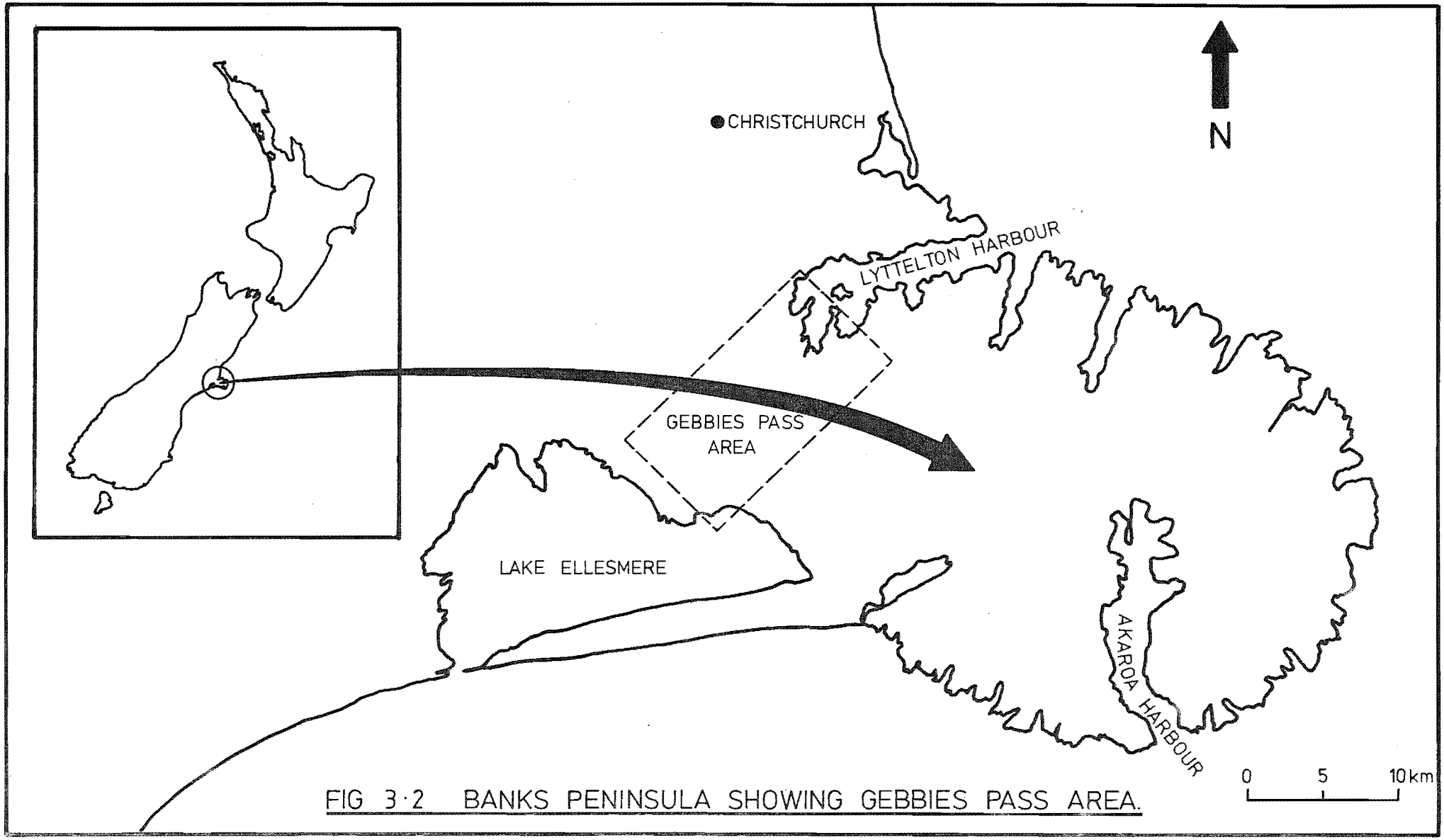

FIG 3·2 BANKS PENINSULA SHOWING GEBBIES PASS AREA.

A sketch of the area detailing the major terrain features is given in Fig.3.3 and an aerial photograph taken from a point north of the region and at a height of 2000m, is given in Fig.3.4. To the west of the saddle lies the Port Hills range which is typically 400-500m high, peaking at Coopers Knob at 570m. The northerly face of these hills is approximately twice the gradient of the southern face. On the eastern side of the Pass there is another range which contains Mt Herbert, which is the most significant single terrain feature in the modelled area.

To the north of the saddle the terrain is of a rougher nature than on the southern side. The other feature to note is that on the northern side, only the Port Hills effectively converge on to the saddle. However, for southerly winds, both the Port Hills and the Mt Herbert range converge quite definitely on to the saddle. To complement the above description, a vertical aerial photograph of the region is presented in Fig. 6.1.

3.2 METEOROLOGY OF BANKS PENINSULA

The effect of the "Roaring 40's" means that westerly winds prevail in all seasons in New Zealand. This flow is subject to considerable local modification, particularly in the South Island, as it passes over mountainous terrain. The result of this is that the Banks Peninsula area receives a predominance of south-westerly winds. The one priviso is during summer when the effect of sea breezes is noted by the regularity of north-easterly winds.

On the Peninsula itself, NW winds, which are predominant in inland Canterbury, are often so modified by the local terrain that they lose their well-defined characteristics of strength and warmth, experienced in inland Canterbury.

The wind rose, Fig.3.5, shows the predominance of SW and NE winds as measured at Christchurch Airport, which is situated inland approximately 10 km from the Peninsula. Figure 3.6 was reproduced from Wards (1976); it shows the wind flow characteristics for the South Island of New Zealand, and also the SW, NE predominance of winds for the Banks Peninsula area.

3.3 MICRO-METEOROLOGY OF THE GEBBIES PASS REGION

There is no local data available specifically for the Gebbies Pass region. Radio towers are situated on the saddle and are soon to be instrumented with cup anemometers and data logger recording equipment. A 10m tower with a cup anemometer is situated to the south of the region but

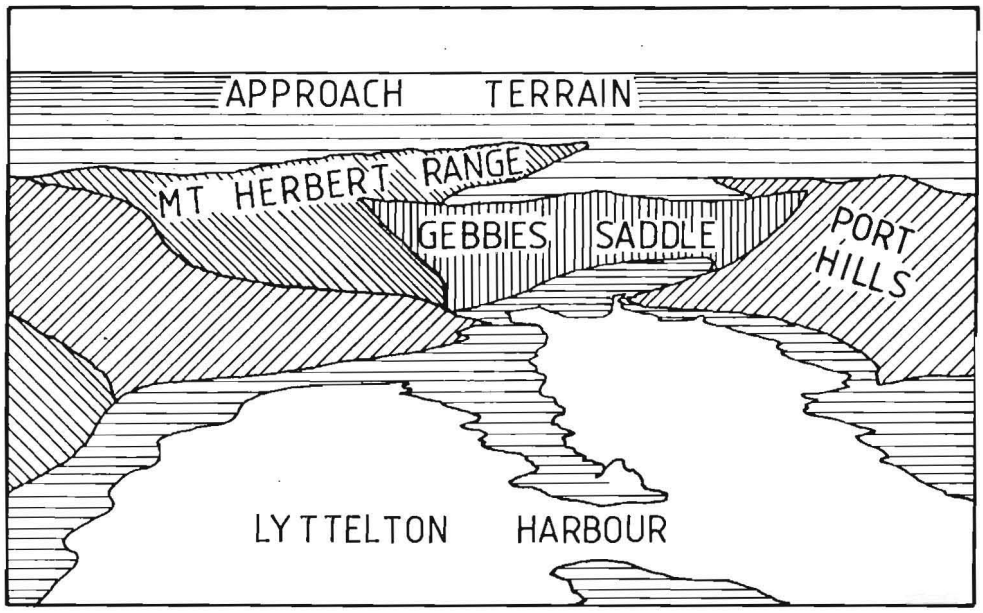

FIG 3·3 SIMPLIFIED DIAGRAM SHOWING MAJOR FEATURES OF MODELLED AREA

704/20

FIG 3·4 AERIAL PHOTOGRAPH OF THE GEBBIES PASS REGION (Altitude – 2,000 m: Position – N.E. of modelled region)

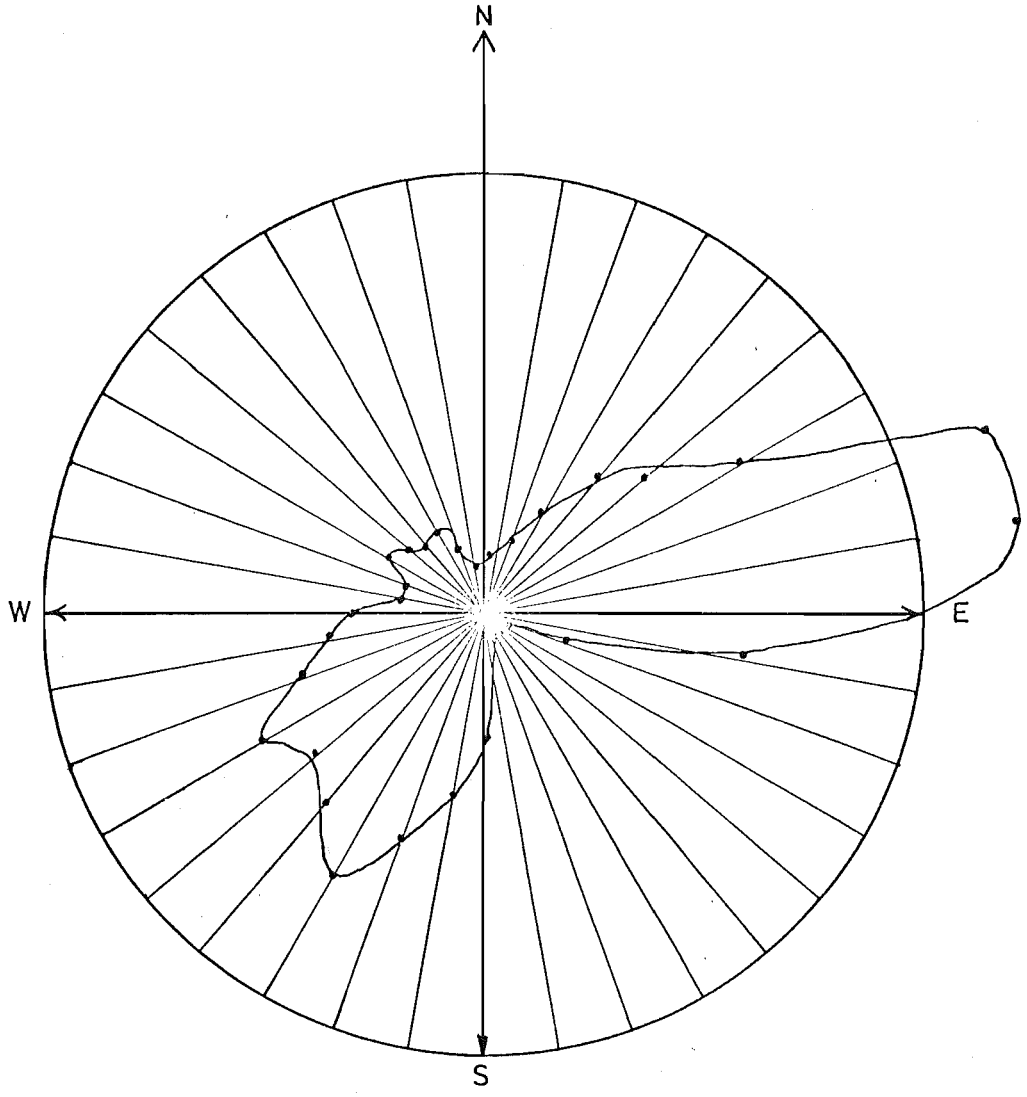

FIG. 3·5 WIND DIRECTION ROSE FOR CHRISTCHURCH AIRPORT.

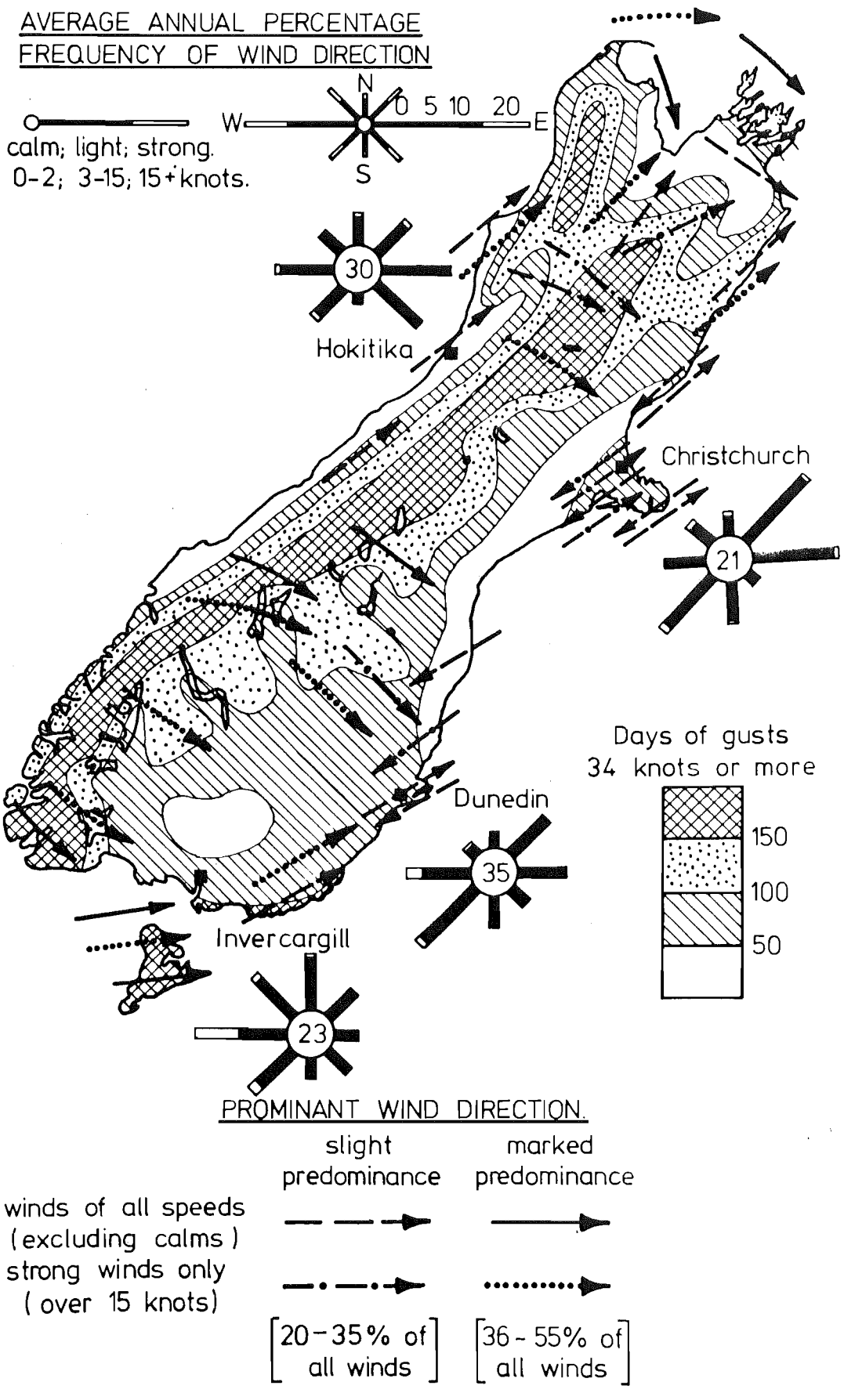

FIG 3·6 ANNUAL WIND FLOW CHARACTERISTICS OVER THE SOUTH ISLAND OF NEW ZEALAND (after Wards)

unfortunately, is of little value on its own.

A wealth of information was obtained from local inhabitants of the area, mainly farmers, who naturally are out on the terrain frequently. They were able to give details of wind directions, stagnation or sheltered areas, and areas of high wind velocities. Although this information had quantitative limitations, it was invaluable in giving the author a "feel" for the area. Much of this information was very localised and often did not correspond to suitable points for analysis. Many of the points suggested as high velocity areas were situated on ridges and hill tops, which one would expect intuitively. However, this additional information was a factor during the selection of sites for analysis.

CHAPTER 4

CRITERIA FOR LABORATORY SIMULATION OF WIND CHARACTERISTICS OVER IRREGULAR TERRAIN

When simulating wind characteristics over irregular terrain, it is essential that the two flow systems are thermally, dynamically, and kinematically similar. This means that after suitable adjustments of units of length, time etc., the equations describing the flow are applicable to both model and prototype.

4.1 BASIC EQUATIONS AND ASSUMPTIONS*

The basic assumptions and equations relevant to modelling of flow over irregular terrain have been outlined by Meroney *et al* (1978). They consider the following:

1. Equation of turbulent momentum transfer.
2. Continuity equation.
3. Equation of state.
4. Poisson's equation.
5. Equation of turbulent heat transfer.
6. Equation of heat transfer from the surface boundary.
7. Equation of turbulent scalar transfer.

These equations and their boundary conditions are reproduced from Orgill *et al* (1971) in Appendix I .

Meroney *et al* discuss the problem of obtaining similarity and suggest that to obtain surface-boundary similarity, the following are required:

a) Surface roughness distribution with "aerodynamically rough" behaviour;
b) topographic relief;
c) surface-temperature distribution;

and for approach flow characteristics similarity, the following are required:

*Taken in part from Orgill, Cermak and Grant (1971)

i) Distribution of mean and turbulent velocities;

ii) distribution of mean and fluctuating temperatures;

iii) zero longitudinal pressure gradient;

iv) if the flow is thermally layered, quality of the ratio of inversion depths is required.

They explain that it is impossible to simulate all of the parameters that they have discussed, many of which have not been included here because they have been shown by other authors, e.g. Raine (1974), not to be significant for topographical modelling. For example, it is not possible to maintain equal Reynolds numbers especially when scales as large as 1:4000 are being used. This simply means that one considers each modelling situation on its merits and models the parameters that theory and/or experience show to be the most significant, as well as giving consideration to the tests and measurements to be made.

One of the requirements suggested by Meroney *et al* for fully rough flow was

$$\frac{U_o L_o}{\nu} > 10^4 - 10^6 \quad \ldots\ldots\ldots\ldots\ldots\ldots\ldots\ldots \quad (4.1)$$

values for the Gebbies Pass model taken at the gradient height and 3mm above the surface are $(0)10^5$ and $(0)10^4$ respectively, thus satisfying the requirement.

Sutton (1953) suggests that the criteria to be met is represented by

$$\frac{u_* \lambda}{\nu} > 100 \quad \ldots\ldots\ldots\ldots\ldots\ldots\ldots\ldots \quad (4.2)$$

for the Gebbies Pass model the value of this term, assuming $\lambda \simeq 0.1$mm, $(0)10^3$. Measurement of λ is extremely difficult but experience would suggest that it lies in the range 0.05-0.2mm for the polystyrene material used for the model construction.

4.2 WIND TUNNEL MODELLING

The topic of wind tunnel modelling will be considered in two sections.

4.2.1 The Simulation of the Atmospheric Boundary Layer

A great deal of literature is available on the subject of the simulation of the atmospheric boundary layer, but unfortunately the vast majority of this data involves the simulation of flow over flat rural terrain or urban areas. Very little work has been documented on flow over complex terrain.

Cermak and Arya (1970) discuss the problems of simulating atmospheric shear flows and they also discuss modelling over topographical features. When considering mountainous terrain, they suggest that artificially

roughened surfaces produce better results by reducing the depth of the viscous layer. However, no mention is made of the construction materials being considered and therefore no quantitative use can be made of their suggestion. One of the aspects of the Gebbies Pass study is to consider the effects of the model surface roughness by studying the model in various states of construction. Cermak and Arya also suggest that in modelling of large areas of topography, again not clearly defined, one may, by necessity, have to exaggerate the vertical scale. However, this suggestion could be questioned in light of work by Nemoto (1961), which suggests that good similarity of the flow pattern is not obtained in such circumstances, particularly close to the surface.

Cook (1973) and Counihan (1973) produced simulations of urban adiabatic boundary layers which were found to agree well with parameter values given by ESDU (1972). The most interesting point from these studies was the approach adopted by Counihan. Instead of approaching the problem by asking ..."What can be used to produce turbulent eddies of some particular shape, size, etc?....", he said ... "How can a certain mean velocity profile and turbulence intensity distribution be produced?" (while still keeping the large scale turbulence required in mind). Hence, his approach was based on modelling the velocity profile and turbulence intensity profile and assuming that this would produce the required form of the complete spectrum. This was in fact, found to be the case.

One of the most useful papers to aid in the simulation of flow over complex terrain is by Counihan (1975) entitled: "Review Paper - Adiabatic Atmospheric Boundary Layers: A Review and Analysis of data from the period 1880-1972." This paper presents field data collected during this period and presents arguments and theories that various studies have developed, leaving the reader to draw his own conclusions from the data. This paper is very useful in providing data with which the wind tunnel simulation can be compared; however, there is an obvious lack of information for flow over complex terrain, and in these areas extrapolation of existing data has to be used.

Raine (1974) discusses the simulation of a rural boundary layer used in a study of wind protection by fences and this is significant because it was carried out in the facility to be used for the Gebbies Pass study. Nemoto (1961) and Raine discuss modelling similarity parameters in detail, Raine suggesting that the main parameters to be considered being:

$$\frac{z}{z_o}, \quad \frac{\sqrt{\overline{U_o^2}}}{\bar{U}_o}, \quad \frac{L_{u_{x_o}}}{z_o}, \quad \frac{U_o z_o}{K_m}, \quad \frac{\varepsilon z_o^2}{\bar{U}^2}, \quad \frac{\lambda_{go}\sqrt{\bar{U}_o^2}}{\nu}, \quad \frac{\lambda_{go}}{L_u}$$

The 'o' subscript denotes the value taken at a reference height. Most of these parameters are interrelated but the first four are the parameters with the most significance. Raine presents definitions and derivations for all of these terms, but only a brief description will be given here.

1. $\frac{\bar{z}}{z_o}$. This parameter requires the linear scaling of all features of the atmospheric flow in the same ratio as the model: prototype. Therefore, it follows that $\frac{z_{om}}{z_{oa}} = \frac{d_m}{d_a}$ etc.

2. $\frac{\sqrt{\overline{U_o}^2}}{\bar{U}_o}$. This is a non-dimensional turbulence intensity function. It should have the same value on the model, at the correctly scaled height, as found on the prototype.

3. $\frac{L_{u_{x_o}}}{z_o}$. This parameter indicates that integral length scales of turbulence must be scaled down according to the linear scaling ratio. Therefore,

$$\frac{L_{u_{o_x}}}{z_o} = \frac{z_{om}}{z_{oa}} = \frac{d_m}{d_a} .$$

The subscript 'a' and 'm' refer to prototype and model respectively.

4. $\frac{U_o z_o}{K_{m_o}}$. This is a turbulent mean flow Reynolds number, and related to the production of turbulence by the action of Reynolds stress on the mean velocity gradient. This parameter requires the correct scaling of:

(a) Mean velocity profile, i.e. $\frac{d\bar{u}}{dz}$.

(b) Reynolds stress profile, i.e. $-\rho\overline{uw}_z$.

The eddy viscosity, K_{m_o} can be related in terms of the Prandtl mixing length, ℓ, and the mean velocity gradient $\frac{d\bar{u}}{dz}$

$$K_{m_o} = \ell^2 \left| \frac{d\bar{u}}{dz} \right| \quad \ldots\ldots\ldots\ldots\ldots\ldots\ldots\ldots\ldots\ldots (4.3)$$

Now the mixing length is related to the integral scale of turbulence in the atmosphere

$$L_{w_x} \simeq 0.5z \quad \text{Pasquill (1961)} \quad \ldots\ldots\ldots\ldots\ldots\ldots (4.4)$$

$$L_{w_x} \simeq 0.4z \quad \text{Teunissen (1970)} \quad \ldots\ldots\ldots\ldots\ldots\ldots \quad (4.5)$$

Counihan concluded that L_{w_x} and z hold for the constant stress layer which can generally be taken as referring to the lower 30% of the boundary layer. Prandtl's derivation of the logarithmic mean velocity profile gives

$$\ell = 0.4z \quad \ldots\ldots\ldots\ldots\ldots\ldots\ldots\ldots\ldots\ldots\ldots\ldots \quad (4.6)$$

Thus, in considering the parameter $\frac{\bar{U}_o z_o}{K_{m_o}}$ the K_{m_o} term suggests correct scaling of the mean velocity gradient and of the length scales of turbulence. As explained above, this parameter will be most significant in the lower 30% of the boundary layer.

These are the most significant similarity parameters for this research and must be generated to produce an accurate model of the atmosphere. However, each modelling situation has to be considered individually because it is very difficult to allocate weightings to these parameters in a way that can be generally applied. Vickery (1965), for example, in considering dynamic excitation of a tall, flexible tower, suggested that the turbulent energy spectrum was the most important parameter and that the velocity profile was relatively unimportant. The research to be carried out for the Gebbies Pass region has the distinct advantage in that field equipment is available to evaluate the area with regard to velocity profiles, turbulence intensity profiles, length scales, energy spectra and Reynolds stresses. Unfortunately, the measurements will only reach 5-10% of the boundary layer height. This data, although limited, will then be used to set the wind tunnel characteristics to those of the prototype.

4.2.2 Topographical Modelling

This area of modelling has, unfortunately, received very little attention especially when one enters the area of complex topography. Golding *et al* (195: suggested that wind tunnel modelling of the topography at possible WECS sites should be made to determine the effects of various terrain features on the flow and structure of the wind.

A great deal of work has been conducted [Astley (1979), Deaves (1975/76), Hardy (1977), Mahrer and Pielke (1975), Taylor (1977)], on numerical analysis of two-dimensional flow over triangular hills, sinusoidal hills and bluffs. This work has been supported by two-dimensional wind tunnel studies, as reported in Table 1.1. Three-dimensional numerical modelling has been discussed by Freeman and Taft (1976); however, they suggest that one of

the most serious limitation of this technique is the very high cost involved, due to the enormous amounts of computer storage required. There was an upsurge in modelling of complex topography in the late 1950's to early 1960's, but since then little has been undertaken. With the need and interest in wind as a renewable energy source, a greater involvement in this area can be expected.

Studies of flow over complex terrain have been conducted; however, many of these have not combined the wind tunnel tests with extensive field measurements. One study that is considered particularly relevant to this research is the Rakaia Gorge study conducted by Meroney *et al* (1978). The wind tunnel phase of the study was carried out in the same facility being used for the Gebbies Pass research, so Meroney's simulation was extremely helpful and provided a basis for obtaining the correct simulation for this study. The scale used for the Rakaia model, 1:5000, was slightly smaller than the Gebbies Pass model, 1:4000.

The most important similarity between the two studies is the approach adopted to provide field data from an extensive area in a short period (one day).

The Gebbies Pass study is more detailed in the following ways:

1) wind tunnel tests and measurements were carried out more extensively;
2) detailed measurements of the structure of the wind to a height of 20m were made in the field;
3) the one day data collection programme was more extensive and the technique used was modified;
4) longer term data was collected at several sites;
5) some wind velocity measurements were taken to much greater heights. Rakaia - 10m : Gebbies Pass - 300m.

Therefore, the Rakaia study will be used in conjunction with those relevant studies from Table 1.1 as a 'yard stick' for the Gebbies Pass study.

4.3 LABORATORY CONSTRAINTS

The practical consideration, which often governs the degree of similarity that can be obtained, is that of the facility itself. The University of Canterbury has a boundary layer wind tunnel with a test section of 1.2m x 1.2m x 12.2m. Boundary layer depth and integral scales are controlled by a combination of square rod grid, fences and surface

roughness. Compared to many other wind tunnels, this facility is fairly basic, but as shown with previous investigations, the simulation required for topographical modelling can be achieved.

There are three parameters which cannot be simulated for this research.

1. Coriolis Parameter

Examination of the momentum conservation equation for atmospheric flow reveals the existence of a Coriolis body force term. This parameter is caused by the spinning motion of the earth and results in a flow direction variation with height, known as the Ekman Spiral. Below 100-150m, thiseffect can be neglected, but for heights above this, the Coriolis effect can be quite significant. Unfortunately, to model this parameter would be immensely difficult and well beyond the facility being used for this study.

2. Density Variations

The variation of density with height is a parameter which can be considered for modelling. Snyder, Britten and Hunt (1978) present results of flow around a hemisphere for stratified conditions, achieved using a fluid medium. Stratification of a liquid is difficult but possible to achieve. However, it is not possible to achieve this variation of density using an atmospheric wind tunnel Numerical models of stratified flow have been produced to evaluate flow régimes over large mountain ranges. Typically, these models are concerned with flow patterns extending up several kilometres.

3. Thermal Stratification

Wind tunnels exist which have the capability to produce a required temperature stratification. Unfortunately, the facility being used for the present study does not have this capability. Therefore, to reduce the significance of this problem, field measurements had to be taken whilst neutrally stable conditions existed. It is difficult to determine the existence of neutrally stable conditions in the field, the rationale used during this study being to ensure that the following conditions applied:

i) large amount of cloud cover (9/10 to 10/10) which reduces the amount of insolation;
ii) high wind speeds > 7 m/s which ensures that mechanical mixing predominates.

The net result of this limitation is that the field and wind tunnel

results are only applicable to neutrally stable conditions which are not a common occurrence over the prototype.

CHAPTER 5

WIND TUNNEL AND INSTRUMENTATION

The following section briefly discusses the wind tunnel facility and the associated equipment used during the modelling facet of the research.

5.1 EQUIPMENT

5.1.1 Atmospheric Boundary Layer Wind Tunnel

The atmospheric boundary layer wind tunnel used during this research was designed by Raine and Stevenson (1977) and built by the University of Canterbury Mechanical Engineering Workshops. A layout of the wind tunnel configuration in its modified form is given in Fig.5.1. Originally it was an open circuit "blower" type system; the fans are now downstream of the working section thus resulting in the tunnel operating below gauge pressure.

The wind tunnel working section is basically of wooden construction which is built up of flanged modules. This system provides ease of construction and maintains the possibility of lengthening the working section if required. One side of the working section is fitted with doors along its entire length, which are constructed with aluminium frames and 6mm thick perspex windows. The tunnel has a screen on the inlet behind which is a honeycomb section consisting of 6cm diameter, 25cm long cardboard tubes followed immediately by another screen. The flow then enters a settling chamber before passing through a contraction having a ratio of 1:2.5. This leads into a second honeycomb, 1cm diameter by 7.5cm long of aluminium construction. An adjustable square rod grid is situated downstream of the honeycomb and is used to generate the desired velocity profile and can also be used to generate turbulence. From the grid the working section is 12.2m long and 1.2m x 1.2m in cross-section; however, the roof is adjustable and can be raised to reduce the effects of model blockage and to ensure a constant velocity or pressure gradient. The rear side wall and roof have flush static pressure tappings in them which allow measurement of the longitudinal pressure gradient.

The existing system uses the Woods 48J½-2 fan arrangement with contra-rotation to reduce swirling effects. The air is drawn in through the working section on the ground floor of the building and then passes up to a mezzanine floor through the fans and is then discharged through a diffuser. The tunnel speed is varied with air pressure pitch control of

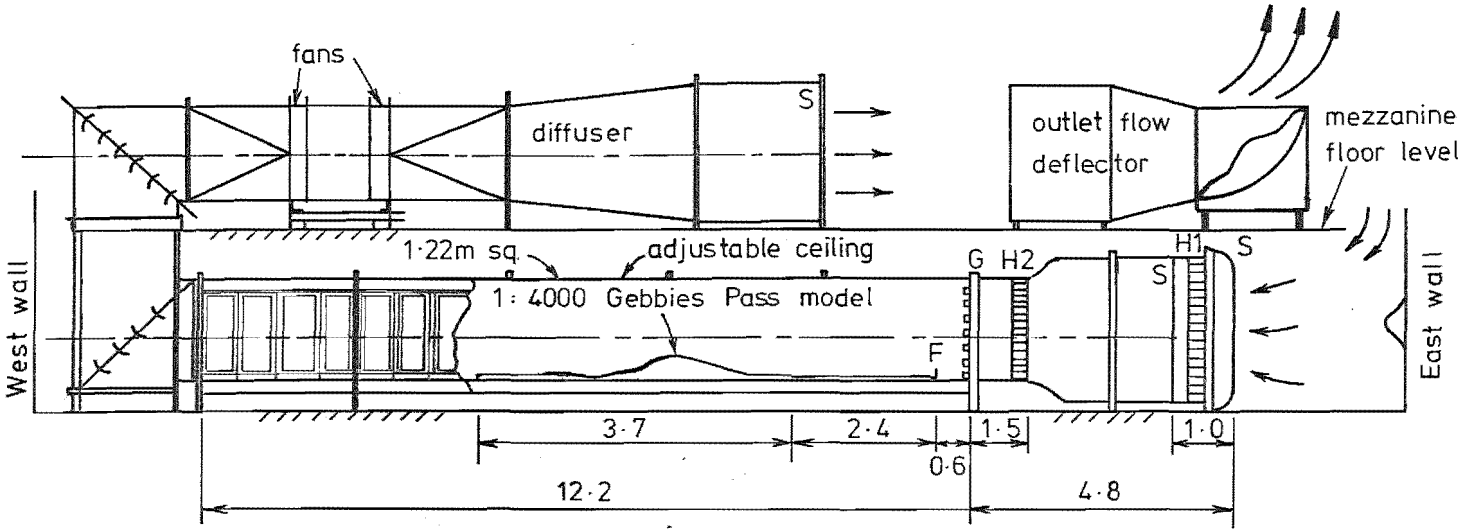

Dimensions are in metres

F: fence
1: 2·5 entrance contraction
S: screens

H1: honeycomb 6cm D. × 25cm
H2: honeycomb 1cm D × 7·5cm
G: grid 2cm × 2cm bars

FIG 5·1 BOUNDARY LAYER WIND TUNNEL, DEPARTMENT OF MECHANICAL ENGINEERING, UNIVERSITY OF CANTERBURY.

the fan blades.

The traverser system designed by Raine (1974) consists of a trolley mounted on a track below the tunnel floor. This is motorized and can travel the full length of the working section with a vertical arm projecting upward through a slot in the tunnel floor. To maintain pressure integrity, a 12.2m zip is mounted along the slot so that the traverser opens the zip ahead of itself and closes it behind itself. The vertical arm carries a horizontal arm which, via a D.C. motor and gearbox, can be moved up and down. The measuring sensors are clamped to the horizontal arm thus providing a longitudinal and vertical positioning capability. A sketch of this system is given in Fig.5.2. Lateral movement has to be carried out manually at present; this is quite a limiting factor for efficient use of the tunnel. The horizontal arm is steadied when in position by activating two air cylinders built into the ends of the horizontal arm. These clamp against the tunnel walls thus reducing sensor movement when taking readings.

The system has, to date, been sufficient for the type of work being undertaken. However, topographical modelling pinpointed some of the limitations of such a system.

5.1.2 Design and Commissioning of a New Traversing System

As described in the previous section, the traverser runs along the middle of the wind tunnel. This presents a major problem when topographical modelling is involved because it is necesssary to cut a section through the model to permit movement of the traverser. It is desirable to keep the number of cuts and joins on the model to a minimum because these features are major discrepancies when a geometric similarity is an important modelling parameter.

It was considered desirable that the sensor should be able to be remotely positioned in a lateral plane so that lateral positioning could be achieved without stopping the wind tunnel. This would also provide a better continuity to the tunnel tests.

The necessity for the system to be operational within a short period precluded a full design analysis approach to this problem.

Some guidance was found in Raine's work since he had made a brief analysis of several traversing options before selecting the present system. In addition to these, the following systems were considered:

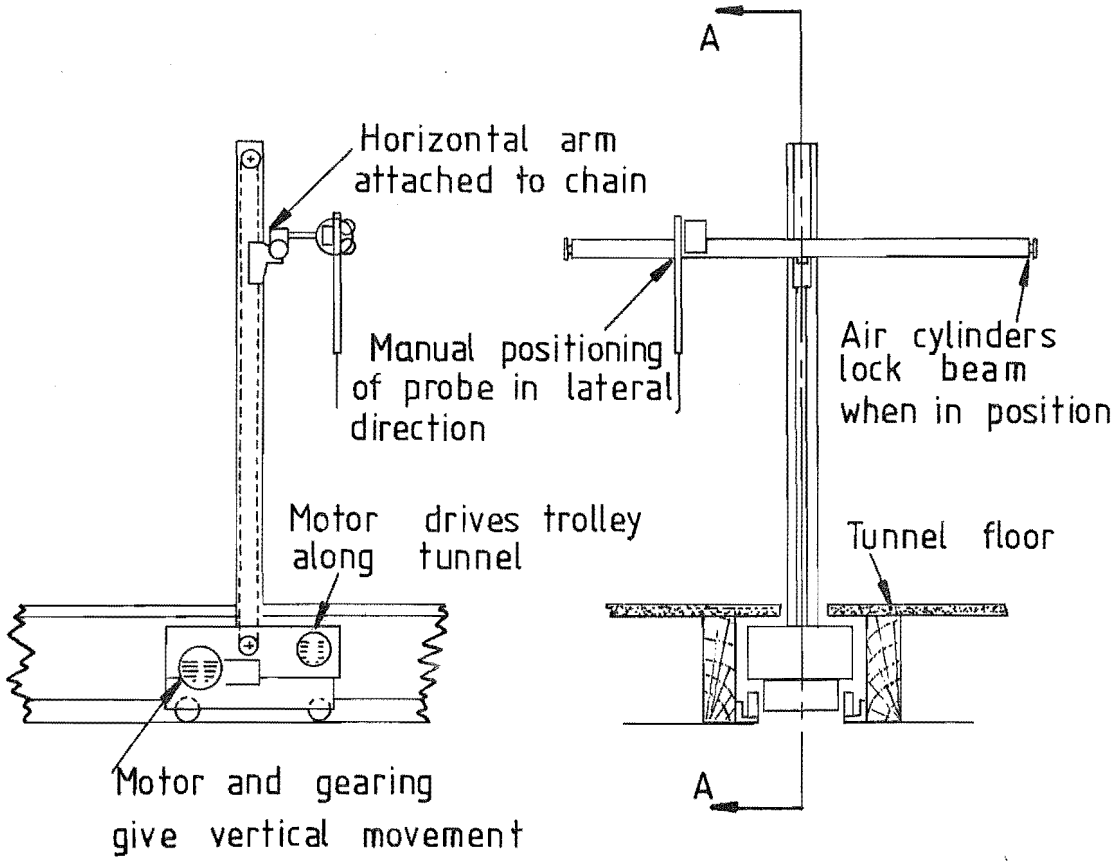

FIG 5·2 SCHEMATIC DIAGRAM OF THE EXISTING TRAVERSER

1. Screwed shafts with direct/indirect stepper motor drive.
2. Rack and pinion system with stepper motor drive.
3. Pulley system powered with stepper motors or D.C. motors.
4. Pantograph system for vertical movement combined with one of the preceeding options for lateral and longitudinal movement.
5. Combinations of 1-4.

The wind tunnel had recently be digitised; the output signals from hot wire anemometry could be connected "on-line" to the Department's HP2100A mini-computer and the data analysed. This facility will be described in Section 5.3.3. There were two long-term objectives also being considered at this stage:

i) A graphical plotter to be connected to the computer, thus plotting the results directly.
ii) The ability of the computer to control the positioning of the probe in the wind tunnel.

This factor was directly related to the design of the traversing system as it meant that a digital drive system had enormous long-term advantages over other systems. For this reason it was decided that stepper motors should provide the basic drive movement. These had the added advantage of ease of position feedback.

Consideration was given to the mounting of the traverser but the limitations of the tunnel construction meant that the roof was the only place through which a traverser could be mounted. However, major problems would be encountered with sealing such a system, so another design was sought.

The obvious solution to this problem was to locate the whole traverser inside the wind tunnel. The major problem to be overcome with this approach was to keep the cross-sectional area, and therefore the blockage, to a minimum whilst maintaining rigidity within the system. The resulting basic shape and degrees of freedom for the traverser are presented in Fig.5.3.

Measurements of the wind tunnel width showed a variation of 3-4mm from the mean value. This posed the problem of how to support the traverser. The design used is presented in Fig.5.4. It uses one rail as a datum and allows the other side to float, thus taking up the tunnel variations.

The resulting traverser is presented in the photographs in Fig.5.5.

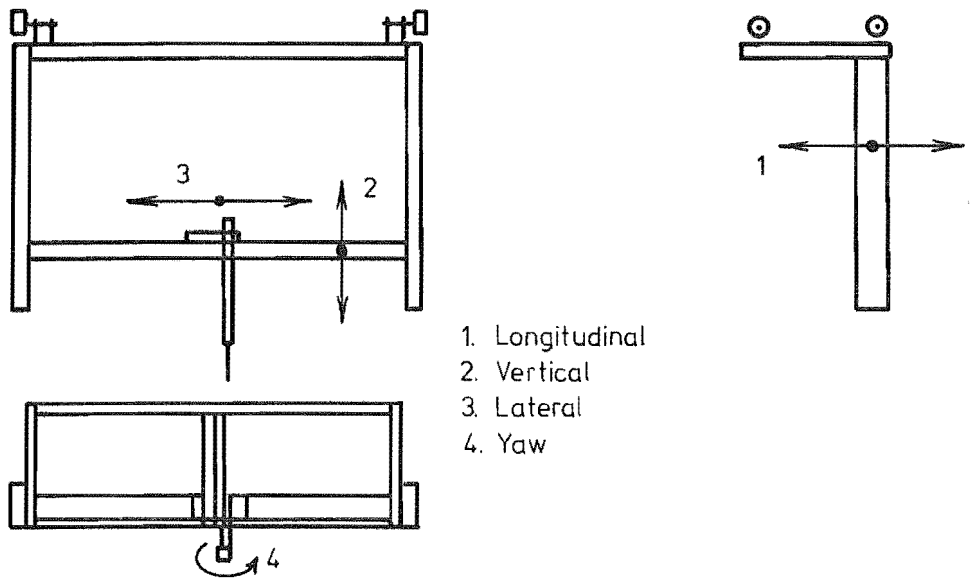

FIG 5·3 BASIC TRAVERSER MOVEMENTS

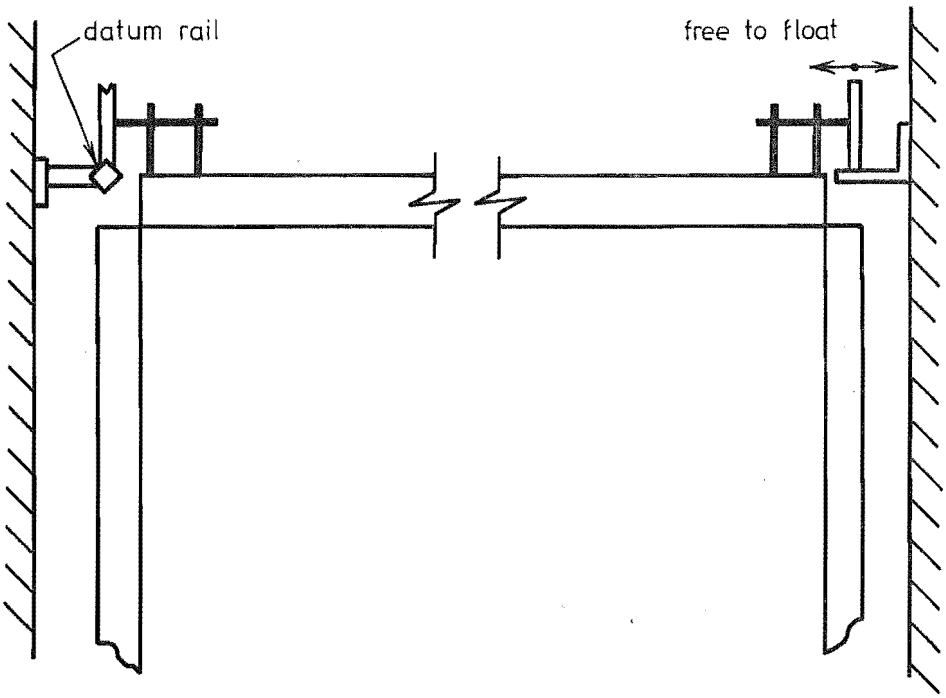

FIG 5·4 TRAVERSER SUPPORT RAILS

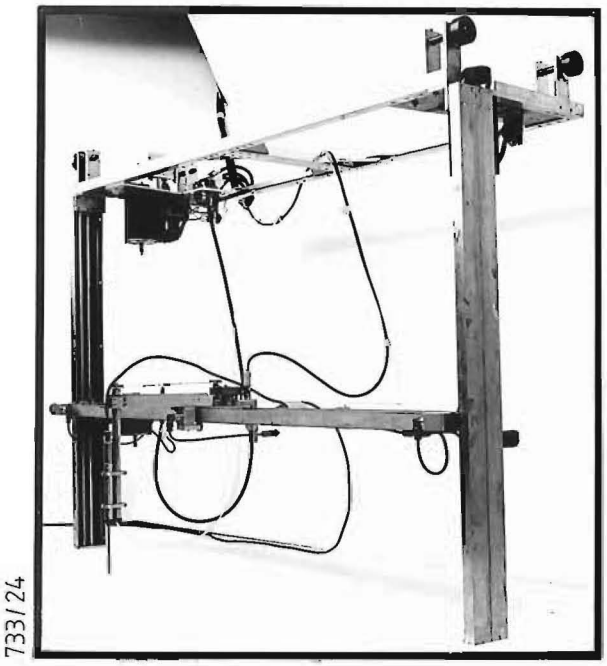

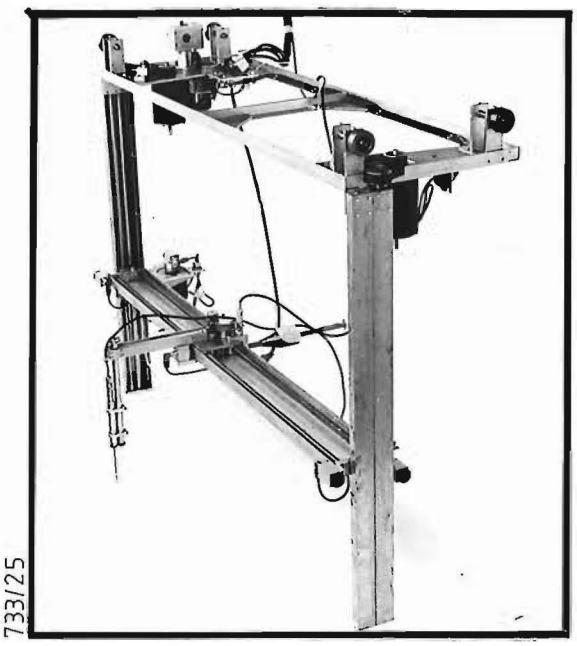

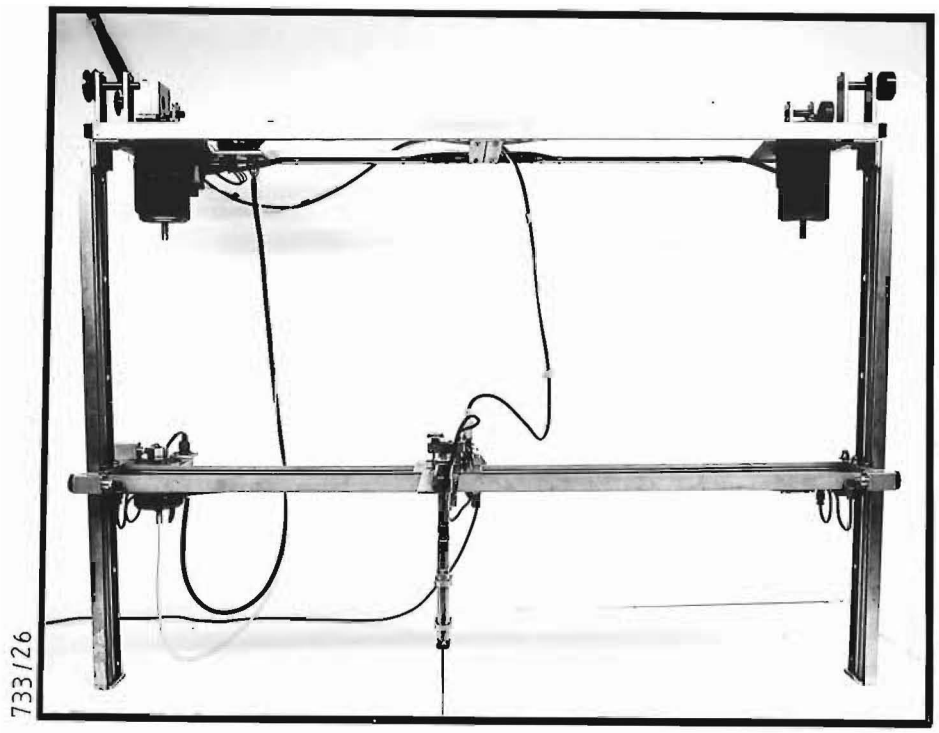

FIG 5·5 VIEWS OF COMPLETED TRAVERSER

Probe positioning was achieved by the following:

1. Longitudinal Positioning:

Movement along the tunnel working section is achieved by means of a variable speed controlled D.C. motor driving through a worm reduction unit to a sprocket. A chain, which is supported on the rail frames, runs the length of the working section and the sprocket runs in this chain. This system gives a positional accuracy of ±3mm. It is proposed that this system will be superseded with a stepper motor drive, thus providing an easier means of position feedback and digital control.

2. Vertical Positioning:

Movement of the horizontal beam in Fig.5.3 is achieved by means of two screw threads, one on each side, driven by stepper motors via timing belts and pulleys. With the stepper motors giving 200 steps per revolution and a thread pitch of 2.5mm, theoretically an increment of 0.02mm is possible. Tests showed that construction tolerances reduced the positioning accuracy to ±0.1mm.

3. Lateral Positioning:

Lateral positioning of the sensor uses a stepper motor driving a trolley which is set inside the main horizontal beam and is located on linear ball races. The connection between the motor and the trolley involves a model wire and capstan system. Positioning accuracy of the trolley is ±1mm.

4. Probe Yaw Positioning

This is achieved with a small stepper motor driving through a gearbox to a wire and capstan. This rotates a small spur gear which, in turn, rotates the probe. Fig.5.6 shows a photograph of this part of the traverser. The housing in which the probe holder fits was machined on an eccentric which allowed the backlash between the spur gears to be reduced to a minimum. The gearbox was necessary due to the large angular increments of the motor; 7.5 degrees. The final system produced a probe increment of 1 degree per motor step.

Controlling the stepper motors necessitated the design and building of electronic control boxes. Two motors, one on each side, provided the vertical positoning. These were both driven from the one controller thus ensuring that they both moved simultaneously. A block diagram of the circuitry involved is given in Fig.5.7. This part of the traverser is still at an elementary stage as feedback from the motors to the controller is still required. The same system, although driving only one motor, is used

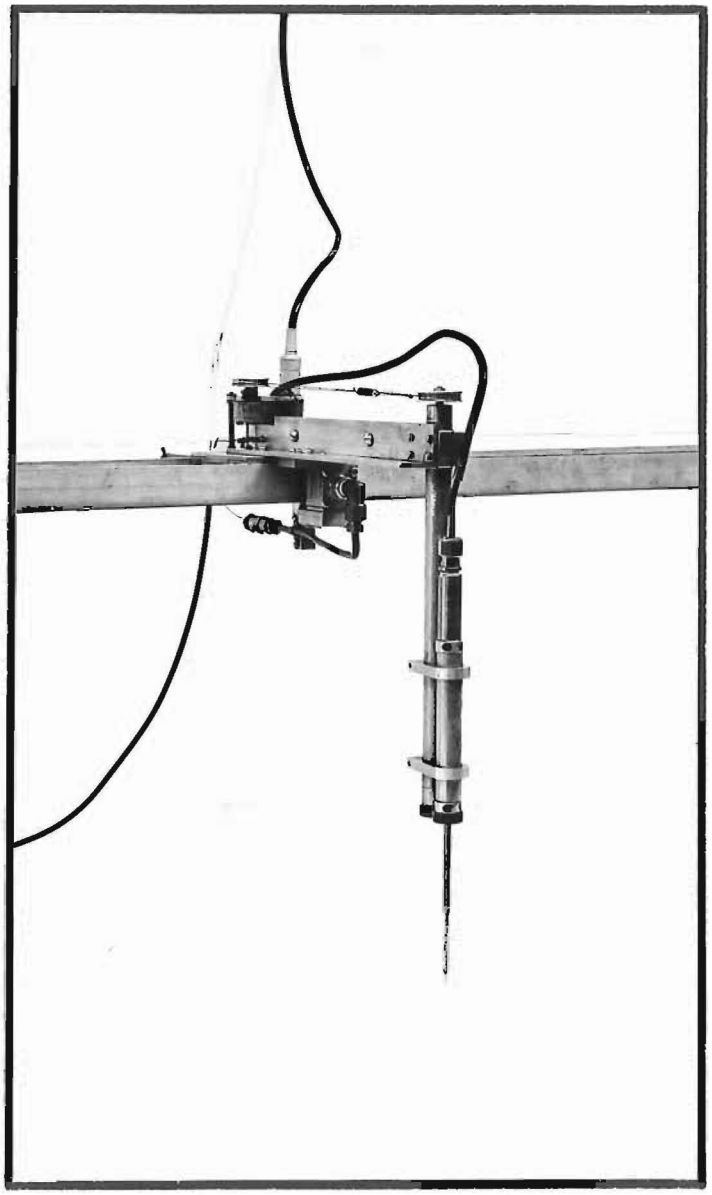

733/23

FIG 5·6 DRIVE MECHANISM FOR PROBE YAW

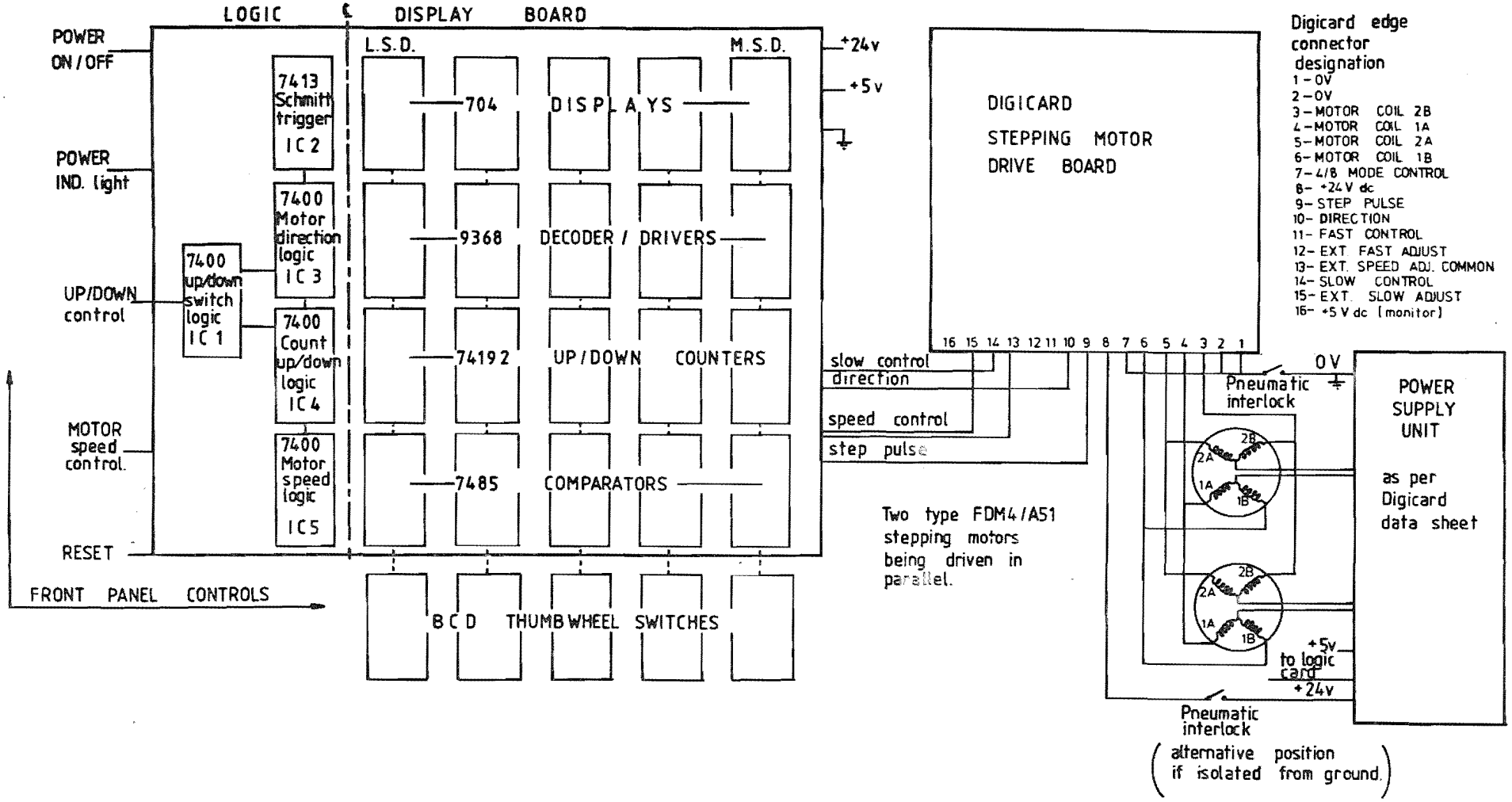

FIG 5·7 SCHEMATIC DIAGRAM OF STEPPER MOTOR CONTROL CIRCUITRY

for the lateral positioning stepper motor.

A mechanical cam system driving limit switches was used to provide pulses for the yaw positioning stepper motor.

5.2 TOPOGRAPHIC MODELS

5.2.1 Banks Peninsula Model

The Geography Department at the University of Canterbury lent a 1:63360 scale model of Banks Peninsula for preliminary tests. The model had a five times exaggerated vertical scale; the effects of vertical scale distortion have been discussed by several authors and are referred to in Chapter 2. The model was 1.2m x 1.5m and was constructed in a terraced form, i.e., built up in layers corresponding to contour lines.

These factors were not significant because this model was not used to produce quantitative results. Some basic flow visualisation tests were carried out to give a general idea of the flow régime over the Peninsula. The dimensions of the model meant that it could only be orientated to simulate easterly and westerly winds.

5.2.2 Topographic Models of Gebbies Pass

The area being modelled has been fully described in Chapter 3. It represents an area of approximately 143 km^2 which reduced on a 1:4000 scale model to an area 2.4m wide and 3.6m long. Since the wind tunnel is only 1.2m wide, the model was sectioned through the middle, this axis representing a NE to SW compass bearing.

Since SSW winds occur frequently in this region, it was desirable that this direction should also be modelled. This was achieved by cutting the model into several sections as shown in Fig.5.8. This clearly shows how the area was divided into three models.

New Zealand Lands and Survey maps S84 and S94, which had a scale of 1:63360, were used as the basis for the model construction. They were photographically enlarged to the 1:4000 scale by the N.Z. Printing Office. This process resulted in the map being reproduced on to stable photographic material. Initially it was intended that paper Ammonia prints would be taken to be used in the model construction. However, severe shrinkage problems were encountered which made accurate model building very difficult. To maintain the greatest accuracy possible, the photographic prints were used for model construction.

The original map had a contour vertical displacement of 75m which required model increments of 19mm. This was considered to be too coarse to be representative, so the contours were linearly interpolated, thus giving model increments of approximately 9mm representing 37.5m prototype increments.

The model base was 9mm thick chipboard, precut to the required shapes shown in Fig.5.8. These pieces were then screwed together leaving a gap of approximately 3mm between the cut faces.

The model was then built on top of the base using expanded polystyrene bead sheets. The contours were cut from the photographic material and traced on to the polystyrene sheet. After cutting several polystyrene contours, they were glued together using a P.V.A. glue. Experience showed that glueing more than five sheets together at a time produced drying problems.

When the model was complete it was cut into the required shapes using a hot wire cutting jig, shown in Fig.5.9. A guide fitted into the gap in the base board provided the correct alignment of the cuts.

The three models resulting from this procedure are shown in Fig.5.10 and will be referred to as Model A, Model B and Model C as shown in the Figure.

5.2.3 Terraced Model

A convention often applied by researchers involved in topographical modelling is to analyse the model in different states of construction. One of the reasons for this is the lack of information regarding the validity and quantitative use of the results obtained.

Therefore, in this research the tests were made with the models in different states of construction. The effects of terracing for complex terrain have been suggested to be a function of the type of model or the type of terrain under test.

Once a library of information of model construction requirements for different types of terrain is available, a researcher will be able to assess the type of model required for a particular terrain type. It is possible that the terraced model may fill one of the categories.

The terraced model was painted with a latex paint to protect and harden the surface and to provide a contrast for flow visualisation analysis.

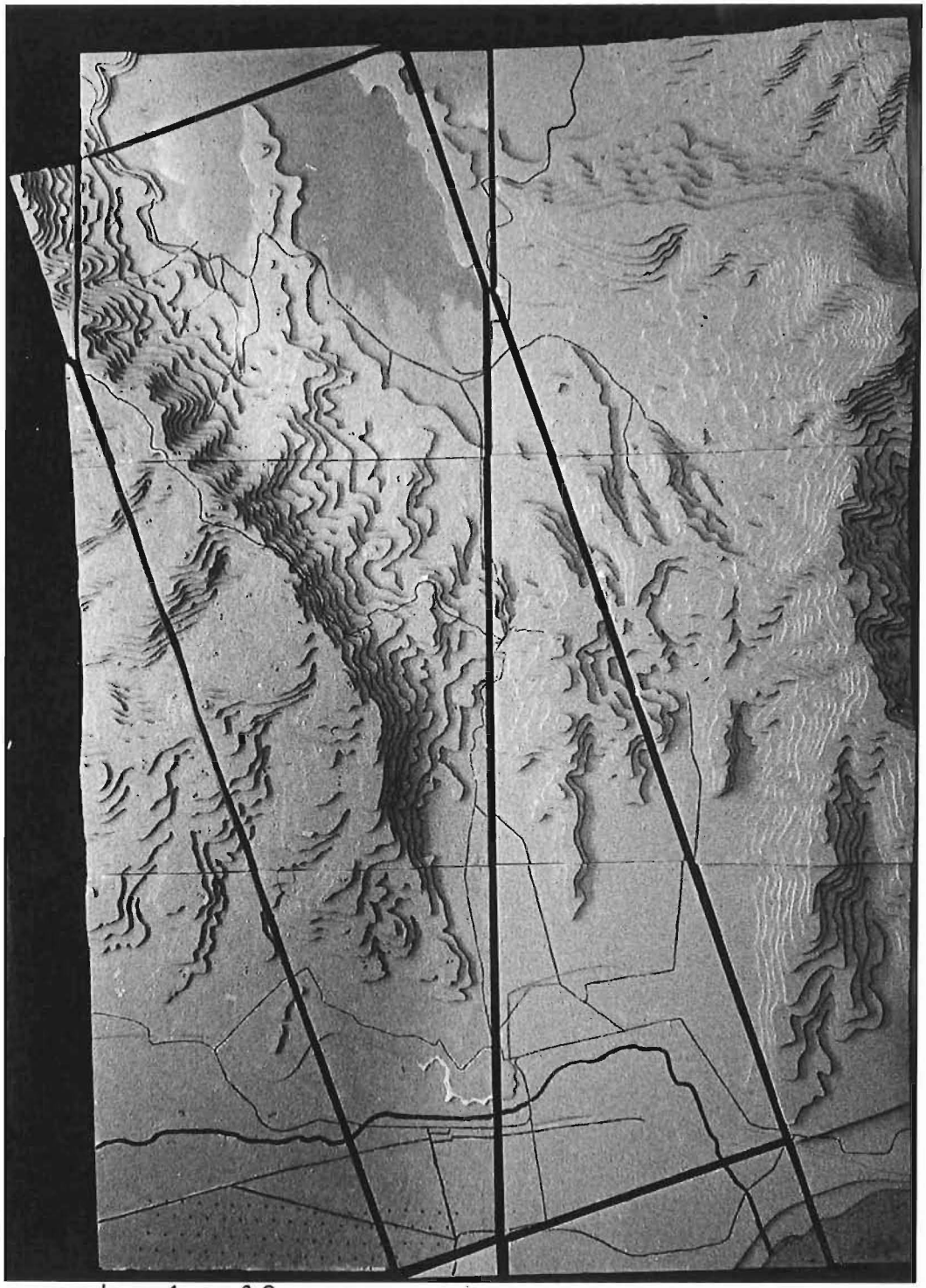

570137

scale: 1cm = 0·2 m

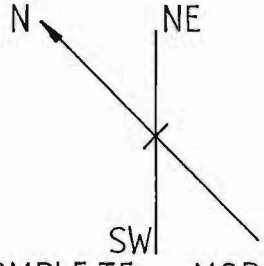

FIG 5·8 AERIAL VIEW OF THE COMPLETE MODEL OF GEBBIES PASS

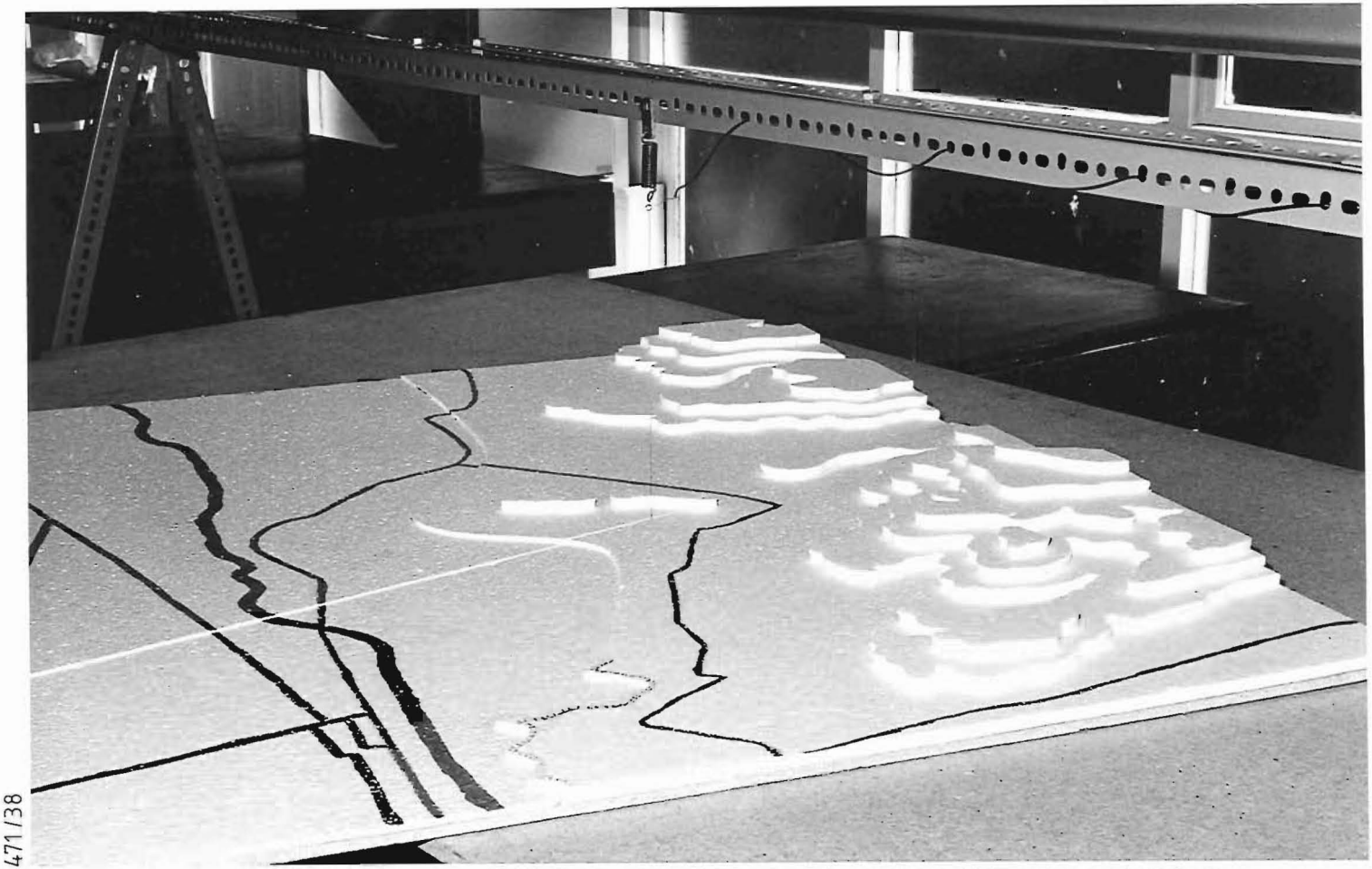

471/38

FIG 5·9 HOT-WIRE CUTTING RIG USED TO SECTION THE MODELS

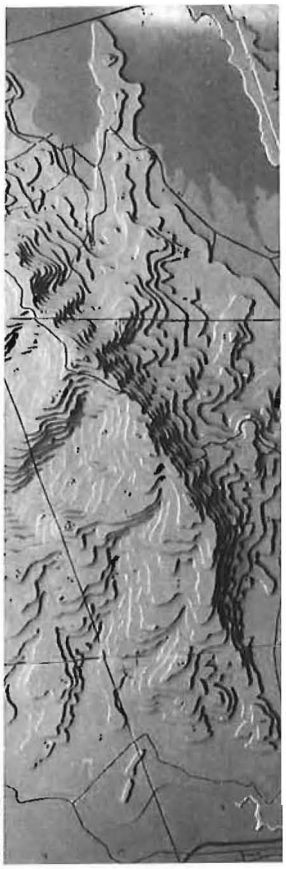

MODEL A

MODEL C

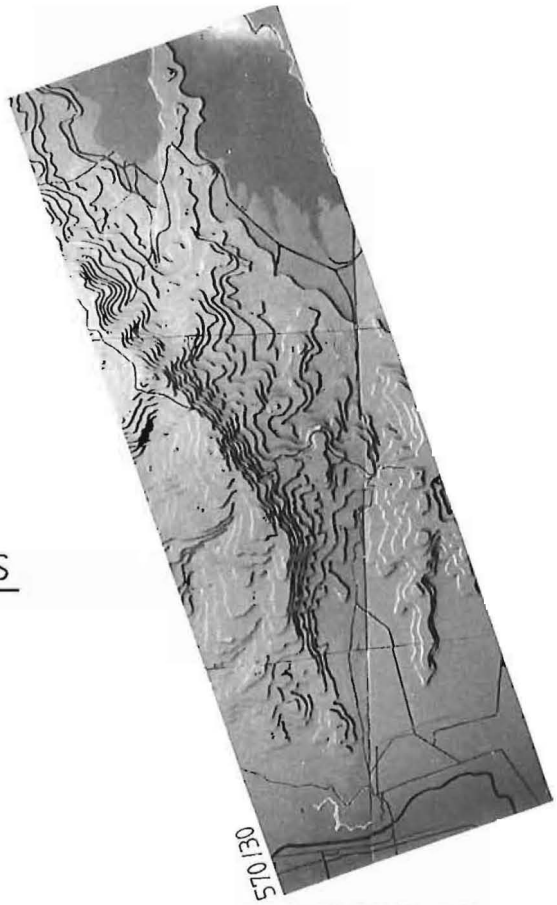

MODEL B

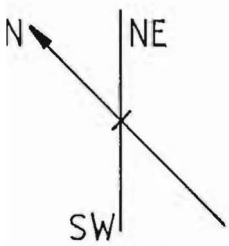

FIG 5·10 INDIVIDUAL MODELS SURVEYED

5.2.4 Contoured Model

After the model had undergone analysis in the terraced form, further constructional changes were made. This involved filling in the contours with a plaster filler material, the particular type used having the distinct advantage of being a non-shrink material which was also easy to work. To aid in this process the Gebbies Pass area was extensively photographed. This provided information not shown on the maps, such as ridge lines, knobs, valleys etc. After the filling-in process, the model was re-painted.

Consideration was given to the type of finish that should be given to the filler. Tests were carried out with variations of mix, ranging from a slimy to a fairly dry mix and using different sized tools for applying the filler. Measurements of velocity and turbulence profiles and roughness length were made above the filler with a smooth finish, spatula finish, and a stippled finish. These revealed that a standard mix of Polyfiller (recommended by the manufacturer) applied with a spatula gave results over a flat surface that were typical of rural terrain.

5.2.5 Roughness Added Model

Many of the small valleys and gullies in the region contain small trees and scrub. These were typically 2-5m high and the nature of the growth in several of these areas suggested that high wind speeds prevailed. This observation was based on the unconventional analysis methods as described in Section 2.2.2

Using photographs in conjunction with maps to locate these areas, roughness was added to represent this vegetation. Meroney *et al* (1978) evaluated two methods of representing shelter belts; they concluded that open stranded wool gave a good representation of established shelterbelts. On this basis it was decided to use this material for the shelterbelts on the Gebbies Pass model.

Modelling of the scrub areas was more difficult because no previous research involving scrub could be found. An intuitative approach was made to this problem. After a great deal of consideration, it was decided that a material called scrim should be used. This is a very open weave sacking similar in appearance to hessian. The rationale for using this was that it has about the right density of material per unit area (hessian was considered too dense), and is about the correct physical height to be representative of the prototype scrub. It was found that the use of double-sided cellotape provided a suitable means of attaching the material to the model.

5.3 FLOW FIELD MEASUREMENTS

Several methods were used to give flow field visualisation including

1. flags;
2. smoke;
3. polystyrene beads.

These techinques are described in this Section.

5.3.1 Visualisation Techniques

Flow over complex terrain is often subject to flow directions being greatly affected by local features. Before useful measurements can be made it is necessary to be aware of any major deviations from the general flow direction. To determine areas of high velocity, high turbulence and signifcant flow direction changes, several techniques were applied.

1. Flags: Small flags, 4mm high x 8 mm long, were made from balsa wood and freely pivoted on a pin which used a small plastic bead as a locating bearing. These were placed on the model at areas of interest and areas where further analysis, both in the field and on the model, would take place. Observations of the flags revealed
   (a) flow direction;
   (b) high turbulence - depicted by the flag fluttering;

2. Smoke: The smoke was applied through a rake which was set up at the same points used for the flags described above. The tunnel was run at a low speed (still producing turbulent flow) and the flow of the smoke recorded with a video unit. The data obtained was somewhat limited because it was difficult to see the smoke close to the model surface. The most useful factors derived from this were the visualisation of turbulent regions and the determination of the gradient height of the flow over the model. Generally, it can be said that the data taken supported the general flow pattern as determined with the other visualisation techniques.

3. Polystyrene beads: Streak lines and regions of relatively low shear were visualised by application of the beads technique. This involved placing small polystyrene beads, measuring 2mm in diameter, upstream of the model. The tunnel was then run slowly and the beads drifted across the model settling in areas of low shear. These areas were recorded and the tunnel speed increased. This process revealed that the pockets of beads that remained were in the most sheltered areas. Areas of vorticity were also noted by swirling pockets of beads. These results are presented and discussed in the following Chapters.

5.3.2 Hot Wire Film Anemometry

Hot wire anemometers have been used for many years as a research tool in fluid mechanics. Recently, the application of anemometry has expanded greatly due to the availability of better equipment and expanded interest in the details of fluid flow. Fig.5.11 shows a typical hot wire anemometer sensor; the dimensions given are typical of this type of sensor. A film type sensor is shown in Fig.5.12. This concept was introduced over ten years ago and is replacing the hot wire anemometer in many applications. This is the type of sensor being used for this research. It possesses the following advantages over an equivalent hot wire sensor;

1. Better frequency response (when electronically controlled) than a hot wire of the same diameter, because the sensitive part of the sensor is distributed on the surface rather than including the entire cross-section, as with a wire.

2. Lower heat conduction to the supports (end loss) for a given length to diameter ratio due to the low thermal conductivity of the substrate material. A shorter sensing length can thus be used.

3. Less susceptible to fouling and easier to clean. A thin quartz coating on the surface resists accumulation of foreign material. Fouling tends to be a direct function of size.

The probes used during this research were the T.S.I. hot film cylindrical sensor type 1210-20. These have a 0.051mm diameter x 1.00mm long sensing element.

A block diagram of a comprehensive system as suggested by TSI is given in Fig.5.13. The boxes marked with asterisks (*) denote equipment that has been used in this research. The system used consists of:

i) 1051-2, monitor and power supply module;
ii) 1054B, constant temperature linearised anemometer unit;
iii) 1056, variable decade accessory unit;
iv) 1076, RMS/True digital voltmeter.

Full details of the equipment and its operation are given in the TSI Operators Manual. The theory of hot wire/hot film anemometry is given by Hinze (1959) and Bradshaw (1971), amongst others.

Until very recently, the output signal from the lineariser had to

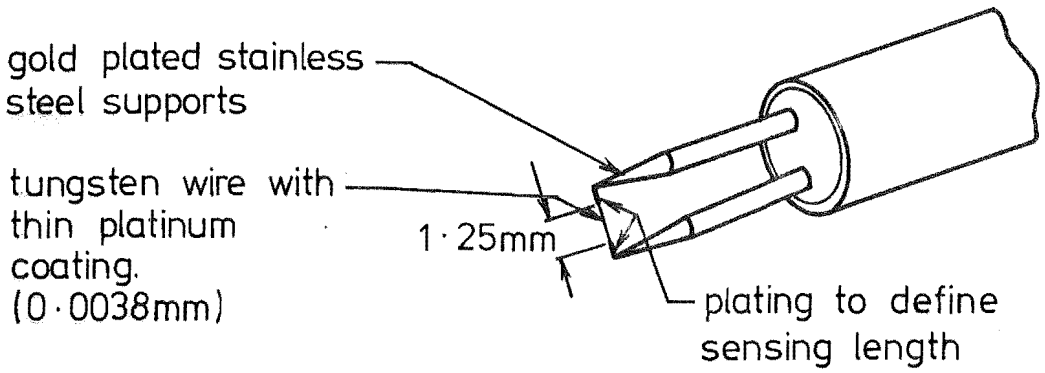

FIG. 5·11 TUNGSTEN HOT WIRE SENSOR AND SUPPORT NEEDLES 0·0038mm DIA.

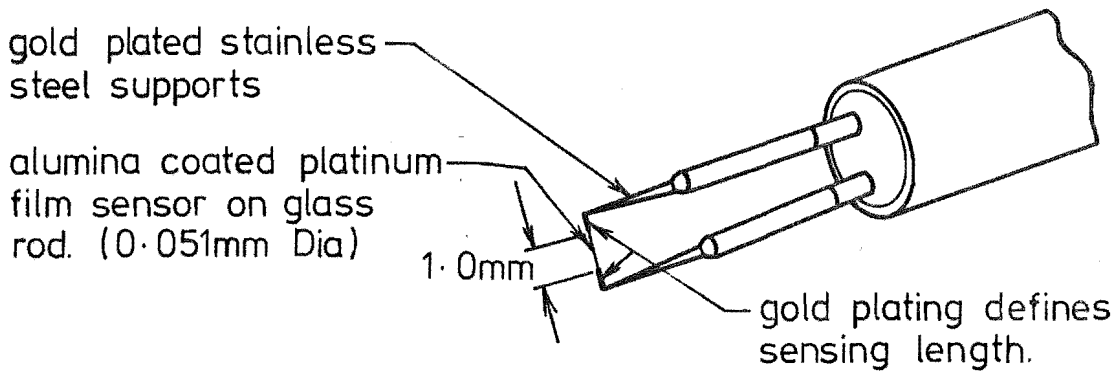

FIG. 5·12 CYLINDRICAL HOT FILM SENSOR AND SUPPORT NEEDLES 0·051mm DIA.

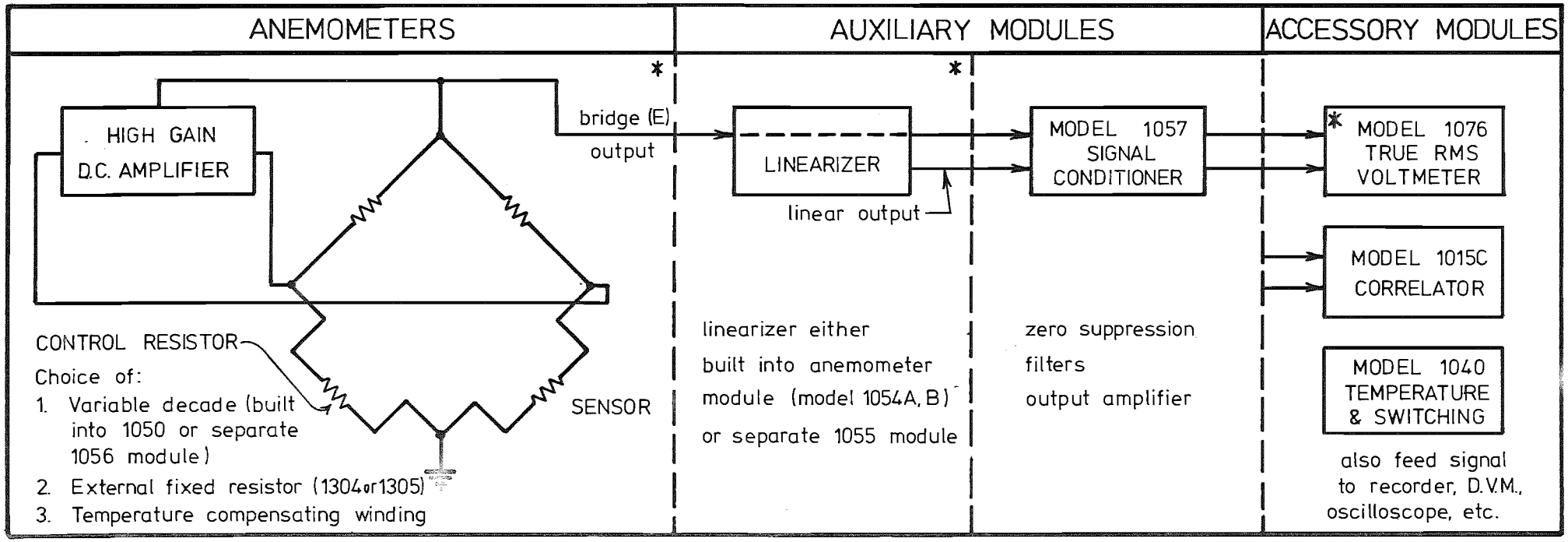

FIG 5·13 BLOCK DIAGRAM FOR A COMPLETE T.S.I. SYSTEM.

be read with voltmeters or passed into analog equipment such as a correlator or spectrometer, to provide information on velocities, auto-correlations and energy spectra.

However, the recent digitising of the wind tunnel by Pearse (1978) has meant that the signal from the lineariser can be fully analysed by the Department's mini-computer.

5.3.3 Data Analysis of the Digitised Wind Tunnel

The data acquisition system uses a centrally located HP 2100A mini-computer which is linked to a number of terminals placed throughout the laboratory. Any digital signal may be transferred from a terminal to the mini-computer which is used to collect and process the signal. The maximum signal throughput rate is 20 kHz.

The hot-wire anemometer signal is converted to a digital signal using a Daytel Systems 8-channel, 12-bit analog to digital converter. The digital signal is sampled at 5000 Hz and stored on magnetic disc. When the required number of samples have been collected, the record is read from the disc and the required record properties calculated. The techniques used to collect the data and calculate the mean, standard deviation, power spectral density function, auto-correlation function, and probability density function of a record are described by Pearse (1978). This also gives a complete description of the computer programs used and discusses the collection of data from two channels. Also presented are the calculation of the coherence and cross-correlation function of two records.

Results obtained using the digital data acquisition system are compared to those obtained using conventional analog techniques. The main advantage of processing the analog signal digitally has been the faster processing times, which allow the required results to be gathered more quickly, or more data to be collected in a given time. The digital system is also more flexible than the analog system, as further quantities may be measured without purchasing special purpose analog equipment.

5.3.4 Pressure Probe Equipment

A standard Prandtl pitot-static tube was used to set the mean velocity of the tunnel at which the measurements were taken. The pressure difference was measured by a Schiltknecht precision liquid micromanometer which had graduations of 0.1mm H_2O. The wind tunnel velocity was set to within

±0.2mm H_2O steady reading before measurements were commenced. A free stream velocity of $\bar{u}$ = 9.8 m/s was used throughout the tests and to further reduce the effects of day-to-day variations, all data was normalised to the free stream velocity as measured at the top of each traverse.

Meroney (1976) in a Battelle Semi-Annual Report, states that in the modelling of hills and ridges, the streamlines are undisturbed at 10 times the model height. The tunnel roof is built in sections and is therefore limited in the degree to which it could be adjusted to follow the model shape. The longitudinal static pressure gradient was measured with a micromanometer; the results of these tests will be reported in later Chapters.

A 5-tube Cobra probe manufactured by United Sensors was used to measure flow directions, yaw, and pitch, over the model. These were measured at points previously used for the flag visualisation tests to provide a correlation between the two methods. The characteristics of this device are given in the United Sensors catalogue and the general theory of this type of probe is given in detail by Bryer and Pankhurst (1971) and Winternitz (1956).

During the tests the probe was rotated about its vertical axis until the pressure difference between the lateral ports was zero, indicating that the probe was aligned with the flow; this angle was recorded. By measuring the pressure difference between the vertical ports and applying the manufacturers' calibration curve, the pitch angle could be calculated.

5.4 EXPERIMENTAL PROGRAMME

Models A, B and C were tested in several states of construction; terraced, contoured and with roughness added. The data extracted from these tests included:

1. Velocities.
2. Turbulence intensities.
3. Auto-correations*.
4. Energy spectra*.
5. Reynolds stresses*.

The procedure used to obtain this data can be summarised by the following steps:

* See Note - page 103.

1. Record barometric pressure and temperature.
2. Calibrate hot film probe (using TSI calibration unit).
3. Place probe on traverser in tunnel and locate at point to be tested.
4. Set probe to initial height (usually 2mm).
5. Start tunnel and settle to operating speed (9.8 m/s).
6. Using information from pressure probe survey, set probe to angle of flow measured.
7. Vary probe angle ± several degrees until flow direction is found (based on maximum output occurring at correct angle).
8. Record measurements from DC and RMS voltmeters.
9. * Run mini-computer programs to produce auto-correlations and energy spectra.
10. Repeat Steps 7 and 8 (possibly 9, if required) at increased heights until the free stream velocity is reached.
11. Move to next point and repeat Steps 6 to 10.
12. When tests are completed, remove probe from tunnel and check calibration. Take readings of pressure and temperature. If significant variations exist, results should be adjusted to take account of drift.

To reduce the effects of thermal drift, the wind tunnel tests were carried out at night when there was generally a small temperature gradient.

NOTE

* Tests involving these measurements were carried out at selected sites of interest and at sites that were accessible with the Department's instrumented portable 20m tower. This will be described in Chapter 6.

CHAPTER 6

FIELD PROGRAMME

This Chapter describes and discusses the Gebbies Pass area and details the sites selected for field measurements. Photographs are used to give the reader a clear description of the area and to provide examples of particular terrain features which were considered relevant to the study. Also given is a description of the various types of field data collected and the equipment involved.

6.1 THE AREA UNDER STUDY

A detailed description of the Gebbies Pass region has been given in Chapter 3. Therefore, in this Chapter, the descriptions will be confined to features that had a direct bearing on the field programme. A vertical aerial photograph of the region is given in Fig.6.1. It was noted that several of the scrub areas and shelterbelts depicted in this photograph had been removed, whilst other shelterbelts had been recently established. This problem arose because of the age of the aerial photographs of this region.

6.1.1 Terrain Features

Scrub stands were typically 2-5m high whilst most of the shelterbelts were 10-25m high. The most significant of these features have been plotted on the map in Fig.6.2. Other features that were typical of the area were cliffs and rocky outcrops where boulders of 5m diameter were not uncommon. Examples of these features are given in Figs 6.3 and 6.4 respectively. Cliffs situated at the southern entry to the modelled area were simulated because they presented a significant front, approximately 0.8 km wide, to the approaching flow. The remaining cliff areas were generally small and were considered, at 1:4000 scale, to be impractical to model specifically.

Similar reasoning was used when considering the rocky outcrops. In this case, it was fortunate that these features were not situated in areas of interest for field measurements, due to their inaccessibility among other reasons.

6.1.2 Data Collecting Sites

Several types of data were collected throughout the region; these are classified as follows:

727/24a

FIG 6·1 VERTICAL AERIAL PHOTOGRAPH OF THE MODELLED REGION

FIG 6·2 MODELLED SHELTER BELTS AND SCRUB AREAS

536/14

FIG 6·3 TYPICAL ROCKY OUTCROPS IN THE REGION

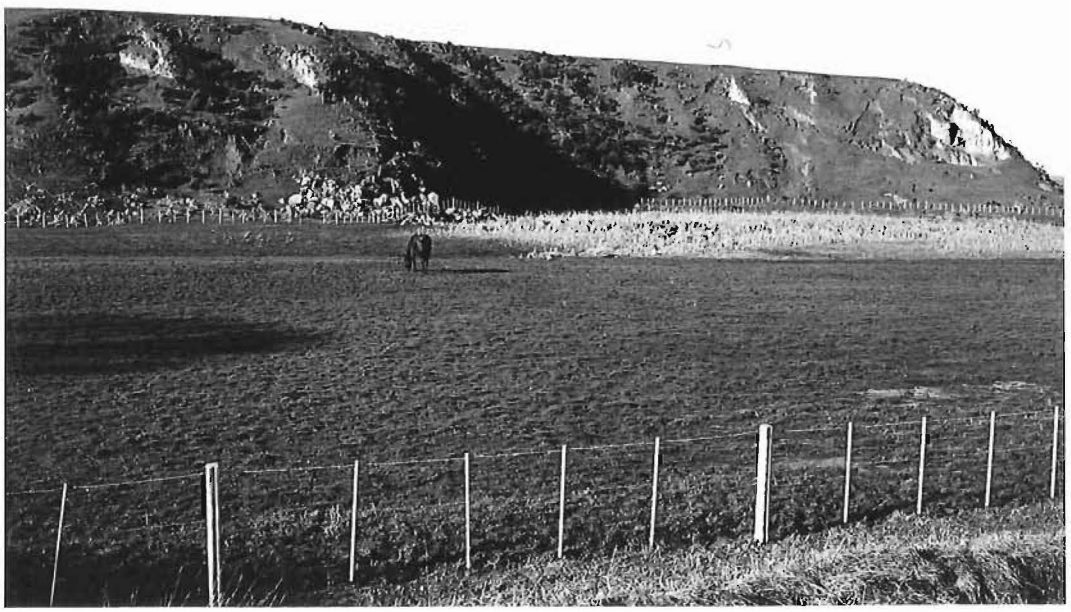

536/20

FIG 6·4 CLIFFS AT THE SOUTHERN BOUNDARY OF THE REGION.

1. One day field data.
2. TALA kite data.
3. In excess of one month duration data.
4. Detailed single point analysis using an instrumented 20m tower.

The map in Fig. 6.5 lists all the points that were measured during the study. Many of these points were measured several times, as will be shown in Chapter 10. Any field data collected will be referred to by the point number given on this map.

The overriding factor to be considered during the selection of the field points was accessibility. Many of the sites selected required 4-wheel drive vehicles to make access possible. Another limiting factor was farm boundaries. Unfortunately, several points had to be omitted because boundary fences (no gates) prevented or made access too complicated.

Every site used was surveyed by the author, on foot, to observe the approach flow conditions, i.e., to note the proximity of hills, ridges, shelterbelts, buildings etc.

6.2 RATIONALE FOR MOBILE SURVEY

The field day data collection used a mobile survey technique whereby teams made measurements throughout the area within a relatively short period of 5-7 hours.

The effectiveness of this technique depends on:

i) The spatial correlation of the wind velocities over the area, approximately 140 km^2 for this study.
ii) The quasi-stationarity of the wind over a 3-6 hour period, this being the time required to cover the area.
iii) The significance of a 5 minute sample at a given point taken once during the 3-6 hour period.

Corotis (1976) examined hourly data from six towers in Northern Illinois and Montana. The report used statistical methods and probability models to determine optimal procedures for survey data.

Meroney *et al* (1978) in their study of the Rakaia Gorge, New Zealand, considered the relevant points from the work of Corotis to their situation as being:

(a) At a given site there are only 2 to 4 statistically independent periods during a day. This suggests an autocorrelation time constant from

FIG 6·5 POSITIONS AND NUMBERS OF ALL FIELD POINTS MEASURED

3.5 - 7 hours. Thus data taken from the same, or a set of towers, erected at a series of nearby stations within a given wind event period may be highly "dependent" or "correlated" to the character of the wind event.

(b) Spatial correlation of wind velocities taken from towers separated by various distances in rolling type terrain revealed that:

Spatial Separation (km)	Maximum Correlation Range $P_{xy} = \frac{R_{xy}}{\sqrt{R_x}\sqrt{R_y}}$
0	0.780 - 0.923
22	0.757 - 0.832
42	0.712 - 0.816
105	0.632 - 0.745
1947	-0.024 - 0.079

That correlation remains as high as 0.7 over a distance of 100 km, suggests that once anemometers are immersed in wind systems of this scale or larger, wind patterns and velocities at nested sites must be strongly related.

(c) Maximum spatial correlation occurred in almost all cases for zero time lag. This suggests that if wind data is available continuously at one site, data taken irregularly at other sites may be normalised by the reference site to a common measurement time.

Corotis (1977) also analysed data at additional sites in the United States chosen on the basis of their geographical diversity, topographical variation, and uniformly promising wind energy potential. These sites reinforced the conclusions arrived at in his 1976 report. Cross correlation remained high between most sites, Fig. 6.6. An additional separation category of 12-13 km revealed correlations between 0.75 and 0.85. The exception was correlations made between Cheyenne and Laramie, Wyoming. These two sites differed in height by 707m and in distance by 85 km. They are separated by the Laramie mountains, which rise to 576m between the two cities. This appears to be a far more accentuated version of the Gebbies Pass region where maximum spatial separation is 14 km and the Gebbies Saddle rises to about 200m.

In the Rakaia Gorge study, Meroney *et al* (1978), the terrain was generally flat. Field data was collected on two days and produced a correlation of

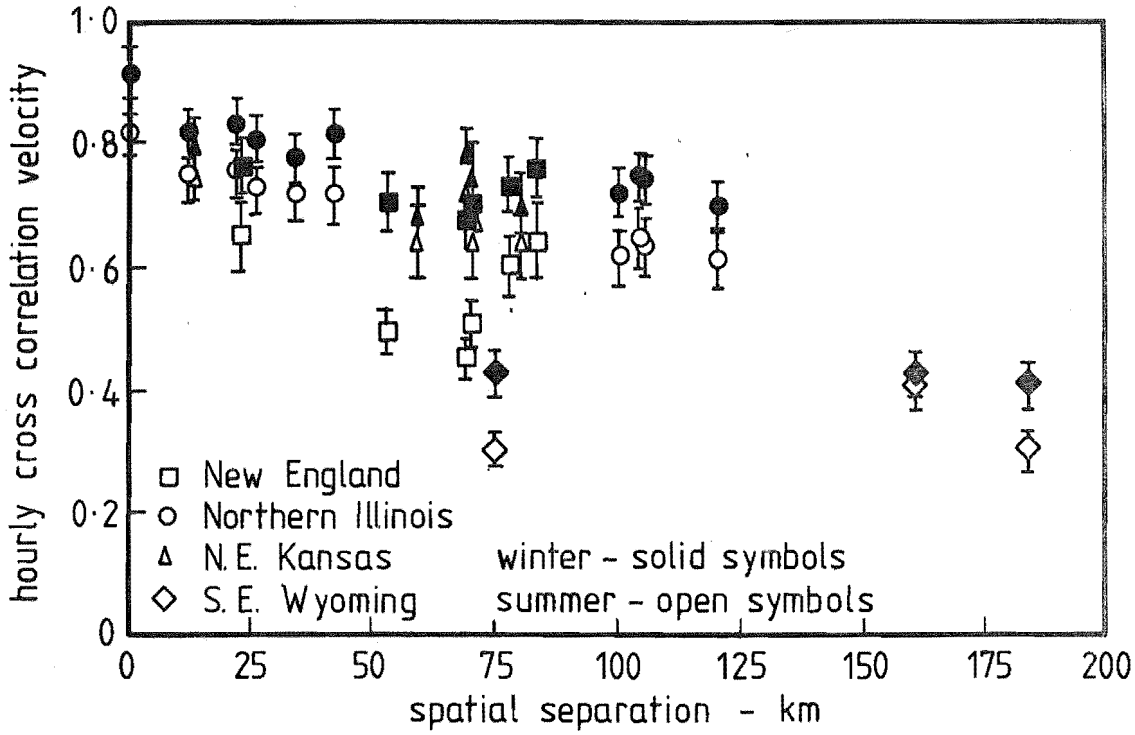

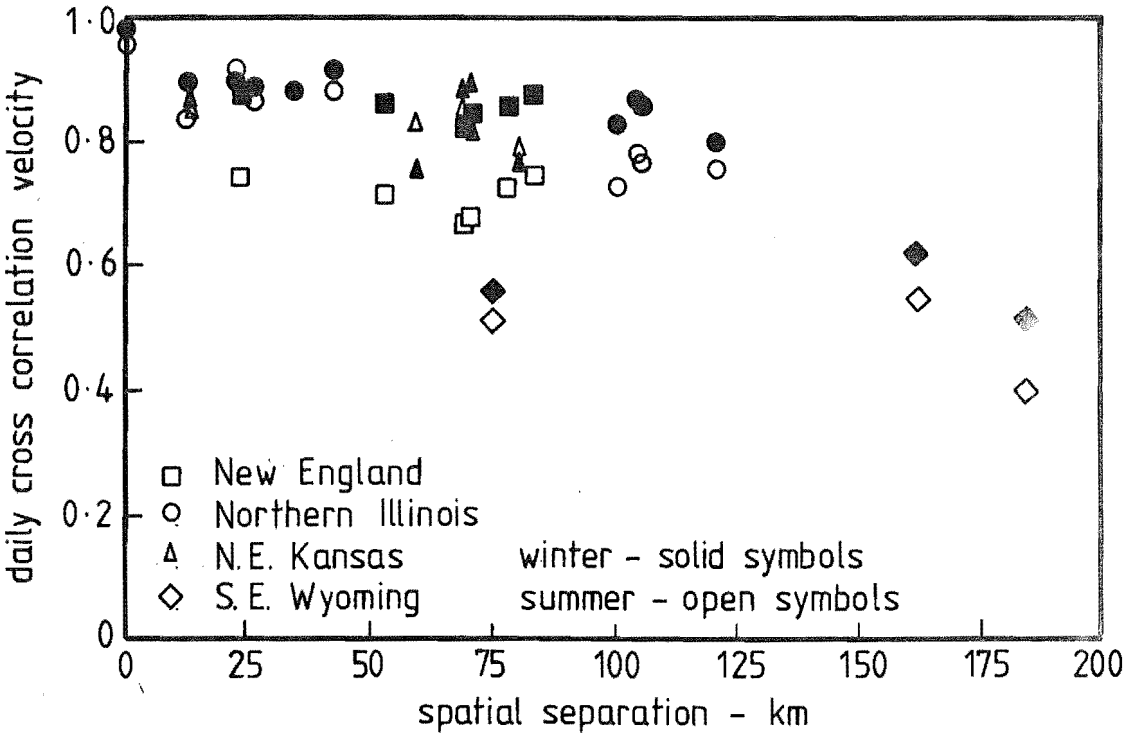

FIG 6·6 MAXIMUM SPATIAL CORRELATION FOR HOURLY AND DAILY VELOCITIES (after Corotis)

0.68. It is hoped that the data collection technique, which has been modified slightly, will produce a higher correlation than this. More detail of the data collection procedure will be given in a later section.

The use of the one day data collection programme is based on the results of Corotis (1976, 1977) and the work of Meroney *et al* (1978). Therefore, assuming this technique to be valid, the results obtained can be directly correlated to the wind tunnel test results to establish the validity of wind tunnel modelling of flow over complex terrain.

6.2.1 Portable Towers and Cup Anemometers

For the one day data collection it was essential to keep the amount and weight of the equipment to a minimum. Although 4-wheel drive vehicles were used, several of the sites required the equipment to be manhandlled for 300-500m. The tower consisted of 5cm diameter thin walled aluminium tubes 5m long, two of these being sleeved together to form a 10m tower. Teams consisted of 3 people, this being the minimum number required to erect a tower safely. A sketch of an erected tower is given in Fig. 6.7. Rimco cup anemometers were attached to the top of the tower with pipe fittings. The features of the low torque Rimco anemometer have been discussed in detail by Sumner (1968).

The anemometer is fitted with a phototransistor electric pulse generator. After amplification, these pulses were fed to a digital counter. The starting speed of the anemometer is approximately 10cm/s, and the instrument operates to 25m/s without damage, providing a pulse rate which is linear within 1.5% over its entire range. All of the anemometers used in this study were calibrated before and after the field programme in the University of Canterbury's 1.22 x 0.91m aerodynamics wind tunnel.

The procedure involved in collecting the data was:

1. Arrive at site and layout equipment.
2. Locate and drive in pegs,
3. Attach anemometer and strap cable to the tower.
4. Test battery level in counter box, make connections and test anemometer.
5. Erect tower.
6. Wait until 1/4 of the hour.
7. Start stop watch and counter.
8. Record wind direction, temperature and make any comments about the site that may be relevant.
9. After 5 minutes, record the counter reading.
10. Carefully lower and dismantle the equipment.

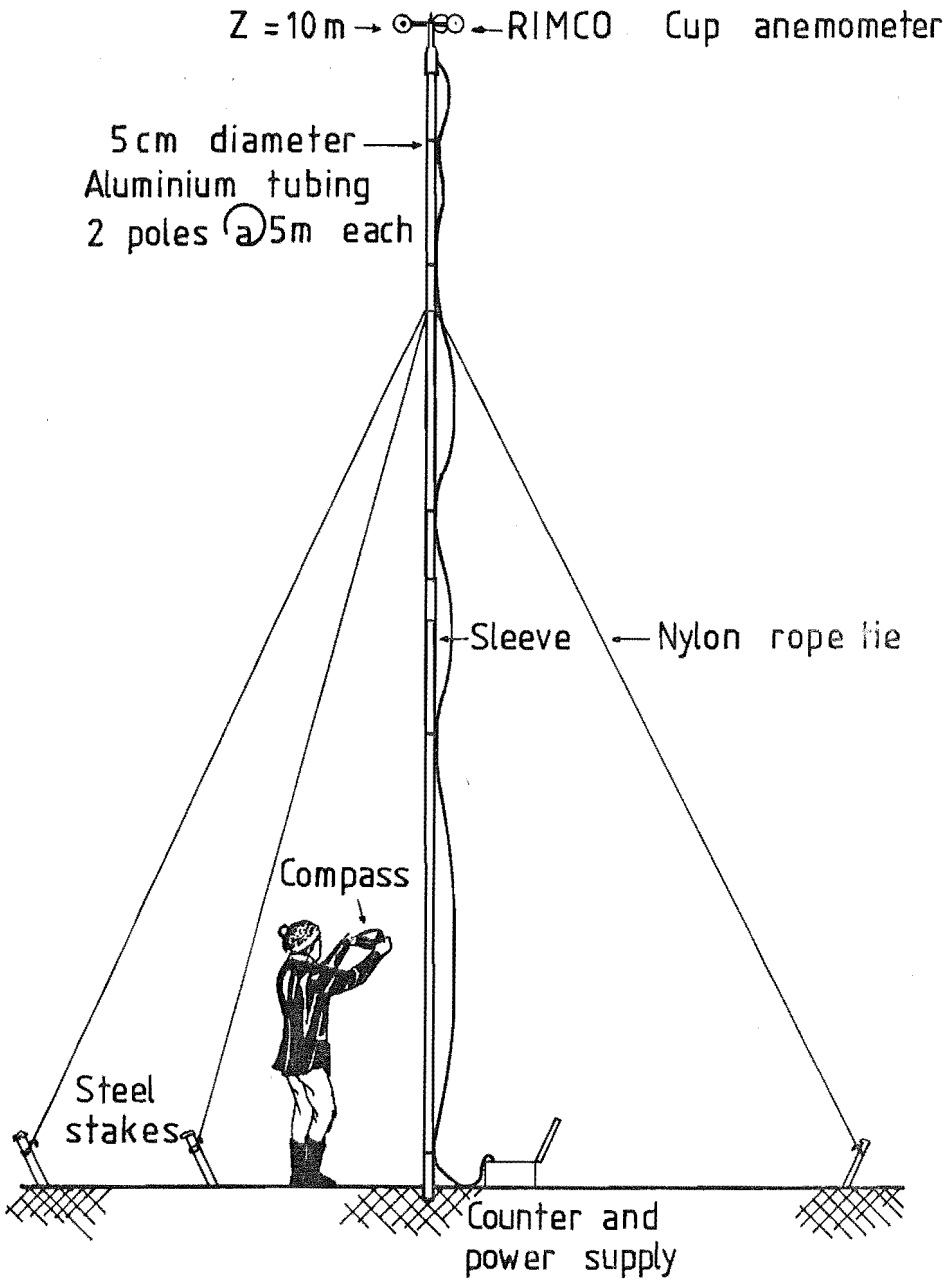

FIG 6·7 PORTABLE TOWER AND ANEMOMETER USED DURING ONE DAY FIELD SURVEYS

This procedure was repeated for several sites during the day. An average field day resulted in measurements from about 15-20 sites.

6.2.2 Tethered Aerodynamically Lifting Anemometer (TALA) Kite Data

This piece of equipment was bought during the latter half of the field programme but was used as extensively as possible.

TALA data is generated from forces exerted on an aerodynamically lifting kite, of the sled design, which is subject to the same aerodynamic laws as an aeroplane. The lift and drag forces on the kite equal the tension on the flying line, which is measured and calibrated as wind speed.

The National Bureau of Standards and the NASA Langley wind tunnels are in 1-2% agreement. The TALA kite has been calibrated in both of these facilities and, as shown in Fig.6.8, are in excellent agreement. In the NBS wind tunnel, TALA showed an accuracy of 2% based on the equation

$$V = 0.5144 \left(\frac{N}{0.01799} \right)^{0.51}$$

where N is the force in newtons

V is the velocity in m/s.

The force on the kite is transmitted through a non-stretch 'kelvar' line, 0.25 mm diameter, to a calibrated spring. A range of springs of varying stiffness is available to enable measurement of wind fields up to 60 m/s.

To determine the altitude of the kite, the manufacturer, Approach Fish Inc. of Clifton Force, Virginia, supply a calibration formula which requires inputs of

1) the observed angle of inclination, θ, (measured with a clinometer);
2) the reel count of line out, N (given by a digital counter which is part of the reel unit).

The expression proposed by the manufacturer is of the form

$$Z = 0.9 \, (0.3N - 2.2 \times 10^{-5} N^2) \, \text{Sin} \, \theta \quad \ldots\ldots\ldots\ldots\ldots\ldots (6.2)$$

where Z is in metres

N is the reel count

θ is the angle of inclination.

A schematic diagram of the method of operation is given in Fig.6.9. Although the manufacturer suggests that this piece of equipment can be operated by one person, it was found that two operators were far more

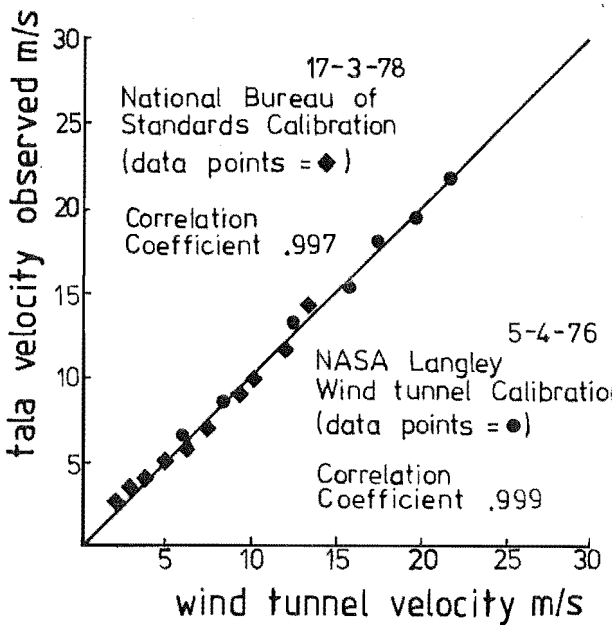

FIG 6·8 WIND TUNNEL CALIBRATION FOR TALA KITE

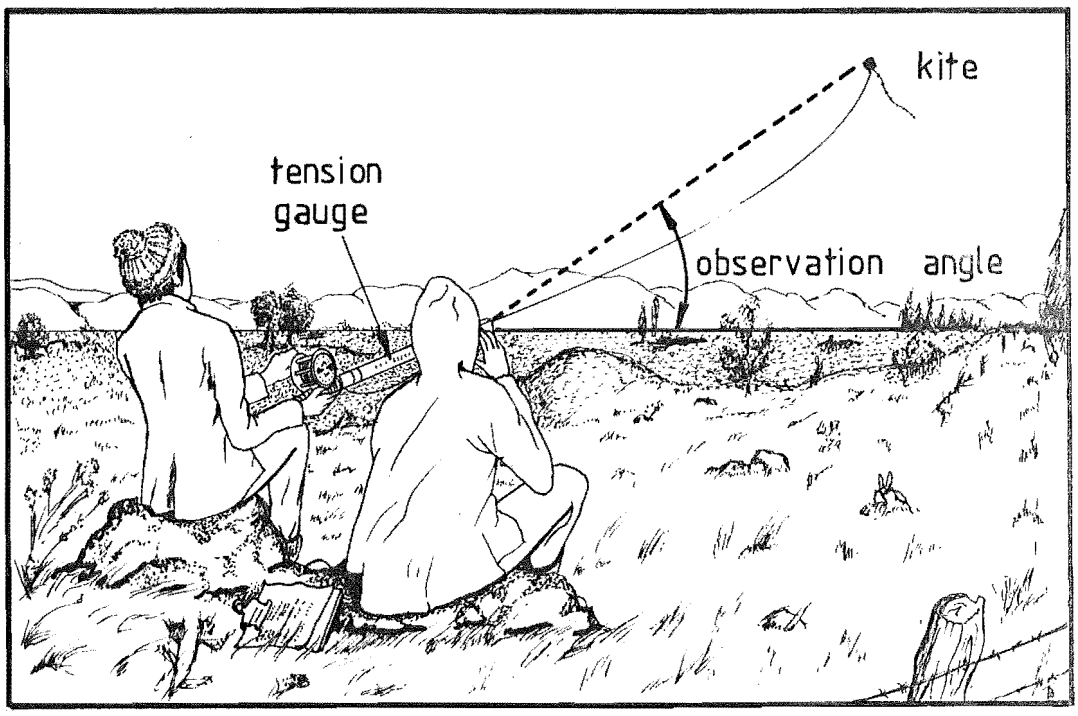

FIG 6·9 OPERATION OF TALA KITE

efficient. One watched the speed indicator whilst the other gave angle readings; typically 10-15 sets of readings were taken at any one height and were averaged.

A tether analysis for a kite anemometer was carried out by Shieh and Frost (1976); the purpose of their study was to establish the cable equations and to determine the accuracy of the manufacturers' altitude equation. These results were also used as the basis for a computer model to determine the kite altitude under different wind régimes. Most of the calibration tests carried out by the manufacturer involved uniform wind flows and there was some doubt as to their applicability in a varying wind régime. The results of this study showed that for uniform flows a slight modification to the altitude formula was necessary. The expression

$$Z = 0.995\ (0.3N - 2.2 \times 10^{-5} N^2)\ \text{Sin}\ \theta \quad \ldots\ldots\ldots\ldots\ (6.3)$$

was shown to give excellent agreement between the computer curve and the calibration curve.

The effect of a variable wind field was found to be very small, i.e., of the order of 0.1%. If the preceeding modification is used for the variable wind field situation, the error in the calculated height is very small - less than 1%. This represents such a small correction that for practical field measurements this error may be neglected. Therefore, Shieh and Frost concluded that the kite anemometer could be used to measure height dependent wind fields on the basis of calibration curves established with uniform wind fields.

6.3 LONG TERM DATA AND DATA LOGGERS

An aspect of this research was to gather data over an extended period which could be used to compare with the one day field data. The New Zealand Wind Energy Task Force made this possible by lending specialised equipment designed specifically for automatic long term wind speed recording. A photograph of the data logger is given in Fig.6.10; these were used in conjunction with Synchrotac 3-cup generator type anemometers. The New Zealand Meteorological Service uses two basic types of anemometer, one being the Hall Effect type which uses a make/break (switch) method of operation. The other type is the generator anemometer, which provides a voltage output proportional to the wind speed. Therefore, since the data loggers use digital signals, the generator anemometer signal is passed through an interface which results in a square wave output.

The logger samples data at an interval, called the averaging interval,

which is selected by the operator and varies from 0.5 - 30 minutes.

Each sample constitutes a "word". Internal storage in the data logger can hold 100 words. Therefore, if an averaging time of 0.5 minute is used the internal storage will be filled in (0.5 x 100) 50 minutes. At this point the contents of the interal storage are transferred on to a cassette tape. The tape used for this equipment lasts for 45 minutes per site; however, the data transfer process only takes a few seconds. This means that using 0.5 minute averaging time, one tape will last approximately 15 days. If the averaging time is increased to 7.5 minutes, the tape life increases to 6 months.

579/17A

FIG. 6·10 DATA LOGGER AND TAPE RECORDER UNIT

6.4 ANEMOMETERS AND FIELD DATA ACQUISITION SYSTEM

The digital data acquisition system used during this research was designed and built at the University of Canterbury. This equipment has been described in detail by Flay (1978) and to a lesser degree, by Bowen (1979). Therefore, only a brief description of the principles of operation will be given here.

6.4.1 Propeller Anemometer

The design and manufacture of the anemometers used in this research was carried out at the University of Canterbury.

The anemometer shaft drives a slotted disc which rotates between two pairs of photo diodes and receivers. Two square waves are thus generated, one from each photo receiver, by the slots passing through each light beam. This enables the velocity and rotational direction of the anemometer propeller to be determined. Bowen (1979) discusses errors and frequency range of this equipment. The form of the signal generated from the anemometer is given in Fig. 6.11.

The propeller used with the anemometer is a four-bladed helicoid propeller. Reasons for the choice of this type of propeller and the details of theory, construction, response and calibration are presented by Flay (1978) and Bowen (1979). In summary, the propeller was constructed with expanded polystyrene which was formed in a steam jacketed mould. The result of this process was a two-bladed propeller with a dovetailed boss. Two of these blades were glued together to form the four-bladed propeller. These were then cut to size, outside diameter, with a hot-wire cutting jig and balanced by adding pins as balancing weights. The propeller was then painted to produce a surface that was more resistant to the weather. A propeller in various states of construction is shown in Fig. 6.12.

6.4.2 Field Data Acquisition System and Recording Equipment

The field data acquisition unit has the capacity to accept and record on to digital magnetic tape any number of triplets, or groups of three, anemometer channels up to a total of 36 anemometers. As discussed in the previous section, the output from the anemometers indicated rotational direction and speed. Since the light chopping disc has 32 windows, it follows that the frequency of the signal was 32 times that of the anemometer

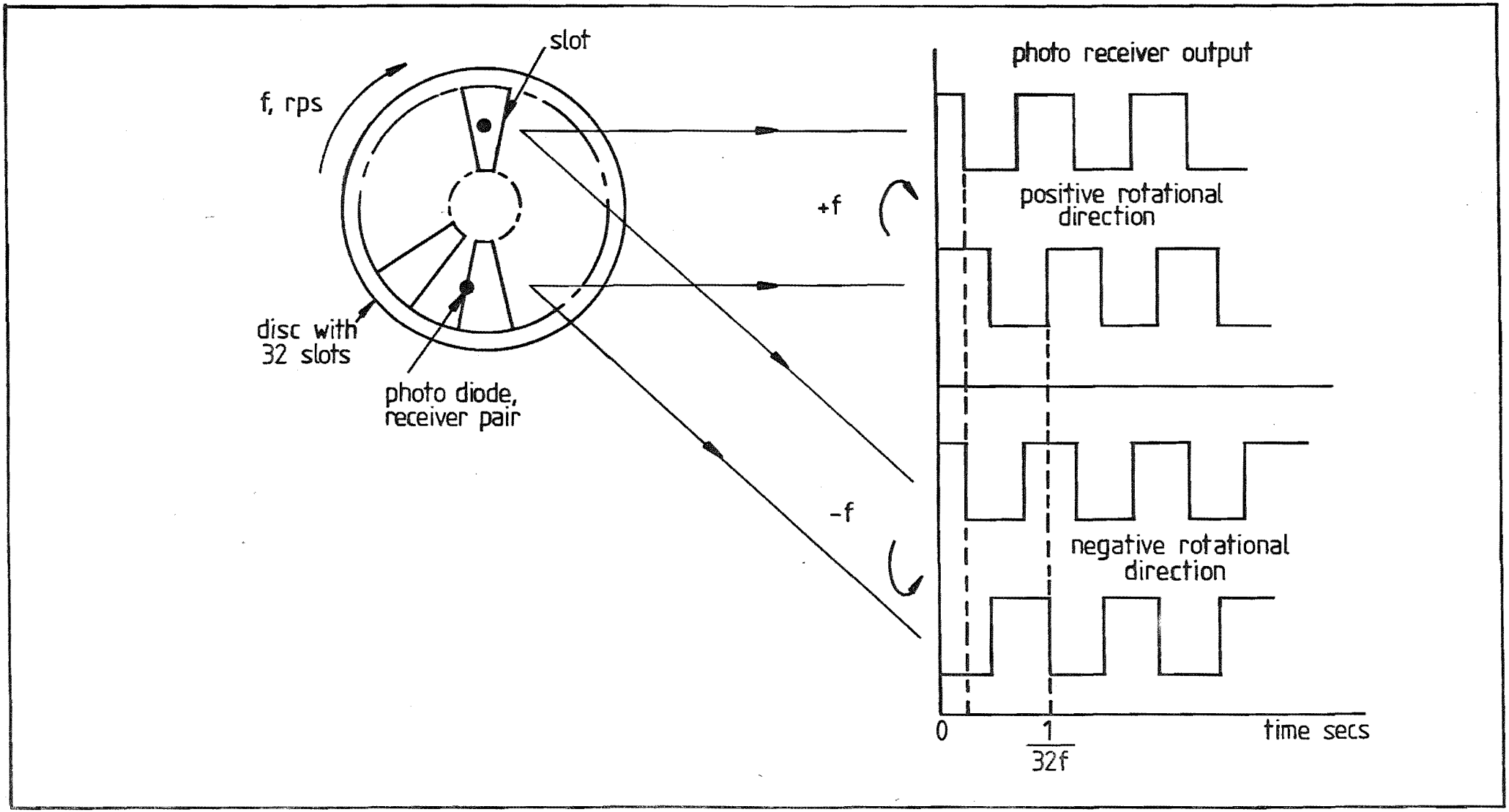

FIG 6·11 SIGNALS GENERATED FROM PHOTO RECEIVERS

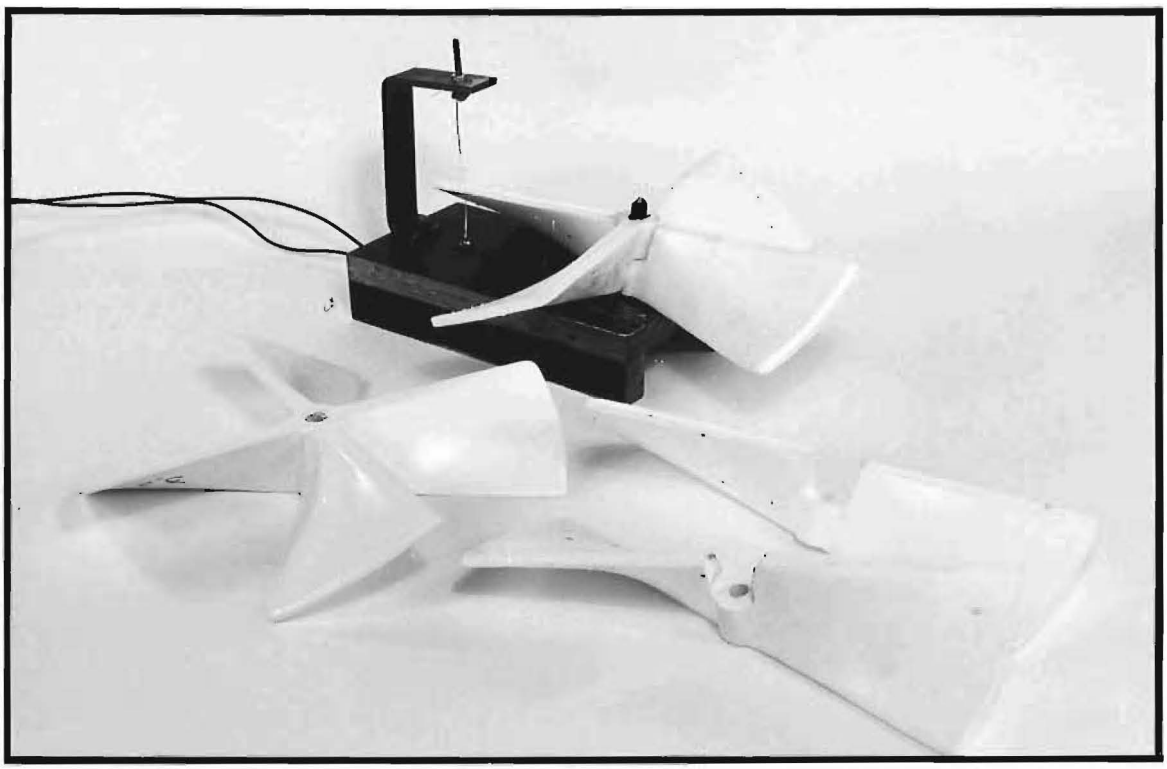

514/41

FIG 6·12 AN ANEMOMETER BLADE DURING SEVERAL STAGES OF CONSTRUCTION.

shaft. The signal from the anemometer was fed, via multicore cables with a maximum length of 1000m, to an 8-bit counter which integrated the counts over selected time periods. Depending upon the direction signal from the anemometer, the counters either count up from 0 to 127 for a positive rotation or down from 256 to 129 for a negative rotation. Thus the counting period had to be selected so that the maximum count stayed within these limits.

To have efficient utilisation of the tape for data storage, the contents from three 8-bit counters were grouped together thus giving 24-bits. This information was then transferred to the buffered formatter via four 6-bit characters. This created the situation where three channels were gated together thus having identical counting periods. For consistency and to aid in computer programming, the three anemometers grouped together were always from a single orthogonal array or triplet. The data was recorded on to a digital seven track tape using a rugged seven track industrial magnetic tape transport, which involved a Kennedy Model 8107 tape deck and a Kennedy 8230C Buffered Formatter. A schematic of the data handling system is given in Fig. 6.13.

To provide capacity for large numbers of anemometers, a time division multiplexor with switch selectable counting periods and with variable channel capacity was developed. Full details of this, its operation and limitations, is given by Flay (1978) and Bowen (1979). The multiplexor and tape recording equipment was installed in a caravan, the power for operation being supplied by a portable 1.5 kVA Markon diesel generator.

6.4.3 The Tower

The tower used in conjunction with the equipment described in the previous sections is 20m high and is of an open lattice construction. It has a triangular cross section which reduces with height thus allowing the top sections to slide down inside the lower ones in a telescoping manner. Mounted on its own trailer, which makes transportation very simple, the overall length is 4m in its fully collapsed state. The side of the triangular section varies from 0.4m at the base to 0.05m at the top triangular section. The pipe diameter of the lattice structure is 32mm and is connected by horizontal straps 40mm wide. At the top, the 25mm diameter pipe is connected by 30mm wide straps occurring approximately every 0.4m apart all the way up the tower.

The tower has a cable and pulley system which is operated with a winch.

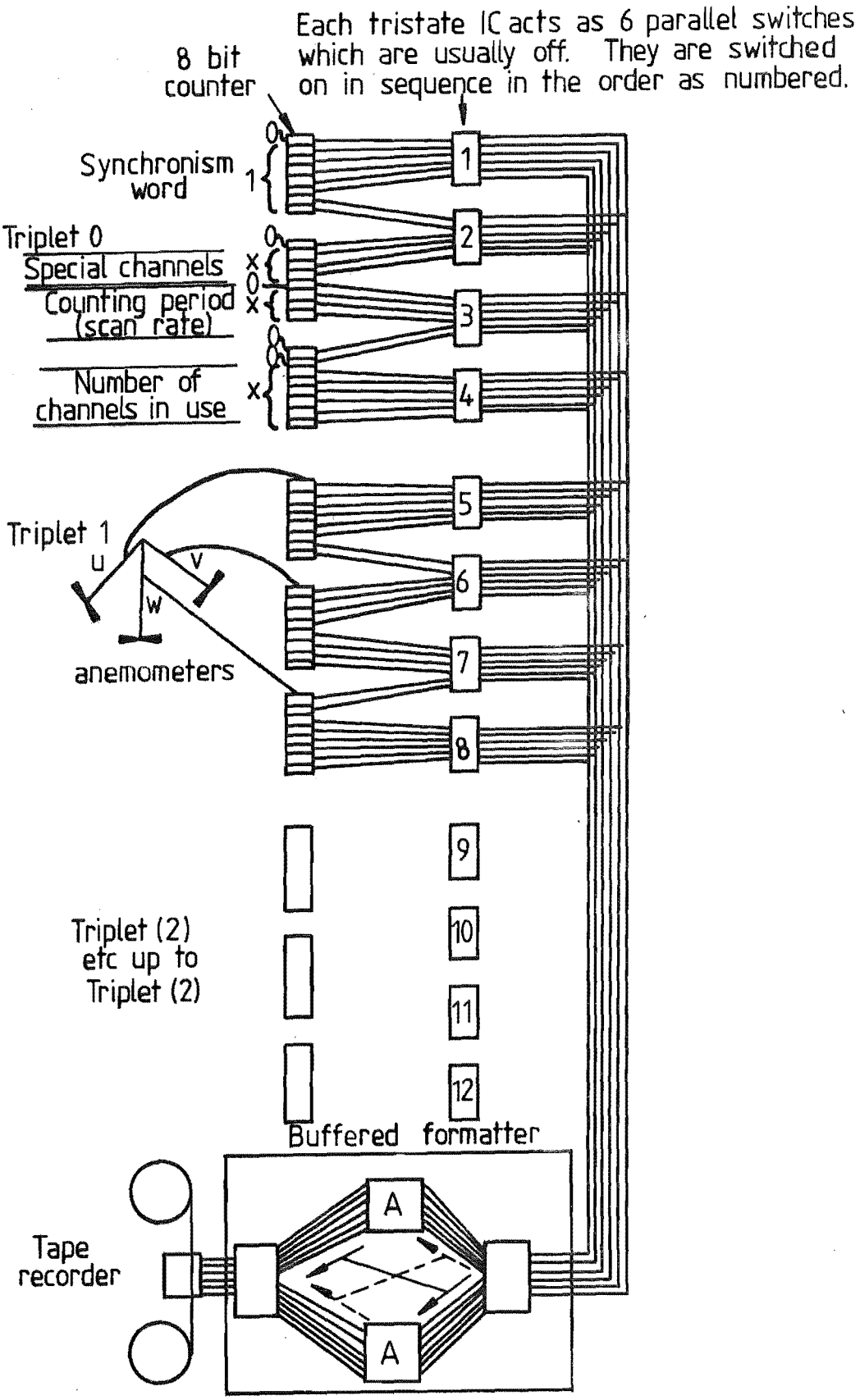

A - 512 x 6 bit word buffer one of which is being filled while the other is having its contents written to tape

x - denotes a bit which can be 0 or 1

FIG 6·13 MAIN FEATURES OF THE DATA PATH FROM ANEMOMETERS TO TAPE STORAGE

The sections rise one at a time, each one moving up until it reaches its end stop, thus leaving an overlap of one section in the other of approximately 0.15m. A steel "keeper" is inserted horizontally between the horizontal straps of the two sections. This process is continued, with anemometers being attached to the tower at the required heights, until the tower is fully extended. The winch is then reversed and all of the tower sections "settle" on to their keepers. At this stage, the guide wires are adjusted to remove any slack and to provide the fine adjustment to bring the tower perpendicular to the terrain; this is usually checked with a theodolite.

The anemometer triplets are mounted on arms which are 0.9m long from the centre of the tower side to the anemometer fastening bracket.

Gill *et al* (1967) have conducted wind tunnel tests to evaluate the influence of the tower on the measured wind velocity for a sensor mounted to record winds from all directions. For this research the direction of the winds to be measured was known; therefore the anemometers were mounted upwind of the tower, the variation of the wind direction being measured being approximately ±20°. The results of Gill *et al* suggest that tower shadow effects would be negligible for this situation.

6.4.4 Purging

Flay (1979) experienced problems with this field equipment during wet weather and when there was a large amount of condensation. This resulted in the anemometers malfunctioning because of corrosion within the anemometer body. There was only one possible mode of entry for the moisture, this being at the point of entry of the propeller shaft into the anemometer body. To prevent this, nitrogen was bled into the anemometer body through a small nipple located at the base of the anemometer body. Details are given in Flay (1978).

Due to the rough nature of the terrain in which this equipment was used and the difficulty of access, it was desirable that a very low flow rate of nitrogen be used. To achieve this, two courses of action were taken:

1. Flow restrictors were included in the system, which ensured an equal flow rate to all anemometers but kept the flow to a minimum.

2. A manifold was built which allowed two nitrogen bottles to be used in parallel, thus increasing the time between bottle changes (although they had to be replaced two at a time).

The nitrogen was passed through a series of regulators which reduced the

pressure to approximately 2.0 kN/m^2, it then passing into a manifold at the base of the tower via a 3.17mm internal diameter nylon tube. From the manifold the nitrogen passed along 1.6mm internal dimater low pressure P.V.C. fluidic tubing, which was attached to the anemometer cables, to a manifold at the triplet support bracket. From there the nitrogen passed through flow restrictors, 0.1mm orifice diameter, into the anemometer body. The circuitry was designed so that a flow meter could be switched into the system, and the pressure adjusted until a flow rate of 30-40 cc/min was achieved. A schematic of the purging system is given in Fig. 6.14. The purging system was found to improve the reliability of the anemometers significantly. During this research the equipment was installed in the field for approximately one year, and during this time only one anemometer failed.

6.4.5 Other Problems Encountered

During the research, problems which were characteristic of the site had to be overcome. One such problem was that of cattle and sheep. A portable electric fence was installed around all the field equipment and this proved a satisfactory solution. The fence construction involved equipment which was simple to erect and easy to transport. The pulse generator operated from a 12 volt car battery with a useful life of about 21 days. Once the cattle in the area were "educated" about the fence, they kept well clear of the equipment, even when the fence was switched off.

Another problem encountered was that of high levels of radio frequency in the area, caused by radio transmission towers located in the Gebbies Pass region. The data logger equipment was not influenced by this as all of the equipment was shielded and earthed. However, the cables used on the 20m tower were not shielded and presented a possible source of error. To prevent this, steel rainwater downpiping was strapped to the tower and all cables were passed down through this. The piping was in lengths of 2m, connected together with cable to provide a good connection so that earthing would be effective. The aluminium cladding of the caravan was expected to provide the necessary shielding for the data acquisition and recording equipment.

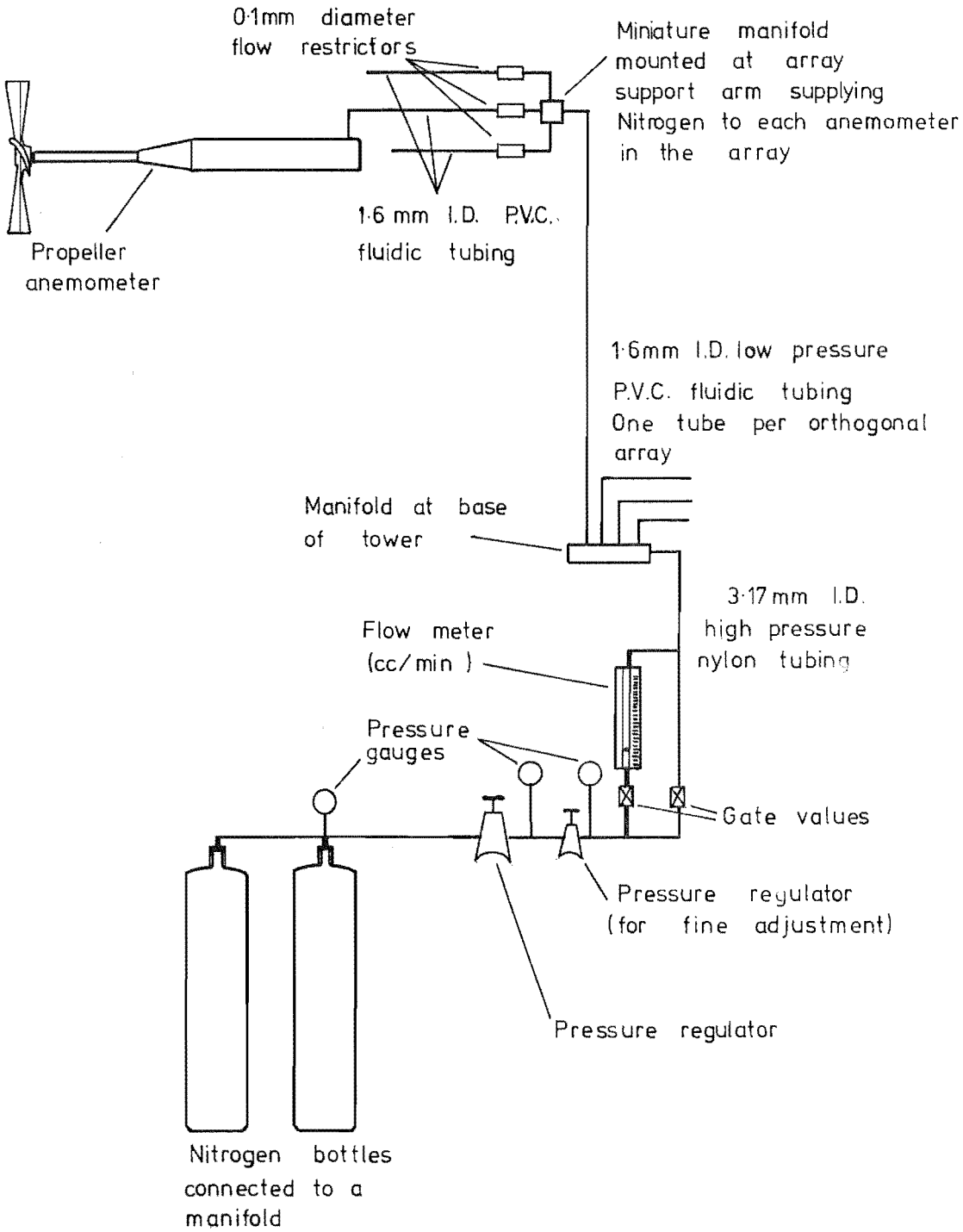

FIG 6·14 SCHEMATIC DIAGRAM OF THE NITROGEN PURGING SYSTEM

CHAPTER 7

MODEL A RESULTS

This Chapter will present the wind tunnel results for model A, see Fig. 5.10, in the terraced, contoured and with roughness added states of construction. Correlations between the results for the various states of construction will be presented and discussed.

A brief description of the flow visualisation results for the preliminary tests involving a model of Banks Peninsula will be given.

A detailed description of the model approach flow conditions will be presented and will be compared with theory and field measurements where possible.

7.1 ANALYSIS OF MODEL A

One of the problems encountered with topographical modelling is the wind tunnel blockage produced by the model itself. If this is significant it can cause local wind speed increases which are a function of the blockage rather than the nature of the terrain being modelled.

Consideration was given to this problem by selecting lateral cross-sections through the model and evaluating the percentage blockage that these presented. The cross sections selected are shown in Fig. 7.1. The actual cross sections and percentage blockages are presented in Figs 7.2 to 7.7. The maximum blockage for model A is seen to be 6.7% which was of some concern. Raine (1974) suggested that blockages should not exceed 5%, otherwise increased velocity due to the blockage would occur. The topic of surface mounted bodies, as opposed to suspended bodies, has not been documented in very much detail. Bowen (1979) evaluated the available literature and concluded that because of the small amount of information available, it was not apparent how the flow would be affected close to the model.

Therefore, he used the same rationale as Raine (1974) which was to keep the model blockage as small as possible; in both cases this was 4-5%.

Pope and Harper (1966) stated that a maximum ratio of frontal area to test section cross-sectional area should be 7.5%, unless errors of several percent could be accepted. This problem was foreseen at the outset of the research and accordingly, recommendations will be presented in the conclusions for this thesis.

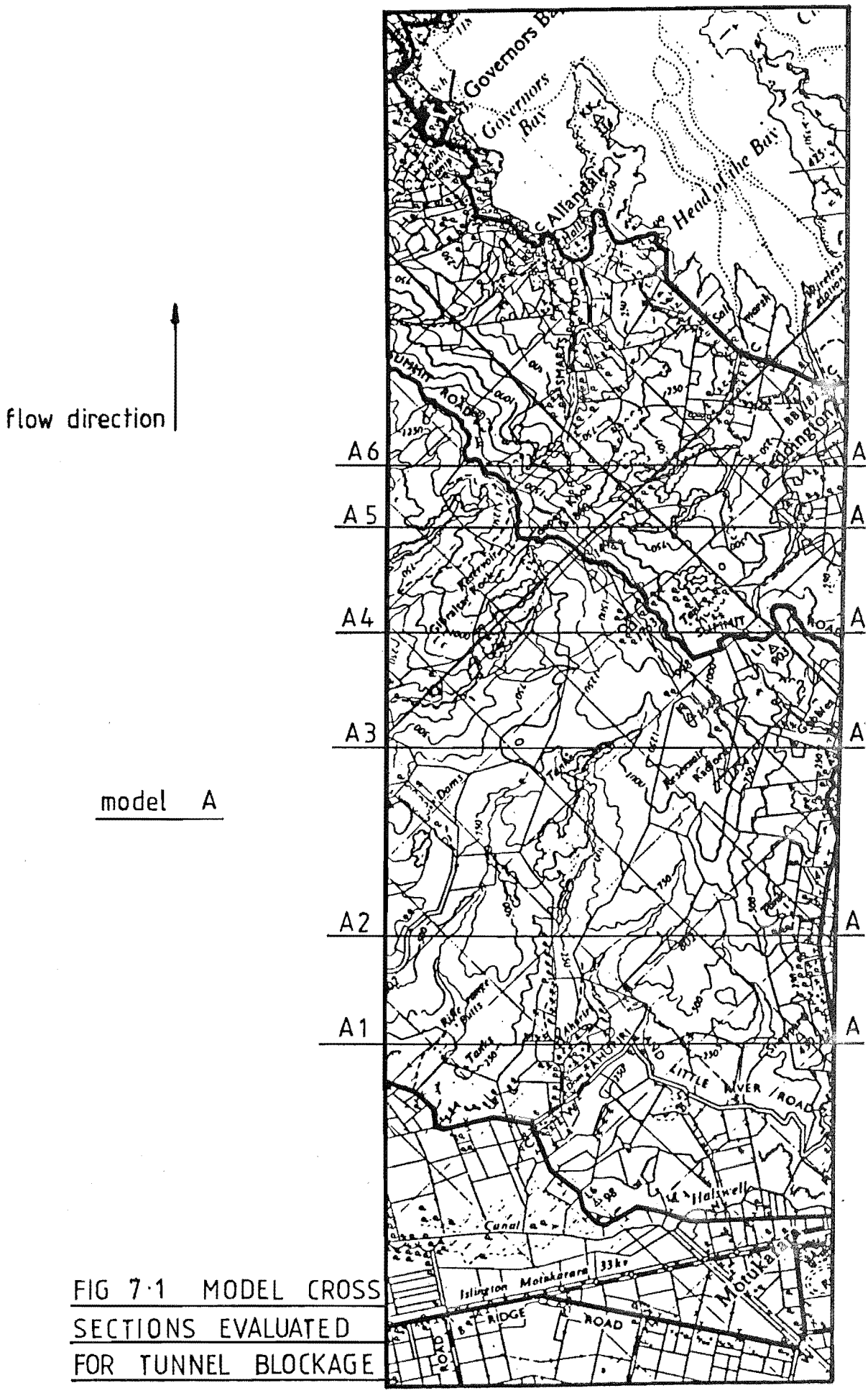

model A

FIG 7·1 MODEL CROSS SECTIONS EVALUATED FOR TUNNEL BLOCKAGE

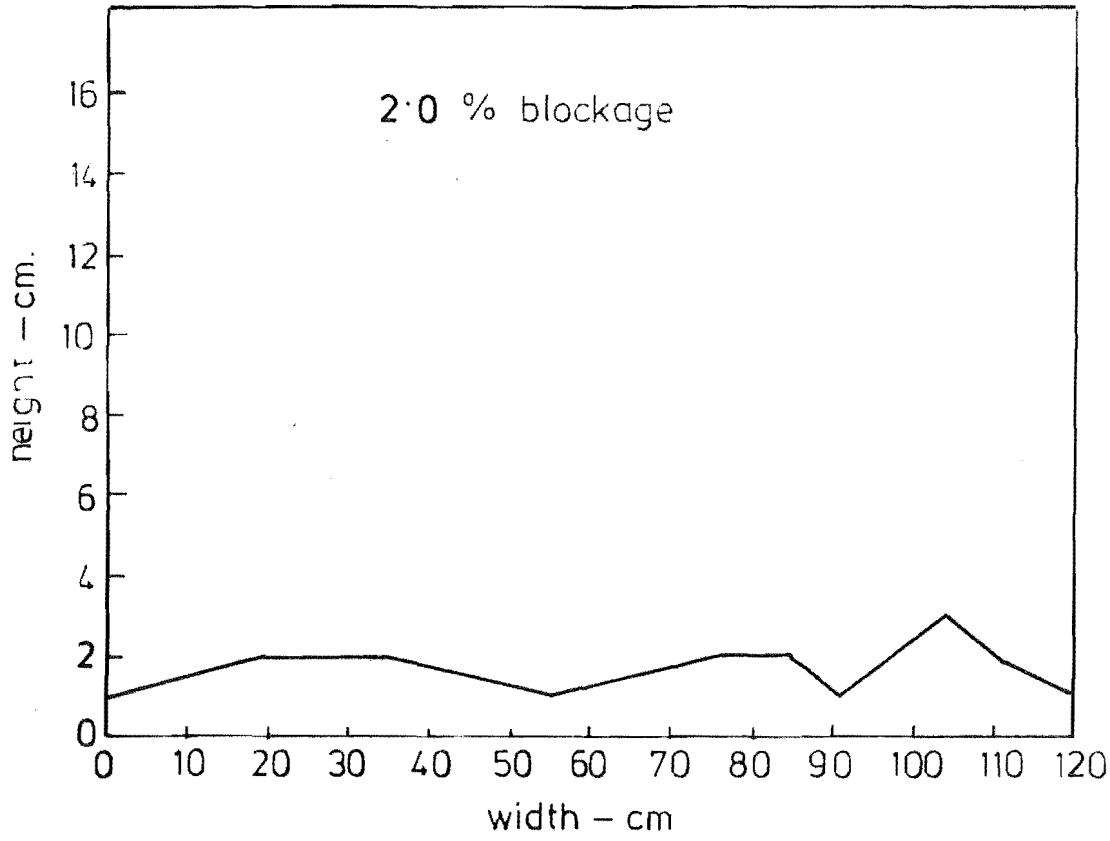

FIG 7·2 MODEL CROSS SECTION A1

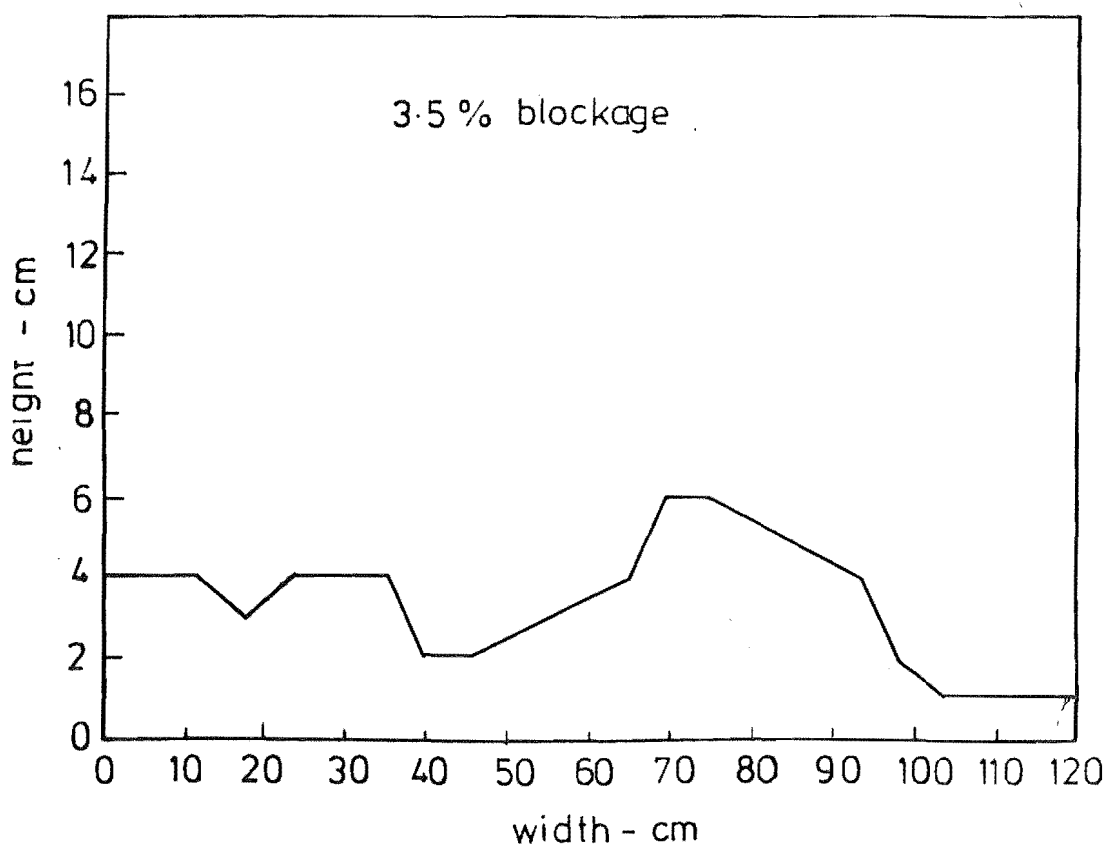

FIG 7·3 MODEL CROSS SECTION A 2

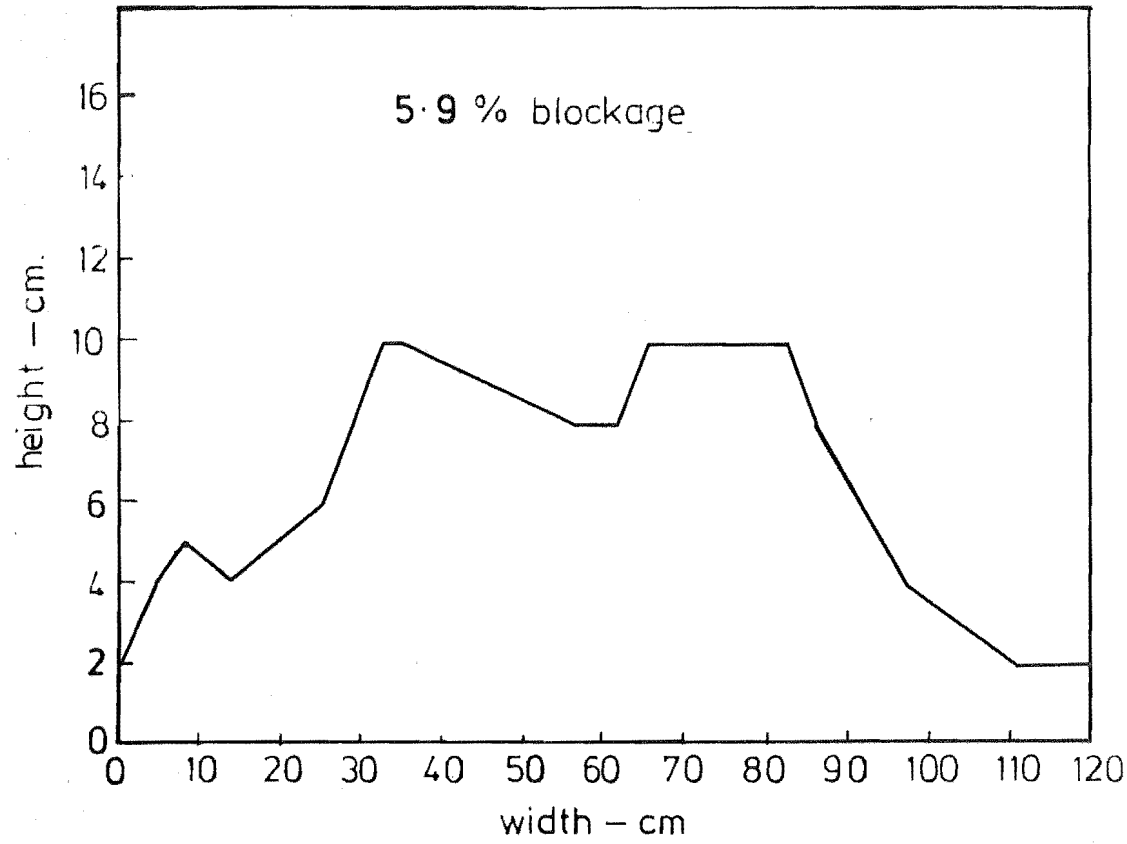

FIG 7·4 MODEL CROSS SECTION A 3

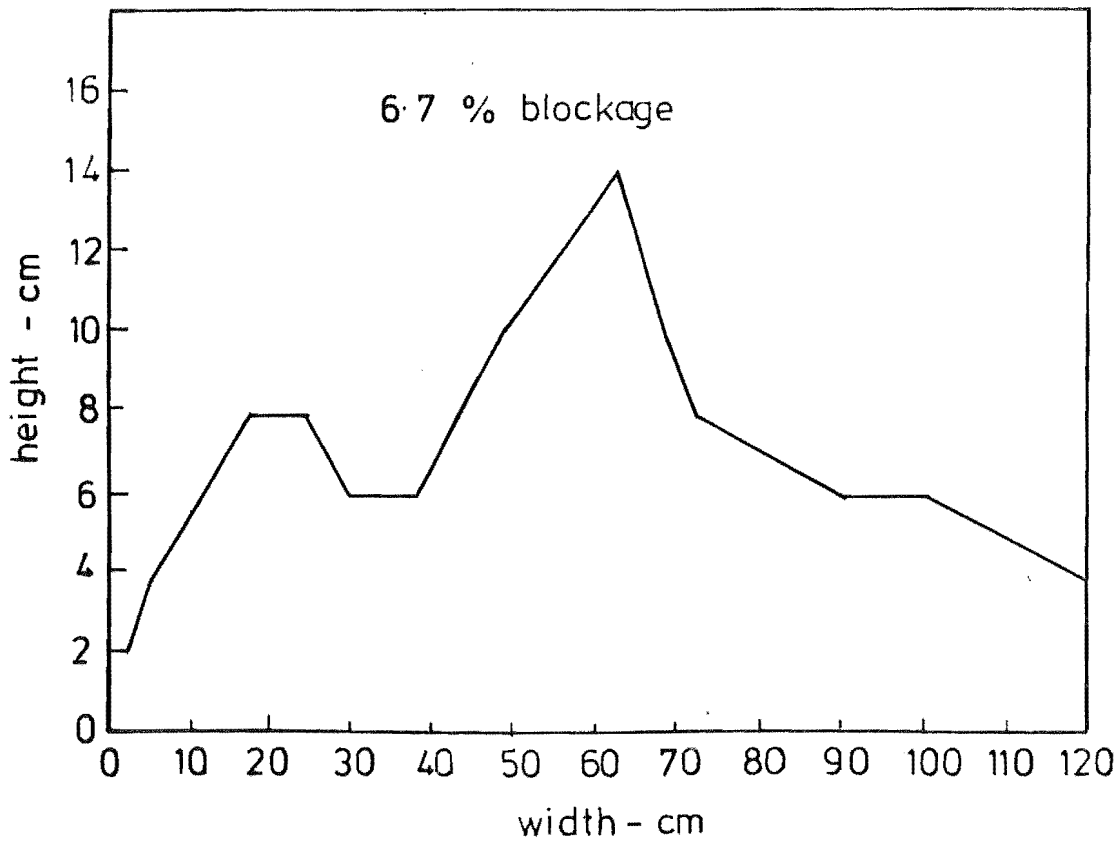

FIG 7·5 MODEL CROSS SECTION A 4

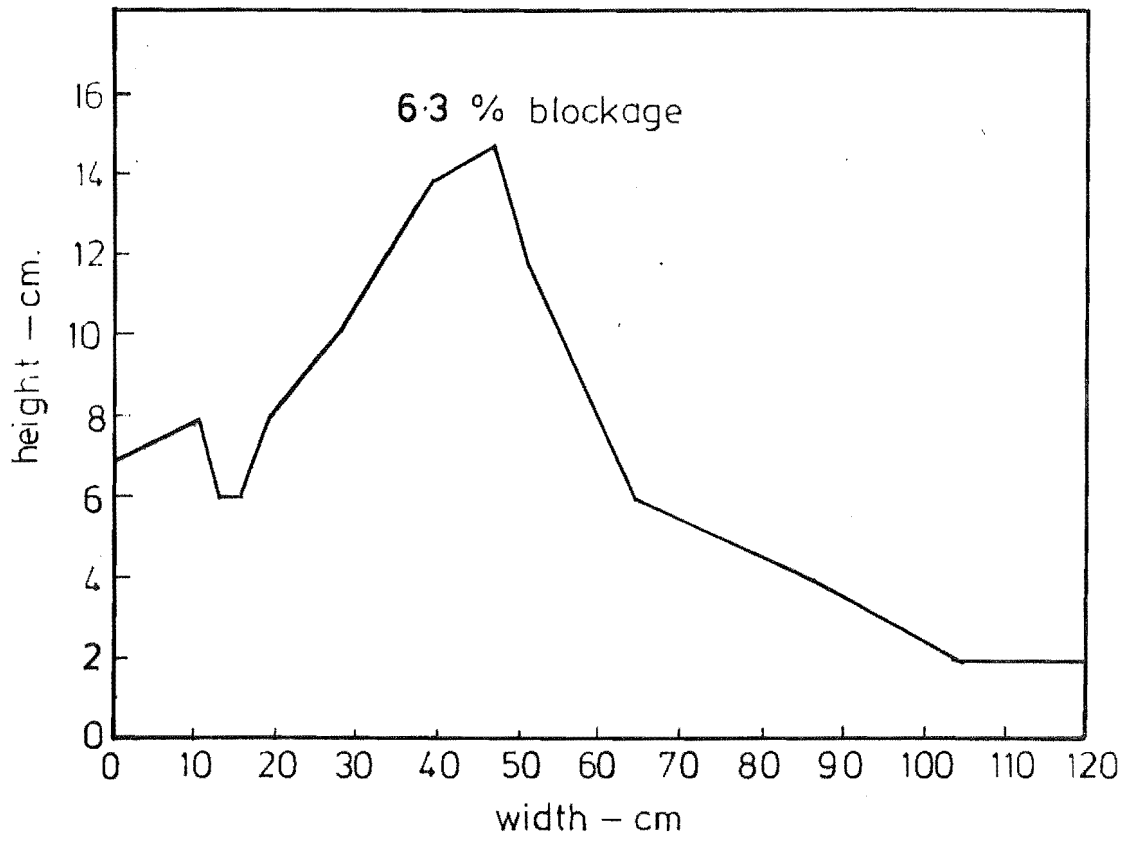

FIG 7·6 MODEL CROSS SECTION A 5

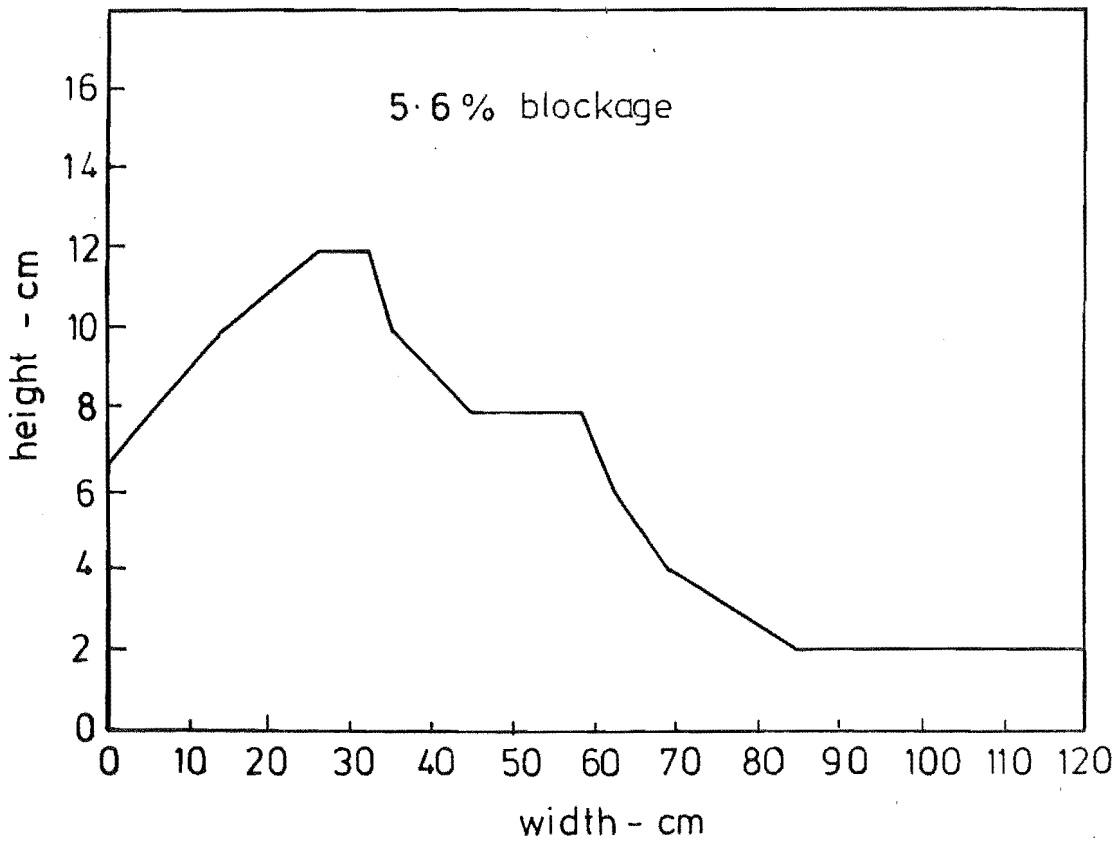

FIG 7·7 MODEL CROSS SECTION A 6

Static pressure tappings are fitted to the roof and side wall at several sections along the working section. At each section the two tappings are connected, as shown in Fig. 7.8, which results in an averaged reading. The positions of these tappings relative to the Gebbies Pass model are presented in Fig. 7.9. The working section roof, which is sub-divided into five sections, was raised such that the pressure variation along the tunnel working section was minimised. Tests showed this to be of the order of 2-3%.

7.1.1 Analysis of Banks Peninsula Model

A model of the whole Banks Peninsula area was borrowed from the Geography Department of the University of Canterbury, and a description of this model was given in Chapter 5.

Due to the dimensions of the model, it could only be aligned in the wind tunnel to represent winds from the east and west. With this major limitation, flow visualisation tests using 2mm diameter polystyrene beads and flags were carried out.

The flag results showed a very strong channelling effect, especially for the easterly winds, through the Gebbies Pass region. The flow was seen to enter the Lyttelton Harbour and follow it around effectively producing a north-east wind approaching the Gebbies Pass saddle. This was significant because, if this happens on the prototype, it means that winds from east to north-east are, in fact, re-directed and flow on to the saddle at right angles.

The bead results confirmed the flow directions predicted by the flags. Beads were deposited on the model, particularly in the Lyttelton Harbour region, as the tunnel speed increased. It was significant to see that the beads cleared out of the harbour and the windward side of Gebbies Pass well before any other areas were cleared. This showed the areas of high wind velocity and it was pleasing to note that the Gebbies Pass region was one such area. The tests were repeated with the model turned through 180°, thus producing west wind conditions. These tests showed very little information that could be used in the Gebbies Pass study and will not be reported here.

7.2 UPSTREAM CHARACTERISTICS

The terrain upstream of the Gebbies Pass region will be described in Chapter 10. However, generally it can be described as flat rural terrain.

The flow approaching the model was analysed and compared with theoretical

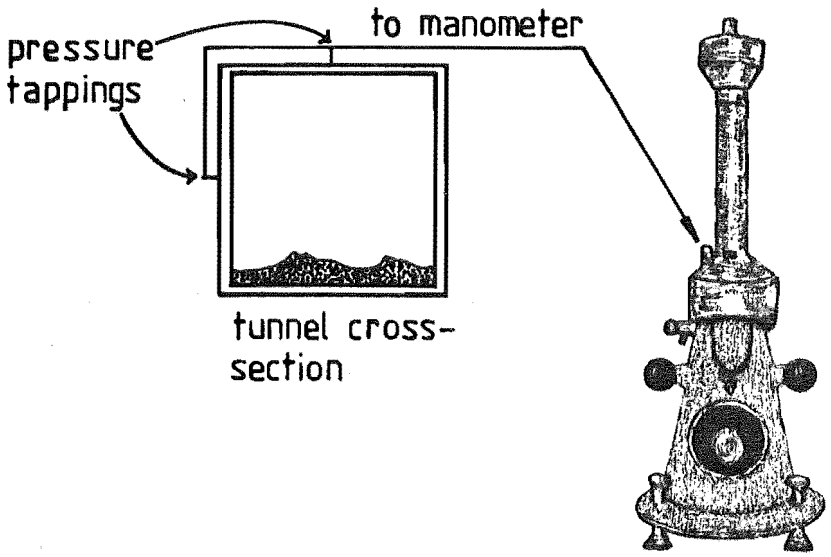

FIG 7·8 PRESSURE TAPPING CONNECTIONS

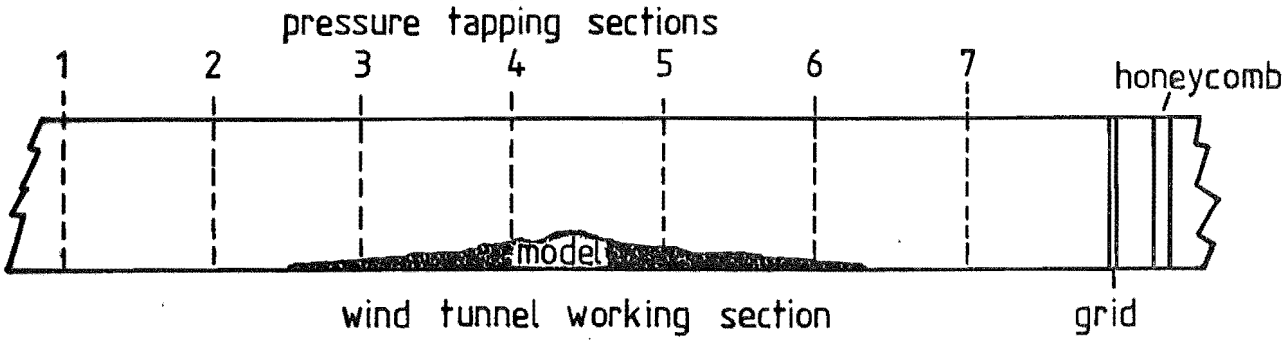

FIG 7·9 PRESSURE TAPPING ARRANGEMENT IN THE WIND TUNNEL WORKING SECTION

models and measurements made in the field.

The terminology for the various sources of data to be used throughout the remainder of this thesis will be as follows:

1) Modelled - refers to the wind tunnel simulation measurements.
2) Measured - refers to field measurements made during this research by the author unless otherwise stated.
3) Theoretical - refers to the results predicted by ESDU, unless another source is specifically stated.

Lateral uniformity tests were carried out upstream of the model. The results of these tests are presented in Fig.7.10. The profile in the centre of the tunnel was used for normalising purposes and readings were then taken to three boundary layer heights. In other tests the vertical uniformity above the boundary layer was tested to five times the boundary layer height.

The modelled power law velocity profile is presented in Fig. 7.11 and suggests a value of the power law index, α, of 0.15 which agrees with values predicted by Counihan (1975) and ESDU (1974).

Counihan (1975) suggested that in the lower 50m of the boundary layer, a log-law velocity profile is more representative. This form of velocity profile has the advantage of providing the value of the roughness length, Z_o, which is an important modelling parameter. This has been discussed in Chapter 2.

From the data collected with the 20m instrumented tower, the Reynolds stress was calculated. This was used to determine the value of the friction velocity from the relationship

$$u_* = \sqrt{-\overline{uw}} \quad \ldots\ldots\ldots\ldots\ldots\ldots\ldots\ldots\ldots\ldots\ldots \quad (7.1)$$

Knowledge of this permits the calculation of the slope of the line to be fitted to the log-law profile. This becomes clear by inspection of the form of the log-law

$$\bar{u}_z = \frac{u_*}{\kappa} \ln\left(\frac{z}{z_o}\right) \quad \ldots\ldots\ldots\ldots\ldots\ldots\ldots\ldots\ldots\ldots\ldots \quad (7.2)$$

where $\frac{u_*}{\kappa}$ is the slope of the line and

κ is the von Karmen constant which is usually taken as 0.4.

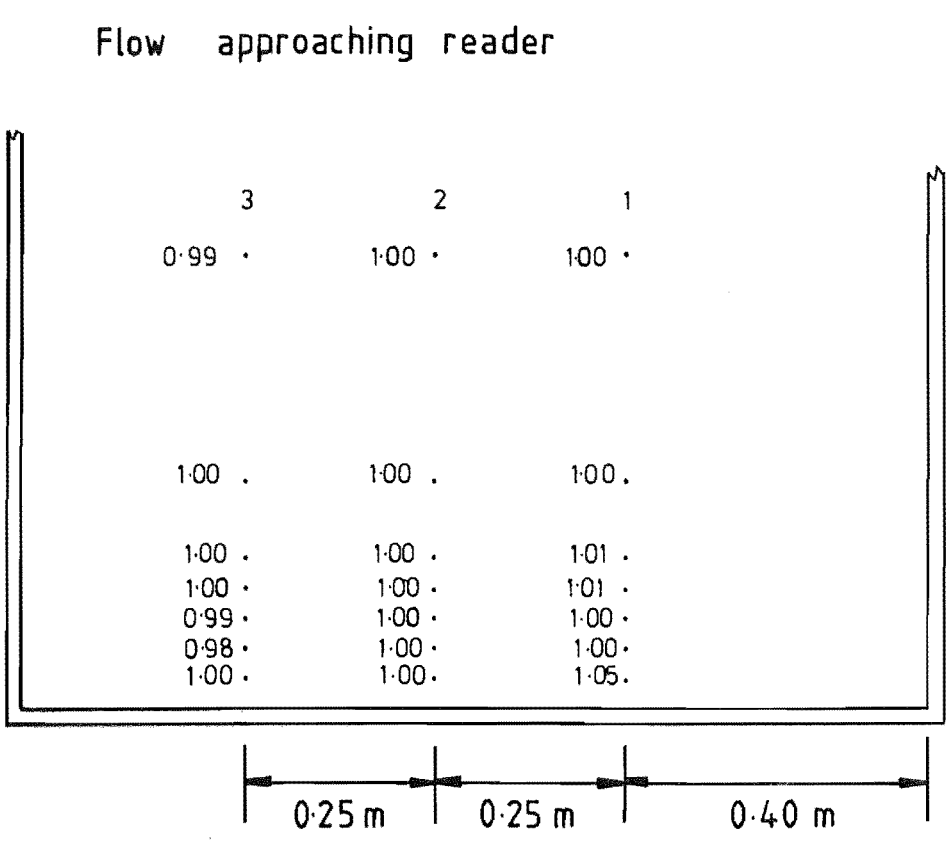

Readings normalized to profile 2

2x Exaggerated vertical scale

FIG 7.10 APPROACH FLOW LATERAL UNIFORMITY FOR MODEL A

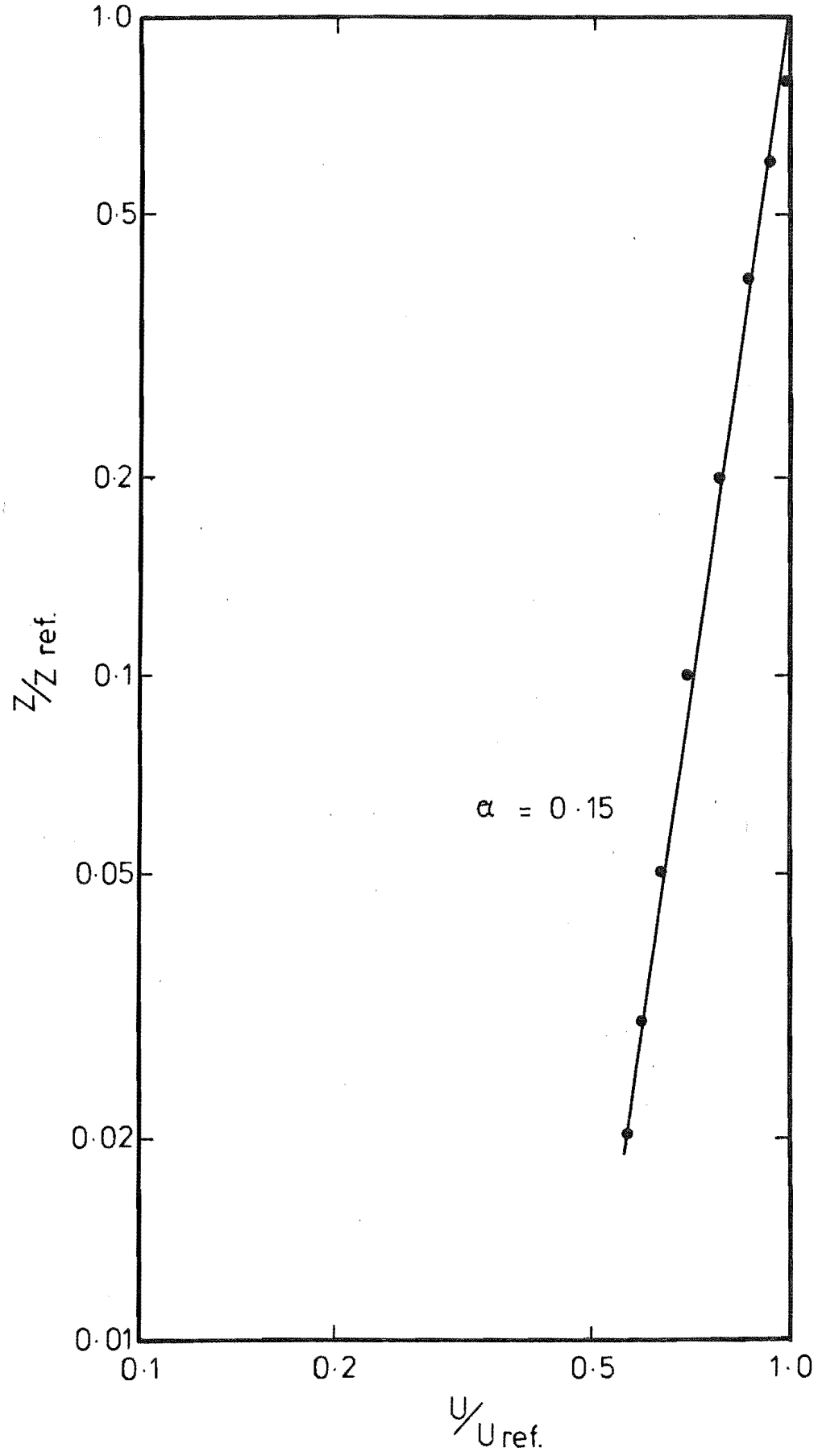

FIG 7·11 UPSTREAM POWER LAW VELOCITY PROFILE

Two modelled profiles, with model A in the wind tunnel, are presented in Fig. 7.12. These are compared with measured log-law velocity profiles which were made at the same site in the field. The measured data consists of field tapes SW1 and SW2, (these will be discussed in Chapter 10) which were recorded using the 20m tower and velocity profiles measured with the TALA kite equipment, these having been described in Chapter 6. The results of all three measuring techniques show an excellent agreement of roughness length values, this being 2 to 3cm. This also agrees very well with values predicted by ESDU (1974) which suggests $z_o \simeq$ 1-5 cm for the type of terrain being modelled.

Turbulence intensity profiles using modelled, measured and theoretical data, are presented in Fig. 7.13. Counihan (1975) suggested that ESDU (considered here as the theoretical curve) generally overestimates the turbulence intensity; therefore the curve proposed by Counihan is also presented for comparison.

Unfortunately, field measurements of this parameter could only be made to 20m above ground height. In this region, all of the curves appear to agree very well. It is interesting to note that despite Counihan's comment regarding the ESDU overestimation, his proposed profile crosses the ESDU profile at about the 100m height.

The modelled longitudinal component of the energy spectrum is presented in Fig. 7.14, and compared with the theoretical model proposed by Harris (1970), which is represented by

$$\frac{nS_u(n)}{\sigma_u^2} = \frac{\frac{2}{3}\left(\frac{nL}{\bar{u}_{10}}\right)}{\left[2 + \left(\frac{nL}{\bar{u}_{10}}\right)^2\right]^{5/6}} \quad \ldots\ldots\ldots\ldots (7.3)$$

where n = frequency

$\bar{u}_{10}$ = velocity at z = 10m

L = scaling length (1800m)

Superimposed on these is the band into which the field measurements taken at the same site, fall. These are discussed in more detail in Chapter 10.

The modelled and measured spectra showed a similar shape and agreed well with the theoretical spectra; in particular, the location of the spectra

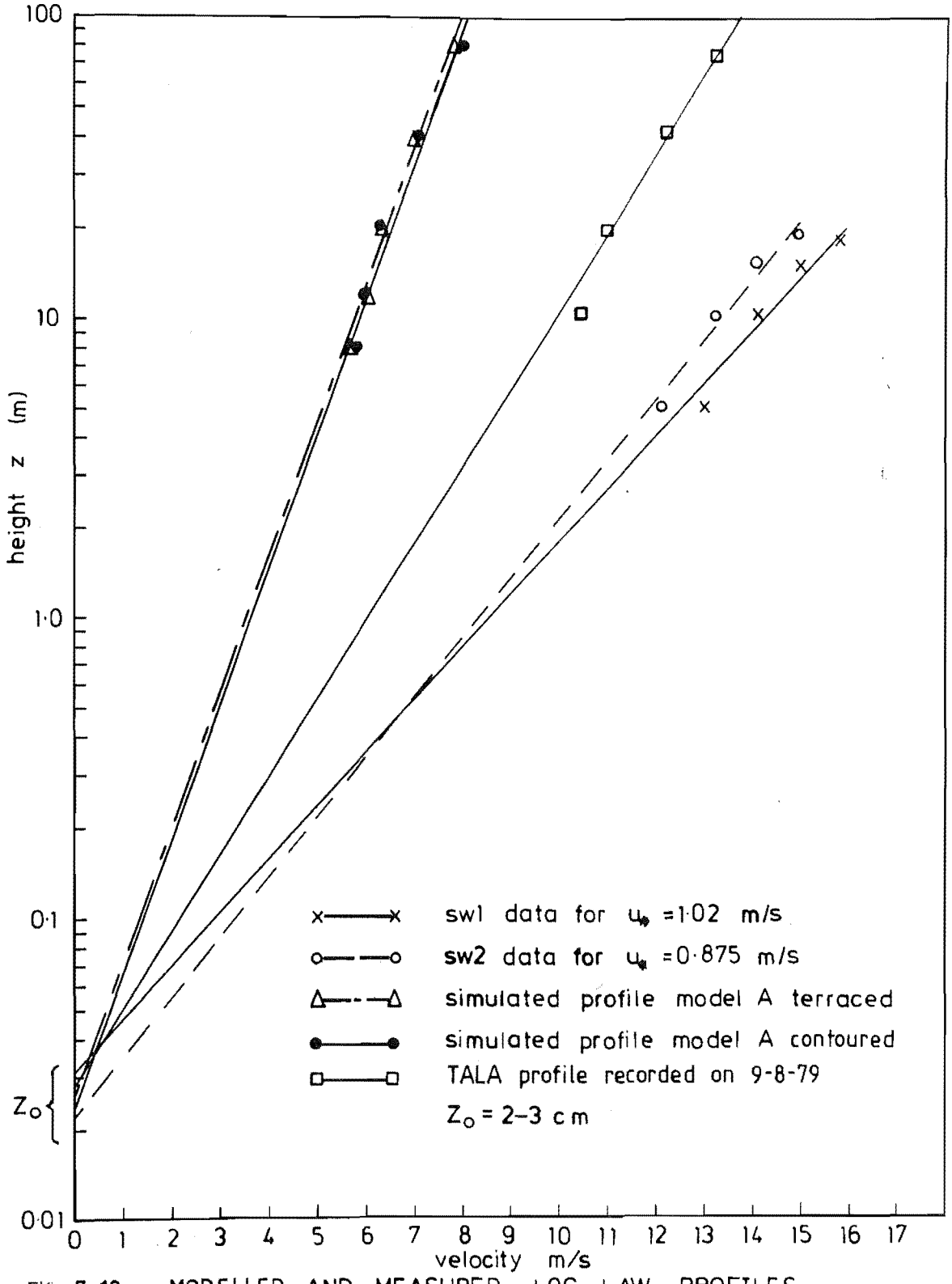

FIG 7·12 MODELLED AND MEASURED LOG–LAW PROFILES

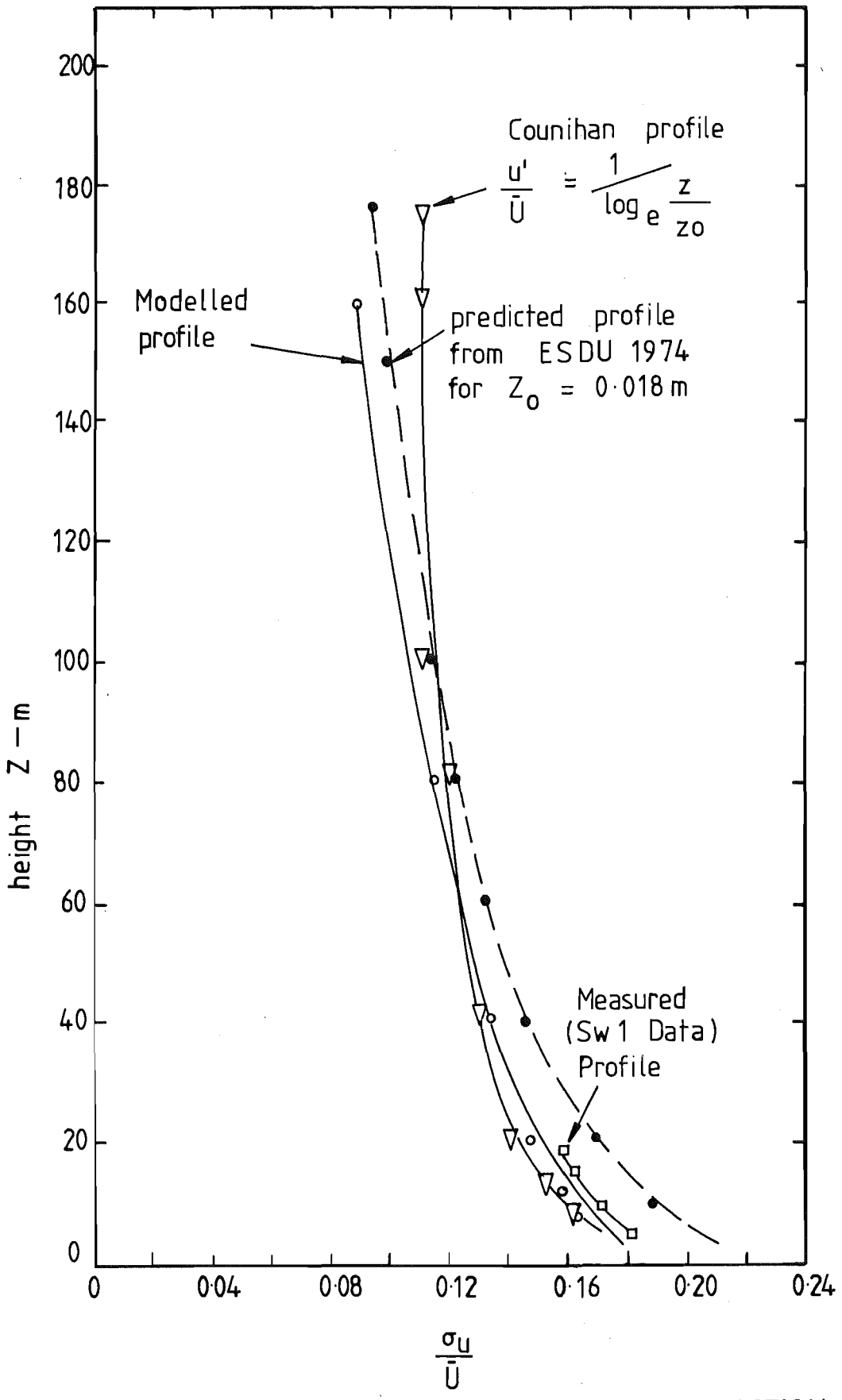

FIG 7·13 COMPARISON OF MODELLED, THEORETICAL AND MEASURED TURBULENCE INTENSITY PROFILES

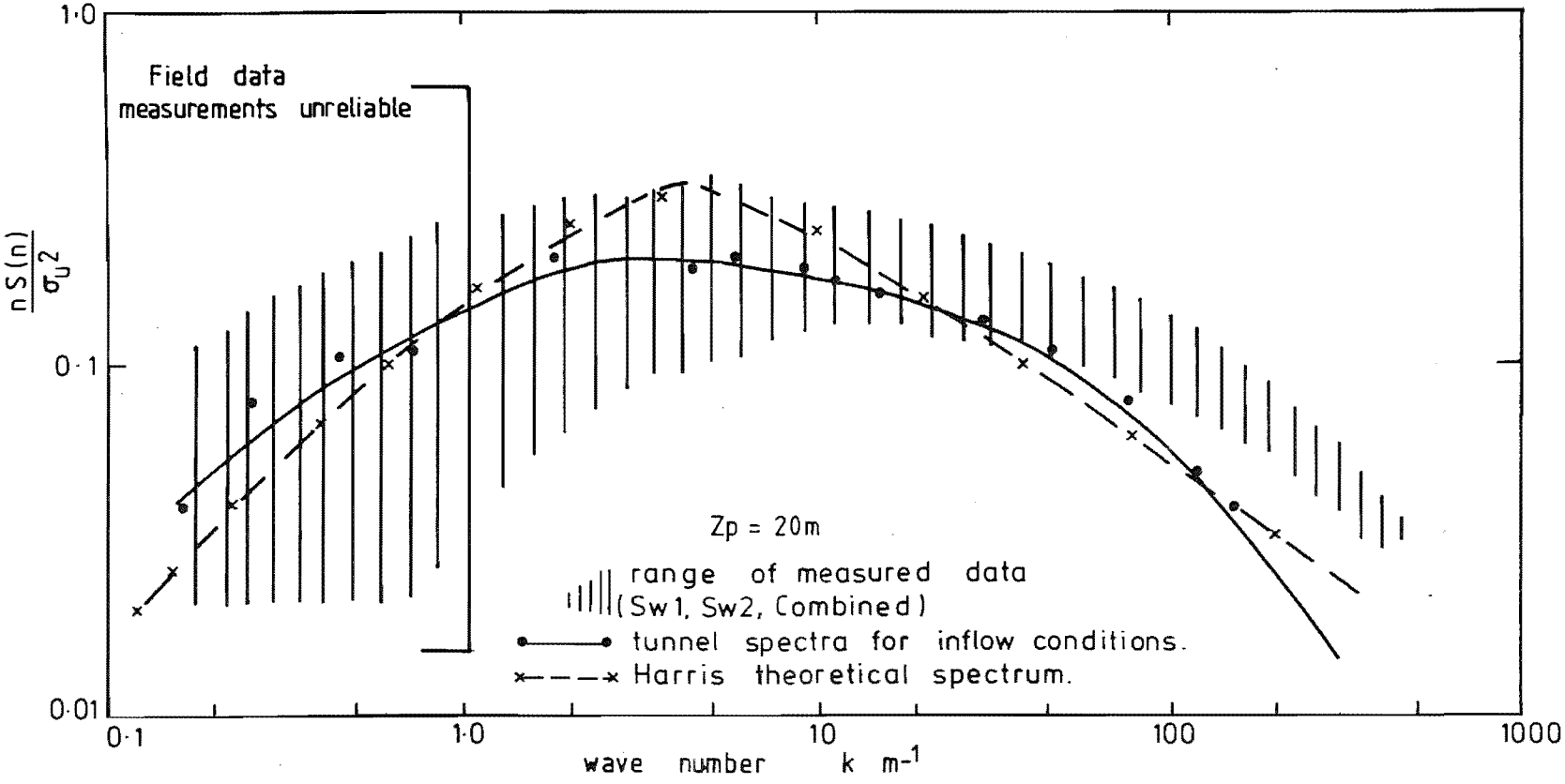

FIG 7·14 COMPARISON OF MODELLED, THEORETICAL AND MEASURED LONGITUDINAL ENERGY SPECTRA FOR Zp=20m.

peak.

Autocorrelation curves are presented in Fig. 7.15, two of the curves being measured in the field and compared to a modelled curve. It is interesting to note the range of values of length scale calculated from these curves, especially when one considers that the field data plotted was collected within 1½ hours during the same wind event.

A summary of the major parameters modelled in this study are presented in Table 7.1 and compared with measured and theoretical values from several sources. The degree of agreement is most encouraging and suggests that suitable inflow similarity on to the model exists.

Parameter	Wind Tunnel Simulation	ESDU (1974)	Tower	Other Sources
δ	400m	490m*	-	300m (1)
α	0.15	0.15	0.16	0.16 (1)
z_o	0.02m	0.02-0.05m	0.03	0.03 (2)
L_{u_x} @ 20m	290m	100m	164m	145m (3)
$-\overline{uw}/u_\delta^2$ @ 20m	0.0022 +	0.0016	0.0023	0.0020
$\frac{u'}{\bar{u}}$ @ 20 m	0.14-0.15	0.16-0.17	0.13-0.14	0.14-0.16(2)

* Derived from ESDU (1974) using the empirical expression

$$z_G = 1000\ z_o^{0.18}\ m$$

(1) Davenport (1963)

(2) Flay (1978)

(3) Counihan (1975)

\+ - See Chapter 8

TABLE 7.1: Summary of modelled parameters

7.3 MODEL A TERRACED

This section presents the wind tunnel results for model A in the terraced form of construction. However, before detailed analysis was carried out, several data collecting points at the southern boundary of the model were used to check the values of several of the parameters described in the previous section.

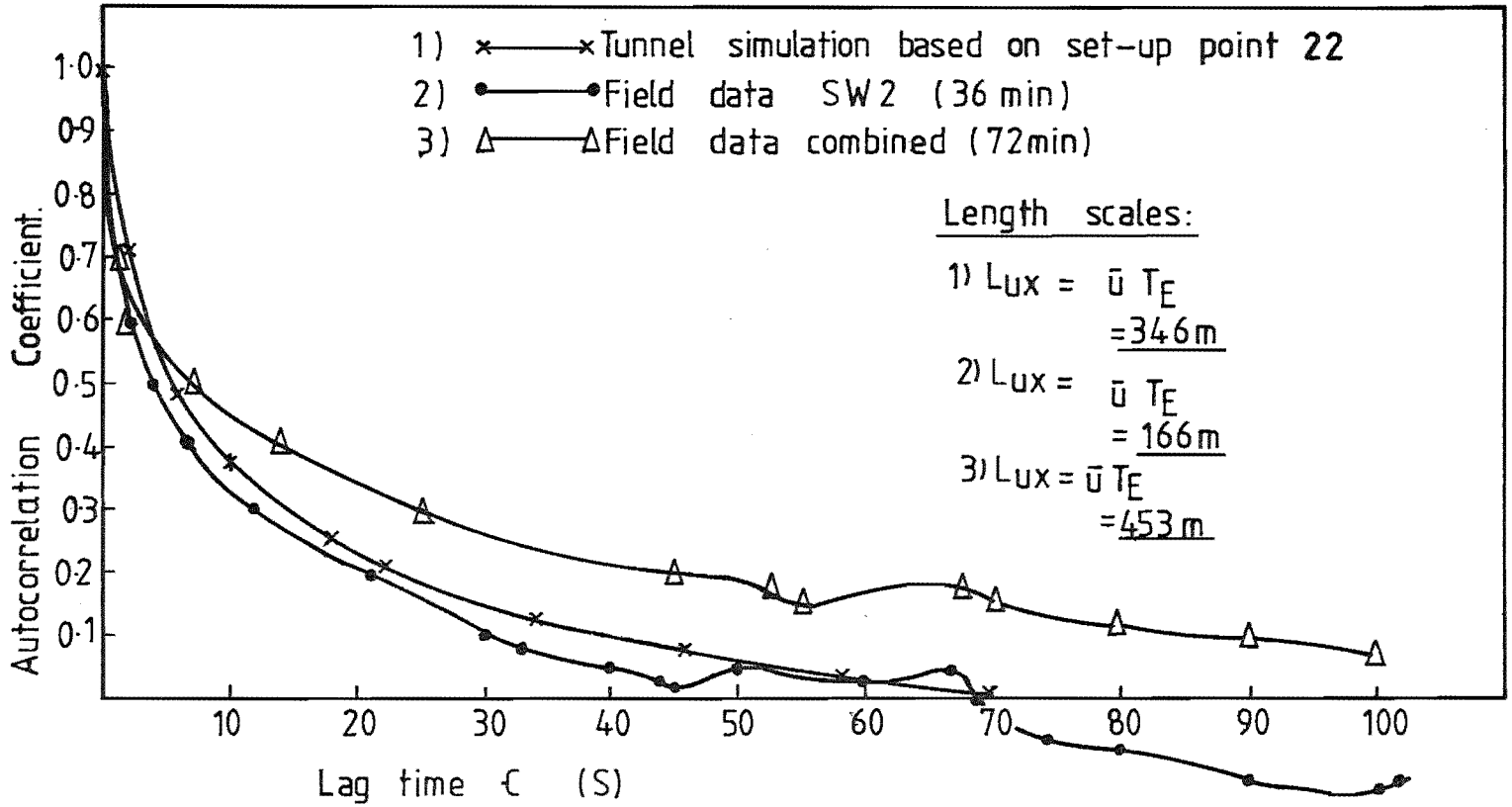

FIG 7·15 AUTOCORRELATION COMPARISONS BETWEEN FIELD AND WIND-TUNNEL SIMULATION

7.3.1 Approach Flow Characteristics

The data collecting points and sections used for Model A are presented in Fig. 7.16; the physical arrangement of the wind tunnel, grid, trip fences etc. is given in Appendix II.

The basis for the site selection of points on the models was to form longitudinal and lateral cross sections over the model. As many of these points as possible were selected to correspond with the sites selected for the field data collection programme.

Isotach (lines of constant velocity) and Isoturb (lines of constant turbulence) lines are plotted along the section to present the reader with a picture of the flow régime over the model. This method of data presentation will be used extensively in this thesis.

Points 53, 22 and 21 on Fig. 7.16 are situated on flat terrain leading to Gebbies Pass. These points were used to evaluate the approach flow uniformity and to check the parameters previously discussed in Section 7.2.

1) Velocity Profiles: Power law velocity profiles for points 21 and 53 are presented in Figs 7.17 and 7.18. These yield the same value for the power law index as was found upstream of the model, which has been shown to agree with other researchers.

The log law form of the velocity profile is presented in Figs 7.19 and 7.20, and these are also in agreement with the upstream profile and yield roughness lengths which are in excellent agreement.

2) Turbulence Intensity Profile: Turbulence intensity profile for point 53 is presented in Fig. 7.21 and is compared with models predicted by ESDU (1974) and Counihan (1975).

The model compares favourably with the theoretical model and that predicted by Counihan (1975).

3) Gradient Height: The gradient height of the boundary layer at all three points was found to be 100mm, which represents 400m on the prototype and is consistent with the upstream condition. It was stated in the previous section that Davenport (1963) suggested a gradient height of 300m for rural terrain. However, Counihan (1975) quotes several other sources which suggest that 300m is too low. Most of the values reported by Counihan suggest the gradient height to be 400-600m for rural terrain, and Counihan himself supports the value of 600m. Since there appears to be a great deal of doubt about the gradient height and in the absence of

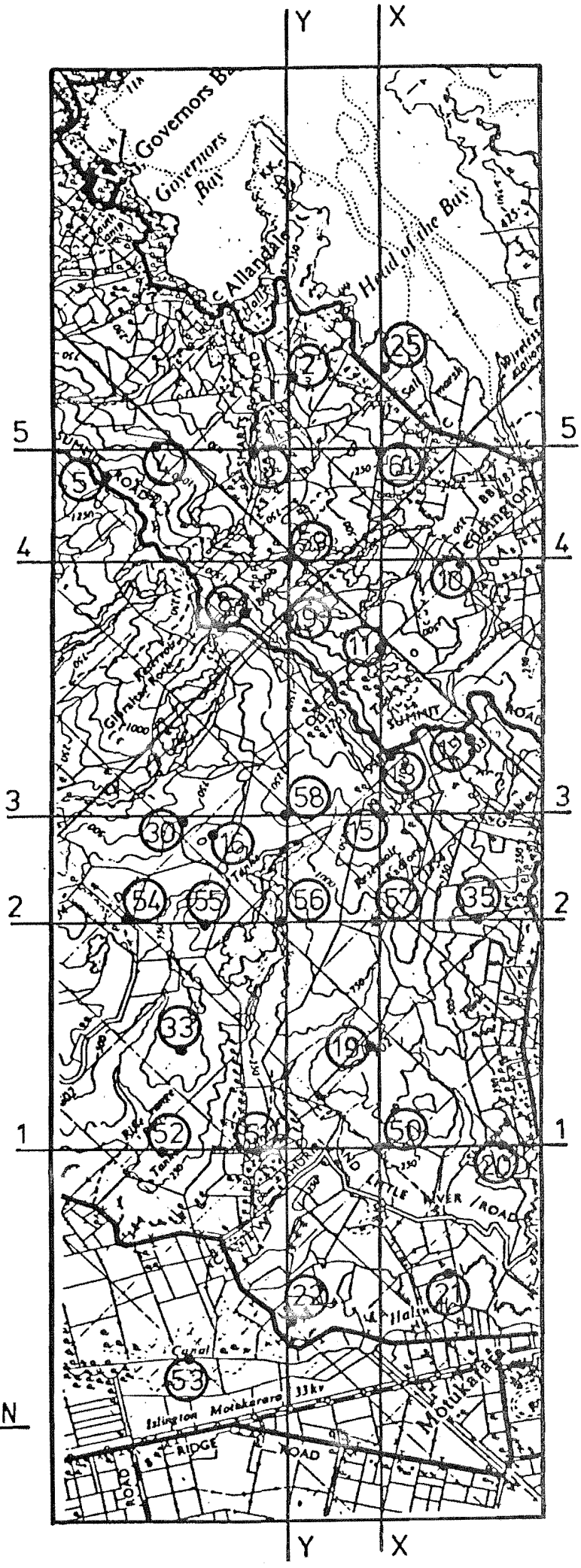
Y
X
5
4
3
2
1
Governors Bay
Governors Bay
Allandale
Head of the Bay
Halfway Bush
Sandy Point
Saltmarsh
Oxford
Edmonton
Glentunnel
Fernmount
Gibraltar Rock
Gibraltar
Summit
Road
Tank
Reservoir
Tank
Tank
Tank

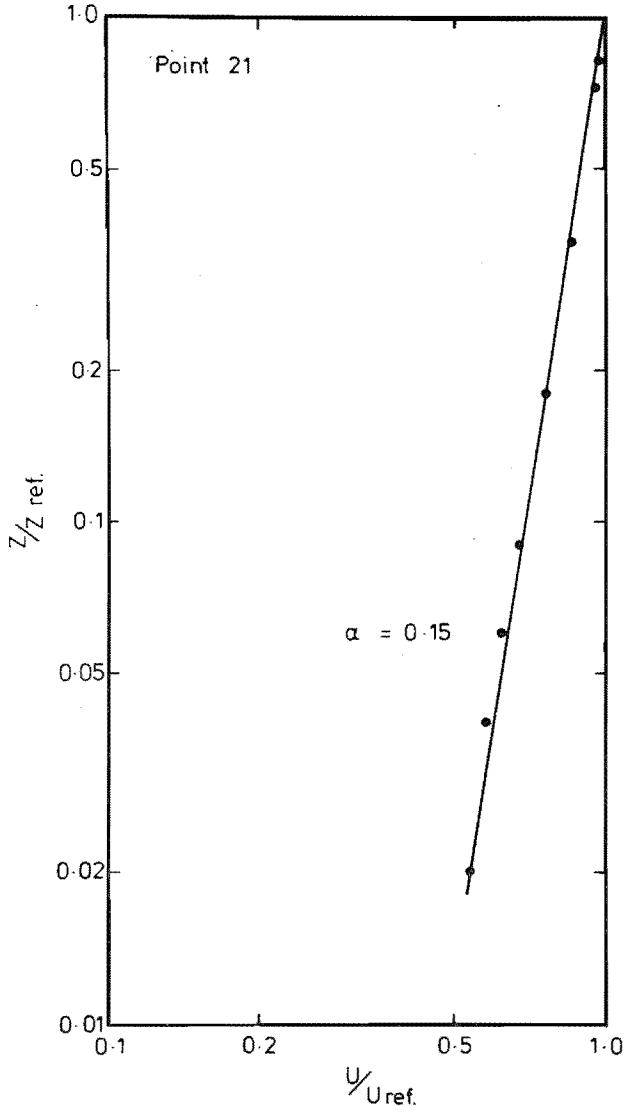

FIG 7.17 POWER LAW VELOCITY PROFILE MODEL A, TERRACED.

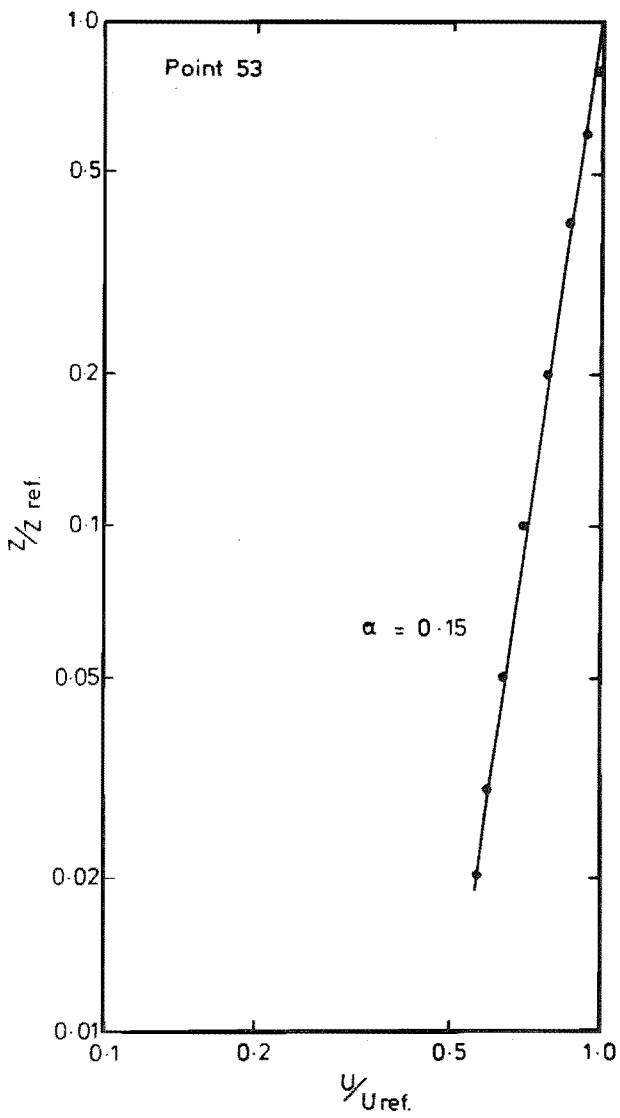

FIG 7.18 POWER LAW VELOCITY PROFILE MODEL A, TERRACED.

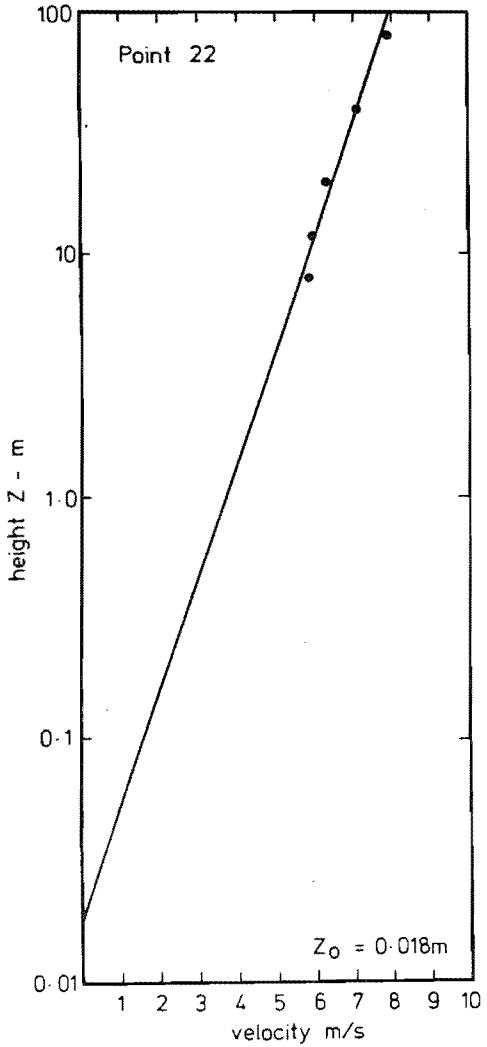

FIG 7.19 LOG LAW VELOCITY PROFILE MODEL A, TERRACED.

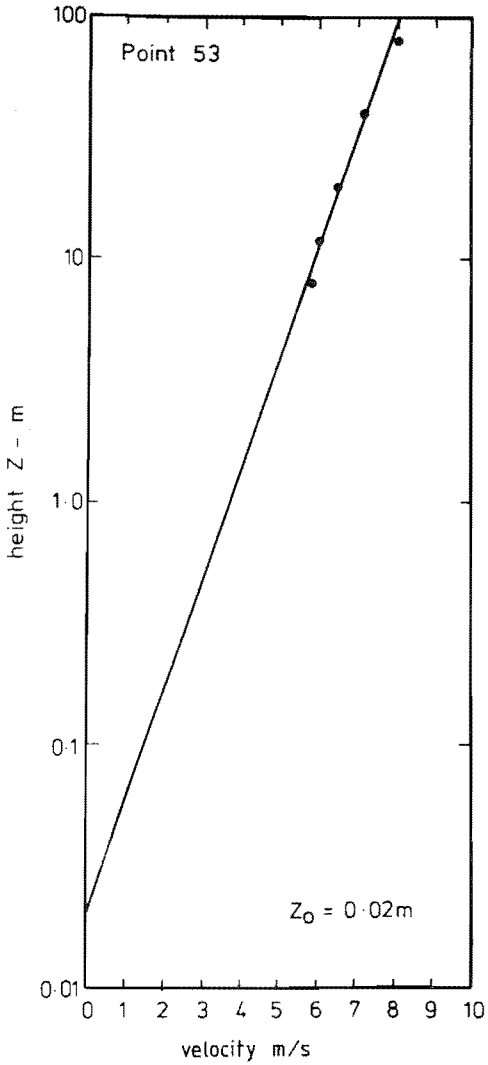

FIG 7.20 LOG LAW VELOCITY PROFILE MODEL A, TERRACED.

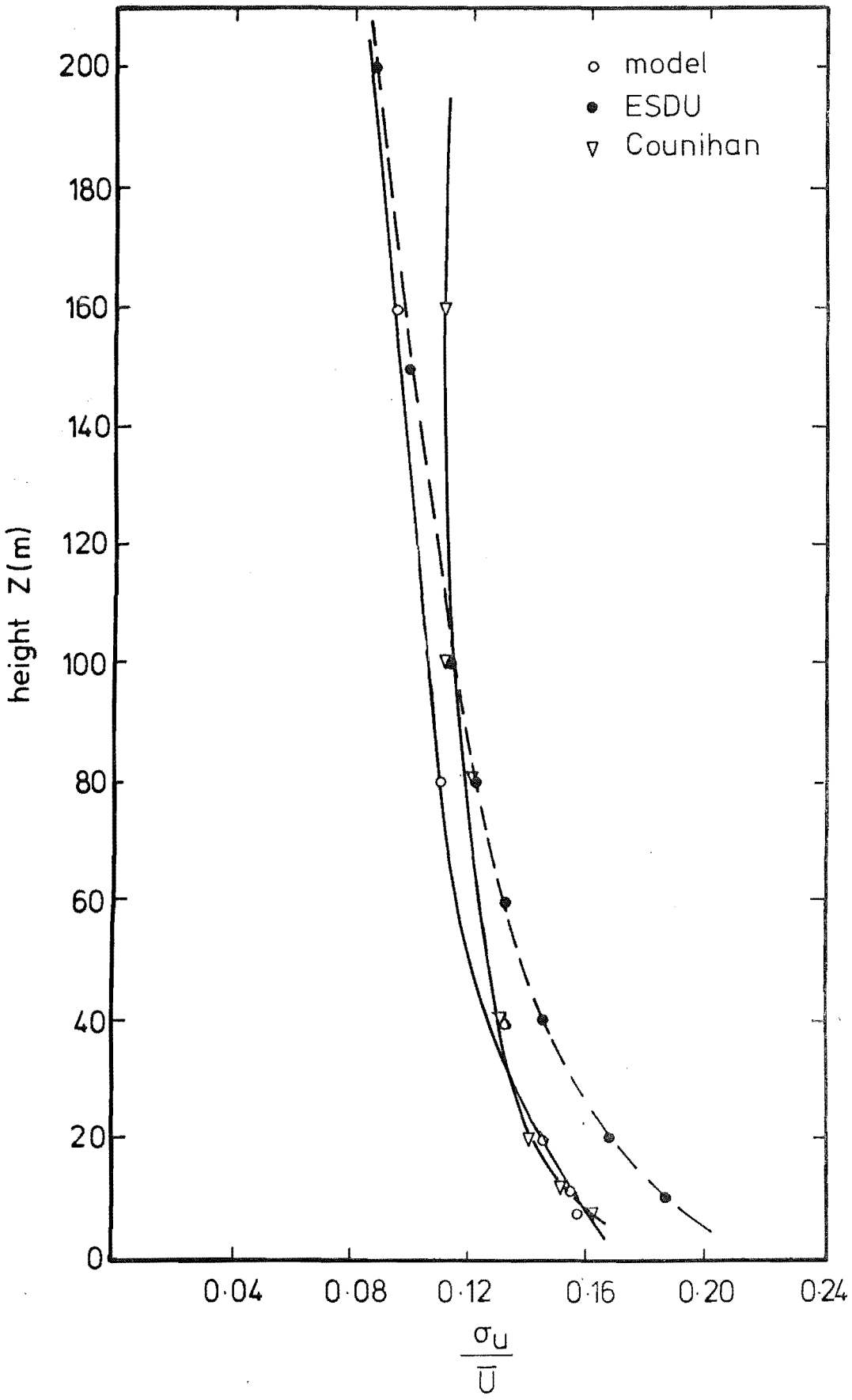

FIG. 7·21 TURBULENCE INTENSITY PROFILE MODEL A, TERRACED. POINT 53.

equipment for the author to make his own measurements; therefore a compromise was adopted and the value of 400m was considered acceptable.

4) Energy Spectrum: Energy spectra for the longitudinal velocity component for points 53 and 22 are presented in Figs 7.22 and 7.23. These are compared with the theoretical model proposed by Harris (1968), which has been discussed in Chapter 2. The modelled spectra matches the theoretical spectrum quite well; this is particularly true for point 22 which is situated in the middle of the tunnel. The peaks of the spectra are of the same order of magnitude which suggest that the length scale of turbulence has been modelled reasonably closely. The suggested value of the length scale L_{u_x} from the spectra is approximately 200m.

Spectra measured at several heights above point 53 are presented in Fig. 7.24. This clearly shows the spectrum peak moving to the left, thus suggesting increasing length scales, which is to be expected, because at greater heights the higher frequencies have decayed and generally the turbulence is of a much lower frequency. It is also interesting to note that at z_p = 40m, the flatness of the peak, which was a characteristic at z_p = 8m, has disappeared. The flatness was basically a function of the model construction material and, at measurements close to the surface, cannot be eliminated.

5) Autocorrelation Coefficients: The autocorrelation curves for points 53 and 21 are presented in Figs 7.25 and 7.26. These have been produced using the digital data collection and processing facility, which has been described in Chapter 5. Length scales have been calculated from the autocorrelation curves using Taylor's hypothesis, and these suggest values for L_{u_x} of 220 - 270m.

A comparison of length scales is presented in Table 7.2, which shows good agreement. This is very encouraging because the value of L_{u_x} is difficult to model and has only been achieved here because of the extra care and effort that was taken to obtain close similarity of the other major parameters such as the roughness length, velocity profile, turbulence intensity profile, and energy spectrum. The Table presents values of the length scale, L_{u_x}, as modelled, measured and predicted by ESDU (1974) and Counihan (1975) at a height of 20m.

Figs 7.27 and 7.28 present isotachs and isoturbs plotted through points 53, 22 and 21. These are encouraging because they confirm the

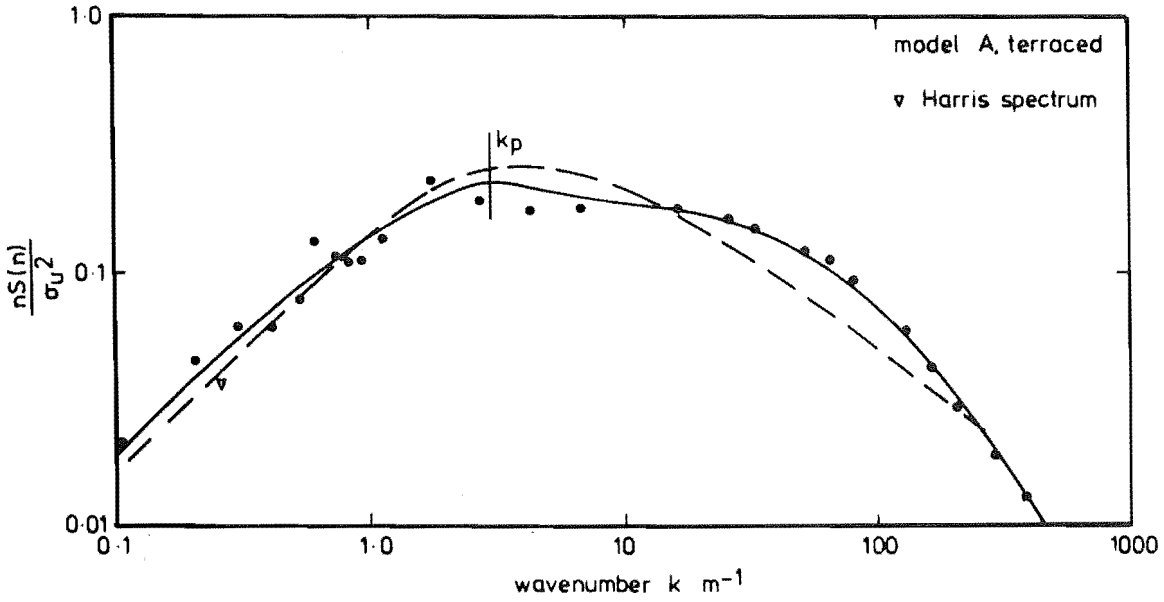

FIG 7.22 ENERGY SPECTRA FOR LONGITUDINAL VELOCITY COMPONENT AT POINT 22, Z_p = 8m

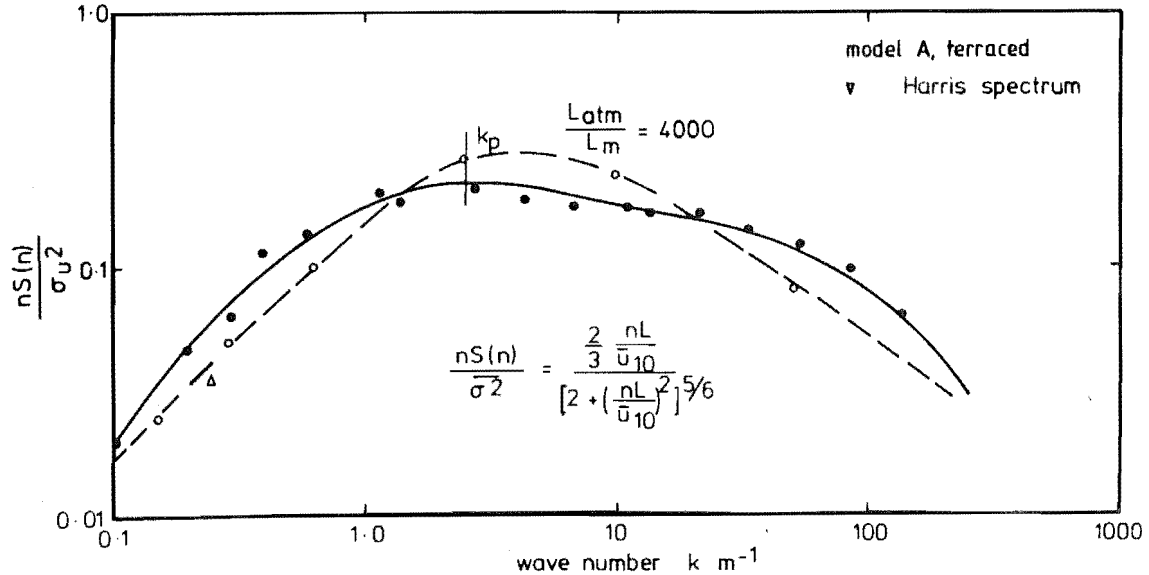

FIG 7.23 ENERGY SPECTRA FOR LONGITUDINAL VELOCITY COMPONENT AT POINT 53, Z_p = 8m

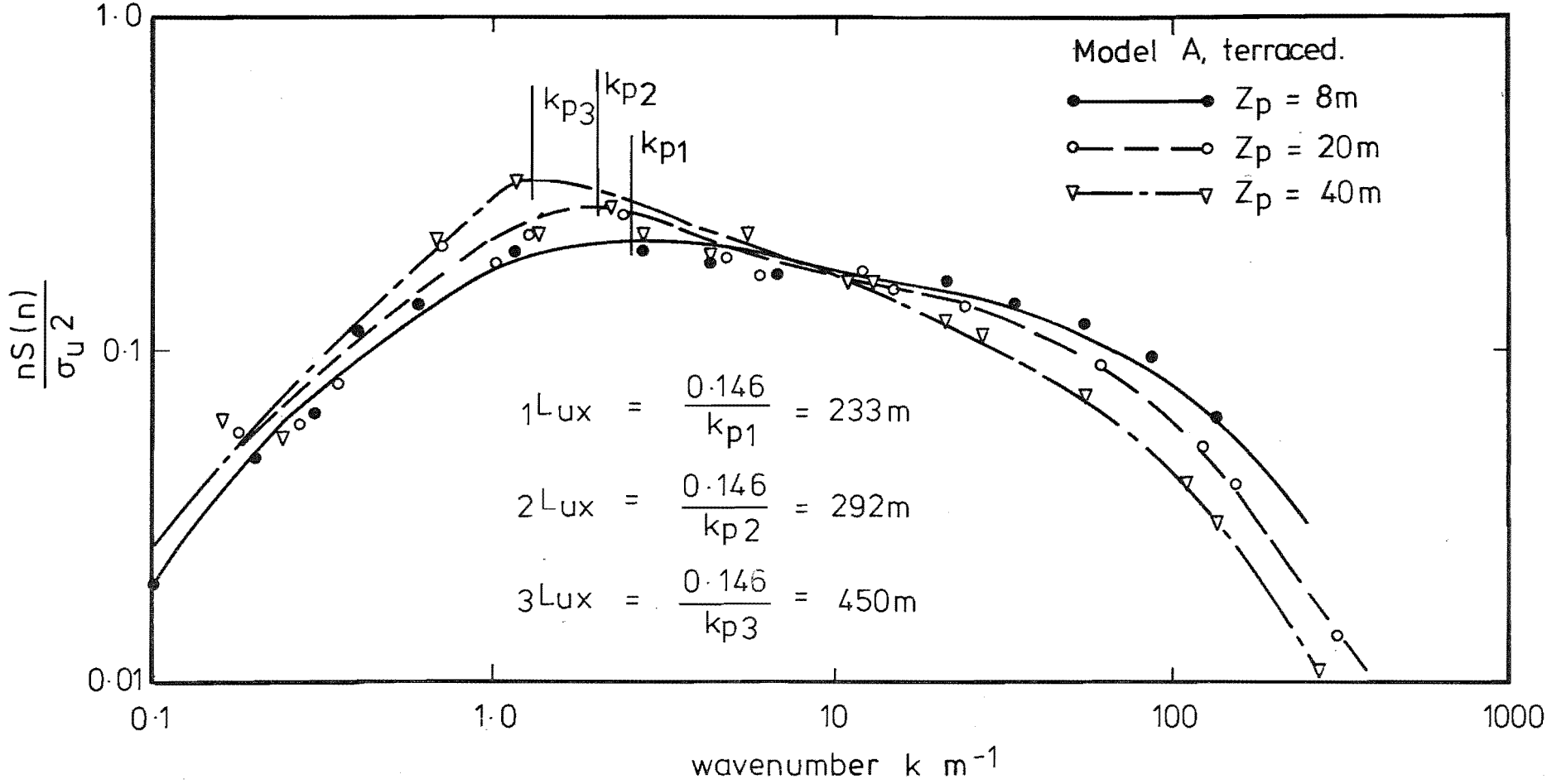

FIG 7·24 SPECTRA AT INCREASING HEIGHTS FOR POINT 53. Z_p = 8m, 20m, 40m.

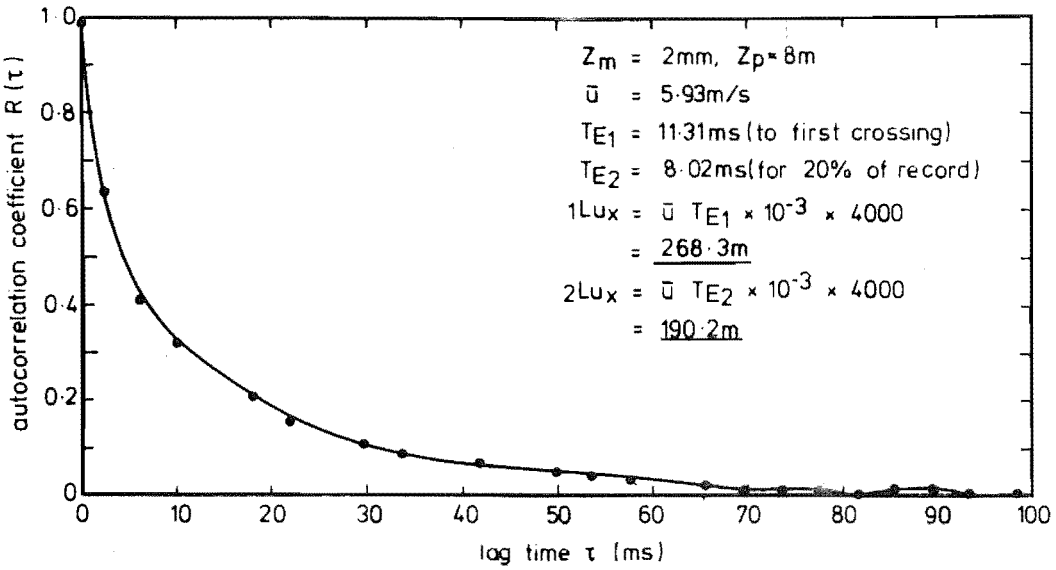

FIG 7.25 AUTOCORRELATION COEFFICIENT FOR LONGITUDINAL VELOCITY COMPONENT AT POINT 21 FOR MODEL A, TERRACED, Z_p = 8m

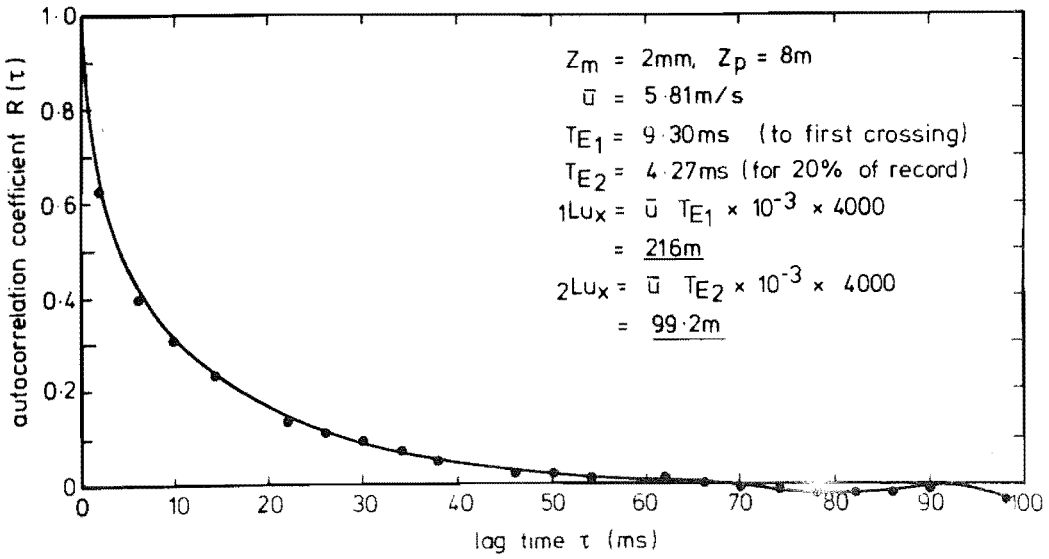

FIG 7.26 AUTOCORRELATION COEFFICIENT FOR LONGITUDINAL VELOCITY COMPONENT AT POINT 53 FOR MODEL A, TERRACED, Z_p = 8m

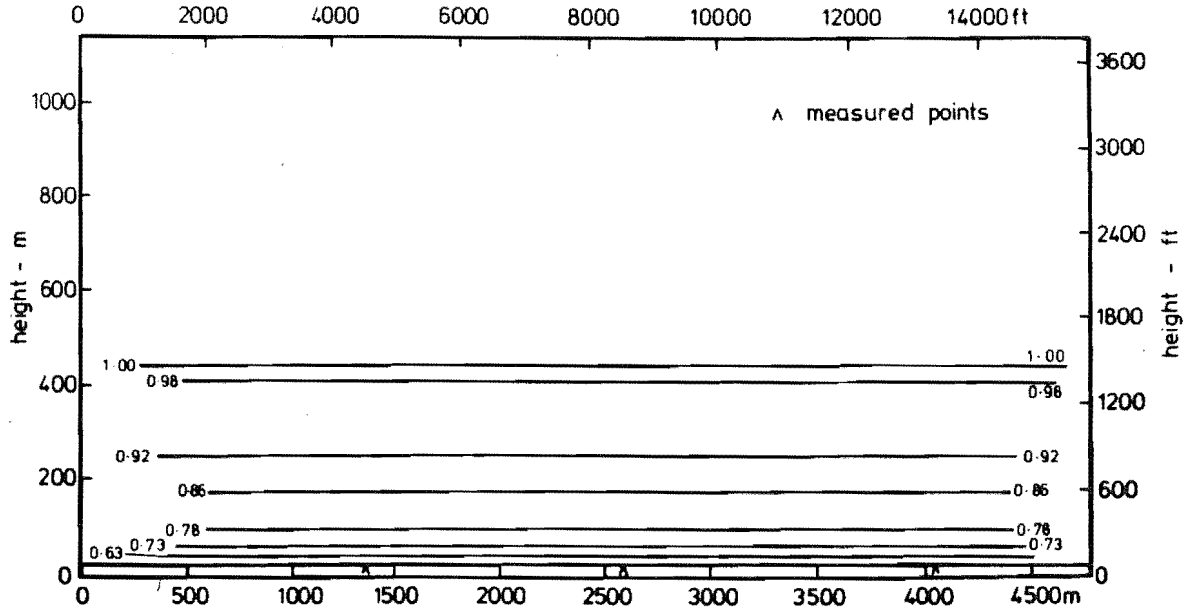

FIG 7.27 ISOTACHS FOR MODEL A TERRACED LATERAL CROSS SECTION UPSTREAM OF MODEL

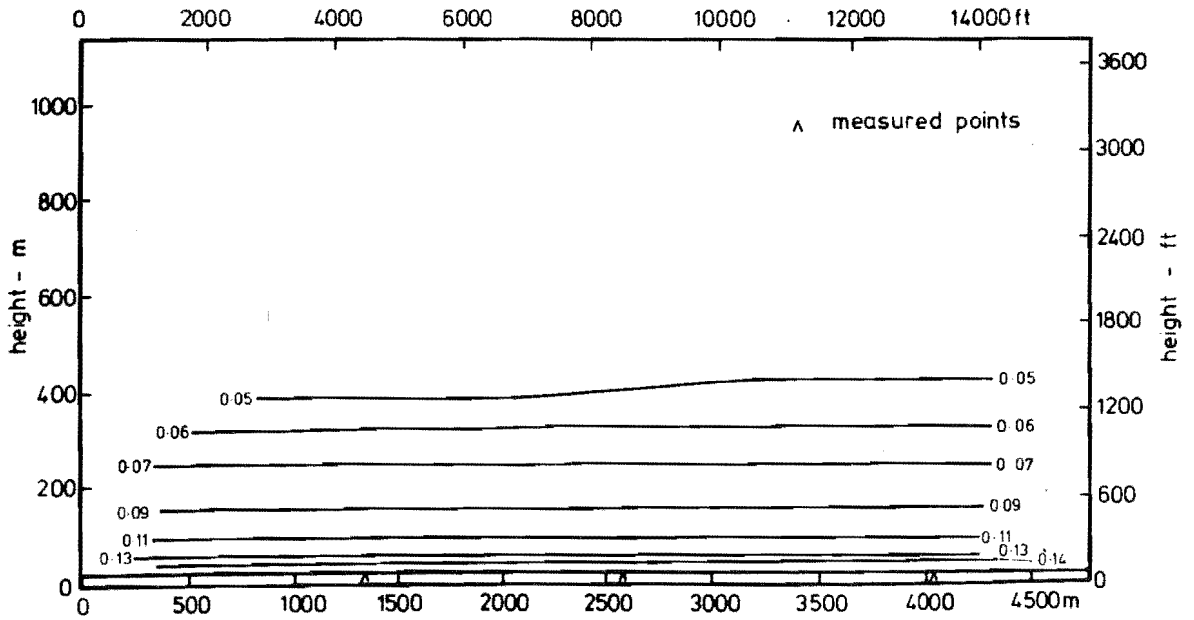

FIG 7.28 ISOTURBS FOR MODEL A TERRACED LATERAL CROSS SECTION UPSTREAM OF MODEL

degree of lateral uniformity and show that the boundary layer depth has established itself at 100mm, which represents the desired 400m on the prototype.

Source	Length scale L_{u_x} at z_p = 20m
Wind tunnel simulation (modelled)	290m (1) 200m (2)
Measured	170-450m (1) 120-180m (2)
Counihan (1975)	145m
ESDU (1974)	100m

(1) Derived from Autocorrelation using Taylor's hypothesis.

(2) Derived from Energy Spectrum using the relationship

$$L_{u_x} = \frac{0.146}{k_p}$$

where k_p is the peak wave number.

TABLE 7.2: Length scale, L_{u_x} comparisons

7.3.2 Flow Visualisation

(1) Polystyrene Beads: Polystyrene beads were placed upstream of the model and the tunnel speed increased until all the beads had moved on to the model. Initially this was recorded with a Video unit mounted in the wind tunnel but the results were so inconclusive and difficult to interpret that this method was abandoned. The method adopted was to record the bead deposition areas prior to increasing the tunnel speed further. Results of the low speed tests, approximately 4.0 m/s, are presented in Fig. 7.29. An interesting feature was the obvious degree of shelter provided by the Port Hills, the passage of beads to this area being along the leeward side of the Port Hills ridge.

The tunnel speed was increased to approximately 5.7 m/s, measured in the free stream. Deposits in the valleys and behind small hills upstream

MODEL A

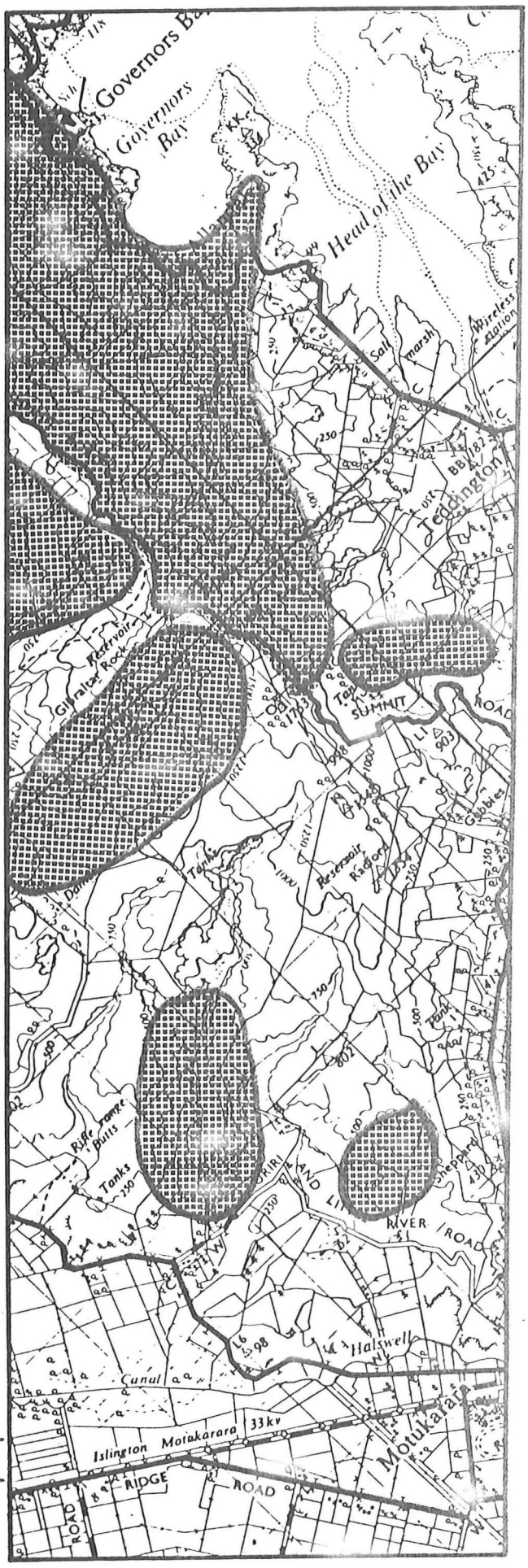

deposits at low speed

FIG 7·29 POLYSTYRENE BEAD DEPOSITION DIAGRAM TERRACED MODEL

of the main ridge disappeared. More interesting was the manner in which the bead deposit in the lee of the Port Hills was reduced. This suggested a very definite flow along the leeward side of the hills. At this stage it was believed that the terraced nature of the construction was enhancing the flow. The results of the high speed tests are presented in Fig. 7.30. Similar tests with the model contoured were expected to support or dismiss this theory, and these will be presented in Section 7.4.

(2) Flags: Miniature flags, as described in Section 5.3.1, were placed on the model analysis points. The flag pivot pin was inserted into the model until the flag centre line was at a height of 7 - 10mm above the model surface. To ensure that all flags were operational, they were initially kept at 90° to the tunnel centre line so that their alignment with the flow could be observed. The tunnel was then run at a velocity of u_∞ = 9.8 m/s which corresponds to the velocity to be used for the pressure probe and hot film surveys.

The flags generally aligned themselves along the tunnel; however, there were some exceptions. In the basin behind point 16, severe flag fluttering was observed, suggesting an area of high turbulence. The polystyrene bead tests were confirmed as the flags on the leeward side of the Port Hills ridge were seen to align themselves with the ridge.

(3) Smoke: Some preliminary tests were carried out using smoke as the visualisation medium. The tests were recorded with a Video unit so that analysis could be carried out over an extended period. Unfortunately, very little information was gained from this because of the inherent problem of diffusion of the smoke. The nett result of this was to disregard this visualisation technique for future tests. The rationale for this was supported by the excellent results being achieved with the beads and flags.

The flow visualisation results, in particular the flag tests, were used as a guide to select points for accurate flow direction tests using a 5-hole Cobra probe.

7.3.3 Pressure Probe Measurements

A United Sensor Cobra probe was used in conjunction with a Setra Systems low range pressure transducer to measure the actual flow directions over the model.

Measurements were made at selected points at heights of 5mm, 20mm and 40mm To determine the flow direction at a point, the Cobra probe, mounted on the

MODEL A

deposits at high speed

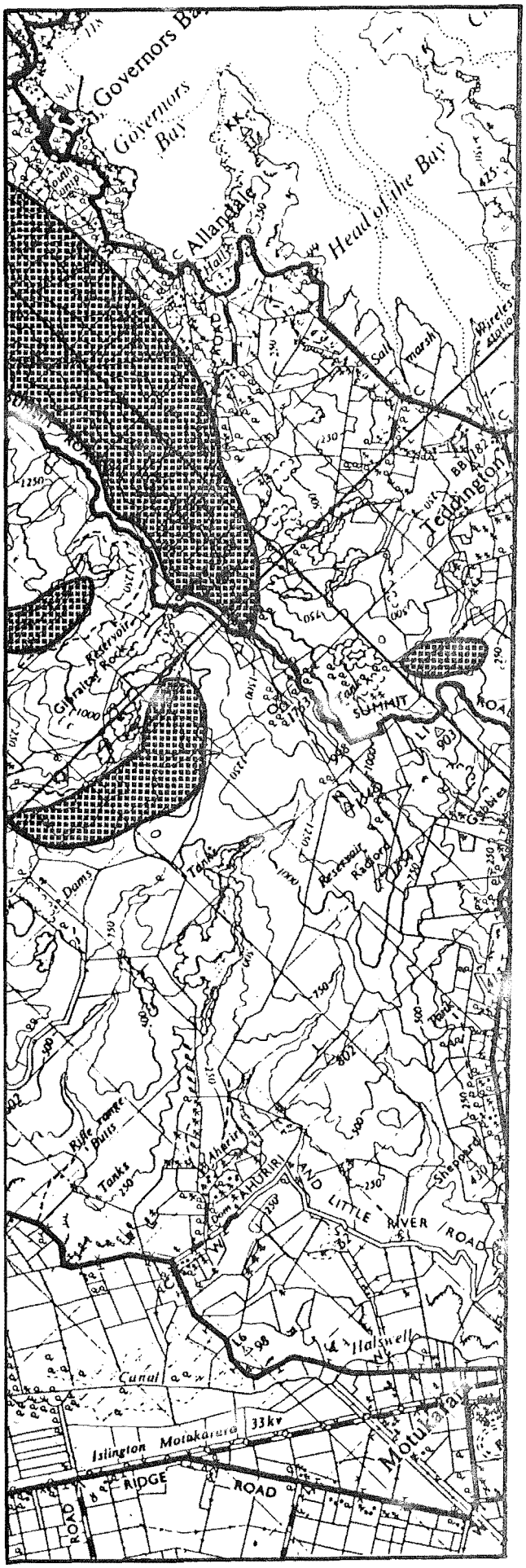

FIG 7·30 POLYSTYRENE BEAD DEPOSITION DIAGRAM, TERRACED MODEL

traverser, was rotated until the outputs from the lateral parts, shown in schematic form in Fig. 7.31, were equalised. The voltage output from the transducer was measured with a T.S.I. DC/RMS Voltmeter type 1076. The results of these tests are presented in Figs 7.32 to 7.34, the 5mm results being extremely close to the results predicted by the flow visualisation analysis. The significance of these tests is highlighted by the degree of flow straightening that occurs between the 5mm and 40mm heights. This effect could not be predicted from the flow visualisation tests and had they been used as a basis for alignment of the hot film probe, major alignment and velocity errors would have resulted.

On the basis of the flow visualisation tests and the pressure probe results, it is reasonable to expect a particularly turbulent region to exist behind the Port Hills ridge where there must be a region where flow passing over the ridge mixes with the flow moving along the leeward side of the ridge.

7.3.4 Hot Film Survey

A description of the equipment involved in the hot film anemometer survey of the wind tunnel models has been given in Chapter 5.

When taking measurements at the analysis points, the procedure utilised the results of the 5-hole pressure probe tests. The hot film probe was set at the flow angle given by the pressure probe tests and then rotated several degrees until a maximum reading was obtained, thus ensuring correct alignment. Vertical traverses of mean velocity and turbulenc intensity were made at the points shown in Fig. 7.16. At many of these points energy spectra and autocorrelation coefficients were measured at heights of 2mm, 5mm and 10mm. However, only a small number of these measurements will be presented here; all of the hot film measurements are presented in a separate report, Neal and Stevenson (1980).

Iso-contour lines for the vertical variation of velocity and turbulence have been prepared for the lateral cross sections 1-5 and the longitudinal cross sections XX and YY. These results are presented in Fig. 7.35 through to Fig. 7.48.

When constructing the iso-contour graphs, the contours were not drawn at pre-determined heights. Instead, contours were drawn for values that occurred at most of the measuring points. This reduced the amount of interpolation, and therefore error, in the plotting process. Care should be taken in trying to compare the iso-contour graphs presented in this thesis, especially since some of the vertical resolution has been lost in

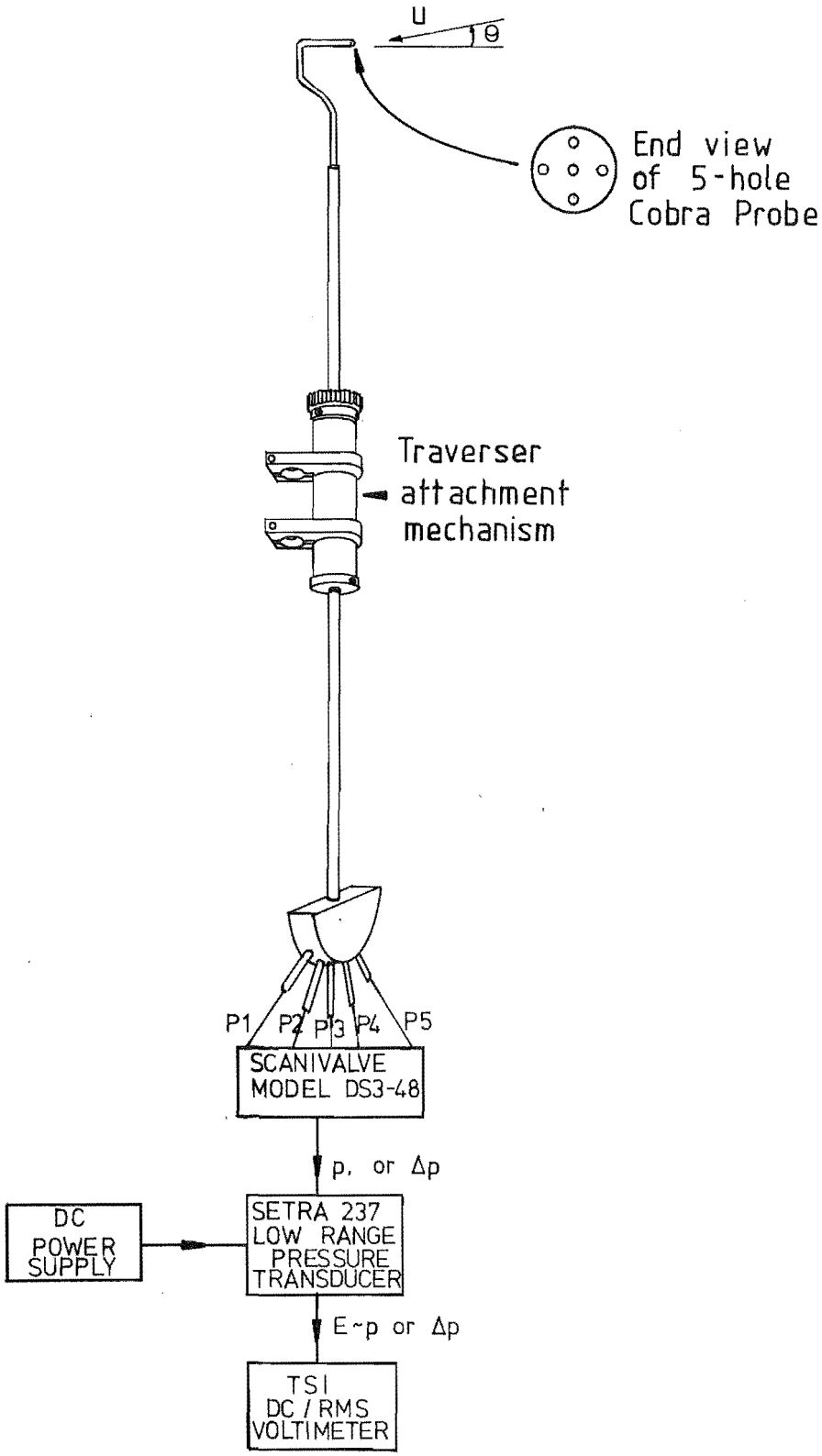

FIG 7-31 SCHEMATIC DIAGRAM OF 5-HOLE COBRA PROBE AND RECORDING EQUIPMENT.

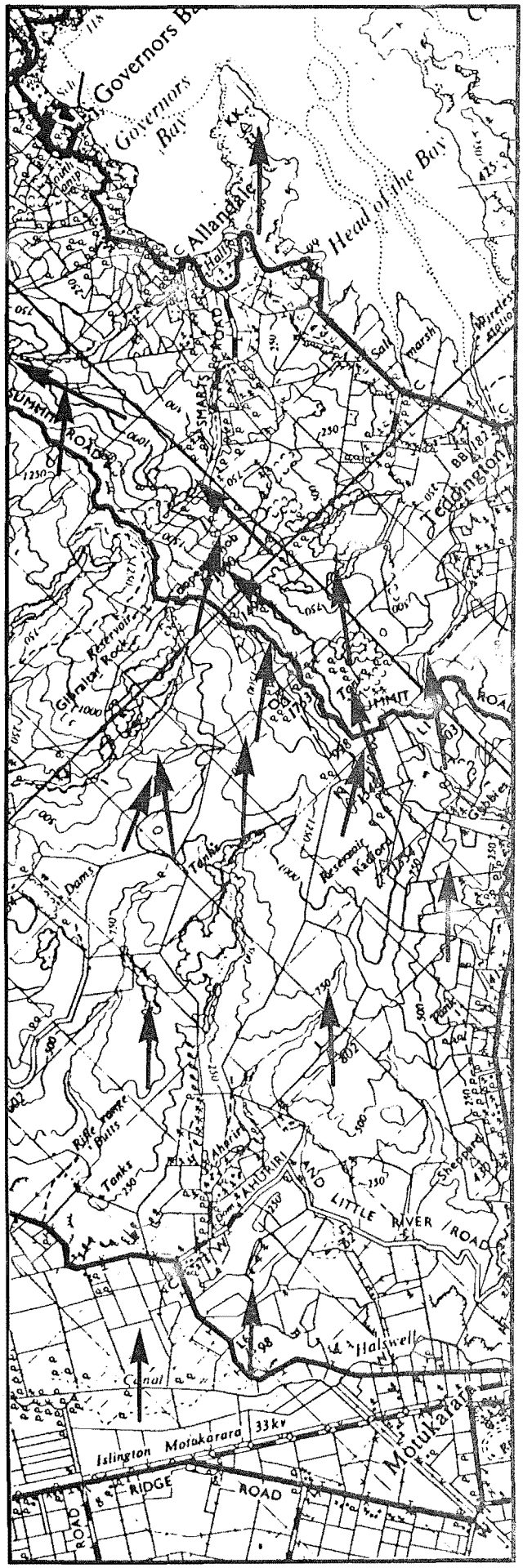

flow regime as measured with 5 hole Cobra probe

FIG. 7·32 FLOW DIRECTIONS OVER MODEL A, TERRACED Z = 5mm

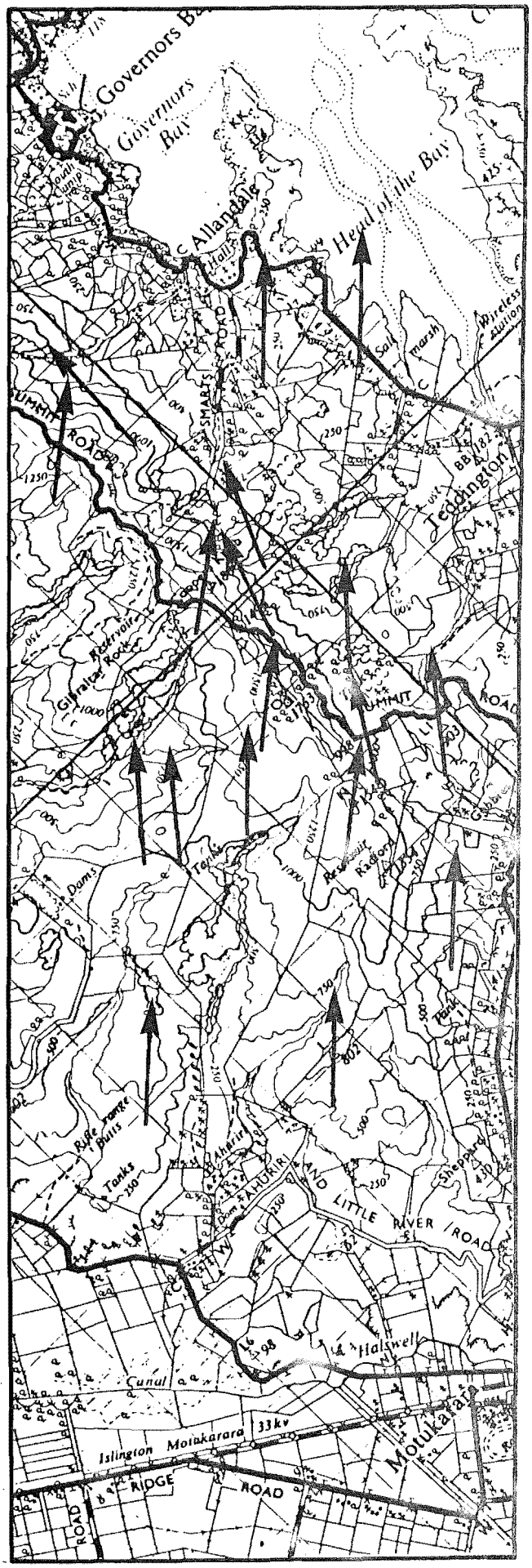

flow regime as measured with 5 hole Cobra probe.

FIG. 7·33 FLOW DIRECTIONS OVER MODEL A, TERRACED Z = 20mm

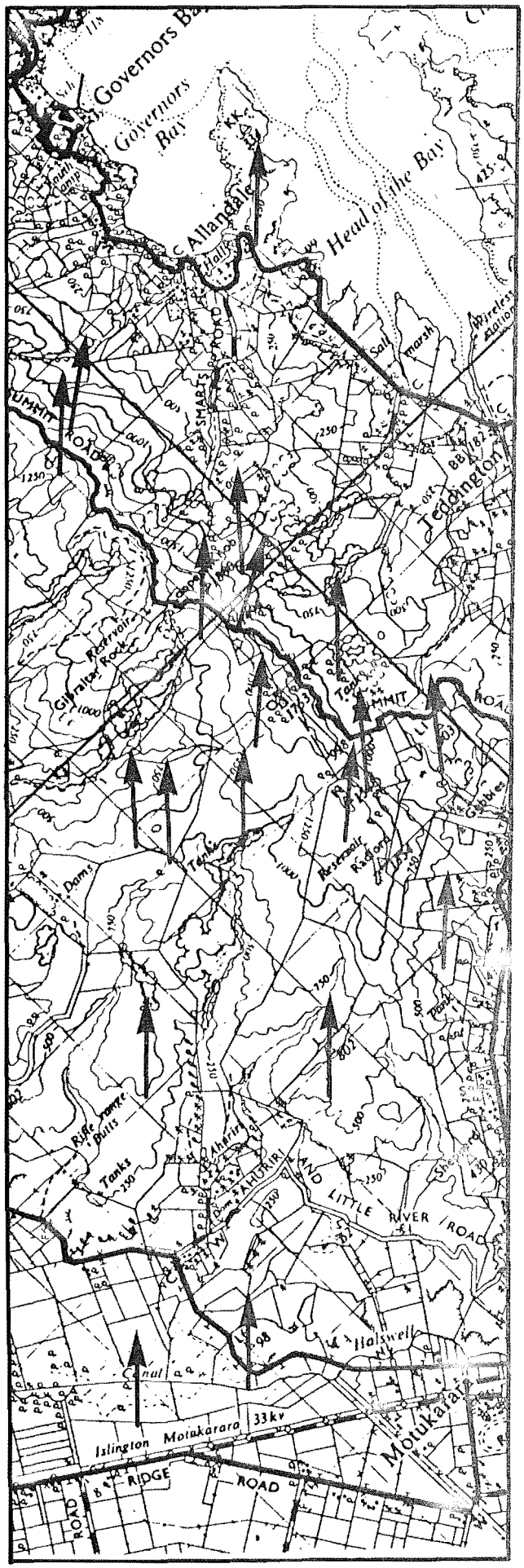

FIG. 7·34 FLOW DIRECTIONS OVER MODEL A TERRACED Z = 40mm

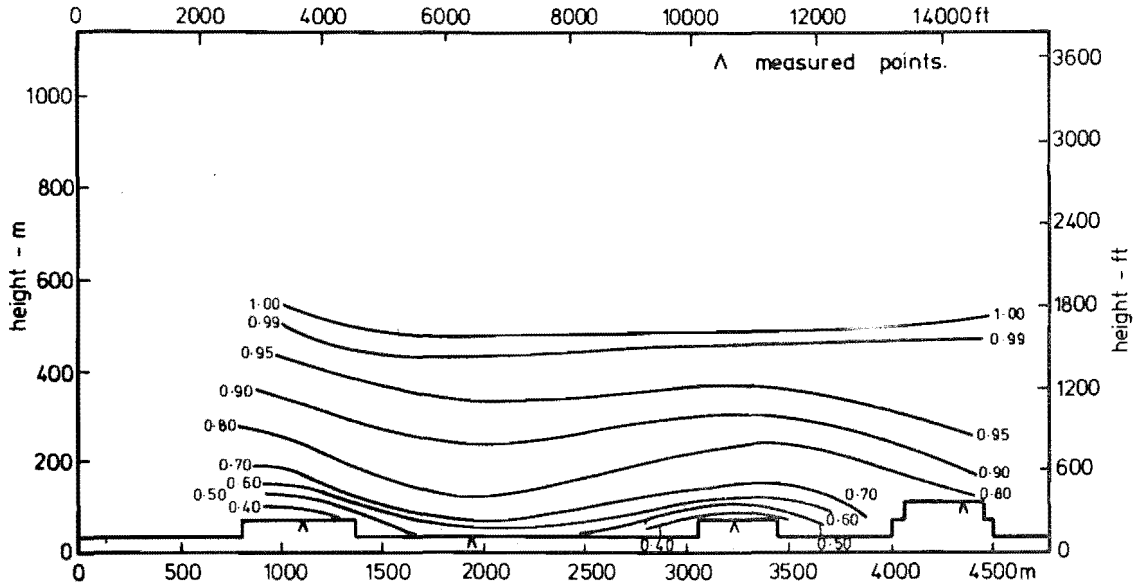

FIG 7.35 ISOTACHS FOR MODEL A TERRACED, LATERAL CROSS SECTION 1.

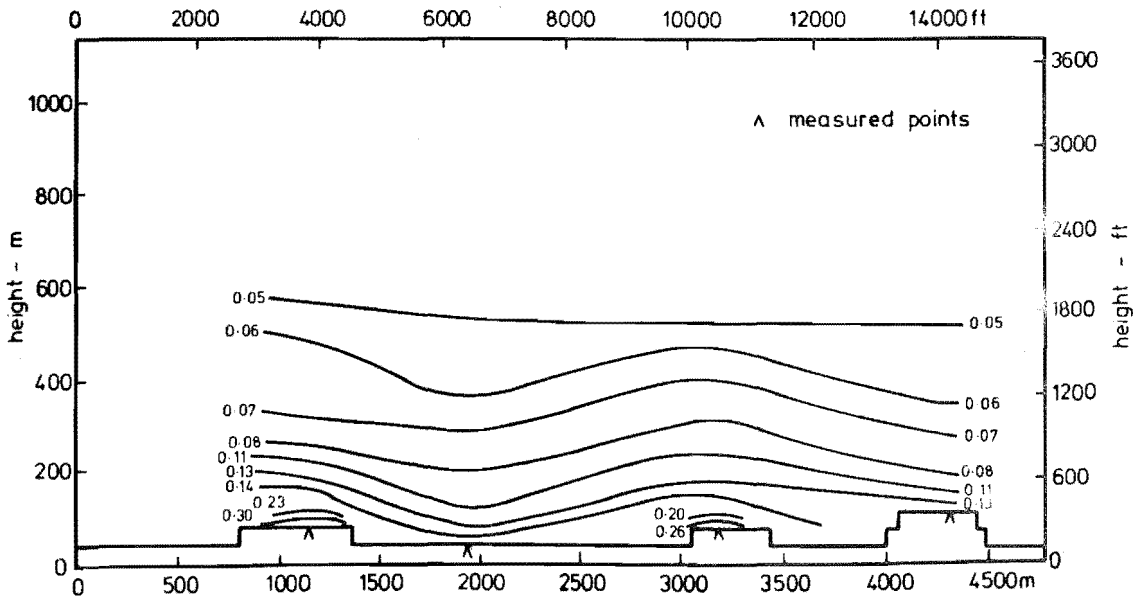

FIG 7.36 ISOTURBS FOR MODEL A TERRACED, LATERAL CROSS SECTION 1

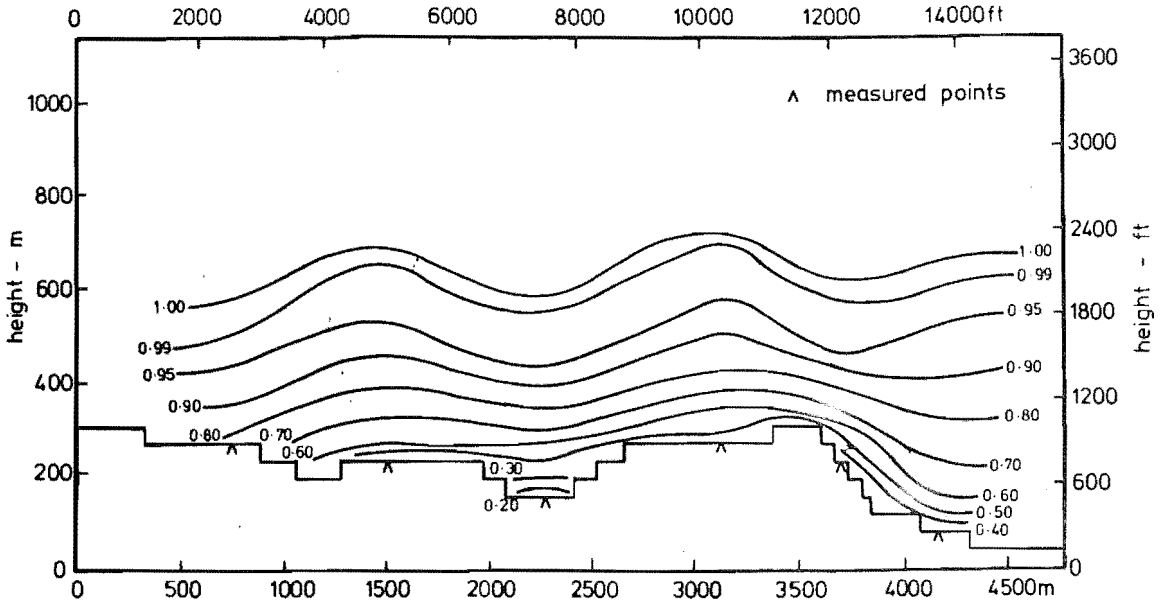

FIG 7.37 ISOTACHS FOR MODEL A TERRACED, LATERAL CROSS SECTION 2

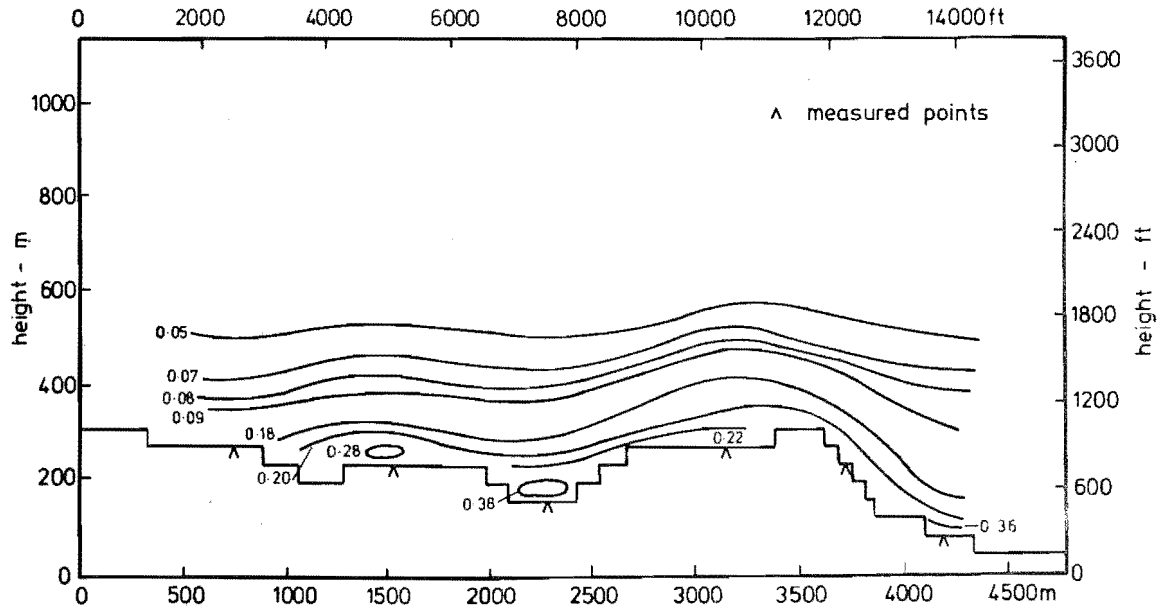

FIG 7.38 ISOTURBS FOR MODEL A TERRACED, LATERAL CROSS SECTION 2

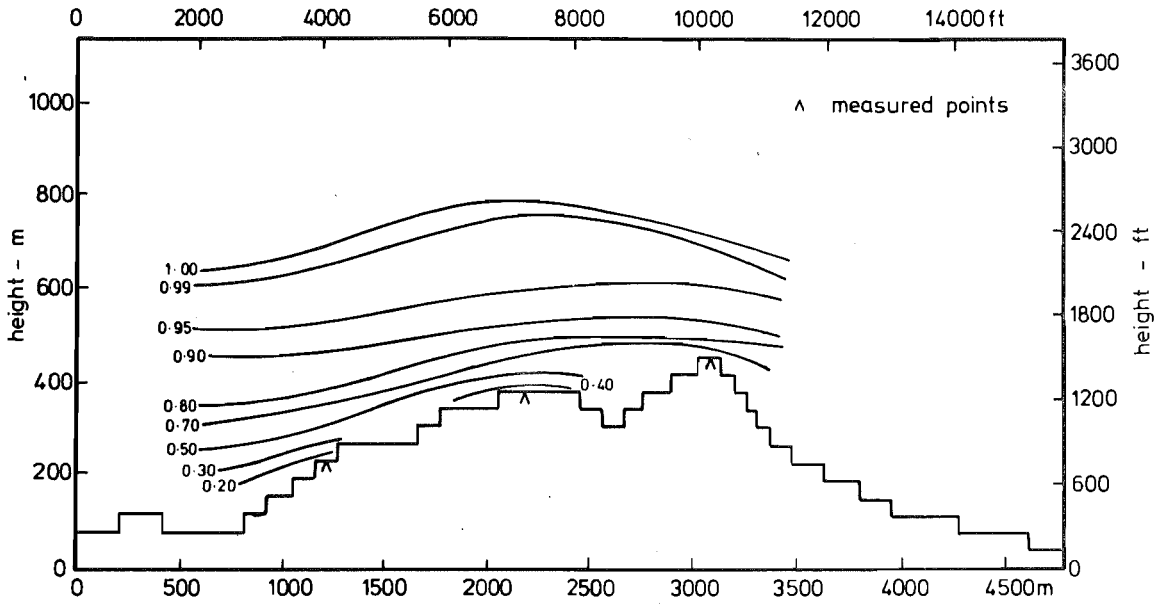

FIG 7.39 ISOTACHS FOR MODEL A TERRACED, LATERAL CROSS SECTION 3

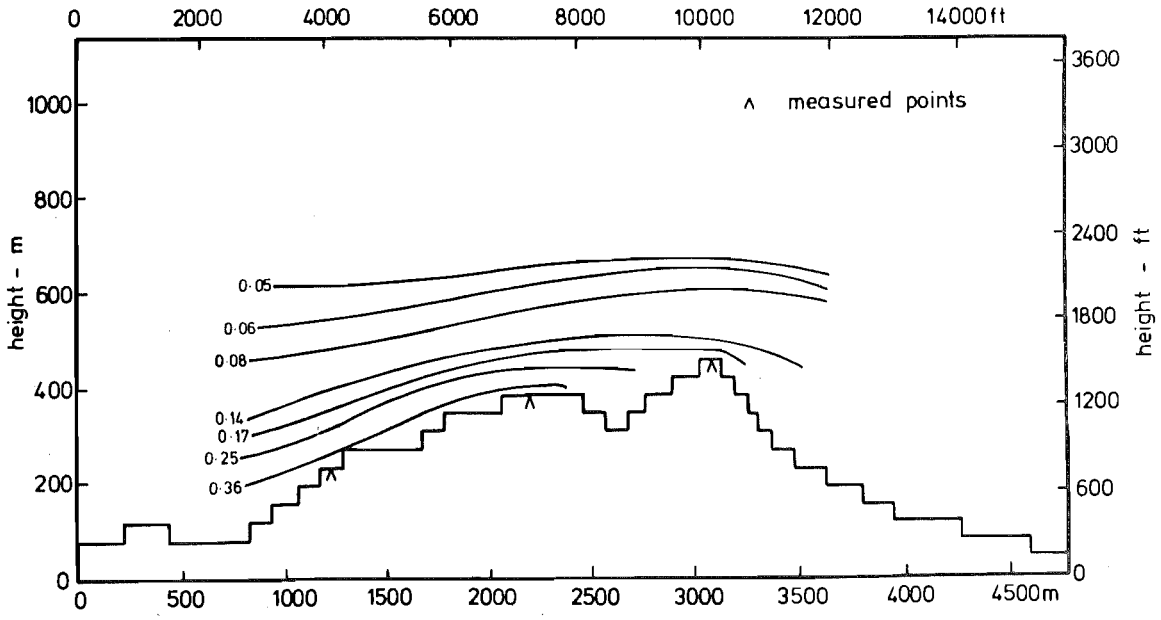

FIG 7.40 ISOTURBS FOR MODEL A TERRACED, LATERAL CROSS SECTION 3

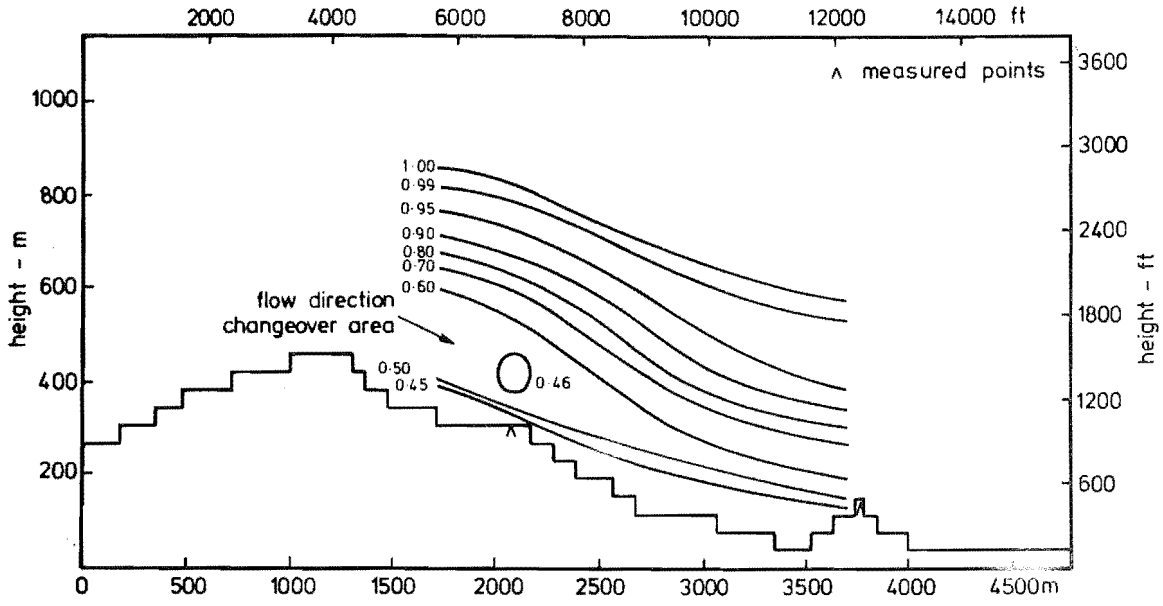

FIG 7.41 ISOTACHS FOR MODEL A TERRACED, LATERAL CROSS SECTION 4.

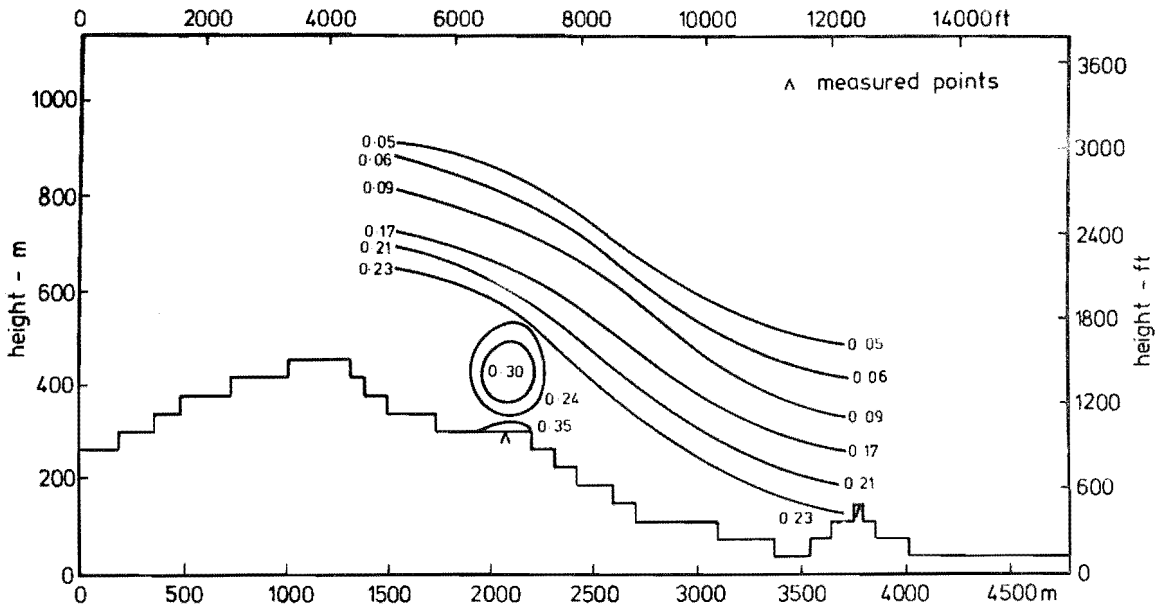

FIG. 7.42 ISOTURBS FOR MODEL A TERRACED, LATERAL CROSS SECTION 4.

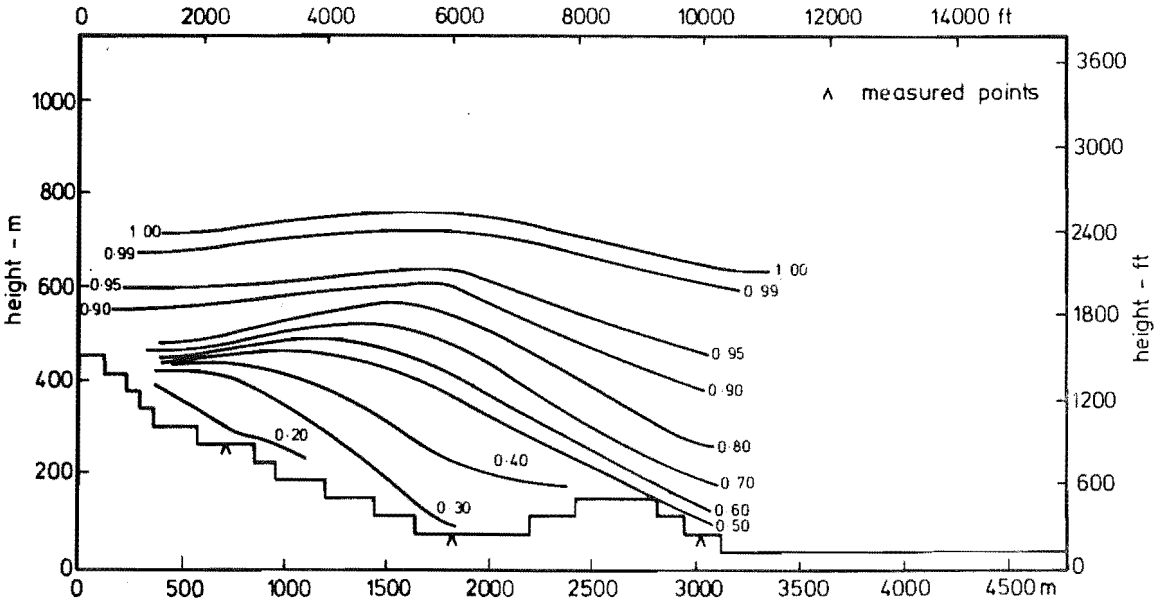

FIG 7.43 ISOTACHS FOR MODEL A TERRACED, LATERAL CROSS SECTION 5.

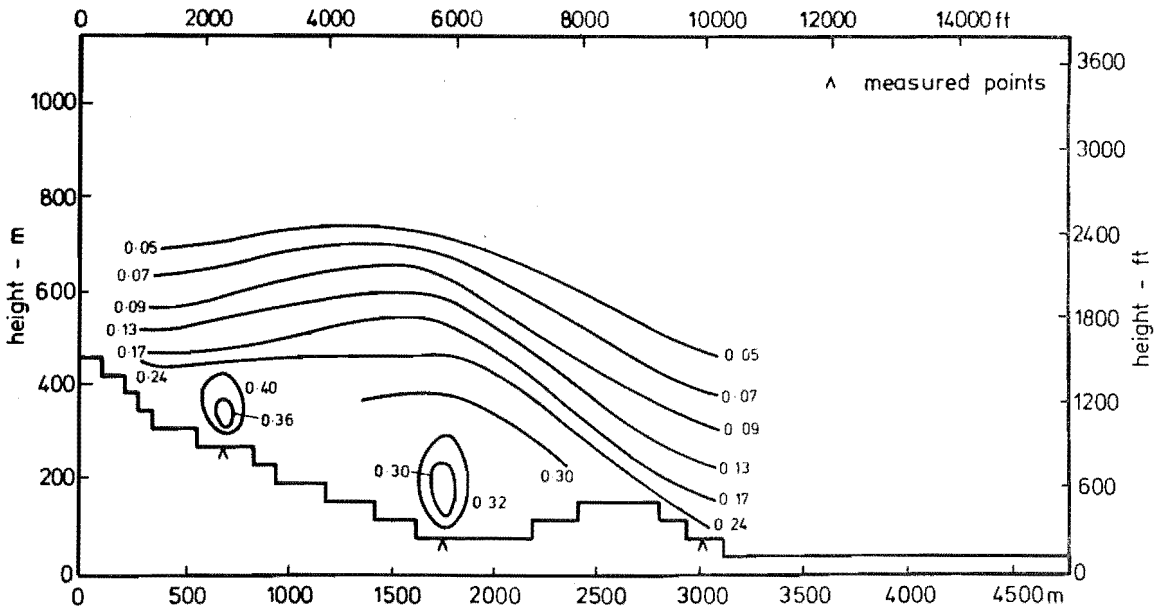

FIG 7.44 ISOTURBS FOR MODEL A TERRACED, LATERAL CROSS SECTION 5

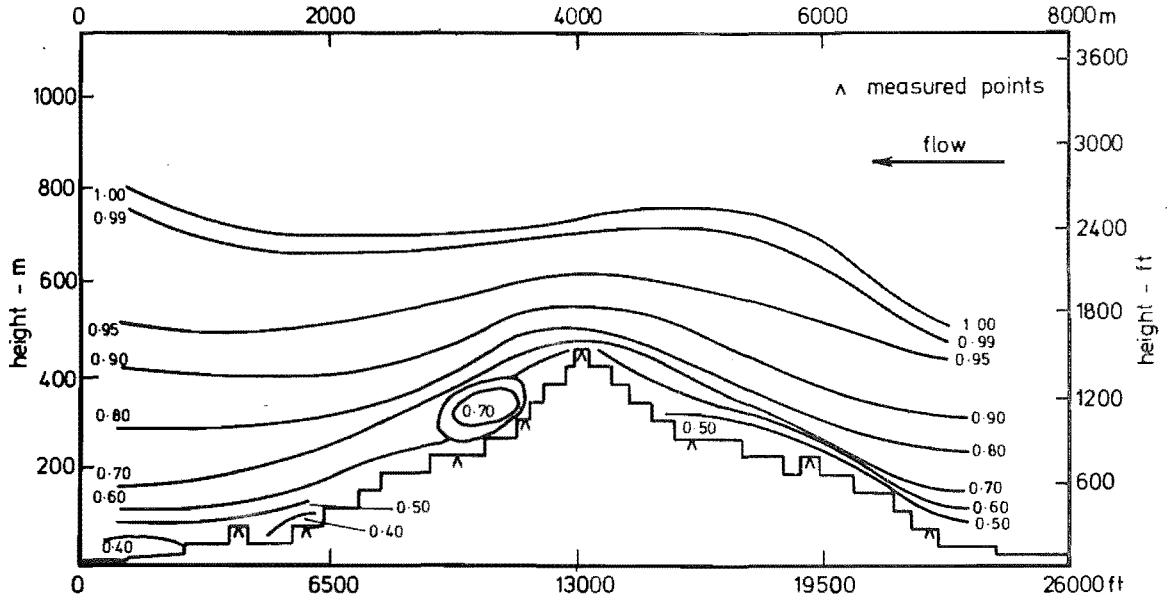

FIG. 7.45 ISOTACHS FOR MODEL A TERRACED, LONGITUDINAL CROSS SECTION XX

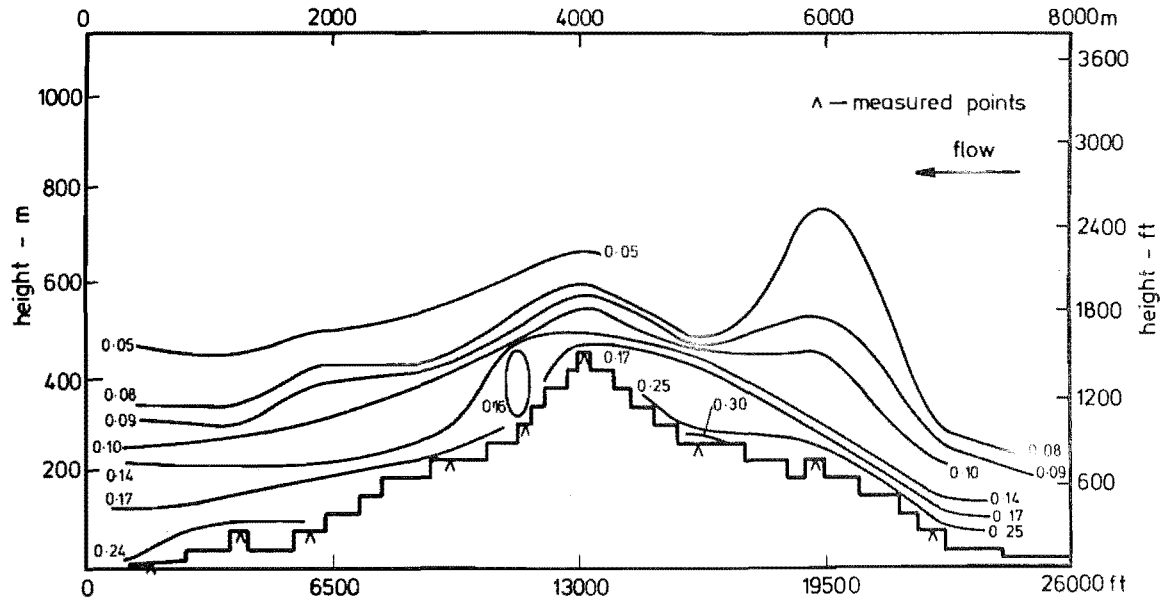

FIG. 7.46 ISOTURBS FOR MODEL A TERRACED, LONGITUDINAL CROSS SECTION XX

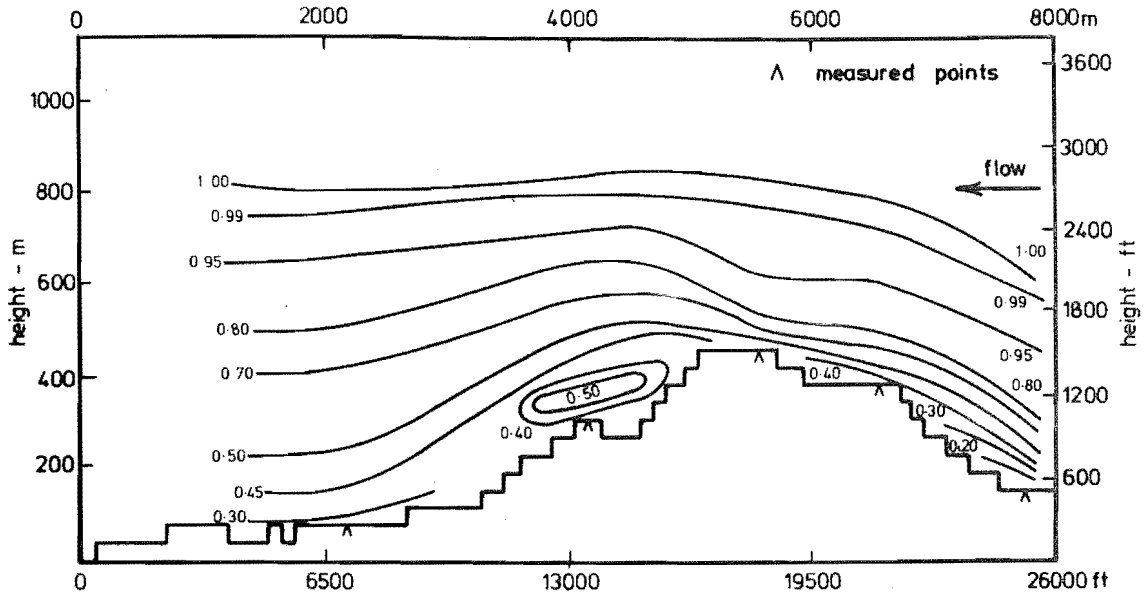

FIG. 7.47 ISOTACHS FOR MODEL A TERRACED, LONGITUDINAL CROSS SECTION YY

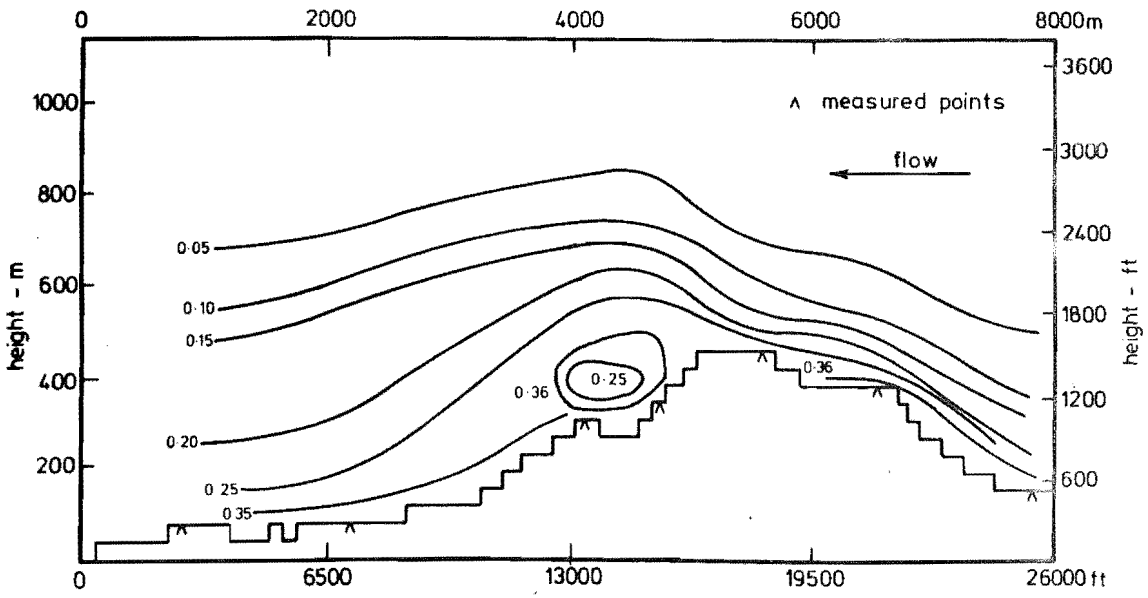

FIG. 7.48 ISOTURBS FOR MODEL A TERRACED, LONGITUDINAL CROSS SECTION YY

the photographic reduction process.

All analyses presented here by the author were carried out using the full-sized original tracings of the data. To compare between, say, terraced and contoured data, the respective graphs could be analysed with one on top of the other, thus clearly showing the differences.

Lateral cross sections 1-3 appear quite straightforward, the contours generally following the basic shape of the terrain. However, it is very important to take care when considering lateral cross sections because the data at any one cross section is very dependent upon the local upstream conditions. For example, the plot of isotachs for lateral cross section 4 does not inform the reader that much of this cross section is on the leeward side of the Port Hills ridge. Therefore, one must either be familiar with the terrain in question or make continual reference to the map of the area. Lateral cross section 2 showed one area of particularly low velocity and high turbulence. This occurred at point 56, which is situated in a valley which opens out to the southern boundary of the model. One would expect the flow to speed up as it progresses further into the narrowing valley. Velocities as low as 20% of the gradient velocity and turbulence intensities as high as 38% were measured at this point. One possible explanation for this is the terraced nature of the model. The vertical faces of the model could be causing the very high turbulence, and thus a reduced velocity because of the close proximity of the sides of the valley.

Lateral cross sections 4 and 5 showed areas of low velocity and high turbulence, particularly below the Port Hills ridge height. The longitudinal cross sections show some very interesting flow patterns. The isotach contours for cross sections XX and YY show the flow pattern along the leeward side of the Port Hills ridge. Interestingly this flow is generally faster than the flow passing over the ridge close to the model surface. It is possible that this pattern of flow is accentuated by the terraced nature of the model.

A further point to note is that the flow up the windward face of the Port Hills ridge for YY is significantly slower than for XX. The physical difference between these two sections is that the slope of the ridge at the YY cross section is much greater than XX. This point prompts the suggestion that when using terraced models, the gradient of the terrain being modelled may be a significant parameter. The information contained

in the iso-contours for model A terraced could be more closely linked to the nature of construction than the nature of the terrain.

Speed-up/down ratios have been calculated for the measured points and are presented in Fig. 7.49. Calculation of these ratios was based on the normalised velocity at a height of Z = 2.5mm for the point divided by the normalised velocity at the same height for the reference point. In the case of model A, point 22 was used for referencing, this point being well upstream of the complex terrain in the middle of the tunnel and close to the actual site used for referencing purposes during the field data collecting programme.

$$\text{Speed-up ratio } \Delta S = \left.\frac{\frac{\bar{u}_{2.5}}{\bar{u}_{\delta}}}{\frac{\bar{u}_{2.5}}{\bar{u}_{\delta}}}\right|_{\text{ref pt}}^{\text{pt}} \times 100 \quad \ldots\ldots\ldots\ldots\ldots \quad (7.4)$$

where $\bar{u}_{\delta}$ is the velocity at the gradient height

$\bar{u}_{2.5}$ is the velocity at 2.5mm which corresponds to a height Z_p = 10m.

Determination of the speed-up ratio areas was extremely subjective due mainly to the large variations from one area to another; however, these results are intended to show trends and hopefully, highlight differences between the various model constructions.

The results clearly show that higher velocities occur on knobs and ridges, which is quite predictable. There appears to be a general slowing of the flow as it approaches the Port Hills range, and this point was noted earlier with longitudinal cross sections XX and YY. The flow does appear to speed-up significantly along the Port Hills ridge, in particular, at Coopers Knob, where there is a 40% speed-up. The conclusions from this data are significant because they suggest that local speed-up effects occur over knobs and ridges as opposed to a general speed-up over the Port Hills ridge. This could be a function of the terraced nature of the model and could be explained by two effects.

Firstly, there could be extra turbulence caused by the terraces close to the model surface, Z < 10mm, thus causing an exaggerated slowing of the flow. This effect would probably be exaggerated even further when the

Terraced Model

$z = 10\,mm$

$Z_p = 40\,m$

$$\frac{\left.\frac{\bar{U}_{10}}{\bar{U}_\delta}\right|_{pt}}{\left.\frac{\bar{U}_{10}}{\bar{U}_\delta}\right|_{ref\ pt}} \times 100$$

141 – 150

121 – 140

101 – 120

81 – 100

71 – 80

61 – 70

0 – 60

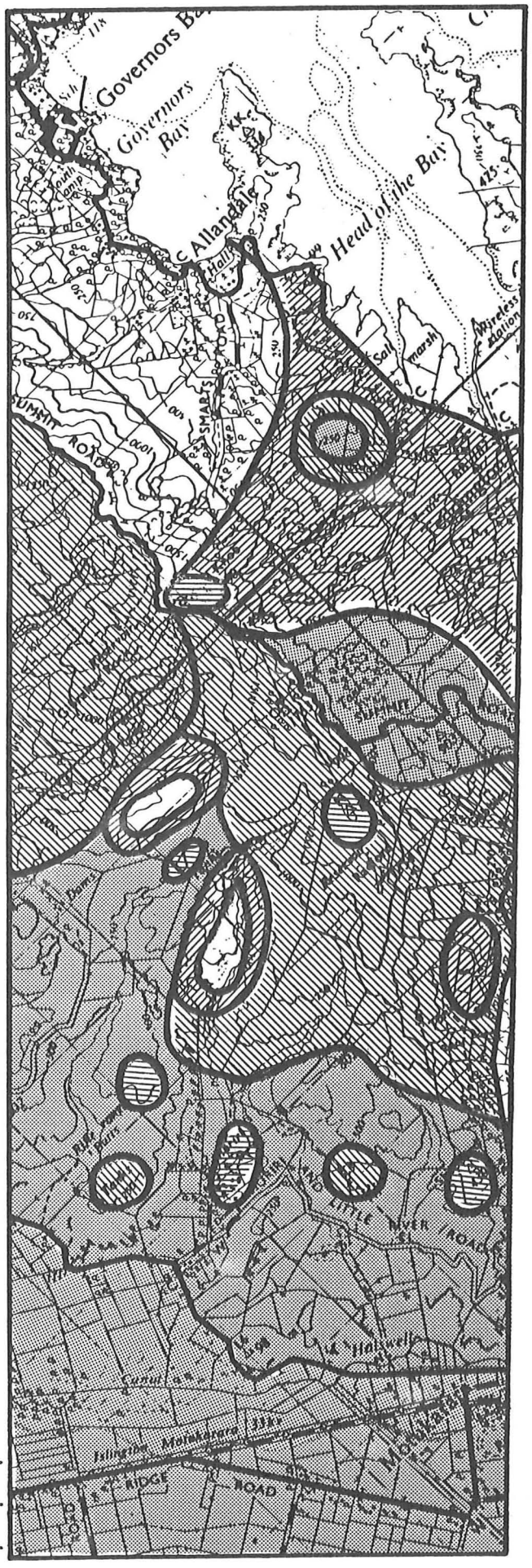

FIG 7·49 SPEED-UP RATIO AREAS FOR MODEL A, TERRACED, $Z_p = 40m$

flow moves up the face of a ridge.

Secondly, in situations where the flow passes on to contours at an acute angle, there is a strong possibility that the flow follows the contours to a large extent. If this is the case, it would be reasonable to expect the flow not to follow the terrain to the same degree when the model has been contoured.

7.4 MODEL A CONTOURED

The terraces on the model were filled in with a polyfiller material as described in Section 5.2.4. After re-painting, the model was set up in the wind tunnel and the approach flow characteristics were checked.

7.4.1 Approach Flow Characteristics

Velocity profile measurements at point 22 and point 53 revealed a power law index, α, of 0.15 and a roughness length, Z_o, of 0.02m, which were identical to the approach flow conditions used for the terraced model. A comparison was made between energy spectra, at a height of 5mm for the terraced and contoured models. This is presented in Fig. 7.50 and shows an excellent agreement between both spectra.

Longitudinal pressure gradient tests showed a very small variation over the model, approximately 1.0%.

Lateral uniformity tests were carried out upstream of the model and showed variations that were not present for the terraced model. The initial results suggested that the model was causing the flow approaching the ridge to speed up. This resulted in a lateral uniformity variation of up to 4.0% which was of some concern. To determine the extent of this effect, the measurements were repeated 0.8m further upstream. The results of this test showed the maximum variation to be 1.2% which was considered quite acceptable. These tests showed that a faster flow could be expected over the model. This increase had to be a function of the new model surface as opposed to any increases in tunnel blockage. The calculation of model cross sections and tunnel blockages used straight lines between the contours, which tended to overestimate the actual model cross sectional area and therefore the percentage of tunnel blockage. Hence, the terraced model produced blockages lower than those given in Section 7.1. It is therefore concluded that satisfactory approach flow conditions existed.

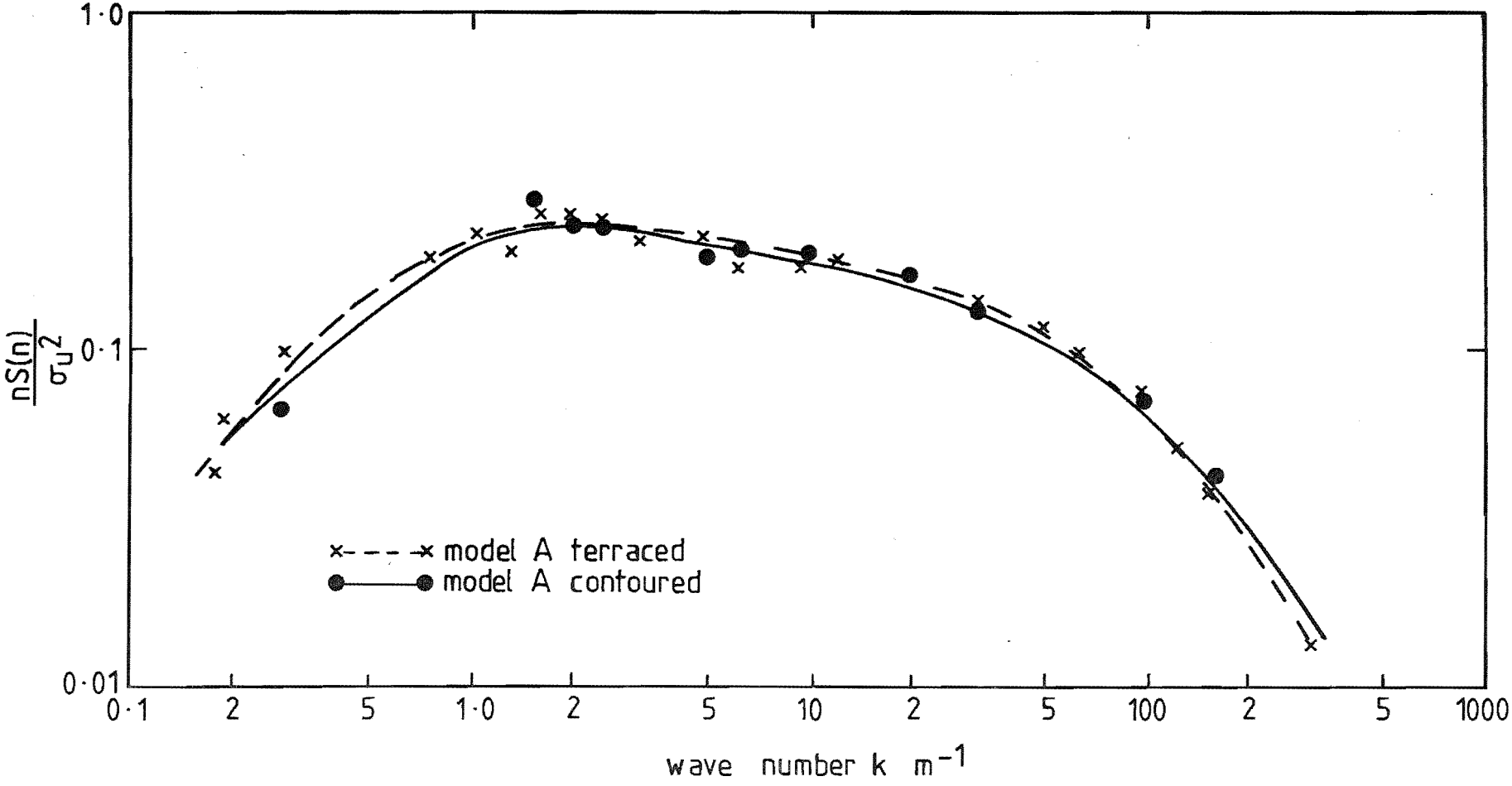

FIG 7·50 COMPARISON OF ENERGY SPECTRA FOR POINT 22 AT Z = 5mm

7.4.2 Flow Visualisation

1) Polystyrene Beads: The polystyrene bead flow visualisation technique was used for the contoured model, a description of the technique being given in Section 7.3.2. Results of the 4.0 m/s tests are presented in Fig. 7.51. If a comparison is made between the bead results for the terraced and contoured models, it is obvious that the size of the bead deposition areas is drastically reduced on the contoured model. In fact, the bead deposits for the contoured model are somewhat similar to the deposits noted for the terraced model at the increased speed, as given in Fig. 7.30. When the wind tunnel speed was increased to approximately 5.7 m/s all the bead deposits were removed from the model. The bead tests for the contoured model were repeated several times and found to be consistent with regard to areas of deposition and total bead removal at the higher speed.

2) Flags: Flow directions over the model were demonstrated with miniature flags. The results of these tests were very similar to those for the terraced model and predicted the wind moving along the leeward side of the Port Hills ridge.

7.4.3 Pressure Probe Measurements

The 5-hole Cobra probe, illustrated in Fig. 7.31, was used to measure actual flow directions over the contoured model. The results of these tests at heights of 5mm, 20mm and 40mm are given in Figs 7.52 to 7.54. These results are extremely close to those obtained for the terraced model. There appears to be a definite flow pattern behind the Port Hills ridge; this was also noted during the analysis of the terraced model. However, with this occurrence on the contoured model, it suggests that the wind flow along the leeward side of the ridge is a feature of the general terrain rather than the terraced nature of the construction. The degree of flow straightening with height also appears to be similar for both states of construction.

7.4.4 Hot Film Survey

The results of the hot film survey for lateral cross sections 1-5 are presented as isotachs and isoturbs in Fig. 7.55 through to Fig. 7.64. The isotachs for cross section 1 show a very similar contour pattern; however, the isoturbs for this cross section show distinct differences. The most notable feature is the reduction of turbulence close to the model surface.

MODEL A

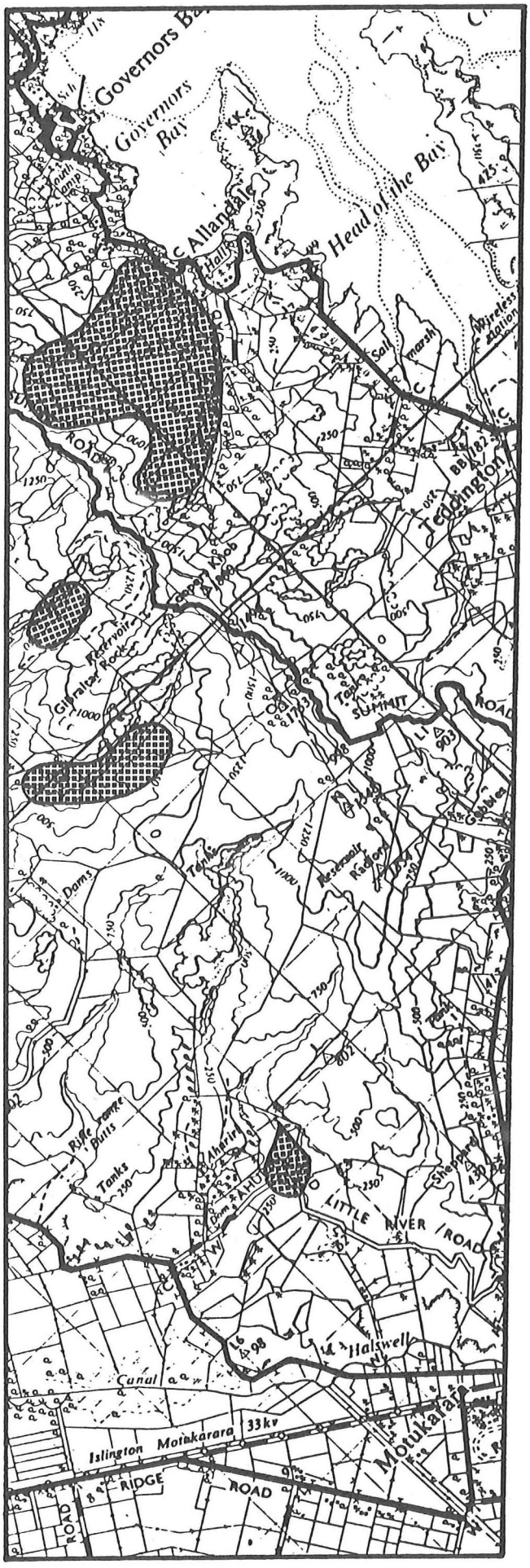

deposits at low speed

FIG 7·51 POLYSTYRENE BEAD DEPOSITION DIAGRAM CONTOURED MODEL

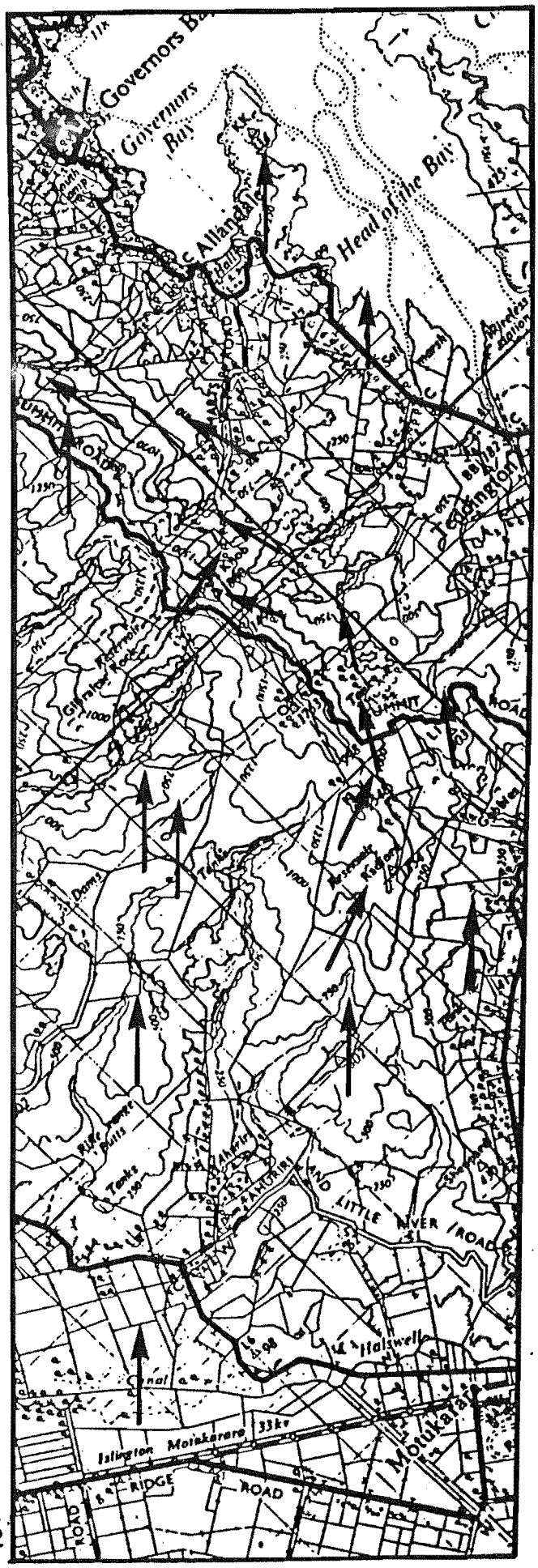

flow regime as measured with 5 hole Cobra probe

FIG. 7·52 FLOW DIRECTIONS OVER MODEL A, CONTOURED Z = 5 mm

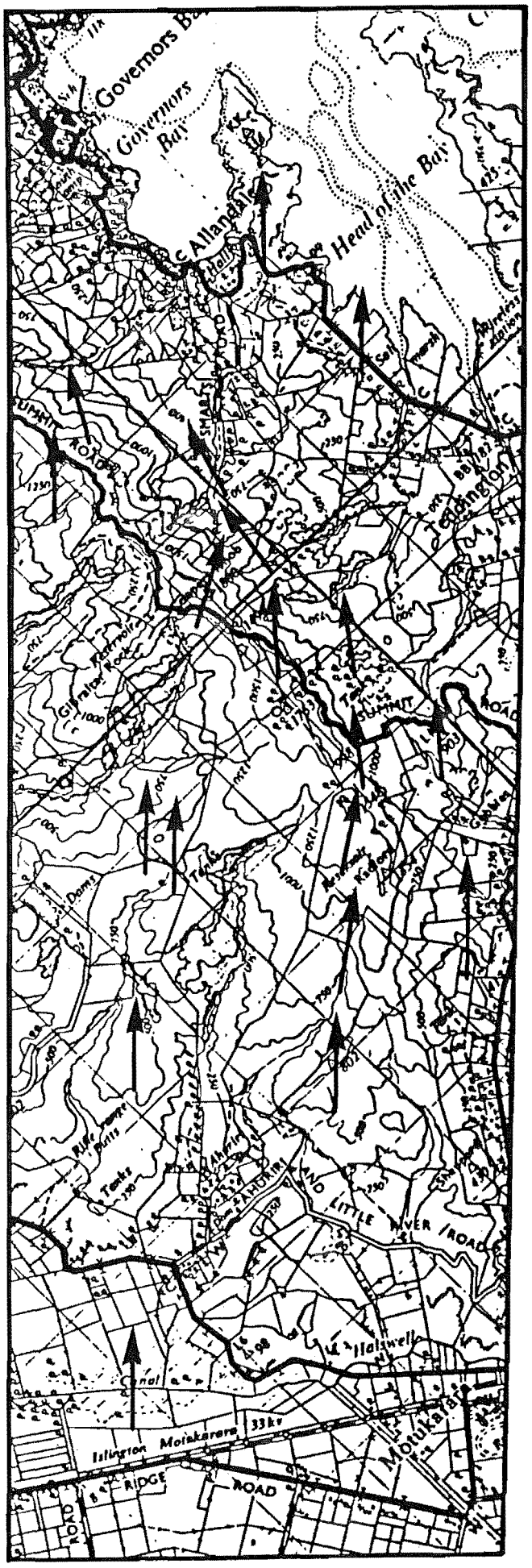

flow regime as measured with 5 hole Cobra probe

FIG. 7·53 FLOW DIRECTIONS OVER MODEL A, CONTOURED Z = 20mm

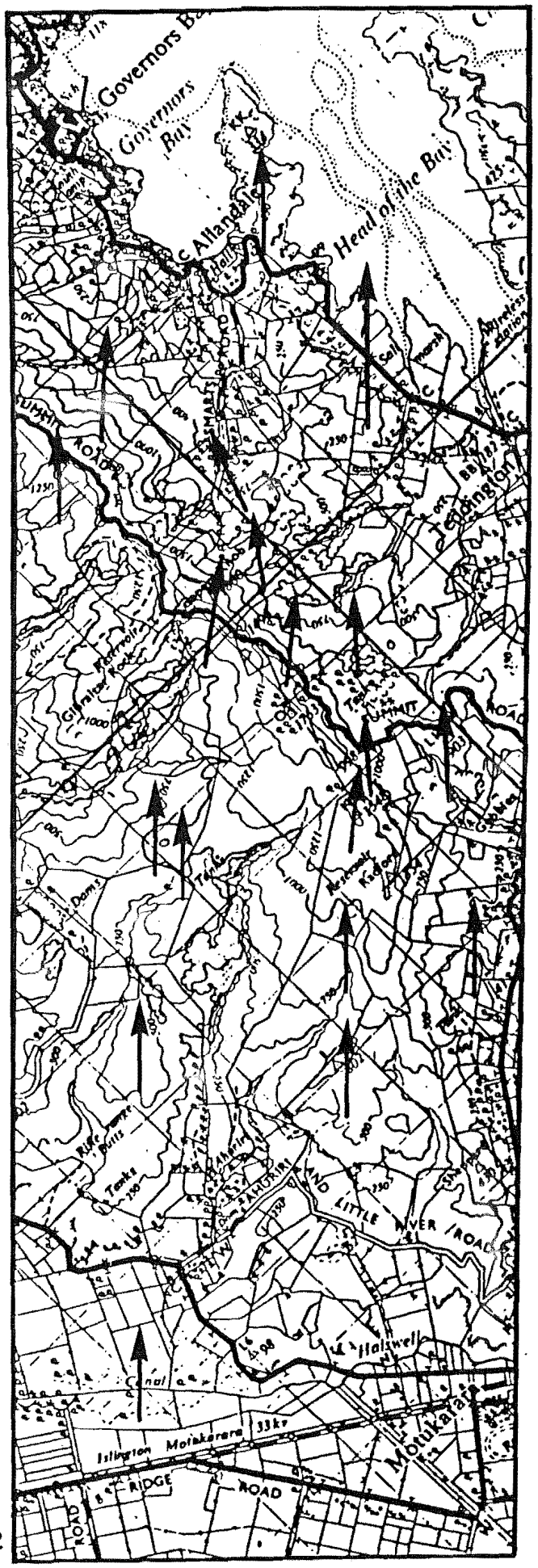

flow regime as measured with 5 hole Cobra probe

FIG. 7·54 FLOW DIRECTIONS OVER MODEL A, CONTOURED Z = 40 mm

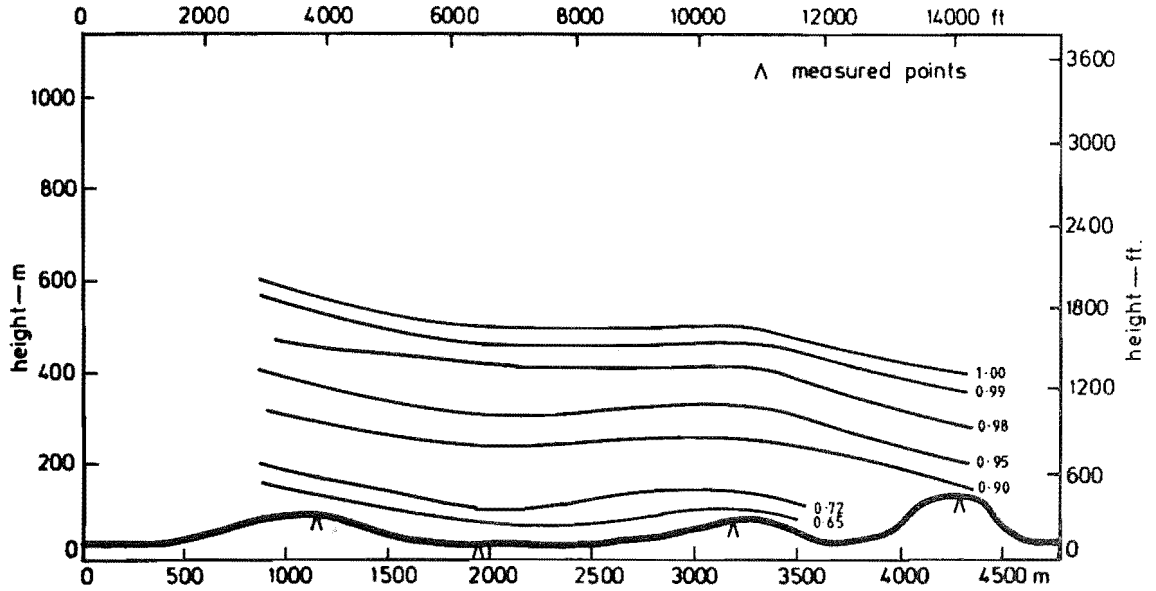

FIG 7.55 ISOTACHS FOR MODEL A, CONTOURED, LATERAL CROSS SECTION. 1

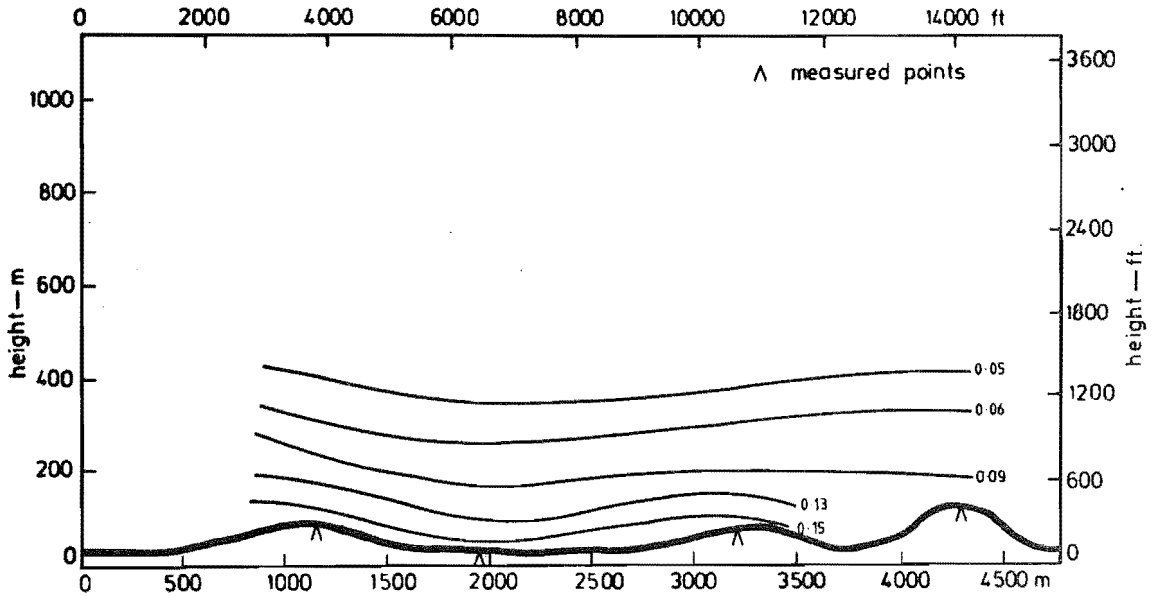

FIG 7.56 ISOTURBS FOR MODEL A, CONTOURED, LATERAL CROSS SECTION. 1

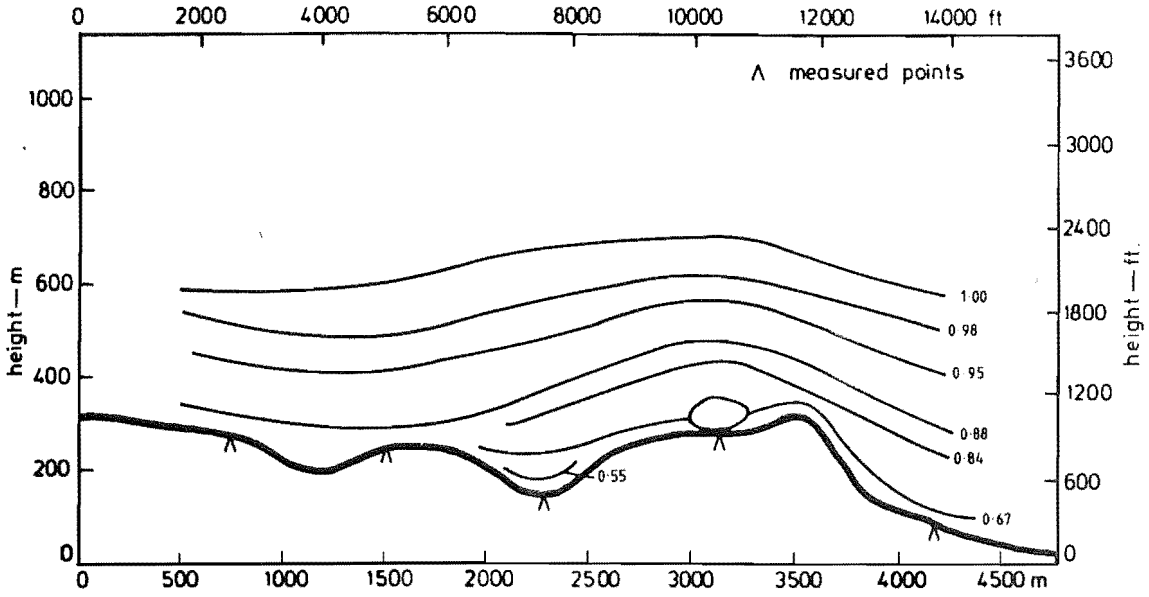

FIG 7.57 ISOTACHS FOR MODEL A, CONTOURED, LATERAL CROSS SECTION. 2

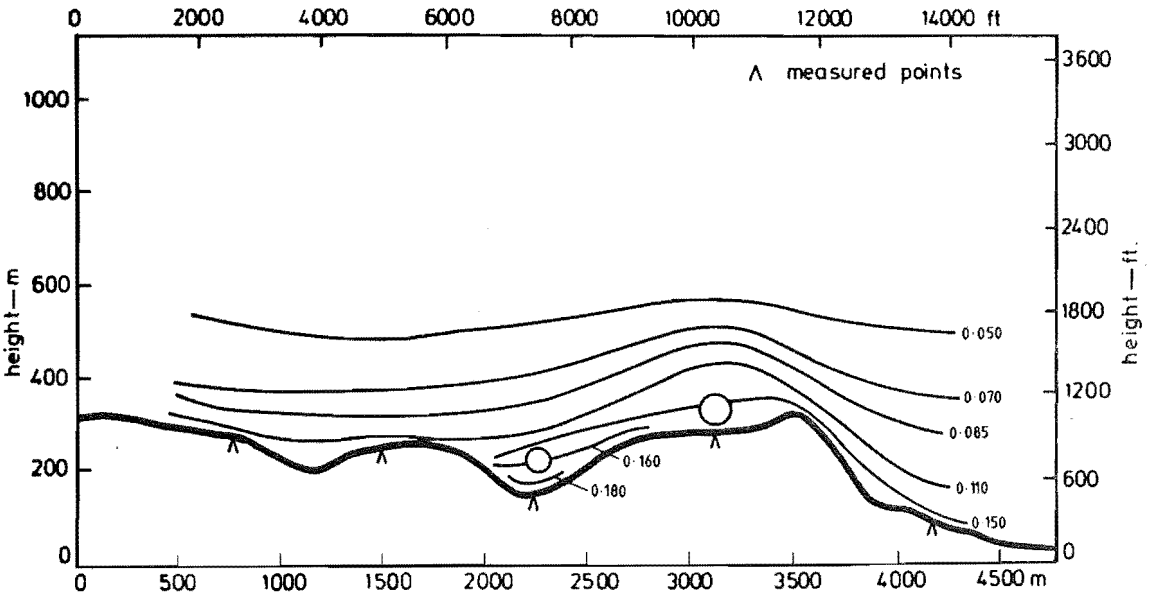

FIG 7.58 ISOTURBS FOR MODEL A, CONTOURED, LATERAL CROSS SECTION. 2

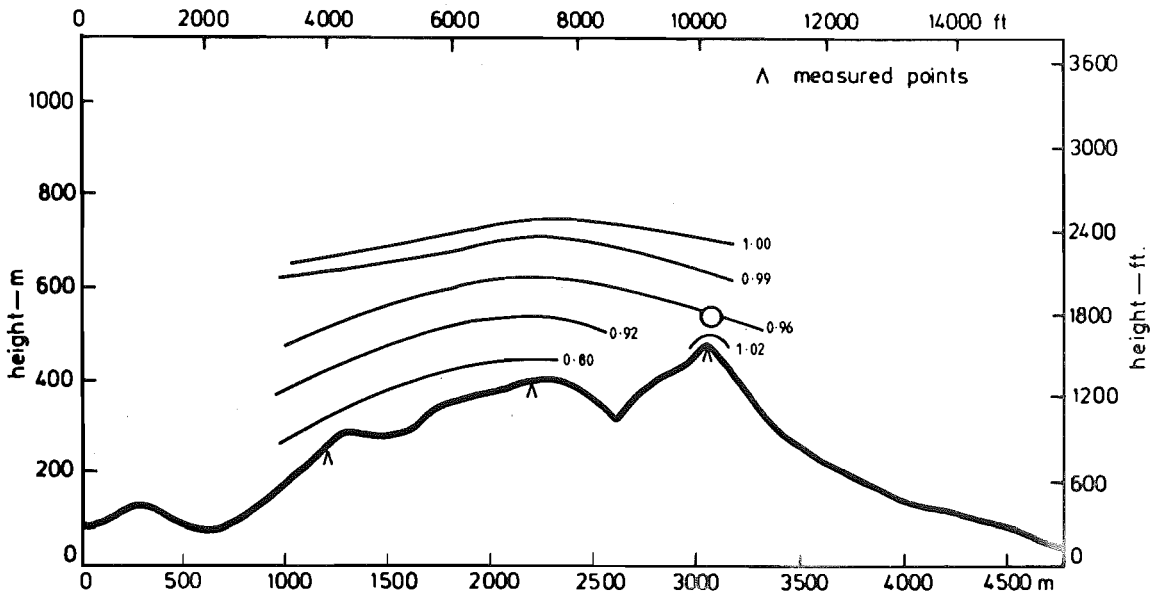

FIG 7.59 ISOTACHS FOR MODEL A, CONTOURED, LATERAL CROSS SECTION. 3

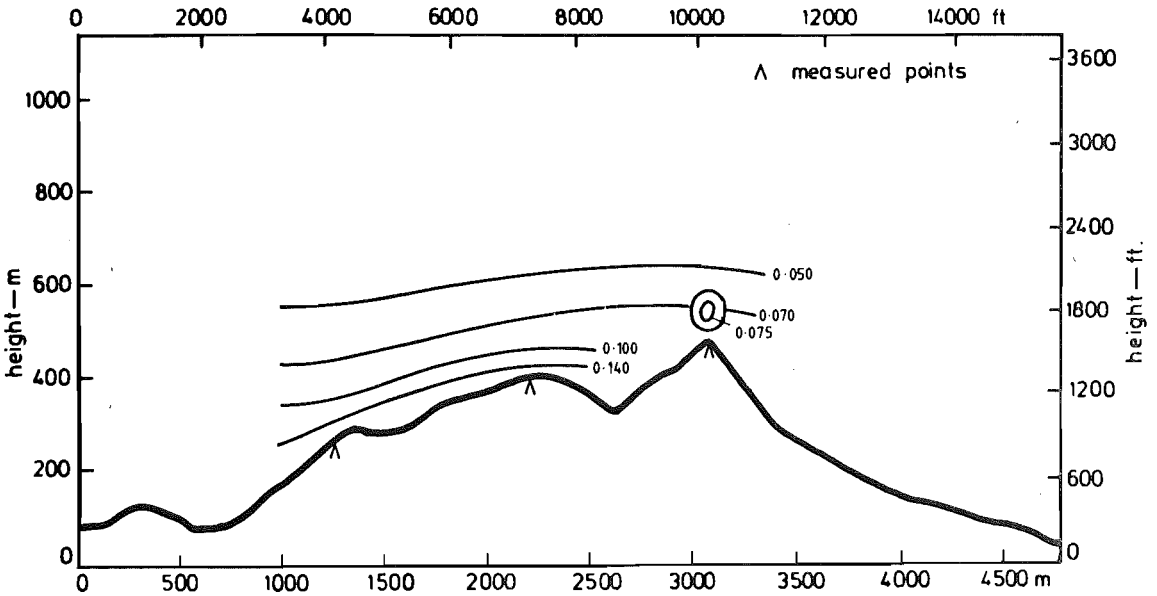

FIG 7.60 ISOTURBS FOR MODEL A, CONTOURED, LATERAL CROSS SECTION. 3

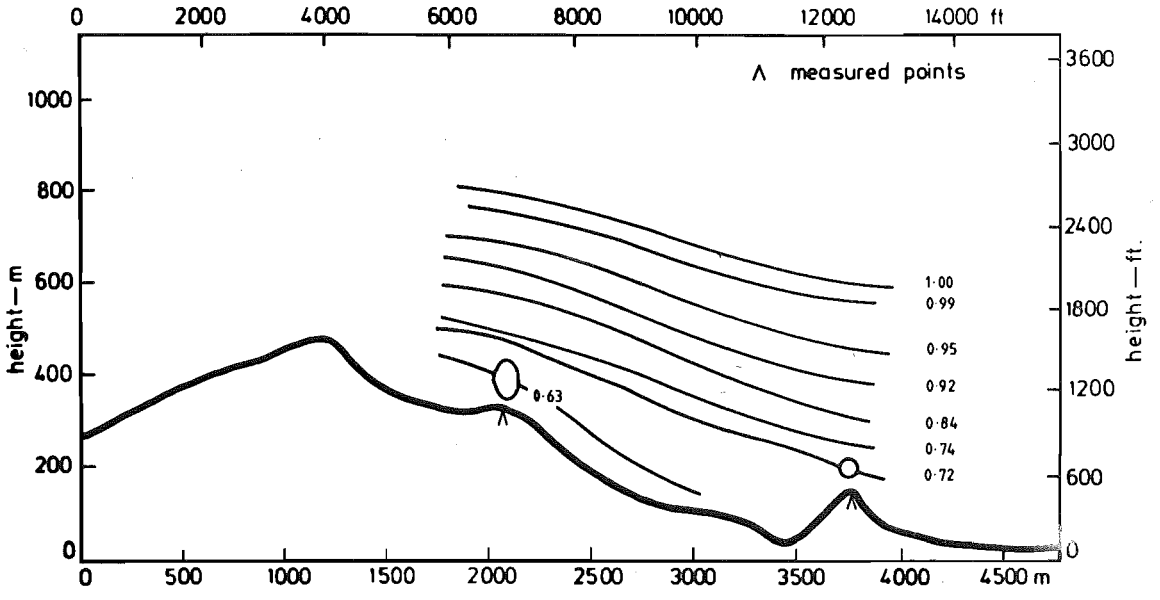

FIG 7.61 ISOTACHS FOR MODEL A, CONTOURED, LATERAL CROSS SECTION. 4

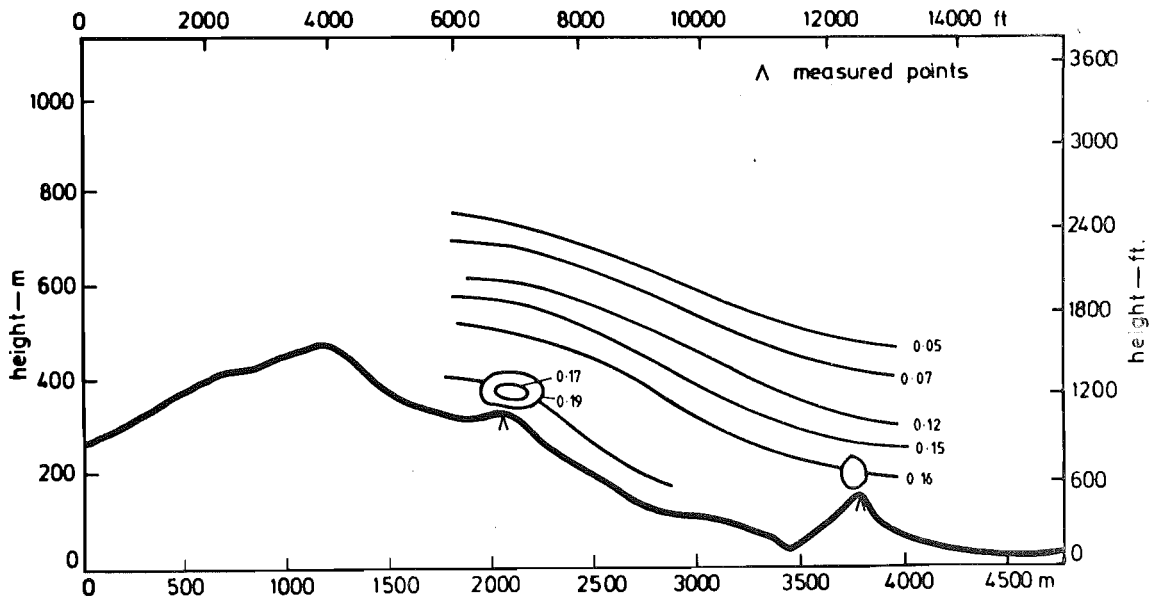

FIG 7.62 ISOTURBS FOR MODEL A, CONTOURED, LATERAL CROSS SECTION. 4

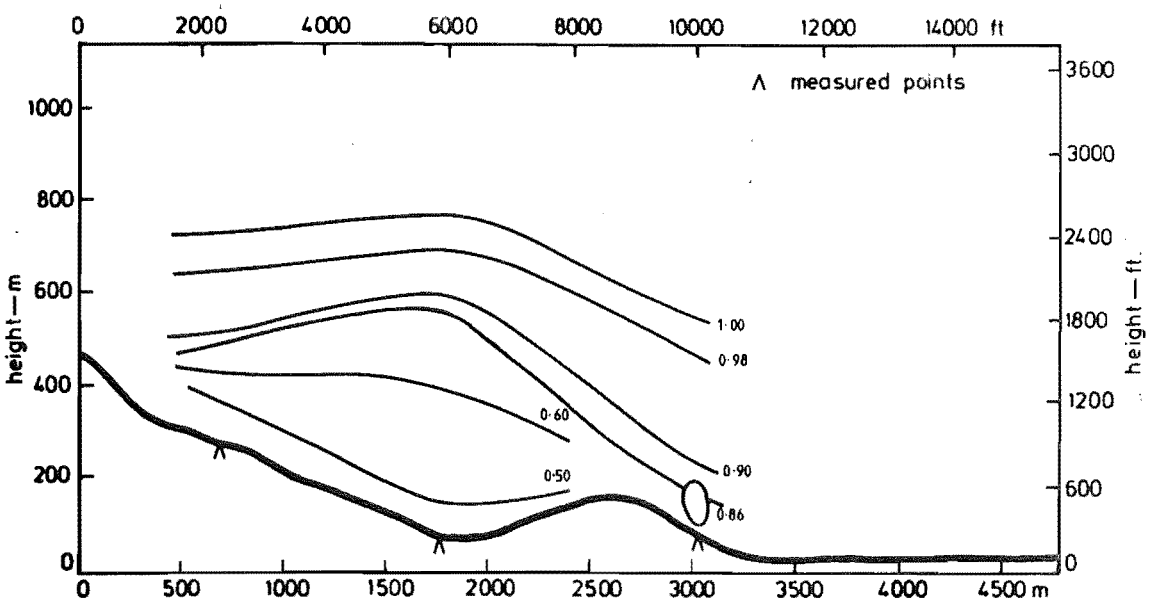

FIG 7.63 ISOTACHS FOR MODEL A, CONTOURED, LATERAL CROSS SECTION. 5

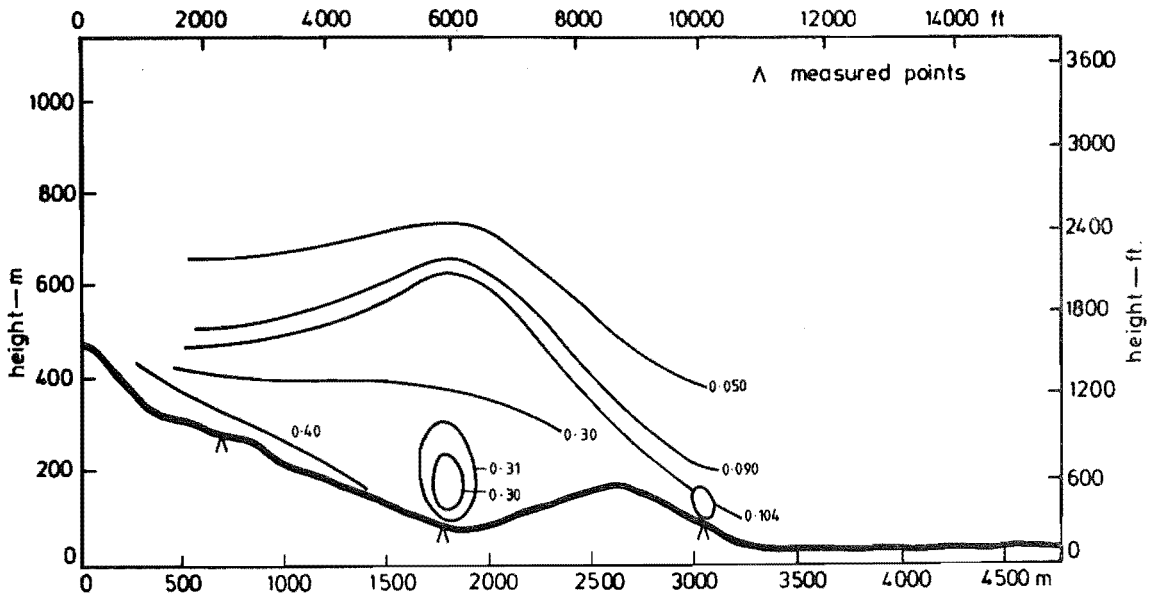

FIG 7.64 ISOTURBS FOR MODEL A, CONTOURED, LATERAL CROSS SECTION. 5

For the terraced model, turbulence intensity values of 20-30% existed but for the contoured model, the maximum turbulence was only 15%.

The isotachs for cross section 2 show that the velocity close to the model surface, i.e., the bottom 10 mm on the contoured model, is substantially faster than was recorded on the terraced model. The other interesting feature is that the contours close to the gradient height followed the model shape quite closely for the terraced model but on the contoured model, the gradient contours appear to have smoothed out and followed the general terrain shape. The isoturb contours for this cross section follow a very similar pattern with the levels of 5% turbulence intensity being almost identical. However, in the bottom 20mm of the flow, dramatic reductions in turbulence occurred over the contoured model.

Cross sections 3, 4 and 5 show the same trends of reduced turbulence close to the model surface and increased speed in the bottom 20mm on the contoured model, whilst exhibiting similar general flow patterns.

Longitudinal cross sections XX and YY are presented in Figs 7.65 to 7.68. The isotach contours show results which were not a feature of the lateral cross sections. Previously it was noted that the gradient height contours followed the shape of the model quite closely for the terraced construction and tended to smooth out over the contoured model. The longitudinal cross section XX produced the opposite result with the contoured model suggesting contours which clearly followed the model closely. The surprising feature is that cross section YY, which is quite close to cross section XX, supports the initial trend with the contoured results presenting a smoothed version of the terraced iso-contours. It is very difficult to provide a clear reason for this other than the fact that cross section XX passes through the end of the Port Hills ridge, and the fact that the terrain drops away on both sides of the cross section may account for the results. On the other hand, cross section YY passes through the Port Hills ridge approximately midway along the ridge.

The other significant point to note in relation to cross section XX is that at point 15, which is at the peak of the hill, the velocity has been increased to produce a local speed-up which is 5% greater than the gradient wind speed. This may not sound particularly significant initially, but it means that the wind speed in the bottom 20m of the atmosphere at

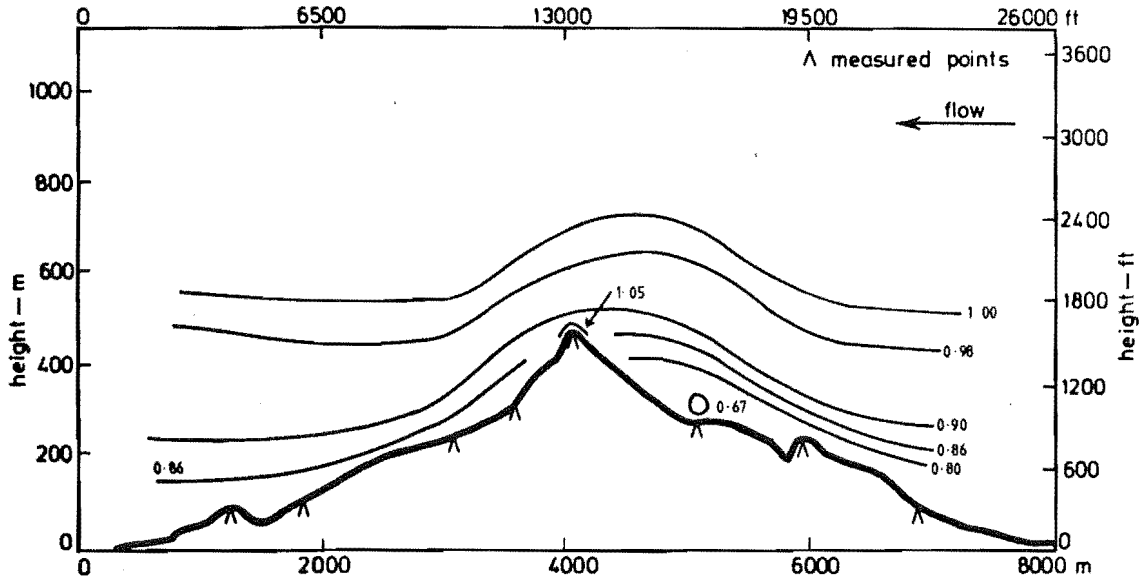

FIG 7.65 ISOTACHS FOR MODEL A, CONTOURED, LONGITUDINAL CROSS SECTION XX

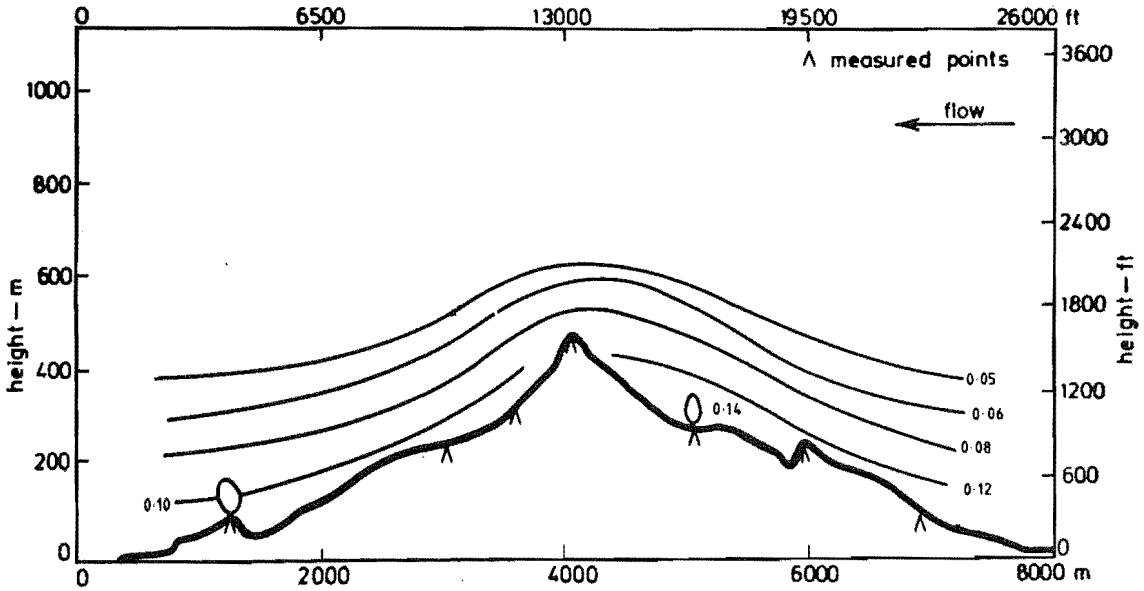

FIG 7.66 ISOTURBS FOR MODEL A, CONTOURED, LONGITUDINAL CROSS SECTION XX

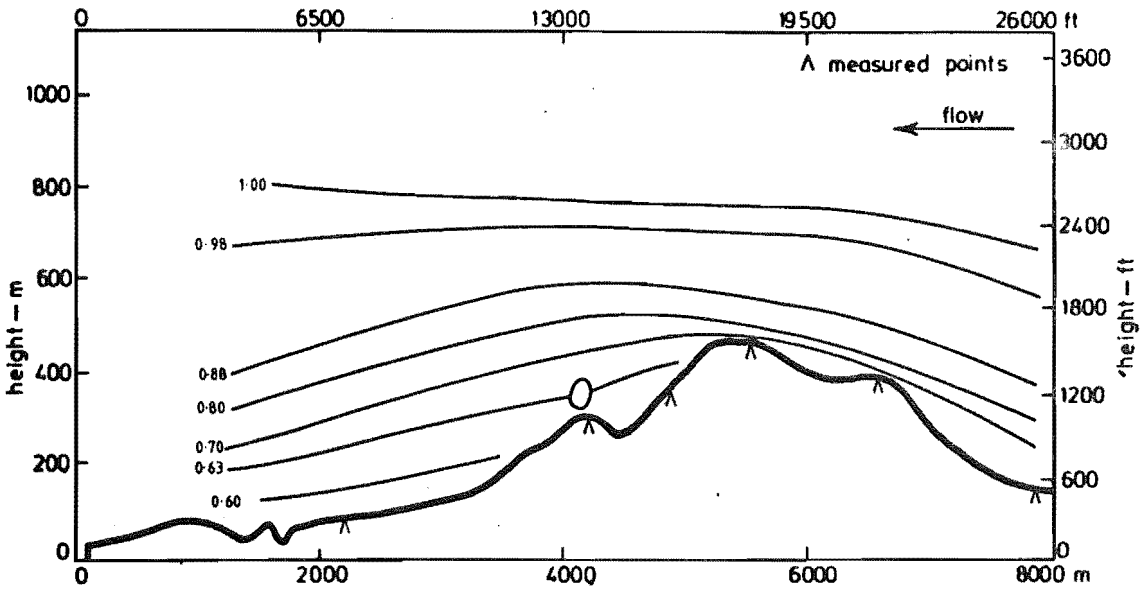

FIG 7.67 ISOTACHS FOR MODEL A, CONTOURED. LONGITUDINAL CROSS SECTION YY

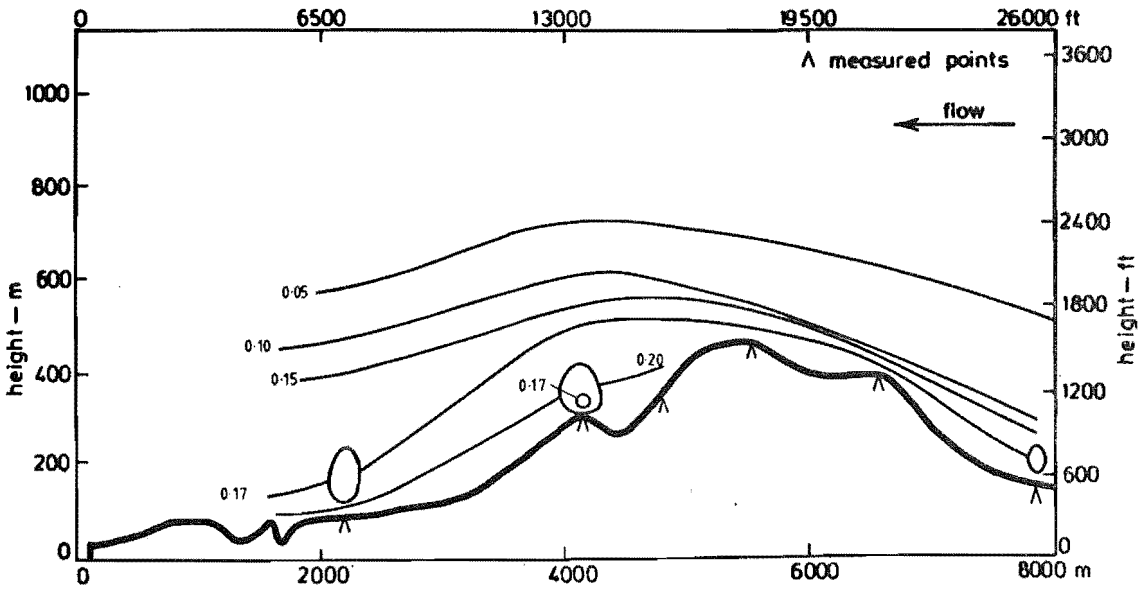

FIG 7.68 ISOTURBS FOR MODEL A, CONTOURED. LONGITUDINAL CROSS SECTION YY

point 15 is approximately the same as the velocity at a height of 400m on the flat rural terrain approaching the region. From the point of view of building a wind turbine to produce power, it makes this feature extremely significant. However, the model must first be tested with roughness added and comparisons made with the results collected in the field.

Isoturb contours for cross section YY have very similar general patterns with the exception that reductions of 50% in the value of the turbulence intensity in the lower 20mm of the contoured model were noted.

An unusual amount of turbulence was noted at point 19, shown in Fig. 7.46, for longitudinal cross section XX. No explanation could be found for this. Measurements at this point were repeated as a check. Reference to the same point on the contoured model shows this effect to have disappeared.

Speed-up ratio areas for Model A contoured are presented in Fig.7.69 for a model height of 10mm. The most interesting feature is the increase in the velocity of the wind moving up the windward face of the Port Hills. A comparison with the speed-up ratio diagram for Model A terraced shows the degree to which this effect has occurred. The areas of higher velocities on the terraced model, hill-tops and knobs, have been retained on the contoured model but yield greater ratios than previously. A typical example is point 15, which was discussed previously when considering the longitudinal cross sections. Its speed-up ratio was increased from 101-120%, see Fig. 7.49, on the terraced model to 121-140%.

The smoothing of the model surface could be expected to increase the flow velocity over the model simply because of the reduction in surface roughness. This was seen to happen during the analysis of the lateral and longitudinal cross sections.

7.4.5 Correlations for Model A, Terraced vs Contoured

This section will present linear correlations based on normalised velocities measured over model A in the terraced and contoured forms of construction.

The theory of the statistical analysis used in this research will be presented in Chapter 11.

Contoured Model

Z = 10 mm

Zp = 40 m

$$\frac{\left.\frac{\bar{U}_{10}}{\bar{U}_\delta}\right|_{pt}}{\left.\frac{\bar{U}_{10}}{\bar{U}_\delta}\right|_{ref\ pt}} \times 100$$

141 – 150

121 – 140

101 – 120

81 – 100

71 – 80

61 – 70

0 – 60

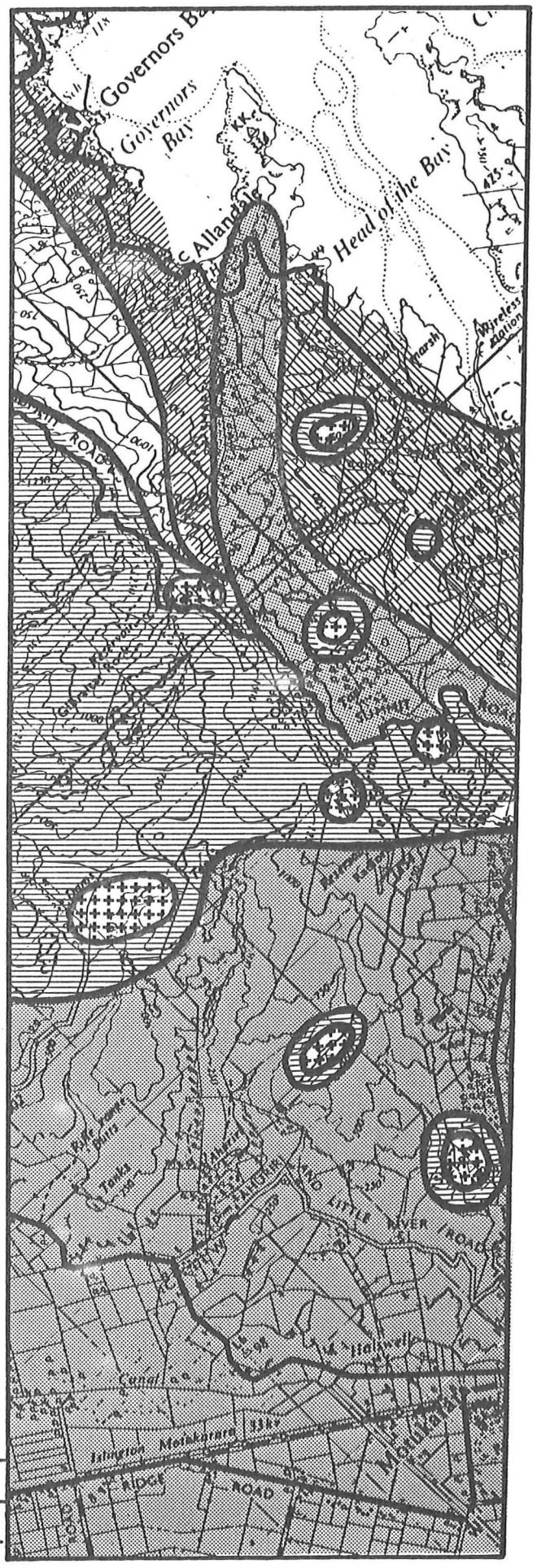

FIG 7·69 SPEED-UP RATIO AREAS FOR MODEL A, CONTOURED, Zp = 40 m

An initial correlation was carried out between the terraced and contoured versions of model A at a height of 5mm. The resulting scatter diagram and least squares regression curves are presented in Fig. 7.70. The correlation coefficient for this data is only 0.55, which suggests a small amount of agreement between the two models. It is reasonable to expect the terracing to significantly influence the results to a height equal to the terraces. In this case the terraces are 9mm thick; therefore further correlations were carried out at 10 and 20 mm heights. The scatter diagram for 10mm, Z_p = 40m, is presented in Fig. 7.71, which also gives the regression curves and the correlation coefficient r. The value of r was 0.57, which suggests a slight improvement when compared with the 5mm results.

The scatter diagram for 20mm, Z_p = 80m, is presented in Fig. 7.72. The correlation coefficient r is 0.73, which represents a significant improvement and supports the argument that the terraces are very important, particularly at heights less than the terrace increment. Unfortunately, at 20mm, the field equivalent is 80m, which is beyond the height of the field measuring equipment used for the one day field data collection programme.

7.5 ROUGHNESS ADDED MODEL

Shelterbelts and major scrub areas were simulated with wool and scrim respectively. A description of the material and the rationale for their use is given in Section 5.2.5.

The approach flow conditions were checked and showed excellent agreement with the inflow conditions previously used for model A. This was most encouraging in terms of repeatability, because large time spans were involved between the analysis of the various models. In some cases the boundary conditions such as the honeycomb, the grid, the roof and the trip fences had been changed or even removed for work being conducted by other researchers. The parameters checked included the power law index, α, the roughness length, Z_o the turbulence intensity profile and the energy spectrum.

7.5.1 Flow Visualisation

1) Polystyrene beads: Tests were carried out on the model to determine the reaction between the beads and the roughness elements. Initial tests showed that the beads became entangled in the wool shelter-

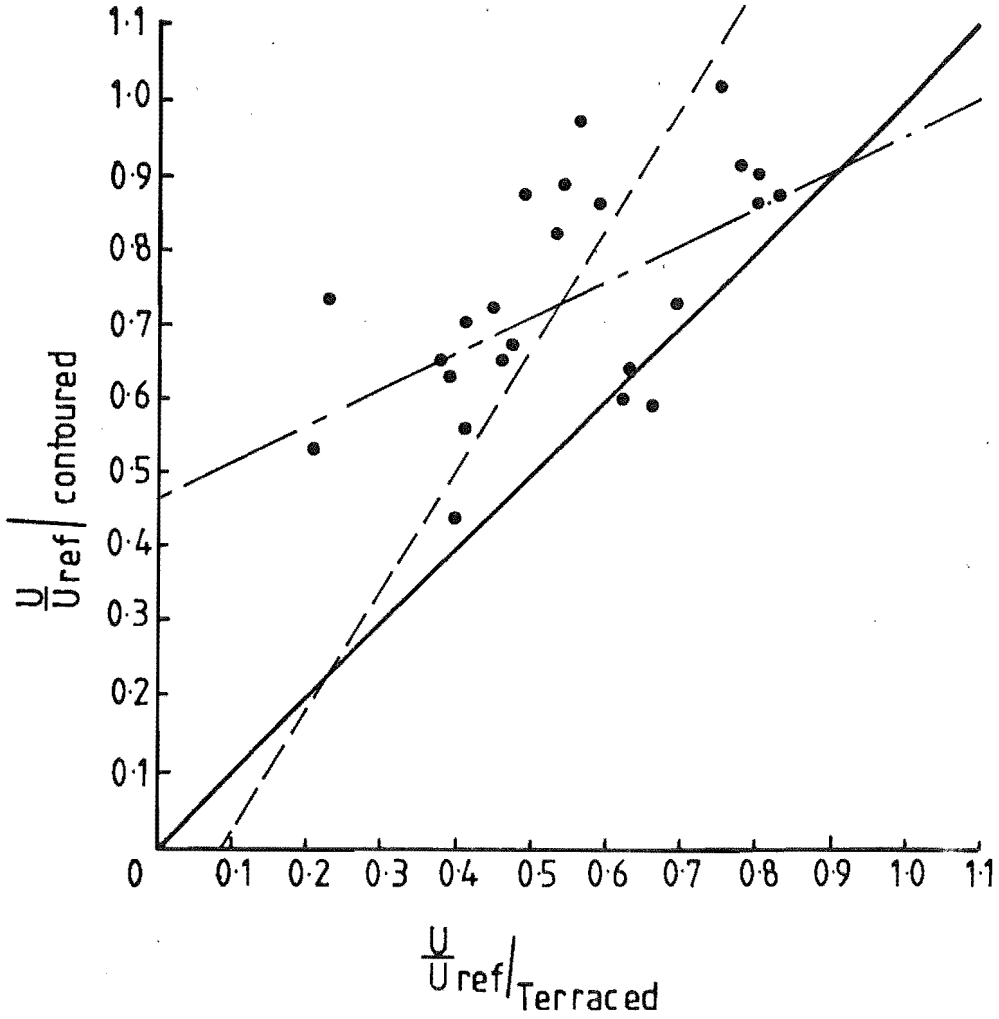

Regression lines

$\frac{U}{U_{ref}}\Big|_{Terraced} = 0.61 \; \frac{U}{U_{ref}}\Big|_{Contoured} + 0.094$

$\frac{U}{U_{ref}}\Big|_{Contoured} = 0.50 \; \frac{U}{U_{ref}}\Big|_{Terraced} + 0.465$

Correlation coefficient $r = 0.55$

FIG 7·70 SCATTER DIAGRAM FOR MODEL A AT Z = 5 mm

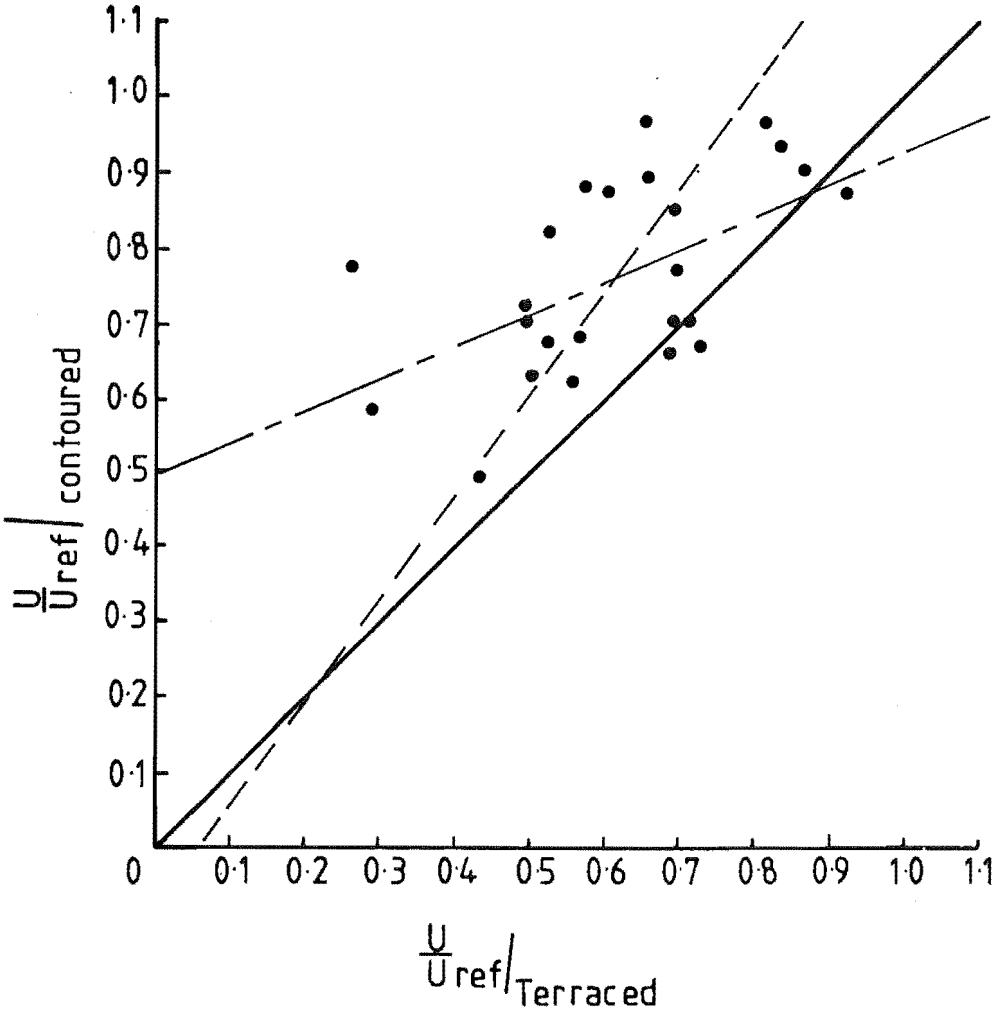

Regression lines

$\frac{U}{U_{ref}}\Big|_{Terraced} = 0.73 \frac{U}{U_{ref}}\Big|_{Contoured} + 0.058$

$\frac{U}{U_{ref}}\Big|_{Contoured} = 0.45 \frac{U}{U_{ref}}\Big|_{Terraced} + 0.487$

Correlation coefficient $r = 0.57$

FIG 7·71 SCATTER DIAGRAM FOR MODEL A AT Z = 10 mm

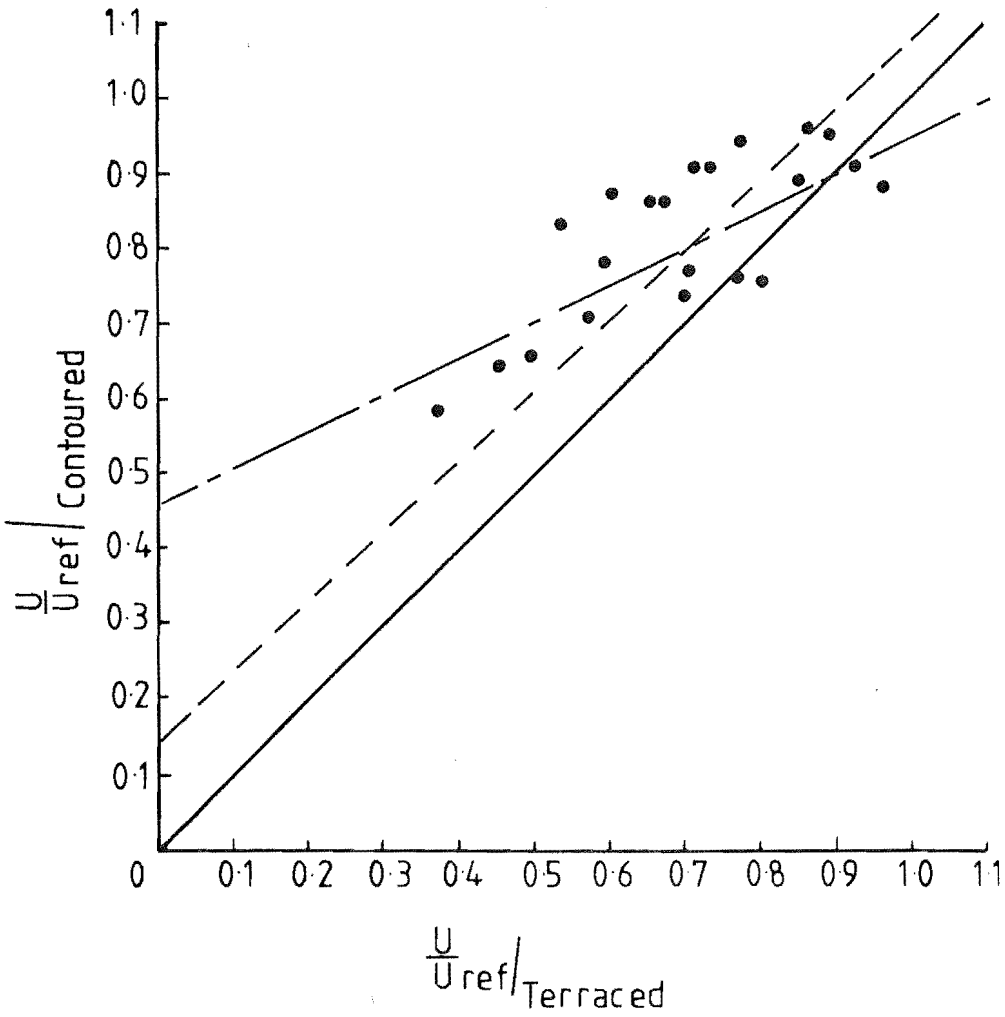

Regression lines

$$\text{- - - - - } \frac{U}{U_{ref}}\Big|_{Terraced} = 1{\cdot}06 \ \frac{U}{U_{ref}}\Big|_{Contoured} - 0{\cdot}160$$

$$\text{- - - - - } \frac{U}{U_{ref}}\Big|_{Contoured} = 0{\cdot}50 \ \frac{U}{U_{ref}}\Big|_{Terraced} + 0{\cdot}461$$

Correlation coefficient $r = 0{\cdot}73$

FIG 7·72 SCATTER DIAGRAM FOR MODEL A AT Z = 20 mm

belts and that they fitted very neatly into the open weave sacking; this made cleaning the model extremely difficult. The problem posed by this situation was the possibility of beads becoming dislodged during the hot film survey of the model. Foreign matter of this size would be capable of breaking a hot-film probe.

However, the tests were useful because they showed a very similar deposition pattern to that recorded for the contoured model. Therefore, a decision was made not to use the bead visualisation technique for the roughness added model in subsequent tests.

2) Flags: The miniature flag visualisation technique posed no problems with the addition of the roughness elements. Extra tests were carried out with the flags to compensate for the lack of bead data. The flags showed the flow directions to be almost the same as for the contoured model. In view of these results, it was considered that the Cobra probe flow direction results from the contoured model could be applied to the roughness added model.

7.5.2 Hot Film Survey

The hot film survey for model A was repeated with the model in the roughness added form of construction. The results of lateral cross sections 1-5 are presented in Fig. 7.73 through to Fig. 7.82; these results will be compared with the contoured model.

The effect of the added roughness is apparent as early as lateral cross section 1, there being a small reduction in the velocity in the bottom 5mm of the boundary layer. However, once above this height, there is a very good agreement between the models. A corresponding increase in turbulence intensity in the lower 5mm is noted in Fig. 7.74. Cross section 2 clearly shows the significant effect produced by the simulated scrub. Point 56, located in a valley at the 2250m position on the base scale, shows a reduction from 0.55 to 0.50 of the gradient speed. However, contour lines above Z = 20mm show a similar trend and are of similar magnitude. Turbulence intensity values at Z = 10mm for point 56 show a change from 18% to 25% which represents a 40% increase. Measurement point 35, 4250m position on base scale, remains much the same for both models. From the raw data, Neal and Stevenson (1980), the ratio for the contoured model and roughness added model at Z = 5mm was 0.65 and 0.68 respectively. At Z = 10mm, both had normalised velocities of 0.70.

The isoturb contours show a corresponding agreement, the most notable

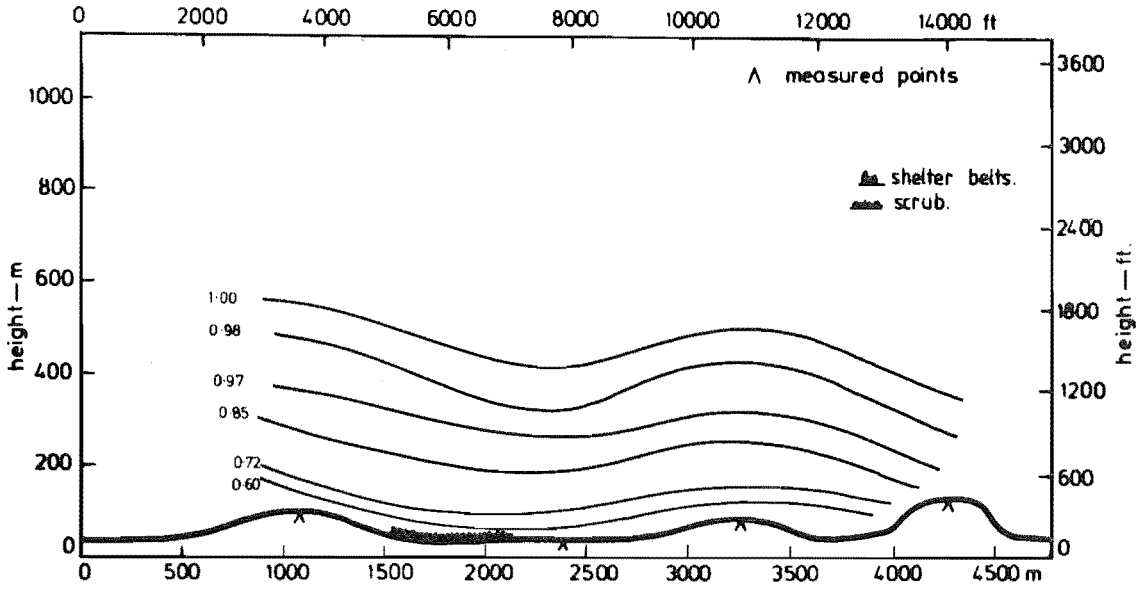

FIG 7.73 ISOTACHS FOR MODEL A WITH ROUGHNESS, LATERAL CROSS SECTION 1

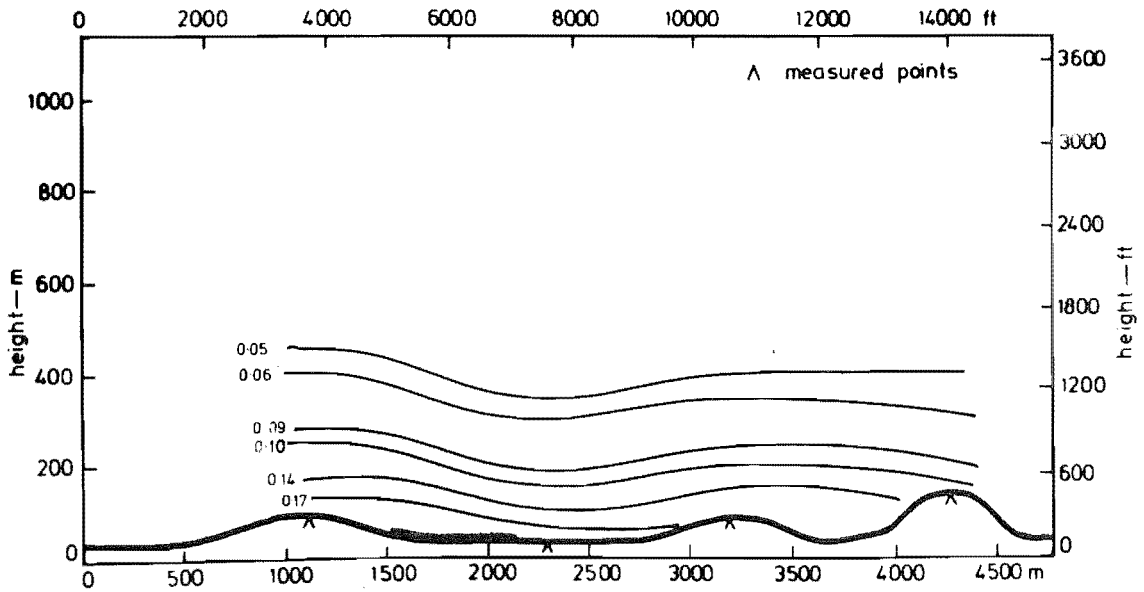

FIG 7.74 ISOTURBS FOR MODEL A WITH ROUGHNESS, LATERAL CROSS SECTION 1

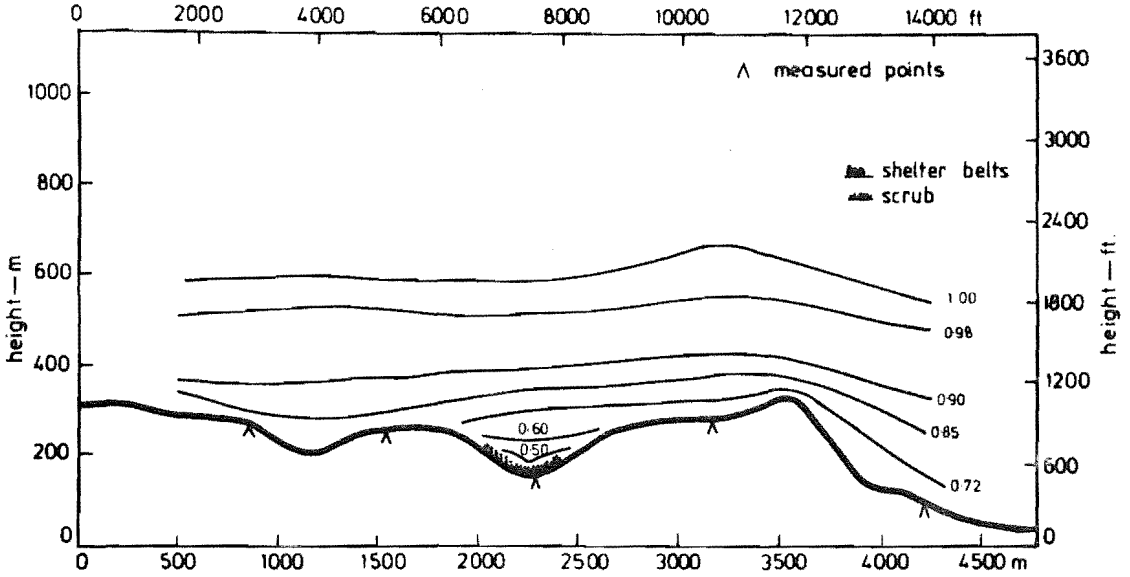

FIG 7.75 ISOTACHS FOR MODEL A WITH ROUGHNESS, LATERAL CROSS SECTION 2

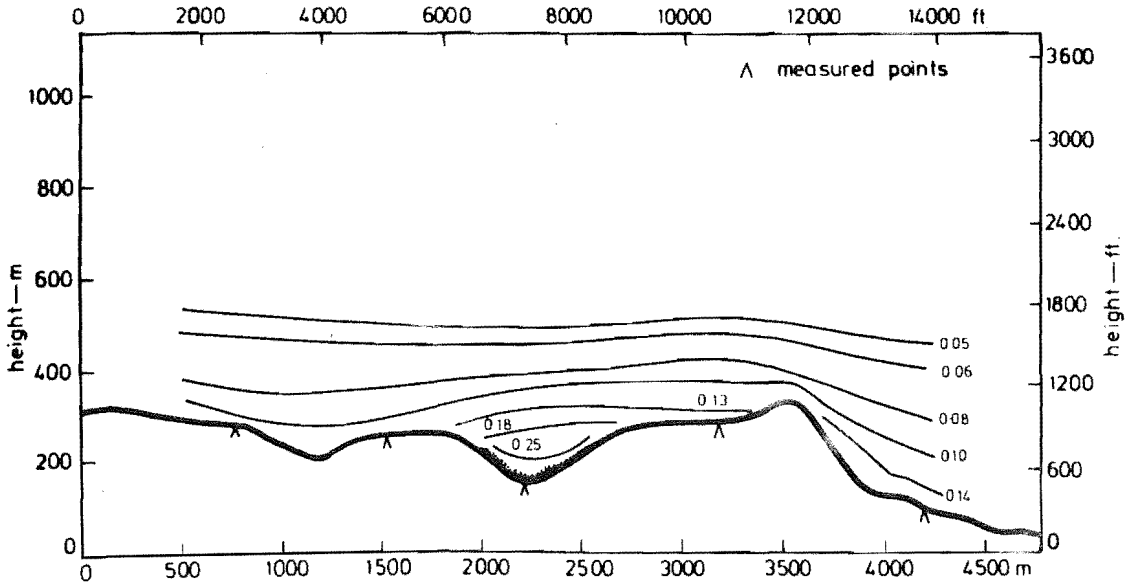

FIG 7.76 ISOTURBS FOR MODEL A WITH ROUGHNESS, LATERAL CROSS SECTION 2

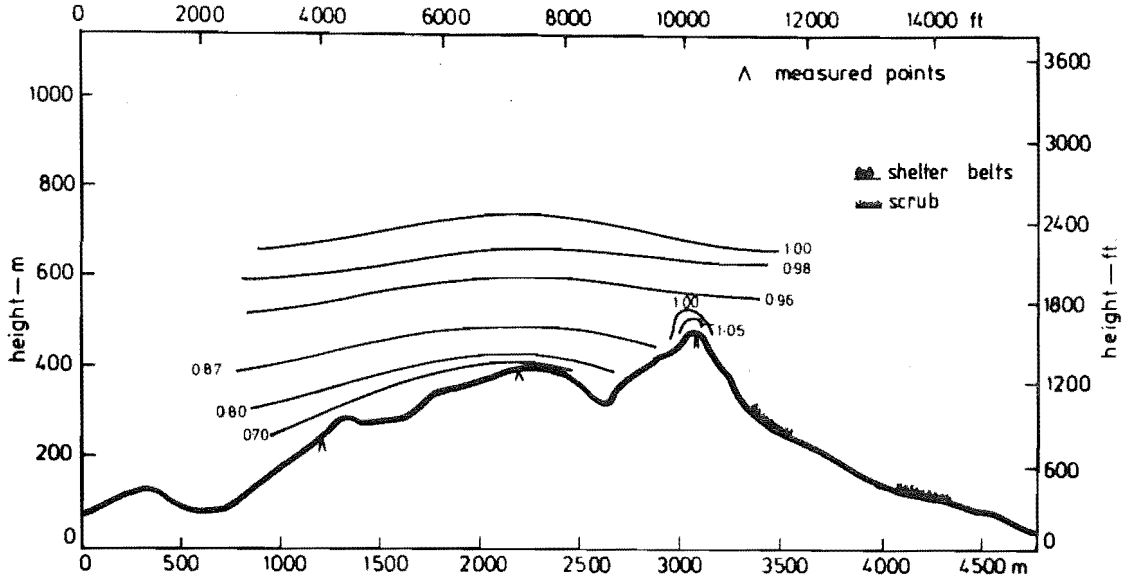

FIG 7.77 ISOTACHS FOR MODEL A WITH ROUGHNESS, LATERAL CROSS SECTION 3

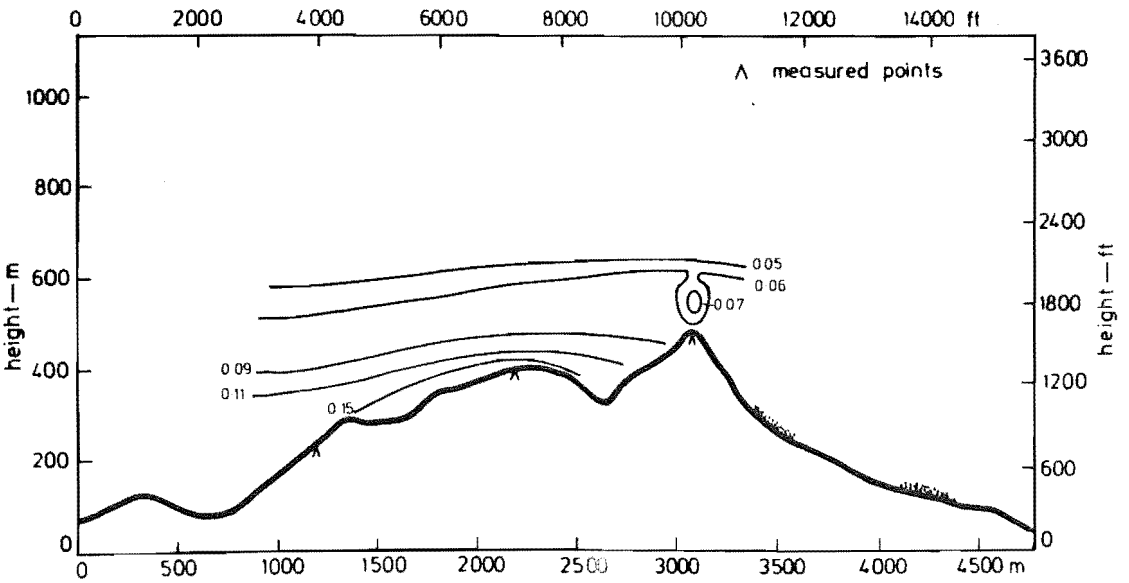

FIG 7.78 ISOTURBS FOR MODEL A WITH ROUGHNESS, LATERAL CROSS SECTION 3

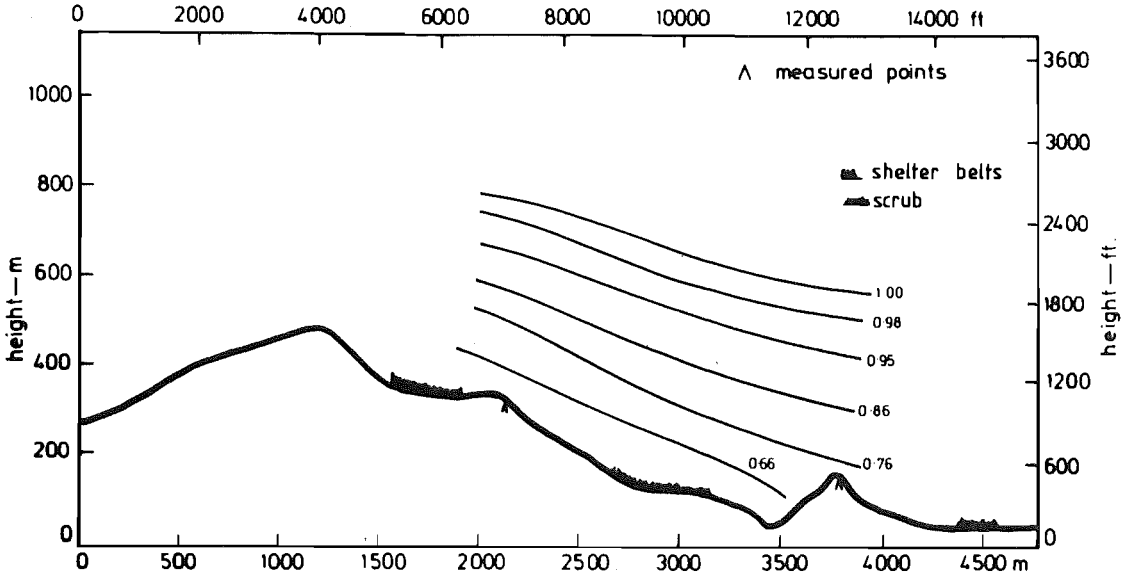

FIG 7.79 ISOTACHS FOR MODEL A WITH ROUGHNESS, LATERAL CROSS SECTION 4

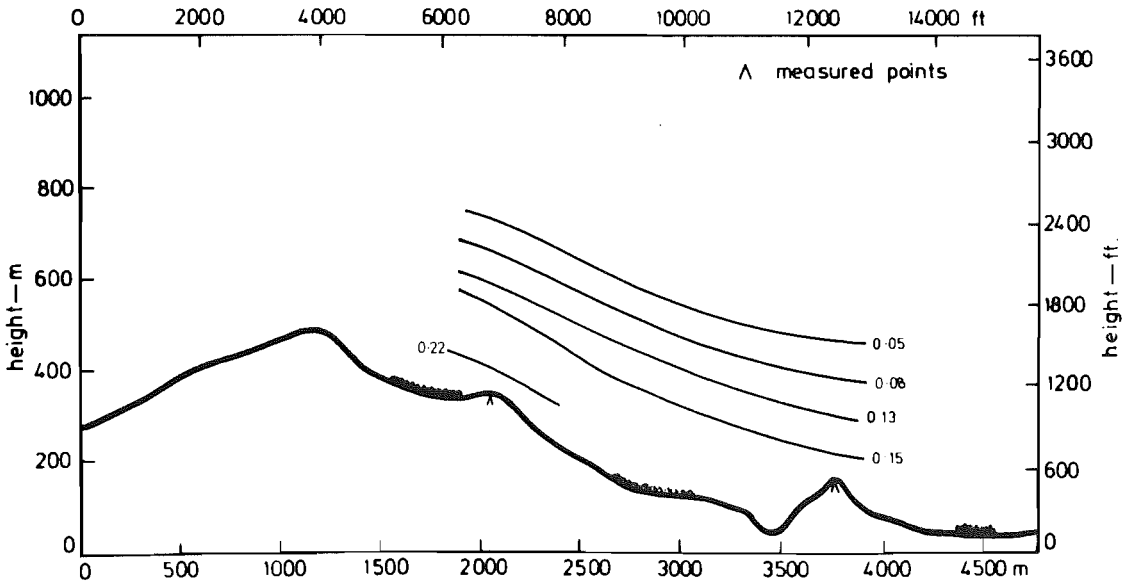

FIG 7.80 ISOTURBS FOR MODEL A WITH ROUGHNESS, LATERAL CROSS SECTION 4

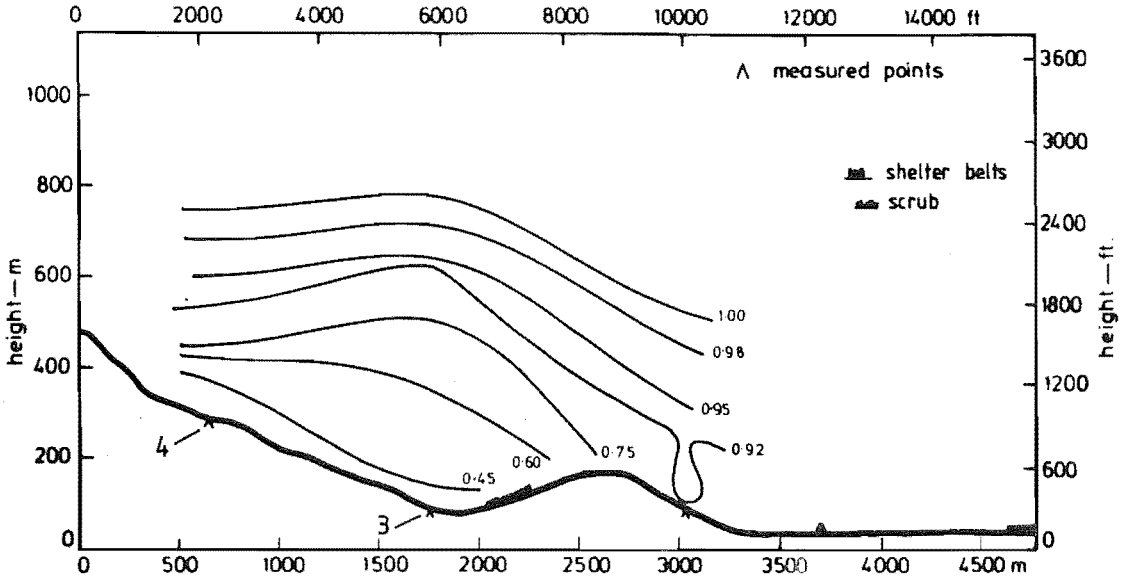

FIG 7.81 ISOTACHS FOR MODEL A WITH ROUGHNESS, LATERAL CROSS SECTION 5

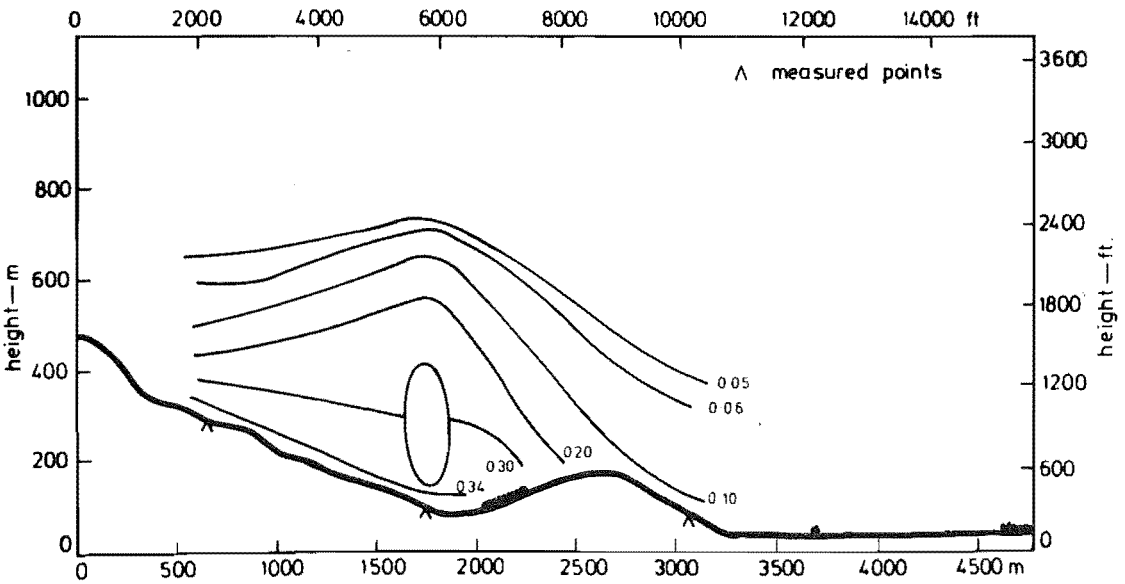

FIG 7.82 ISOTURBS FOR MODEL A WITH ROUGHNESS, LATERAL CROSS SECTION 5

feature being that on the roughness added model, the isoturb contours below the 5% contour remain very flat in comparison with the contoured model where the isoturb contours closely followed the terrain shape.

The isotachs for cross section 3 are very similar to those for the contoured model. Interestingly, there is a slight increase in the velocity below 10mm at point 15, this being at the top of the hill at the 3250m base scale position. Point 58, at the 2250m position, shows a decrease in velocity in the lower 10mm of the boundary layer. This point shows an increase in turbulence intensity close to the model surface, $Z < 10mm$. Modelled scrub noted in cross section 2 could be the cause of this reduced velocity and increased turbulence. With the exception of point 58, the isoturb contours are in good agreement between the two models.

Cross section 4 is located just behind the Gebbies Pass Saddle. The isotach contours above $Z = 50mm$ are almost identical for both the roughness added and contoured models. The interesting feature is that the flow in the 2-50mm region on the roughness added model appears to have increased in comparison with the contoured model. It is very difficult to formulate sound reasoning to explain this feature at this stage of the study. However, this effect is noted and will be discussed in detail in Chapter 8.

The isoturb contours for both models are very similar except those close to the surface at point 59. In view of the increased velocity at this point one would expect a slight reduction in the turbulence intensity; in fact, the results show an increase from 19% to 22% at this point.

The isotach contours for this cross section are in excellent agreement with those for the contoured model at heights above 40mm. The flow close to the surface above points 4 and 3 has slowed from 0.50 to 0.45 of the gradient wind speed. The 0.60 contour appears closer to the surface on the roughness added model than the contoured. This is particularly true between the 2000 - 2500m region on the base scale. The location of this part of the contour is very difficult because the contour can only be accurately located at points 3 and 4. After this it is not known how the flow changes. The contours above this which can be located at point 61 can only be used as a guide.

Iso-contours for the longitudinal cross sections XX and YY are presented in Figs 7.83 to 7.86. Isotach contours for longitudinal cross section XX suggest a slowing of the flow approaching point 15, located at the 4000m point on the base scale. This effect is most significant in the bottom 40mm of

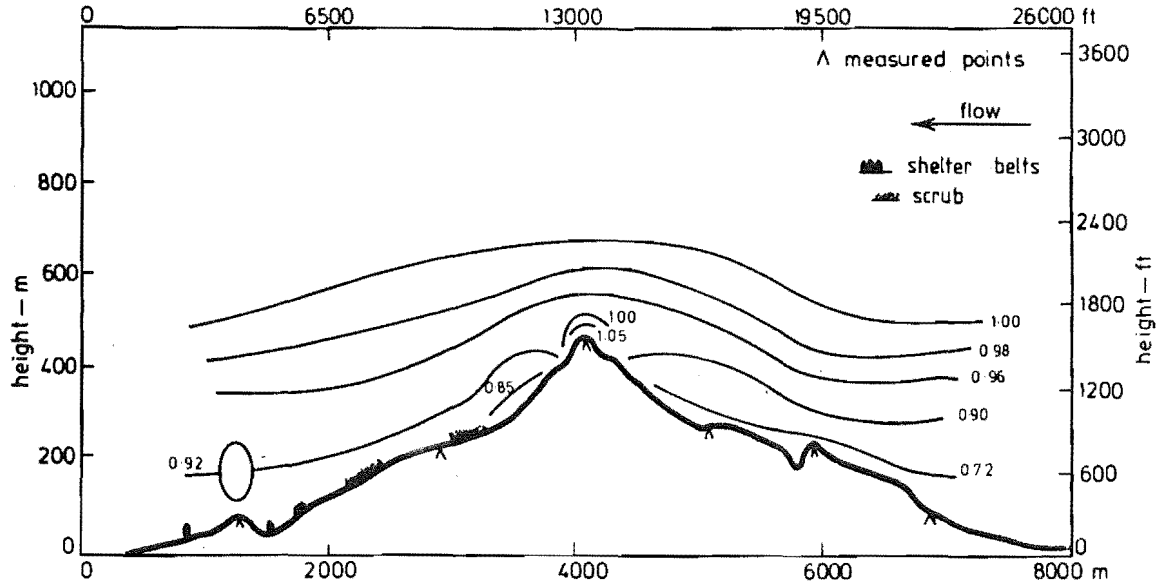

FIG 7.83 ISOTACHS FOR MODEL A WITH ROUGHNESS, LONGITUDINAL CROSS-SECTION XX

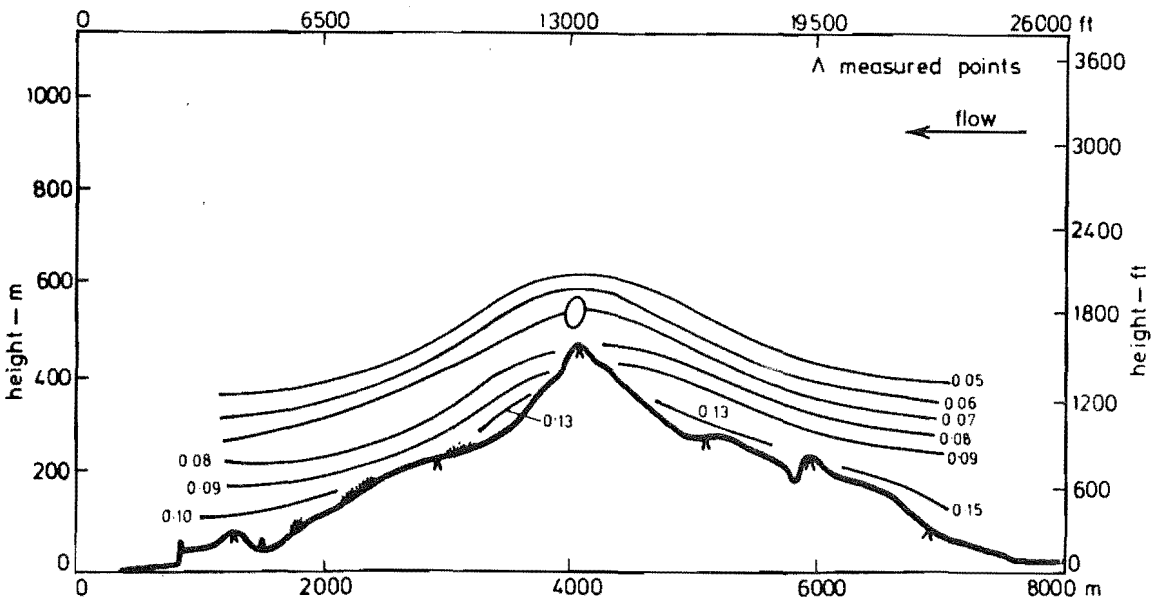

FIG 7.84 ISOTURBS FOR MODEL A WITH ROUGHNESS, LONGITUDINAL CROSS-SECTION XX

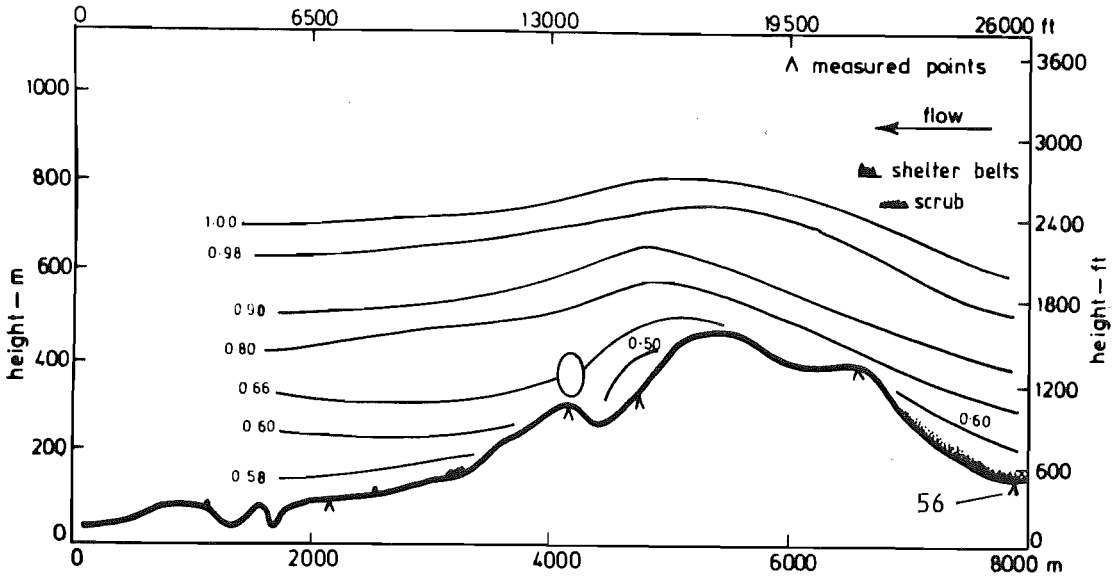

FIG 7.85 ISOTACHS FOR MODEL A WITH ROUGHNESS, LONGITUDINAL CROSS-SECTION YY

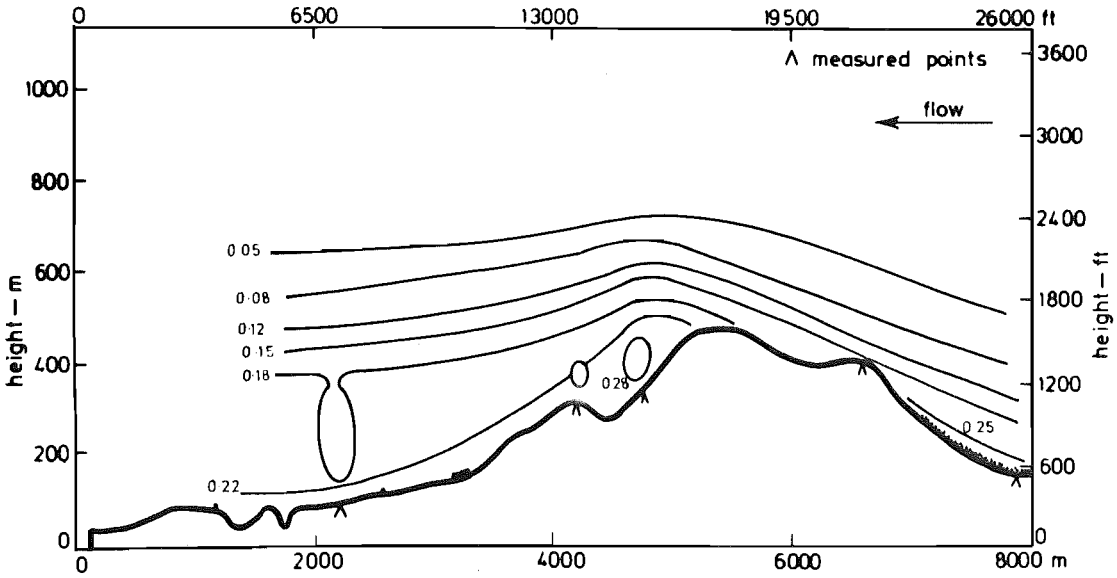

FIG 7.86 ISOTURBS FOR MODEL A WITH ROUGHNESS, LONGITUDINAL CROSS-SECTION YY

the boundary layer. At the gradient height the most relevant feature is the amount of smoothing of the contours over the terrain in comparison with the contoured model which was seen to follow the terrain closely, see Fig. 7.65.

The isoturb contours for this cross section show an excellent agreement in shape to those for the contoured model. There is a marked increase in turbulence intensities in the lower 40mm of the boundary layer. This is most apparent in the flow moving up the southern face of the Port Hills ridge.

The isotach contours for longitudinal cross section YY show that the contours on the southern face of the Port Hills ridge are in excellent agreement with the contoured model both in shape and magnitude. The exception to this is in the lower 20mm of the boundary layer at point 56, which is located in the middle of an extensive area of scrub. Above this point there is a significant reduction of velocity. One the leeward side of the Port Hills the flow is, generally, slowed below that recorded on the contoured model.

The isoturb contours follow a similar pattern as described for the isotach contours. Point 56 has a significant increase in turbulence intensities close to the model surface, $Z < 20mm$, and the turbulence in the lee of the Port Hills has undergone a small increase. Table 7.3 presents the normalised velocities and gradient heights for model A in the contoured and roughness added forms close to the model surface. From this data the magnitude of the variations can be seen. It is apparent that many of the variations are within the expected experimental error of $\pm 2\%$, this being the error in reading the velocity from the voltmeter.

Speed-up ratio areas for the roughness added model are presented on the map in Fig.7.87. A comparison of the speed-up ratio areas for the contoured and roughness added models shows a very strong agreement. The approach to the Port Hills ridge is almost identical for both models. The Gebbies Pass Saddle and the region directly behind it show increased velocity. However,it must be remembered that the boundaries between the various speed-up regions are difficult to determine accurately and can only be used as an indication of the flow régime. Points 15 and 12, the 141-150% speed-up regions, show an increase compared to the contoured model. No explanation for this can be advanced at this stage; however these points are discussed in more detail for models B and C in the following chapters.

During the analysis of longitudinal cross section XX, it was noted that the isotach contours were not as smooth as those for many of the other cross

Height Z (mm)					
	Lateral Cross Section 1				
δ	120 (120)	120 (120)	110 (110)	10 (60)	
5	0.56 (0.50)	0.59 (0.51)	0.65 (0.60)	0.91 (0.90)	
3	0.51 (0.42)	0.54 (0.46)	0.63 (0.56)	0.90 (0.89)	
	52	51	50	20	
	Lateral Cross Section 2				
δ	80 (80)	90 (90)	140 (110)	110 (100)	130 (120)
5	0.87 (0.81)	0.87 (0.80)	0.53 (0.49)	0.67 (0.72)	0.65 (0.68)
3	0.85 (0.76)	0.86 (0.74)	0.50 (0.40)	0.65 (0.66)	0.64 (0.66)
	54	55	56	57	35
	Lateral Cross Section 3				
δ	110 (110)	90 (90)	60 (50)		
5	0.73 (0.65)	0.70 (0.71)	1.02 (1.05)		
3	0.70 (0.61)	0.58 (0.61)	1.06 (1.08)		
	30	58	15		
	Lateral Cross Section 4				
δ	120 (110)	110 (110)			
5	0.63 (0.66)	0.72 (0.76)			
3	0.60 (0.65)	0.72 (0.76)			
	59	10			
	Lateral Cross Section 5				
δ	120 (120)	180 (180)	120 (110)		
5	0.31 (0.34)	0.43 (0.41)	0.89 (0.92)		
3	0.30 (0.32)	0.42 (0.39)	0.89 (0.91)		
	4	3	61		
	Longitudinal Cross Section XX				
δ	120 (110)	60 (50)	110 (100)	80 (70)	110 (110)
5	0.89 (0.92)	1.02 (1.05)	0.67 (0.72)	0.82 (0.88)	0.65(0.60)
3	0.89 (0.91	1.06 (1.08)	0.65 (0.66)	0.77 (0.86)	0.63(0.56)
	61	15	57	19	50
	Longitudinal Cross Section YY				
δ	180 (160)	120 (110)	120 (120)	90 (90)	140 (110)
5	0.53 (0.52)	0.63 (0.66)	0.44 (0.42)	0.70 (0.71)	0.53 (0.49)
3	0.49 (0.48)	0.60 (0.65)	0.42 (0.40)	0.58 (0.61)	0.50 (0.40)
	2	59	9	58	56

Values in brackets are for roughness added model.

TABLE 7.3: Normalised velocity readings close to model surface for Model A. Contoured and with roughness added.

Roughness added Model

Z = 10 mm

Zp = 40 m

$$\frac{\bar{U}_{10}/\bar{U}_{\delta}\,|_{pt}}{\bar{U}_{10}/\bar{U}_{\delta}\,|_{ref\ pt}} \times 100$$

141 - 150

121 - 140

101 - 120

81 - 100

71 - 80

61 - 70

0 - 60

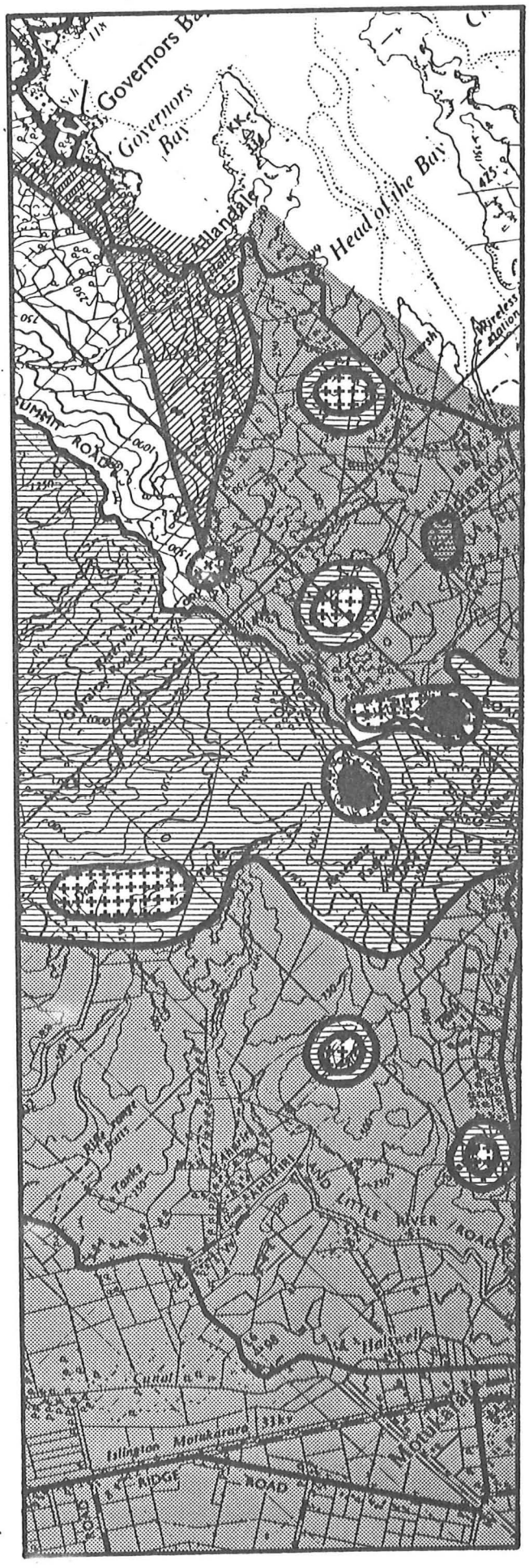

FIG 7·87 SPEED-UP RATIO AREAS FOR MODEL A WITH ROUGHNESS ADDED

Zp = 40m

sections. The speed-up ratio diagram could explain this effect, it clearly showing that 4 of the points used in the XX cross section have speed-up ratios equal to or greater than 40%. The points involved are 19, 15, 11 and 61 as given in Fig. 7.16. These regions have complex regions of flow acceleration and deceleration which could explain the iso-contour variations.

7.5.3 Correlations for Model A, Contoured vs Roughness Added

Scatter diagrams for model A contoured against roughness added model are presented in Figs 7.88 to 7.90. An extremely high correlation of 0.97 occurred at the 5mm height and was found to decrease slightly to 0.96 at 10mm and 0.94 at 20mm.

A test was carried out to show the effect of the shelterbelts and scrub on the correlation results. Points located downstream of scrub areas or shelterbelts were chosen for analysis, but only seven such points could be found. These points were correlated with the contoured model and yielded a correlation coefficient of 0.97. The tests were repeated using seven points on exposed sites, the sites selected being close to those used for the previous test. The correlation coefficient for these points was 0.99.

The results of these tests suggest that the shelterbelts and scrub roughness are having an effect on the flow but because there are so few of these points, the effect is almost completely masked.

7.5.4 Comparisons Between the 3 Forms of Construction

To demonstrate the effect of the surface finish used on the model, the values of several parameters will be compared.

1) Velocity Profiles: A comparison of velocity profiles for points 12, 15, 56, and 59 are given in Fig. 7.91 through to Fig. 7.94.

Points 12 and 15 are situated on top of a ridge and hill respectively, see Fig. 7.16. The profiles clearly show the reduction in velocity that occurred over the terraced model. The contoured and roughness added profiles are almost identical and the velocity at the gradient height, 240m, is shown to be almost the same for all three forms of construction.

Point 56, which was discussed during the analysis of lateral cross section 2, shows the significant velocity reductions that occurred in the bottom 20mm of the boundary layer, i.e., bottom 80m in Fig. 7.93.

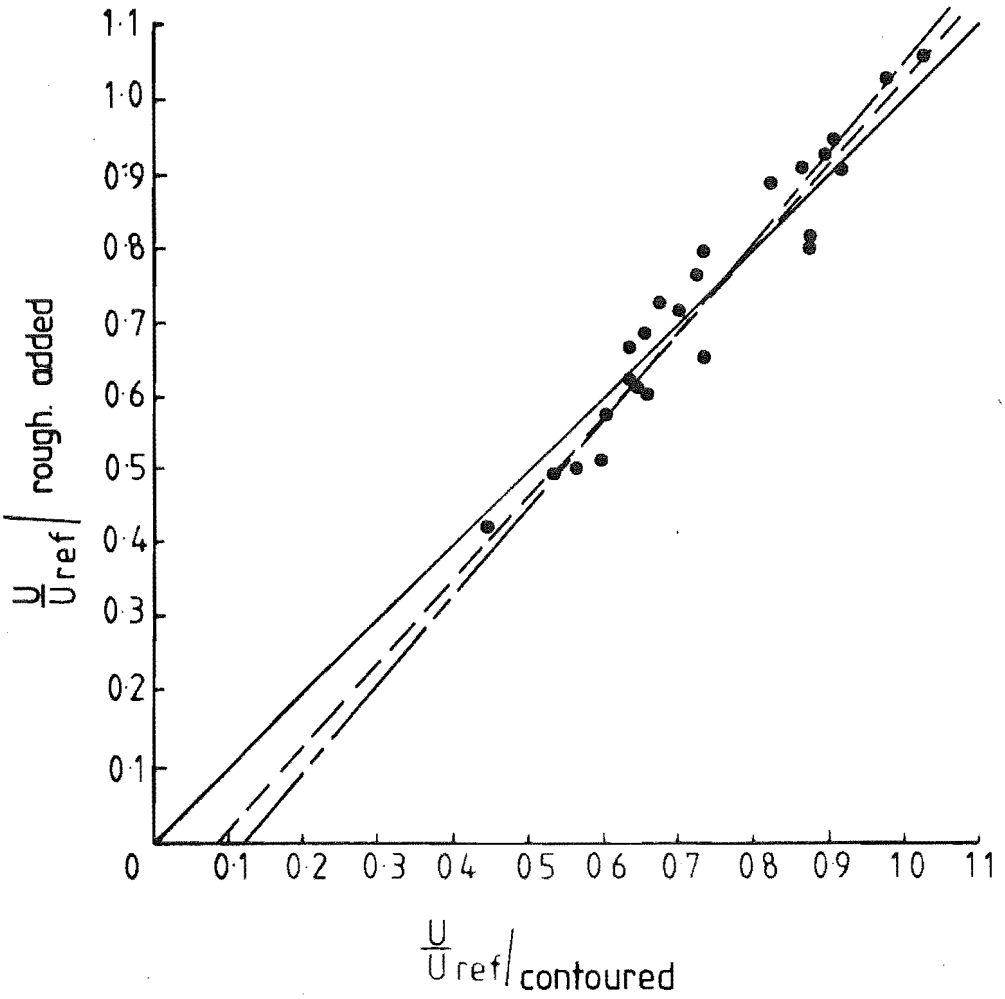

Regression lines

$$\text{– – – –}\quad \frac{U}{U_{ref}}\Big|_{contoured} = 0{\cdot}84\ \frac{U}{U_{ref}}\Big|_{rough.\ added} + 0{\cdot}120$$

$$\text{– · – · –}\quad \frac{U}{U_{ref}}\Big|_{rough.\ added} = 1{\cdot}11\ \frac{U}{U_{ref}}\Big|_{contoured} + 0{\cdot}085$$

Correlation coefficient $r = 0{\cdot}97$

FIG. 7·88 SCATTER DIAGRAM FOR MODEL A AT Z = 5 mm.

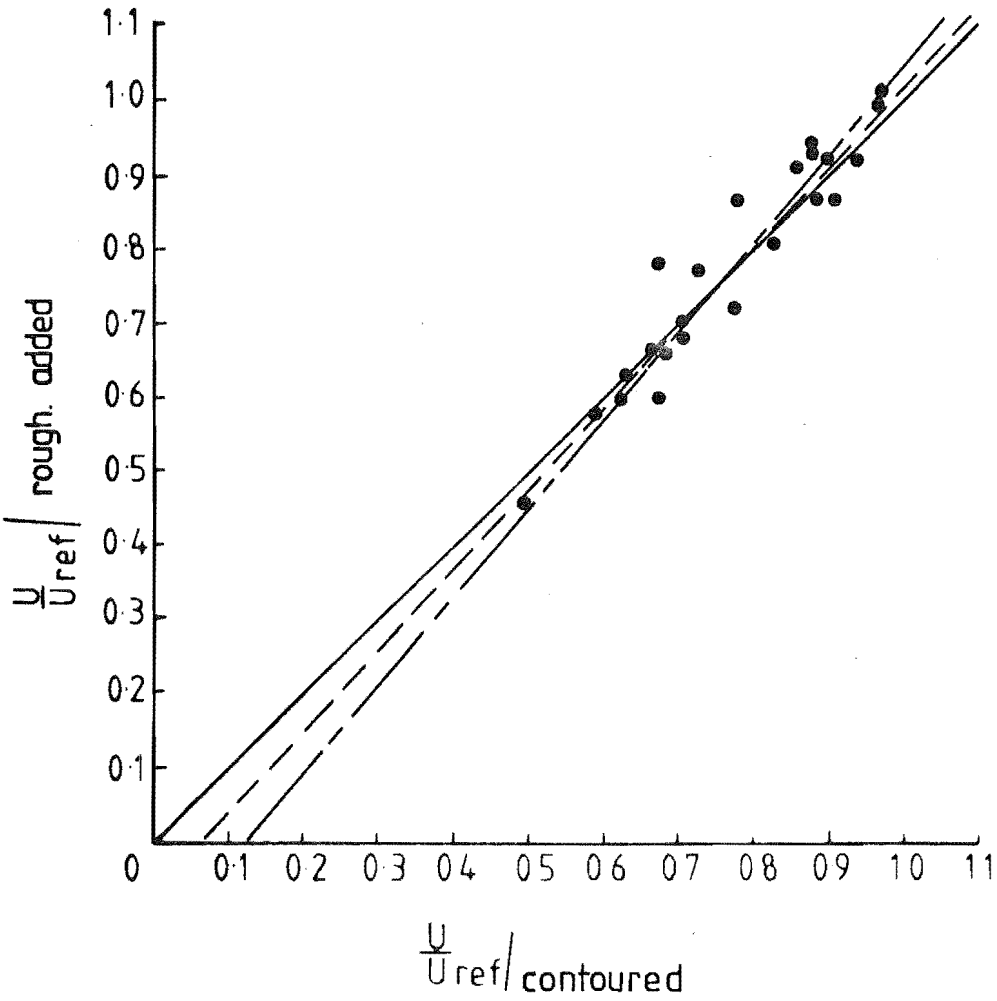

Regression lines

$\frac{U}{U_{ref}}\Big|_{contoured} = 0{\cdot}83 \quad \frac{U}{U_{ref}}\Big|_{rough.\ added} + 0{\cdot}124$

$\frac{U}{U_{ref}}\Big|_{rough.\ added} = 1{\cdot}09 \quad \frac{U}{U_{ref}}\Big|_{contoured} - 0{\cdot}068$

Correlation coefficient $r = 0{\cdot}96$

FIG. 7·89 SCATTER DIAGRAM FOR MODEL A AT Z = 10 mm.

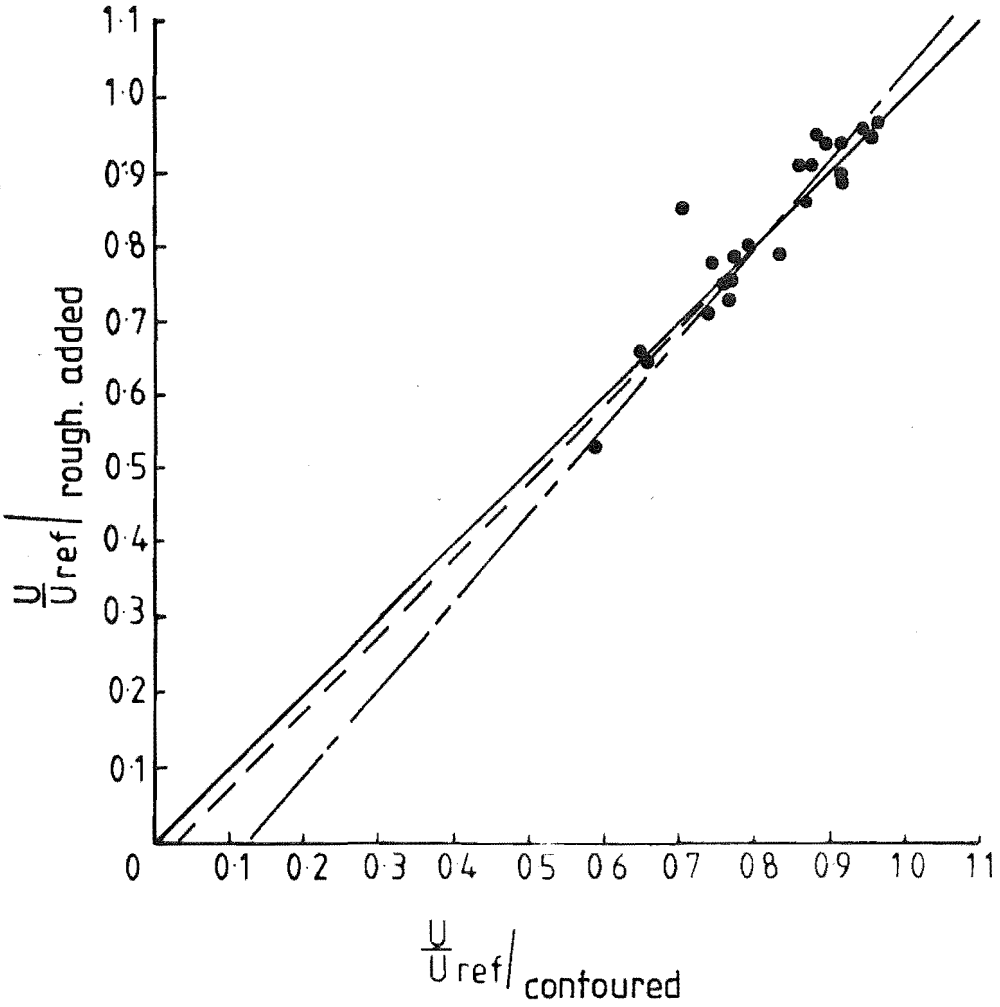

Regression lines

$$\text{- - - -}\quad \frac{U}{U_{ref}}\Big|_{contoured} = 0\cdot 85\,\frac{U}{U_{ref}}\Big|_{rough.\ added} + 0\cdot 120$$

$$\text{- — - —}\quad \frac{U}{U_{ref}}\Big|_{rough.\ added} = 1\cdot 03\,\frac{U}{U_{ref}}\Big|_{contoured} - 0\cdot 023$$

Correlation coefficient $r = 0\cdot 94$

FIG. 7·90 SCATTER DIAGRAM FOR MODEL A AT Z = 20 mm.

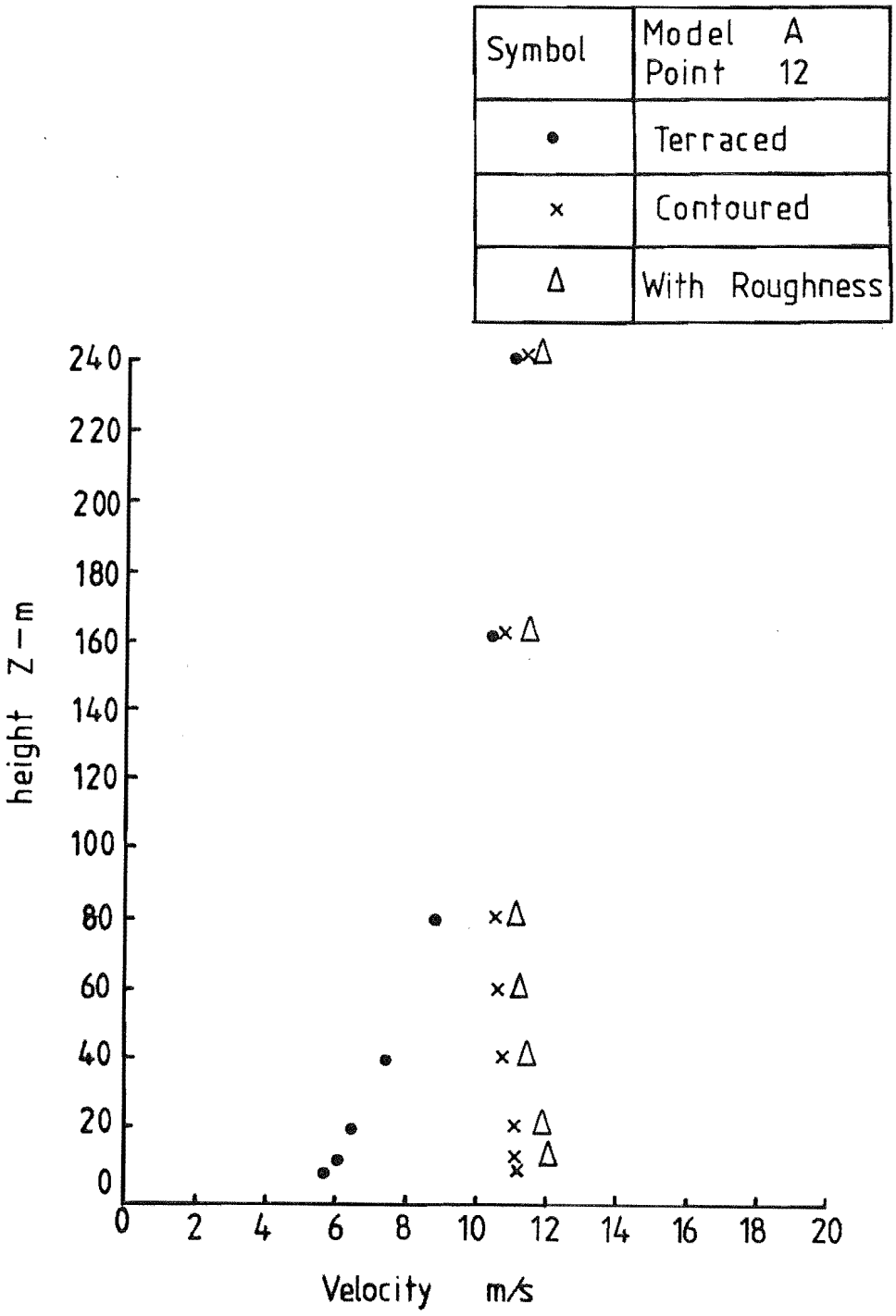

FIG 7·91 COMPARISON OF VELOCITY PROFILES FOR MODEL A POINT 12

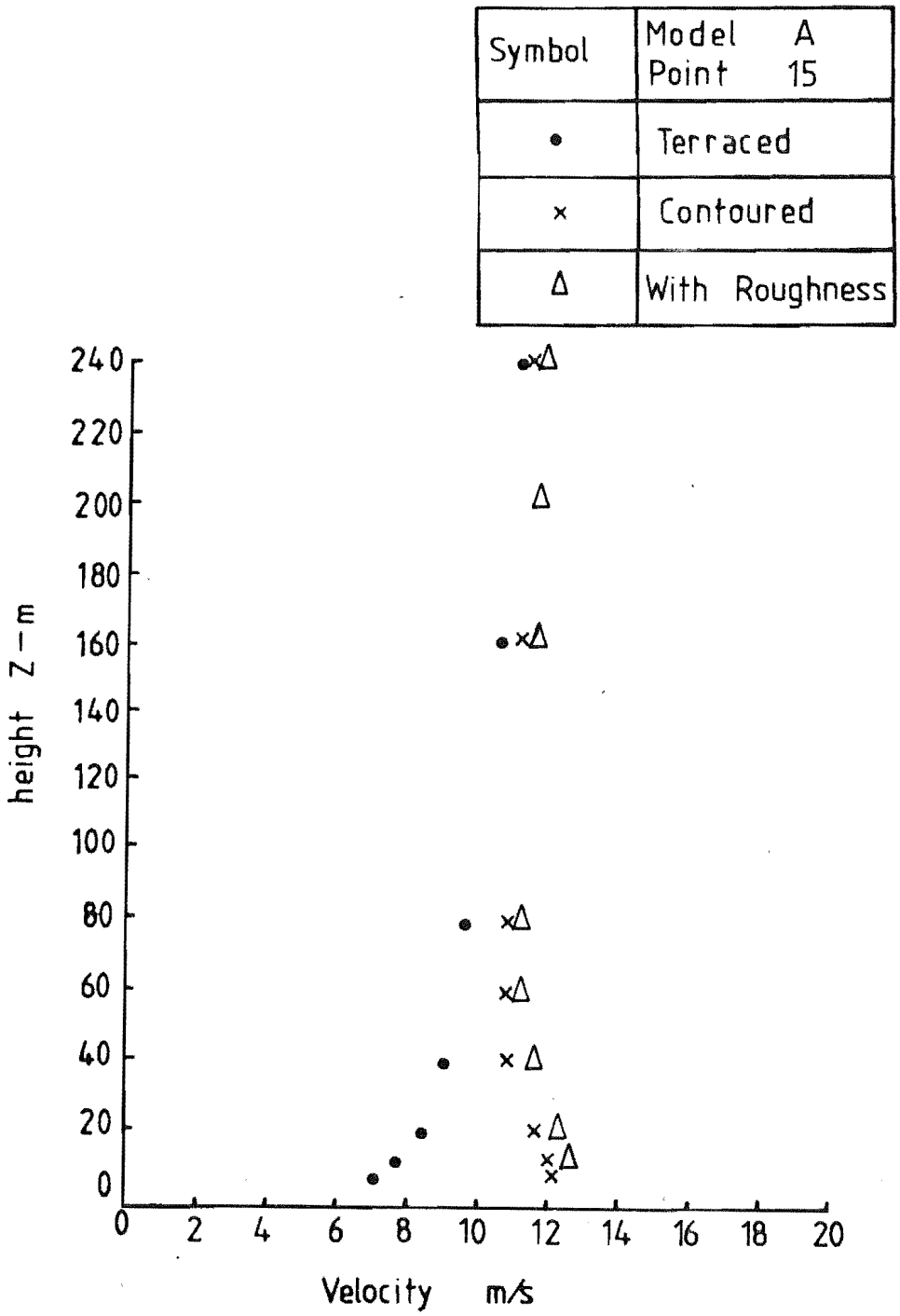

FIG 7·92 COMPARISON OF VELOCITY PROFILES FOR MODEL A POINT 15

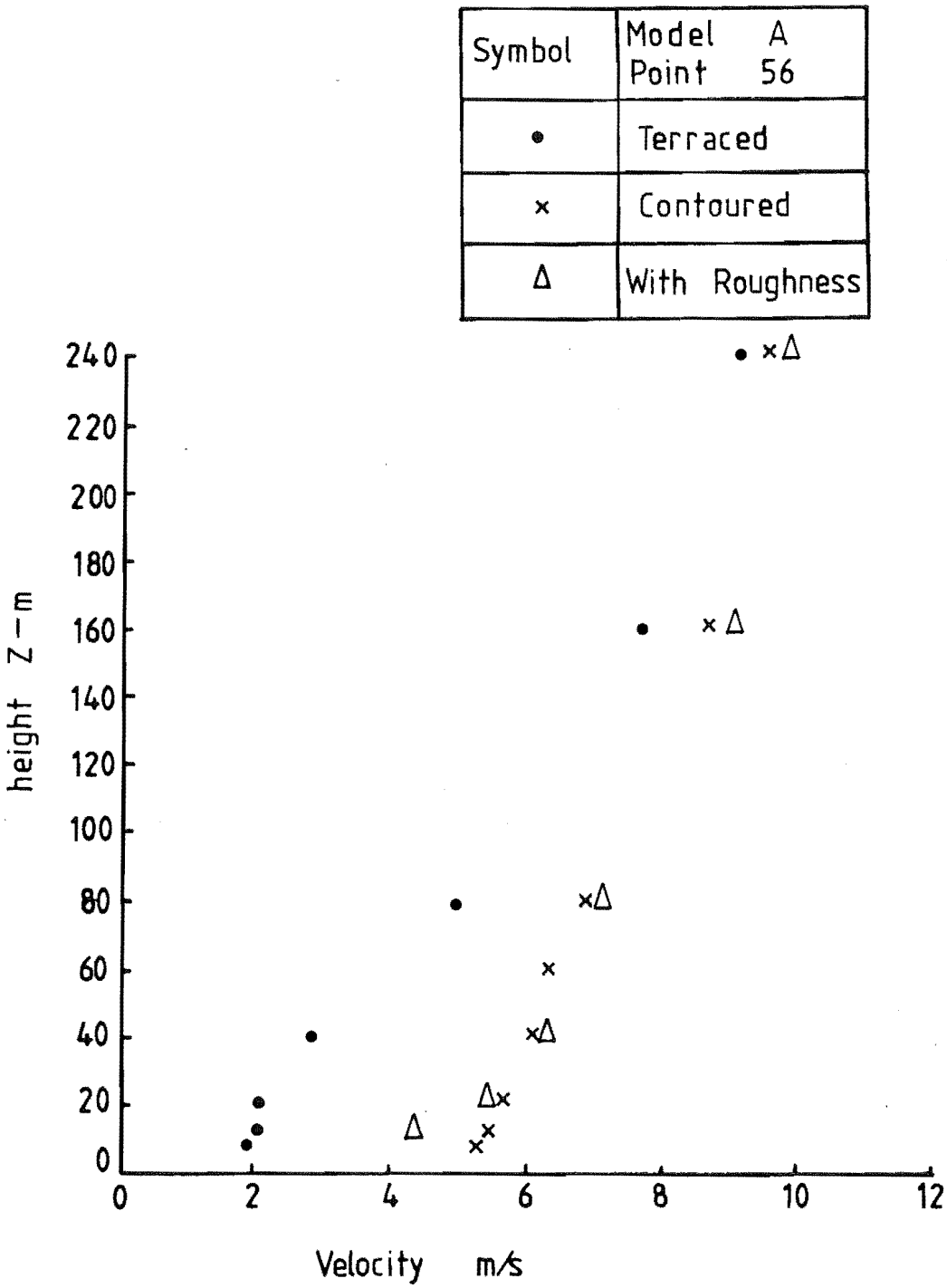

FIG 7·93 COMPARISON OF VELOCITY PROFILES FOR MODEL A POINT 56

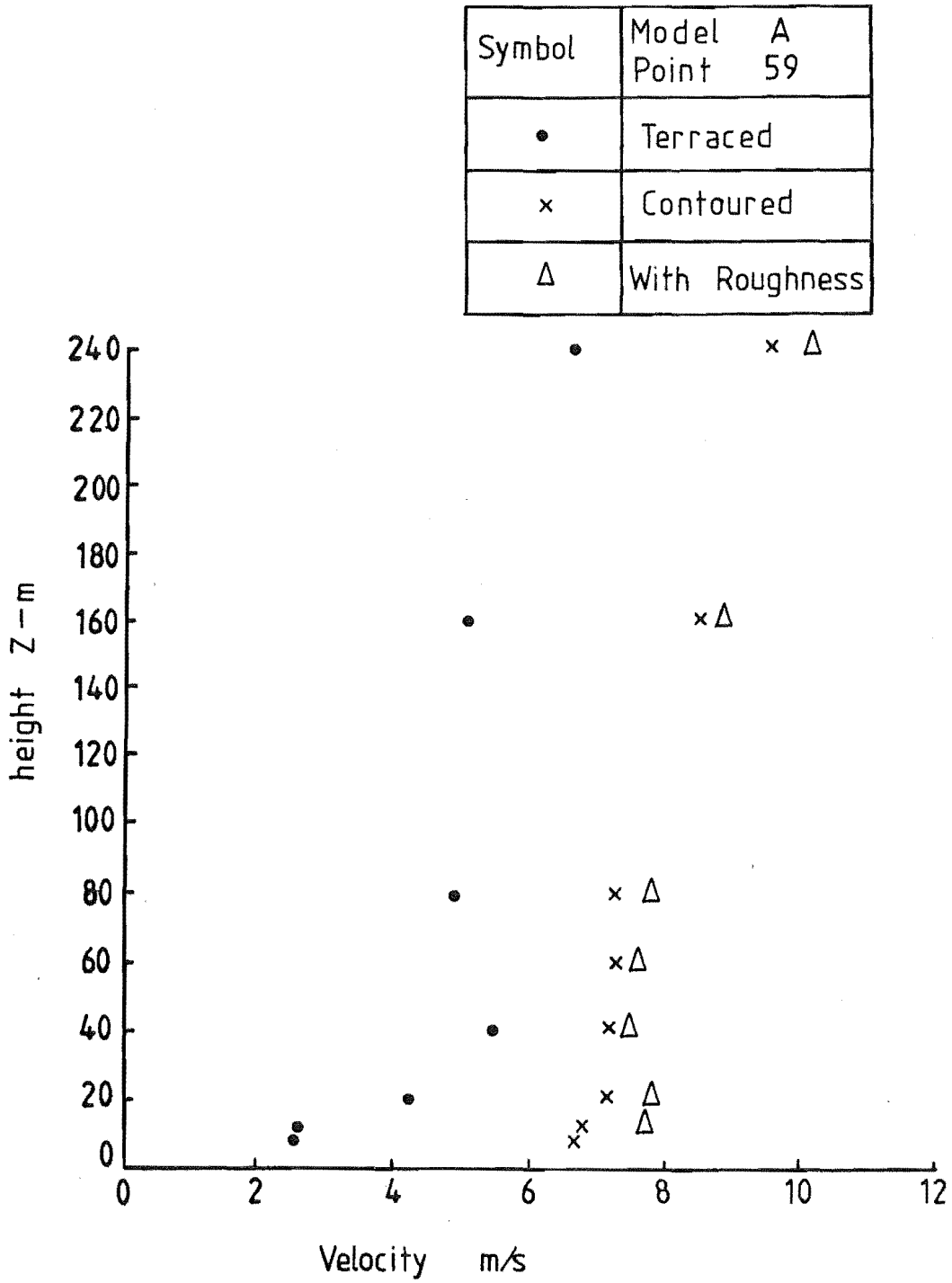

FIG 7·94 COMPARISON OF VELOCITY PROFILES FOR MODEL A POINT 59

The gradient height of the boundary layer at this point occurred at 440m; however, even at 240m, the velocities for all the profiles are very close. The effect of the modelled scrub is apparent in the bottom 20m of the boundary layer, the addition of the roughness being seen to reduce the mean velocity significantly.

Point 59 is situated behind the Port Hills ridge and is in an area where flow passing over the Port Hills mixes with that passing along the leeward side of the hills, as was shown with the flag and Cobra probe tests. The velocity profile suggests that contouring the model produced a general increase in velocity which extends some distance above 240m.

2) Turbulence Intensity Profiles: The turbulence intensity profiles for points 15 and 12 are presented in Fig. 7.95, and show the effect caused by the terraced form of construction. The turblence intensity values are much higher for this form of construction and have a significant effect up to a height of 40mm, 160m on the prototype. The profiles for the contoured and roughness added models are very close, the slight increase in velocity shown in the velocity profiles accounting for the turbulence profiles for the roughness added model being less than for the contoured model.

Turbulence profiles for points 11 and 61 are presented in Fig. 7.96. Point 11 is situated on the leeward side of the Port Hills ridge and is directly behind a small scrub area. The turbulence intensity profile does not appear to be influenced by the upstream roughness elements. Both points 11 and 61 show the dramatic difference produced by the terraced form of construction and the similarity between the contoured and roughness added models.

A detailed discussion of these effects is given in Chapters 8 and 9 which also included the results for models B and C.

3) Autocorrelation Curves: Autocorrelation curves for points 58 and 59 are presented in Fig. 7.97. These have been plotted for the three states of construction. From the autocorrelation curve, the length scale of turbulence can be determined based on Taylor's Hypothesis (Section 2.1.5).

Point 58 is on the windward face of the Port Hills and has several shelterbelts and a large area of scrub in its approach flow. The length scale, L_{u_x}, for the terraced form is much lower than for the other models.

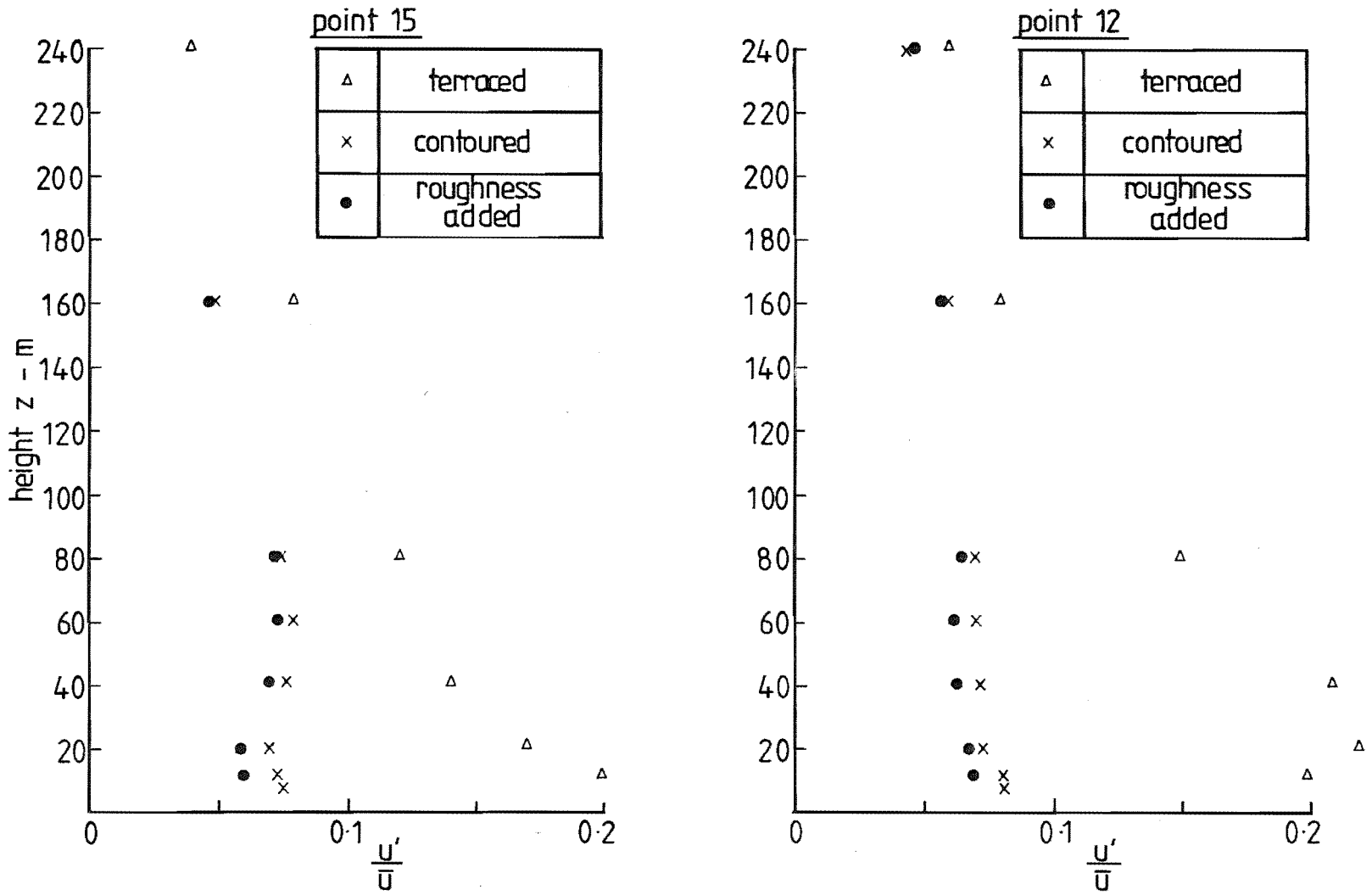

FIG. 7·95 COMPARISON OF TURBULENCE INTENSITY PROFILES FOR THE VARIOUS FORMS OF CONSTRUCTION

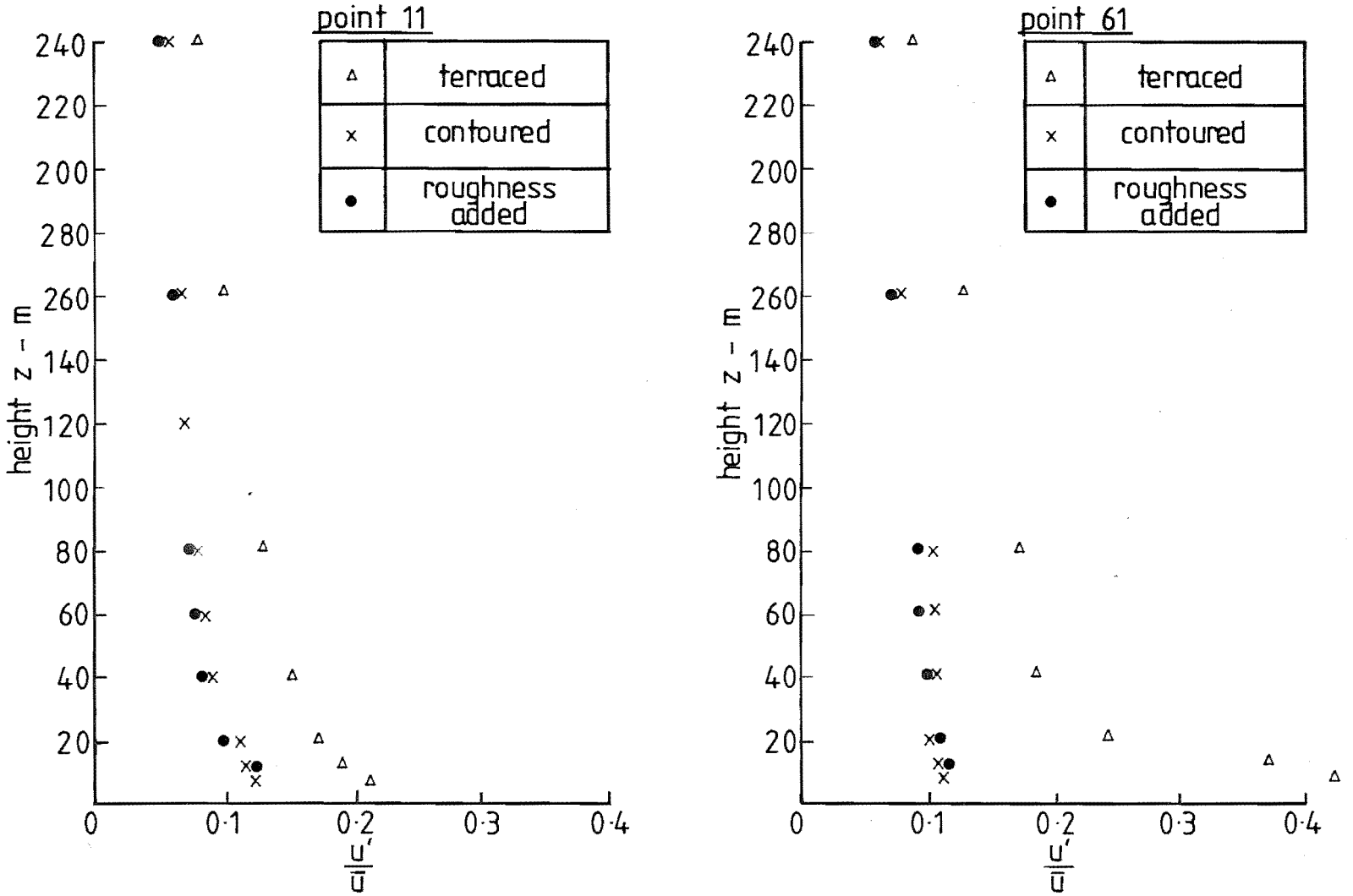

FIG. 7·96 COMPARISON OF TURBULENCE INTENSITY PROFILES FOR THE VARIOUS FORMS OF CONSTRUCTION

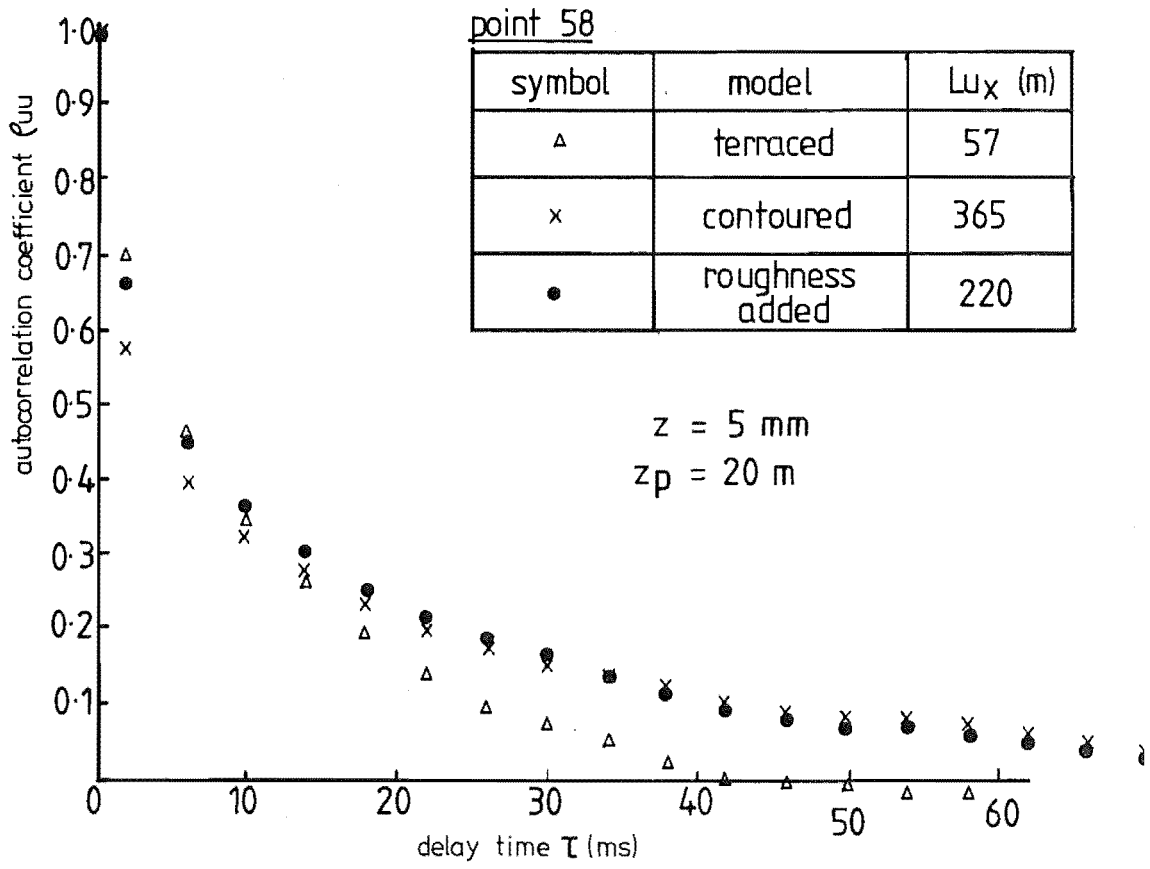

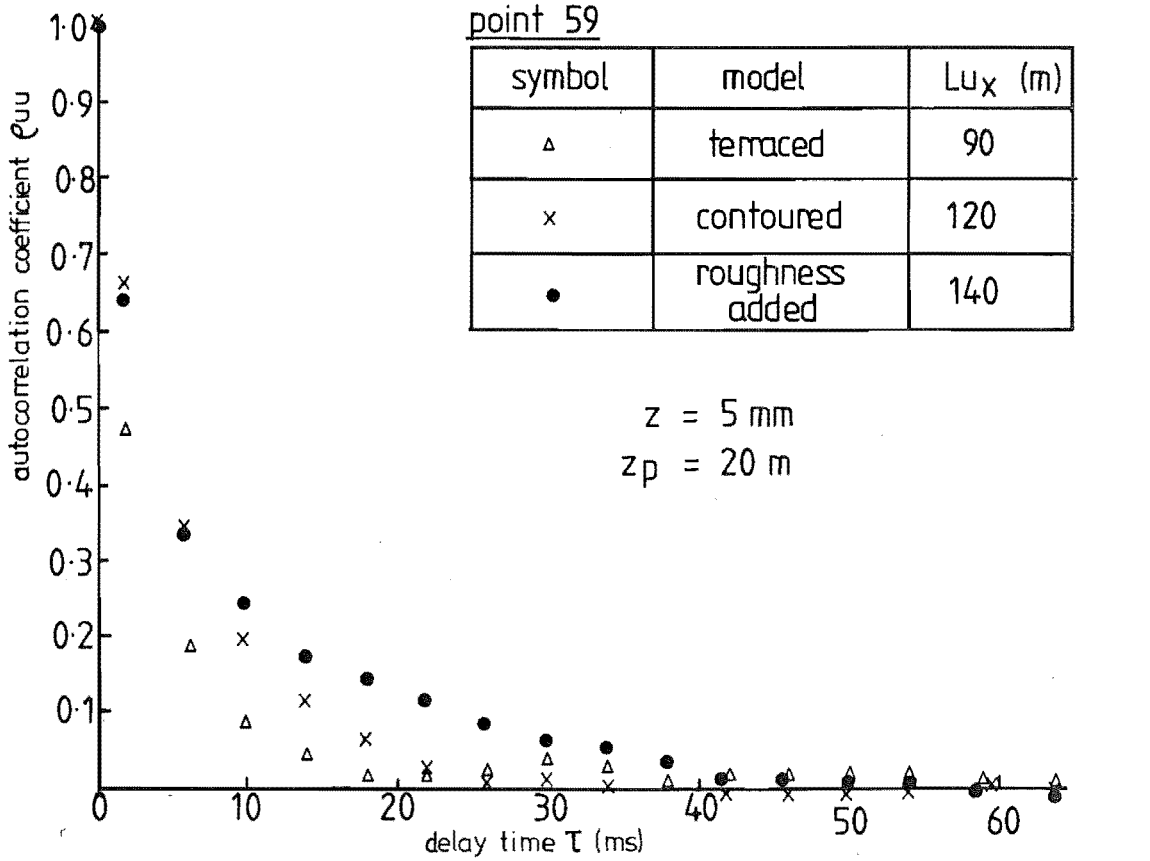

FIG. 7·97 AUTOCORRELATION CURVES FOR THE VARIOUS FORMS OF CONSTRUCTION

This is indicative of higher frequency turbulence which is probably being generated by the terraces and the fact that the mean velocity is significantly reduced at this point on the terraced model.

The contoured and roughness added length scales are very close, the slight reduction in L_{u_x} for the roughness added model probably being caused by the upstream roughness.

Point 59 is located on the leeward side of the Port Hills ridge and also shows a small value of L_{u_x} for the terraced model. The contoured and roughness added values are very similar, probably being due more to the general location rather than the local roughness. In other words, L_{u_x} is determined by general terrain features rather than the small amount of added surface roughness.

4) Energy Spectra: The longitudinal component of the energy spectrum at 5mm for point 58 is presented in Fig. 7.98. The spectra does not have a well-defined peak, this feature appearing to be characteristic of topographic modelling with small scales. Meroney *et al* (1978) also found this trend and concluded that the approach flow to the model did not have sufficient fetch to 'break-up' the larger scale turbulence being generated by the upstream grid. Unfortunately, the grid is necessary to generate the appropriate velocity profile. The peak wave number indicated by the spectra for the roughness added model is $2.1m^{-1}$. The length scale of turbulence is calculated using the relationship

$$L_{u_x} = \frac{0.146}{k_p} \quad \ldots\ldots\ldots\ldots\ldots\ldots\ldots\ldots\ldots\ldots\ldots\ldots\ldots\ldots\ldots\ldots\ldots\ldots\ldots\ldots\ldots\ldots(7.5)$$

where k_p is the peak wave number.

Allowing for the linear scaling, the length scale becomes

$$L_{u_x} = \frac{584}{k_p} \quad \ldots\ldots\ldots\ldots\ldots\ldots\ldots\ldots\ldots\ldots\ldots\ldots\ldots\ldots\ldots\ldots\ldots\ldots\ldots\ldots\ldots\ldots(7.6)$$

The energy spectra for point 59 is presented in Fig. 7.99. Considering the physical location of this point, it is surprising that the resulting spectra have a shape which resembles the theoretical curves proposed by other researchers such as Harris, Panofsky, Teunissen. One possible explanation is that the rough nature of the approach terrain, in particular, the effects of the Port Hills ridge upstream of this point,

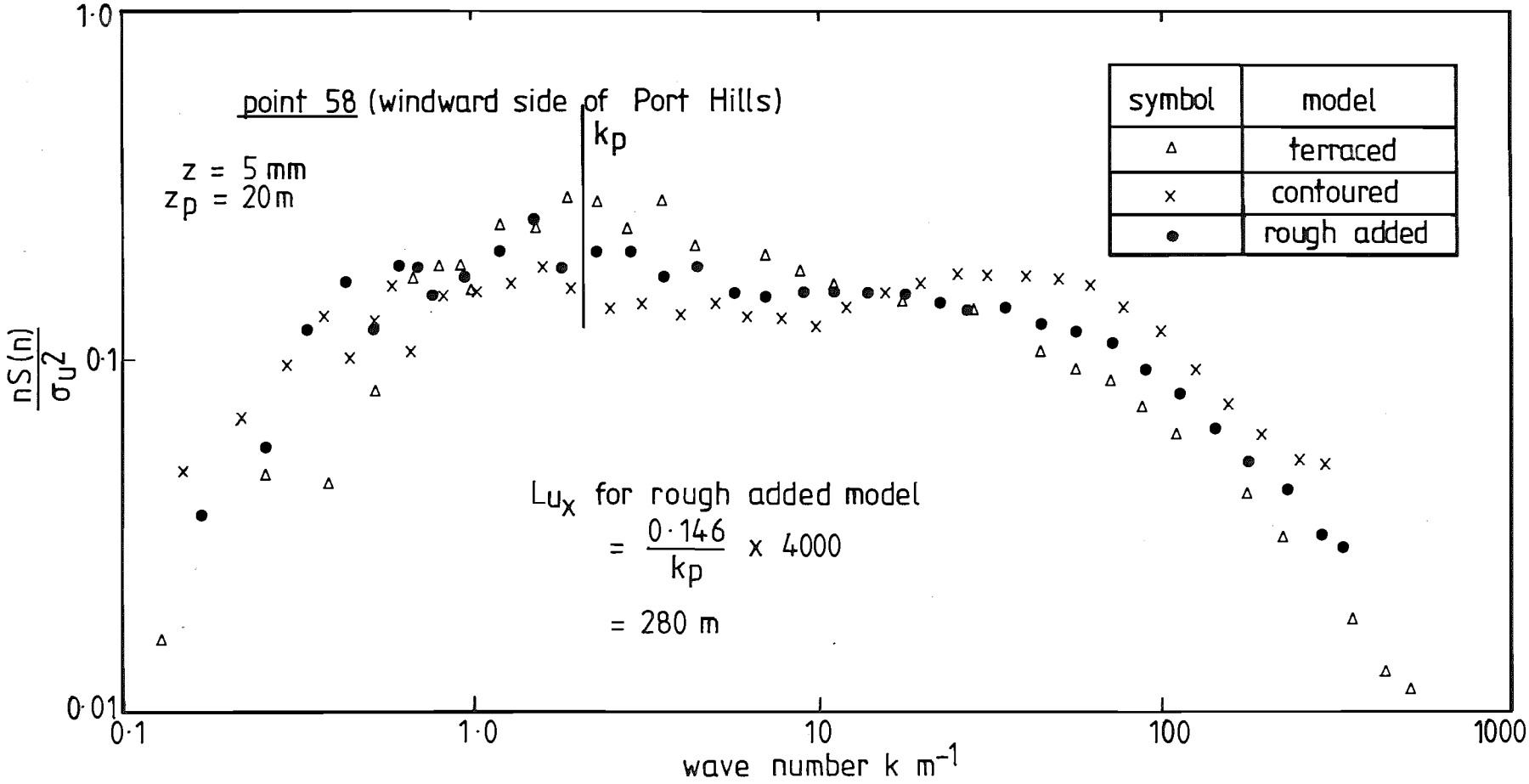

FIG. 7·98 COMPARISON OF ENERGY SPECTRA FOR POINT 58, Z_P = 20 m

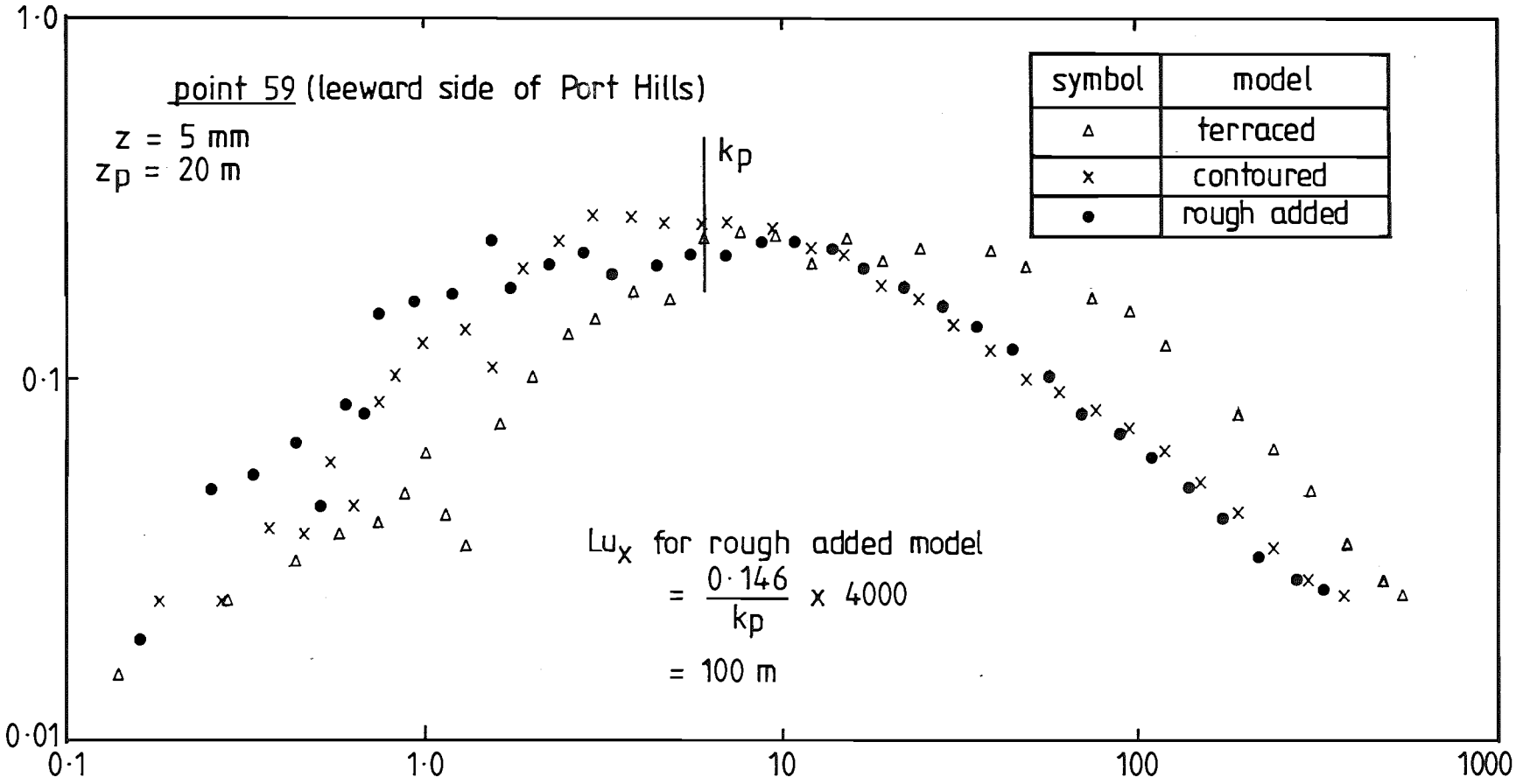

FIG. 7·99 COMPARISON OF ENERGY SPECTRA FOR POINT 59, Z_P = 20 m

has 'broken-up' the larger scale turbulence from the grid, as described earlier.

One should not place too much emphasis on the horizontal positions of the various curves in this figure. The base scale of non-dimensionalised wave number is given by

$$k = \frac{nz}{\bar{u}} \qquad \ldots\ldots\ldots\ldots\ldots\ldots\ldots\ldots\ldots\ldots\ldots\ldots\ldots\ldots\ldots\ldots\ldots\ldots\ldots\ldots\ldots\ldots (7.7)$$

where n = frequency

z = height

$\bar{u}$ = mean velocity.

In the case of the terraced model, the velocity at point 59 was very much less than that for the contoured model. Therefore, this factor is the major reason for the terraced spectra being displaced to the right of the other curves.

The resulting length scales for points 58 and 59 are presented in Table 7.4 for comparison with those evaluated from the autocorrelation curves.

z_p m	Point	L_{u_x} (m)	
		Spectra	Autocorrelation
20	58	280	220
20	59	100	140

Table 7.4: Comparison of length scales for Model A with roughness added.

To give an indication of the variation of the length scales (and therefore turbulence over the model), energy spectra at four points along cross section YY are presented in Fig. 7.100 for the model in the roughness added form. Although the curves are similar in the higher wave number region, it must be remembered that the mean velocity varies significantly from point to point, therefore having a direct effect on the horizontal axis position of the curve. The resulting length scales for these points are given in Table 7.5.

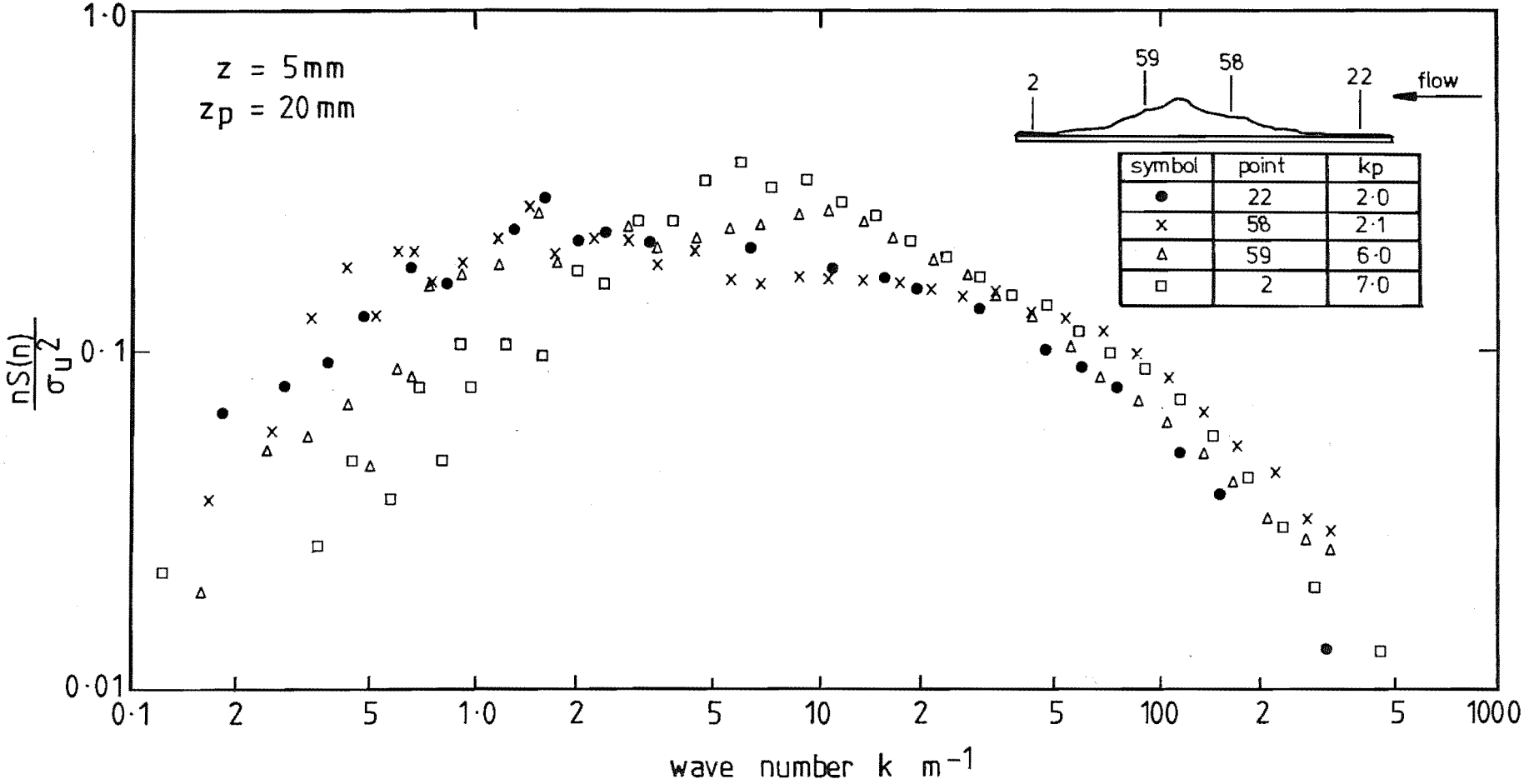

FIG. 7·100 VARIATION OF ENERGY SPECTRA ALONG SECTION YY, Zp = 20 m

z_p (m)	Point	k_p m^{-1}	L_{u_x} (m)
20	22	2.0	290
20	58	2.1	280
20	59	6.0	100
20	2	7.0	84

Table 7.5: Length scale variations along cross section YY

The results show a trend for the length scale to decrease as the flow passes over the model. This is to be expected because, as the flow passes over the roughness of the model, so it causes a greater transfer of momentum up into the boundary layer, resulting in the average frequency of the turbulence to increase, i.e., the length scale to decrease.

7.6 CONCLUSIONS

Analysis of the actual model showed that the percentage of tunnel blockage produced by model A was acceptable. The lack of information on the topic of blockage was highlighted.

Approach flow conditions which agree with theoretical proposals and with field measurements made by serveral researchers, including the author, were shown to have been essentially achieved.

The terraced model results suggest areas of low velocity and particularly high turbulence, $\frac{u'}{\bar{u}} > 30\%$, in the bottom 10mm of the boundary layer. The speed-up ratio diagram suggested that there was a general slowing down of the flow on the windward face of the Port Hills ridge. Pearse (1979) showed the effects of roughness on the flow over two dimensional triangular hills and concluded that the addition of roughness on a triangular hill of slope 1:2 produced a speed-up effect. However, for a hill with slope 1:20, the roughness slowed the flow. The southern face of the Port Hills, with a slope of 1:15, while noting that the ridge is not at right angles to the flow, supported these results.

Velocities and turbulence intensity values, particularly those close to the model surface, i.e., Z < 10mm, were very different from the terraced model. Velocity values were generally higher and turbulence intensity values reduced by up to 50%.

The speed-up ratio map showed that the windward side of the Port Hills ridge was subjected to higher velocities than for the terraced model.

There was a poor correlation, only 0.55, between the terraced and contoured models.

The general flow features for the roughness added model were very similar to those for the contoured model. The speed-up ratio areas did not differ significantly and the high correlation coefficient of 0.97 confirmed the similarities between the two models. The significance of modelling the shelterbelts and scrub areas was shown to be doubtful at the heights measured. However, below the height of 2mm, minimum height measured, this might not be the case. Analysis of points located downstream of these features still yielded a correlation of 0.96.

CHAPTER 8

MODEL B RESULTS

The results of the wind tunnel tests over model B, see Fig. 5.10, will be presented and discussed in this Chapter. The results for model B in the terraced, contoured and with roughness added forms of construction will be compared with each other, measured results and theoretical models.

8.1 ANALYSIS OF MODEL B

Consideration was given to the problem of wind tunnel blockage caused by the presence of the model. The cross sections evaluated are presented on the map in Fig. 8.1 and the percentage blockages are presented in Figs 8.2 to 8.7. The maximum blockage presented by the model is 5.8% which is considered as being acceptable under the conditions discussed in Section 7.1.

8.1.1 Approach Flow Characteristics

Vertical uniformity above the gradient height and lateral uniformity up to three boundary layer heights were measured upstream of the model. From the results it was concluded that a satisfactory level of uniformity, similar to that used for model A, had been achieved. The results of the lateral uniformity tests are presented in Fig. 8.8.

The modelled power law velocity profile is presented in Fig. 8.9 and is in agreement with that measured for model A. The turbulence intensity profile, Fig. 8.10, is also in good agreement with model A and theoretical predictions. The log-law velocity profile for point 40, Fig. 8.11, suggests a roughness length of 0.018m which is in excellent agreement with theory and model A.

In general, the required approach flow conditions stipulated and produced for model A were reproduced satisfactorily for the model B analysis.

8.2 MODEL B TERRACED

The data collection sections and points used for this model are presented on the map in Fig. 8.12. Pressure gradient measurements were made over the model and showed a maximum variation of 1%, which was considered satisfactory.

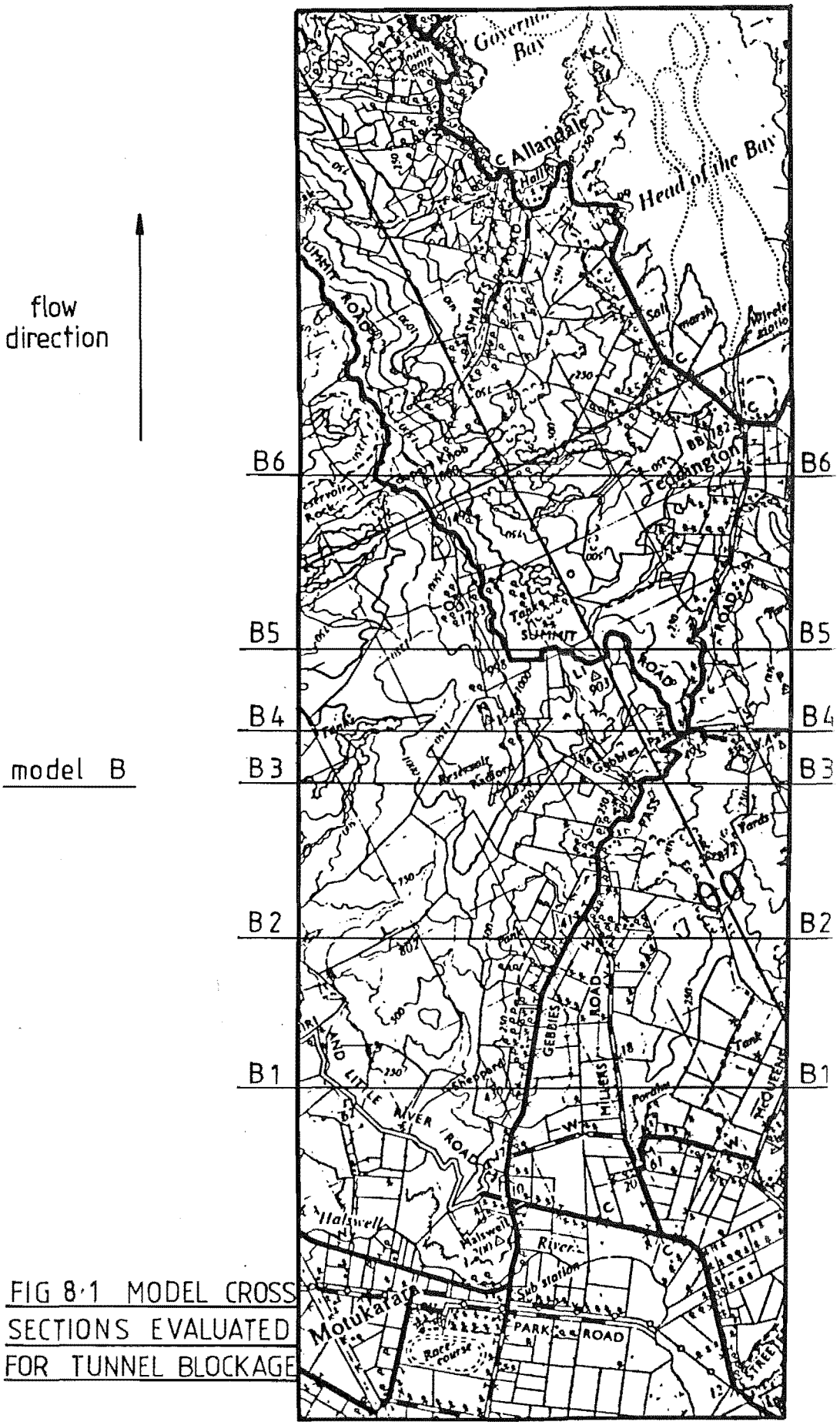

FIG 8·1 MODEL CROSS SECTIONS EVALUATED FOR TUNNEL BLOCKAGE

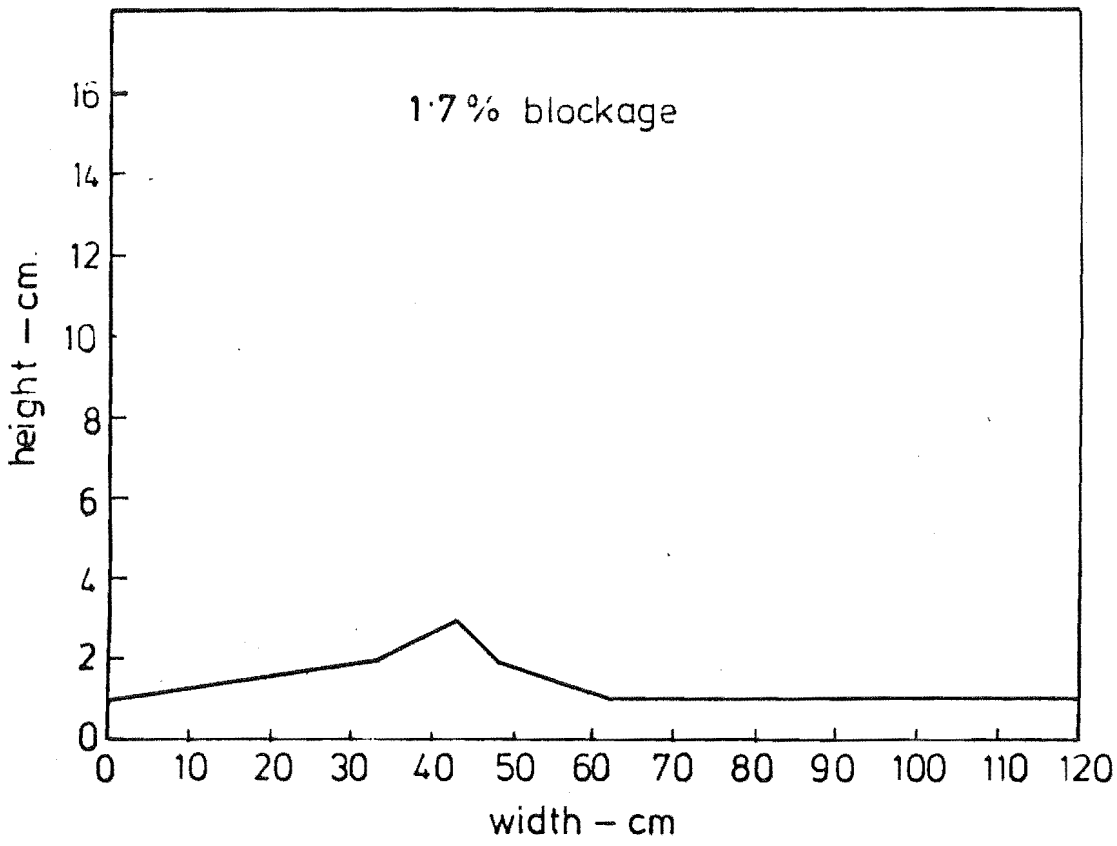

FIG 8·2 MODEL CROSS SECTION B 1

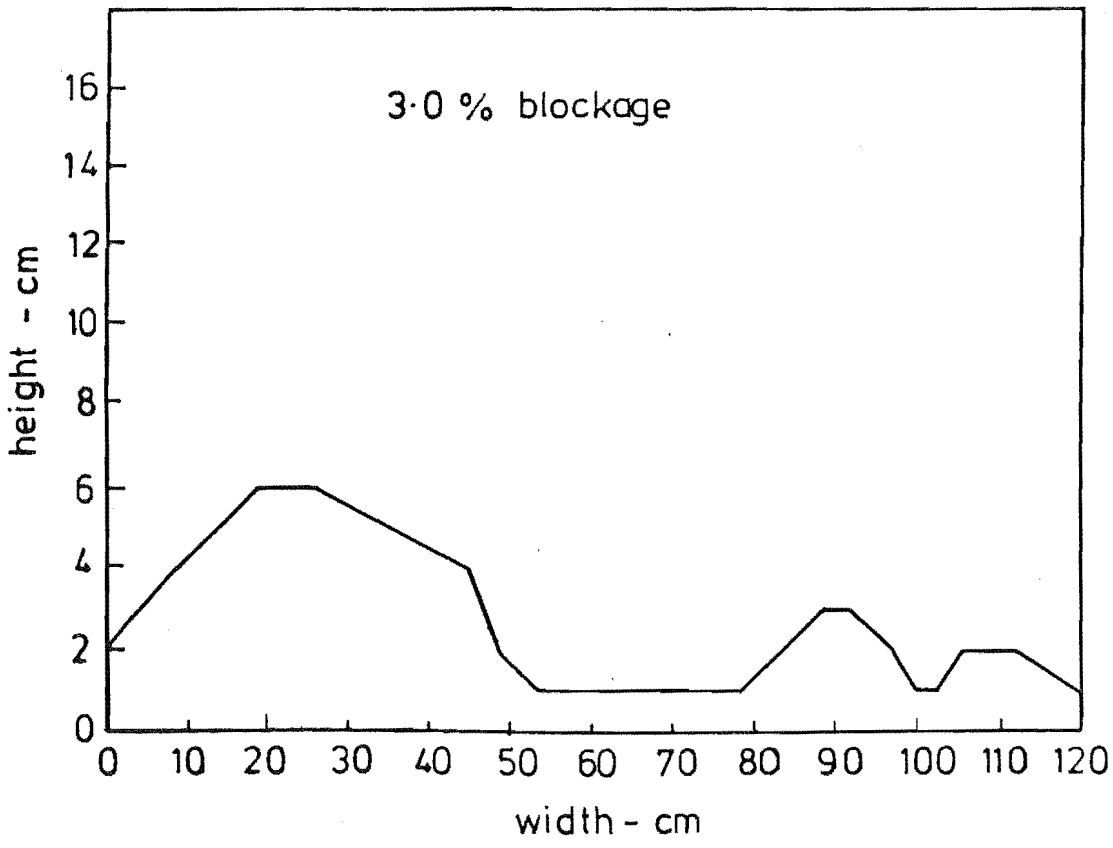

FIG 8·3 MODEL CROSS SECTION B 2

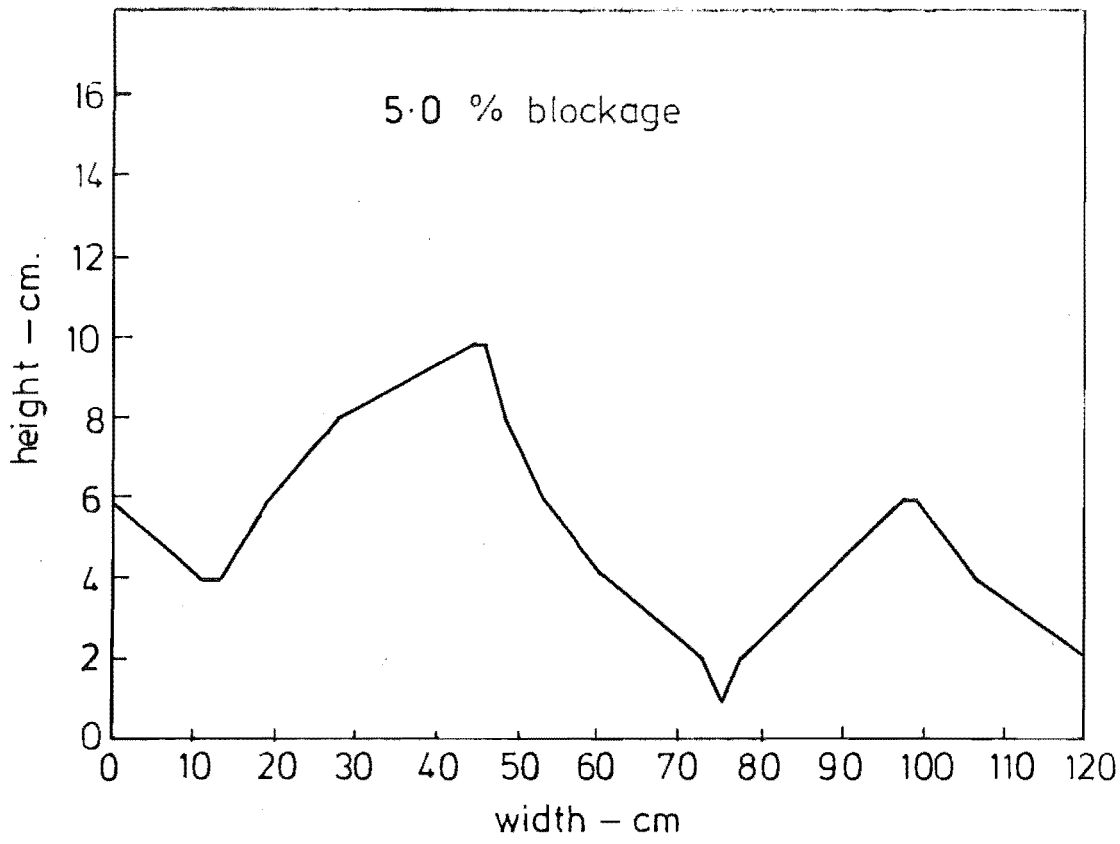

FIG 8·4 MODEL CROSS SECTION B 3

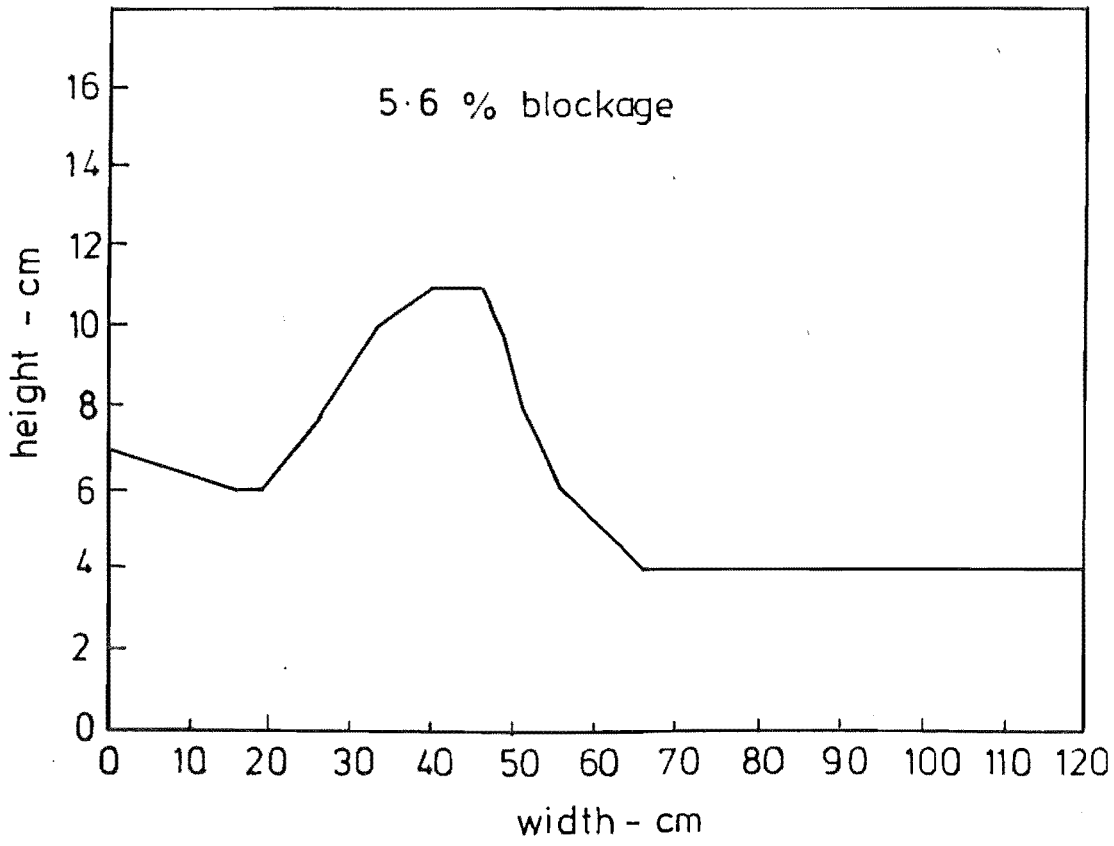

FIG 8·5 MODEL CROSS SECTION B 4

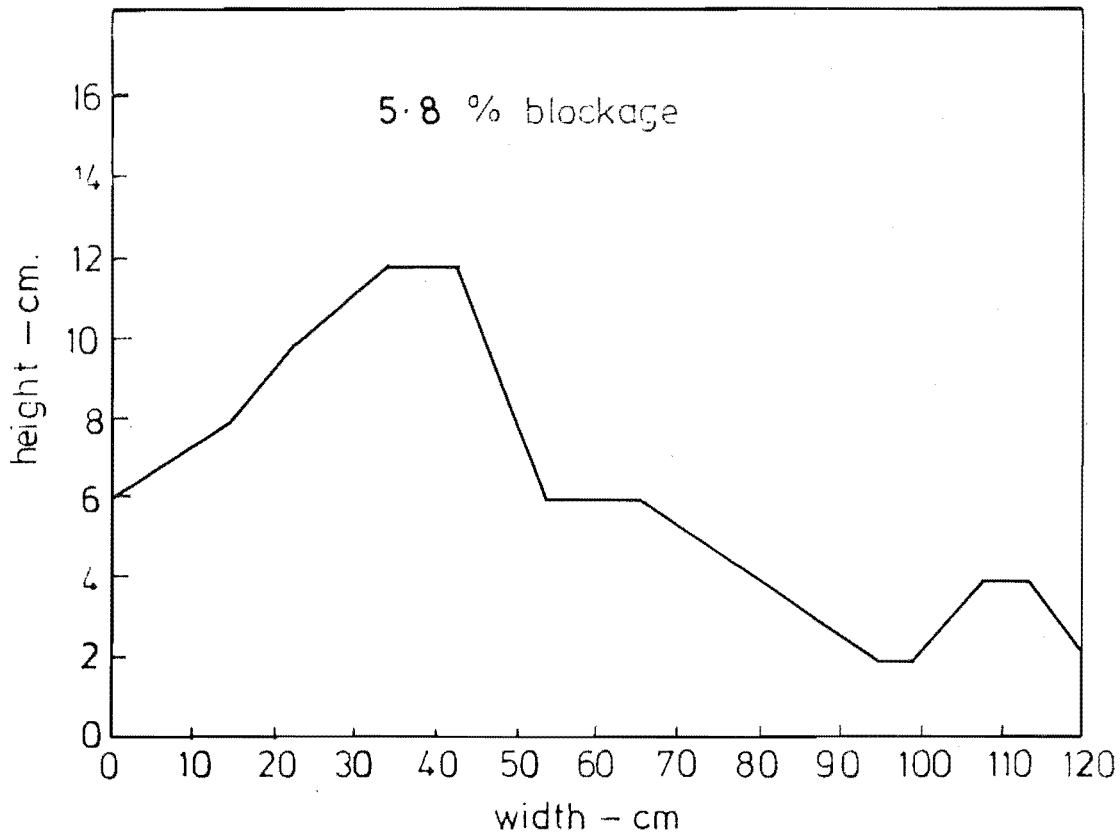

FIG 8·6 MODEL CROSS SECTION B 5

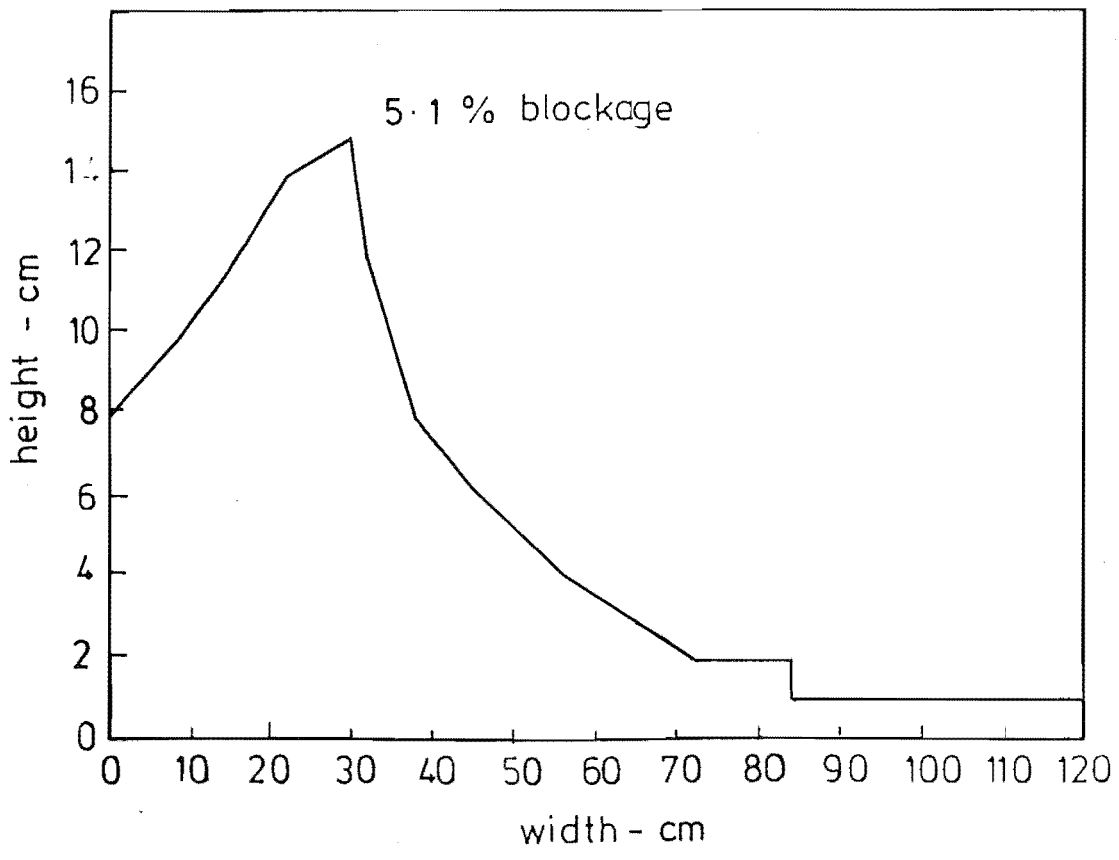

FIG 8·7 MODEL CROSS SECTION B 6

Flow approaching reader.

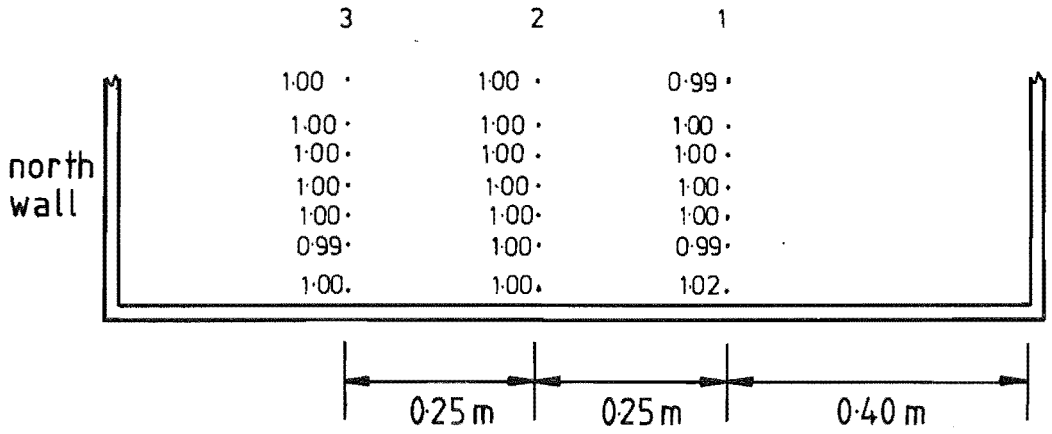

Readings normalized to profile 2

2 x Exaggerated vertical scale.

FIG 8·8 APPROACH FLOW LATERAL UNIFORMITY FOR MODEL B

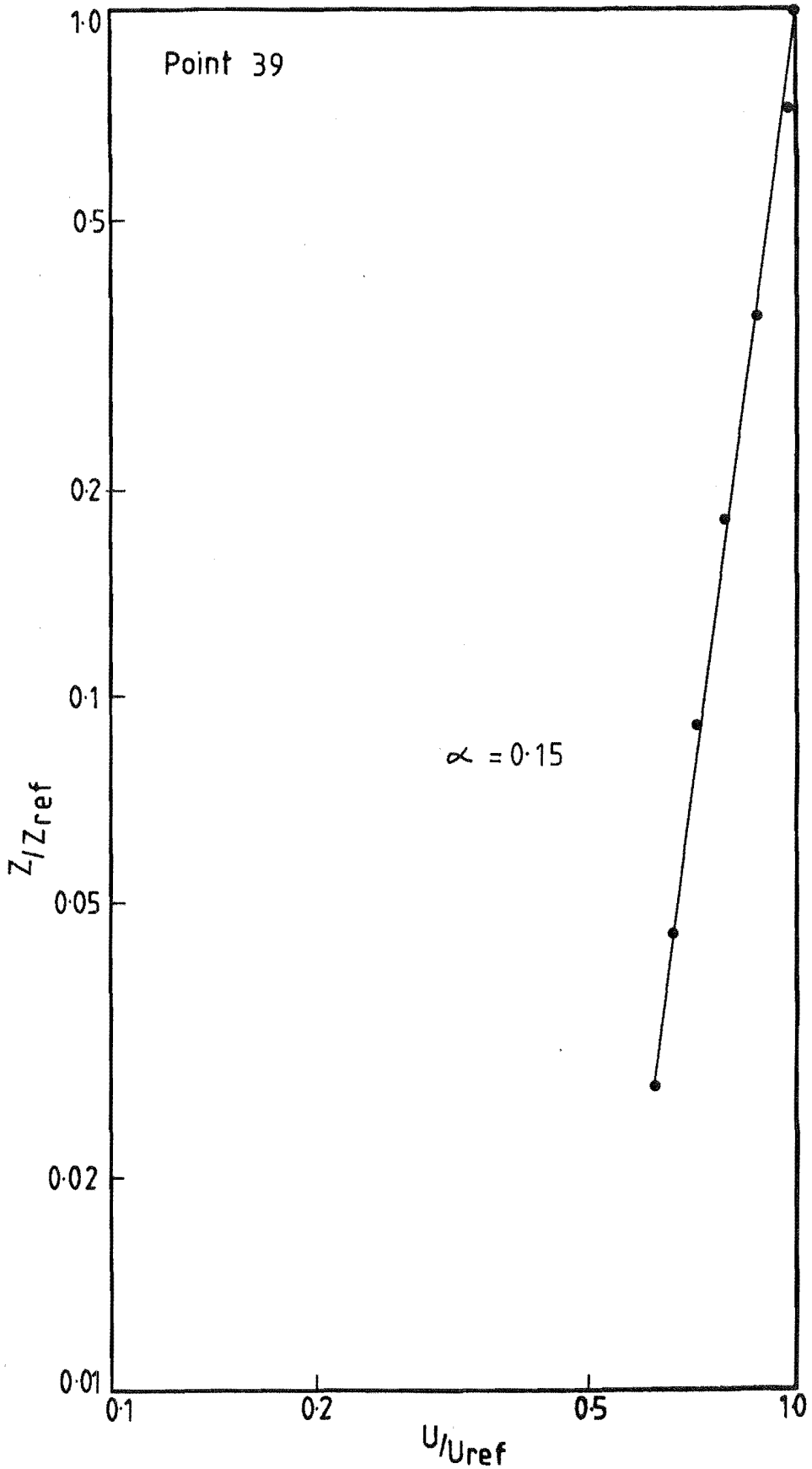

FIG 8·9 POWER LAW VELOCITY PROFILE
MODEL B TERRACED

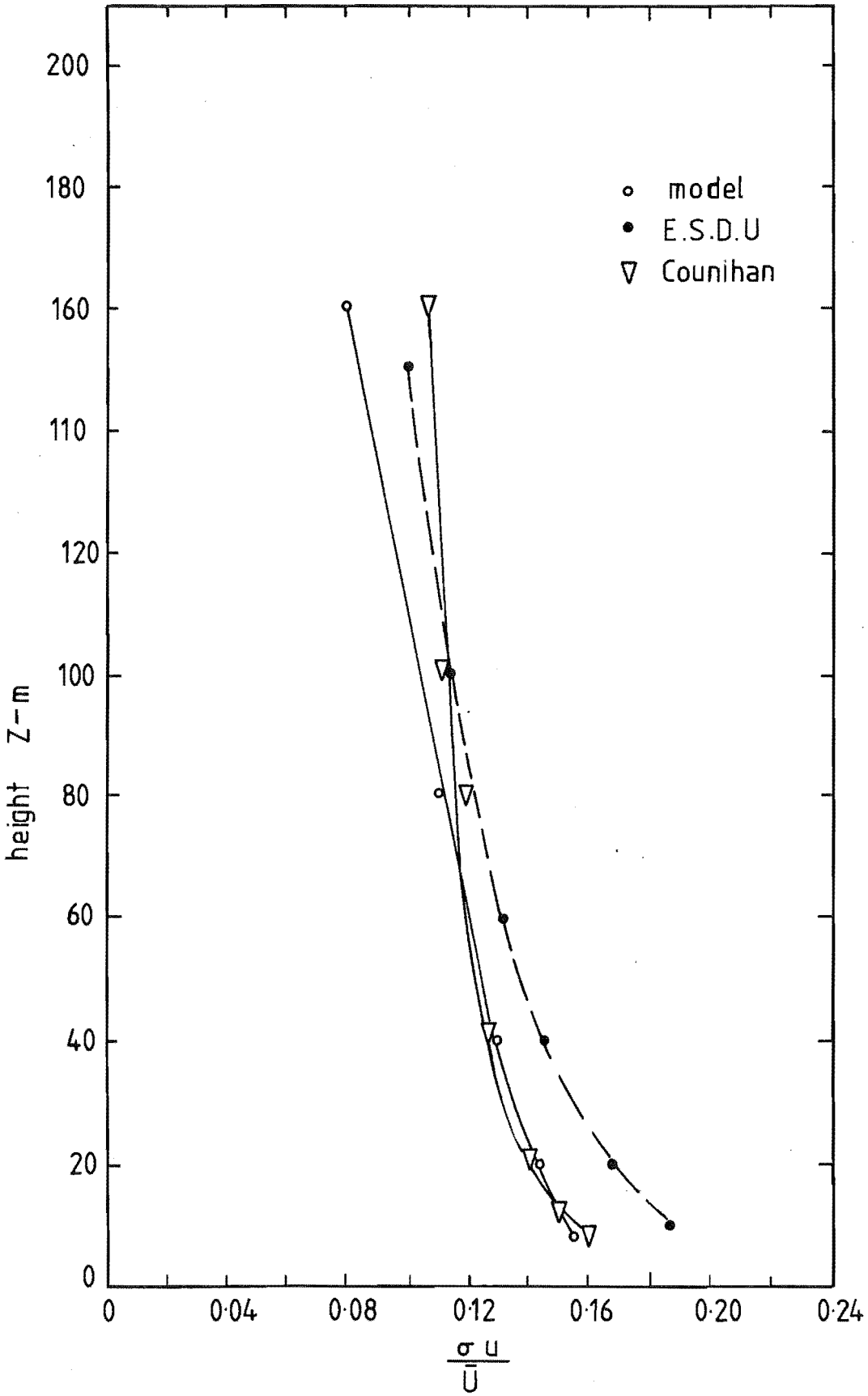

FIG 8·10 APPROACH FLOW TURBULENCE INTENSITY PROFILE MODEL B TERRACED

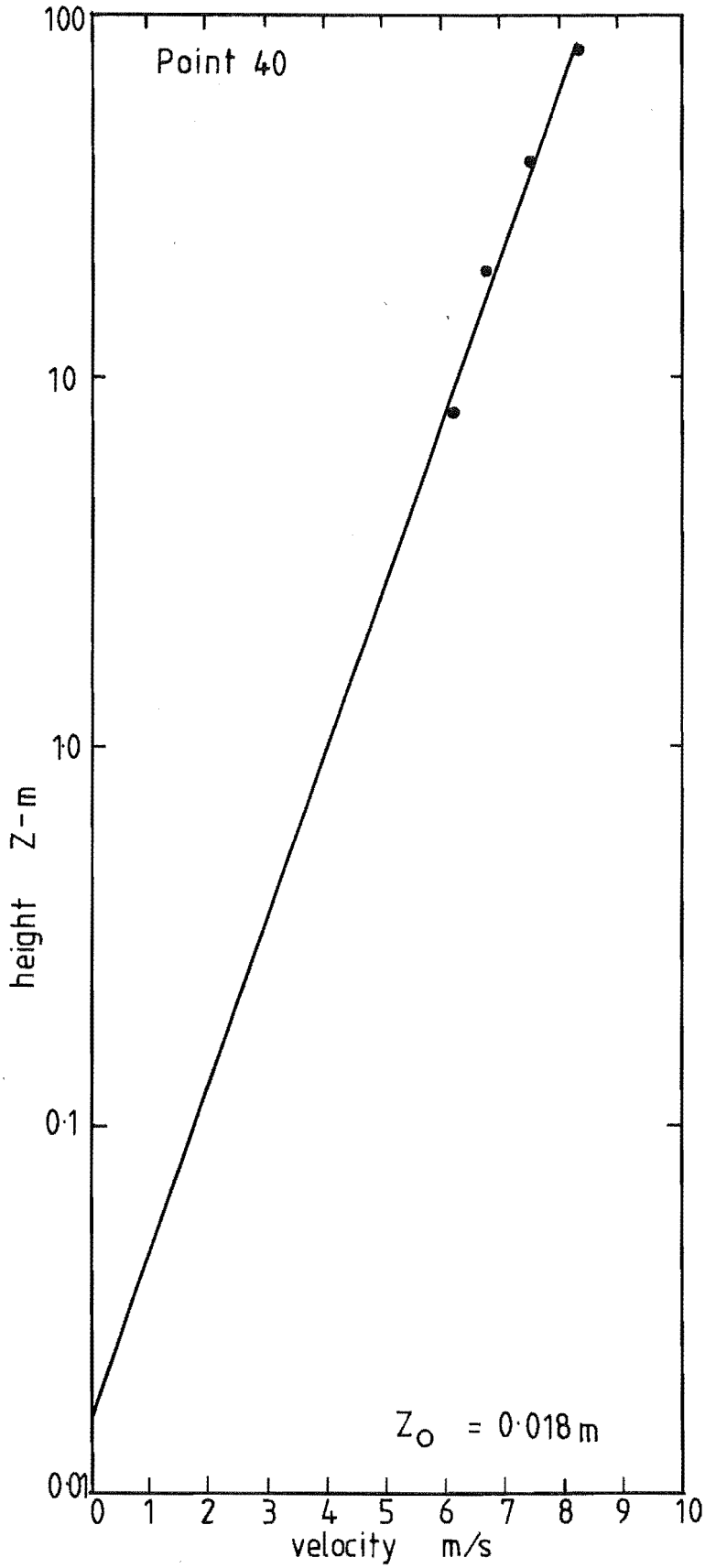

FIG 8·11 LOG LAW VELOCITY PROFILE
MODEL B, TERRACED

flow direction

model B

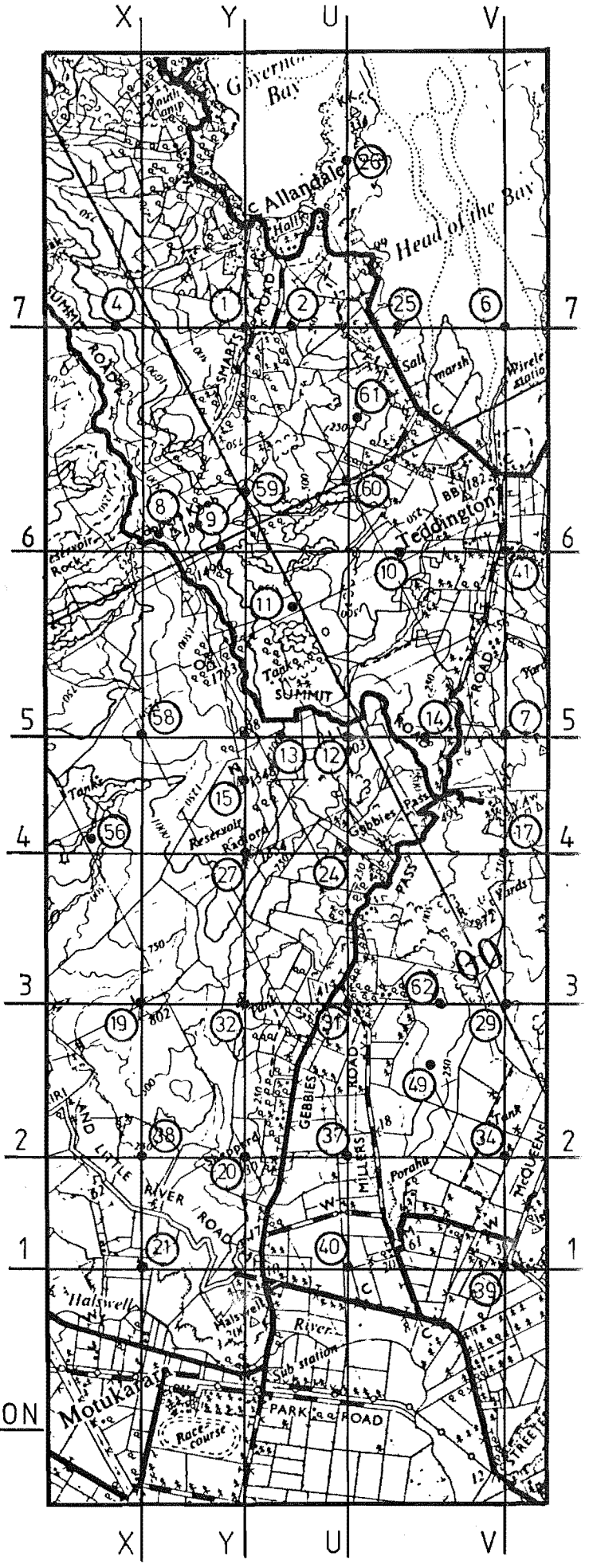

FIG 8·12 DATA COLLECTION SECTIONS AND POINTS

8.2.1 Flow Visualisation

(1) Polystyrene Beads: Polystyrene beads were placed upstream of the model. The tunnel was then run slowly until all the beads had moved on to the model. The tunnel was then run with a free stream velocity of approximately 4.0 m/s and the bead depositions recorded, the results of this test being presented in Fig. 8.13. A few of the windward valleys appeared to be sheltered; other than this, most of the beads were removed. The sizes of the deposition areas were very much smaller than those found on Model A, when the tunnel speed was increased to 5.7 m/s, free stream velocity, the deposition areas were reduced significantly, as shown in Fig. 8.14.

(2) Flags: Miniature flags, as described in Section 5.3.1, were placed on the model at most of the analysis points. With the tunnel free stream velocity set to 9.8 m/s, the flag alignments were noted. Generally, the flags were found to align themselves along the tunnel. The few points that did deviate significantly from the general trend were noted for pressure probe analysis.

8.2.2 Pressure Probe Measurements

The five hole cobra probe was used to measure the actual flow directions indicated by the flow visualisation analysis. The measurements were made at three heights, 5mm, 20mm and 40 mm. The number of points analysed did not warrant the presentation of the results on a map as for those of Model A. However, the actual readings are presented by Neal and Stevenson (1980) in tabular form. The results clearly show a high degree of flow straightening between the 5mm and 40 mm heights.

8.2.3 Hot Film Survey

The results of the hot film survey for lateral cross sections 1-7 are presented in Figs 8.15 to 8.28.

The isotachs and isoturbs for lateral cross section 1 are almost horizontal. This cross section is approximately 0.4m downstream from the start of the model but is well upstream of any of the major terrain features. The degree of lateral uniformity that exists at this cross section is comparable to the upstream isotachs and isoturbs for model A, Fig. 7.27, and Fig. 28 respectively.

The isotachs for lateral cross section 2 can be seen to follow the contours quite closely in the bottom 40mm, but undergo a smoothing as the height increases. A similar pattern is apparent in the isoturbs for this cross section.

MODEL B

Deposits at low speed

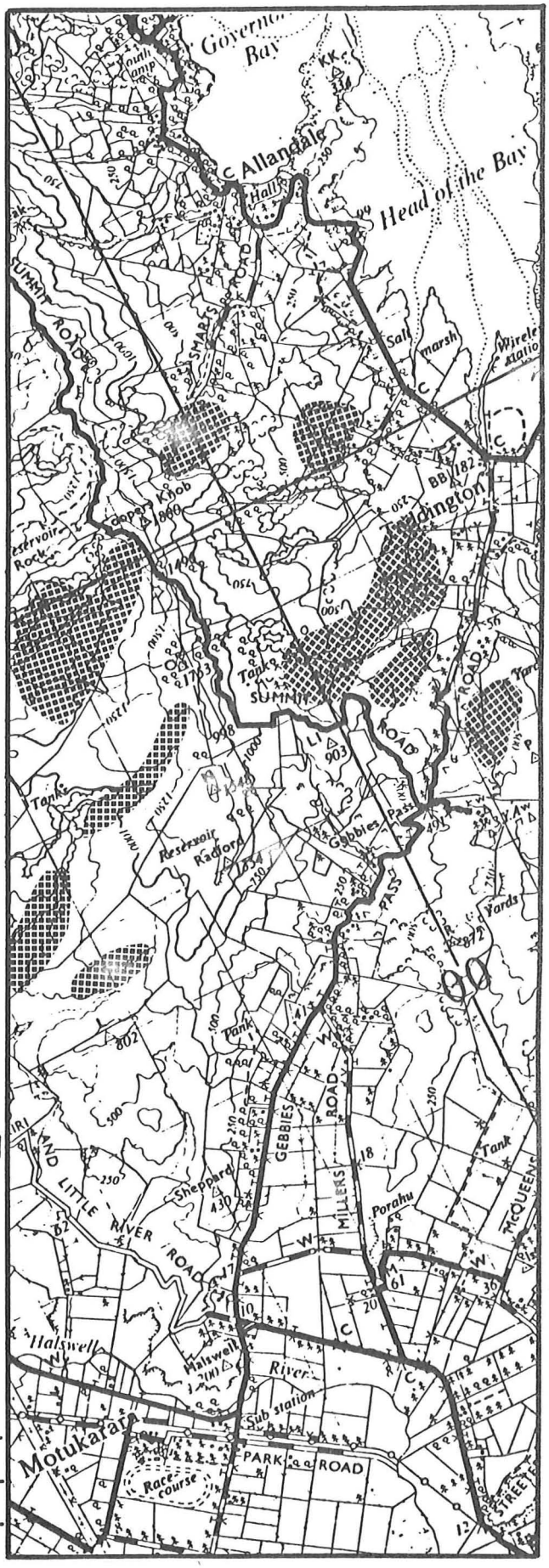

FIG 8·13 POLYSTYRENE BEAD DEPOSITION DIAGRAM, TERRACED MODEL

MODEL B

Deposits at high speed

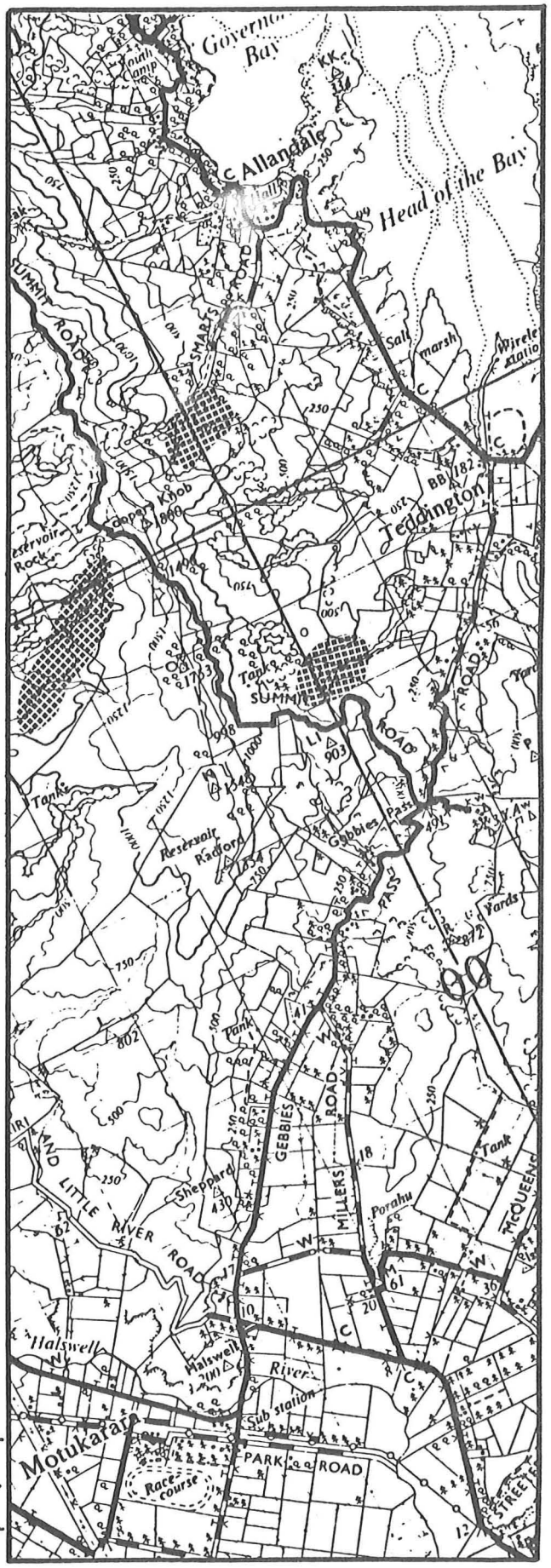

FIG 8·14 POLYSTYRENE BEAD DEPOSITION DIAGRAM TERRACED MODEL.

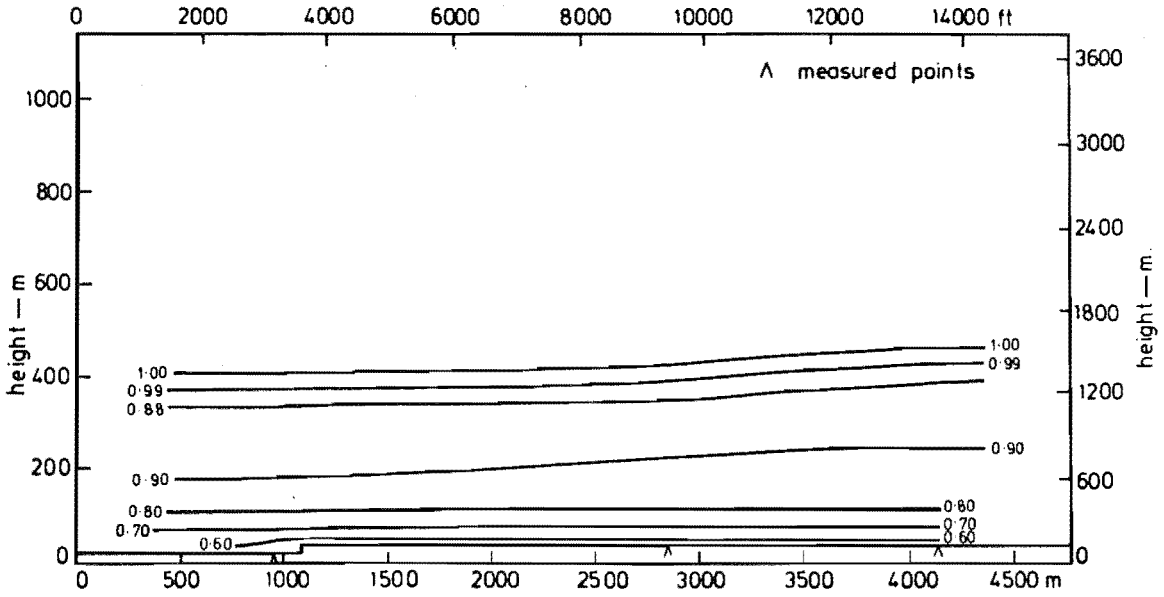

FIG 8.15 ISOTACHS FOR MODEL B TERRACED, LATERAL CROSS SECTION. 1

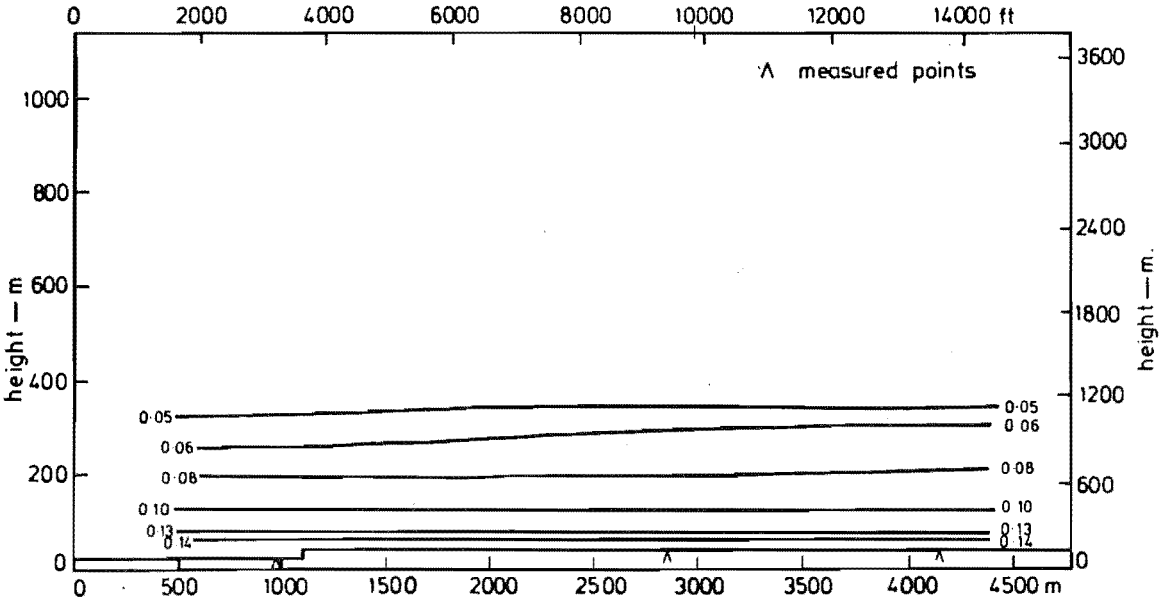

FIG 8.16 ISOTURBS FOR MODEL B TERRACED, LATERAL CROSS SECTION. 1

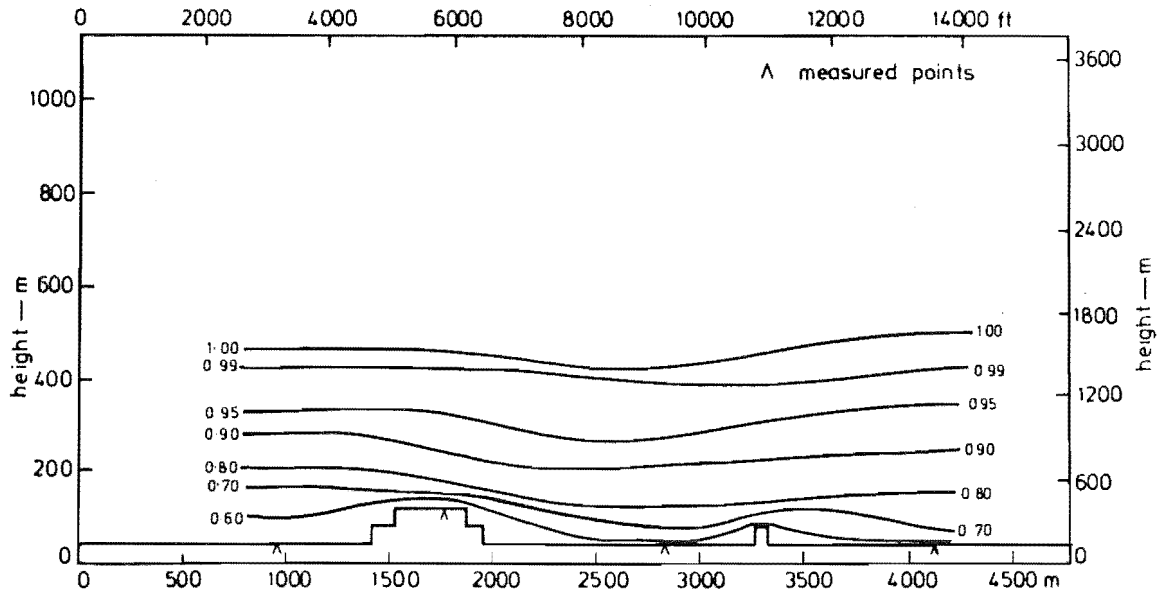

FIG 8.17 ISOTACHS FOR MODEL B TERRACED, LATERAL CROSS SECTION. 2

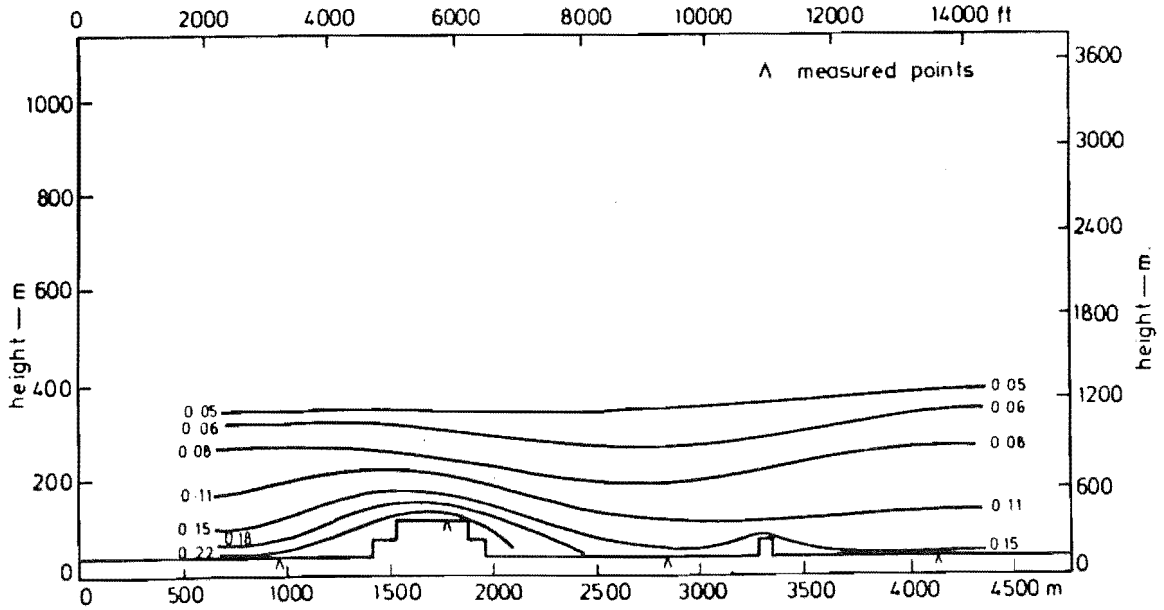

FIG 8.18 ISOTURBS FOR MODEL B TERRACED, LATERAL CROSS SECTION. 2

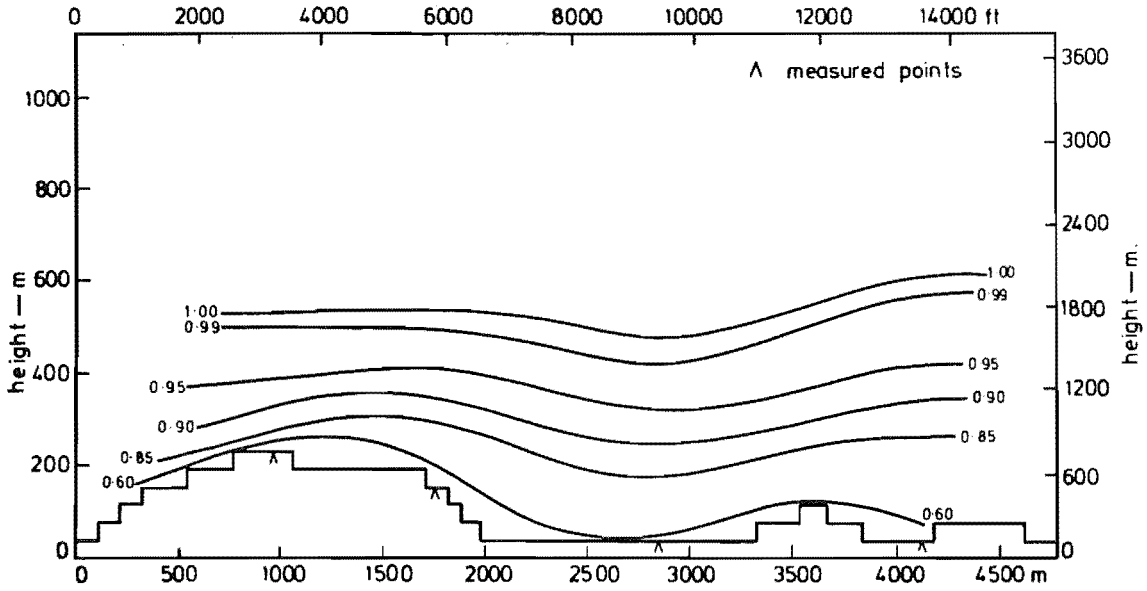

FIG 8.19 ISOTACHS FOR MODEL B TERRACED, LATERAL CROSS SECTION. 3

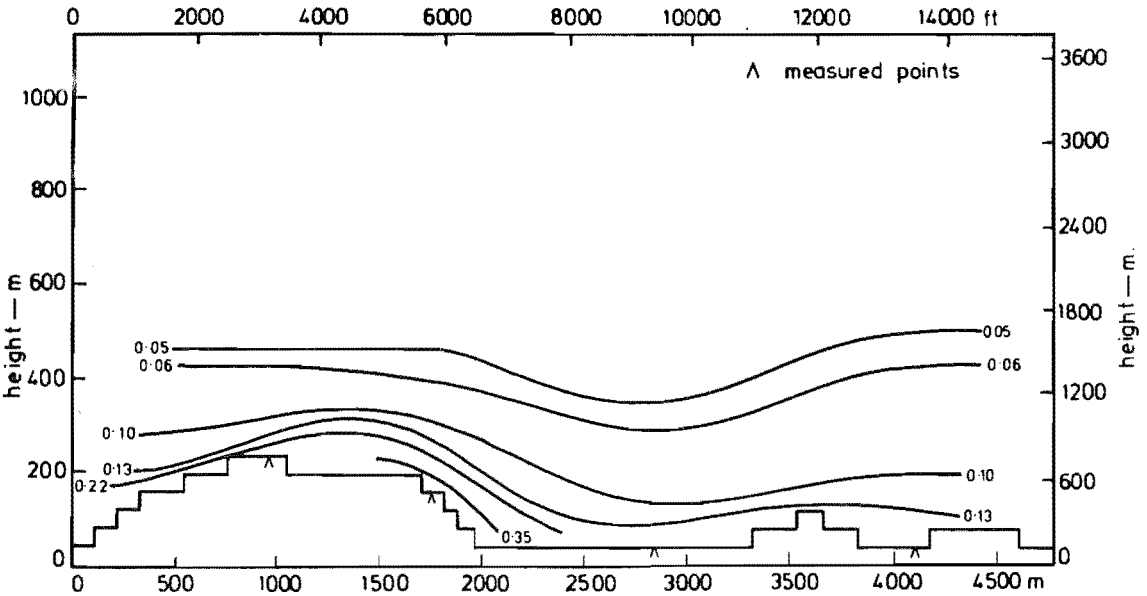

FIG 8.20 ISOTURBS FOR MODEL B TERRACED, LATERAL CROSS SECTION. 3

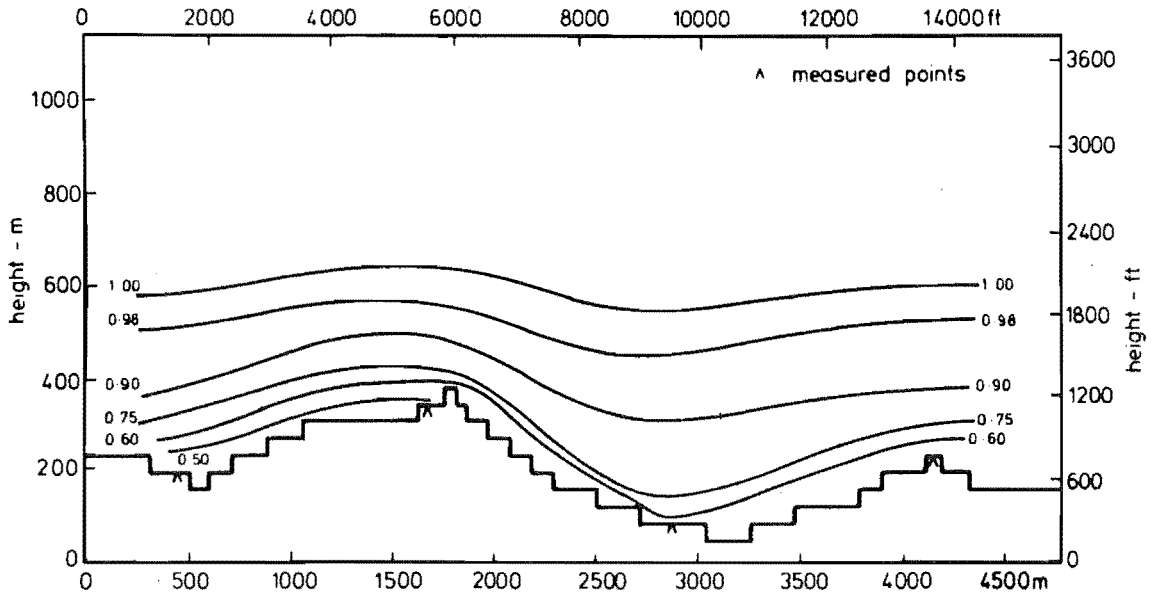

FIG 8.21 ISOTACHS FOR MODEL B TERRACED, LATERAL CROSS SECTION 4.

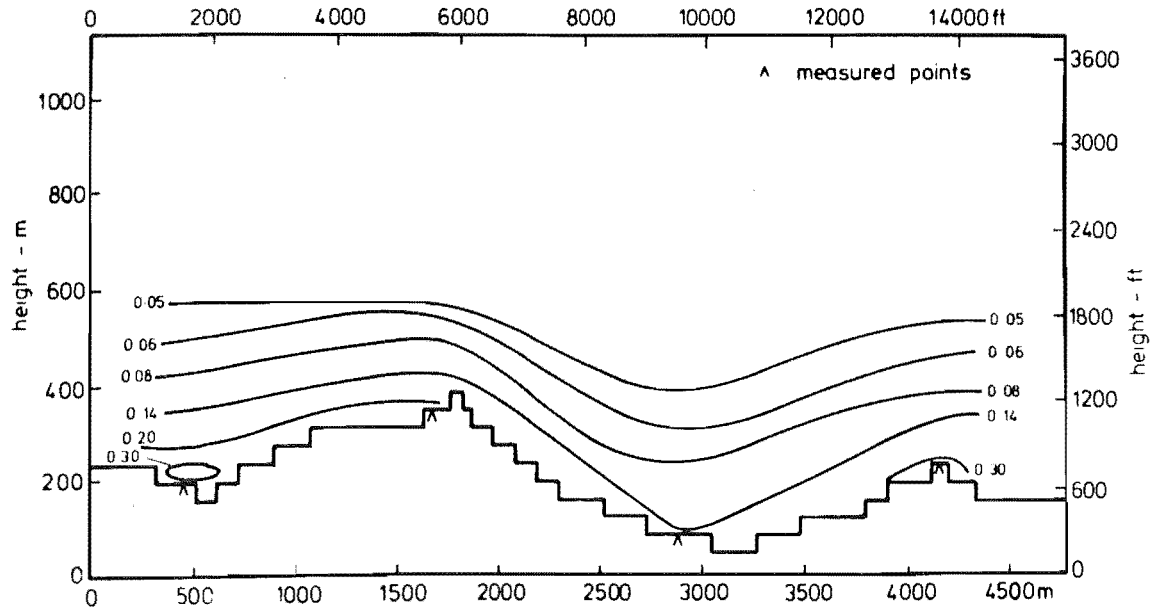

FIG 8.22 ISOTURBS FOR MODEL B TERRACED, LATERAL CROSS SECTION 4

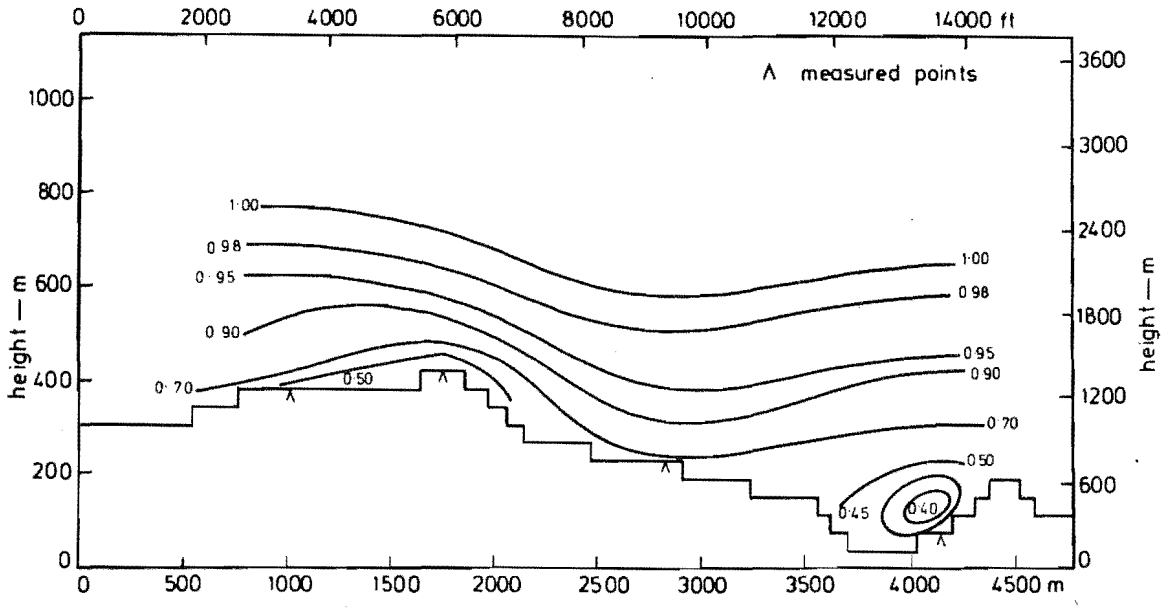

FIG 8.23 ISOTACHS FOR MODEL B TERRACED, LATERAL CROSS SECTION. 5

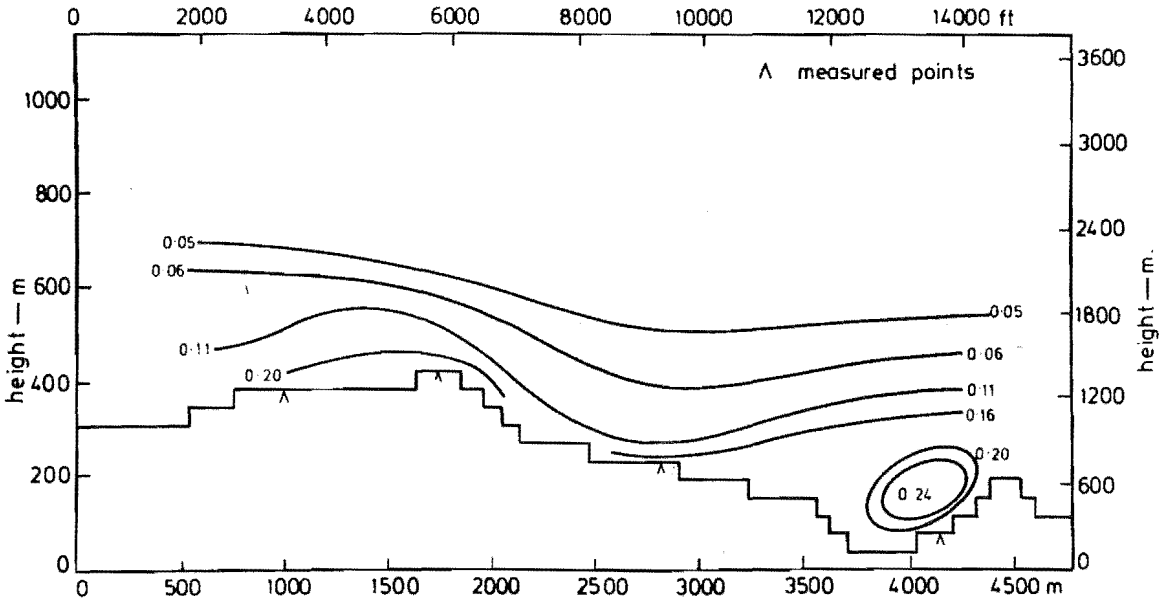

FIG 8.24 ISOTURBS FOR MODEL B TERRACED, LATERAL CROSS SECTION 5

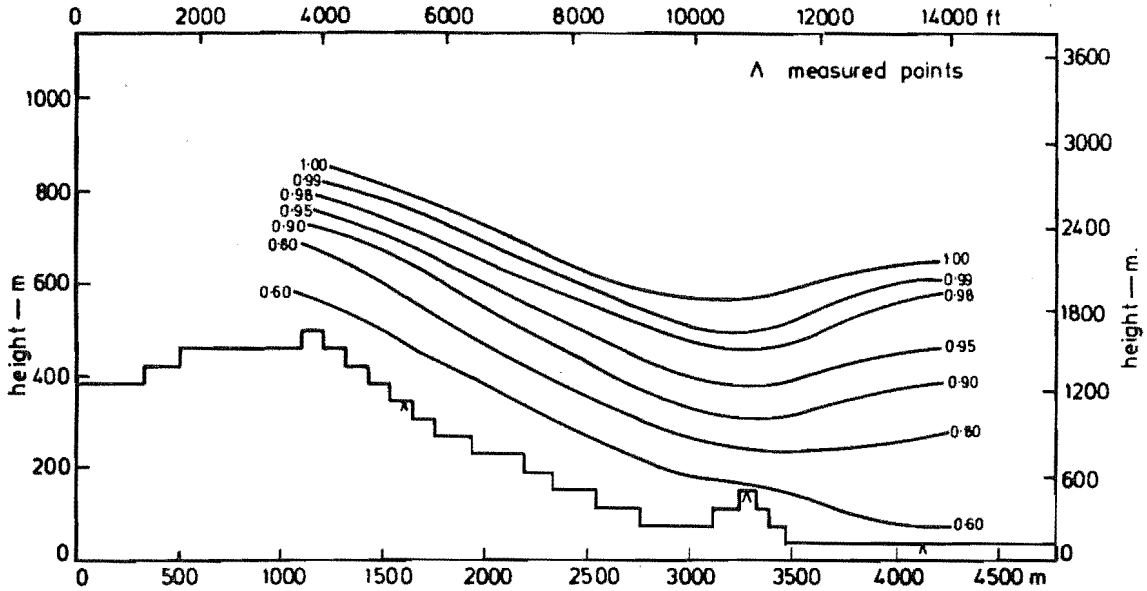

FIG 8.25 ISOTACHS FOR MODEL B TERRACED, LATERAL CROSS SECTION. 6

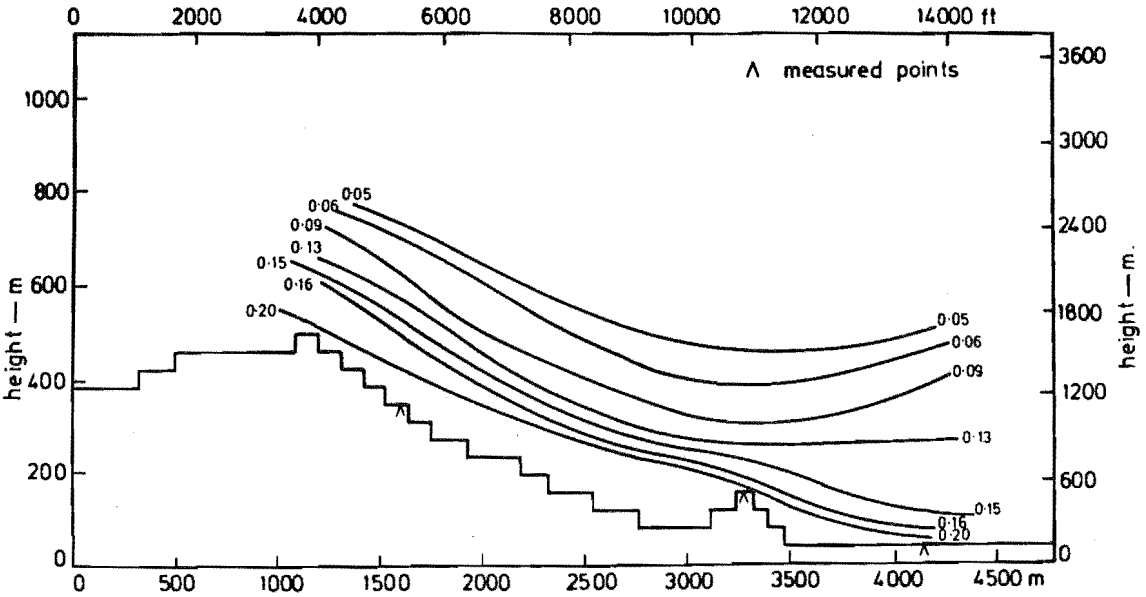

FIG 8.26 ISOTURBS FOR MODEL B TERRACED, LATERAL CROSS SECTION. 6

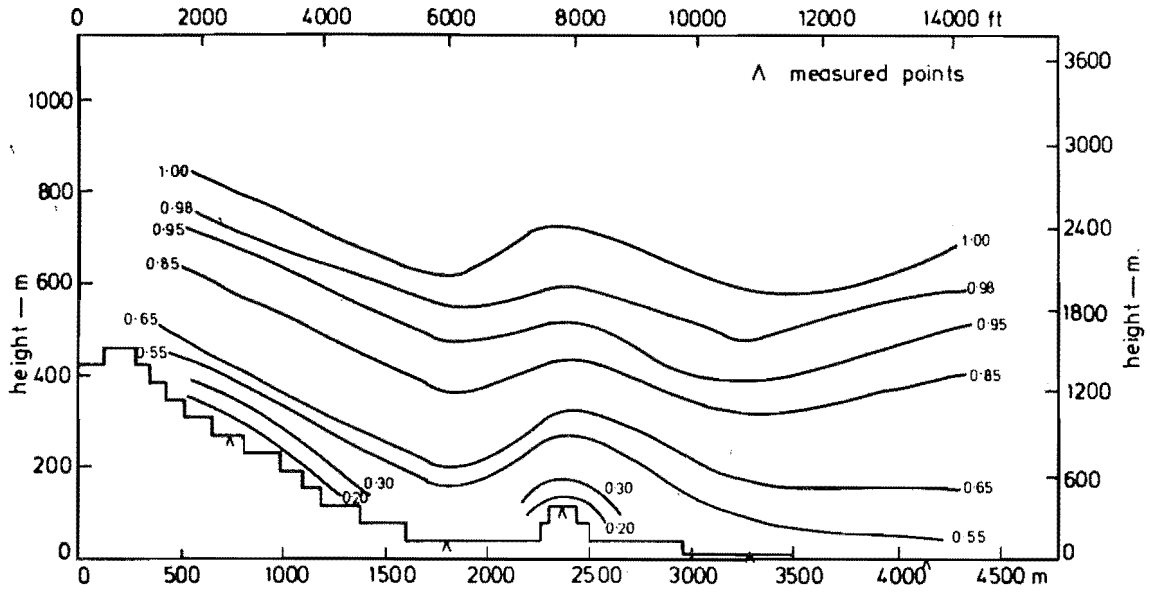

FIG 8.27 ISOTACHS FOR MODEL B TERRACED, LATERAL CROSS SECTION. 7

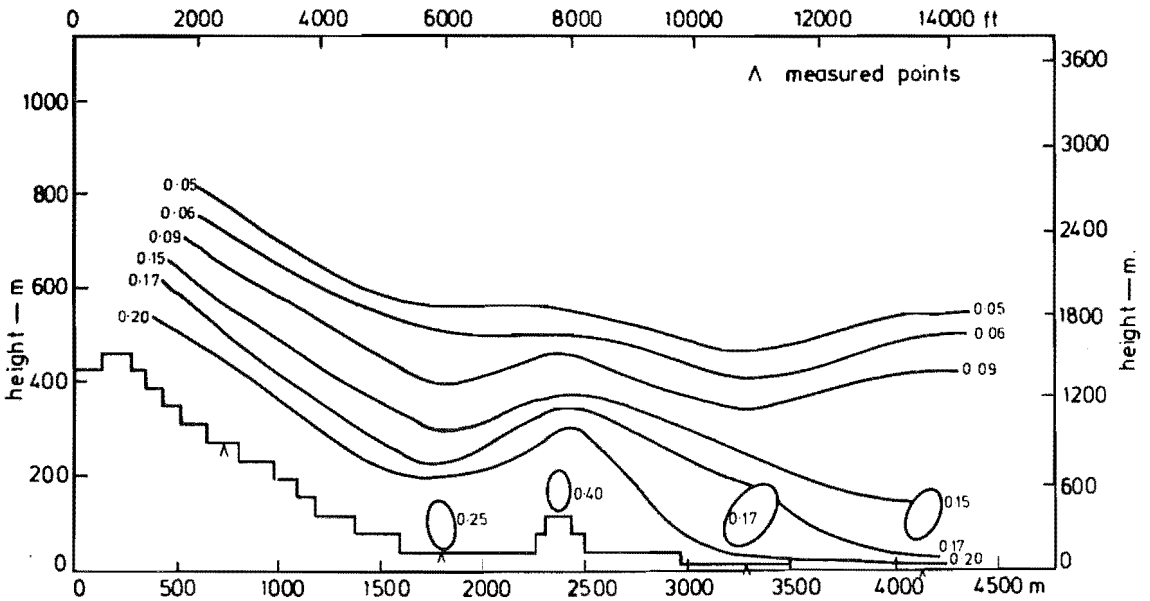

FIG 8.28 ISOTURBS FOR MODEL B TERRACED, LATERAL CROSS SECTION 7

Lateral cross section 3 shows a very similar trend with the contours close to the model surface following the terrain shape very closely. The interesting feature to note is that for all cross sections so far considered, the bottom isotach contour has remained constant at 0.6. To reach point 19, located at the 1000m point on the base scale, the flow has moved up five terraces, and yet the velocity and turbulence intensity values close to the surface have remained essentially the same as they were well upstream of this cross section.

With the exception of point 56, located at the 500m point on the base scale, which is situated in a valley, the trend pointed out for cross section 3 is maintained. The lowest isotach contour is 0.6 and it follows the terrain closely. At the gradient height, this effect has been smoothed out to a large extent; however, the general form of the terrain is visible in this contour. The isoturb contours for cross section 4 follow the terrain very closely at all heights up to the 5% contour. The highest turbulence occurs at point 56 and has a value of 30%. This point, when analysed on model A, had a turbulence contour of 0.38%. The isotach contour difference is even greater. For model A, the equivalent contour was 0.30 compared with 0.50 for model B.

Lateral cross section 6, which is on the leeward side of the Port Hills ridge, maintains the trend of the contours following the terrain closely. The results of the lateral cross sections suggest that the flow over the terraced model at the lower heights, $Z < 40mm$, is not affected by the terracing nor the general terrain and has, in fact, stayed fairly close to the inflow condition. However, there could be two actions working against each other - the terrain could be causing the flow to speed up but the terracing nullifying this effect. If this is the case, the contoured model should show an appreciable speed-up of the flow.

Lateral cross section 7 is well downstream of the Port Hills ridge and consequently shows areas of low velocity and high turbulence. In particula point 2, located at the 2300m point on the base scale, has a velocity contour of 0.2 and a turbulence intensity of 40% in the bottom 20mm of the boundary layer. The longitudinal cross sections are presented in Figs 8.29 to 8.36.

Little can be said about longitudinal cross sections XX, YY and UU, these clearly reflecting the results of the lateral cross sections. The flow appears to have passed over the terraces and general terrain features with a minimum of disturbance to the contours.

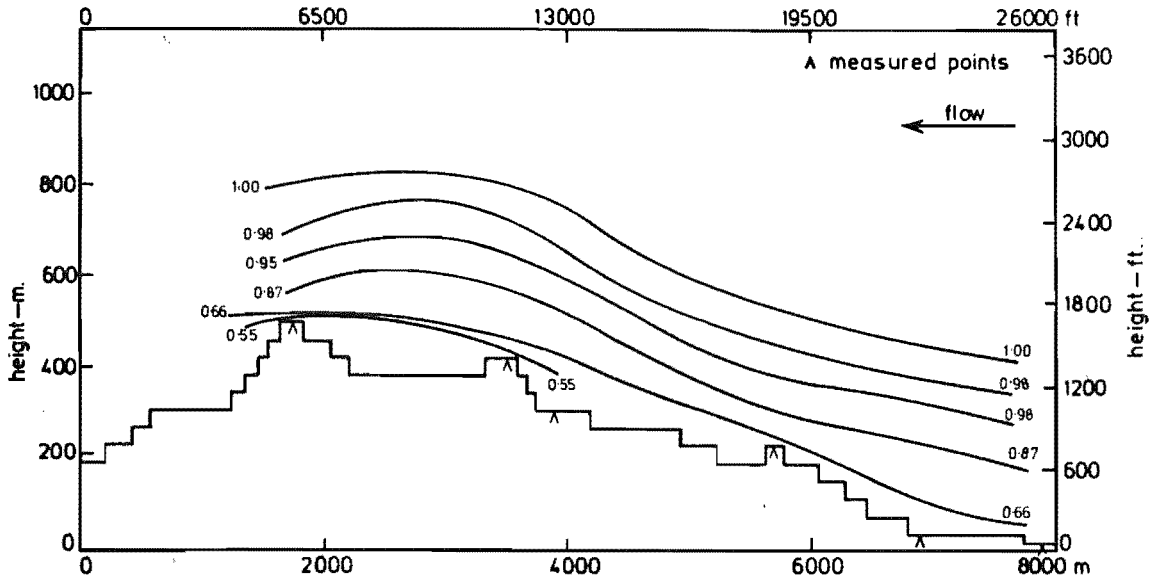

FIG 8.29 ISOTACHS FOR MODEL B TERRACED, LONGITUDINAL CROSS SECTION XX

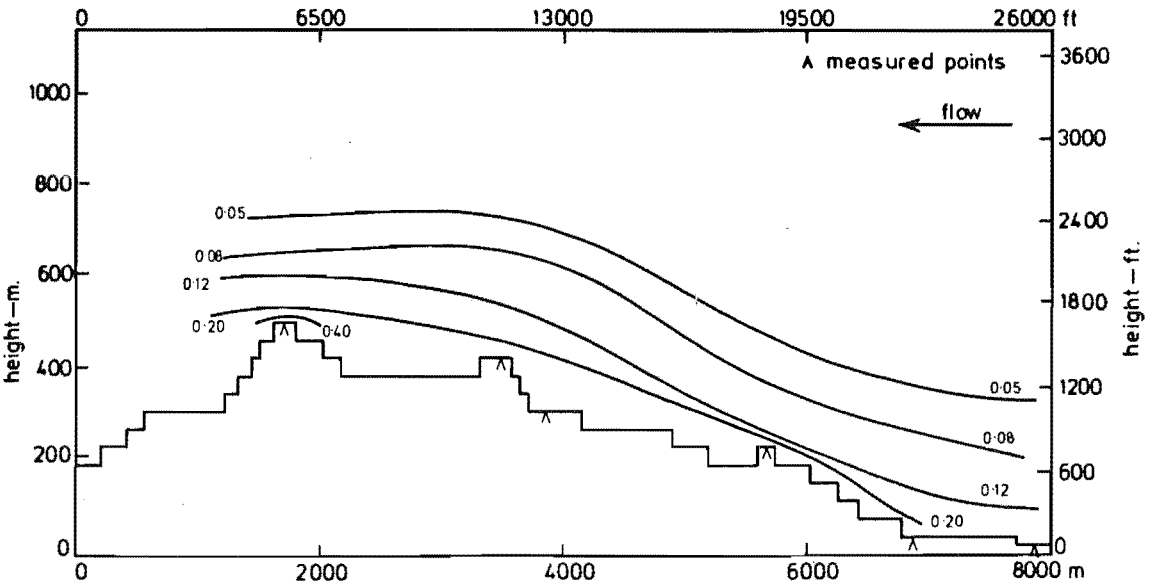

FIG 8.30 ISOTURBS FOR MODEL B TERRACED, LONGITUDINAL CROSS SECTION XX

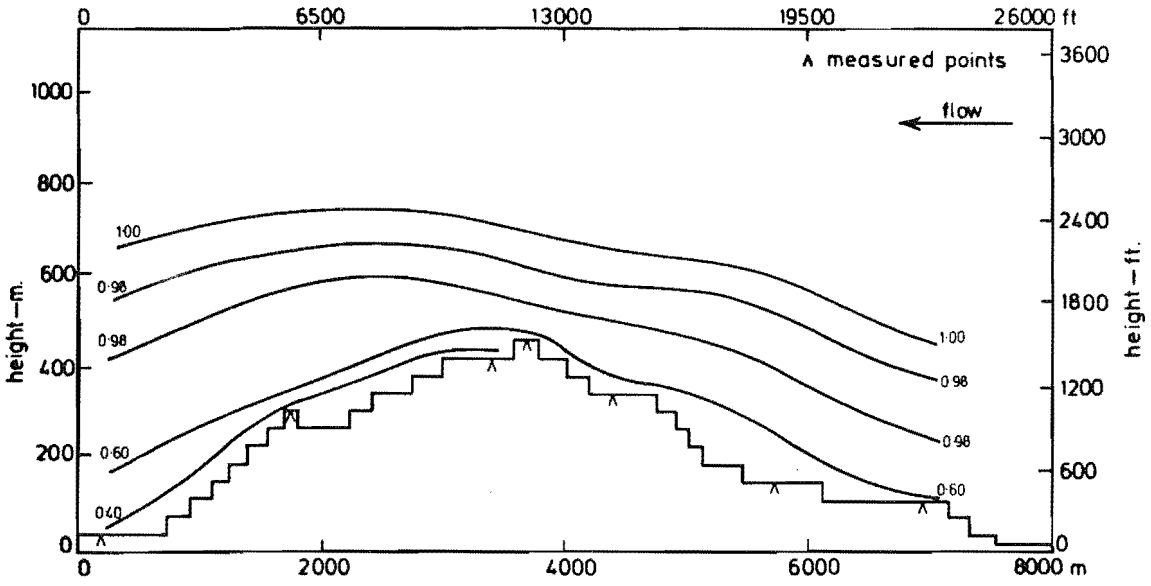

FIG 8.31 ISOTACHS FOR MODEL B TERRACED, LONGITUDINAL CROSS SECTION YY

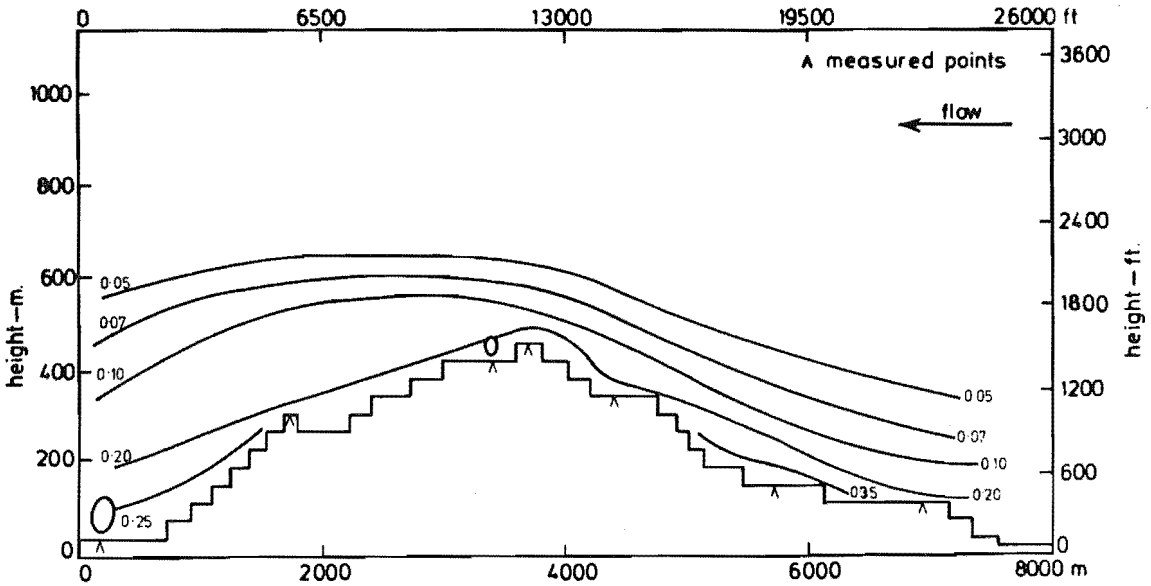

FIG8.32 ISOTURBS FOR MODEL B TERRACED, LONGITUDINAL CROSS SECTION YY

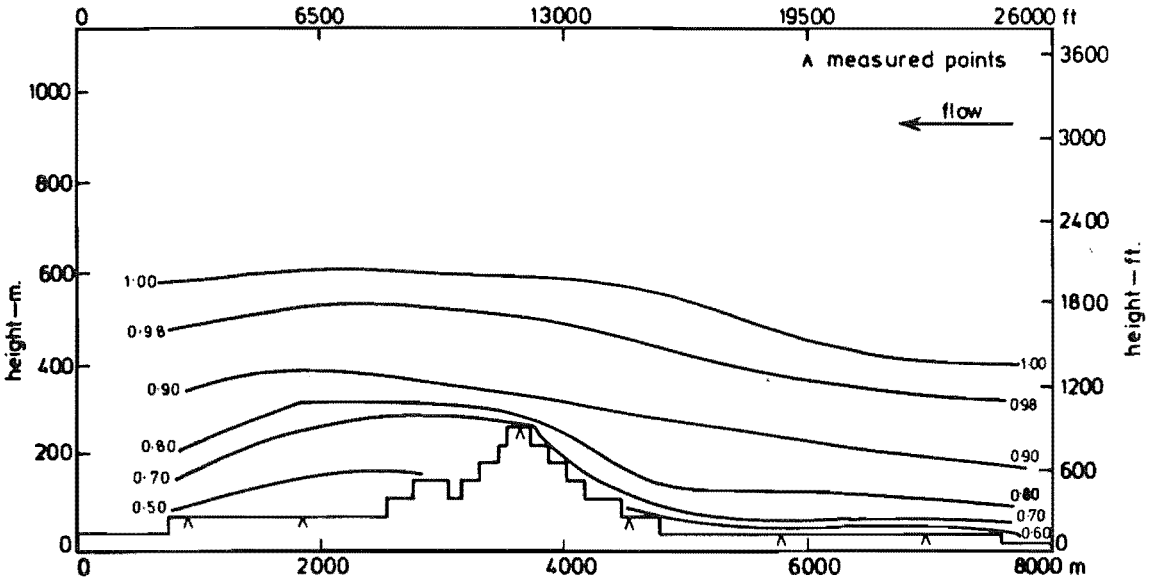

FIG 8.33 ISOTACHS FOR MODEL B TERRACED, LONGITUDINAL CROSS SECTION UU

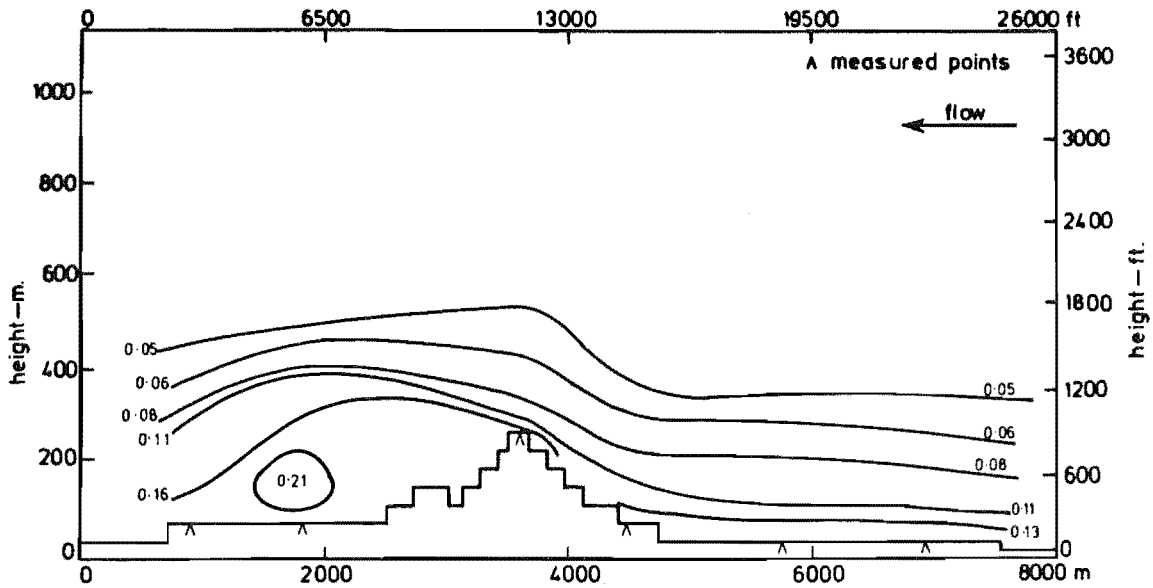

FIG 8.34 ISOTURBS FOR MODEL B TERRACED, LONGITUDINAL CROSS SECTION UU

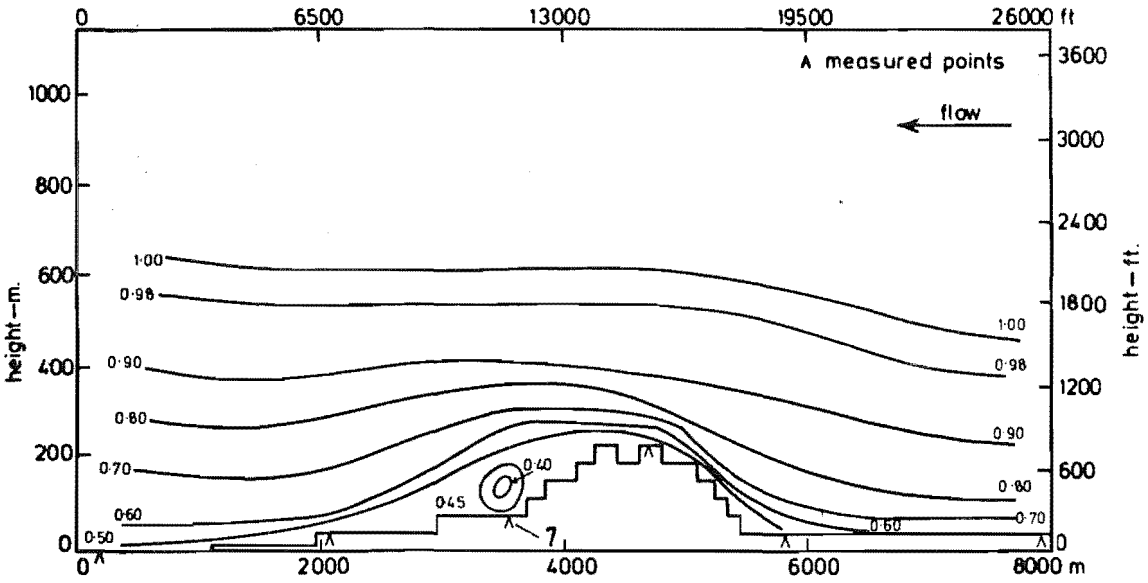

FIG 8.35 ISOTACHS FOR MODEL B TERRACED, LONGITUDINAL CROSS SECTION VV

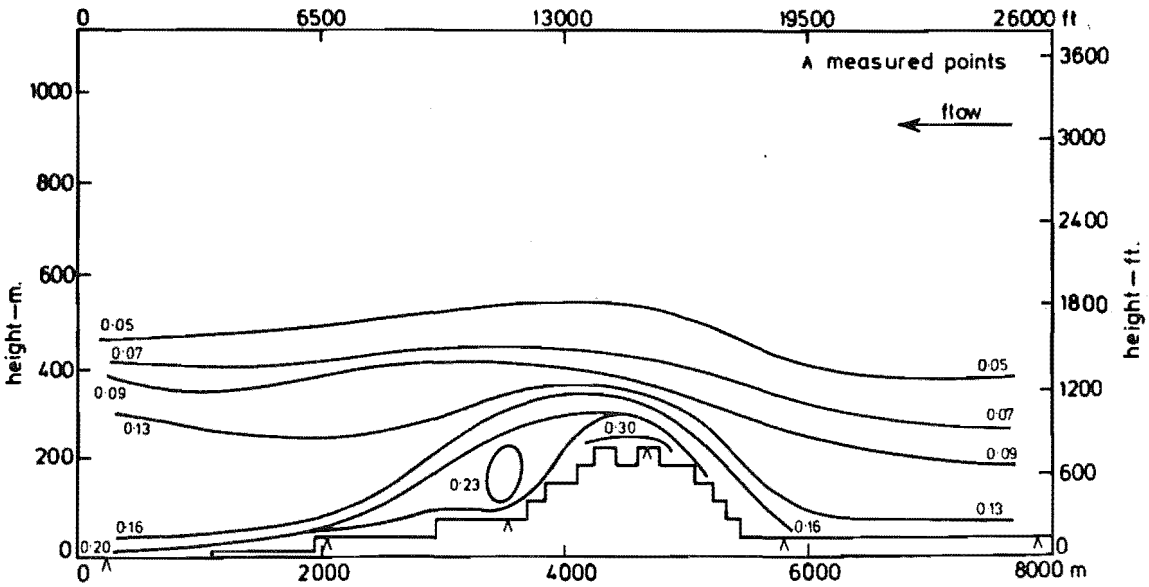

FIG 8.36 ISOTURBS FOR MODEL B TERRACED, LONGITUDINAL CROSS SECTION VV

However, longitudinal cross section VV does show one particular feature. At point 7, indicated on cross section, Fig. 8.36, a region of low velocity and high turbulence was recorded. This could be caused by several factors, two of which are:

1) Separation from the small hill immediately upstream of this point.
2) The influence of the flow direction change at a point close to point 7.

The region where the road passes over the Gebbies Pass saddle is located at the road junction close to points 7 and 17 on the map in Fig. 8.12. The flow was noted during the flow visualisation tests to be passing over this point at an angle veering towards point 7 from the road junction.

Cross sections XX and VV must be viewed with caution due to the proximity of the tunnel walls. Cross section XX is approximately 0.45m from the tunnel side wall and section VV only 0.2m from the opposite side wall. This point should be considered when analysing these cross sections.

The speed-up ratio areas for the terraced model are presented in Fig. 8.37. The interesting feature which is very clearly shown in this Figure is the uniformity of the flow over the model. This point was alluded to during the analysis of the lateral cross sections but is summed up concisely in the speed-up ratio area diagrams. The small speed increases which have occurred are confined to the most pronounced knobs on the model. The speed-up at these points does not exceed 120%, remembering that a 100% speed-up means that the velocity is the same as at the reference point.

The results for model B terraced, suggest that the slight change of flow direction, SW for model A and SSW for model B, has caused significant changes in the flow regime over the general terrain features; however, this could be accentuated by the terraced form of construction which was seen to be significant on model A.

8.3 MODEL B CONTOURED

The model terraces were filled in with Polyfiller, as described in Section 5.2.4. The model was then set up in the wind tunnel and the approach flow characteristics checked.

8.3.1 Approach Flow Characteristics

Velocity profile measurements at points 40 and 39 showed that the power law index α remained at 0.15, the same as that measured for the

Terraced Model

Z = 10mm

Zp = 40m

$$\frac{\left.\frac{\bar{U}_{10}}{\bar{U}_{\delta}}\right|_{pt}}{\left.\frac{\bar{U}_{10}}{\bar{U}_{\delta}}\right|_{ref\ pt}} \times 100$$

141 – 150

121 – 140

101 – 120

81 – 100

71 – 80

61 – 70

0 – 60

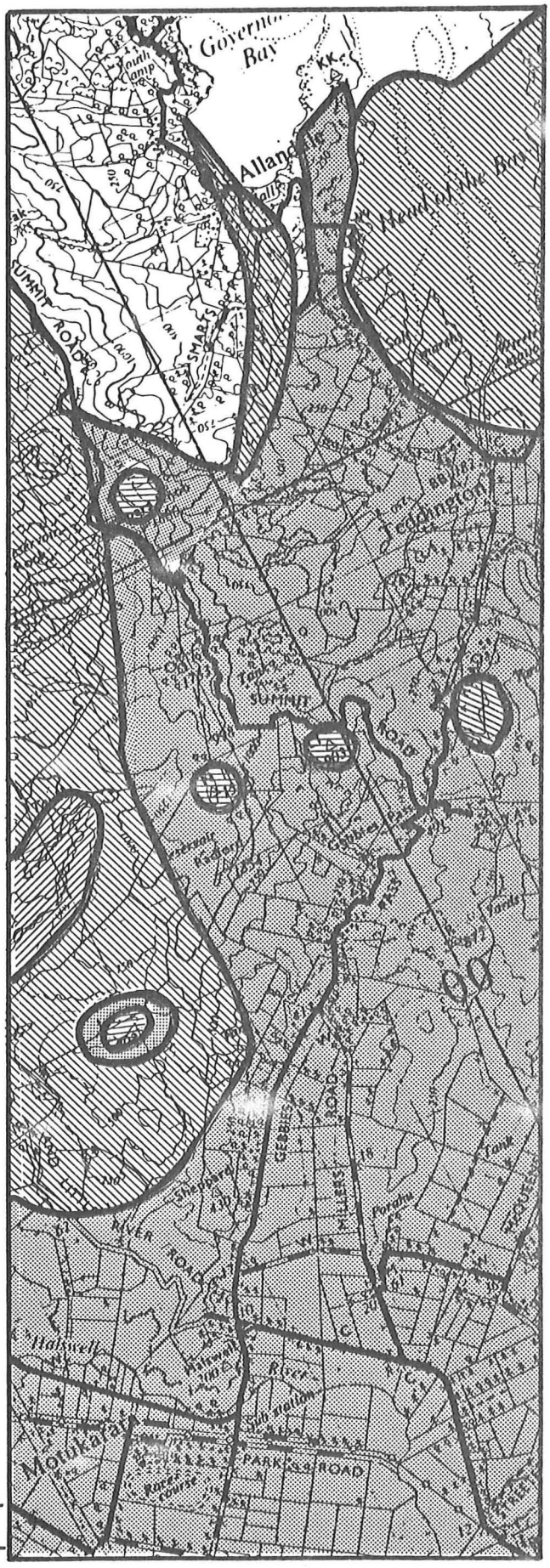

FIG 8·37 SPEED-UP RATIO AREAS FOR MODEL B, TERRACED, Zp = 40m

terraced model and previously for model A.

Longitudinal pressure gradient tests showed that a very small variation, less than 1.0%, existed over the model.

Lateral uniformity tests showed a variation which was very close to that for the terraced model. Other parameters checked were the roughness length and turbulence intensity profile; these also confirmed that the approach flow conditions had been reproduced.

8.3.2 Flow Visualisation

(1) Polystyrene Beads: The polystyrene bead flow visualisation tests were carried out initially with a tunnel free stream velocity of 4.0 m/s. A small pocket of beads deposited behind point 59, see the map in Fig. 8.12. Several other hills and knobs had small deposits on their leeward side. However, the results were not considered significant enough to present in the form of a deposition diagram. When the tunnel speed was increased to a free stream velocity of 5.7 m/s, all the beads were quickly removed from the model. This had not been the case when the model was in the terraced form. The tendency for the sheltered areas to decrease when the model is contoured was also noted for model A.

(2) Flags: The miniature flags were seen to generally align themselvers with the tunnel, the exception to this being the flag in the Pass itself. This point is not numbered but is at the junction of the roads on the Gebbies Pass saddle between points 7 and 17 on Fig. 8.12. The flow at this point deviated from the direction along the tunnel by approximately 20°. This feature was also noted for this model in the terraced form of construction. The other points to have significant flow directional change were point 56 (which aligned with the valley in which it is situated), and point 4 (which aligned itself with the Port Hills ridge in a similar manner to that observed with the model terraced).

Several of the flags indicated turbulence by their fluttering at points 19, 8, 1, 58, 2, 10 and 12, as given in Fig. 8.12.

8.3.3 Pressure Probe Measurements

After consideration of the flow visualisation results, it was decided that the pressure probe flow direction tests would be superfluous. Only two points beingused for analysis were affected and for these, the angles measured over the terraced model were used.

8.3.4 Hot Film Survey

The results of the hot film survey for lateral cross sections 1-7 are presented as isotachs and isoturbs in Figs 8.38 to 8.51 These cross-sections will be discussed and compared with the results for the terraced model.

At cross section 1, the isotach and isoturb contours show a high degree of lateral uniformity and are almost identical to those for the terraced model. The isotachs for cross section 2 suggest higher velocities in the bottom 10mm of the boundary layer than were recorded on the terraced model. Only point 38, located at the 1000m position in the base scale, differs from this as it remains the same as for the terraced model. The isoturb contours show that the higher velocity areas have corresponding turbulence intensity reductions. The contours generally follow the terrain but to a lesser degree than indicated on the terraced model.

The isotach contours for cross section 3 suggest a slight increase in velocity in the bottom 10mm of the boundary layer. There appears to be a smoothed region at the 0.90 to 0.95 contour heights. The flow above this height has a wavey form which is out of phase with the results from the terraced model. This effect cannot be readily explained at this point. Isoturb contours show a slight reduction in magnitude close to the model surface, but the general shape is similar to the terraced contours.

Cross section 4 isotachs and isoturbs follow the pattern of cross sections 2 and 3. Cross section 5 is situated along the actual saddle. This could be unclear from the terrain cross section given in this Figure, particularly as the terrain altitude at the 4000m point on the base scale, is substantially lower than the general terrain. A short distance to the south of cross section 5 there is no evidence of this valley but lateral cross section 4 shows this quite clearly. From the Gebbies Pass road junction, see Fig. 8.12, the terrain descends very steeply in the northerly direction and the road winds down into this valley. However, the terrain to the south of cross section 5 presents an unbroken barrier across the valley floor. This can clearly be seen in Fig. 3.3.

The saddle generates high velocities over it, as shown by the isotachs for this cross section. The isotach contours agree in shape with those over the terraced model but close to the model surface, $Z < 10mm$. there are significant velocity increases.

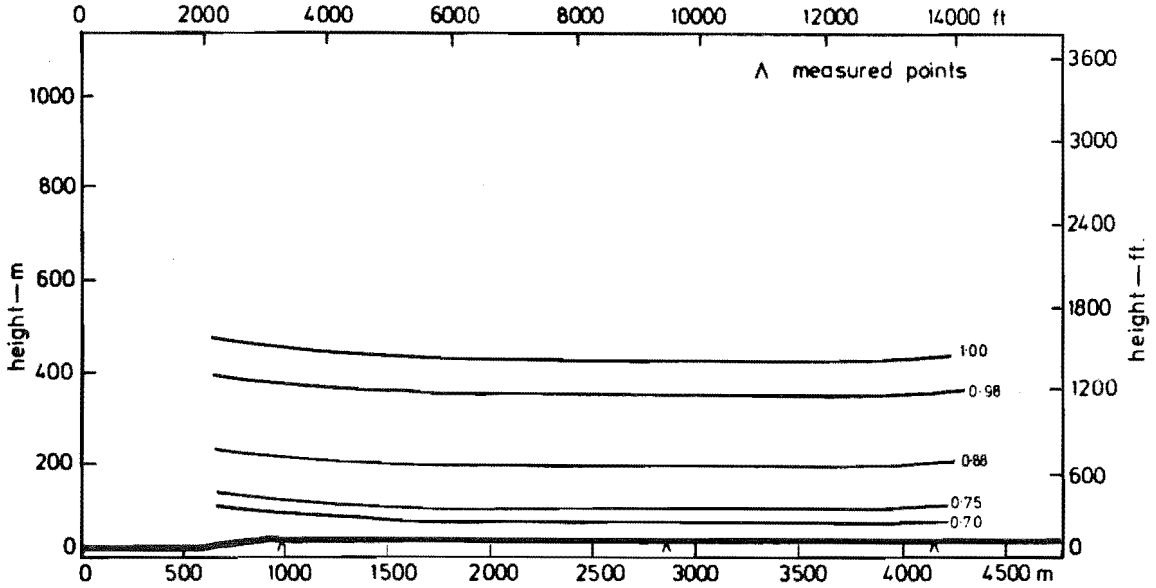

FIG 8.38 ISOTACHS FOR MODEL B CONTOURED, LATERAL CROSS SECTION. 1

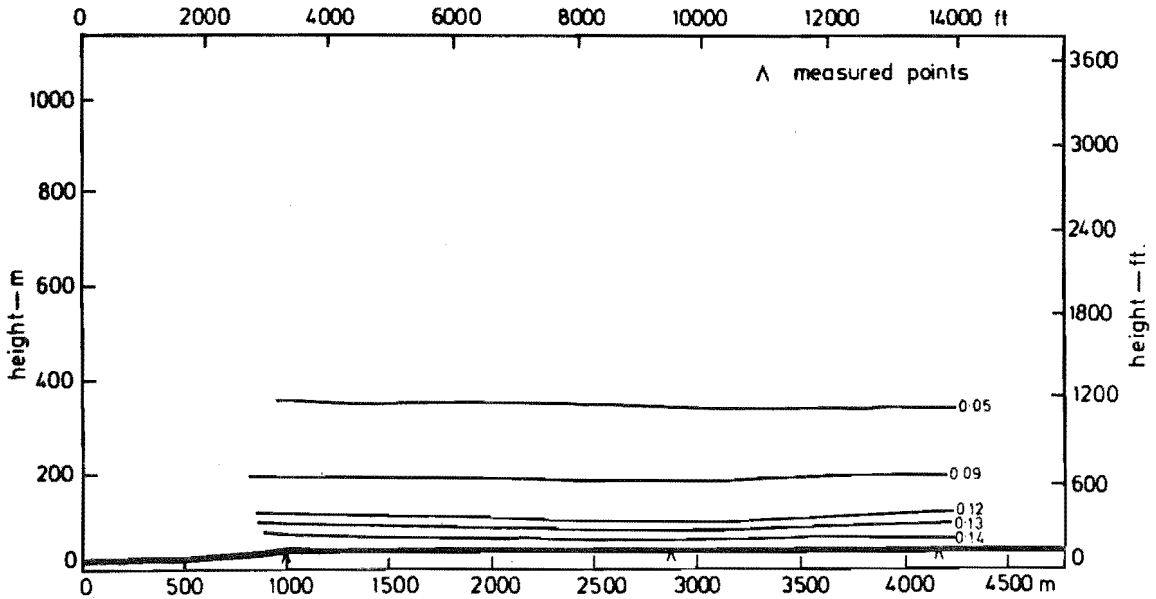

FIG 8.39 ISOTURBS FOR MODEL B CONTOURED, LATERAL CROSS SECTION. 1

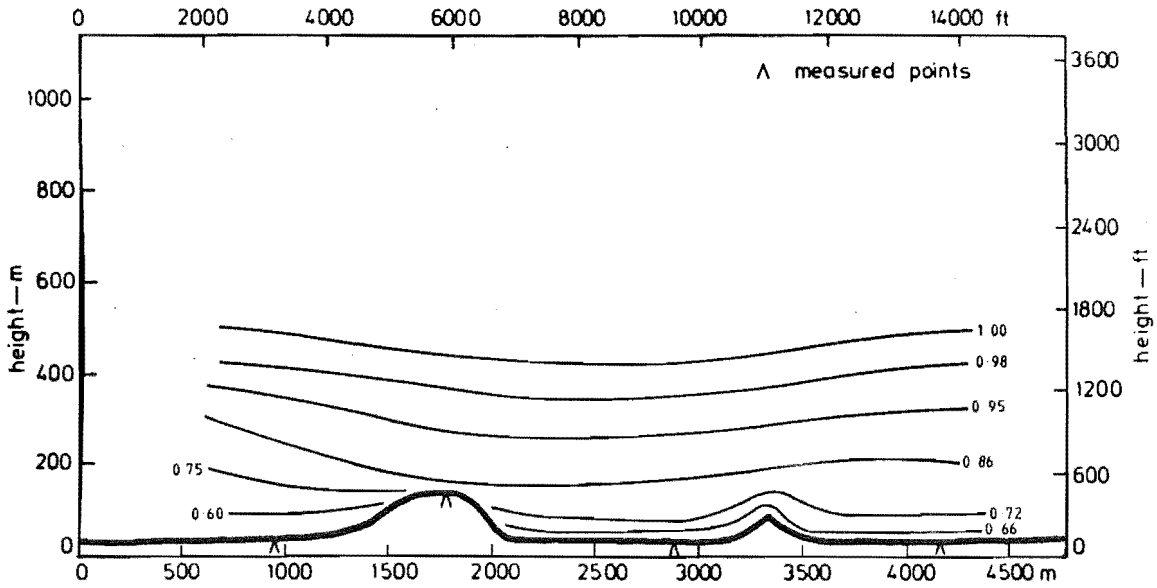

FIG 8.40 ISOTACHS FOR MODEL B, CONTOURED, LATERAL CROSS SECTION. 2

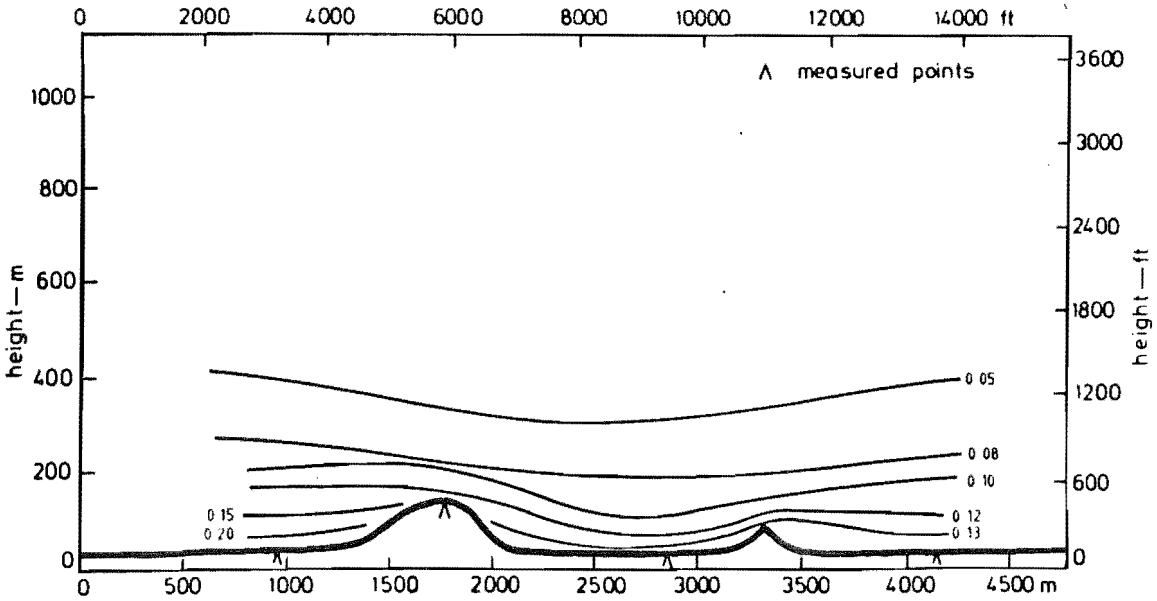

FIG 8.41 ISOTURBS FOR MODEL B, CONTOURED, LATERAL CROSS SECTION. 2

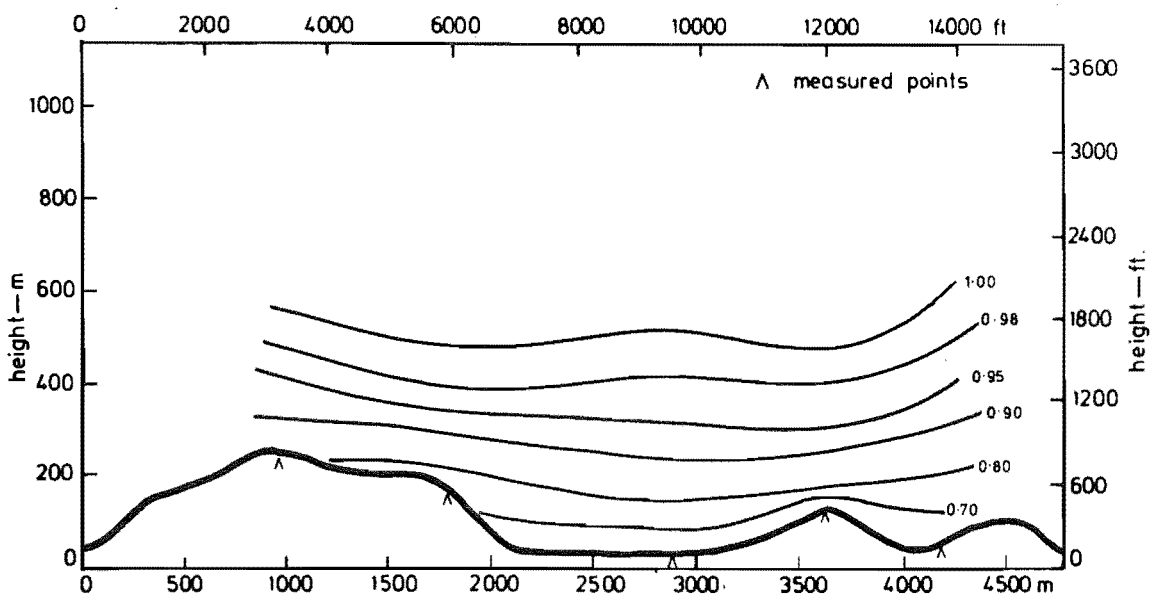

FIG 8.42 ISOTACHS FOR MODEL B CONTOURED, LATERAL CROSS SECTION. 3

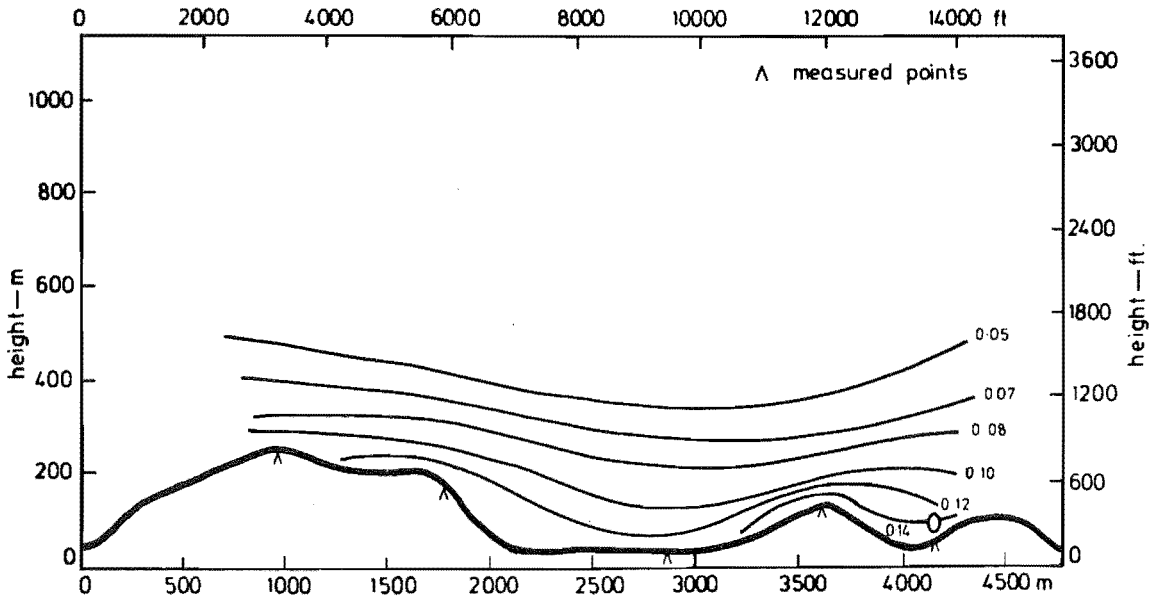

FIG 8.43 ISOTURBS FOR MODEL B CONTOURED, LATERAL CROSS SECTION. 3

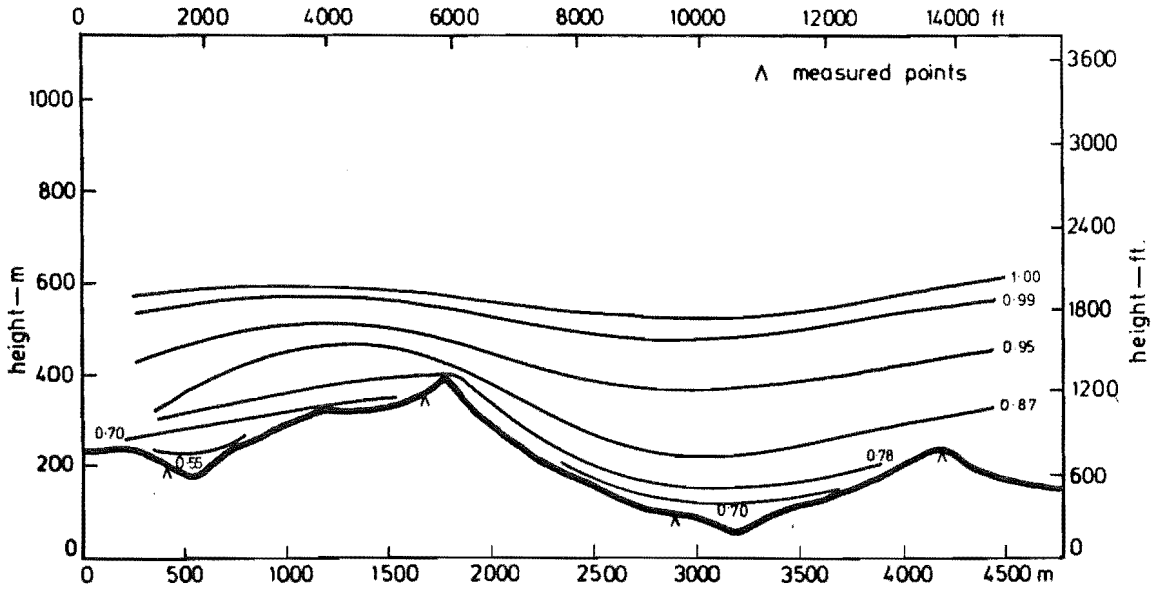

FIG 8.44 ISOTACHS FOR MODEL B CONTOURED, LATERAL CROSS SECTION 4

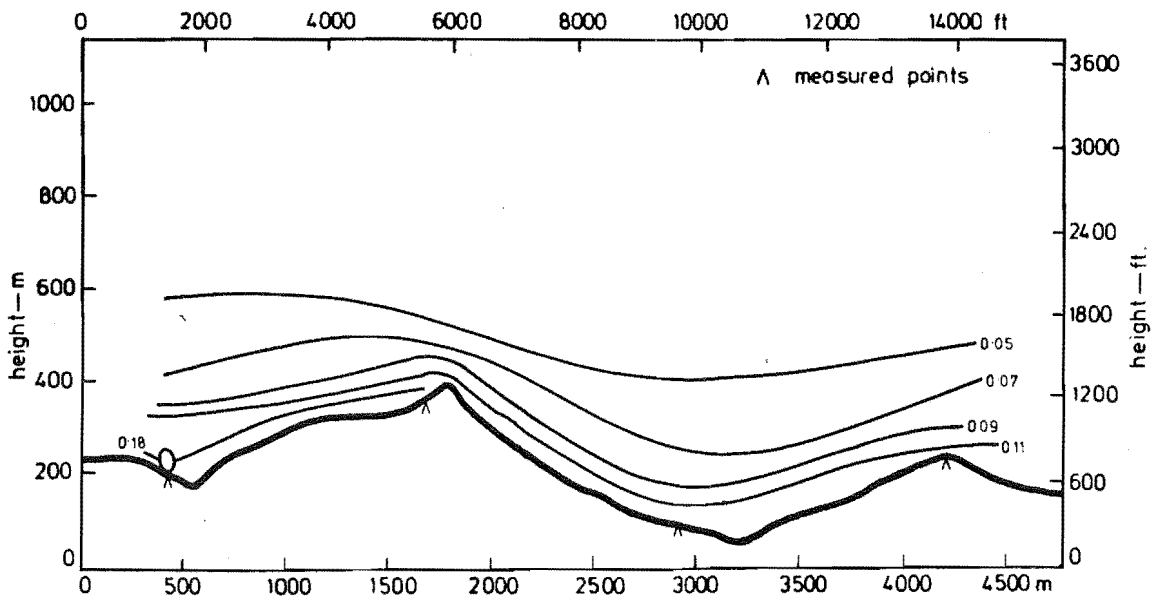

FIG 8.45 ISOTURBS FOR MODEL B CONTOURED, LATERAL CROSS SECTION 4

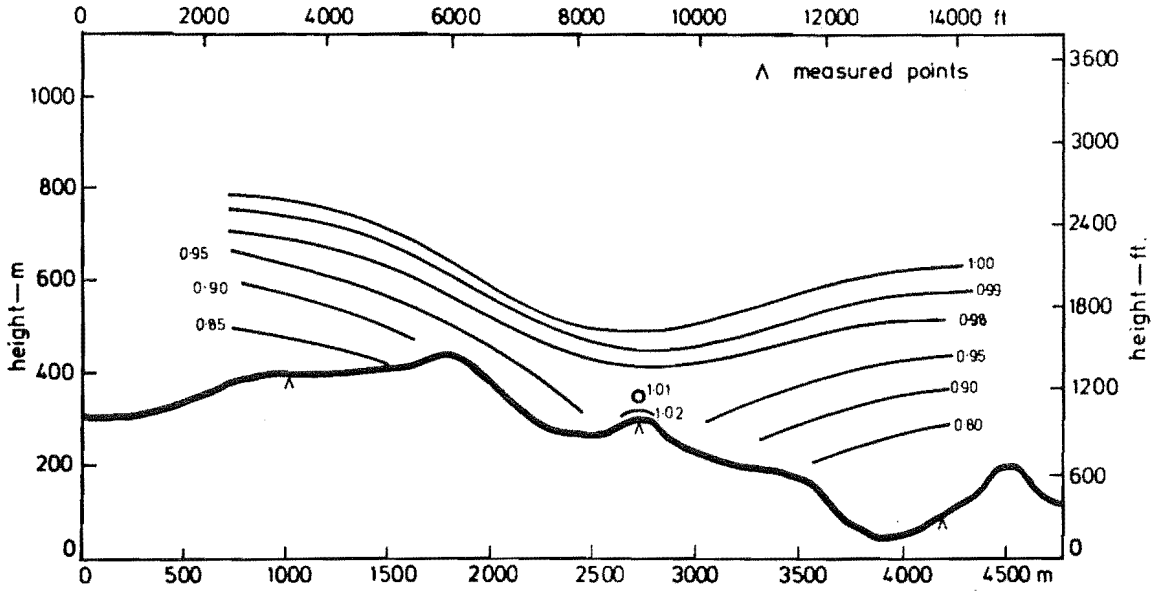

FIG 8.46 ISOTACHS FOR MODEL B CONTOURED, LATERAL CROSS SECTION. 5

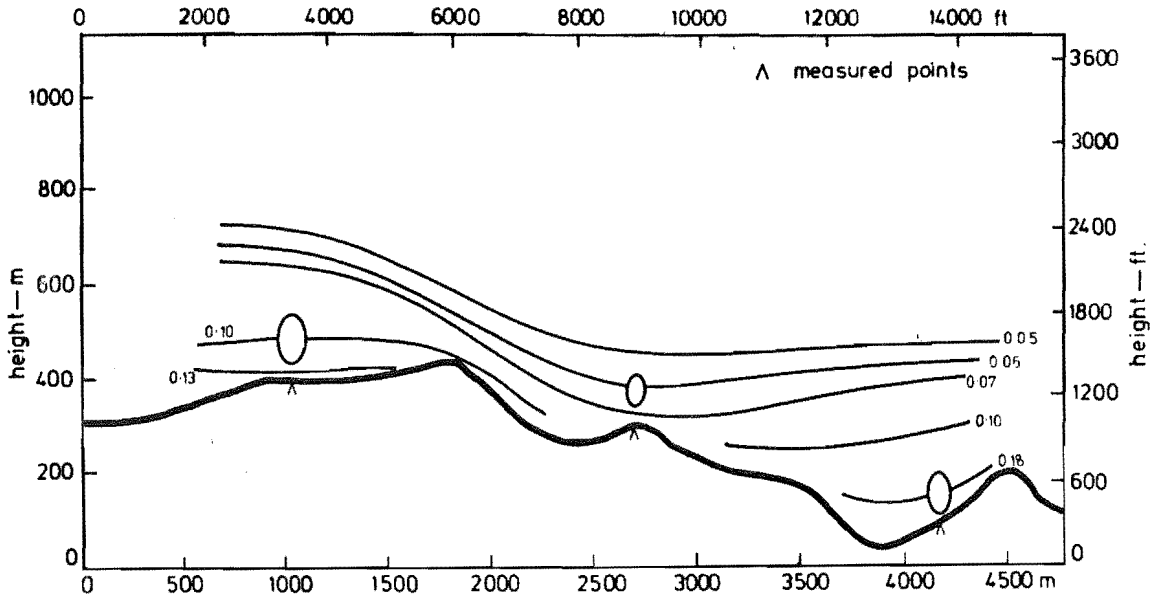

FIG 8.47 ISOTURBS FOR MODEL B CONTOURED, LATERAL CROSS SECTION. 5

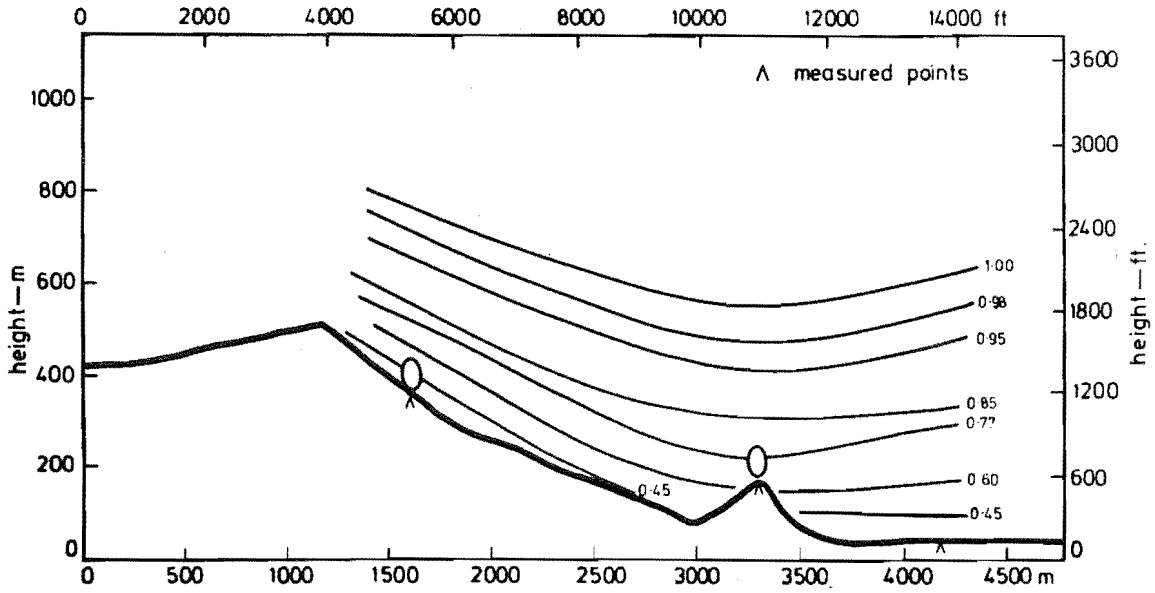

FIG 8.48 ISOTACHS FOR MODEL B CONTOURED, LATERAL CROSS SECTION. 6

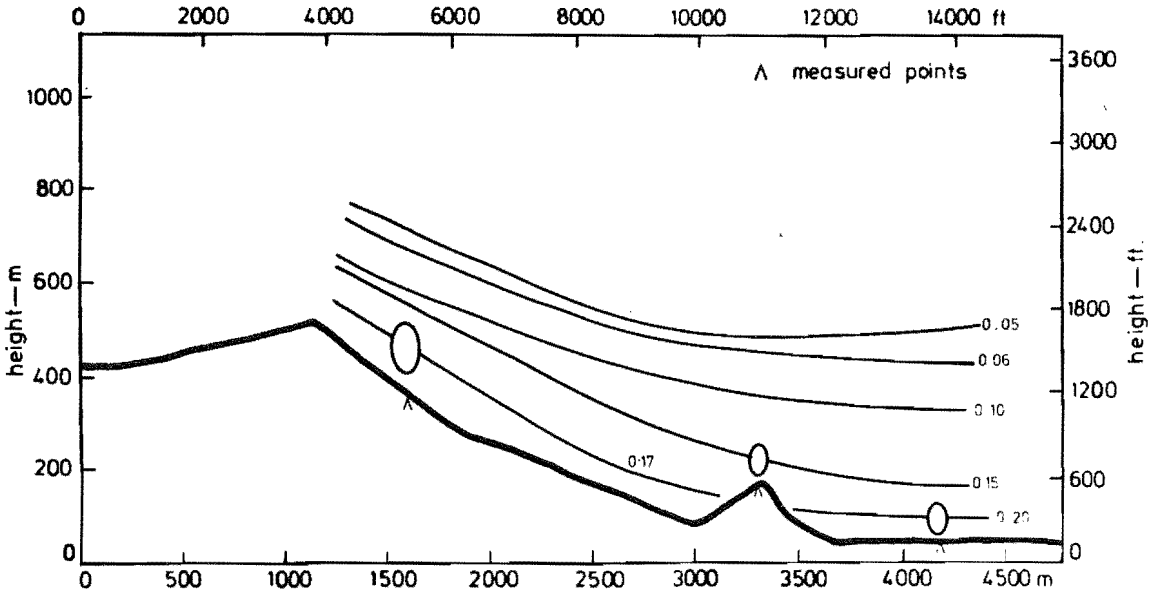

FIG 8.49 ISOTURBS FOR MODEL B CONTOURED, LATERAL CROSS SECTION. 6

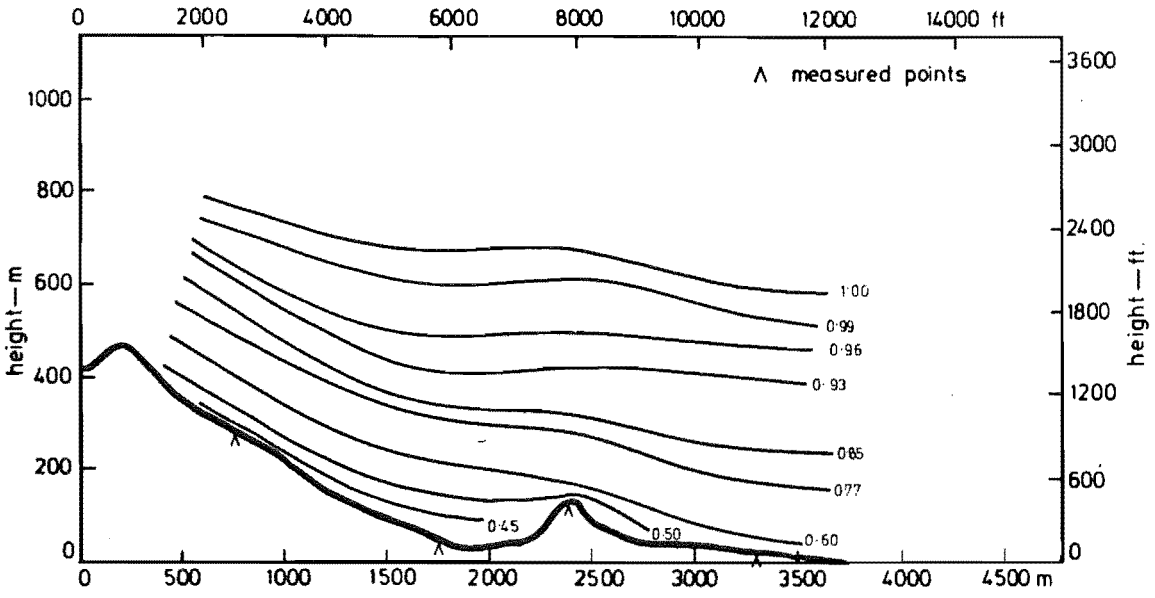

FIG 8.50 ISOTACHS FOR MODEL B CONTOURED, LATERAL CROSS SECTION. 7

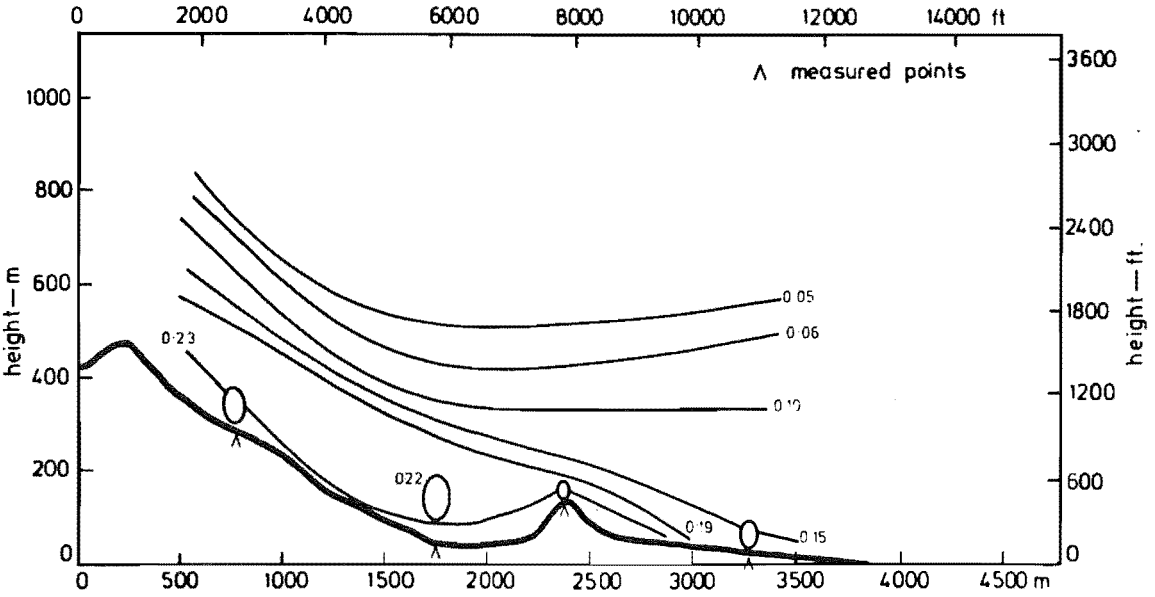

FIG 8.51 ISOTURBS FOR MODEL B CONTOURED, LATERAL CROSS SECTION. 7

There is a corresponding reduction in turbulence intensity values close to the model surface. The 5% turbulence intensity contour has the same shape as for the terraced model but is slightly lower above the saddle. This is to be expected as a reduction in turbulence intensity close to the surface means that the mixing does not extend as far into the boundary layer as it would for the model with a rougher surface.

Isotach contours for cross section 6 are almost the same as for the terraced model, the contoured model curves appearing to have a smoother shape over the terrain. Point 41, located at the 4100m position on the base scale, suggests a slowing of the velocity close to the model surface. There is no obvious explanation for this effect.

Isoturb contours are essentially the same for both the contoured and terraced models.

Cross section 7 follows the general trend with an increase in isotach values close to the model surface combined with a general smoothing of the contours. Likewise, the isoturb contours show a reduction in magnitude close to the surface and have a smoothed appearance.

The isotach and isoturb contours for the longitudinal cross sections are presented in Figs 8.52 to 8.59.

On cross section XX, the isotachs on the windward side of the Port Hills ridge at the 7000m position on the base scale, suggest a slight slowing of the flow. This is contrary to the remainder of the cross section where generally there is an increase in velocity, particularly close to the model surface. The contours at heights greater than 40mm are generally the same for both the contoured and terraced models.

The most significant changes in the isoturb contours occur on the top of hills and knobs where significant reductions in turbulence intensity were observed.

Isotachs on the YY cross section show a general increase in velocity and a slight smoothing of the contours. The isoturbs show a significant reduction in turbulence intensity on the windward side of the Port Hills ridge. Terraced model values of 35% have been reduced to 12% at point 32, 5900m position on the base scale.

The isotach contours for cross section UU show that the flow approaching

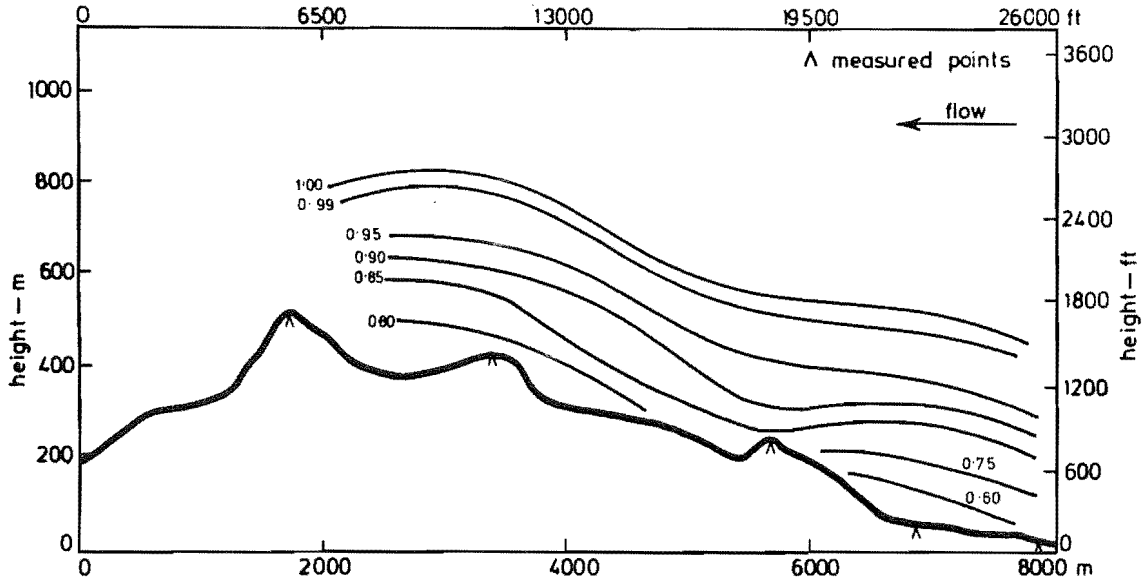

FIG 8.52 ISOTACHS FOR MODEL B CONTOURED, LONGITUDINAL CROSS SECTION XX

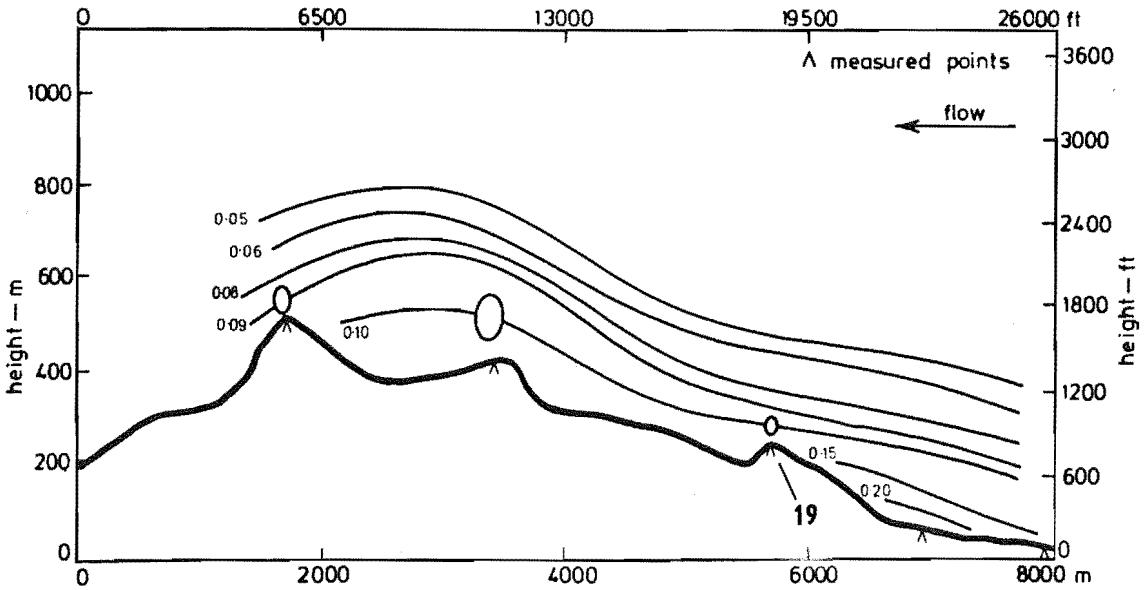

FIG 8.53 ISOTURBS FOR MODEL B CONTOURED, LONGITUDINAL CROSS SECTION XX

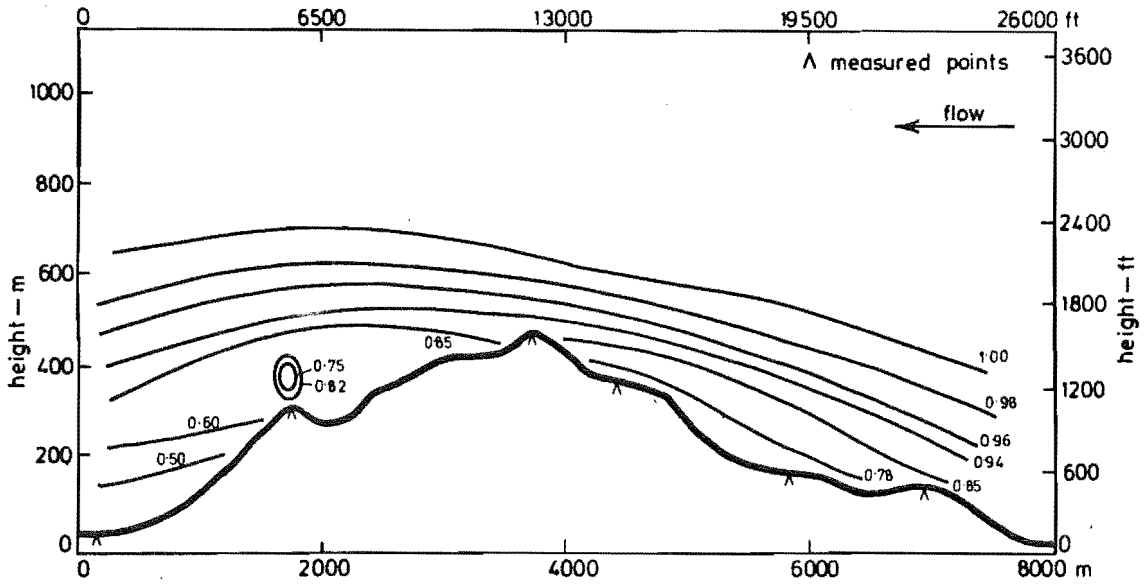

FIG 8.54 ISOTACHS FOR MODEL B CONTOURED, LONGITUDINAL CROSS SECTION YY

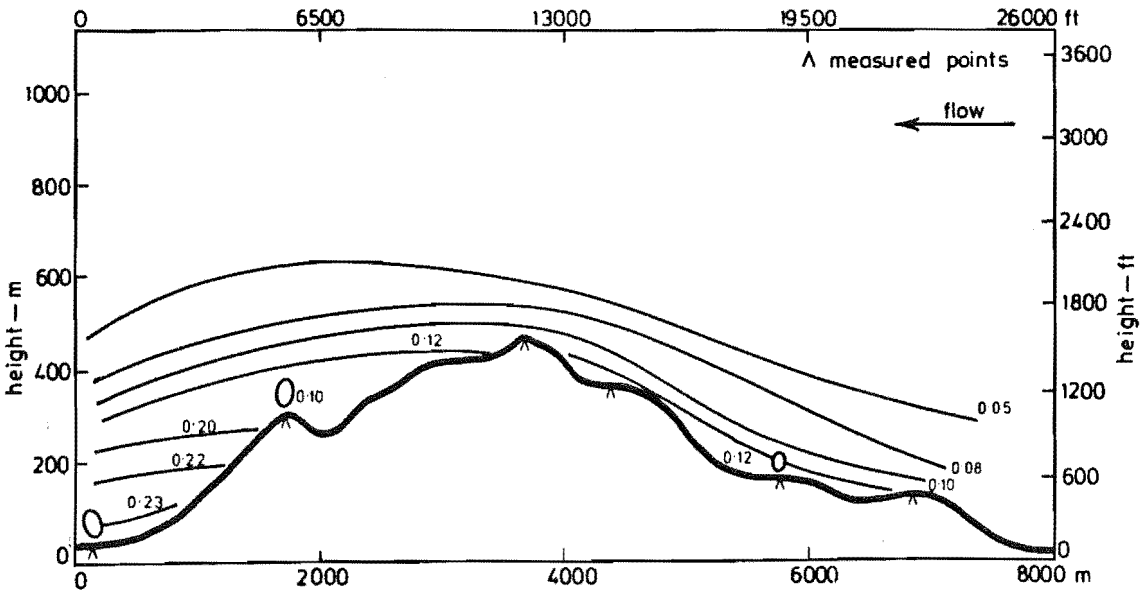

FIG 8.55 ISOTURBS FOR MODEL B CONTOURED, LONGITUDINAL CROSS SECTION YY

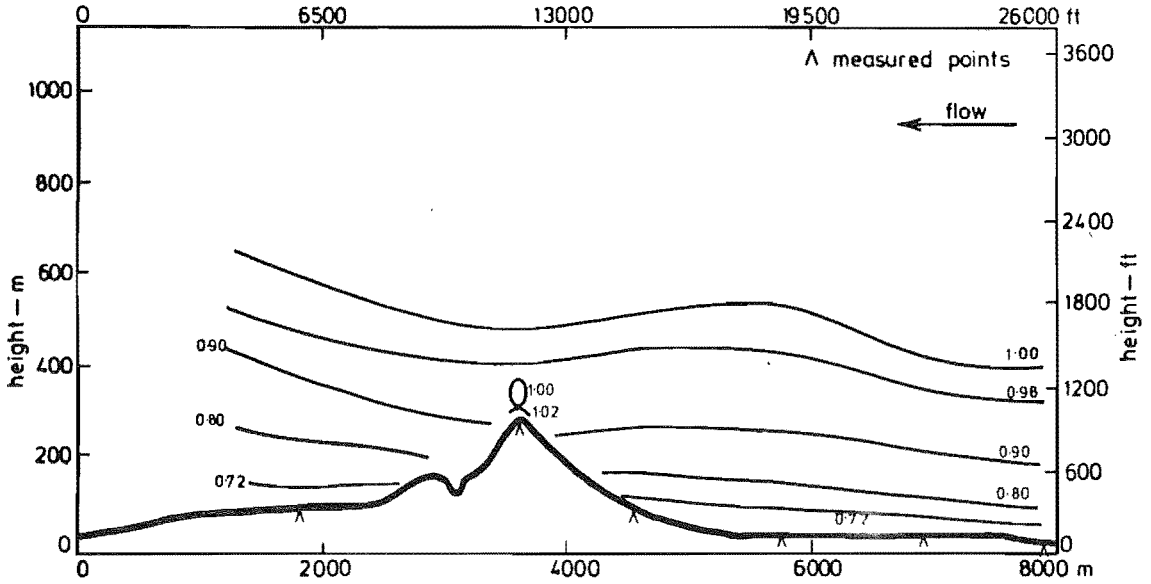

FIG 8.56 ISOTACHS FOR MODEL B CONTOURED. LONGITUDINAL CROSS SECTION UU

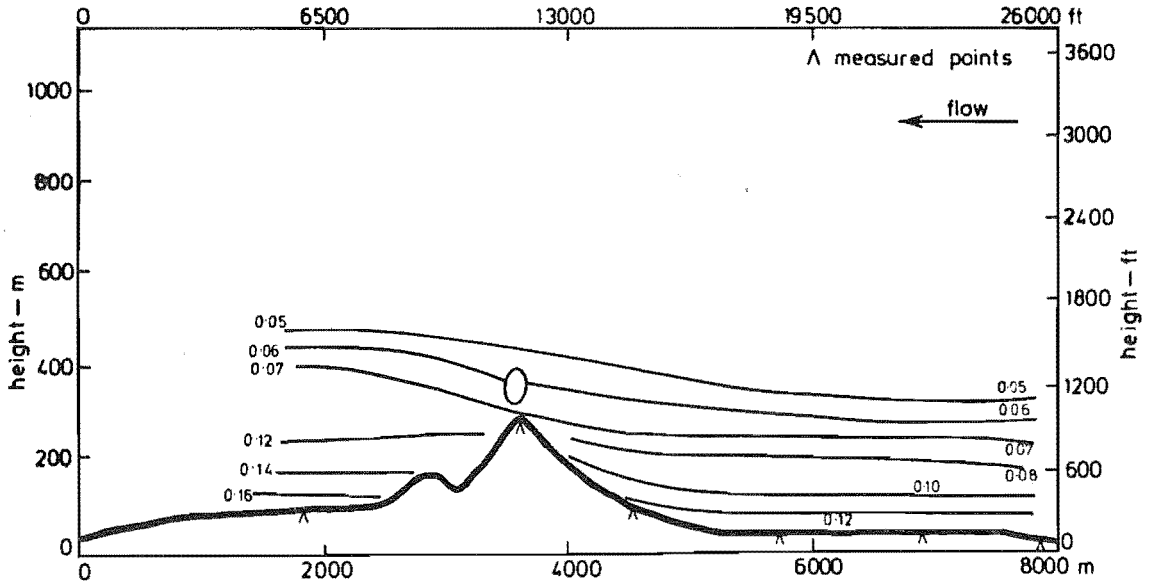

FIG 8.57 ISOTURBS FOR MODEL B CONTOURED. LONGITUDINAL CROSS SECTION UU

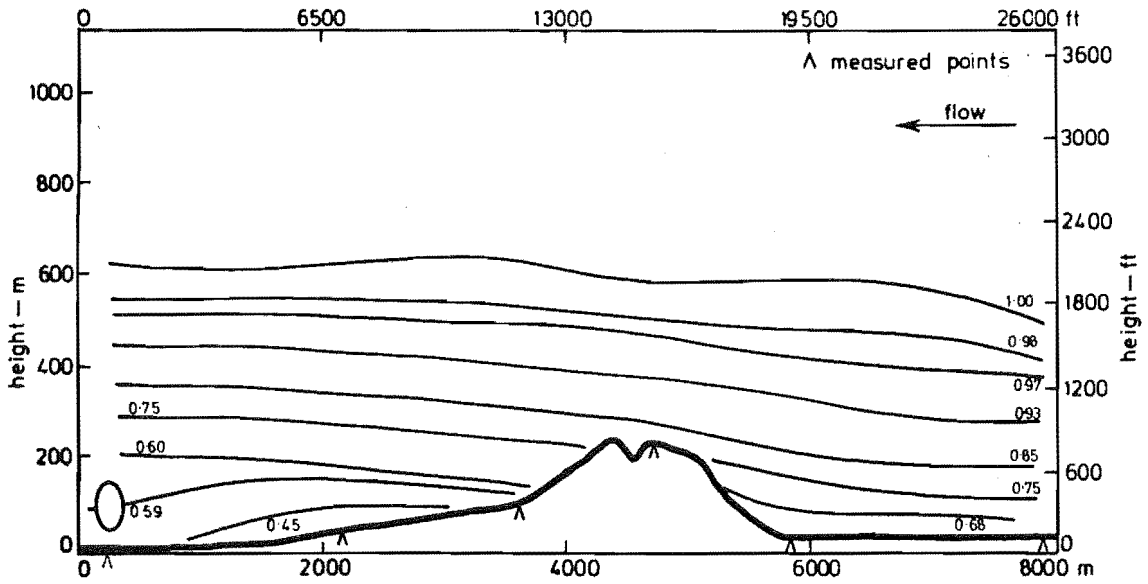

FIG 8.58 ISOTACHS FOR MODEL B CONTOURED, LONGITUDINAL CROSS SECTION VV

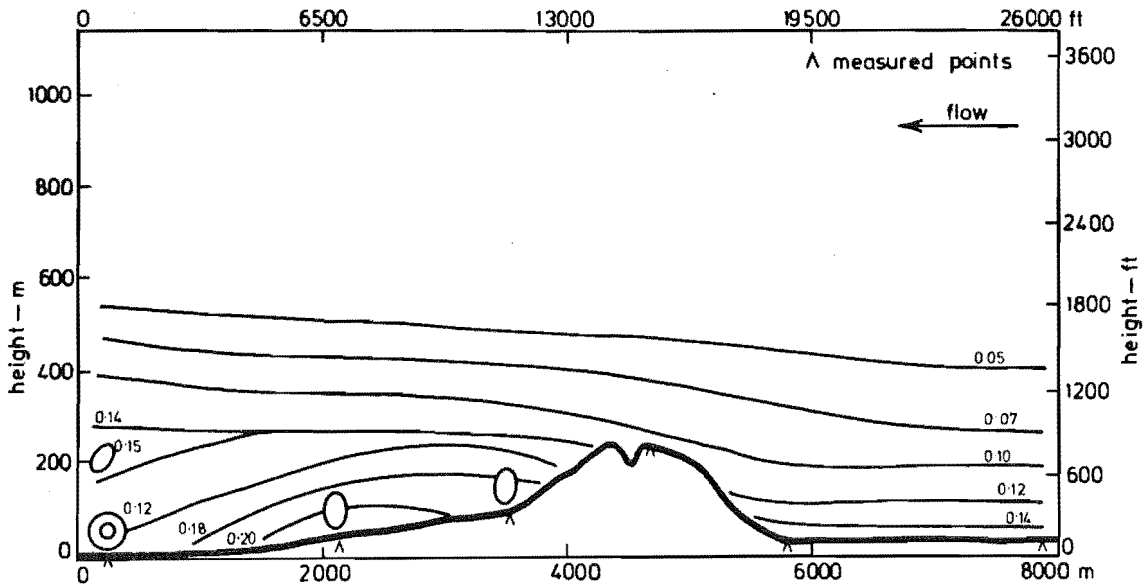

FIG 8.59 ISOTURBS FOR MODEL B CONTOURED, LONGITUDINAL CROSS SECTION VV

the Gebbies Pass saddle is virtually the same for the terraced and contoured models. Velocities on the leeward side of the saddle are generally faster on the contoured model. The most significant difference is the degree of speed-up on the saddle itself. Point 12, 3800m position on the base scale, indicates velocities close to the surface, Z < 5mm, greater than the gradient velocity. This appears to have had the effect of reducing the gradient height at this point quite significantly. Therefore, the resulting gradient height contour has a wavey shape.

Isoturb contours for the terraced and contoured models are markedly different. On the leeward side of the saddle the turbulence intensity is drastically reduced and the contours are much smoother. The windward contours are similar for both models.

Little can be said about longitudinal cross section VV. Both the isotach and isoturb contours are similar in shape and magnitude to those measured over the terraced model.

The speed-up ratio areas for the contoured model are presented in Fig. 8.60. There are several major differences between the speed-up ratio areas for the terraced and contoured models. One difference is that the flow over the contoured model is generally faster at all levels. This is particularly clear on the windward face of the Port Hills ridge and along the ridgelines of both the Port Hills and the Gebbies Pass saddle. The valley leading to the saddle from the south does not seem to be experiencing higher wind velocities. However, it must be remembered that this is the situation at one height only.

Another feature is that ridges and knobs appear to be more significant than the general terrain effects; however, the high velocities on the saddle, point 12, could be the result of a combination of these factors.

8.3.5 Correlations for Model B, Terraced vs Contoured

The scatter diagrams for model B terraced vs contoured for heights of 5mm, 10mm and 20mm are presented in Figs 8.61, 8.62 and 8.63 respectively. At the 5mm height, a correlation coefficient of 0.61 was measured, based on data from 30 points. This compares with a correlation of 0.55 for the same states of construction on model A. The apparent improvement can probably be explained by the differences in terrain between models A and B. The major feature on model A was the Port Hills ridge, which was situated across the wind tunnel. This produced significant slowing of the flow on the windward face of the ridge as was noted in Chapter 7.0. In the case of

Contoured Model

Z = 10mm

Zp = 40m

$$\frac{\bar{U}_{10}/\bar{U}_6|_{pt}}{\bar{U}_{10}/\bar{U}_6|_{ref\ pt}} \times 100$$

141–150

121–140

101–120

81–100

71–80

61–70

0–60

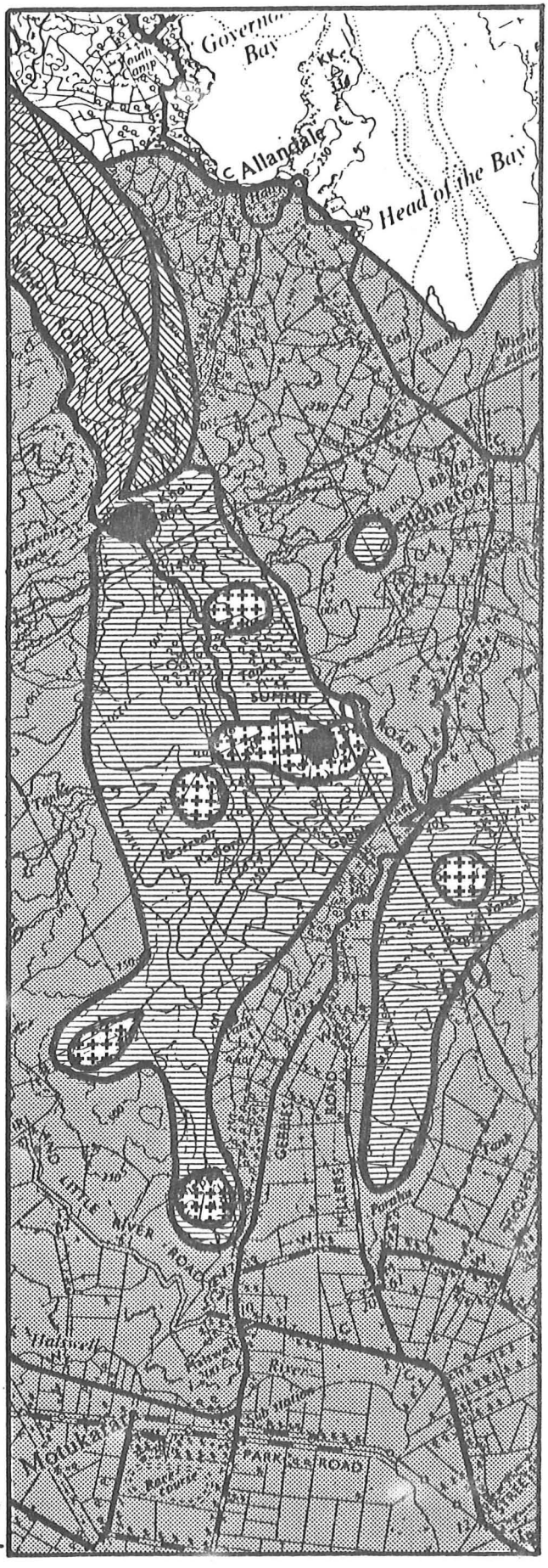

FIG 8·60 SPEED-UP RATIO AREAS FOR MODEL B CONTOURED, Zp = 40m

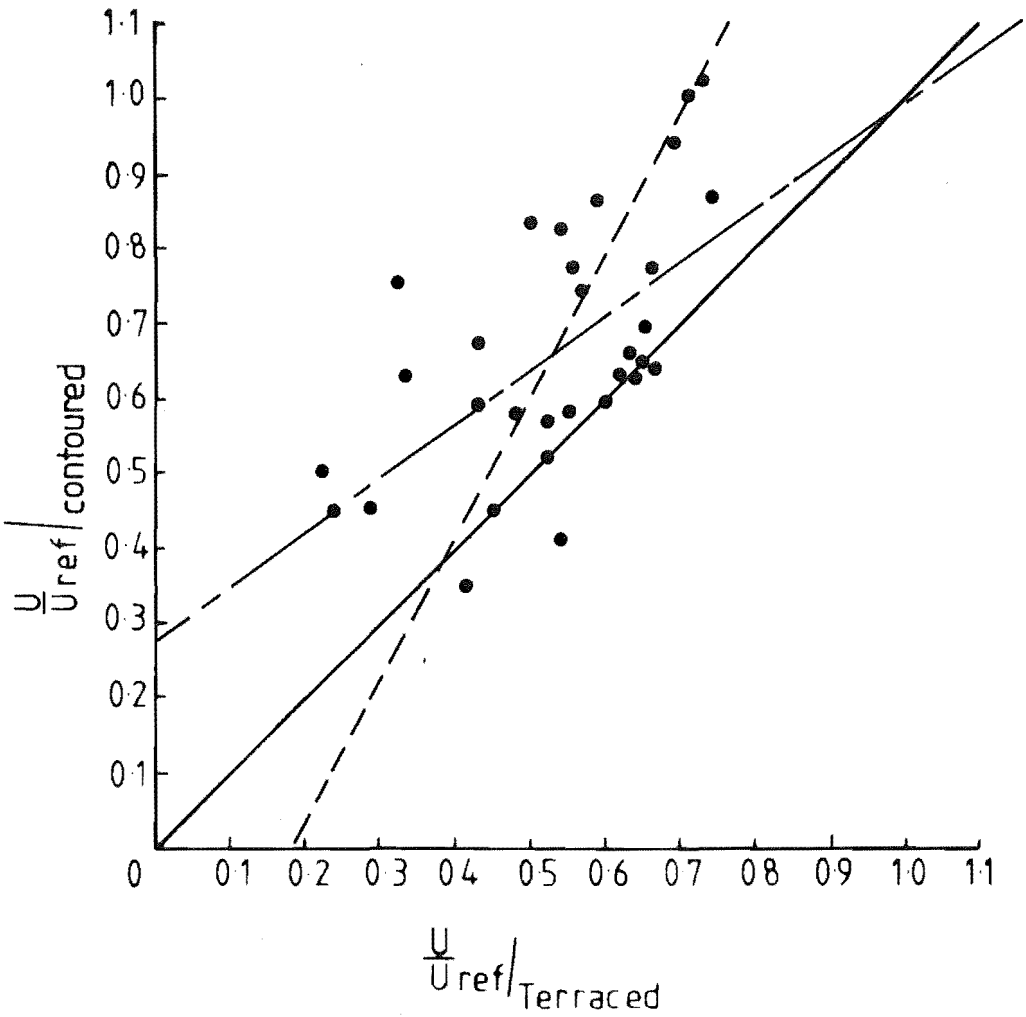

Regression lines

$$\text{- - - -}\quad \frac{U}{U_{ref}}\Big|_{Terraced} = 0{\cdot}52\ \frac{U}{U_{ref}}\Big|_{Contoured} + 0{\cdot}184$$

$$\text{- - — - -}\quad \frac{U}{U_{ref}}\Big|_{Contoured} = 0{\cdot}73\ \frac{U}{U_{ref}}\Big|_{Terraced} + 0{\cdot}276$$

Correlation coefficient $r = 0{\cdot}61$

FIG. 8·61 SCATTER DIAGRAM FOR MODEL B AT Z = 5 mm.

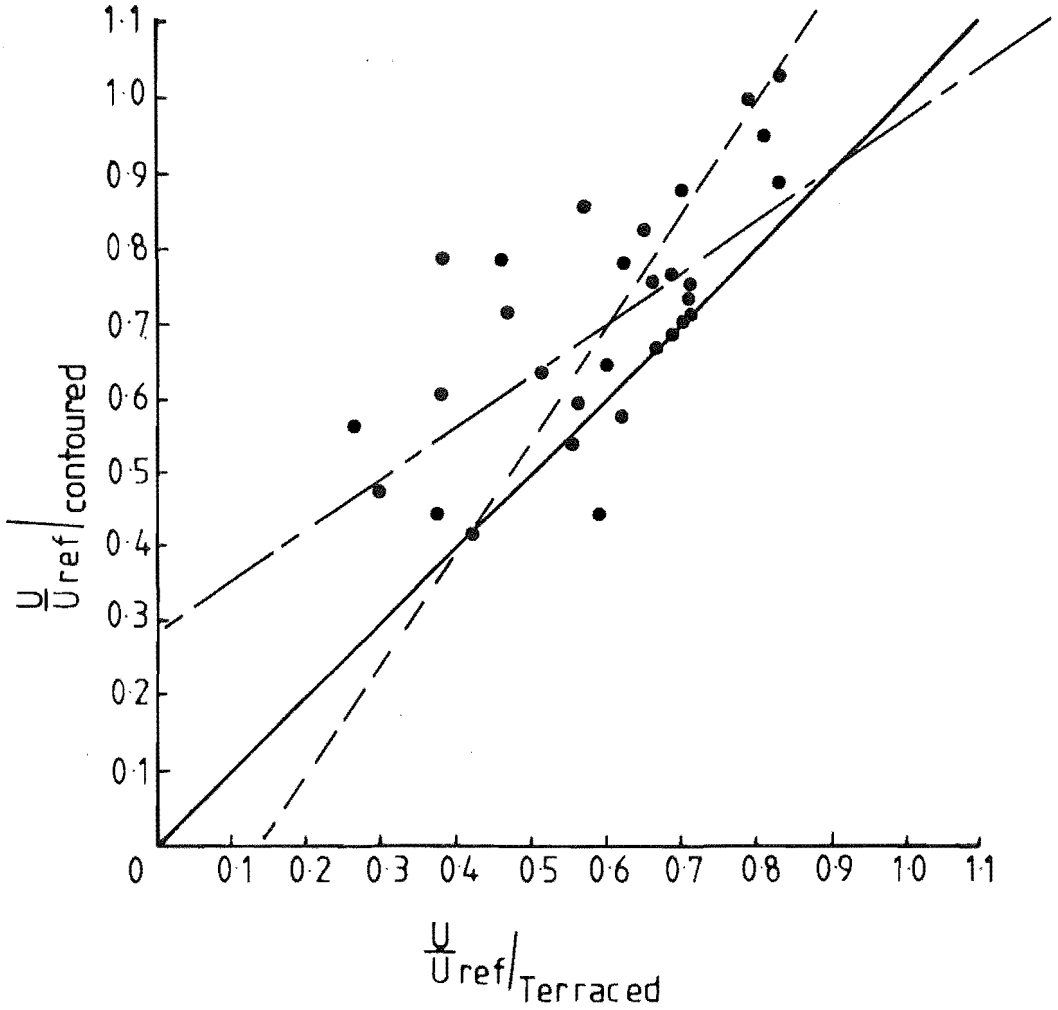

Regression lines

$$- - - - \frac{U}{U_{ref}}\Big|_{Terraced} = 0 \cdot 67 \frac{U}{U_{ref}}\Big|_{Contoured} + 0 \cdot 130$$

$$- - - - \frac{U}{U_{ref}}\Big|_{Contoured} = 0 \cdot 68 \frac{U}{U_{ref}}\Big|_{Terraced} + 0 \cdot 290$$

Correlation coefficient $r = 0 \cdot 67$

FIG. 8·62 SCATTER DIAGRAM FOR MODEL B AT Z = 10 mm.

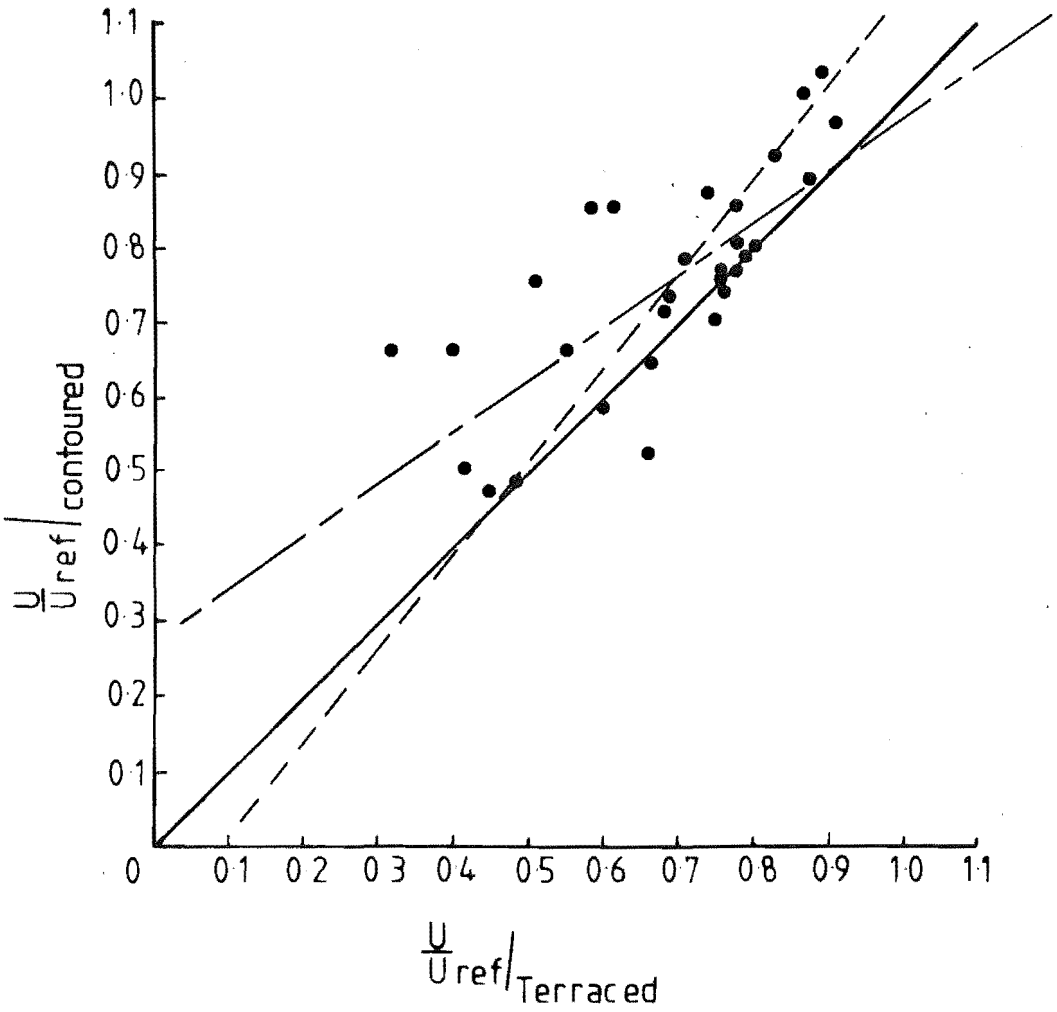

Regression lines

$$- - - - \frac{U}{U_{ref}}\Big|_{Terraced} = 0 \cdot 80 \ \frac{U}{U_{ref}}\Big|_{Contoured} + 0 \cdot 080$$

$$- - - - \frac{U}{U_{ref}}\Big|_{Contoured} = 0 \cdot 69 \ \frac{U}{U_{ref}}\Big|_{Terraced} + 0 \cdot 278$$

Correlation coefficient $r = 0 \cdot 74$

FIG. 8·63 SCATTER DIAGRAM FOR MODEL B AT Z = 20 mm.

model B, the ridge has been aligned, to a greater extent, with the tunnel. The net result is that this feature has a less significant effect on the flow. The second major factor to be considered is the number of points used for the correlation calculation.

On model A, 24 points were used compared with 31 for model B. The signficance of this is the location of the points. There are more points on the flat approach terrain for model B than for model A. These, naturally, produce results which will improve the correlation coefficient because they are affected only to a small degree by the contouring process.

As the height is increased, so the correlation improves to 0.67 at 10mm and 0.74 at 20mm. At the 20mm height, the correlation is the same as for model A. A correlation of 0.74 suggests that the terraced data at this height could be quite useful. It is becoming apparent from the wind tunnel results that there could be a use for terraced models, particularly for general flow régimes over complex topography. However, both the results from model A and model B have shown that close to the model surface, $Z < 10mm$ or $Z_p < 40m$ for the present study, terraced models are not representative of the flow régime.

8.4 ROUGHNESS ADDED MODEL

The roughness elements were added to model B in the same manner as for model A.

The approach flow conditions were checked and showed excellent agreement with the flow used for the earlier studies of model B.

8.4.1 Flow Visualisation

Polystyrene bead tests were not repeated for the model in this form of construction, the reasons for this being presented in Section 7.5.1.

Flag tests were repeated and indicated that no significant flow direction changes had occurred as a result of the addition of the roughness elements.

8.4.2 Hot Film Survey

The lateral cross section isotach and isoturb contours for the roughness added model are presented in Figs 8.54 to 8.77.

The isotach contours for cross section 1 show no changes from those recorded for the contoured model. The isoturb contours do show an increase in turbulence intensity close to the model surface, $Z < 5mm$.

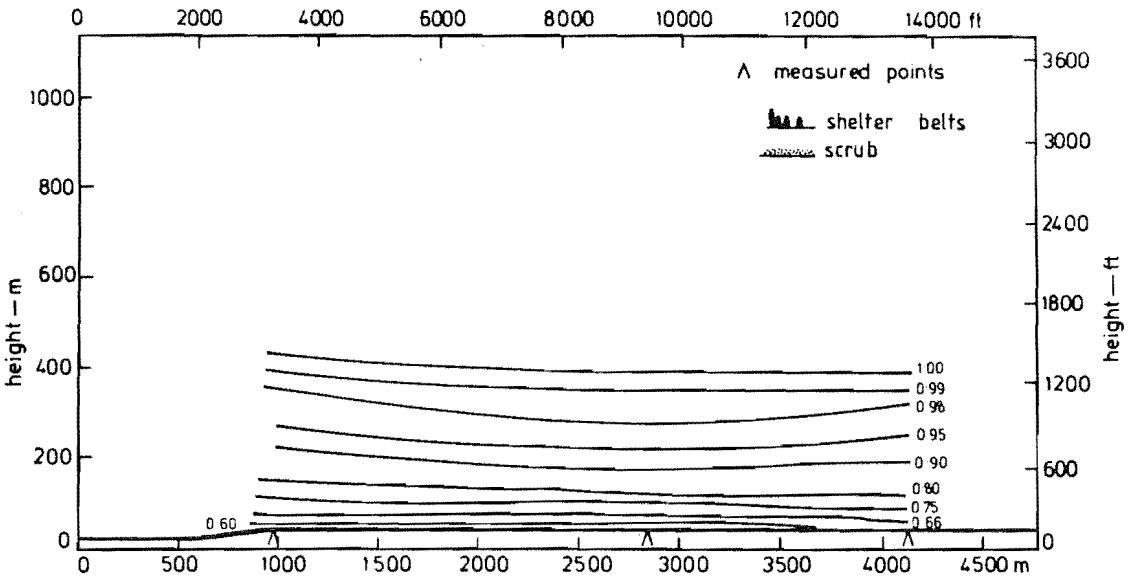

FIG 8.64 ISOTACHS FOR MODEL B WITH ROUGHNESS, LATERAL CROSS SECTION. 1

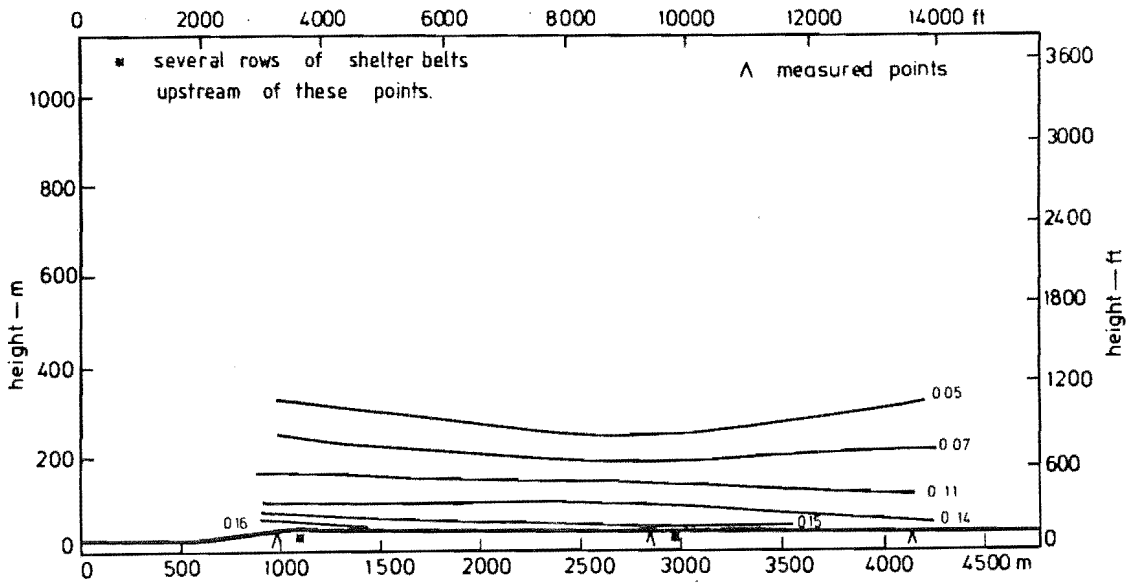

FIG 8.65 ISOTURBS FOR MODEL B WITH ROUGHNESS, LATERAL CROSS SECTION. 1

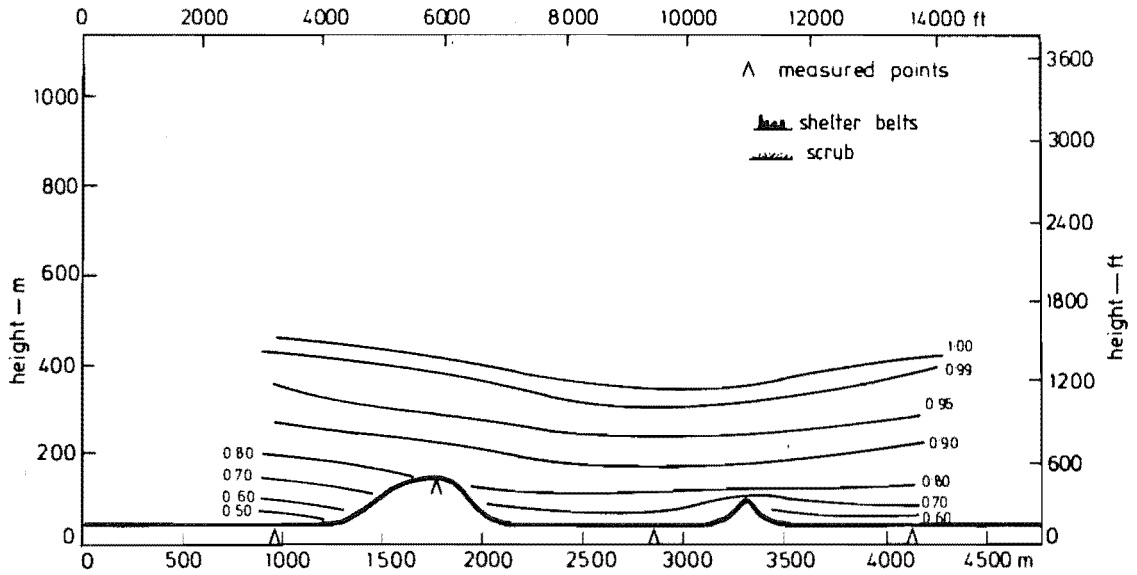

FIG 8.66 ISOTACHS FOR MODEL B WITH ROUGHNESS, LATERAL CROSS SECTION. 2

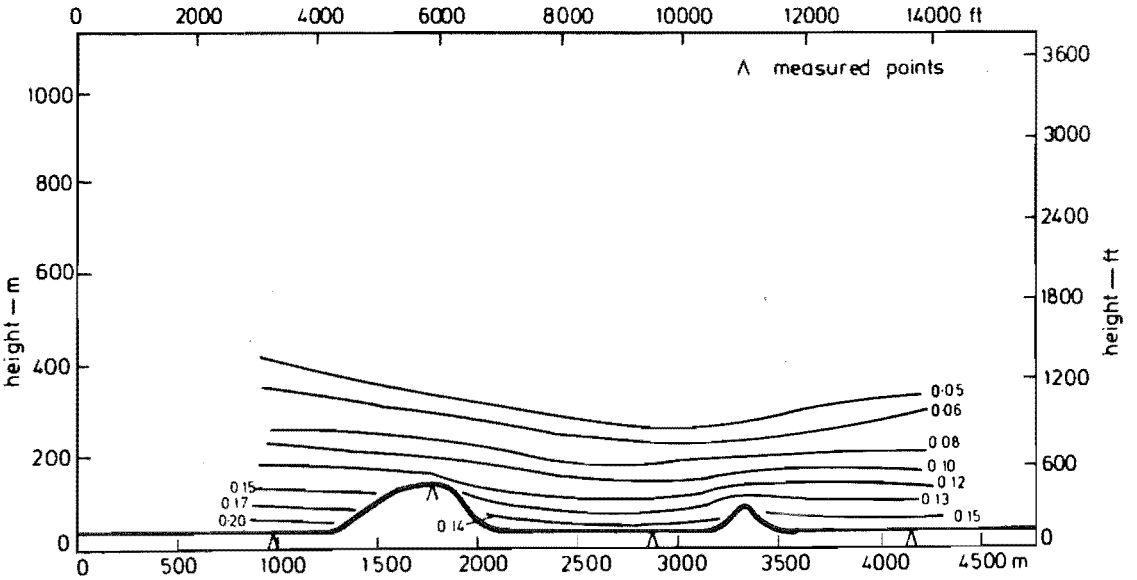

FIG 8.67 ISOTURBS FOR MODEL B WITH ROUGHNESS, LATERAL CROSS SECTION. 2

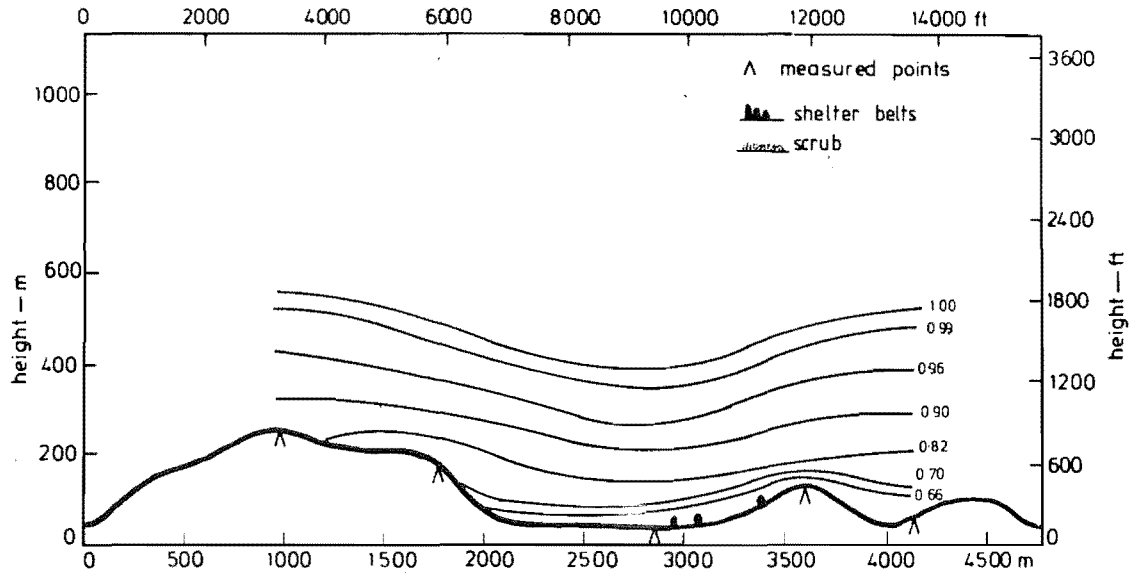

FIG 8.68 ISOTACHS FOR MODEL B WITH ROUGHNESS, LATERAL CROSS SECTION. 3

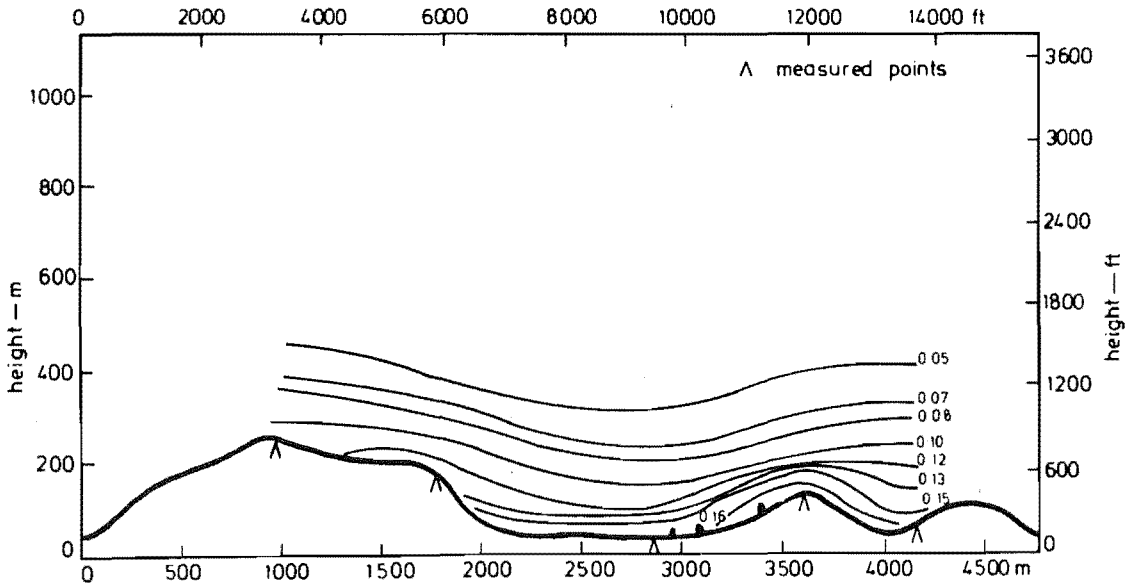

FIG 8.69 ISOTURBS FOR MODEL B WITH ROUGHNESS, LATERAL CROSS SECTION. 3

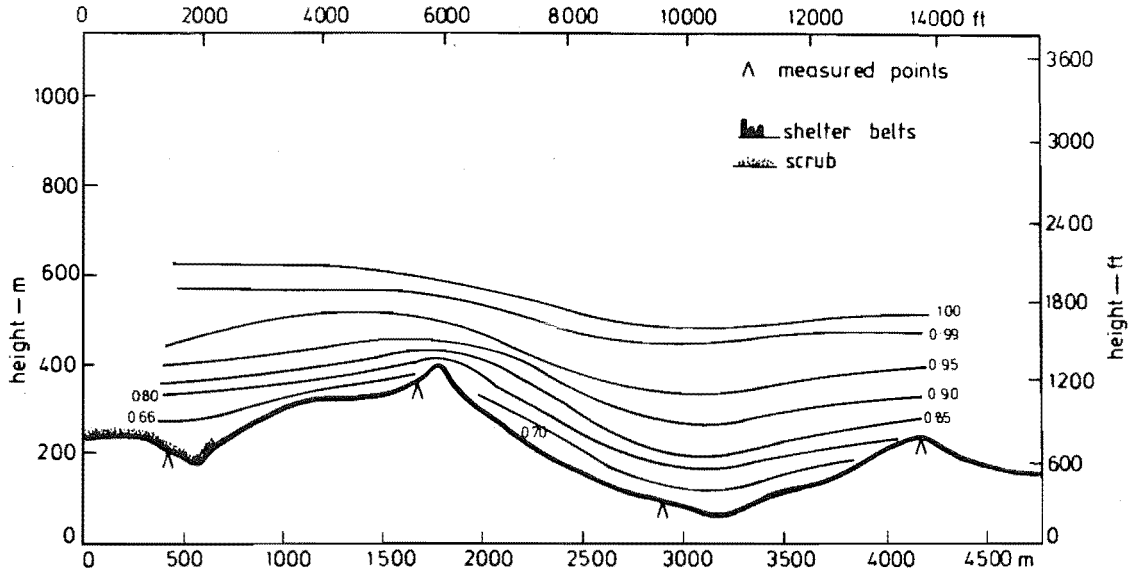

FIG 8.70 ISOTACHS FOR MODEL B WITH ROUGHNESS, LATERAL CROSS SECTION. 4

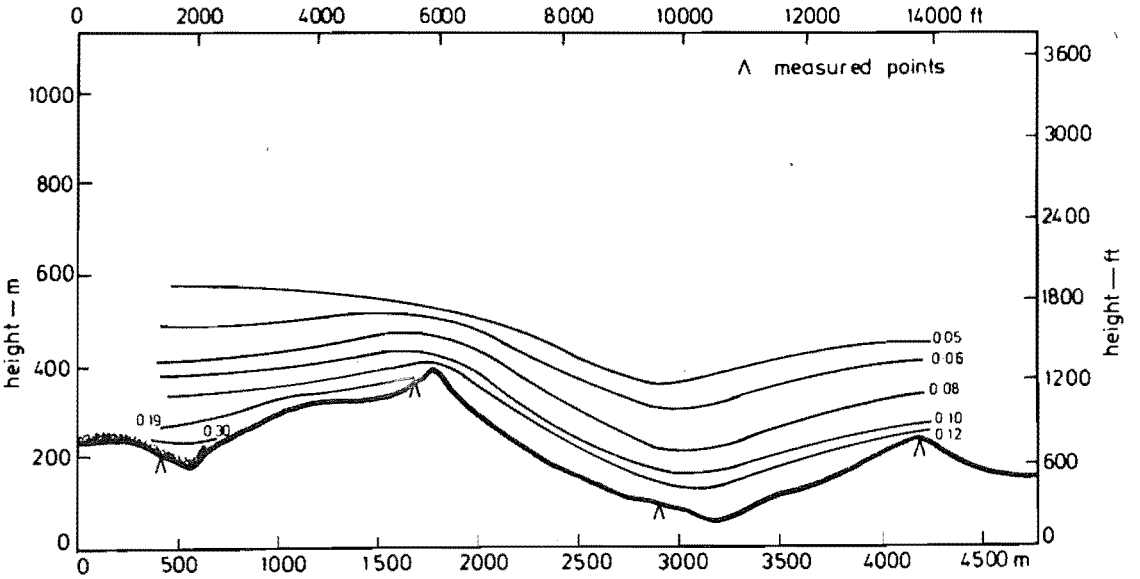

FIG 8.71 ISOTURBS FOR MODEL B WITH ROUGHNESS, LATERAL CROSS SECTION. 4

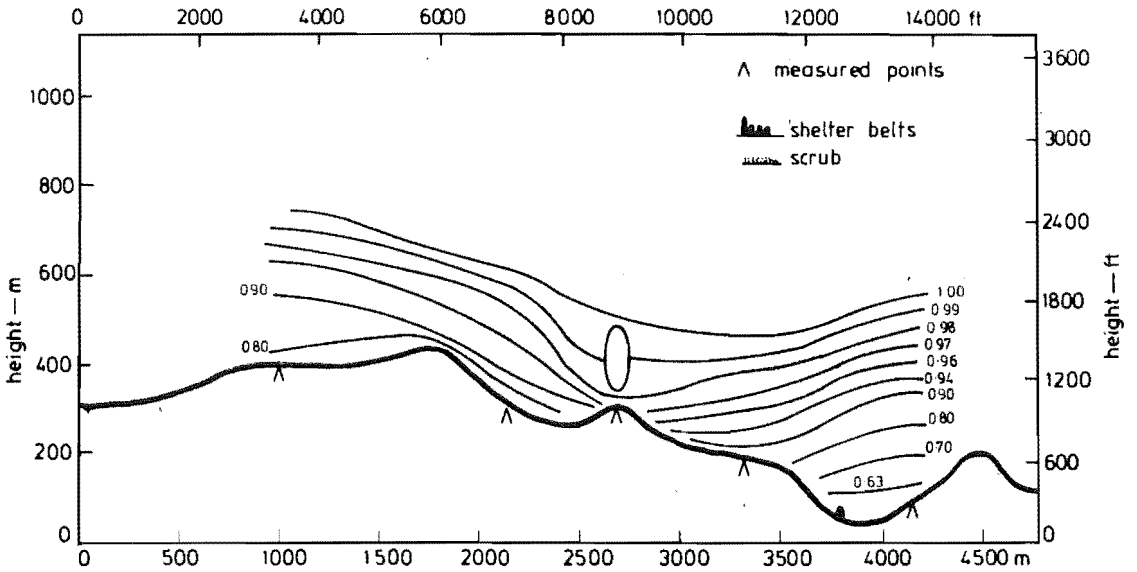

FIG 8.72 ISOTACHS FOR MODEL B WITH ROUGHNESS, LATERAL CROSS SECTION 5

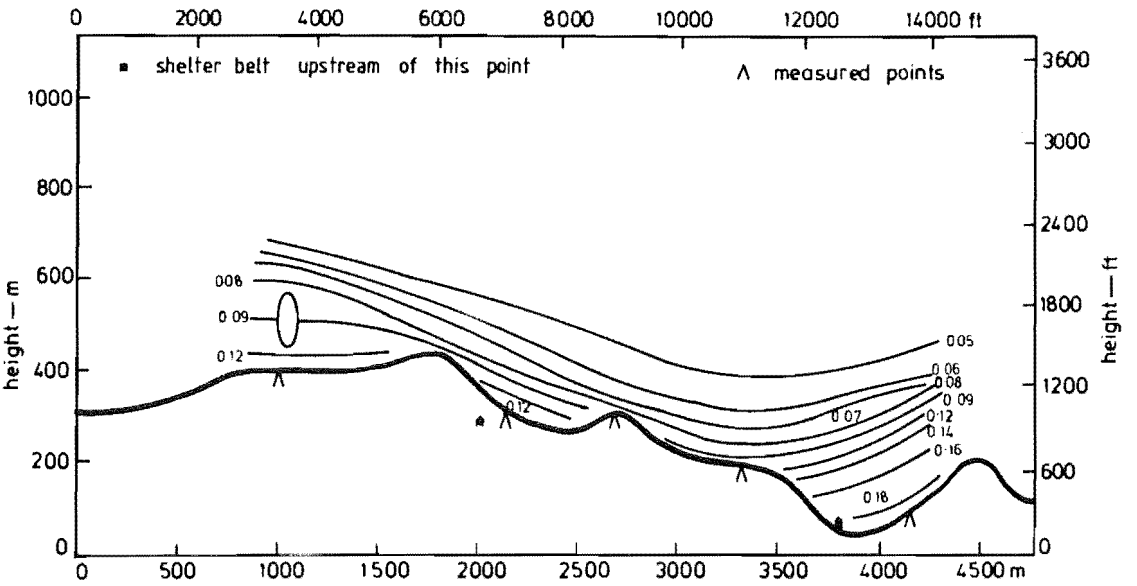

FIG 8.73 ISOTURBS FOR MODEL B WITH ROUGHNESS, LATERAL CROSS SECTION 5

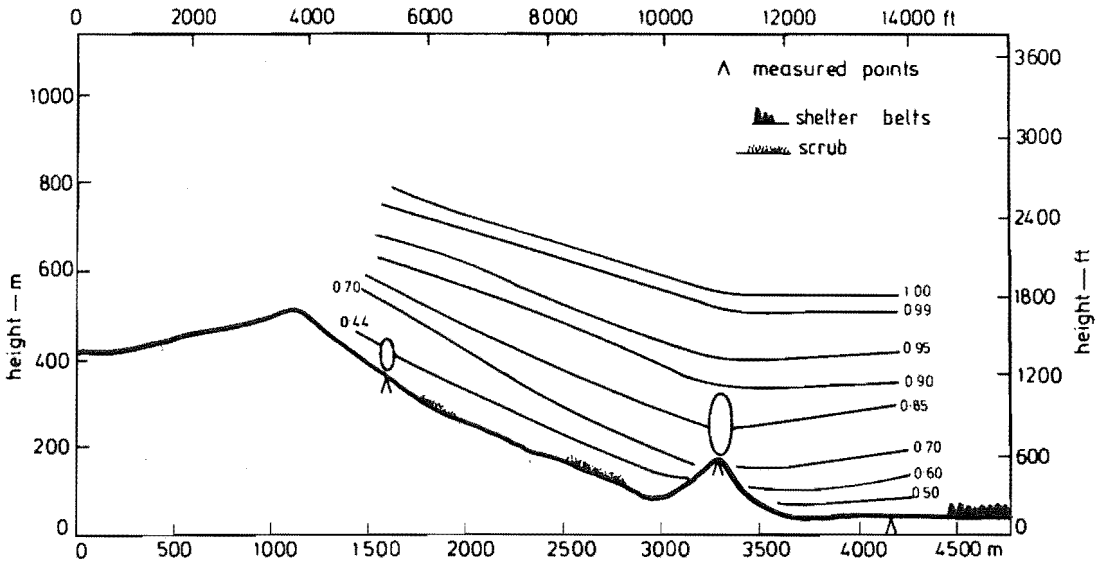

FIG 8.74 ISOTACHS FOR MODEL B, WITH ROUGHNESS, LATERAL CROSS SECTION 6

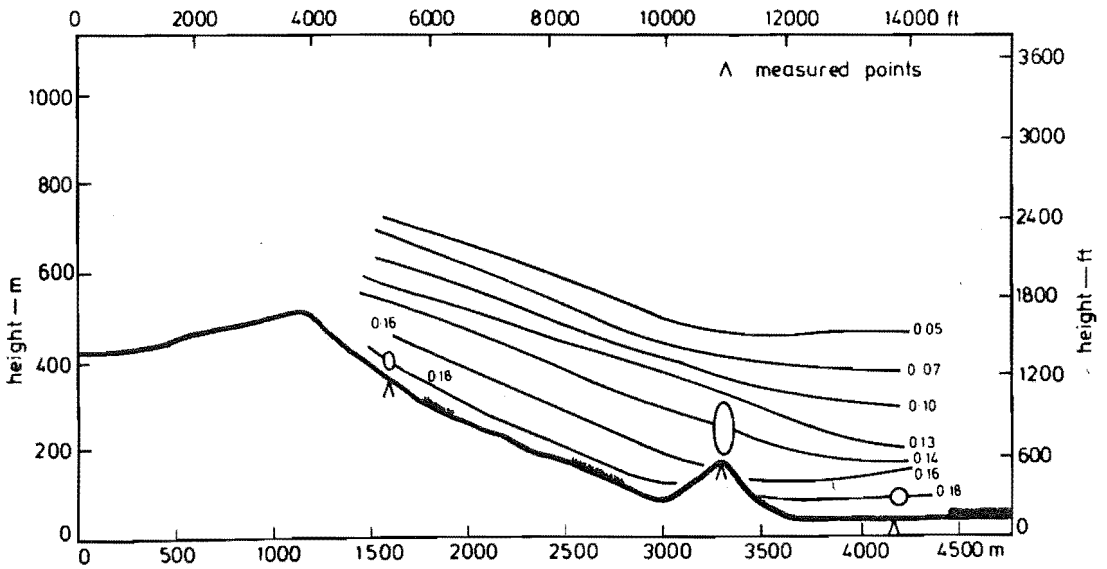

FIG 8.75 ISOTURBS FOR MODEL B WITH ROUGHNESS, LATERAL CROSS SECTION 6

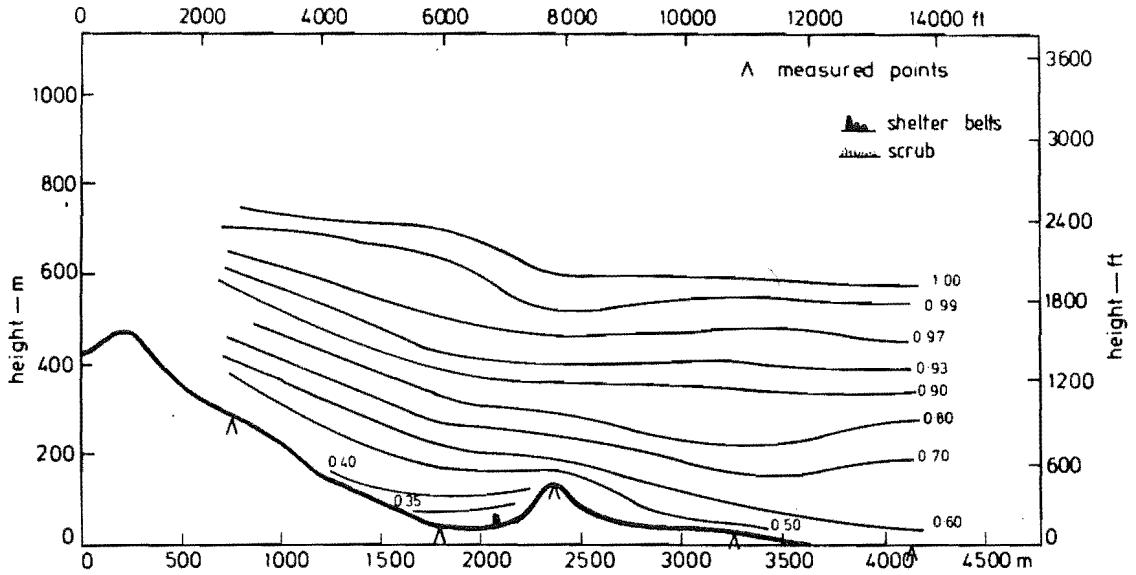

FIG 8.76 ISOTACHS FOR MODEL B WITH ROUGHNESS, LATERAL CROSS SECTION 7

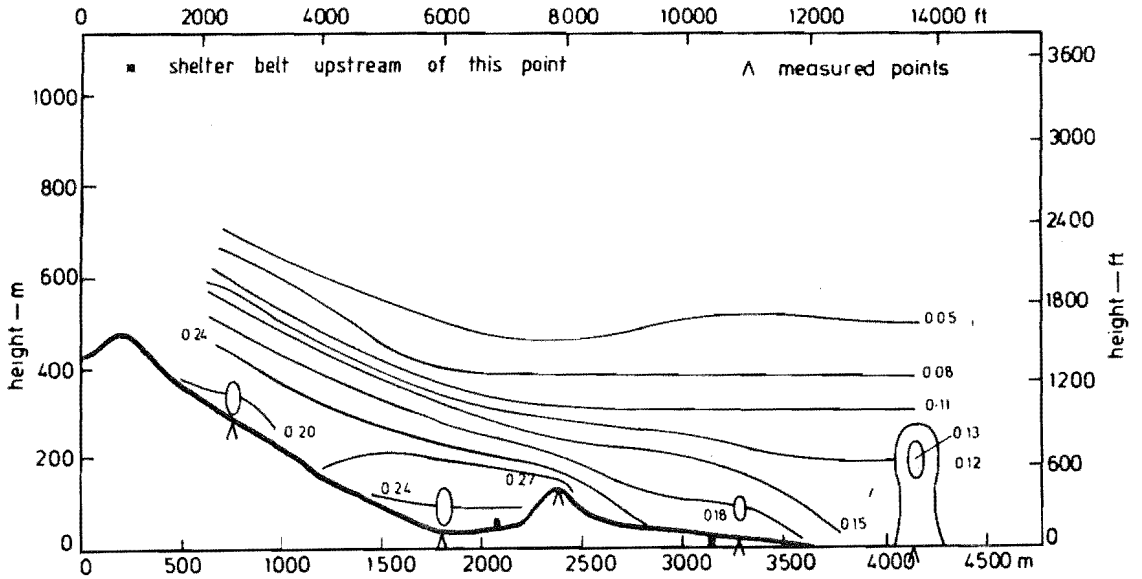

FIG 8.77 ISOTURBS FOR MODEL B WITH ROUGHNESS, LATERAL CROSS SECTION 7

This effect is caused by the shelterbelts directly upstream of this cross section. It is not clear why the 5% contour dips signifnicantly in the middle of the cross section between base scale positions 2000m and 3500m.

For cross section 2, the isotach contours indicate a reduction of velocity close to the model surface; however, the general shape of the contours remains the same as for the contoured model. The isoturb contours are almost identical to the contoured model, although there are small increases in turbulence intensity between the 2000m and 4000m base scale positions. These are caused by the several rows of shelterbelts on the approach terrain.

Cross section 3 exhibits the same trends with reduced isotach values close to the surface and corresponding isoturb increases. The contours generally follow the terrain shape more closely than those of the contoured model.

The isotachs for cross section 4 are almost identical to those for the contoured model. Point 56, located at the 500m position on the base scale, shows a reduction in velocity which can be attributed to the presence of the extensive scrub area surrounding it. The isoturb contours are affected in the same manner with an increase in turbulence intensity at point 56 from 18% on the contoured model to 30% above the scrub.

For cross section 5, the isotach contours show a general slowing of the flow close to the model surface. Point 12, see Fig. 8.12, shows a significant reduction in velocity which can only be attributed to the added upstream roughness. The isoturb contours are similar to those for the contoured model but show a small increase in turbulence intensity in the bottom 10mm of the boundary layer.

Cross section 6 does not show any significant variations from the results for the contoured model.

Cross section 7 shows that significant changes in both the isotachs and isoturbs have occurred. The isotach contour close to the model surface is reduced from 0.60 on the contoured model to 0.50 on the roughness added model.

Isoturbs close to the model surface generally show an increase in turbulence intensity. Point 6, located at the 4000m position on the base scale, shows a constant level of turbulence up to approximately 50mm, 200m on prototype. This point is situated on mud flats, which were represented

by smooth chip (particle) board. The reduction in roughness over this surface could be influencing the lower part of the boundary layer, i.e., reducing the turbulence intensity directly above the surface. As the height increases, so the turbulence being measured becomes a function of the upstream terrain, resulting in the extended area of 12% turbulence.

Longitudinal cross sections XX, YY, UU and VV are presented in Figs 8.78 to 8.85.

The isotach and isoturb contours for longitudinal cross section XX are essentially the same for both the contoured and roughness added models. The cross section plotted does not extend very far on to the flat approach terrain and therefore does not show the effect of the shelterbelts.

Similarly, cross section YY is is essentially the same for both forms of construction. The only point to note is a small increase in turbulence values on the leeward side of the Port Hills ridge, base scale points 0 to 2000m.

The isotach contours for cross section UU clearly show differences in comparison to the contoured model. The windward side of the Gebbies Pass saddle shows definite velocity reductions in the bottom 10mm of the boundary layer. Velocity reductions on the saddle at point 12, are also significant. The contours on the leeward side of the saddle are almost the same as for the contoured model. The same pattern applies to the isoturbs for this cross section, as shown in Fig. 8.83.

Similarly, cross section VV indicates small changes in the windward contours close to the model surface, but generally the flow patterns are much the same.

Table 8.1 presents the normalised velocities and gradient heights for the cross sections measured for model B in the contoured and roughness added forms. From this data the magnitude of the variations can be seen and it is apparent that many of these are within the experimental error of the data recording procedure.

The speed-up ratio areas are presented on the map in Fig. 8.86. A comparison with the speed-up ratio areas in Fig. 8.60 clearly shows the general slowing of the flow approaching the Gebbies Pass saddle. However, velocities on the tops of knobs and ridges appear to be slightly higher than those on the contoured model. The information to be gained from these diagrams is not the location of the boundaries between the various speed-up

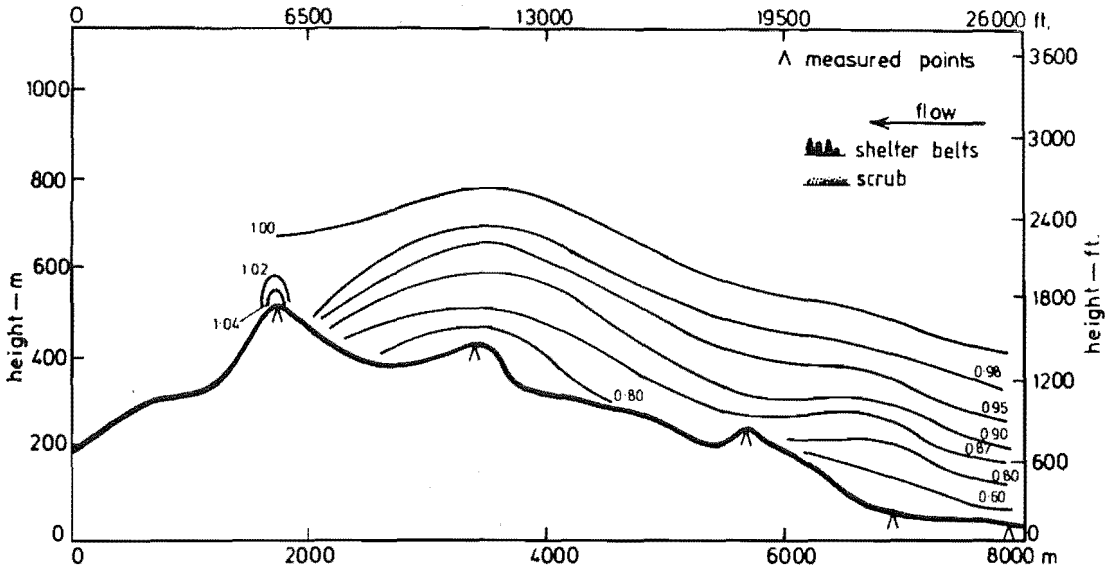

FIG 8.78 ISOTACHS FOR MODEL B WITH ROUGHNESS, LONGITUDINAL CROSS-SECTION XX

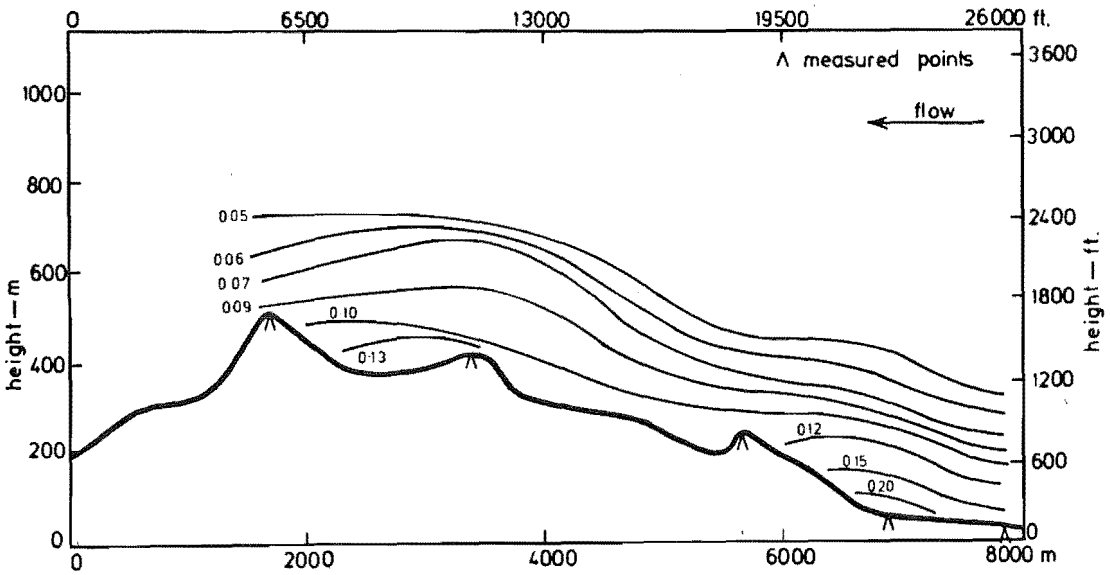

FIG 8.79 ISOTURBS FOR MODEL B WITH ROUGHNESS, LONGITUDINAL CROSS-SECTION XX

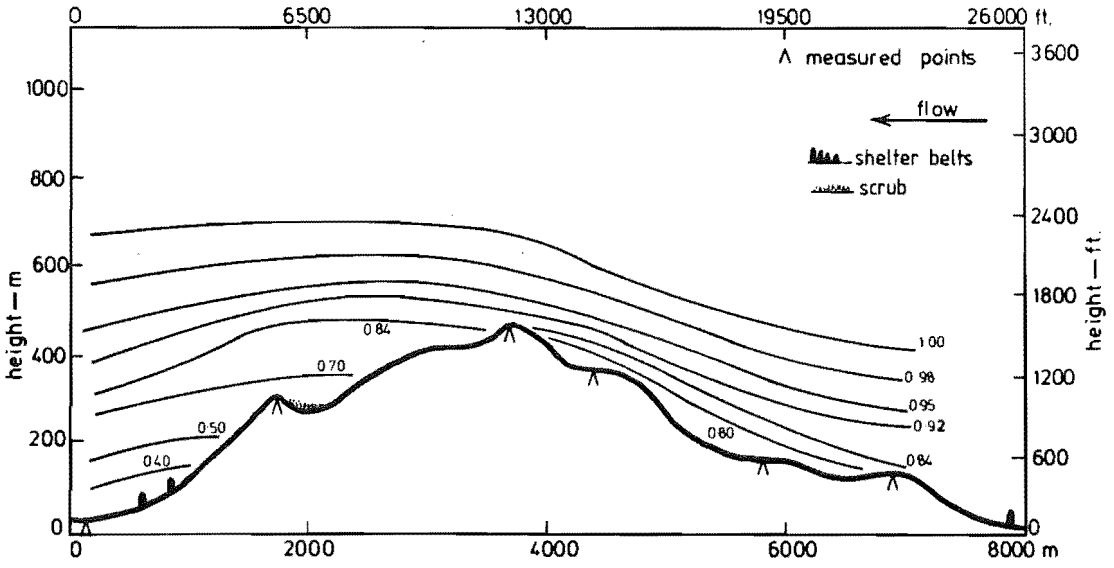

FIG 8.80 ISOTACHS FOR MODEL B WITH ROUGHNESS, LONGITUDINAL CROSS-SECTION YY

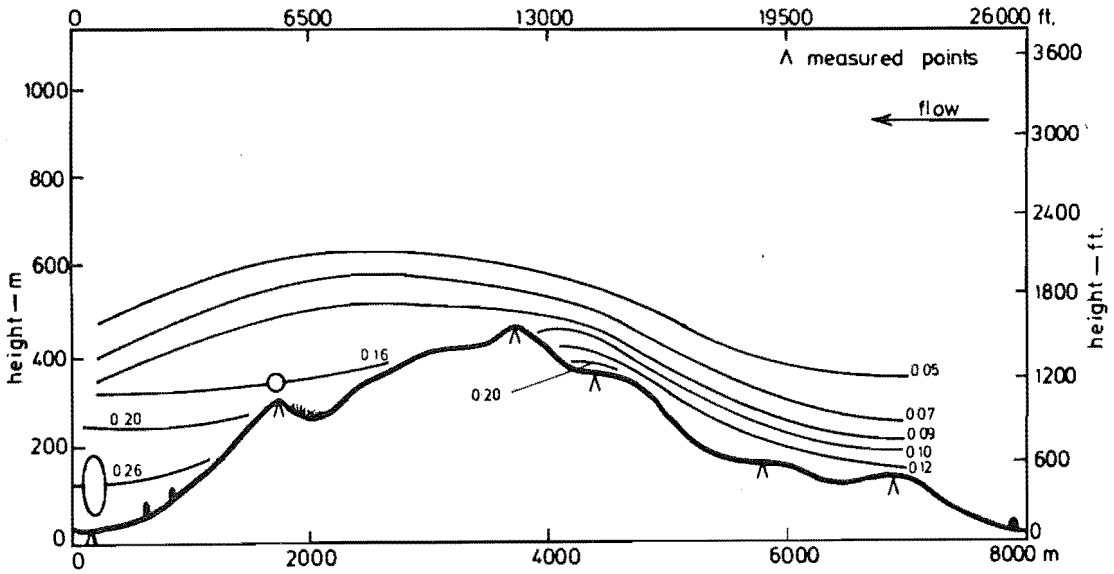

FIG 8.81 ISOTURBS FOR MODEL B WITH ROUGHNESS, LONGITUDINAL CROSS-SECTION YY

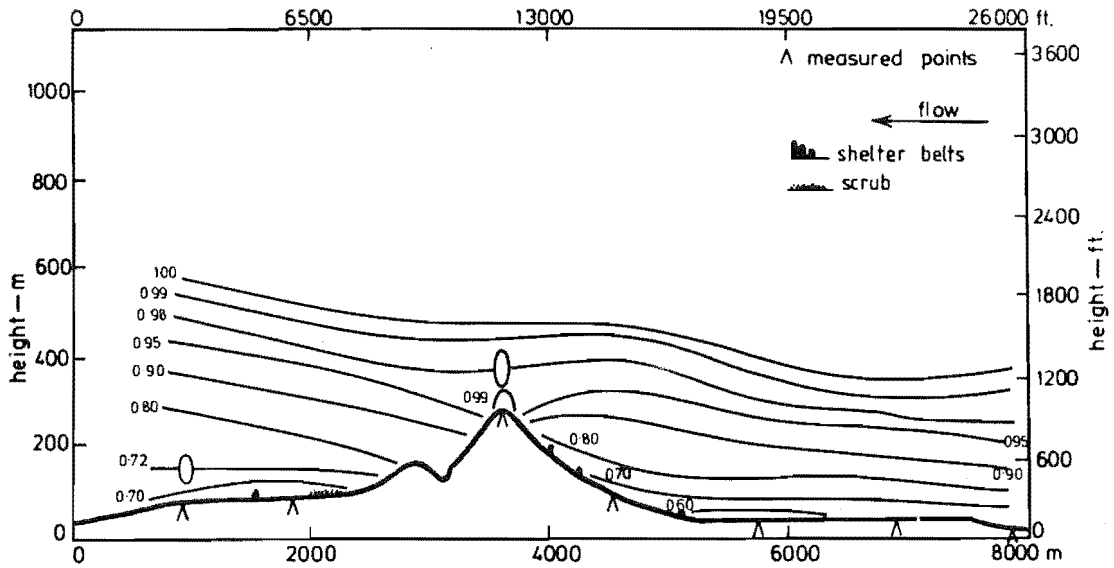

FIG 8.82 ISOTACHS FOR MODEL B WITH ROUGHNESS, LONGITUDINAL CROSS-SECTION UU

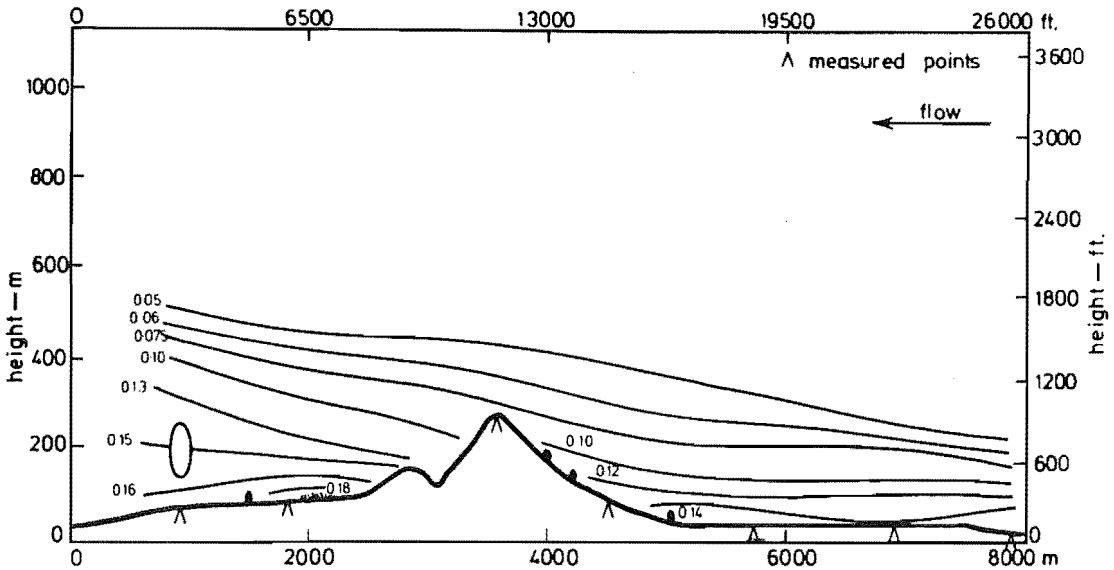

FIG 8.83 ISOTURBS FOR MODEL B WITH ROUGHNESS, LONGITUDINAL CROSS-SECTION UU

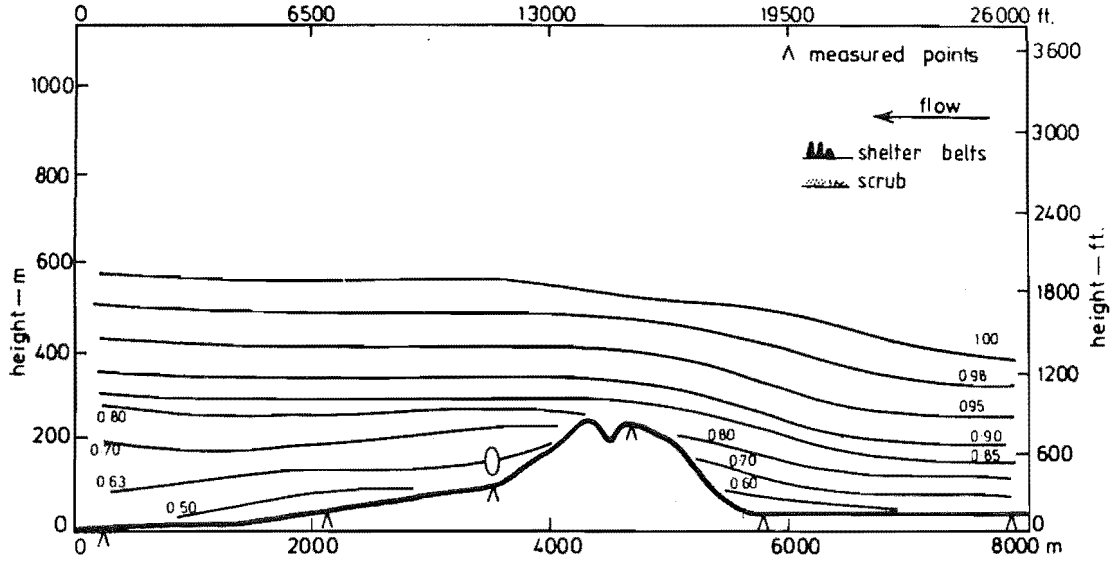

FIG 8.84 ISOTACHS FOR MODEL B WITH ROUGHNESS, LONGITUDINAL CROSS-SECTION VV

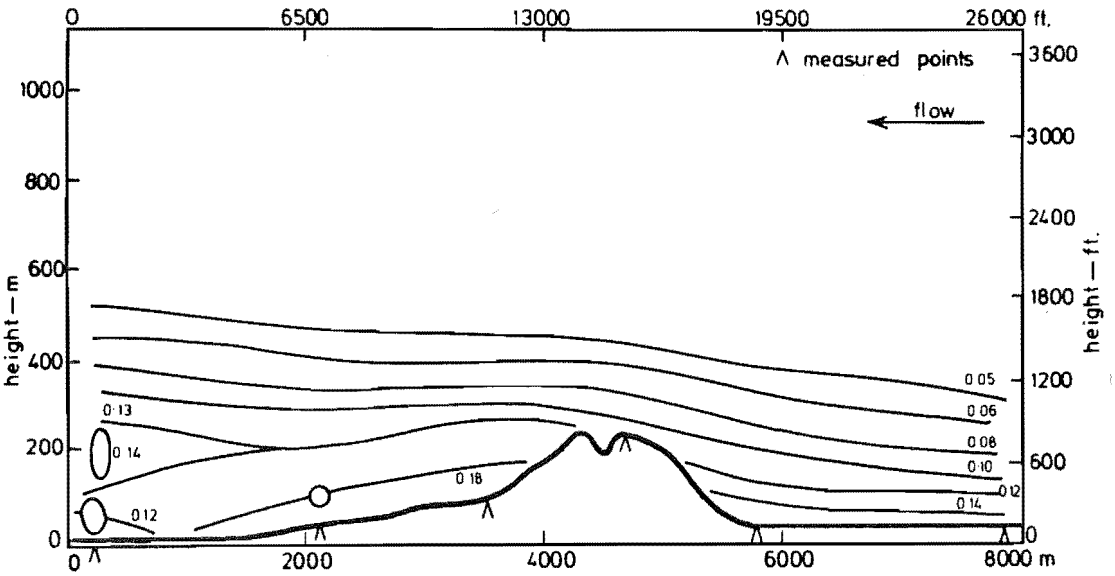

FIG 8.85 ISOTURBS FOR MODEL B WITH ROUGHNESS, LONGITUDINAL CROSS-SECTION VV

Height Z (mm)					
	Lateral Cross Section 1				
δ	110 (100)	100 (90)	110 (90)		
5	0.60 (0.60)	0.65 (0.60)	0.64 (0.65)		
3	0.55 (0.55)	0.60 (0.56)	0.60 (0.62)		
	21	40	39		
	Lateral Cross Section 2				
δ	120 (110)	80 (70)	100 (80)	120 (100)	
5	0.45 (0.44)	0.86 (0.84)	0.66 (0.64)	0.63 (0.61)	
3	0.39 (0.38)	0.84 (0.82)	0.62 (0.61)	0.59 (0.57)	
	38	20	37	34	
	Lateral Cross Section 3				
δ	80 (80)	80 (80)	130 (90)	90 (90)	150 (120)
5	0.86 (0.87)	0.74 (0.75)	0.63 (0.59)	0.66 (0.66)	0.58 (0.56)
3	0.84 (0.86)	0.69 (0.72)	0.59 (0.55)	0.64 (0.62)	0.54 (0.53)
	19	32	31	62	29
	Lateral Cross Section 4				
δ	100 (110)	60 (60)	110 (100)	90 (70)	
5	0.52 (0.40)	0.63 (0.66)	0.69 (0.70)	0.83 (0.83)	
3	0.48 (*)	0.52 (0.51)	0.64 (0.68)	0.80 (0.82)	
	56	27	24	17	
	Lateral Cross Section 5				
δ	100 (90)	60 (80)	50 (50)	140 (120)	
5	0.74 (0.76)	0.84 (0.77)	1.02 (0.99)	0.59 (0.63)	
3	0.61 (0.64)	0.82 (0.76)	1.02 (0.98)	0.59 (0.62)	
	58	13	12	7	
	Lateral Cross Section 6				
δ	110 (110)	100 (100)	150 (130)		
5	0.45 (0.42)	0.77 (0.85)	0.41 (0.52)		
3	0.44 (0.43)	0.77 (0.85)	0.41 (0.49)		
	9	10	41		
	Lateral Cross Section 7				
δ	130 (120)	150 (120)	160 (150)	160 (150)	
5	0.45 (0.47)	0.50 (0.46)	0.58 (0.49)	0.57 (0.58)	
3	0.44 (0.47)	0.47 (0.43)	0.55 (0.47)	0.54 (0.55)	
	4	2	25	6	

Values in brackets are for roughness added model.

TABLE 8.1: Normalised velocity readings close to model surface for Model B. Contoured and with roughness added.

Height Z (mm)												
	Longitudinal Cross Section XX											
δ	110	(100)	120	(110)	80	(80)	100	(90)	15	(30)		
5	0.60	(0.60)	0.45	(0.44)	0.86	(0.87)	0.74	(0.76)	1.01	(1.03)		
3	0.55	(0.55)	0.39	(0.38)	0.84	(0.86)	0.61	(0.64)	1.00	(1.04)		
	21		38		19		58		8			
	Longitudinal Cross Section YY											
δ	80	(70)	80	(80)	60	(60)	40	(50)	100	(100)	160	(170)
5	0.86	(0.84)	0.74	(0.75)	0.63	(0.66)	0.93	(0.92)	0.82	(0.73)	0.35	(0.32)
3	0.84	(0.82)	0.69	(0.72)	0.52	(0.51)	0.92	(0.91)	0.83	(0.73)	0.31	(0.30)
	20		32		27		15		59		1	
	Longitudinal Cross Section UU											
δ	100	(90)	100	(80)	130	(90)	110	(100)	50	(50)	130	(110)
5	0.65	(0.60)	0.66	(0.64)	0.63	(0.59)	0.69	(0.70)	1.02	(0.99)	0.67	(0.65)
3	0.60	(0.56)	0.62	(0.61)	0.59	(0.55)	0.64	(0.68)	1.02	(0.98)	0.65	(0.59)
	40		37		31		24		12		60	
	Longitudinal Cross Section VV											
δ	110	(90)	120	(100)	150	(120)	90	(70)	140	(120)	150	(130)
5	0.64	(0.65)	0.63	(0.61)	0.58	(0.56)	0.83	(0.83)	0.59	(0.63)	0.41	(0.52)
3	0.60	(0.62)	0.59	(0.57)	0.54	(0.53)	0.80	(0.82)	0.59	(0.62)	0.41	(0.49)
	39		34		29		17		7		41	

Height Z (mm)												
	Longitudinal Cross Section XX											
δ	110	(100)	120	(110)	80	(80)	100	(90)	15	(30)		
5	0.60	(0.60)	0.45	(0.44)	0.86	(0.87)	0.74	(0.76)	1.01	(1.03)		
3	0.55	(0.55)	0.39	(0.38)	0.84	(0.86)	0.61	(0.64)	1.00	(1.04)		
	21		38		19		58		8			
	Longitudinal Cross Section YY											
δ	80	(70)	80	(80)	60	(60)	40	(50)	100	(100)	160	(170)
5	0.86	(0.84)	0.74	(0.75)	0.63	(0.66)	0.93	(0.92)	0.82	(0.73)	0.35	(0.32)
3	0.84	(0.82)	0.69	(0.72)	0.52	(0.51)	0.92	(0.91)	0.83	(0.73)	0.31	(0.30)
	20		32		27		15		59		1	
	Longitudinal Cross Section UU											
δ	100	(90)	100	(80)	130	(90)	110	(100)	50	(50)	130	(110)
5	0.65	(0.60)	0.66	(0.64)	0.63	(0.59)	0.69	(0.70)	1.02	(0.99)	0.67	(0.65)
3	0.60	(0.56)	0.62	(0.61)	0.59	(0.55)	0.64	(0.68)	1.02	(0.98)	0.65	(0.59)
	40		37		31		24		12		60	
	Longitudinal Cross Section VV											
δ	110	(90)	120	(100)	150	(120)	90	(70)	140	(120)	150	(130)
5	0.64	(0.65)	0.63	(0.61)	0.58	(0.56)	0.83	(0.83)	0.59	(0.63)	0.41	(0.52)
3	0.60	(0.62)	0.59	(0.57)	0.54	(0.53)	0.80	(0.82)	0.59	(0.62)	0.41	(0.49)
	39		34		29		17		7		41	

Values in brackets are for roughness added model.

TABLE 8.1 (Continued): Normalised velocity readings close to model surface for Model B. Contoured and with roughness added.

Roughness added Model

$Z = 10\,mm$

$Z_p = 40\,m$

$$\frac{\bar{U}_{10}/\bar{U}_6\,|_{pt}}{\bar{U}_{10}/\bar{U}_6\,|_{ref\ pt}} \times 100$$

151 - 180

141 - 150

121 - 140

101 - 120

81 - 100

71 - 80

61 - 70

0 - 60

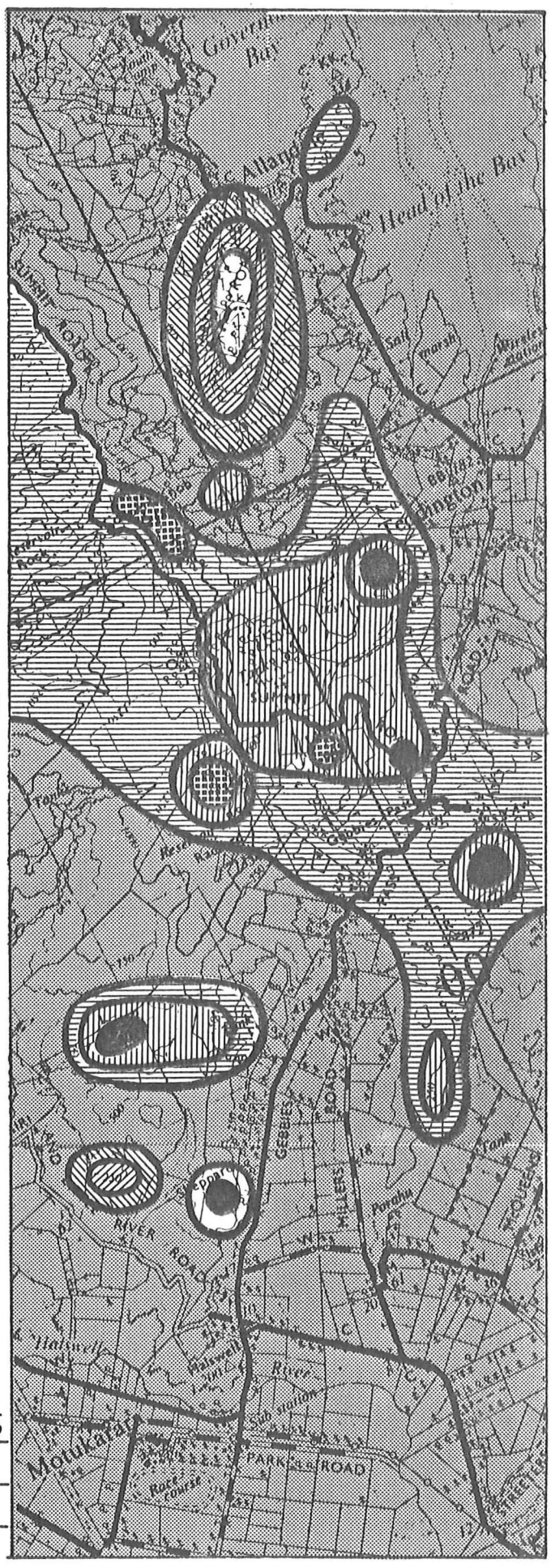

FIG 8·86
SPEED-UP RATIO AREAS FOR MODEL B WITH ROUGHNESS ADDED
Z_p = 40m

ratios, but the general areas of higher velocities and the variation of the magnitude of the speed-up. In terms of these factors, Fig. 8.86 clearly shows the favourable speed-up effects of the whole of the Gebbies Pass saddle, which could be the result of a funnelling effect.

Probably the most significant point arising from the hot film survey was the general slowing of the flow close to the model surface after the addition of the roughness elements.

This was the expected effect, but it was one that was not clearly apparent during the analysis of model A. However, model B does have significantly more added roughness by way of shelterbelts in the approach flow part of the model. It will therefore be interesting to compare the correlation coefficient values for models A and B.

Extremely high correlation coefficients in excess of 0.96 were calculated for model A, which showed that the addition of the roughness had little effect.

8.4.3 Correlations for Model B, Contoured vs Roughness Added

The scatter diagrams for data at heights of 5mm, 10mm and 20mm are presented in Figs 8.87, 8.88 and 8.89 respectively.

Using 31 observations or data pairs, a high correlation of 0.94 was produced. This is very close to the correlation for model A with similar forms of construction. Model B does have more shelterbelts on it than model A, and their effect was evidenced in the slowing of the flow in the lower regions of the boundary layer. The slightly lower correlation for model B compared with model A is probably the result of this fact.

The correlation at 10mm is 0.91 and at 20mm, 0.94. These variations are so small that it is considered unrealistic to try to explain them. The results for model B are essentially the same as for model A, and show that in terms of velocities, the addition of roughness elements at this scale has a very small effect on the magnitude of those velocities.

Models A and B in the roughness added forms were compared using data points common to both. Based on 15 data points, a correlation of 0.76 was calculated for the 5mm height, and 0.87 for the 20mm height. The points in the flat approach terrain were not included because they could increase the correlation unduly. Of the 15 points, 7 were on the leeward side of the Port Hills ridge, 3 were on the top of the major terrain features, and the remaining 5 were on the windward face of the Port Hills. This result

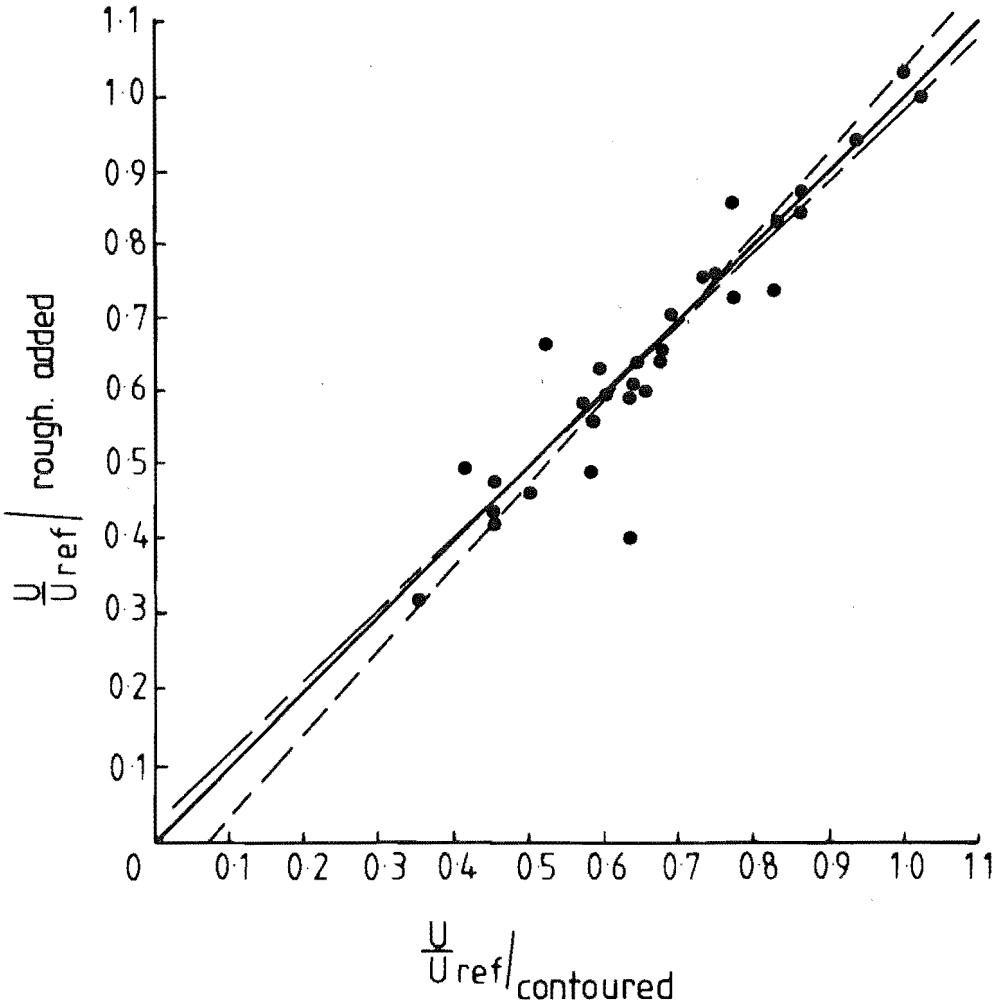

Regression lines

$$- - - - \frac{U}{U_{ref}}\Big|_{contoured} = 0 \cdot 90 \frac{U}{U_{ref}}\Big|_{rough.\ added} + 0{\cdot}078$$

$$- \text{——} - - \frac{U}{U_{ref}}\Big|_{rough.\ added} = 0 \cdot 98 \frac{U}{U_{ref}}\Big|_{contoured} + 0{\cdot}002$$

Correlation coefficient $r = 0{\cdot}94$

FIG. 8·87 SCATTER DIAGRAM FOR MODEL B AT Z = 5 mm.

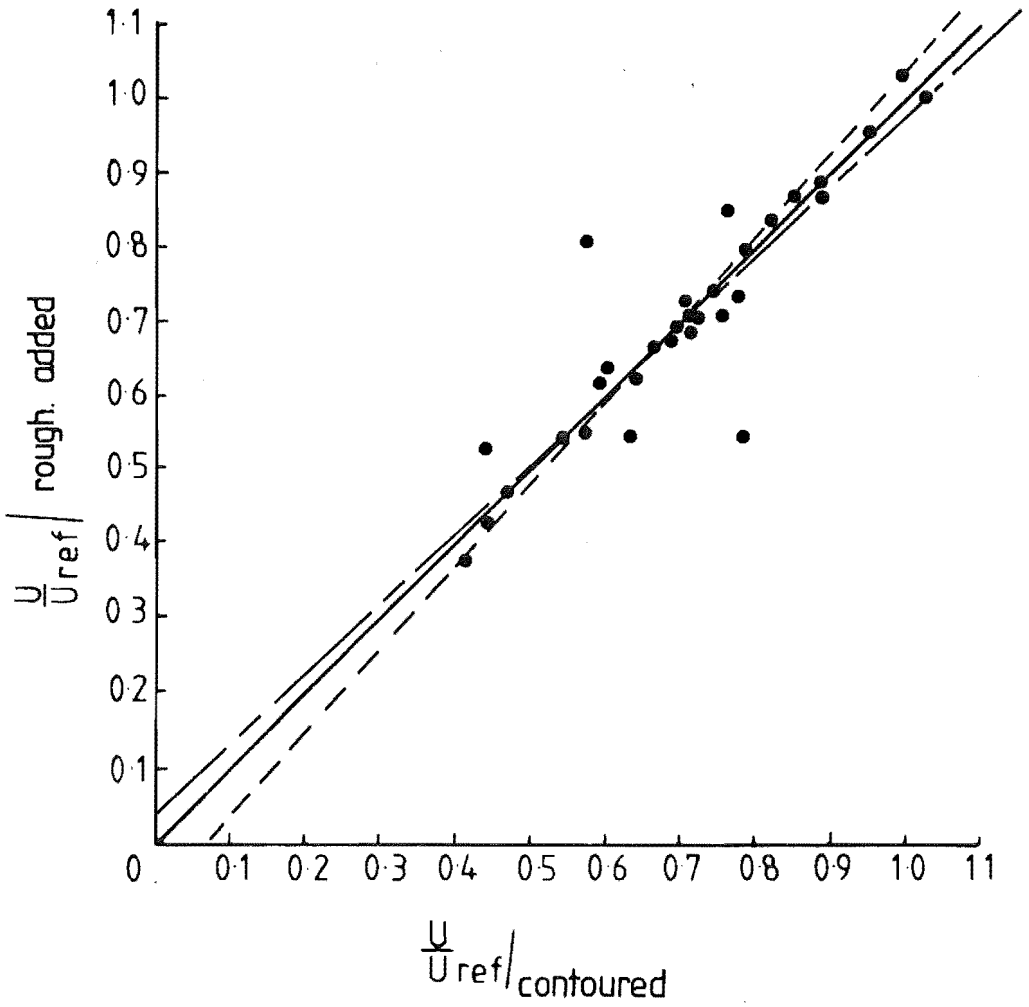

Regression lines

$$- - - - \; \frac{U}{U_{ref}}\Big|_{contoured} = 0 \cdot 88 \; \frac{U}{U_{ref}}\Big|_{rough.\ added} + 0{\cdot}087$$

$$- \text{——} - - \; \frac{U}{U_{ref}}\Big|_{rough.\ added} = 0 \cdot 93 \; \frac{U}{U_{ref}}\Big|_{contoured} + 0{\cdot}043$$

Correlation coefficient $r = 0{\cdot}91$

FIG. 8·88 SCATTER DIAGRAM FOR MODEL B AT Z = 10 mm.

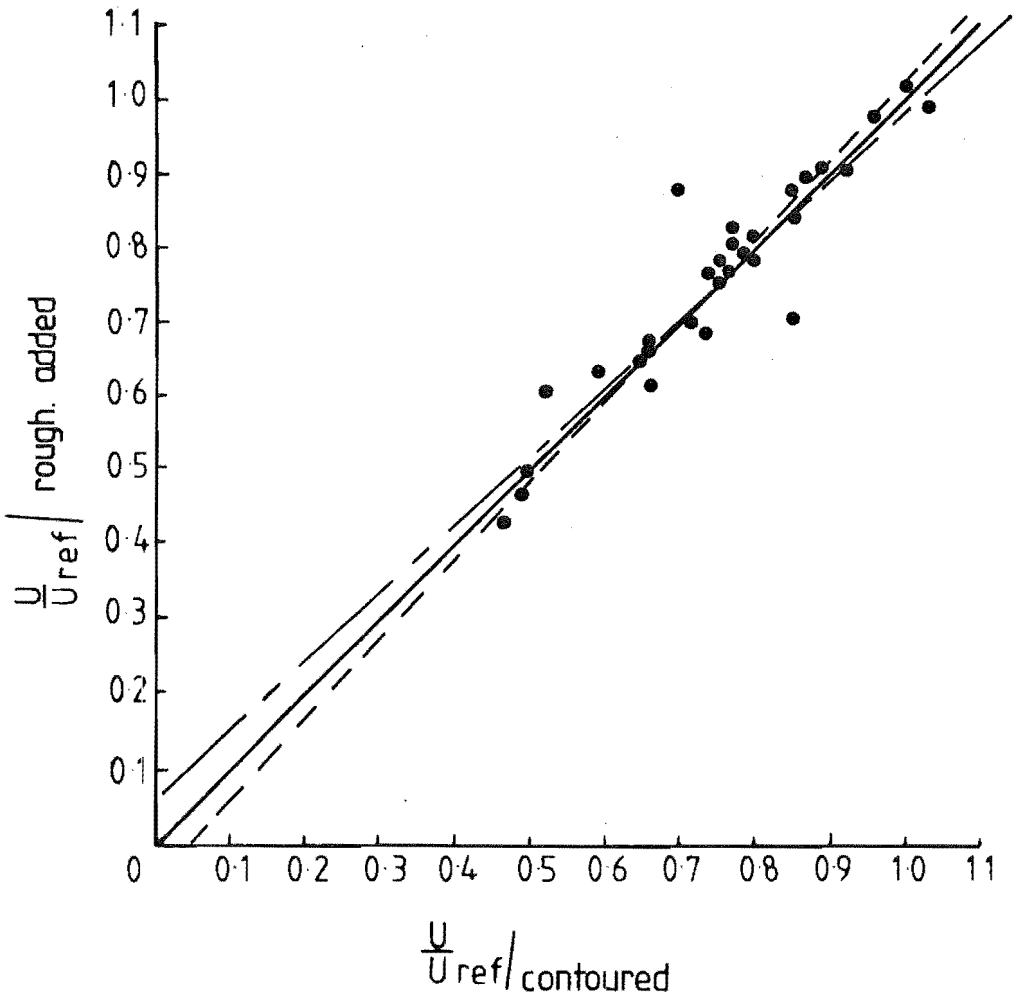

Regression lines

$$\text{- - - -}\quad \frac{U}{U_{ref}}\Big|_{contoured} = 0\cdot 94\ \frac{U}{U_{ref}}\Big|_{rough.\ added} + 0\cdot 043$$

$$\text{- - - -}\quad \frac{U}{U_{ref}}\Big|_{rough.\ added} = 0\cdot 93\ \frac{U}{U_{ref}}\Big|_{contoured} + 0\cdot 049$$

Correlation coefficient $r = 0\cdot 94$

FIG. 8·89 SCATTER DIAGRAM FOR MODEL B AT Z = 20 mm.

was viewed with confidence because it suggested that, for the roughness added model, there existed a reasonable level of correlation between the two wind directions. This information might be useful during the field phase of the research.

8.4.4 Reynolds Stress Profiles

It will be shown in Chapter 10 that the wind direction for the measured data was SSW, which coincides with the alignment of model B. Therefore, this model was used for most of the comparisons between the modelled and measured results. The $\rho\overline{uw}$ Reynolds stress profile was measured at several points along a longitudinal cross section of Model B. Those points measured were 40, 12, 10 and 25.

The resulting profiles are presented in Fig. 8.90 and show some interesting features. Approach flow point 40 was measured twice, and showed a good degree of repeatability, which was regarded as very encouraging. Point 12 is located on the top of the saddle where, as was shown in Section 8.4.1, high velocities and low turbulence intensities prevailed. This feature explains the general reduction in $\rho\overline{uw}$ values recorded at this point.

Point 10 is situated on the top of an isolated conical hill which experienced local velocity speed-up close to the model surface. This feature is demonstrated by the low $\rho\overline{uw}$ values close to the surface. The profile shows a dramatic increase in $\rho\overline{uw}$ up to a height of 100m. This corresponds to the height of the saddle upstream of this point, suggesting that turbulence being generated by the saddle is having an influence.

Confirmation of this was noted at point 25, where an increase in $\rho\overline{uw}$ was found at a height of 320m, which again corresponds very closely to the height of the saddle upstream.

8.4.5 Comparisons Between the Three Forms of Construction

To demonstrate the effect of the surface finish used on the model, the values of several parameters will be compared.

1) Velocity Profiles: The velocity profile for point 31 is presented in Fig. 8.91 and shows no significant variation between the three forms of construction. The roughness added model does show a very small reduction in velocity in the bottom 40m, which is caused by the added roughness. This point is not influenced by the terraces because it is well upstream of the major terrain features.

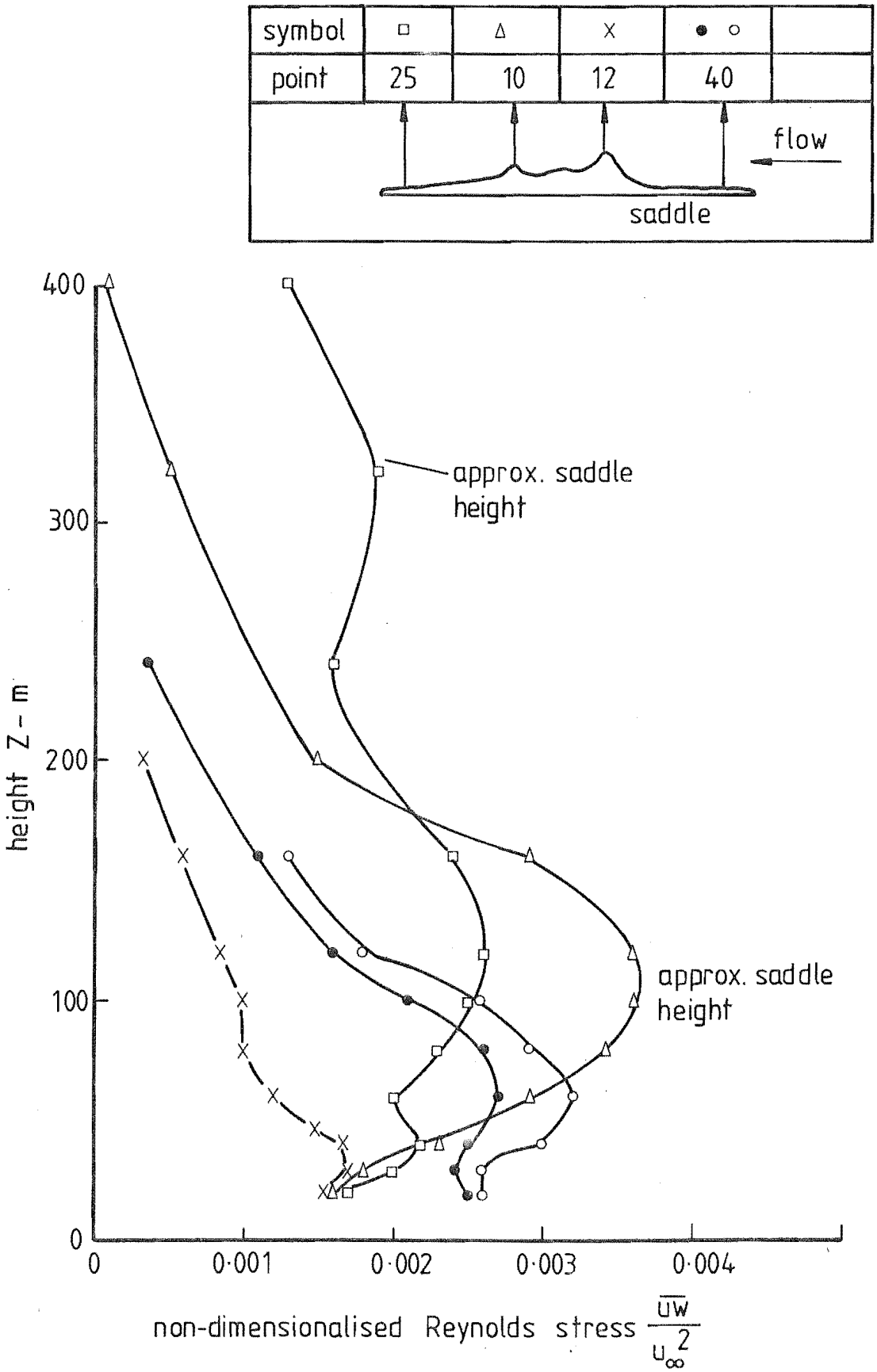

FIG 8·90 VARIATION OF $\rho\overline{uw}$ REYNOLDS STRESS OVER MODEL B

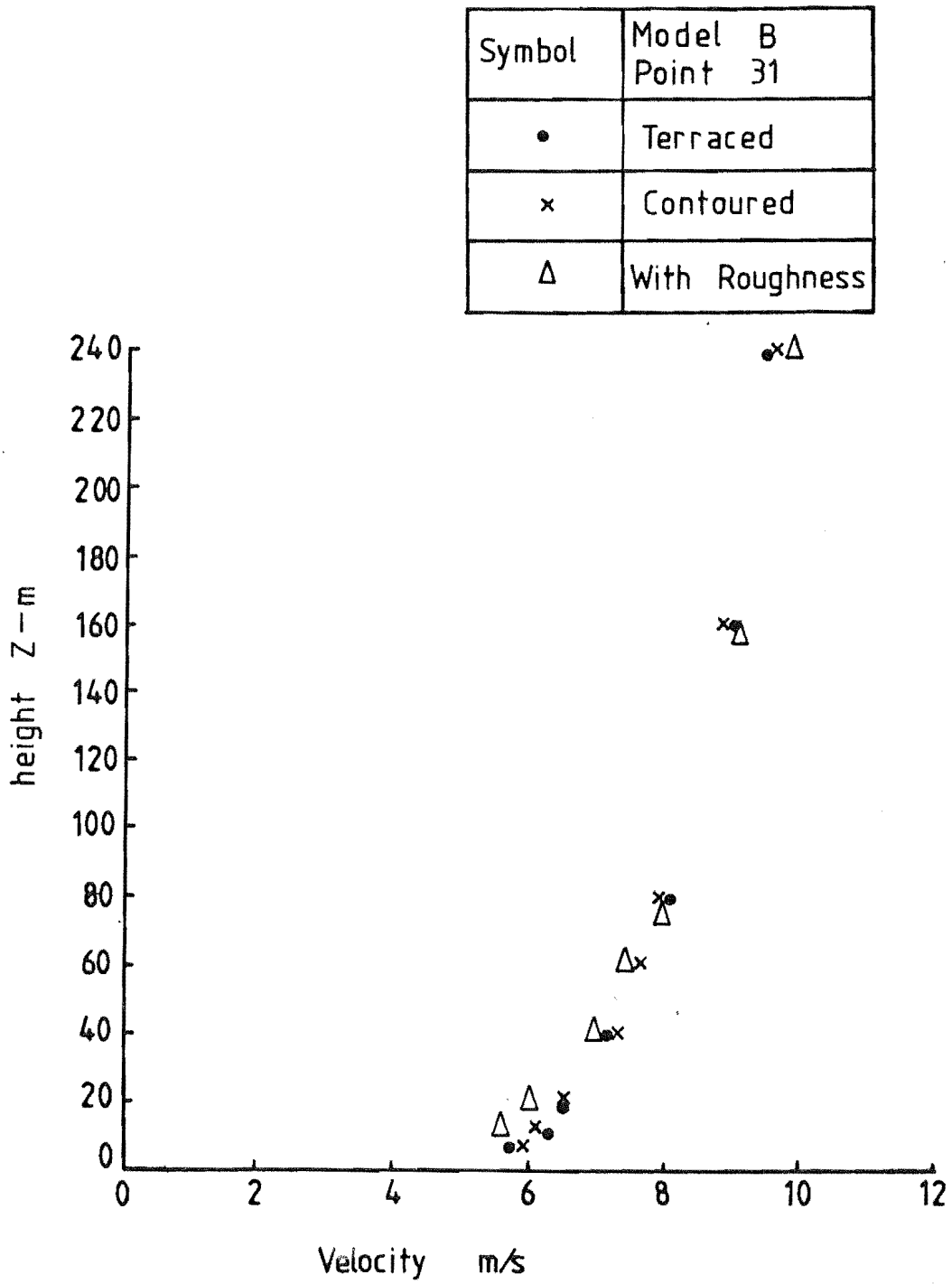

FIG 8·91 COMPARISON OF VELOCITY PROFILES FOR MODEL B POINT 31

Velocity profiles for points 15 and 12 are presented in Figs 8.92 and 8.93 respectively. The results for both points are almost identical and clearly show the velocity reductions resulting from the terraced form of construction. The contoured and roughness added profiles are almost identical, primarily due to these sites being very exposed. It is interesting to note that, although point 15 is at the top of a higher ridge than point 12, the velocity at point 12 is generally higher than that for point 15. This could be caused by a funnelling effect on the flow over the saddle. This explanation could also be applied when analysing the speed-up ratio areas in Fig. 8.86.

Point 2 is situated on the leeward side of the Port Hills ridge, and the velocity profile for the point is presented in Fig. 8.94. These results clearly show the effect of the terraces in slowing the flow, and they also show the significant degree of slowing caused by the addition of the roughness elements.

2) Turbulence Intensity Profiles: The turbulence intensity profile for point 40 is presented in Fig. 8.95. This point is far upstream of the major terrain features and therefore the terraced and contoured profiles are almost identical. In the roughness added form, several shelterbelts were added upstream of this point and these explain the increase in turbulence in the bottom 80m of the boundary layer.

This effect is duplicated at point 31, which is situated on the flat terrain in the approach to the Gebbies Pass saddle. The turbulence intensity profile for this point is given in Fig. 8.96.

The turbulence intensity profile for point 12 is presented in Fig. 8.97. This profile shows the effects of the various forms of construction very clearly. The terraced model shows turbulence intensity values of twice the magnitude of those for the other forms of construction.

The contoured and roughness added profiles are almost identical, which is explained by the exposed nature of this point.

The turbulence intensity profile for point 60 is presented in Fig. 8.98. This point is located on the leeward side of the Gebbies Pass saddle. Turbulence values are generally significantly greater for all forms of construction. The terraced model shows the highest level of turbulence and the contoured model the lowest. The effect of adding roughness is to

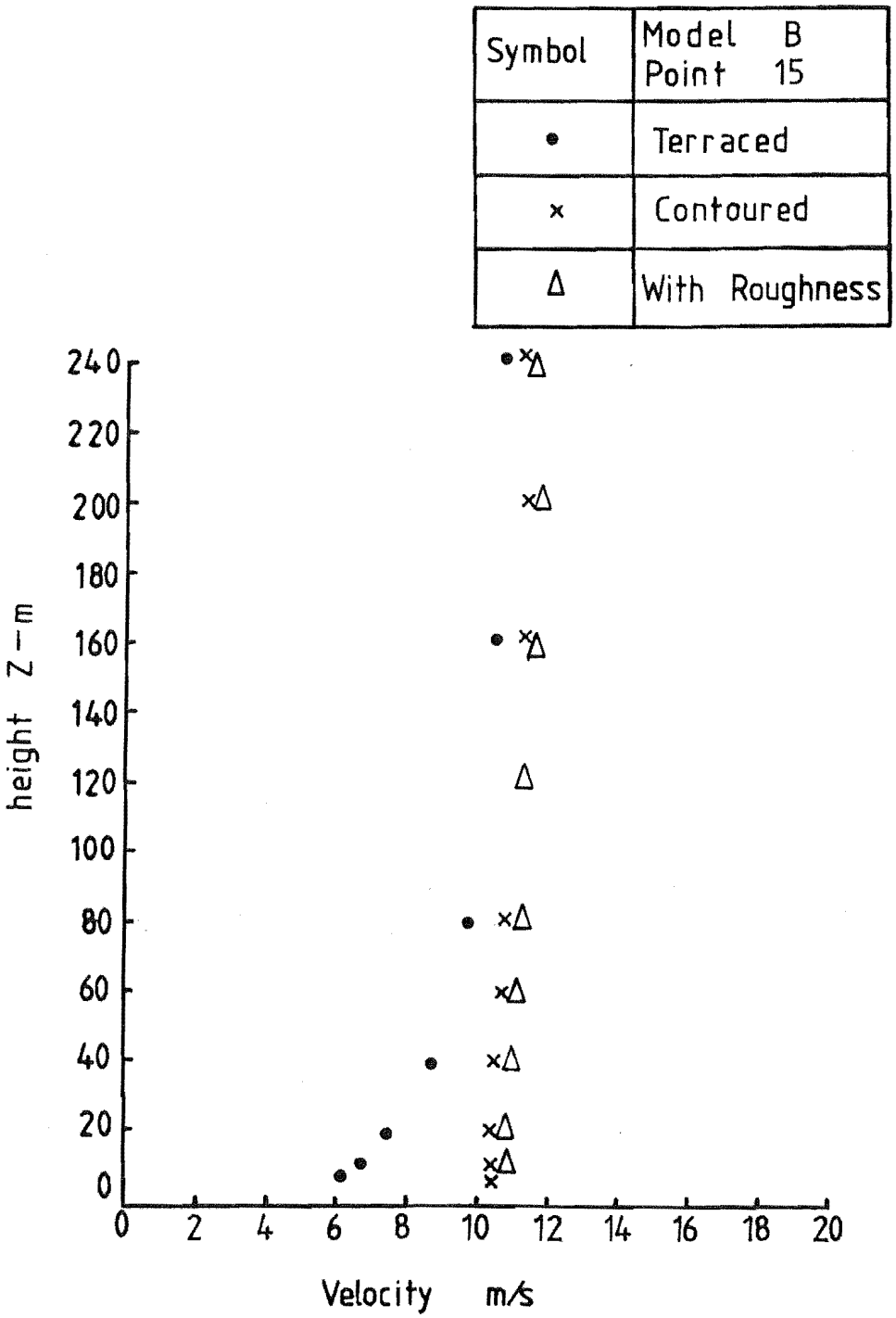

FIG 8·92 COMPARISON OF VELOCITY PROFILES FOR MODEL B POINT 15

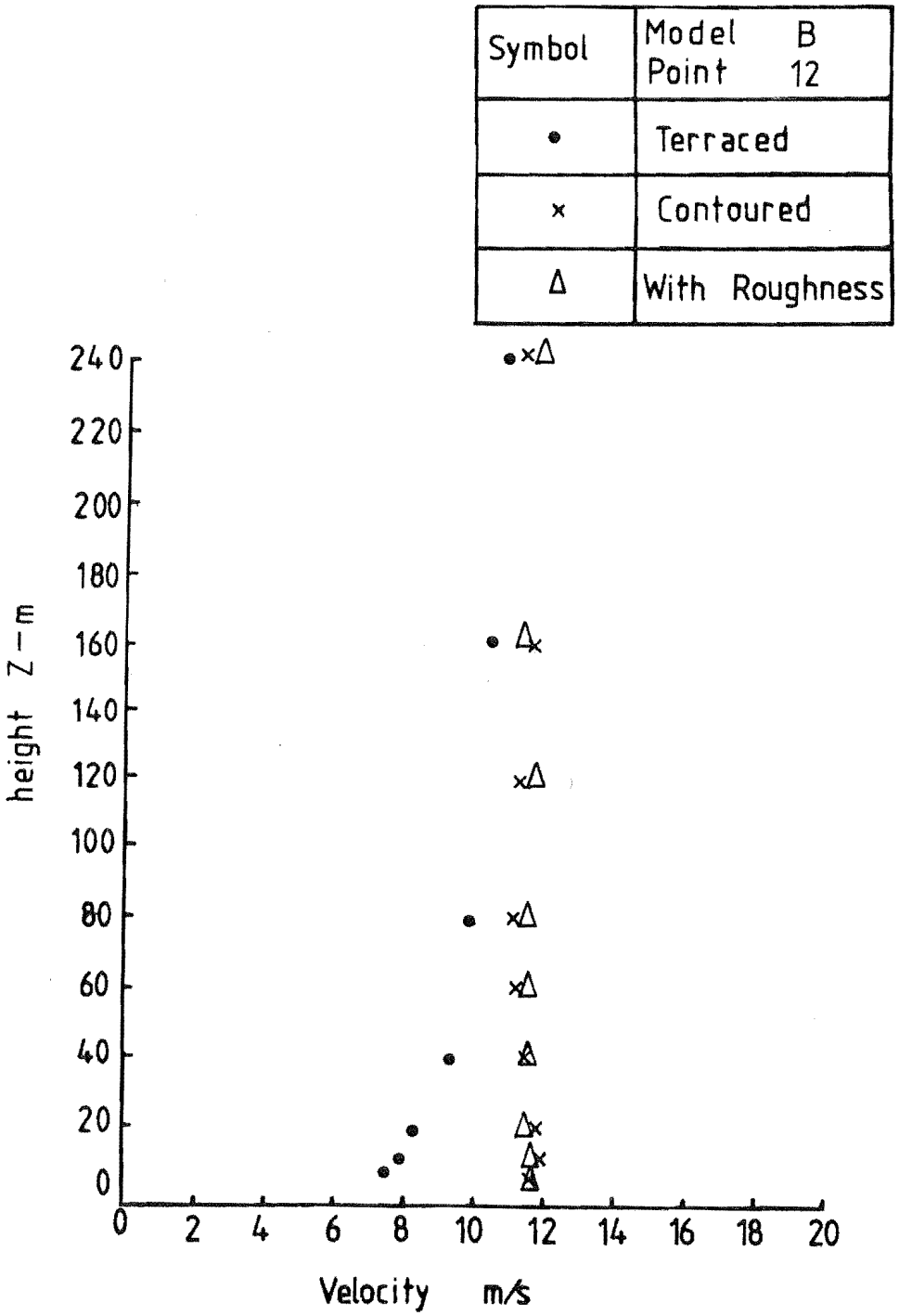

FIG 8·93 COMPARISON OF VELOCITY PROFILES FOR MODEL B POINT 12

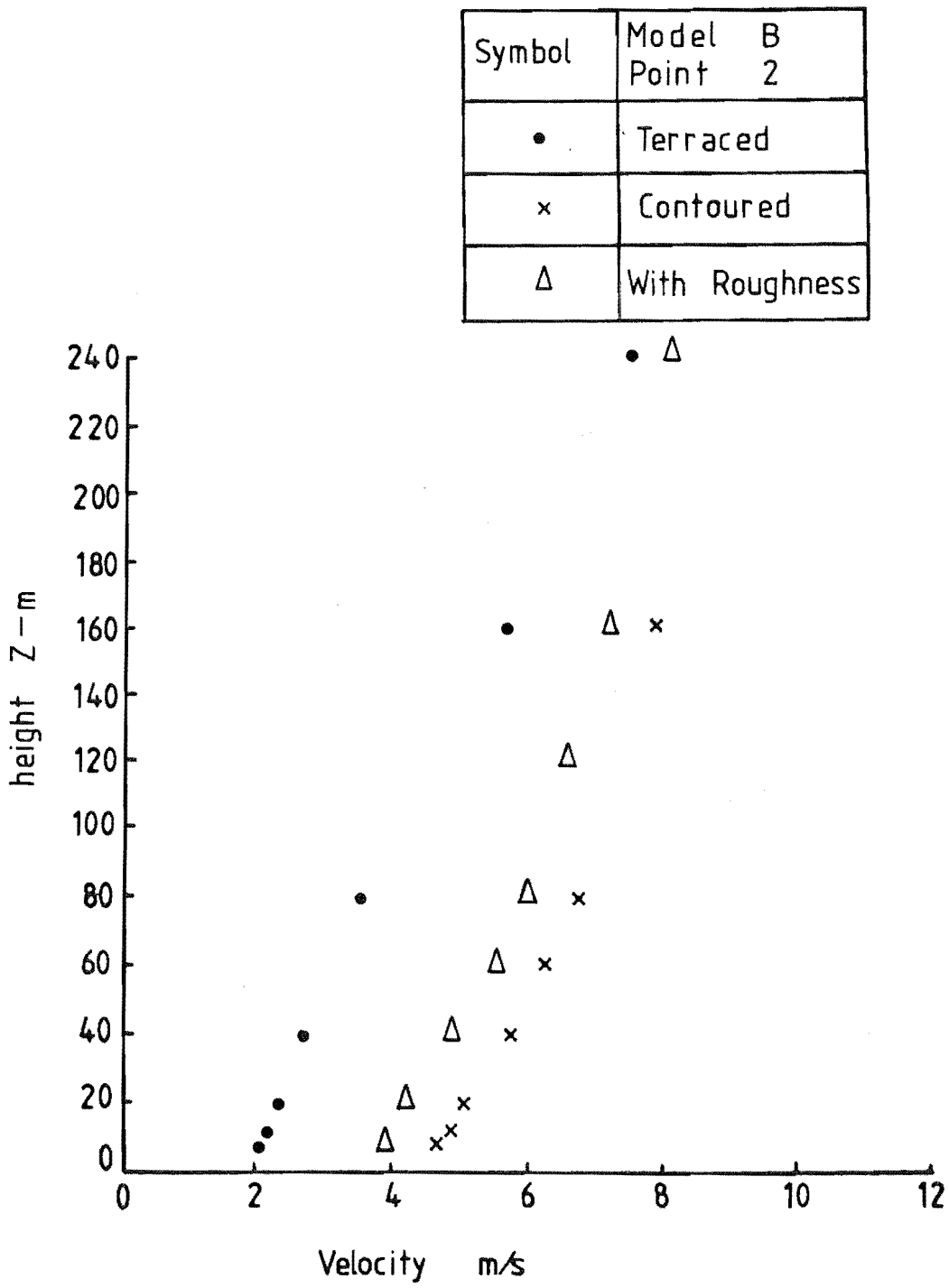

FIG 8·94 COMPARISON OF VELOCITY PROFILES FOR MODEL B POINT 2

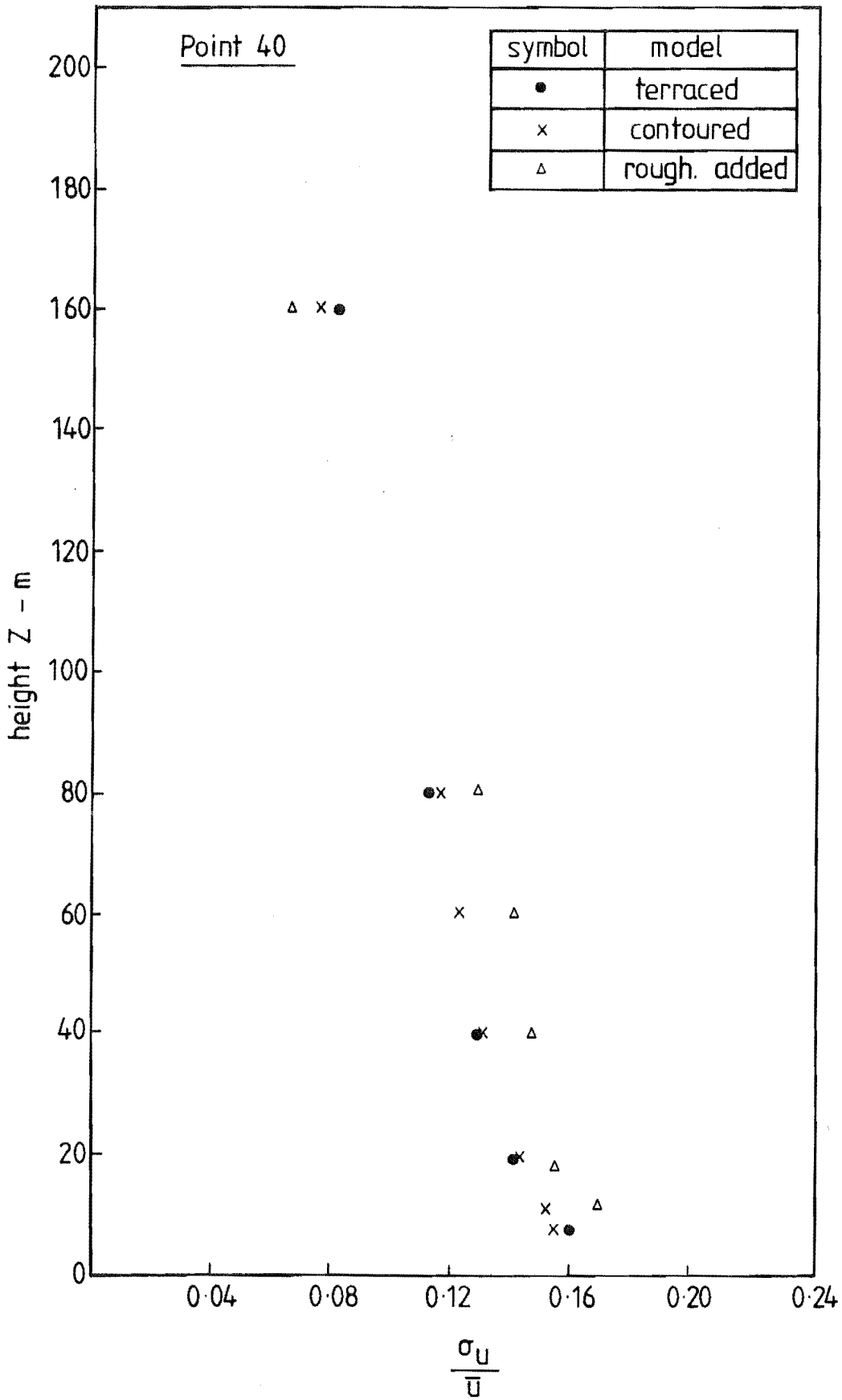

FIG. 8·95 TURBULENCE INTENSITY PROFILE COMPARISONS

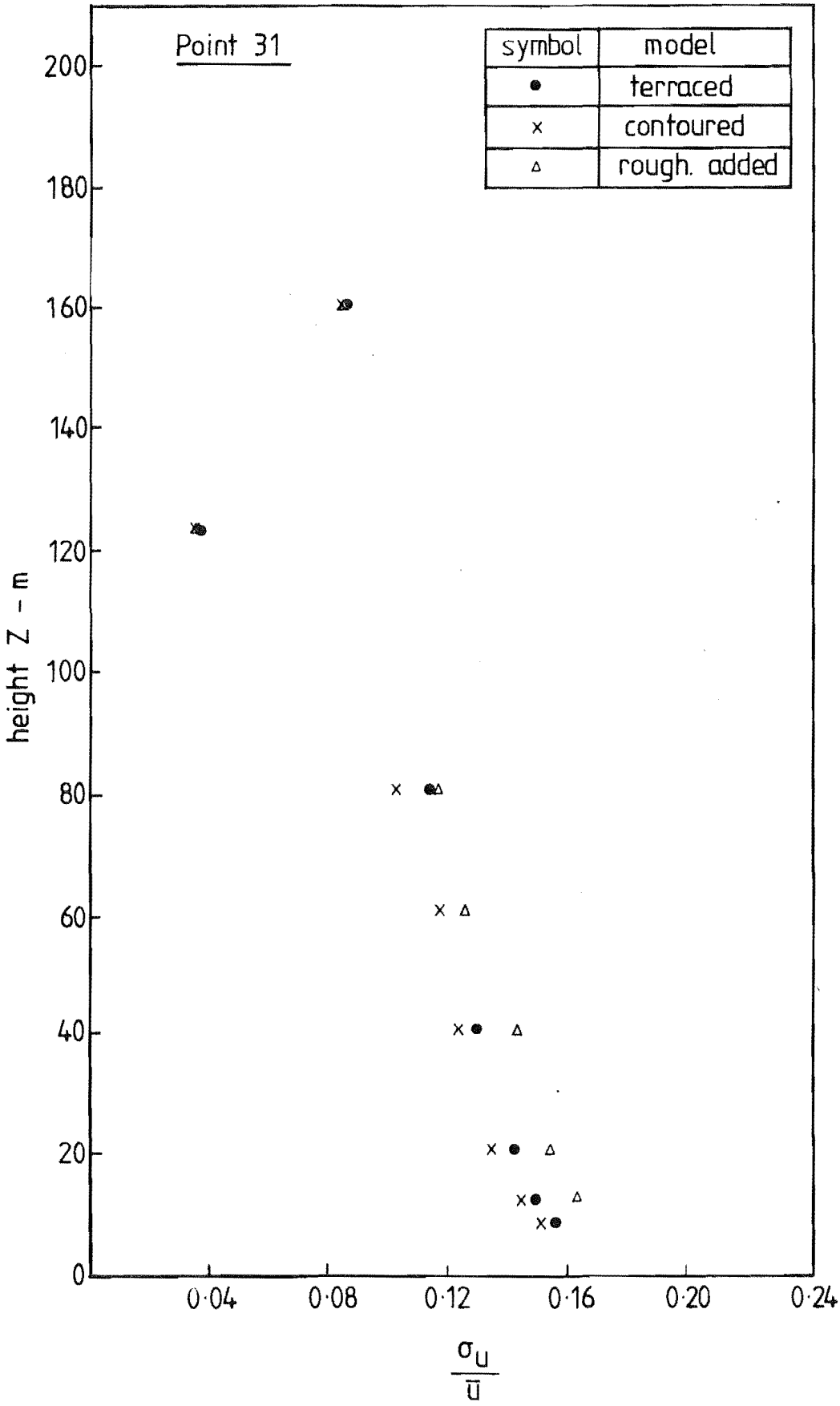

FIG. 8·96 TURBULENCE INTENSITY PROFILE COMPARISONS

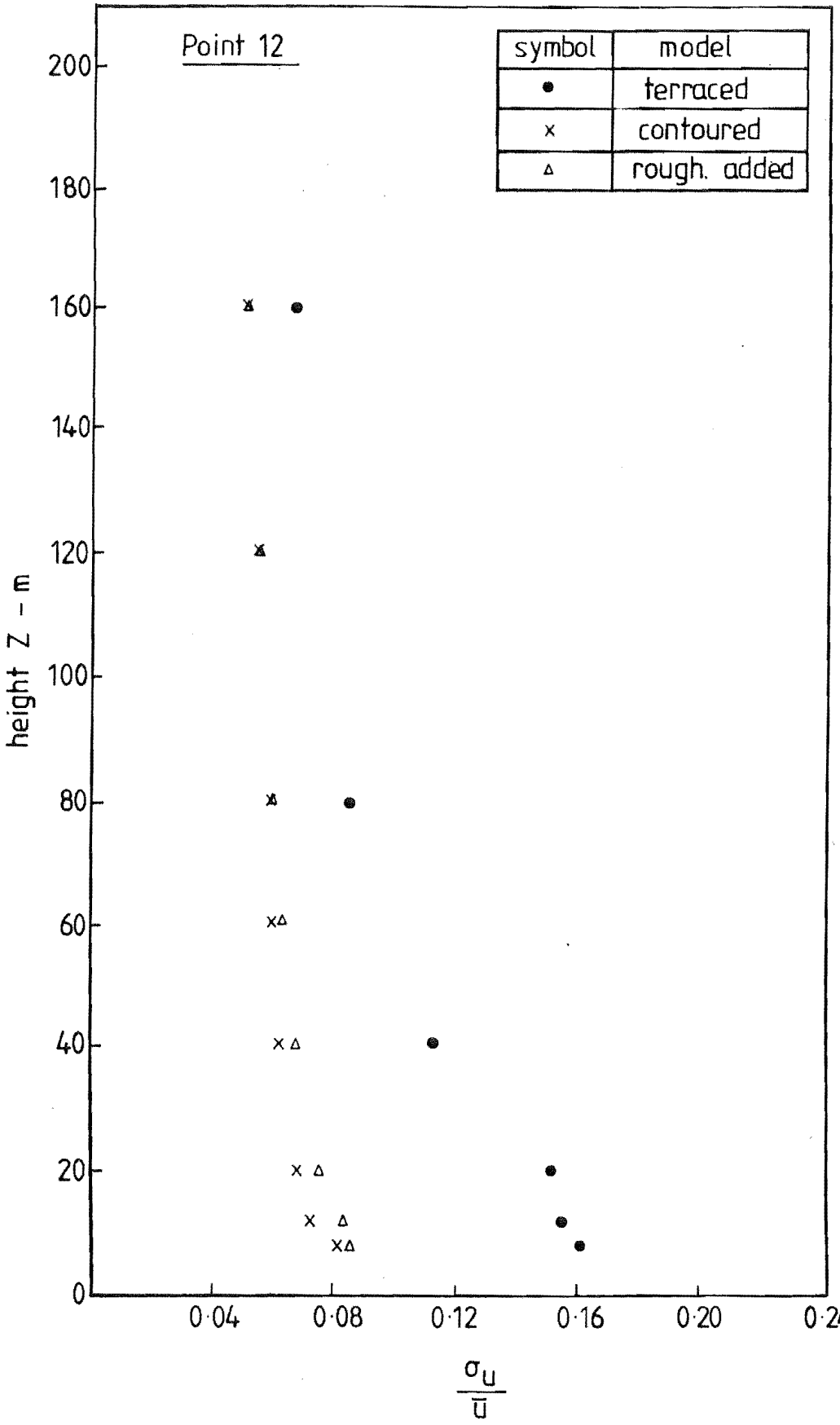

FIG. 8·97 TURBULENCE INTENSITY PROFILE COMPARISONS

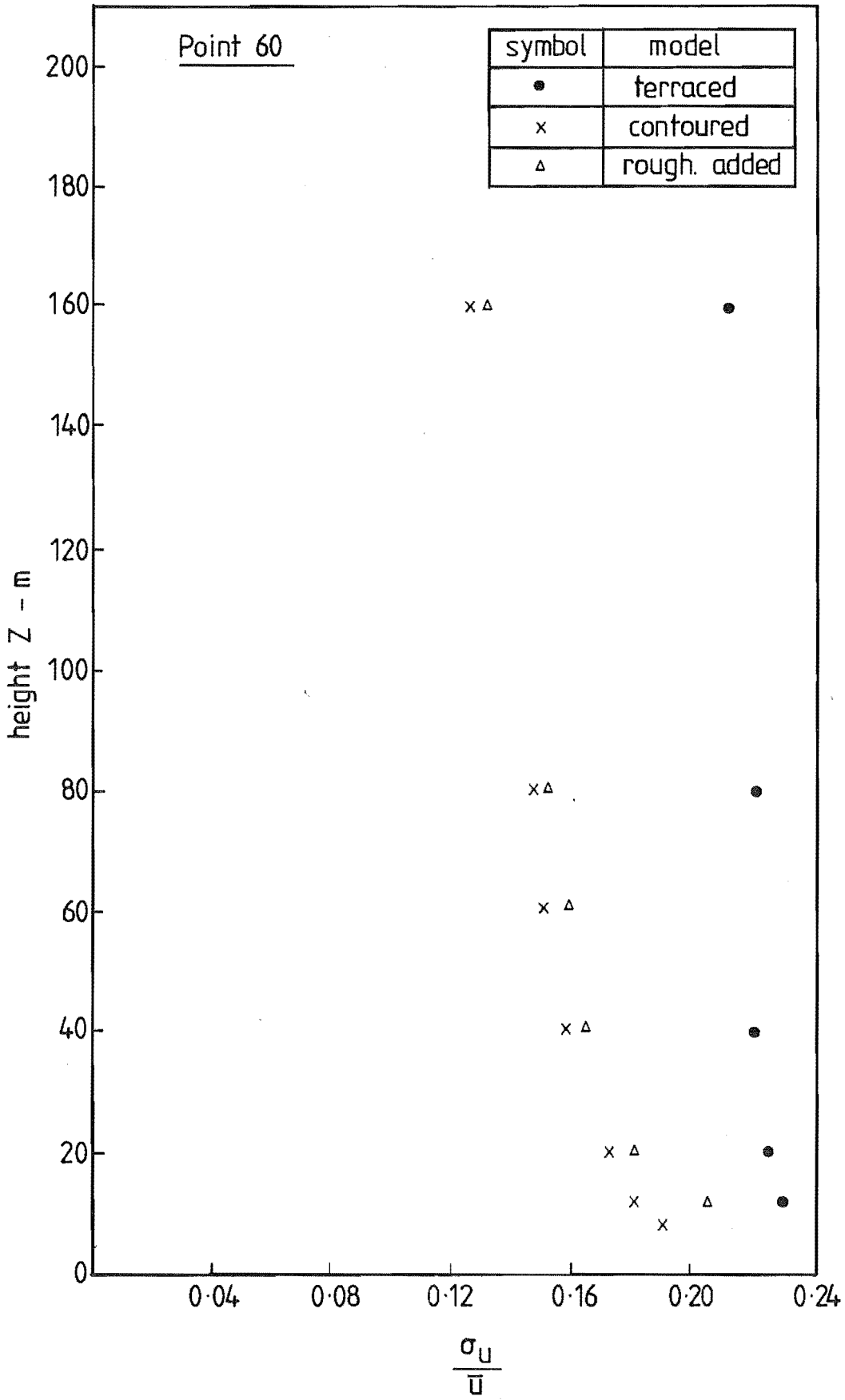

FIG. 8·98 TURBULENCE INTENSITY PROFILE COMPARISONS

increase the turbulence close to the model surface, Z < 10mm, which is to be expected.

3) Energy Spectra: The longitudinal component of the energy spectrum for point 12 is plotted in Fig. 8.99 to show the variation with the various forms of construction. Included on this graph is the spectrum for point 12 in the model A configuration.

The amount of high frequency energy appears to vary with the degree of roughness. The terraced model shows the largest amount of high frequency energy which is reduced drastically on the contoured model and then increased significantly by the addition of the roughness elements. However, there appears to be very little movement of the spectral peak although, on a log-log scale, a very small change can result in a significant variation of the calculated length scale.

The difference in the position of the spectral peaks for point 12, using models A and B, is very large. The spectra for model A suggest a higher peak wave number, resulting in a smaller value of the length scale, L_{u_x}. This result is reasonable because, on model A, point 12 is probably influenced by the southern end of the Port Hills ridge, therefore creating more turbulence and reducing the length scale value.

A further two points along longitudinal cross sections UU were analysed to provide an indication of the variation of turbulence over the saddle. Point 31 was considered on the windward side of the saddle and the longitudinal component of the energy spectrum for this point is given in Fig. 8.100.

There are very few major terrain features upstream of this point capable of influencing the results. It is clear from this Figure that the addition of the roughness elements increased the amount of high frequency energy and moved the curve back towards the terraced curve.

Point 60 is located on the leeward side of the saddle. The spectra for this point are presented in Fig. 8.101. Unfortunately, this point was omitted for analysis in the terraced state of construction and can only be compared for the other forms of surface finish. The positions of the spectral peaks and general shapes of the curves are in excellent agreement. Point 60 demonstrates that the general terrain upstream of the point dominates the shape and position of the curve. A comparison of length scale values will demonstrate this point.

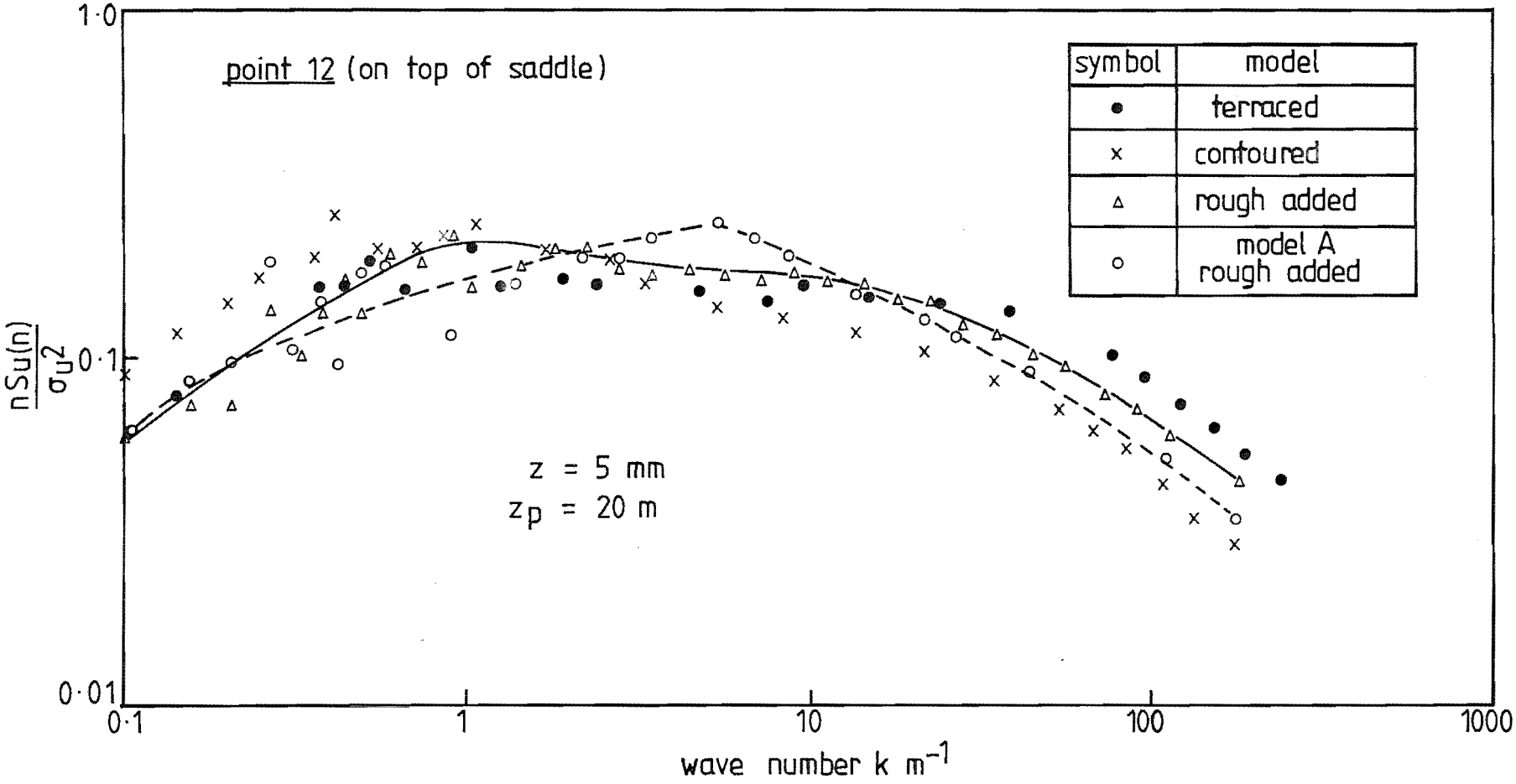

FIG. 8·99 COMPARISON OF ENERGY SPECTRA FOR POINT 12, Zp = 20 m

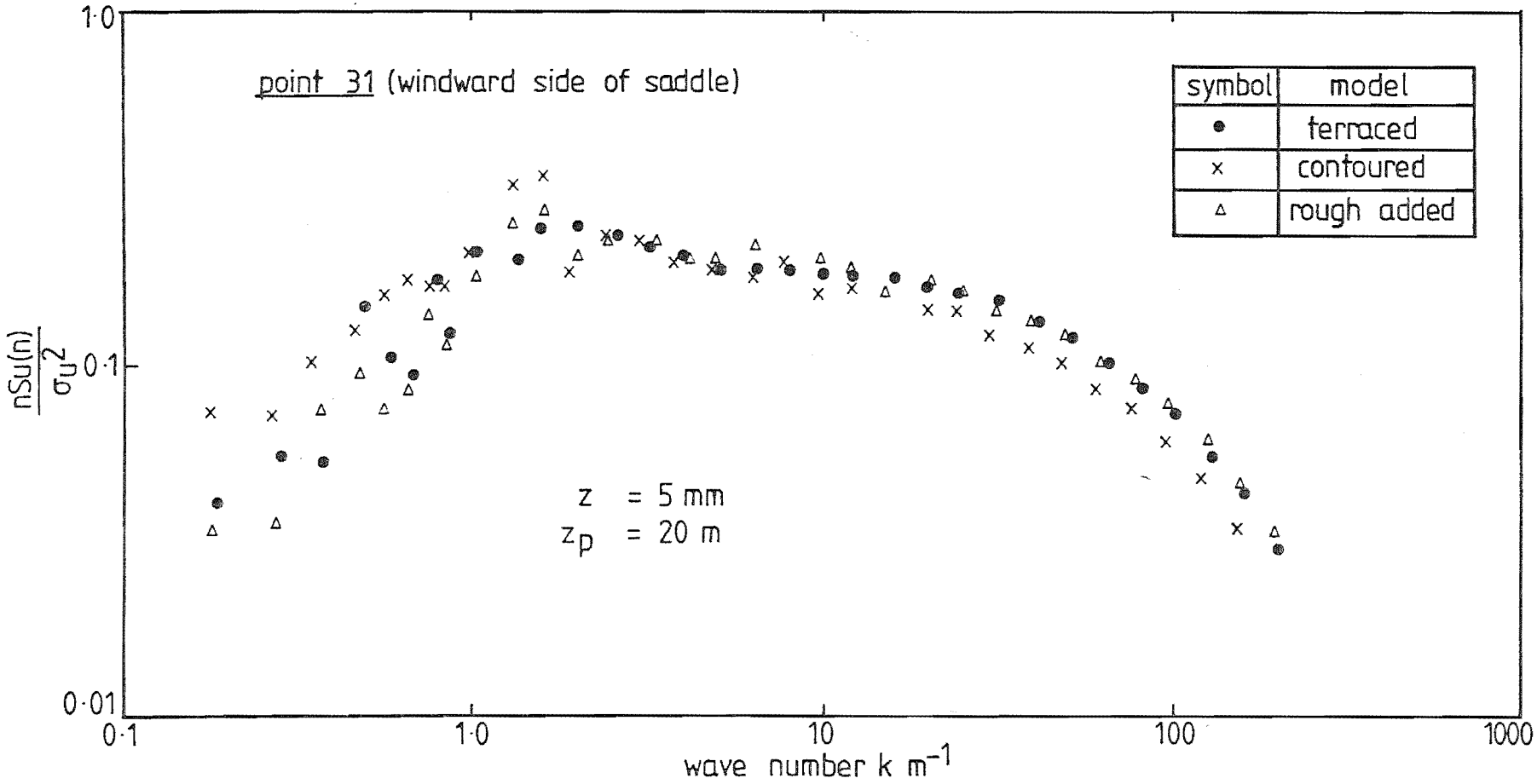

FIG. 8·100 COMPARISON OF ENERGY SPECTRA FOR POINT 31, Z_p = 20 m

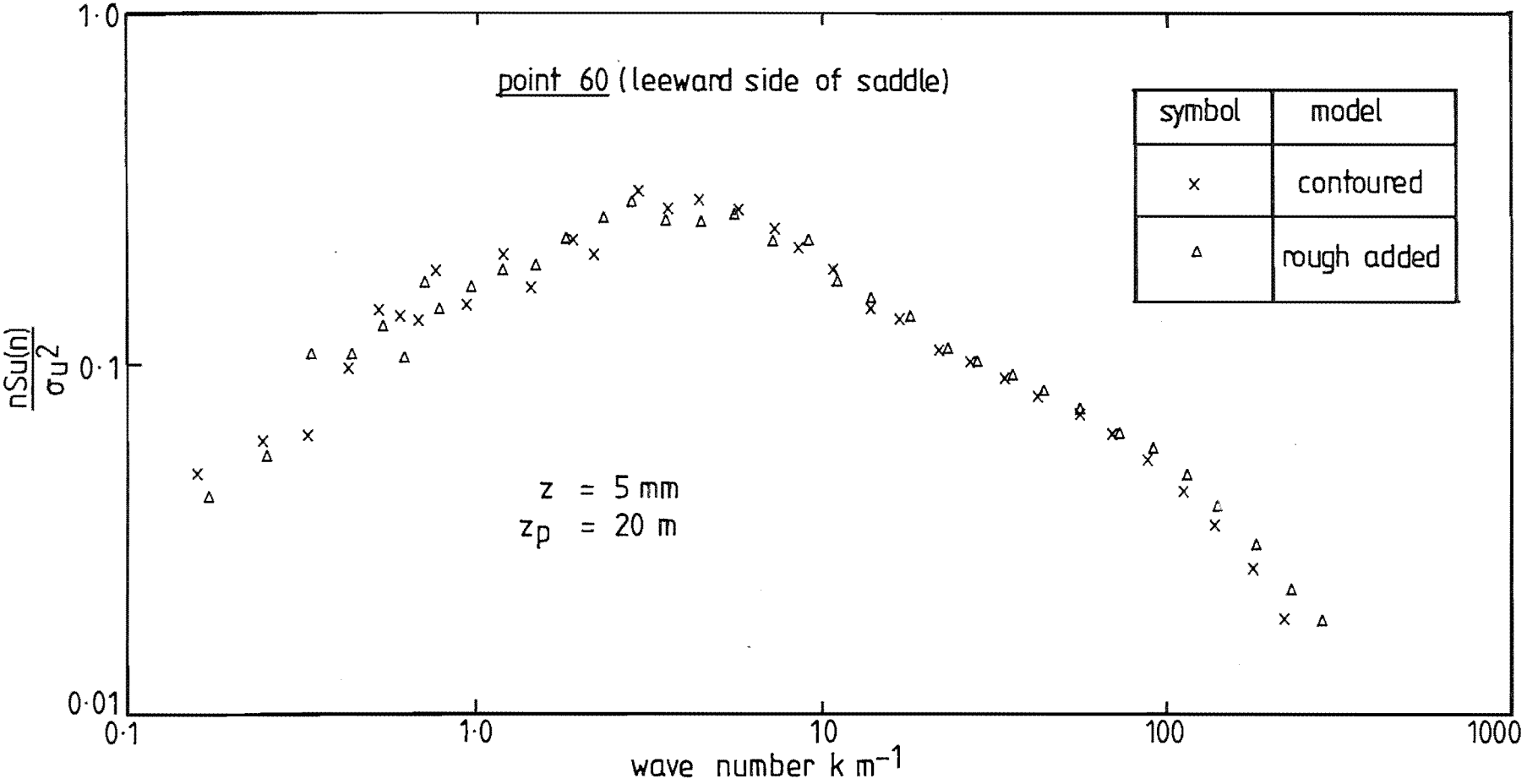

FIG. 8·101 COMPARISON OF ENERGY SPECTRA FOR POINT 60, ZP = 20 m

4) Length Scales: The L_{u_x} length scale component was calculated using the spectral peak method and the autocorrelation method, these having been described in Section 2.1.5.

The variations in the length scale for the flow over the saddle are presented in Table 8.2.

Z_p (m)	Point	k_p (m^{-1})	L_{u_x} (m) Spectra	Autocorrelation T_i	Autocorrelation T_e
20	31	2.0	290	257	245
20	12	1.2	480	600	450
20	60	3.0	190	330	280

T_i - area under curve to first crossing

T_e - time for coefficient to fall to 0.368

TABLE 8.2: Variation of Length Scales over Gebbies Pass Saddle for Model B with Roughness Added

The length scales arising from the autocorrelation data are in reasonable agreement and are in agreement with the spectra based values for points 31 and 12. However, for point 60, there are conflicting results.

The value of L_{u_x} at point 31 is in agreement with the upstream length scale reported in Chapter 7 during the establishment of the current approach flow characteristics, see Section 7.2. This result is reasonable since there are no major terrain features upstream of this point.

The length scale at point 12 is significantly larger than at the upstream points. As the flow is accelerated over the saddle, the turbulence is effectively "stretched" in the longitudinal direction, resulting in the higher value of L_{u_x}.

The resulting length scales for point 60 can be explained in two ways:

1) If the larger value (suggested by the autocorrelation curve) is accepted it is suggested that the elongation effects of the flow over the saddle are

affecting this point downstream.

2) If the lower value (suggested by the spectral peak) is used, then the elongating effects have been completely masked by the extra turbulence induced by the saddle itself, which results in L_{u_x} values less than those in the approach flow.

It is the latter case that is supported by the author, because the spectrum at point 60 is very well defined and the peak wave number was determined with confidence. Secondly, Taylor's hypothesis is not valid in situations of high turbulence, which is a feature of the flow régime at point 60.

8.5 COMPARISONS BETWEEN MODEL B AND FIELD DATA

The wind direction during the one day field data collection remained between SSW - SW. The speed-up ratios for several points are presented for comparison in Table 8.3.

Model B Point	Field Point	Model B (with rough)	Velocity Ratios Field					
			December			May		August
			11	13	14	16	17	9
39	5	1.00	-	0.96	0.89	0.98	0.86	0.86
17	7	0.98	1.06	0.87	0.96	0.86	0.89	0.87
12	15	1.58	1.46	1.61	1.55	1.90	1.43	1.48
10	24	1.37	1.13	-	-	1.67	1.36	-
25	29	0.76	1.13	-	0.80	0.72	0.75	-

TABLE 8.3: Velocity Ratio Comparisons Between Model B (roughness added) and field

These results are encouraging because they suggest an agreement between the modelled situation and the field. Comparisons and correlation calculations for model and field will be presented in Chapter 11.

8.6 CONCLUSIONS

The model was shown to present a maximum wind tunnel blockage of 5.8% which was considered acceptable.

The orientation of model B meant that the Port Hills ridge had less significance. This was highlighted in flow visualisation tests where very little deviation of the flow from along the tunnel direction was observed.

The terraced model produced results that were significantly different from those for the other forms of construction. Generally, however, velocities and higher turbulence were a feature of the terraced model. The resulting correlation between the terraced and contoured models was low, 0.61 at the 5mm height, although higher than the corresponding correlation for model A. It was concluded that this was due primarily to the reduced influence of the Port Hills ridge. The roughness added model showed a slowing of the flow, particularly in the bottom 5mm of the boundary layer.

The resulting correlation between the contoured and roughness added models was high, 0.94 at the 5mm height. However, this was lower than the equivalent correlation for model A, probably due to the effect of the roughness elements on model B.

Points common to both models A and B provided a fairly high correlation of 0.76 at a height of 5mm, and 0.87 at a height of 20mm.

The $\rho\overline{uw}$ Reynolds stress profiles measured along longitudinal cross section YY showed three features:

1) The approach flow profile at point 40 showed a constant value up to 40 - 50m which agreed with theoretical predictions of a constant value of $\rho\overline{uw}$ in the constant shear stress layer. Point 40 also showed excellent repeatability.

2) The magnitude of $\rho\overline{uw}$ was significantly reduced at point 12 (situated on top of the saddle).

3) The $\rho\overline{uw}$ Reynolds stress generally increased in the lee of the Gebbies Pass saddle with notable increases in the value of $\rho\overline{uw}$ at the saddle height. This indicated the presence of additional turbulence generated by the general saddle terrain.

The effects of the various forms of construction were demonstrated with velocity and turbulence intensity profiles. The terraced form of construction was shown to vary significantly from the other forms. Several

points indicated significant variations between the contoured and roughness added forms of construction.

The spectrum for point 12 (on the saddle) showed significant differences between models A and B, particularly in the location of the spectral peak. For model A, the peak occurred at a higher wave number, suggesting a smaller length scale. This was explained by the presence of the southern portion of the Port Hills ridge influencing the flow approaching point 12 on model A. The feature common to both models was the "stretching" of the turbulence passing over the saddle, this being noted by the substantial increase in L_{u_x} at the saddle.

CHAPTER 9

MODEL C RESULTS

The results of the wind tunnel tests over model C, see Fig. 5.10, will be presented and discussed in this Chapter. Due to the poor correlations between the terraced and contoured models, model C was not analysed in the terraced form.

9.1 ANALYSIS OF MODEL C

Model C contains the Mt Herbert Range, which is quite large and therefore warranted consideration in terms of wind tunnel blockage. The cross sections evaluated for this purpose are presented on the map in Fig. 9.1, and the resulting percentage blockages are presented in Figs 9.2 to 9.7. The maximum blockage presented by the model is 6.7% which occurs at cross section 5 passing through Mt Herbet itself. A blockage of this magnitude was of some concern but could not be avoided. Blockages in excess of this were encountered on model A and the rationale adopted has been discussed in Section 7.1.

9.1.1 Approach Flow Characteristics

Lateral uniformity tests were carried out upstream of the model and showed that a satisfactory level of uniformity existed with the maximum variation being 3.7% at vertical profile 3, this being upstream of the major terrain feature - i.e., the Mt Herbert Range.

The results of the lateral uniformity tests are presented in Fig. 9.8.

Several parameters were checked using points 43 and 44, see Fig.9.14, which are situated upstream of the first cross section.

The modelled power law velocity profiles for these points are presented in Figs 9.9 and 9.10. They yield a power law index α of 0.15 to 0.16 which is in agreement with that used on models A and B.

The log-law profiles for these points are presented in Figs 9.11 and 9.12; they have been extrapolated to determine the value of the roughness length Z_o. A value of 0.018 - 0.02m was suggested which is identical to that used on models A and B.

A turbulence intensity profile for the approach flow is presented

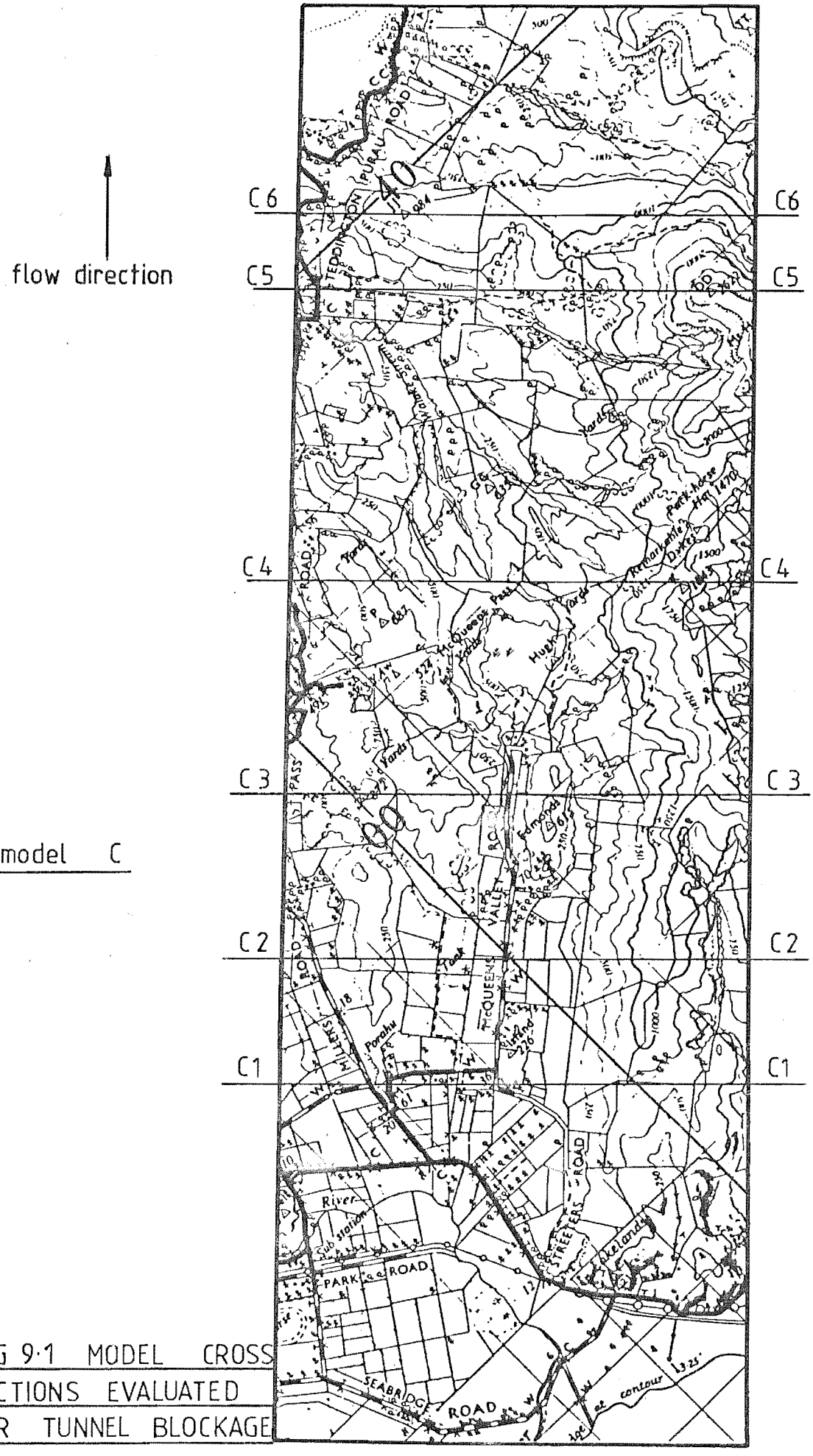

FIG 9·1 MODEL CROSS SECTIONS EVALUATED FOR TUNNEL BLOCKAGE

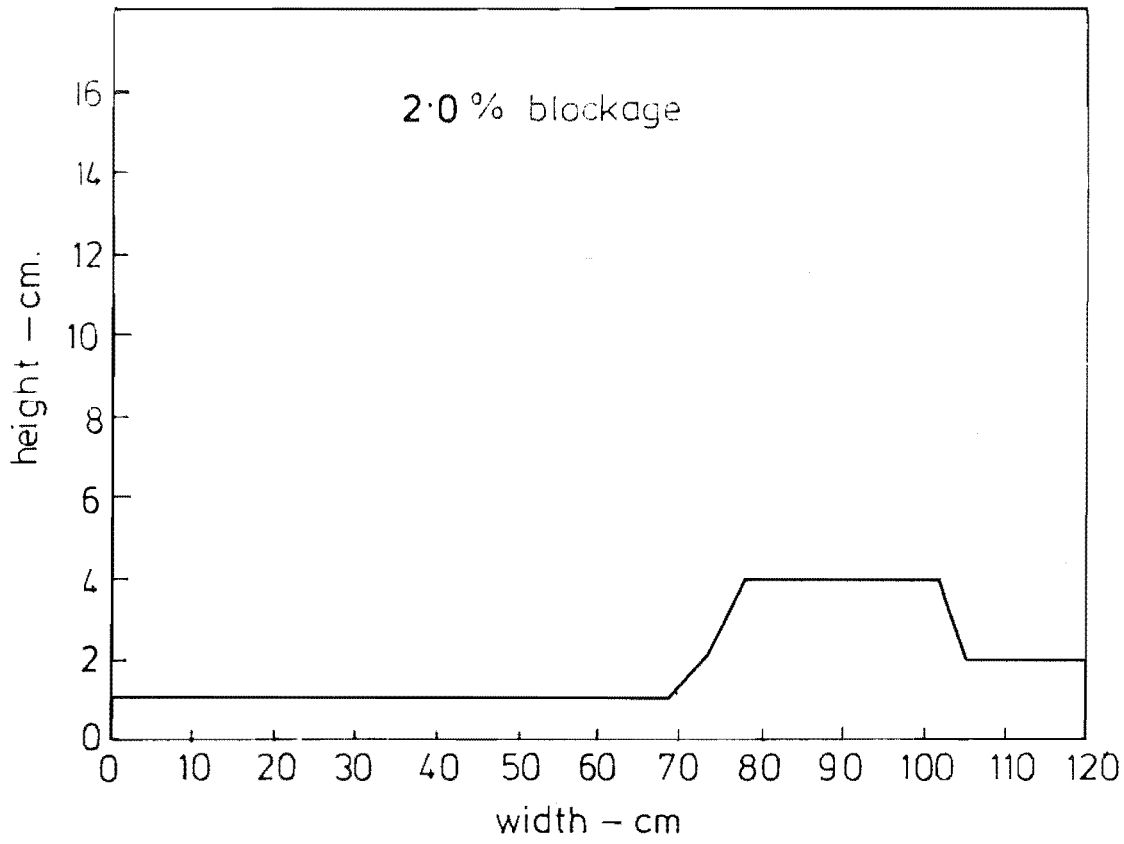

FIG 9·2 MODEL CROSS SECTION C 1

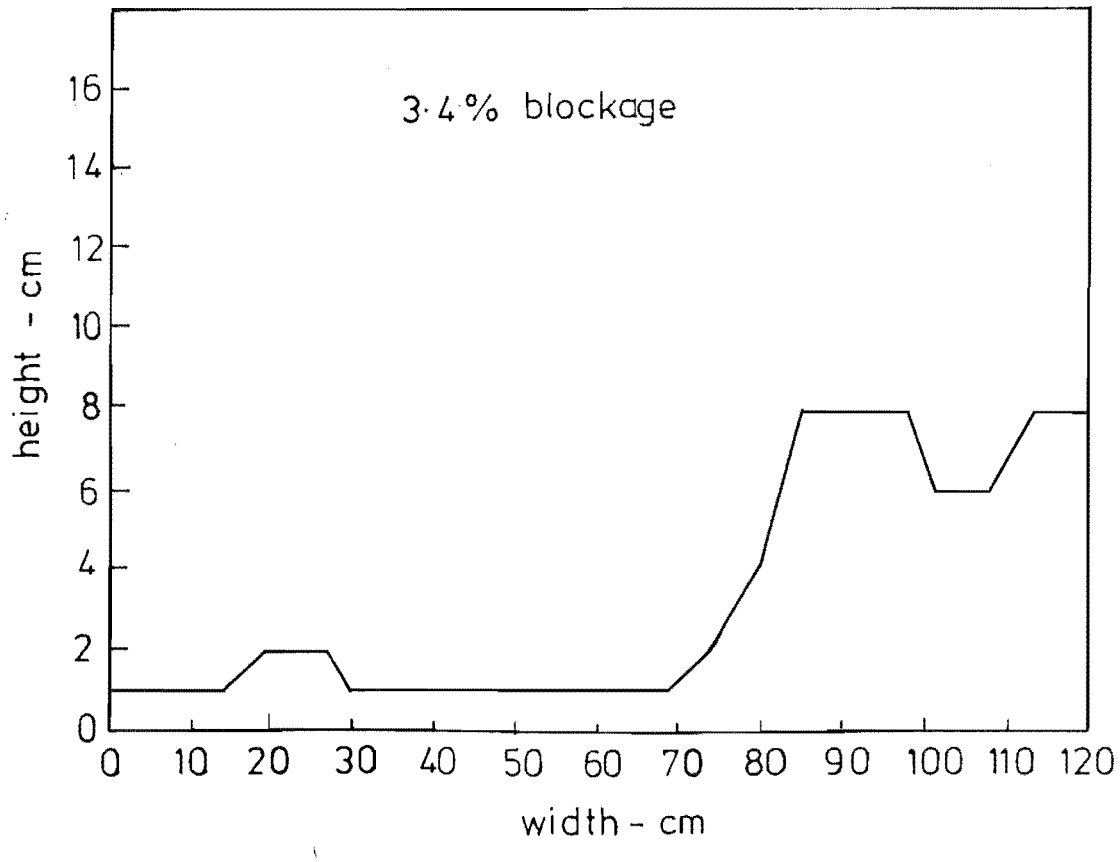

FIG 9·3 MODEL CROSS SECTION C 2

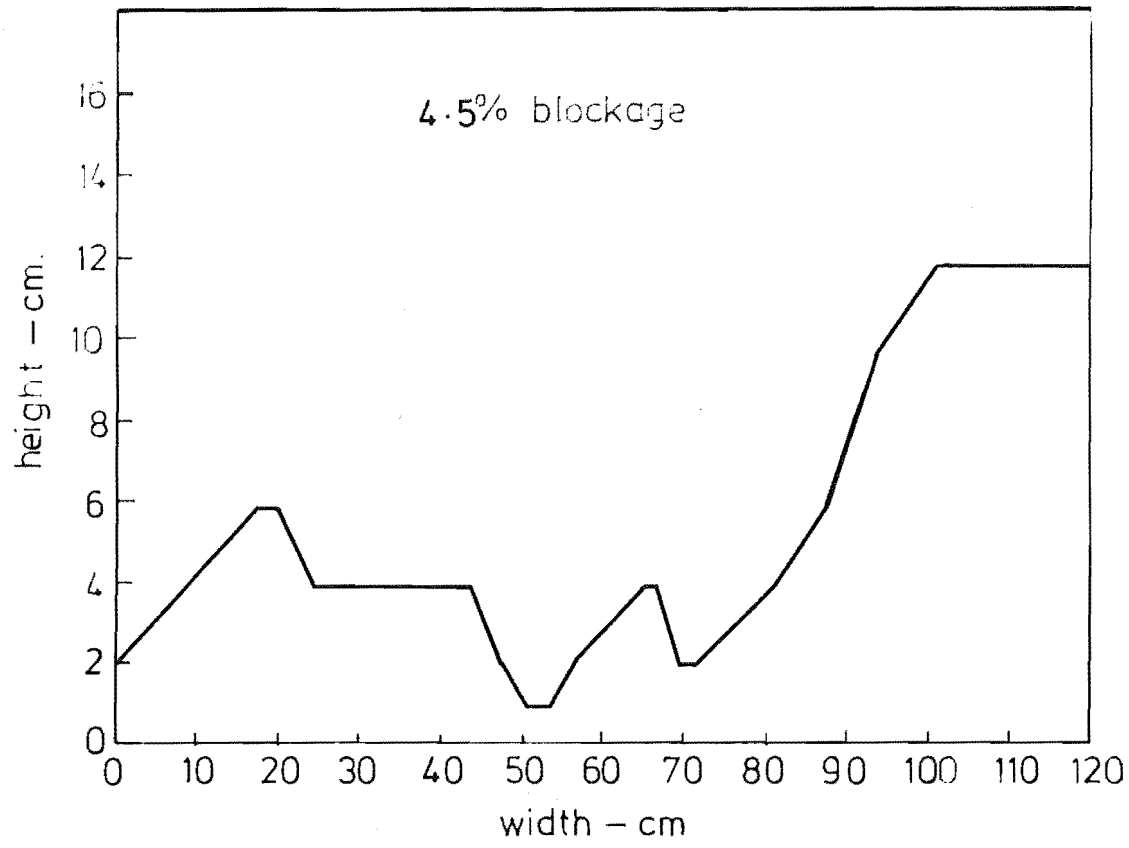

FIG 9·4 MODEL CROSS SECTION C 3

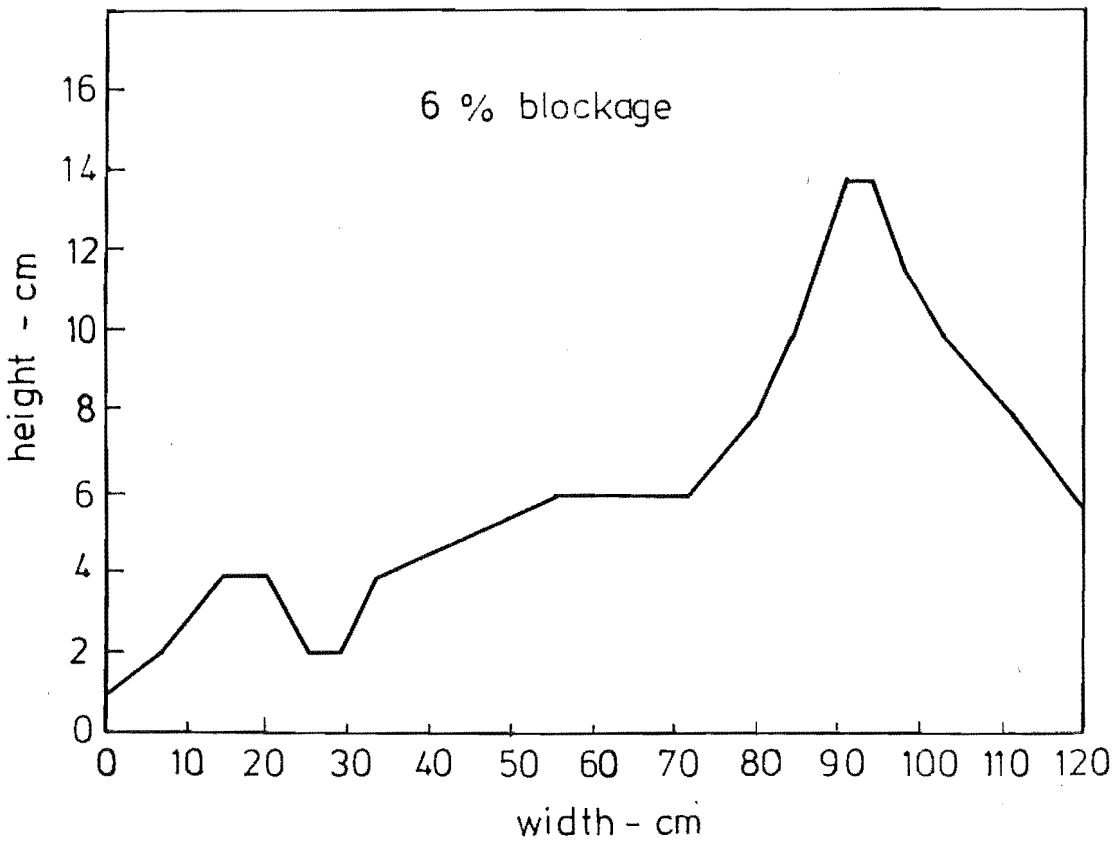

FIG 9·5 MODEL CROSS SECTION C 4

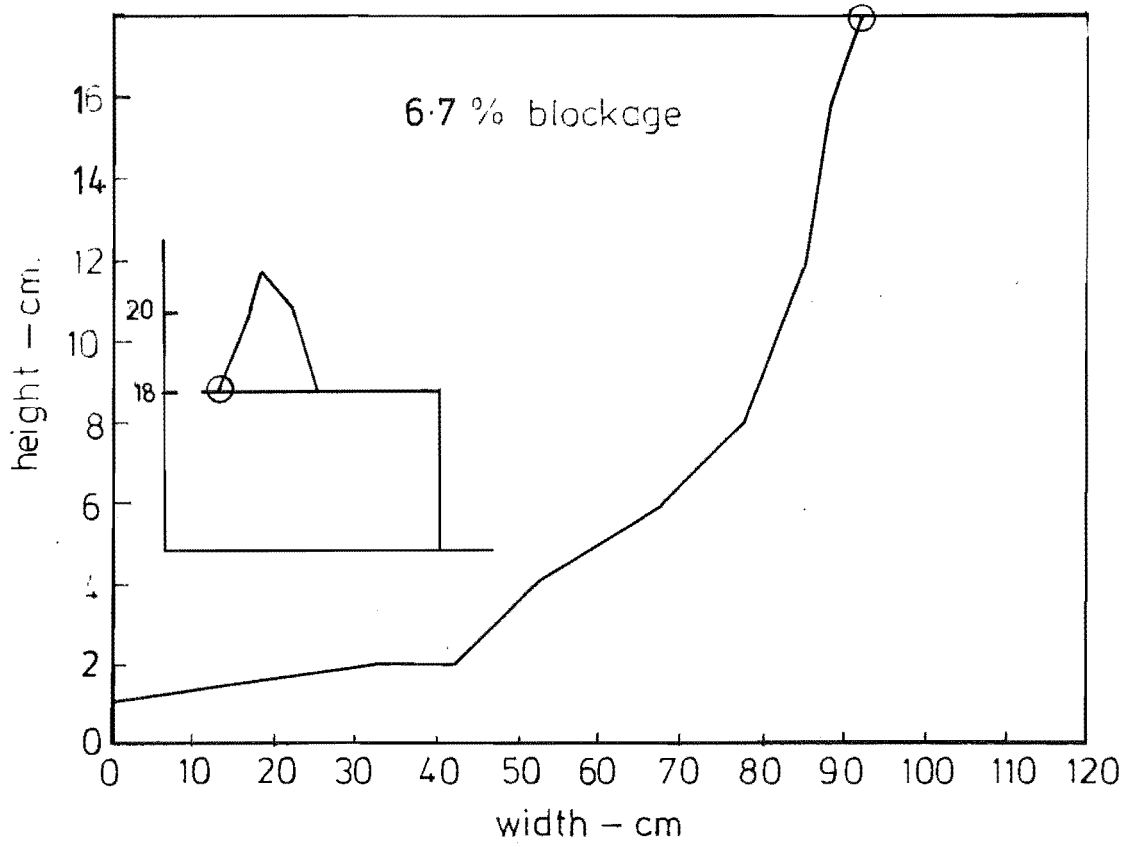

FIG 9·6 MODEL CROSS SECTION C 5

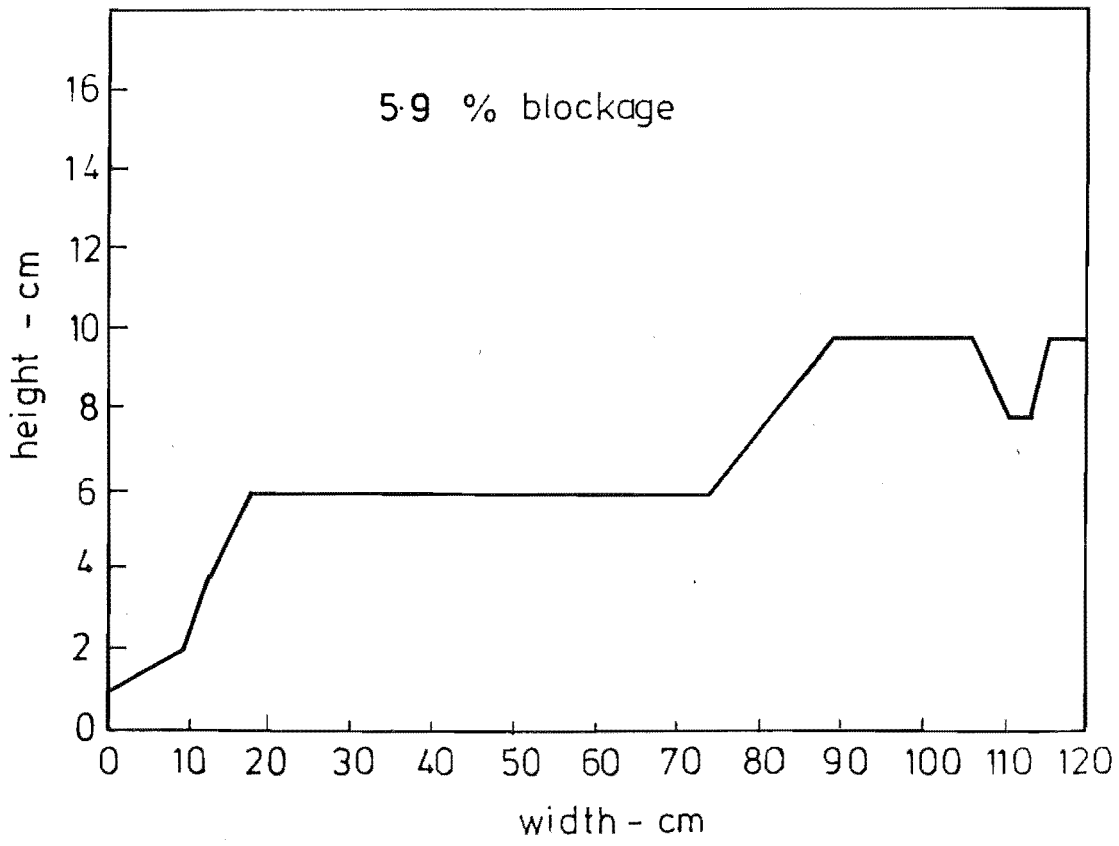

FIG 9·7 MODEL CROSS SECTION C6

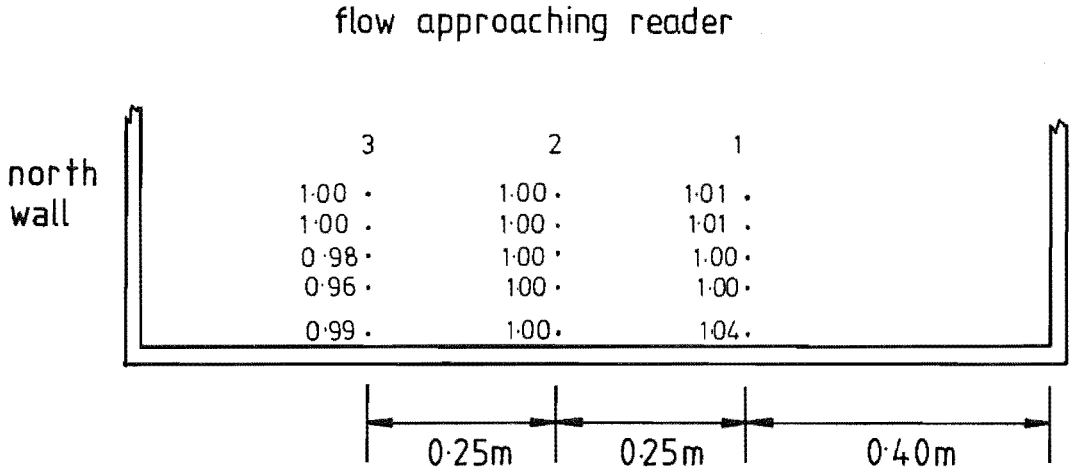

Readings normalized to profile 2

2x Exaggerated vertical scale

FIG 9·8 APPROACH FLOW LATERAL UNIFORMITY FOR MODEL C

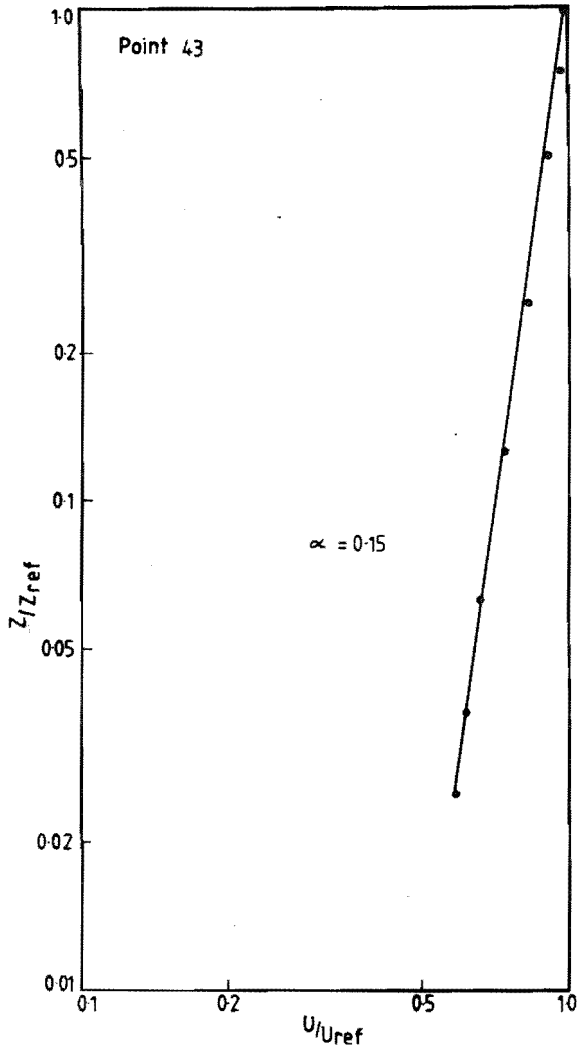

FIG 9.9 POWER LAW VELOCITY PROFILE MODEL C, CONTOURED

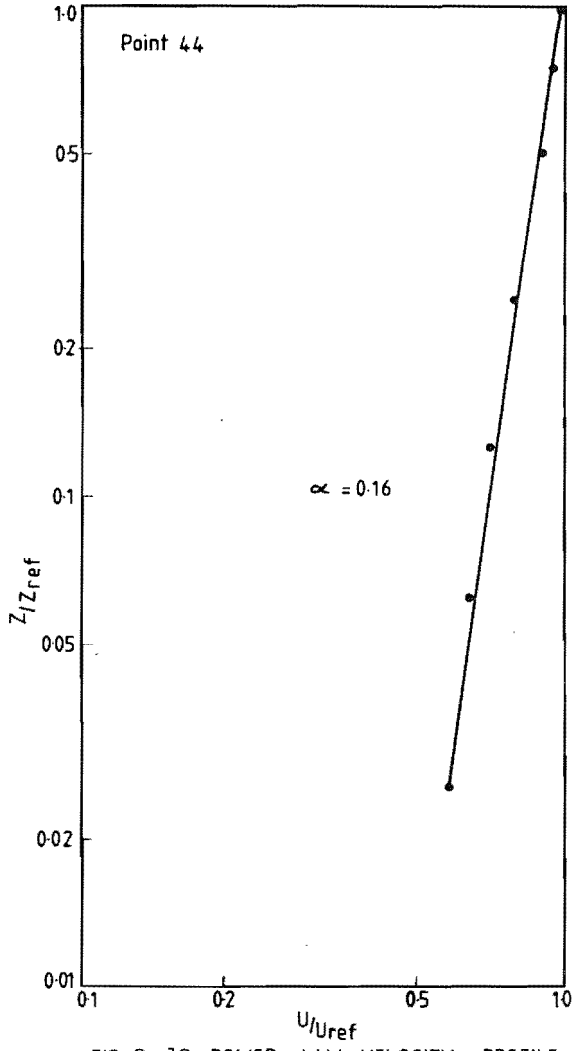

FIG 9.10 POWER LAW VELOCITY PROFILE MODEL C, CONTOURED

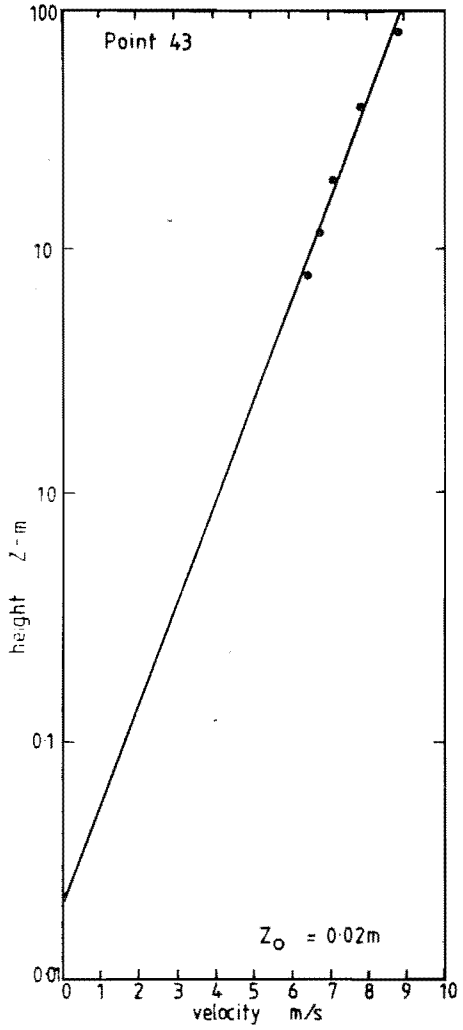

FIG 9.11 LOG LAW VELOCITY PROFILE
MODEL C, CONTOURED

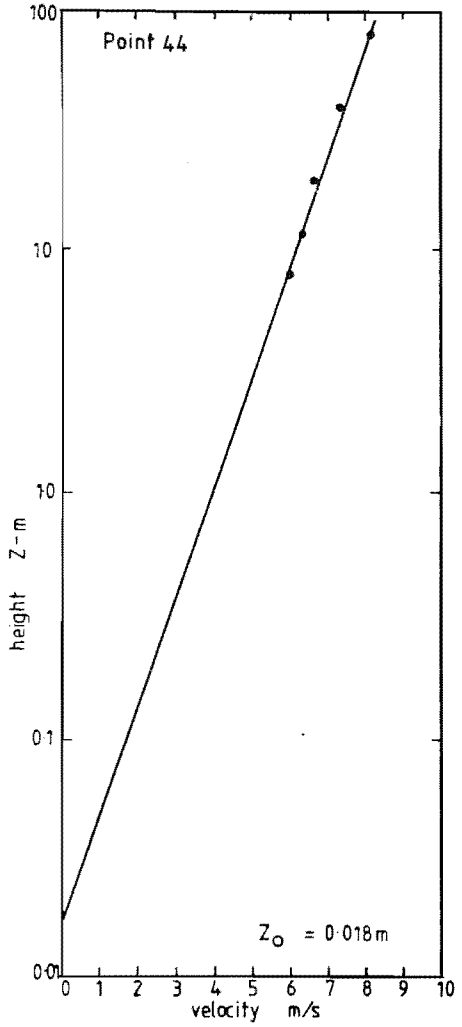

FIG 9.12 LOG LAW VELOCITY PROFILE
MODEL C, CONTOURED

in Fig. 9.13 and is in good agreement with those for the previous models.

In general, the required approach flow conditions stipulated and produced for the previous models were reproduced satisfactorily for the model C analysis.

9.2 MODEL C CONTOURED

Pressure gradient measurements were made along the tunnel over the region of the model and resulted in a maximum variation of 1.6%.

The data collection sections and points are presented on the map in Fig. 9.14.

9.2.1 Flow Visualisation

1) Polystyrene Beads: The polystyrene bead tests revealed that model C was generally more exposed than would be expected for terrain having the complexity of this model. The results of the low speed (4.0 m/s) test are presented in Fig. 9.15, and show that small bead deposits occurred in the lee of Mt Herbert and behind a significant ridge. This ridge extends from trig station JJ, close to grid number 40 on Fig. 9.15, across to Mt Herbert and has an almost constant height at its crest. The beads were observed to pass over this ridge with very little deviation from along the tunnel direction. The high degree of turbulence, noted by the behaviour of the beads deposited behind the ridge, suggested that separation could be occurring at the ridge crest, and the hot film survey might demonstrate this more clearly.

When the tunnel freestream velocity was increased to 5.7 m/s, essentially all beads were removed.

2) Flags: The miniature flags were placed on the analysis points and revealed that no points were subject to significant deviations from along the tunnel direction.

9.2.2 Pressure Probe Measurements

The confidence gained in the flag results meant that this aspect of the analysis could be omitted for the analysis of model C. All tests strongly suggested that there were no major flow direction changes.

9.2.3 Hot Film Survey

The results of the hot film survey for lateral cross sections 1 - 4 are presented in Figs 9.16 to 9.23.

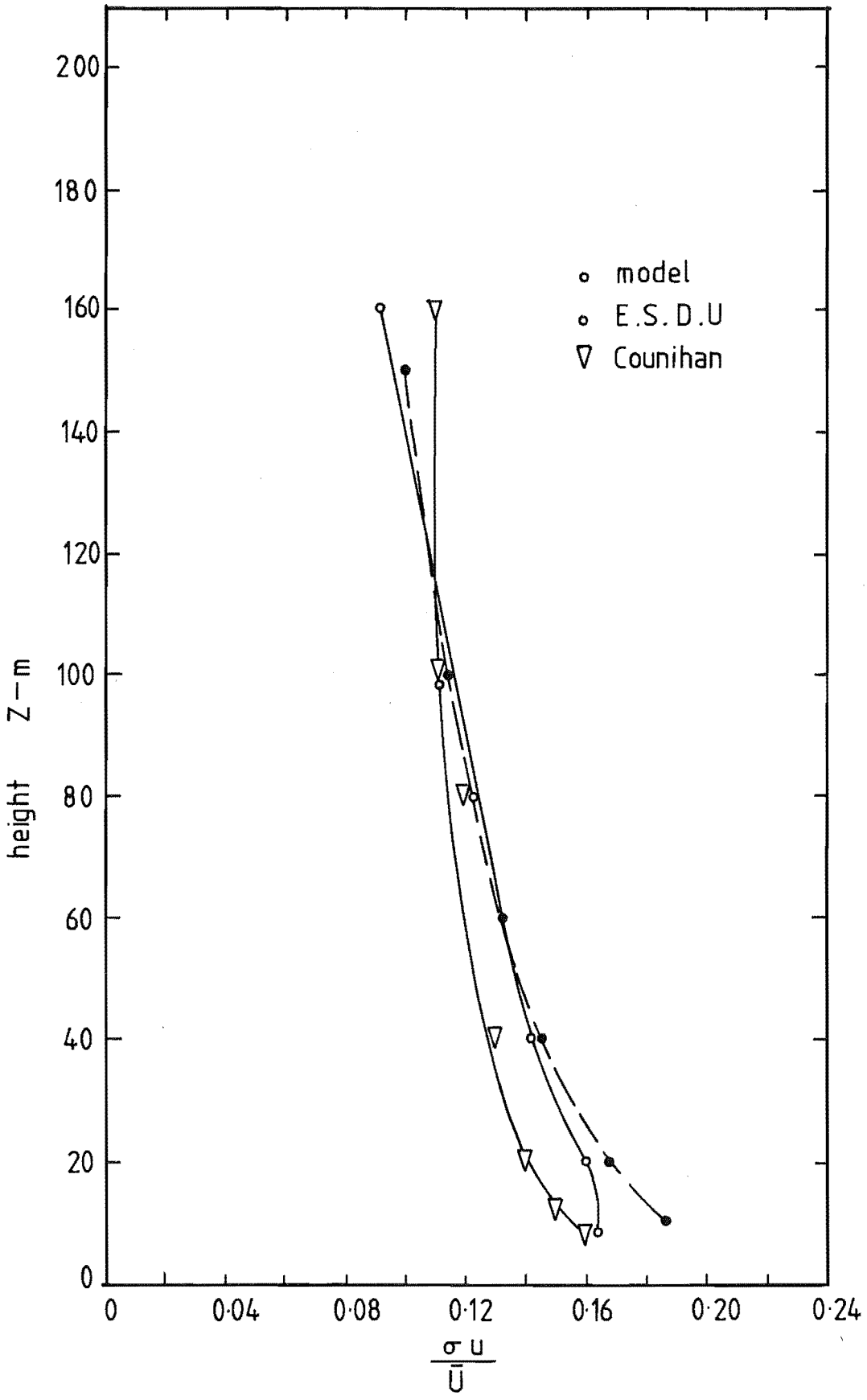

FIG. 9·13 APPROACH FLOW TURBULENCE INTENSITY PROFILE, MODEL C CONTOURED

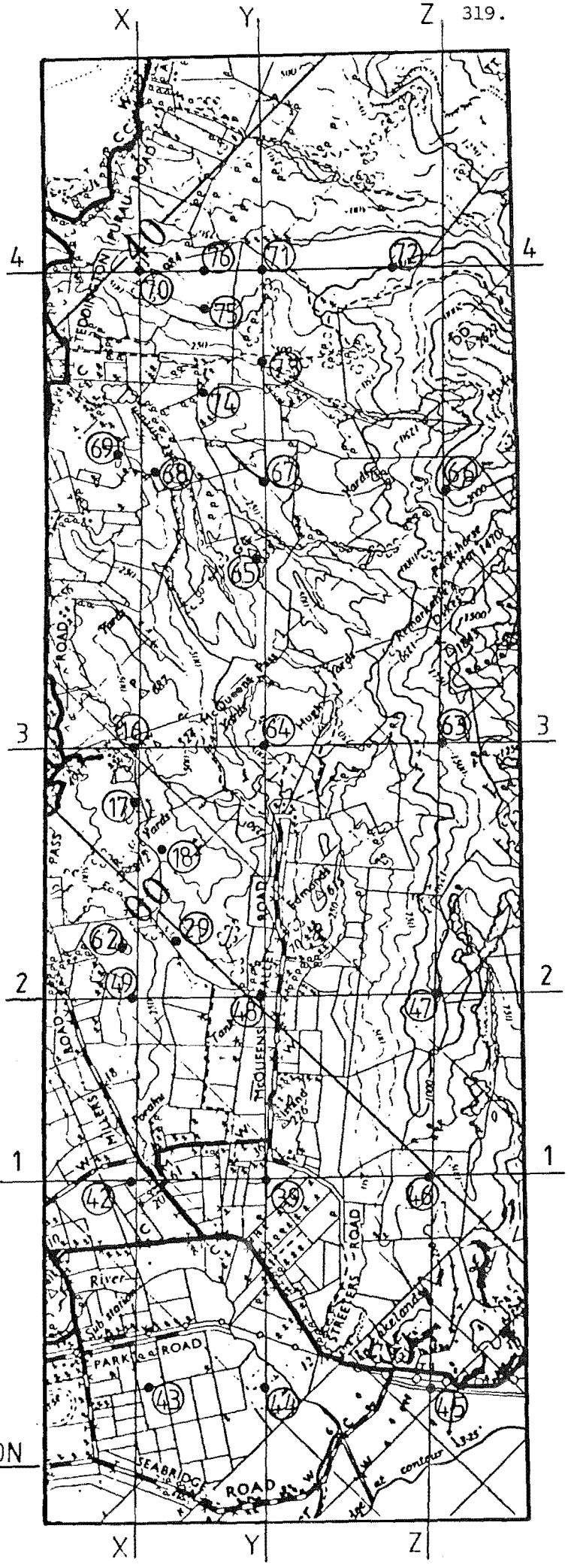

FIG. 9·14 DATA COLLECTION SECTIONS AND POINTS

MODEL C

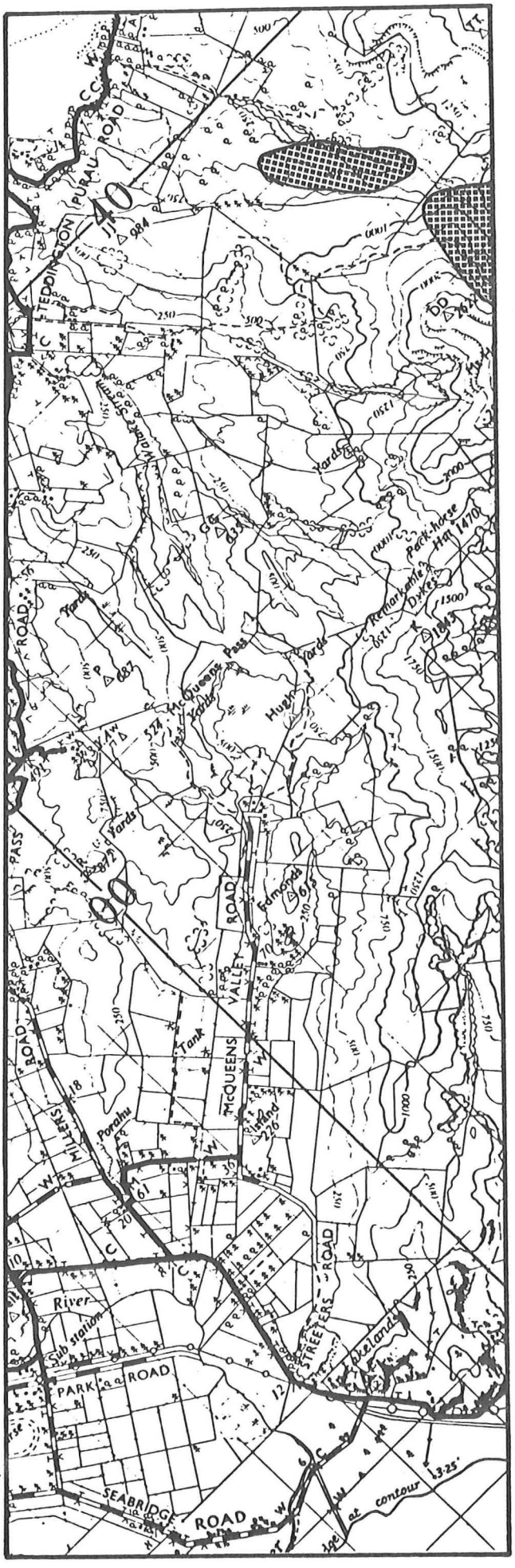

deposits at low speed

FIG. 9·15 POLYSTYRENE BEAD DEPOSITION DIAGRAM CONTOURED MODEL

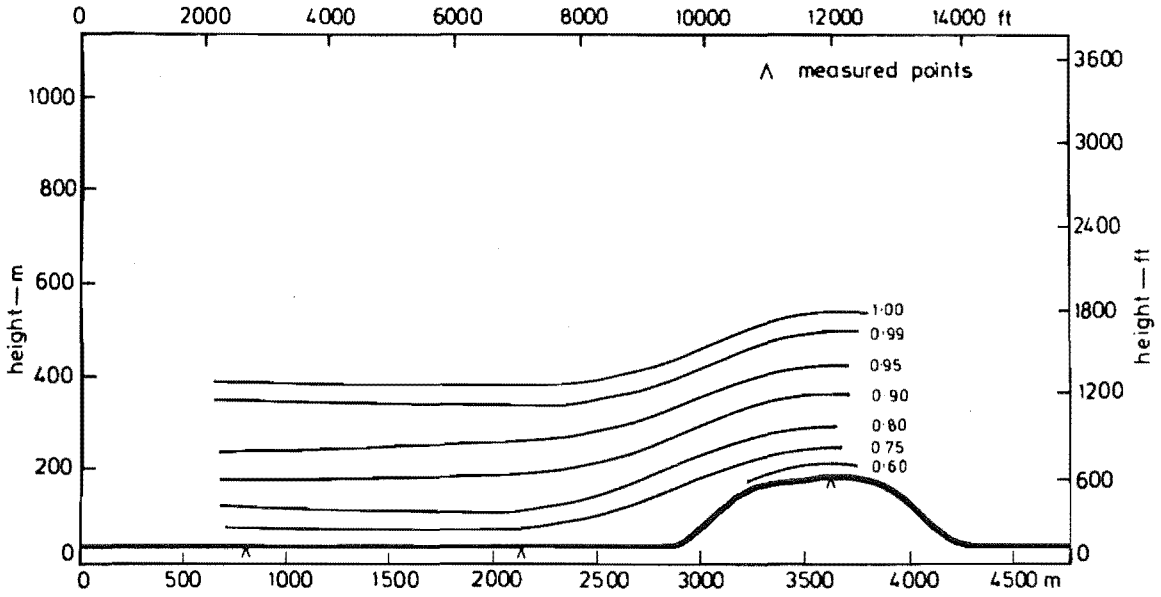

FIG 9.16 ISOTACHS FOR MODEL C CONTOURED, LATERAL CROSS SECTION. 1

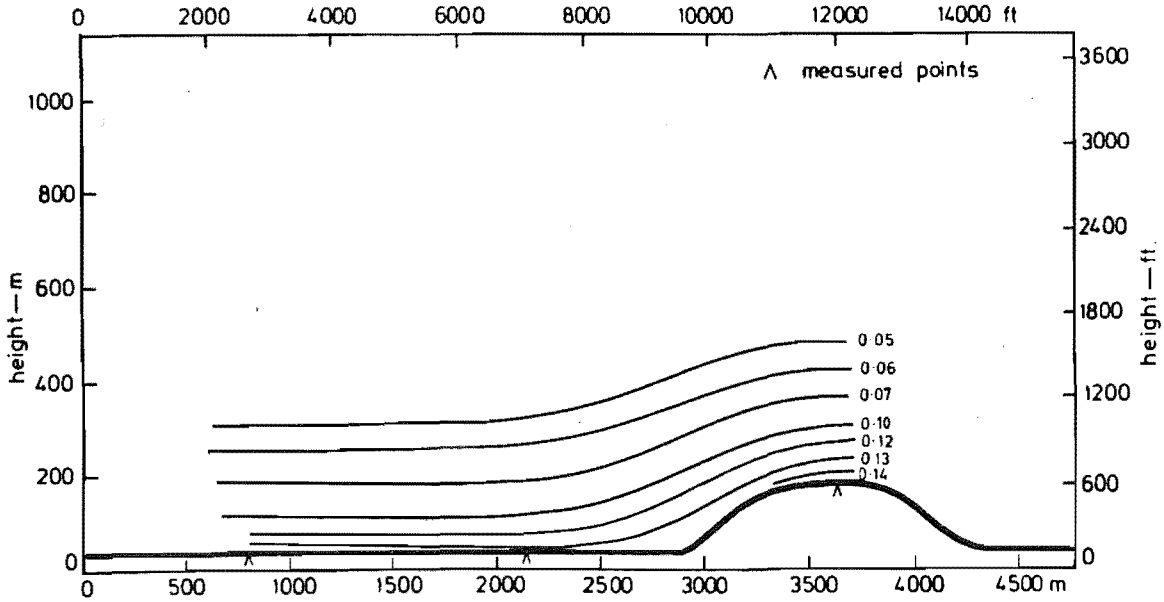

FIG 9.17 ISOTURBS FOR MODEL C CONTOURED, LATERAL CROSS SECTION. 1

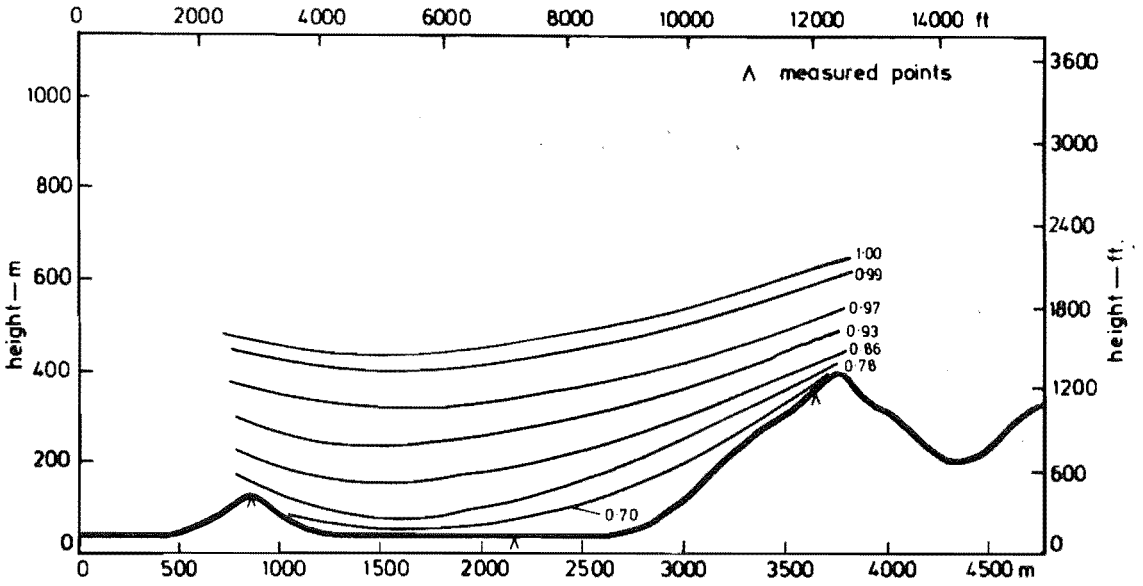

FIG 9.18 ISOTACHS FOR MODEL C CONTOURED, LATERAL CROSS SECTION. 2

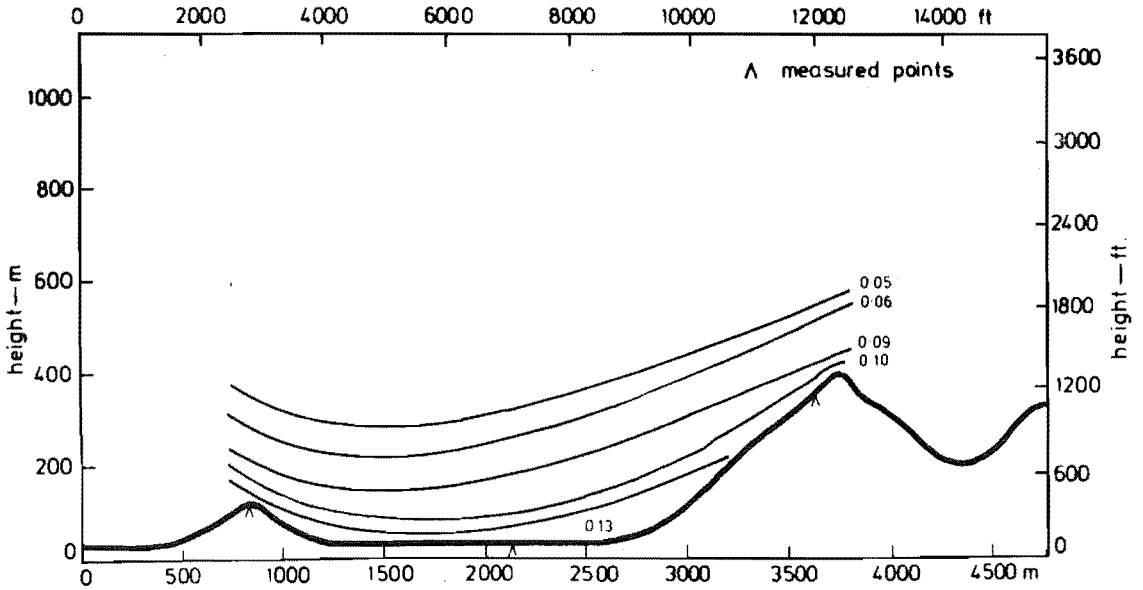

FIG 9.19 ISOTURBS FOR MODEL C CONTOURED, LATERAL CROSS SECTION. 2

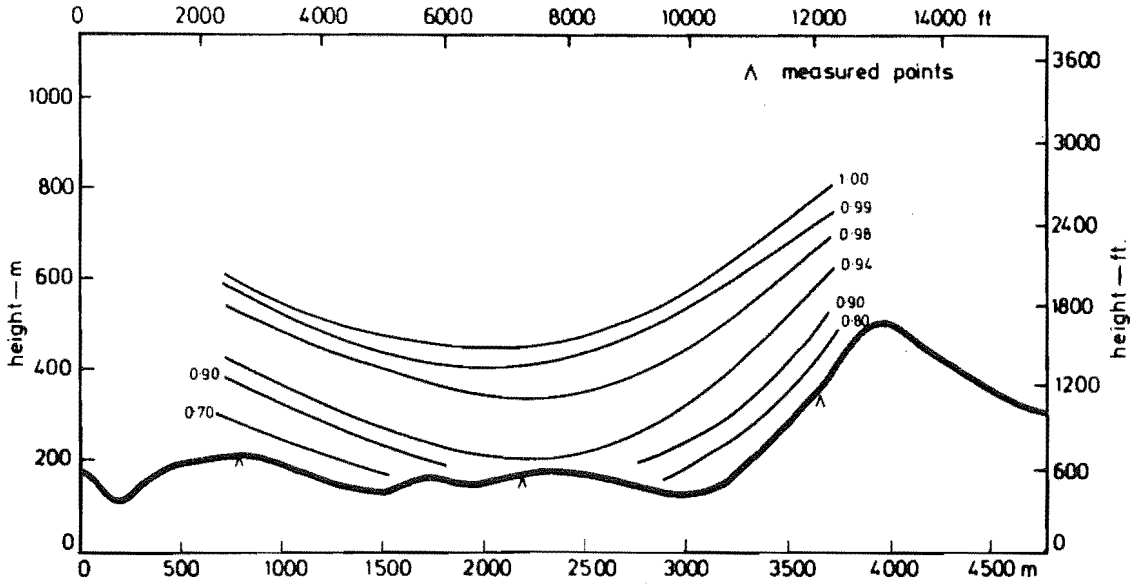

FIG 9.20 ISOTACHS FOR MODEL C CONTOURED, LATERAL CROSS SECTION. 3

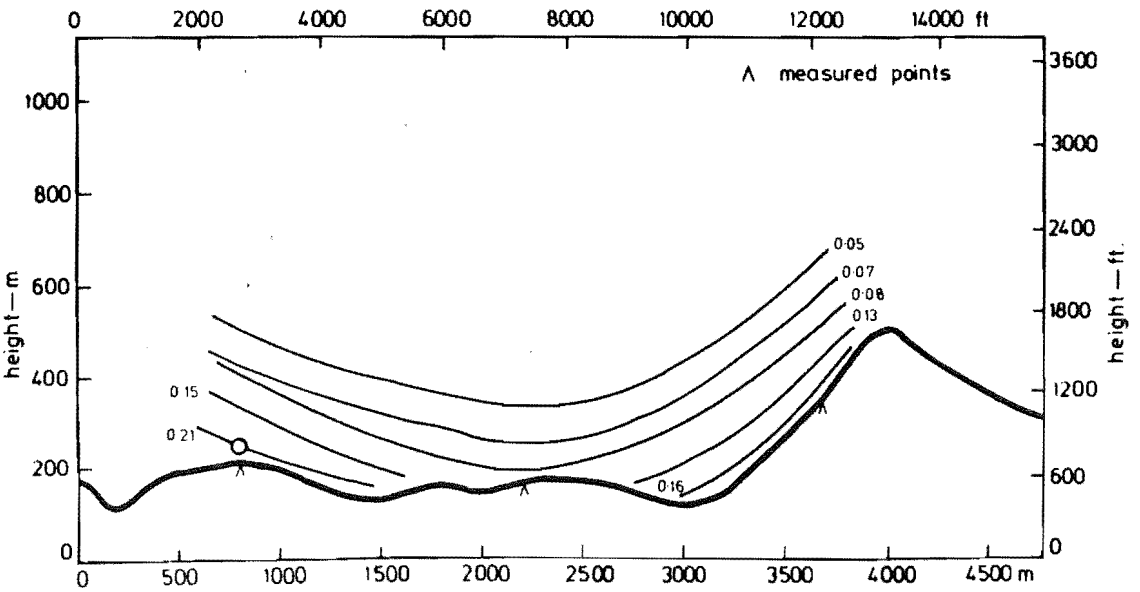

FIG 9.21 ISOTURBS FOR MODEL C CONTOURED, LATERAL CROSS SECTION. 3

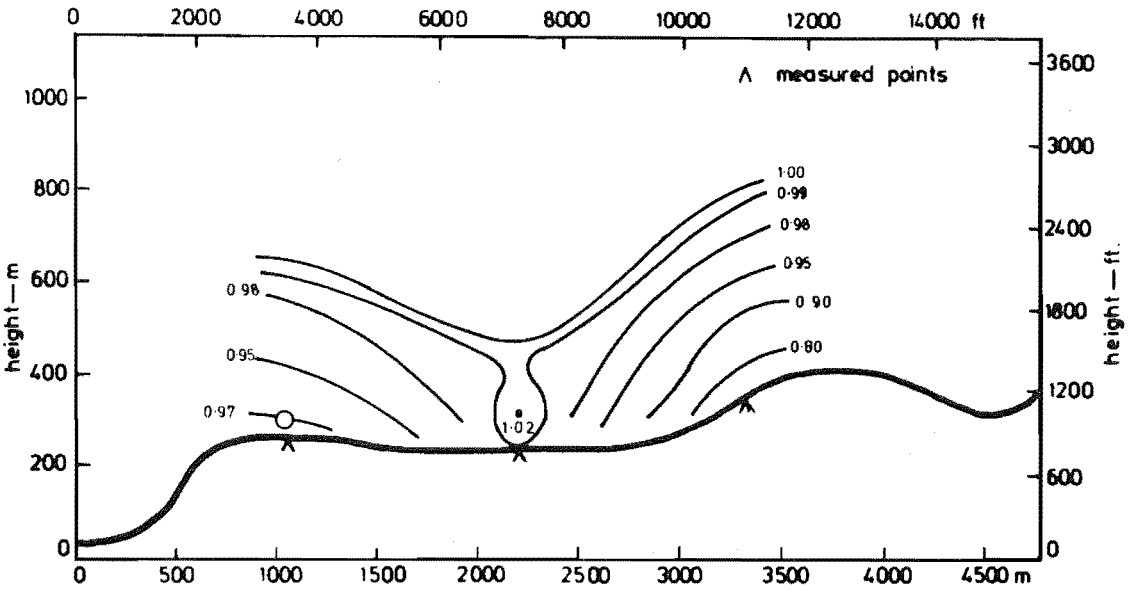

FIG 9.22 ISOTACHS FOR MODEL ℄ CONTOURED, LATERAL CROSS SECTION. 4

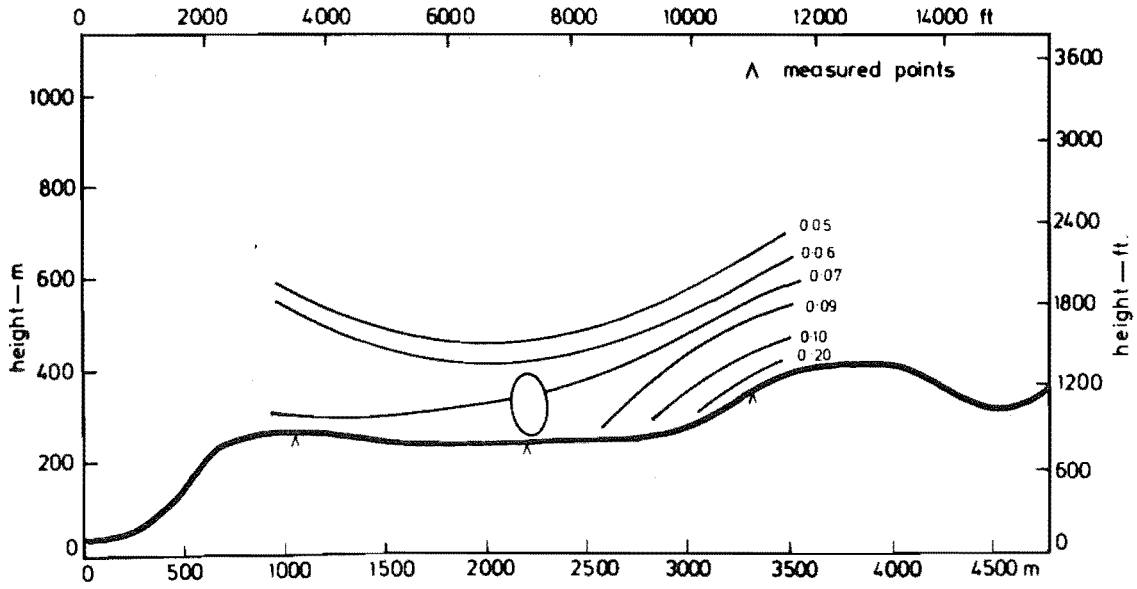

FIG 9.23 ISOTURBS FOR MODEL ℄ CONTOURED, LATERAL CROSS SECTION. 4

Both the isotach and isoturb contours for cross section 1 follow the terrain closely, and show a high level of lateral uniformity on the flat terrain.

The isotach contours for cross section 2 follow the general terrain shape closely. They also suggest high velocities close to the model surface, the bottom contour being 0.70. The isoturb contours show no deviations from the general trend of following the terrain and being reduced in areas of high velocity.

Lateral cross section 3 is situated on the Gebbies Pass saddle and is almost an extension of lateral cross section 3 used on model A. The isotach contours indicate relatively high velocities close to the model surface. Point 64, 2250m position on base scale, shows high velocities in the lower part of the boundary layer. This point is situated on the top of a hill which is at the end of a long valley, representing a miniature saddle situation. The lower velocities indicated for point 16 are explained by the upstream terrain. This point is in the lee of a significant hill upon which point 17 is situated.

The isoturbs for cross section 3 follow the general terrain shape closely with the highest turbulence being recorded at point 16, 21%.

The isotach contours for cross section 4 suggest that a very complex situation exists along the top of the main ridge. This situation is further complicated by the actual upstream terrain features. Data for a base scale position in excess of 3000m must be treated very cautiously because Mt Herbert is situated upstream of this cross section. This fact, combined with wall effects, could be influencing the flow régime to a greater extent than was considered applicable to models A and B. The isotach contours show a particularly significant velocity speed-up at point 71, located at the 2250m base scale position. The interesting feature is that the high velocities do not extend laterally along the ridge. A possible reason for this is the approach terrain to point 71. It can be seen on the map in Fig. 9.14 that a gully is located on the face of the main ridge leading directly to point 71. The isotach contours could be reflecting a channelling of the flow caused by this feature.

The isoturb contours for this cross section follow a similar pattern to the isotachs, with low values of turbulence intensity close to the surface, this being indicative of the higher velocities. Point 72 shows a significantly higher value of turbulence intensity in the bottom 10mm of the

boundary layer. The cross section does not show that point 72 is situated behind a small ridge which is the probable cause of the extra turbulence.

The isotach and isoturb contours for the longitudinal cross sections are presented in Figs 9.24 to 9.29.

The isotach contours for cross section XX suggest that the flow is not greatly disturbed by the terrain. The 0.96 contour is affected significantly by the ridge at the 400m position on the base scale. The contours above 0.96 again have a smooth, undisturbed shape.

The isoturb contours also show a smooth passage over the model and follow the general terrain closely. The 18% and 20% turbulence intensity contours are generated behind a significant ridge and their high values could be an indication that point 16, indicated on Fig. 7.25, and point 17 (upstream of point 16) are in a separated region.

The isotach contours for cross section YY suggest that a complex flow situation exists. The contours approaching the Gebbies Pass saddle, and the ridge at the 4000m base scale position, are quite straightforward and predictable. However, the region behind the Gebbies Pass saddle is rather complex because the terrain drops to a low level before rising to the large ridge. In this valley or depression, the flow has a complex nature. The velocity below the upstream ridge height is low with turbulence intensities of about 20%. It is possible that the flow is separating from the Gebbies Pass saddle. However, if this were the case, one could have expected beads to have been deposited in this region, but this did not happen.

Longitudinal cross section ZZ passes along the ridge line of the Mt Herbert range. The hill at the 1000m base scale position (measurement point 66) is not the ridge discussed in the other longitudinal cross sections; reference to Fig. 9.14 and the position of point 66 will show this. The isotach contours for this cross section suggest that the flow over the rough terrain is generally undisturbed. Point 66, indicated on the isotach diagram, shows particularly high velocities which extend vertically 200m. The isoturb contours for point 66 do not indicate an area of constant turbulence intensity as has been noted in many of the other areas where high velocities were recorded.

The speed-up ratio areas for model C are presented on the map in Fig. 9.30.

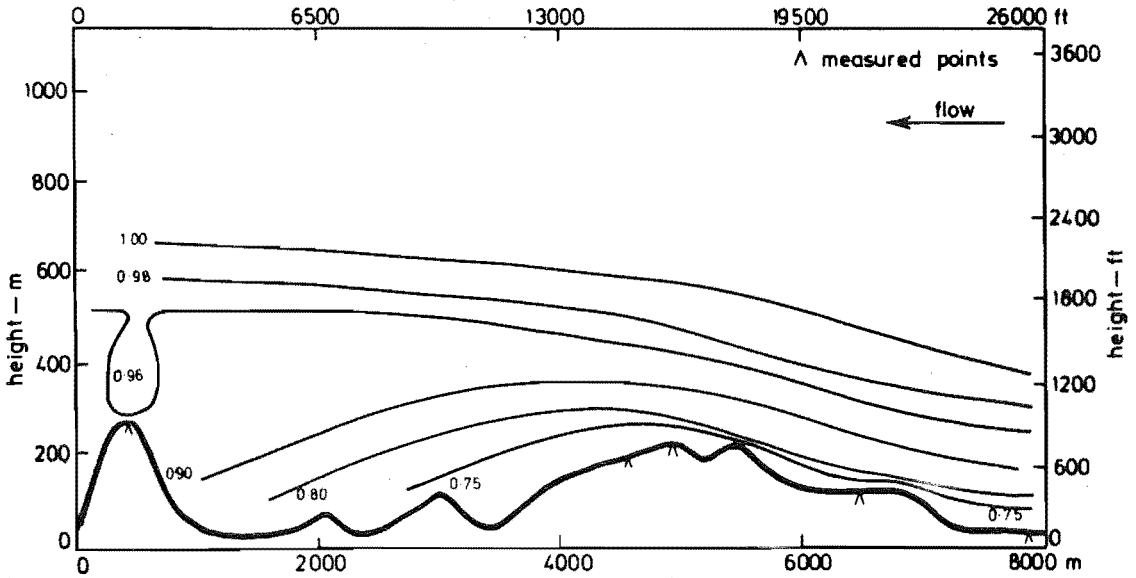

FIG 9.24 ISOTACHS FOR MODEL C CONTOURED, LONGITUDINAL CROSS SECTION XX

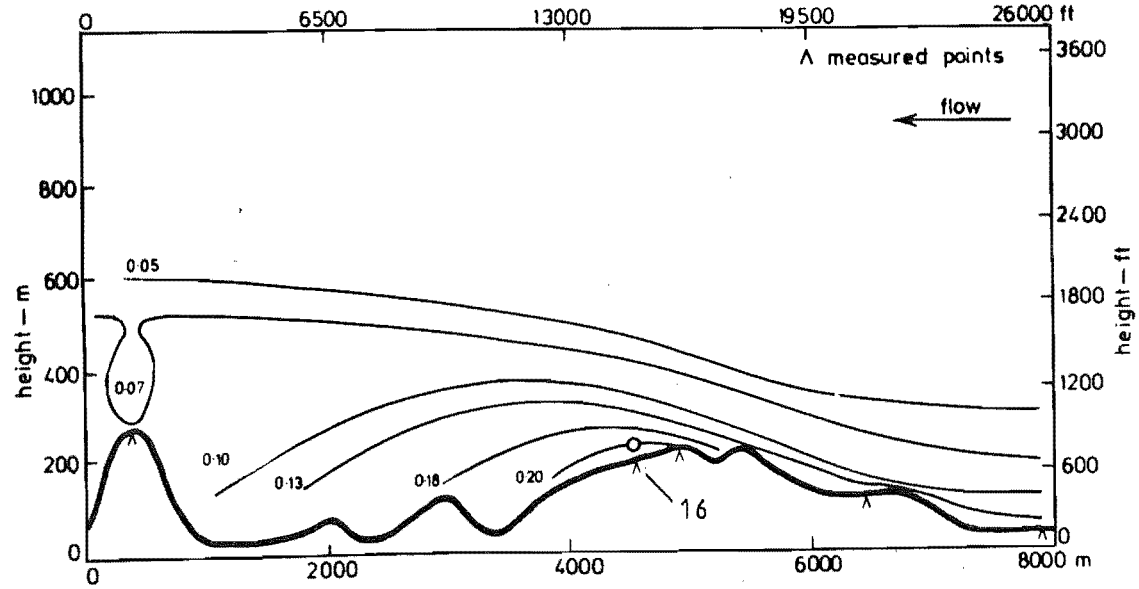

FIG 9.25 ISOTURBS FOR MODEL C CONTOURED, LONGITUDINAL CROSS SECTION XX

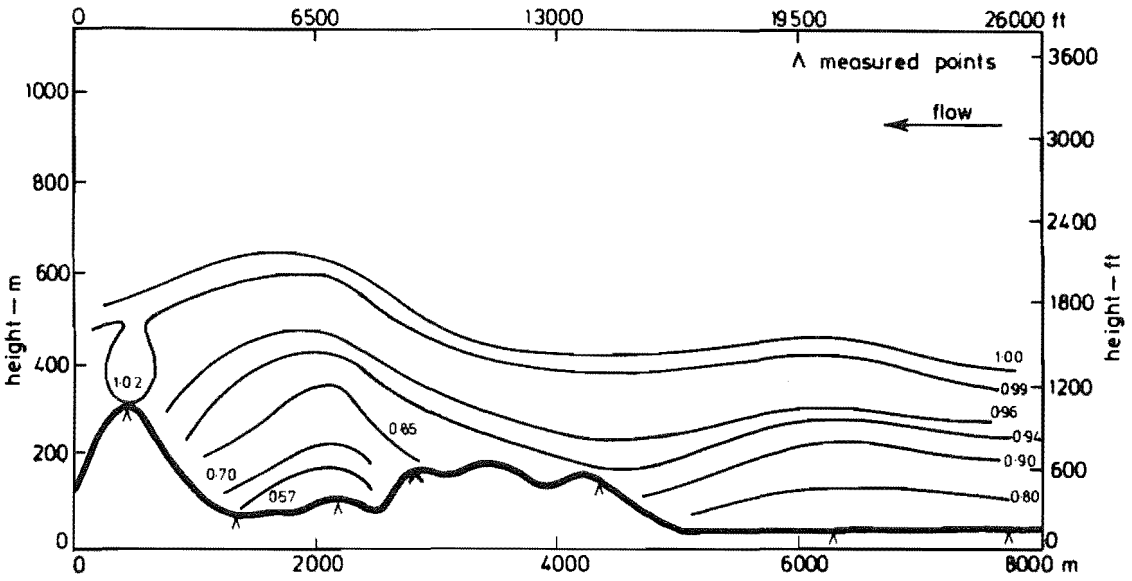

FIG 9.26 ISOTACHS FOR MODEL C CONTOURED, LONGITUDINAL CROSS SECTION YY

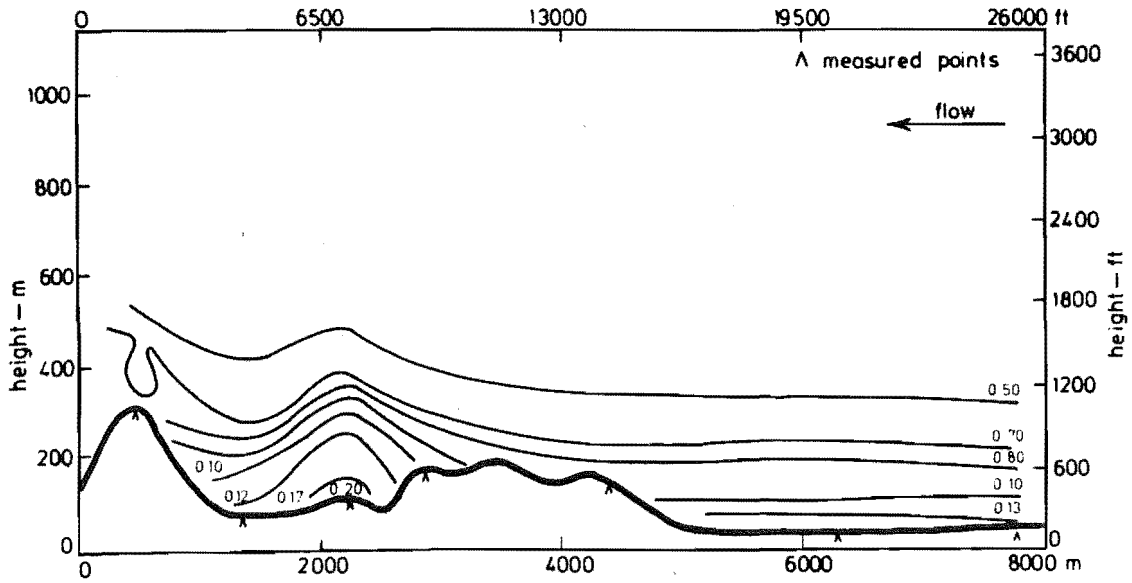

FIG 9.27 ISOTURBS FOR MODEL C CONTOURED, LONGITUDINAL CROSS SECTION YY

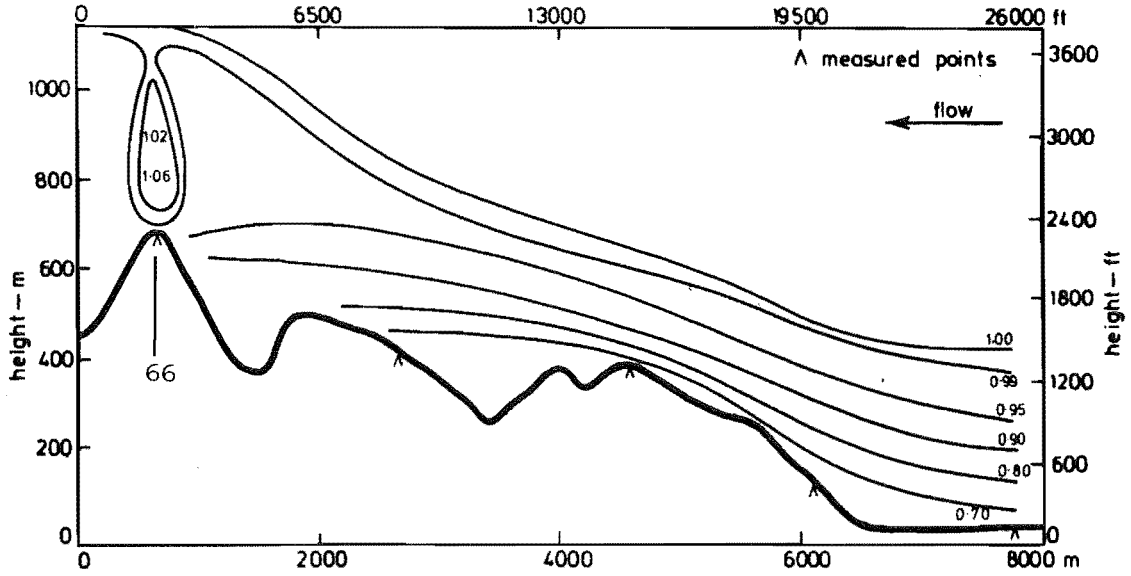

FIG 9.28 ISOTACHS FOR MODEL C CONTOURED. LONGITUDINAL CROSS SECTION ZZ

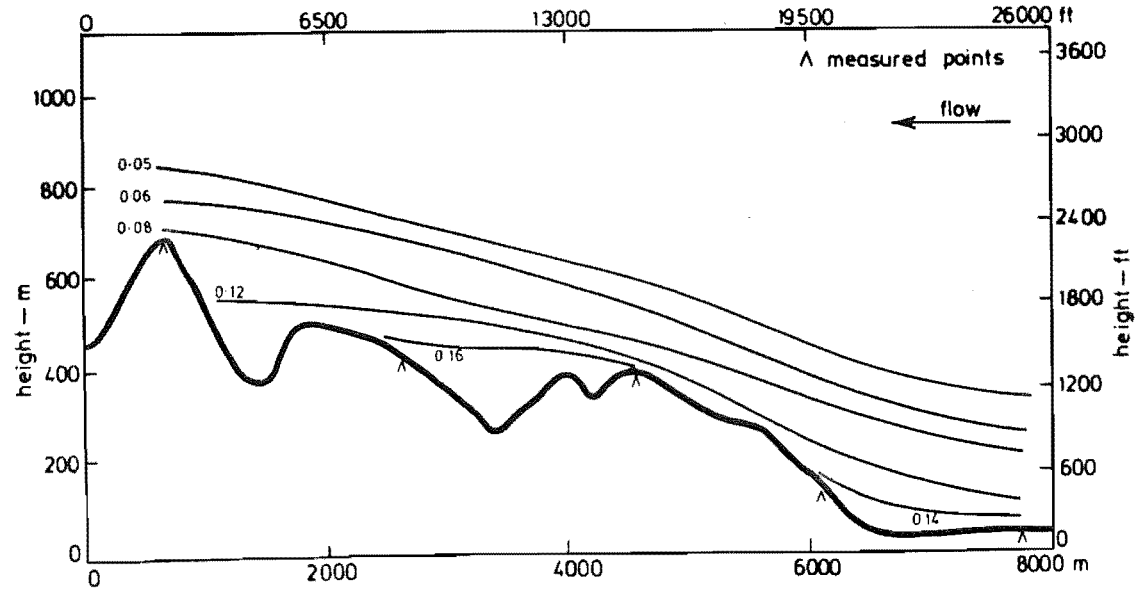

FIG 9.29 ISOTURBS FOR MODEL C CONTOURED. LONGITUDINAL CROSS SECTION ZZ

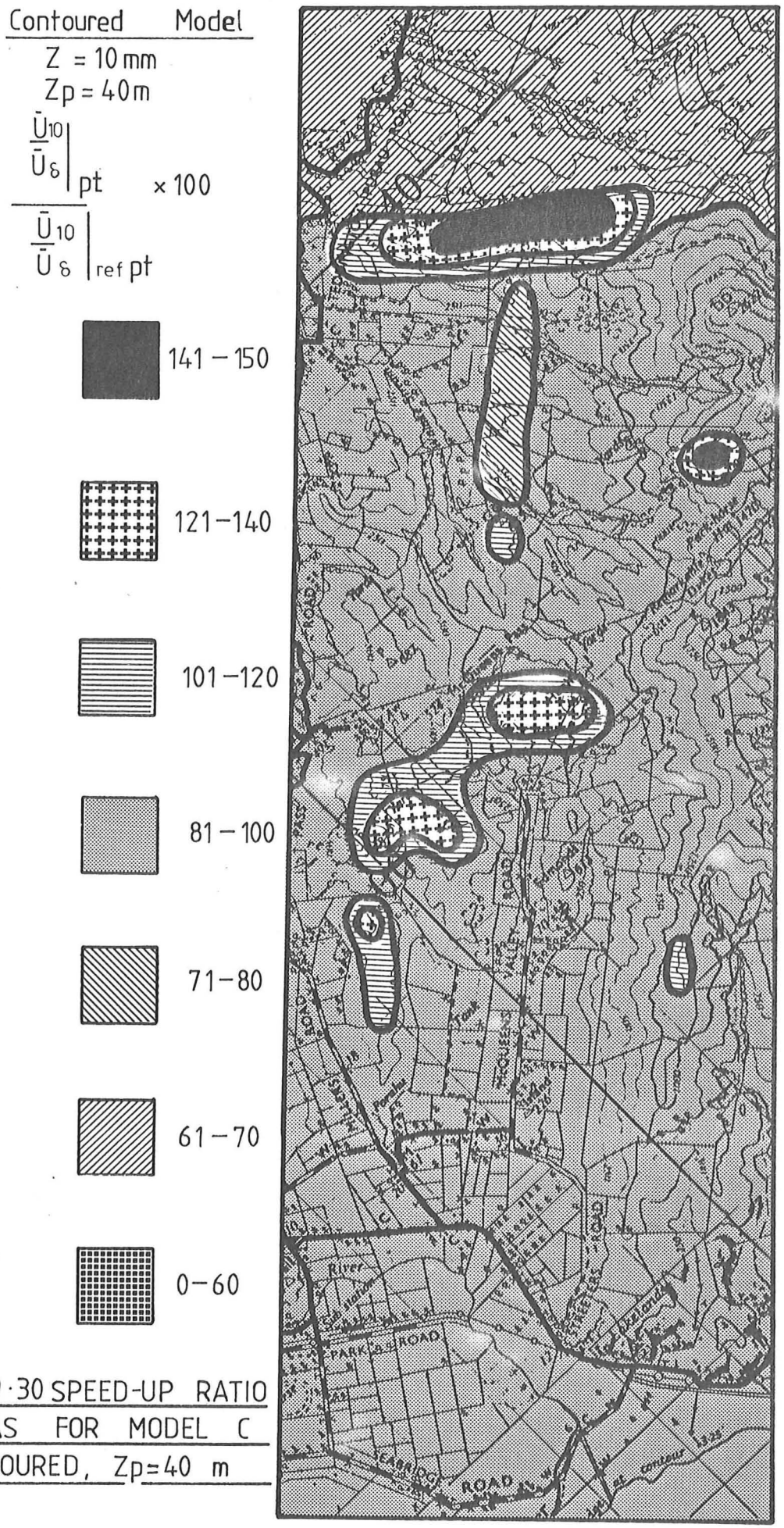

FIG. 9·30 SPEED-UP RATIO AREAS FOR MODEL C CONTOURED, Zp=40 m

This shows that there is generally very little change in the flow over model C. Speed-up was found on the saddle region and on isolated hills and knobs. The most significant speed-up occurred on the lateral ridge at lateral cross section 4.

9.3 ROUGHNESS ADDED MODEL

The roughness elements were added to model C in the same manner as that used for models A and B.

The approach flow conditions were checked and showed excellent agreement with the flow used for the analysis of the model in the contoured form.

9.3.1 Flow Visualisation

Polystyrene bead tests were not repeated for the model in this form of construction, the reasons for this being detailed in Section 7.5.1.

Flag tests were repeated and indicated that no significant flow direction changes had occurred as a result of the addition of the roughness elements.

9.3.2 Hot Film Survey

The lateral cross section isotach and isoturb contours are presented in Figs 9.30 to 9.38.

The isotach contours for cross section 1 show a slight velocity reduction in the bottom 5mm of the boundary layer. The contours above this height are almost identical for both the contoured and roughness added models. The isoturb contours for this cross section are significantly different to those for the contoured model. Point 42, located at the 800m base scale position, has several shelterbelts upstream and these have resulted in a turbulence intensity increase from 13% to 16%. The other points on this cross section show a smaller increase in the bottom 5mm of the boundary layer. The general shape of the contours above this height are in excellent agreement with those for the contoured model.

The isotach contours for cross section 2 show a significant reduction in velocity from 0.70 to 0.60 in the bottom 5mm of the boundary layer. The contours above this height show little change.

The isoturb contours show a significant increase in the bottom 5mm of the boundary layer. The effect of this increase is extended up to the 5% contour which is also moved upwards slightly.

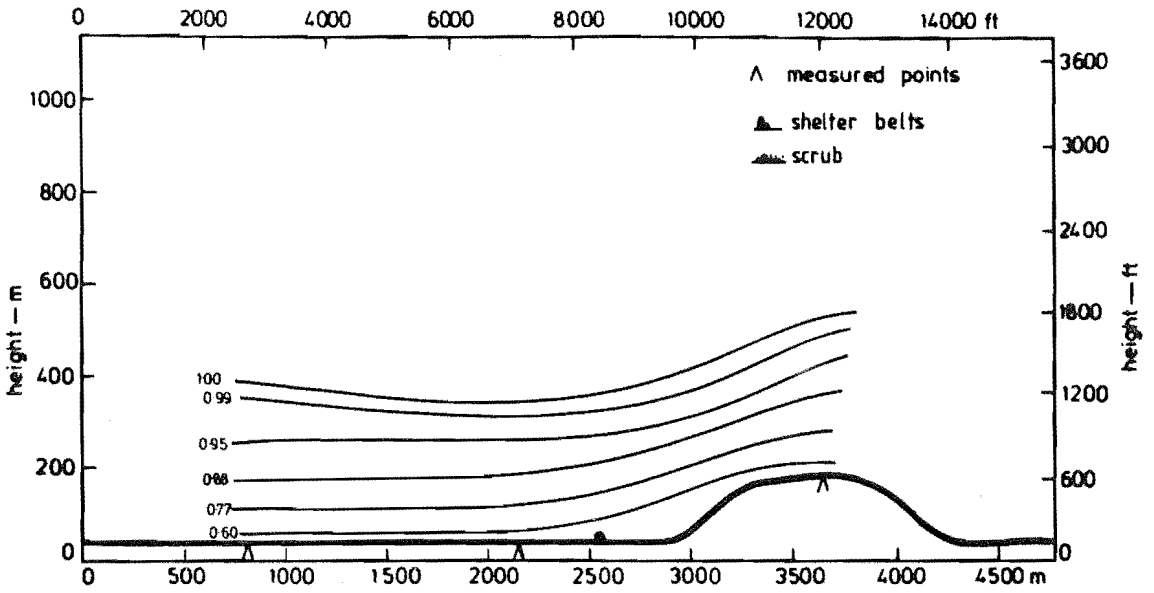

FIG 9.31 ISOTACHS FOR MODEL C WITH ROUGHNESS, LATERAL CROSS SECTION 1

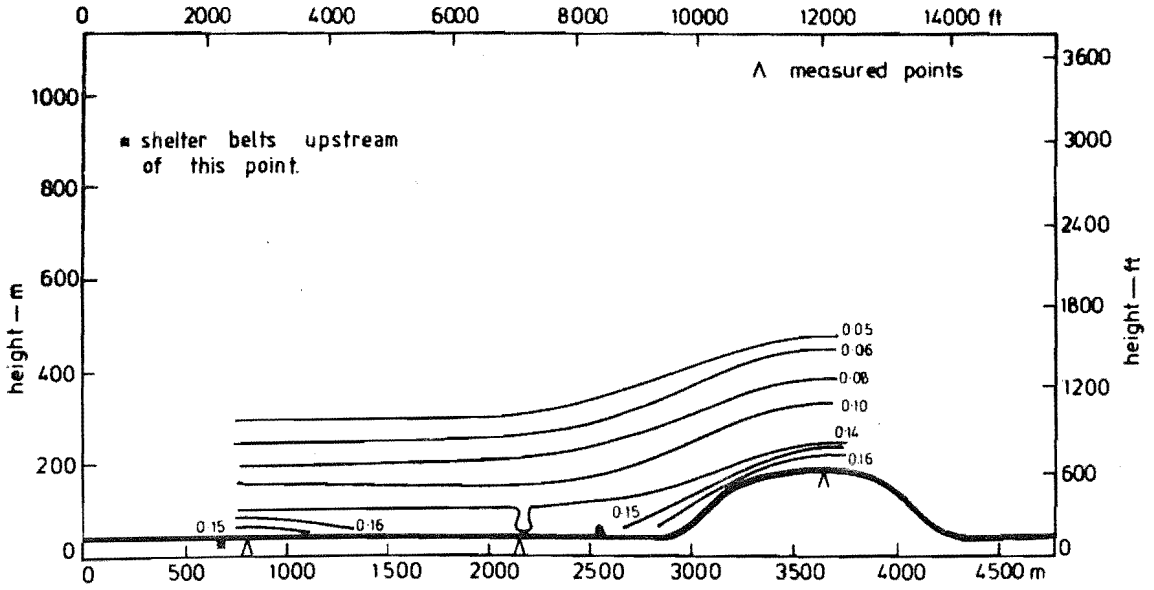

FIG 9.32 ISOTURBS FOR MODEL C WITH ROUGHNESS, LATERAL CROSS SECTION 1

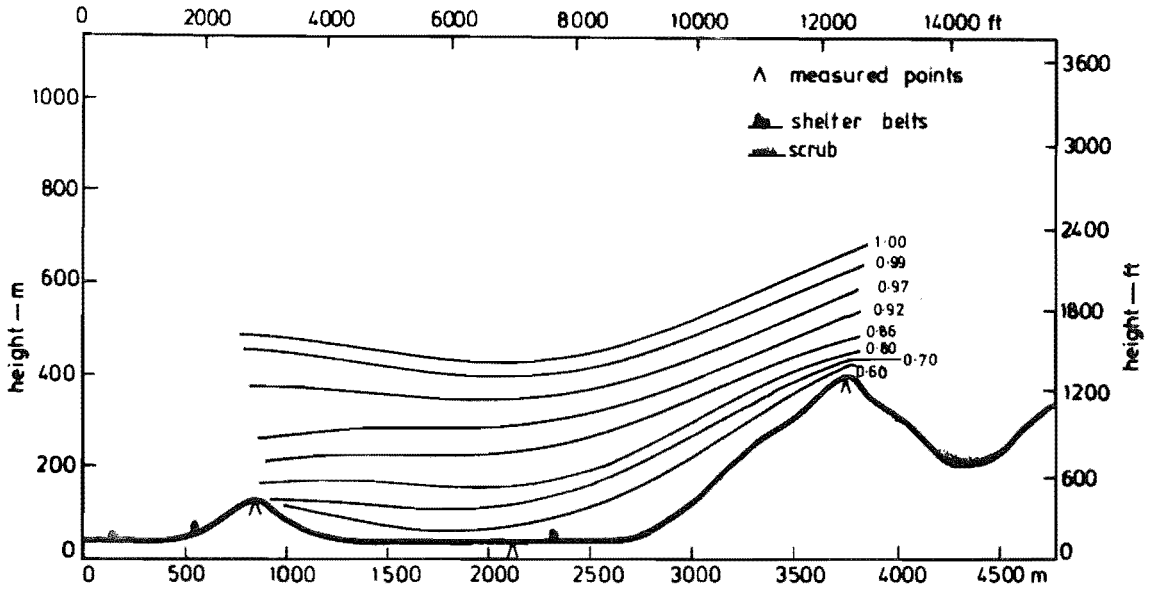

FIG 9.33 ISOTACHS FOR MODEL C WITH ROUGHNESS, LATERAL CROSS SECTION 2

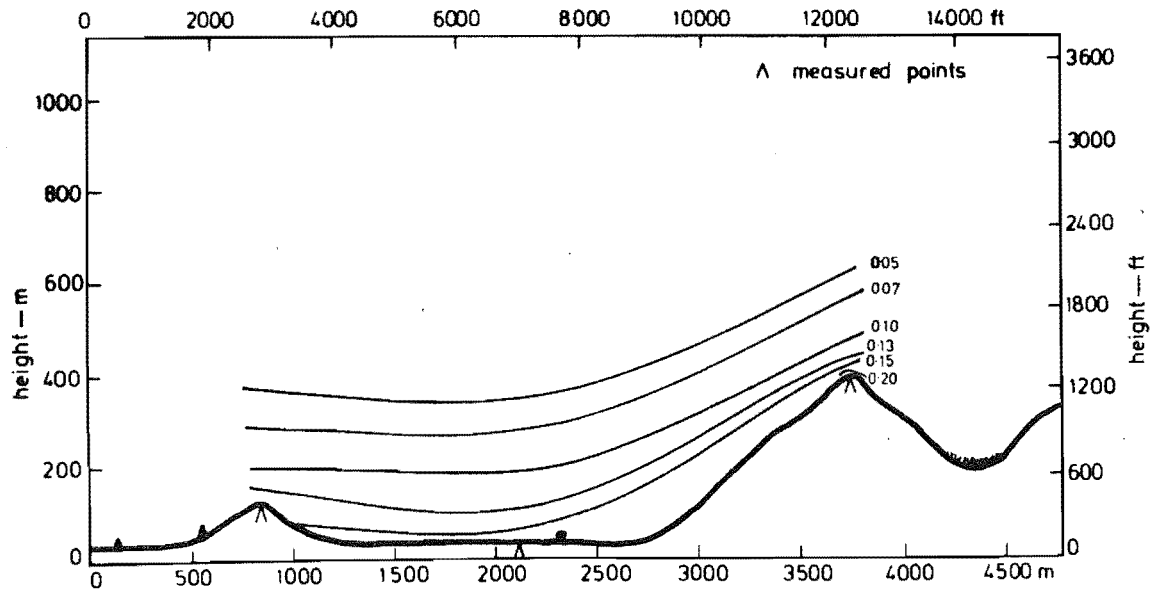

FIG 9.34 ISOTURBS FOR MODEL C WITH ROUGHNESS, LATERAL CROSS SECTION 2

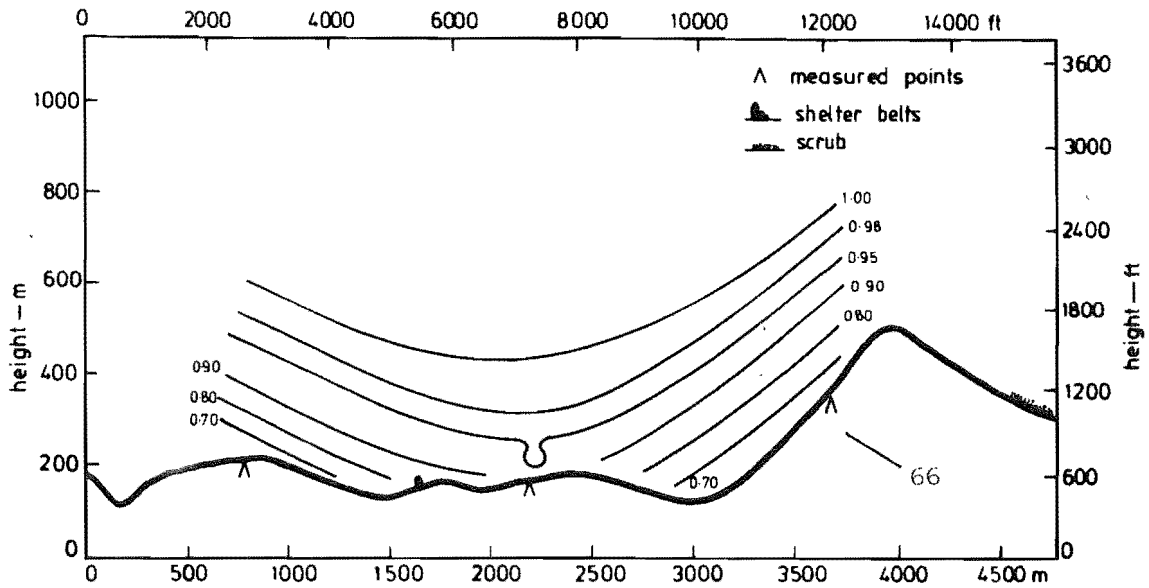

FIG 9.35 ISOTACHS FOR MODEL C WITH ROUGHNESS, LATERAL CROSS SECTION 3

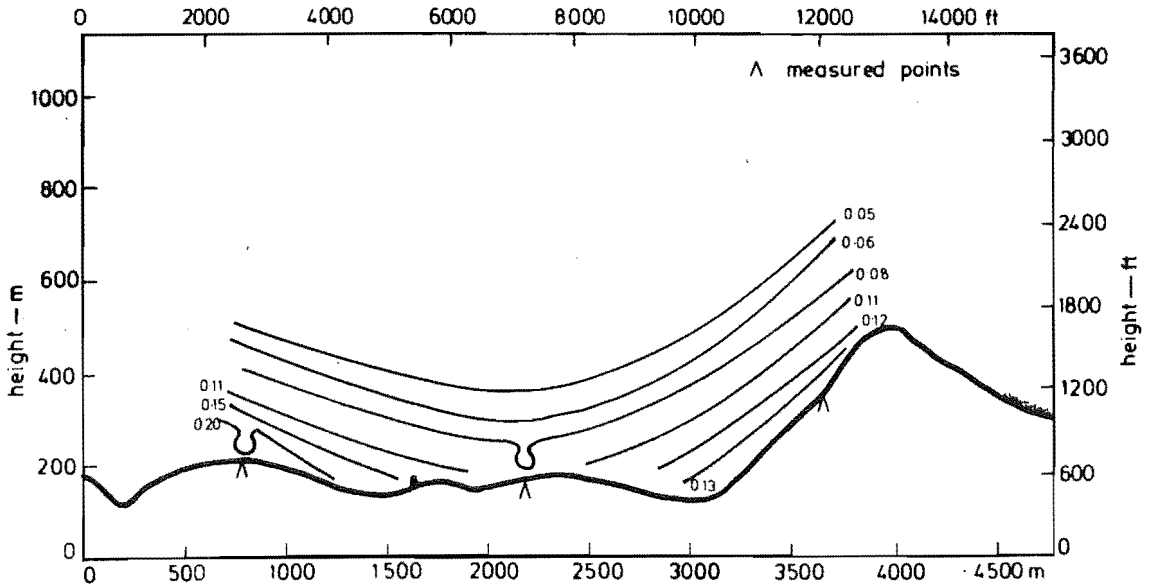

FIG 9.36 ISOTURBS FOR MODEL C WITH ROUGHNESS, LATERAL CROSS SECTION 3

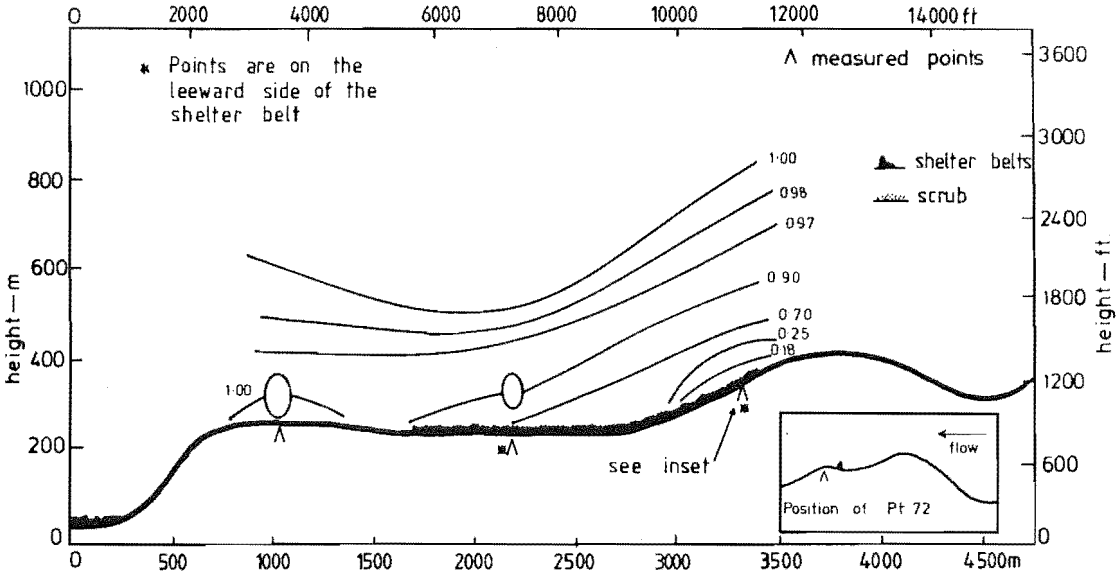

FIG 9.37 ISOTACHS FOR MODEL C WITH ROUGHNESS, LATERAL CROSS-SECTION 4

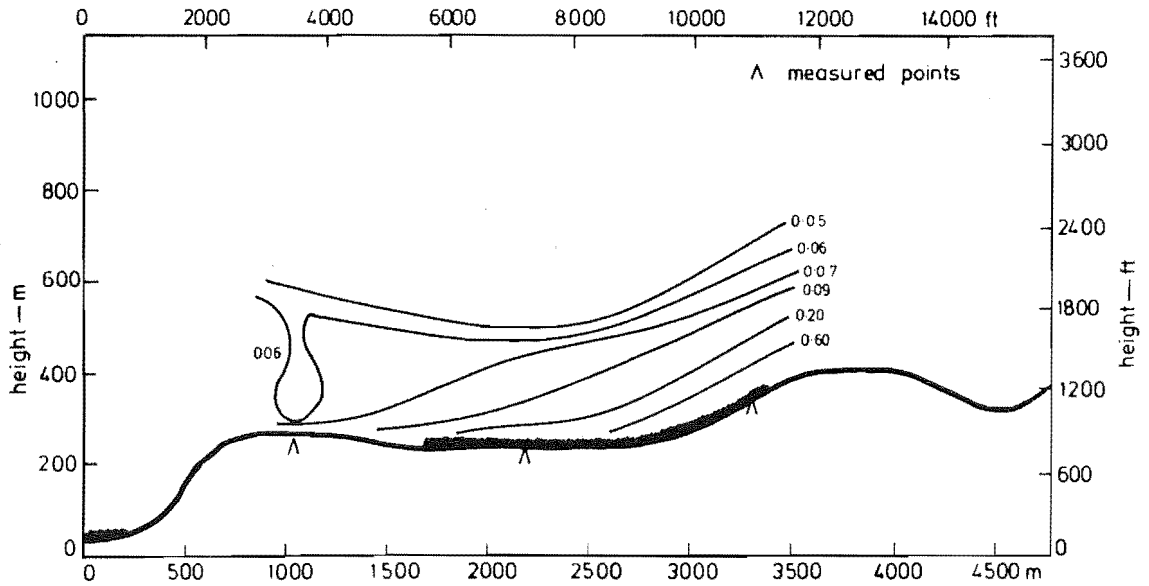

FIG 9.38 ISOTURBS FOR MODEL C WITH ROUGHNESS, LATERAL CROSS SECTION 4

Cross section 3 shows local variations in the isotach contours. Close to the surface, i.e. Z < 10mm, the flow at point 63 is significantly reduced. However, this is not a general trend since the other points measured on this cross section show, essentially, no change. The isoturb contours demonstrate the same pattern.

The effect of adding the roughness elements shows a significant change in the isotach contours at cross section 4. The flow is being affected by the shelterbelt indicated and also a large area of scrub, not shown on the cross section, which is a feature of the windward face of the ridge. The velocity close to the surface at point 72 has been reduced from 0.80 to 0.25 at a height of 10mm. Generally, the effect of the roughness has been to smooth the contours and reduce the level of speed-up close to the model surface.

The isoturb contours show very high levels of turbulence intensity at point 72, $\frac{u}{\bar{u}} > 60\%$. This is an isolated case as the remainder of the ridge shows only small turbulence intensity increases. The contours above 40mm are essentially the same for both models.

The longitudinal cross section results are presented in Figs 9.39 to 9.44.

The isotach contours for both models are essentially the same. The vertical positions of the contours in the 2000m base scale region are difficult to locate because of the lack of data for this area. Consequently, one cannot place too much emphasis on the contours in this region.

The isoturb contours suggest higher turbulence levels in the approach flow close to the model surface. Otherwise, the contours have a very limited shape and their magnitudes are very close.

The isotach contours for longitudinal cross section YY indicate a definite slowing of the flow in the bottom 50mm of the boundary layer. The most significant variation in velocity is on the ridge at the 500m base scale position. The velocity close to the surface has been reduced from 1.02 to 0.70. This is attributed directly to the added roughness immediately upstream. The isoturb contours show increased turbulence intensity values at the points where velocity reductions were noted. There is a general increase in turbulence intensity close to the surface along the whole section. The isotach contours for cross section ZZ show a reduction in velocity approaching the rougher terrain. This feature prevails over the whole section except at point 66, where an increase in

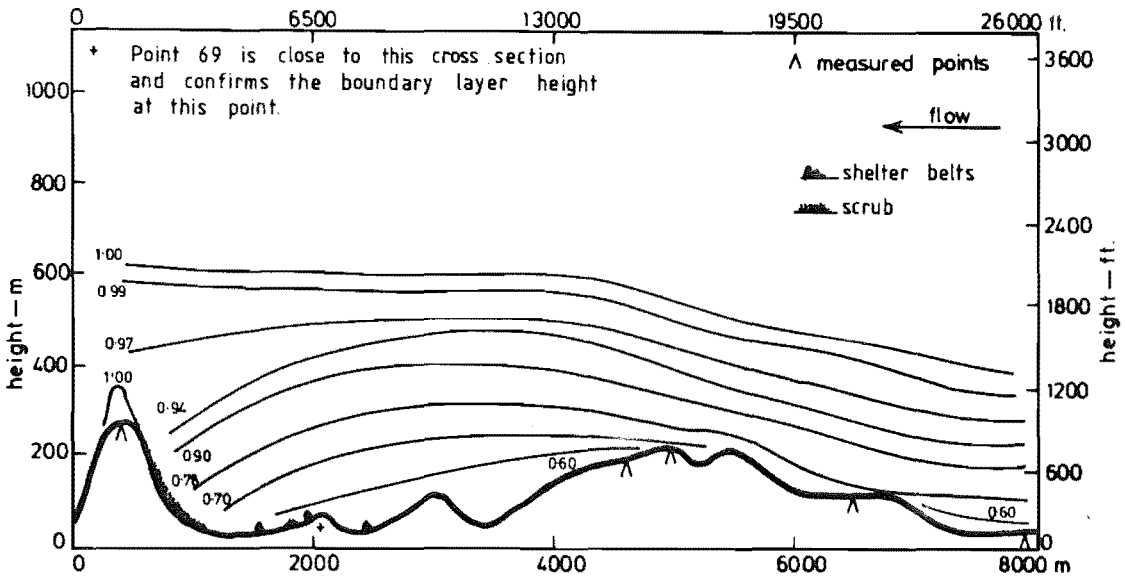

FIG 9.39 ISOTACHS FOR MODEL C WITH ROUGHNESS, LONGITUDINAL CROSS-SECTION XX

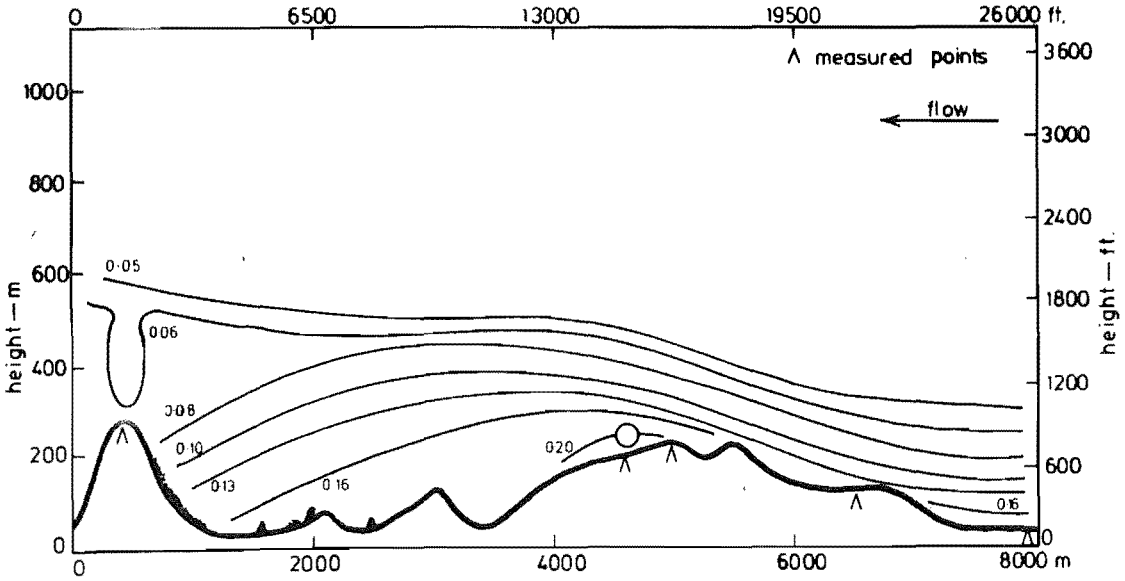

FIG 9.40 ISOTURBS FOR MODEL C WITH ROUGHNESS, LONGITUDINAL CROSS-SECTION XX

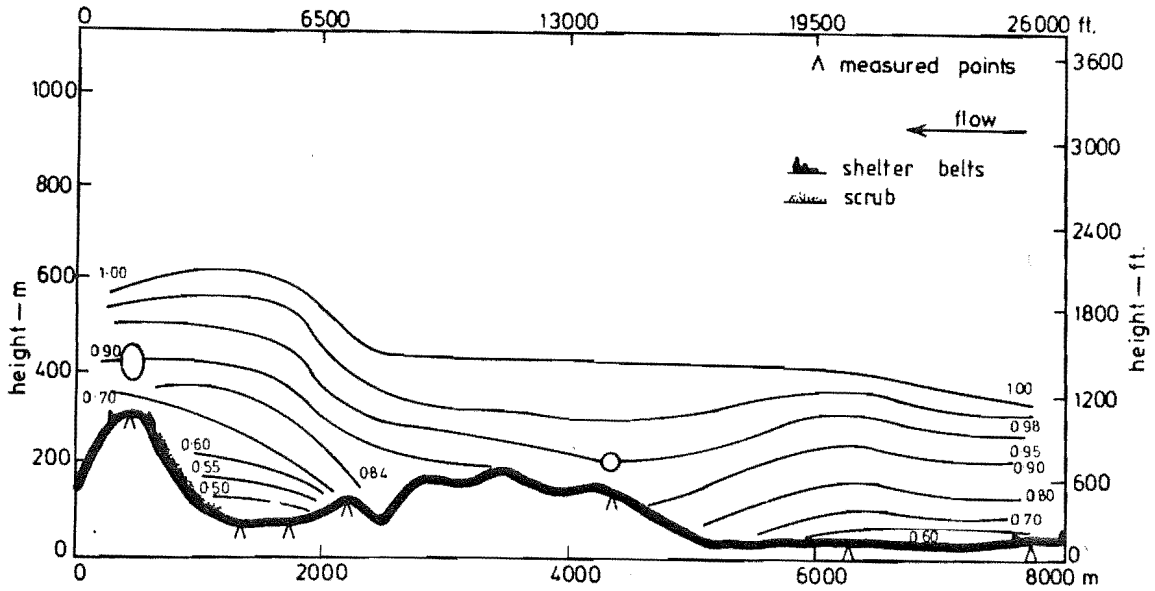

FIG 9.41 ISOTACHS FOR MODEL C WITH ROUGHNESS, LONGITUDINAL CROSS-SECTION YY

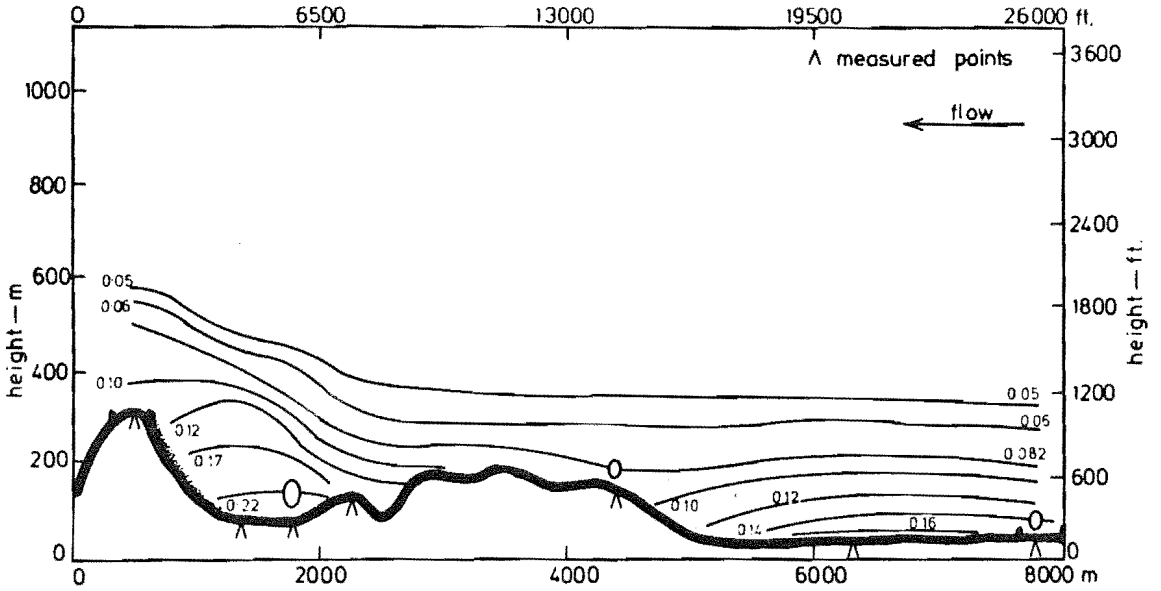

FIG 9.42 ISOTURBS FOR MODEL C WITH ROUGHNESS, LONGITUDINAL CROSS-SECTION YY

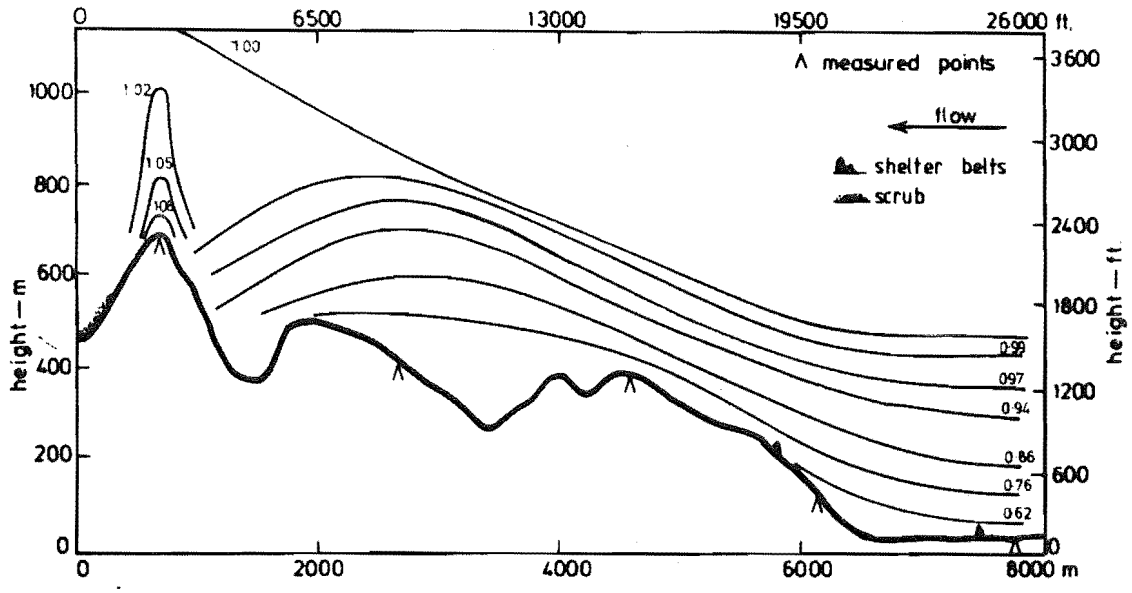

FIG 9.43 ISOTACHS FOR MODEL C WITH ROUGHNESS, LONGITUDINAL CROSS-SECTION ZZ

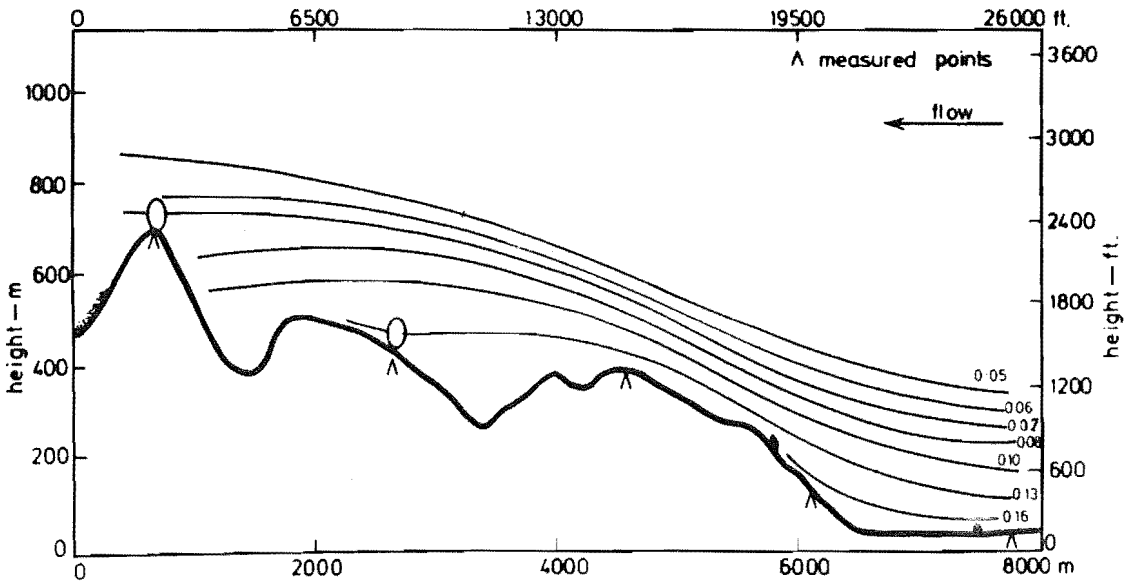

FIG 9.44 ISOTURBS FOR MODEL C WITH ROUGHNESS, LONGITUDINAL CROSS-SECTION ZZ

velocity was noted. Although the method of representing the contours at this point differs for the two models, the magnitude of the velocity is only increased by a small amount. To fully understand what is happening at this point, one would need to carry out a detailed measurement programme each side of the crest. It has been a feature of this study that knobs and ridges often exhibited complex velocity variations. The aims of the research could not be met if every such point were analysed in the required detail. However, this highlights one of the difficulties encountered in the presentation of data measured on complex terrain. In general, the contours for the two models are very close. The isoturb contours for cross section ZZ show an increase in the approach terrain and a slight reduction at point 66; otherwise, the contours for both models are in good agreement.

The normalised velocities for the 3mm and 5mm heights for model C are presented in tabular form in Table 9.1.

The speed-up ratio areas for the roughness added model are presented on the map in Fig. 9.45. Generally, the speed-up ratio areas are the same as for the contoured model, see Fig. 9.30 for comparison. The exceptions to this mainly occur on the lateral ridge, cross section 4. The extent of the 141-150% area has been significantly reduced together with an increase in the low speed area. This effect is reasonable when one considers the large amount of roughness added in this region. In particular, point 72 which is located in a hollow behind a shelterbelt (see inset in Fig. 9.38) shows a velocity ratio reduction from the 81-100% to the 0-60% range. A couple of the points suggest small increases, most of these points being very close to the demarcation between ranges and therefore a small change of 1 or 2% in the measured velocity can be misconstrued on the speed-up ratio area diagram as being a significant change.

9.3.3 Correlation Between Model C, Contoured vs Roughness Added

The scatter diagrams for model C contoured vs roughness added velocities are presented for heights of 5mm, 10mm and 20mm in Figs 9.46 to 9.48 respectively.

A particularly interesting result was obtained in the correlation analysis. The results of several sets of correlation calculations using different sample sizes, n, are presented in Table 9.2.

In all previous calculations, all points measured were included in the correlation calculations. When this approach was adopted for model C, using 28 points, a poor correlation of 0.64 was calculated for the 5mm

Height Z(mm)								
	Lateral Cross Section 1							
δ	90	(90)	90	(80)	90	(90)		
5	0.68	(0.59)	0.67	(0.60)	0.65	(0.62)		
3	0.64	(0.55)	0.62	(0.56)	0.62	(0.57)		
	42		39		46			
	Lateral Cross Section 2							
δ	90	(90)	110	(100)	70	(70)		
5	0.77	(0.76)	0.63	(0.57)	0.70	(0.61)		
3	0.72	(0.71)	0.58	(0.52)	0.61	(0.52)		
	49		48		47			
	Lateral Cross Section 3							
δ	100	(100)	70	(70)	110	(110)		
5	0.57	(0.58)	0.94	(0.94)	0.65	(0.63)		
3	0.55	(0.56)	0.92	(0.93)	0.62	(0.61)		
	16		64		63			
	Lateral Cross Section 4							
δ	100	(90)	35	(25)	60	(70)	120	(120)
5	0.97	(1.01)	1.06	(0.96)	1.02	(0.19)	0.56	(0.16)
3	0.95	(0.97)	-	(0.90)	1.03	(0.15)	0.50	(0.16)
	70		76		71		72	

Values in brackets are for roughness added model.

TABLE 9.1: Normalised velocity Readings close to Model Surface for Model C. Contoured and with roughness added.

Height Z (mm)						
	Longitudinal Cross Section XX					
δ	90 (90)	90 (90)	90 (80)	100 (100)	100 (90)	
5	0.68 (0.59)	0.77 (0.76)	0.73 (0.73)	0.57 (0.58)	0.97 (1.01)	
3	0.64 (0.55)	0.72 (0.71)	0.70 (0.70)	0.55 (0.56)	0.95 (0.97)	
	42	49	17	16	70	
	Longitudinal Cross Section YY					
δ	90 (80)	110 (100)	70 (70)	90 (80)	150 (140)	60 (70)
5	0.67 (0.60)	0.63 (0.57)	0.94 (0.94)	0.84 (0.84)	0.44 (0.45)	1.02 (0.19)
3	0.62 (0.56)	0.58 (0.52)	0.92 (0.93)	0.85 (0.85)	0.41 (0.42)	1.03 (0.15)
	39	48	64	65	73	71
	Longitudinal Cross Section ZZ					
δ	90 (90)	70 (70)	110 (110)	130 (120)		
5	0.65 (0.62)	0.70 (0.61)	0.65 (0.63)	1.06 (1.08)		
3	0.62 (0.57)	0.61 (0.52)	0.62 (0.61)	1.02 (1.07)		
	46	47	63	66		

Values in brackets are for roughness added model.

TABLE 9.1 (Continued): Normalised Readings close to Model Surface for Model C. Contoured and with roughness added.

Roughness added model

$Z = 10mm$

$Z_p = 40m$

$$\left.\frac{\bar{u}_{10}}{u_\delta}\right|_{pt} \times 100$$

$$\left.\frac{\bar{u}_{10}}{u_\delta}\right|_{ref.\ pt.}$$

	151 - 170
	141 - 150
	121 - 140
	101 - 120
	81 - 100
	71 - 80
	61 - 70
	0 - 60

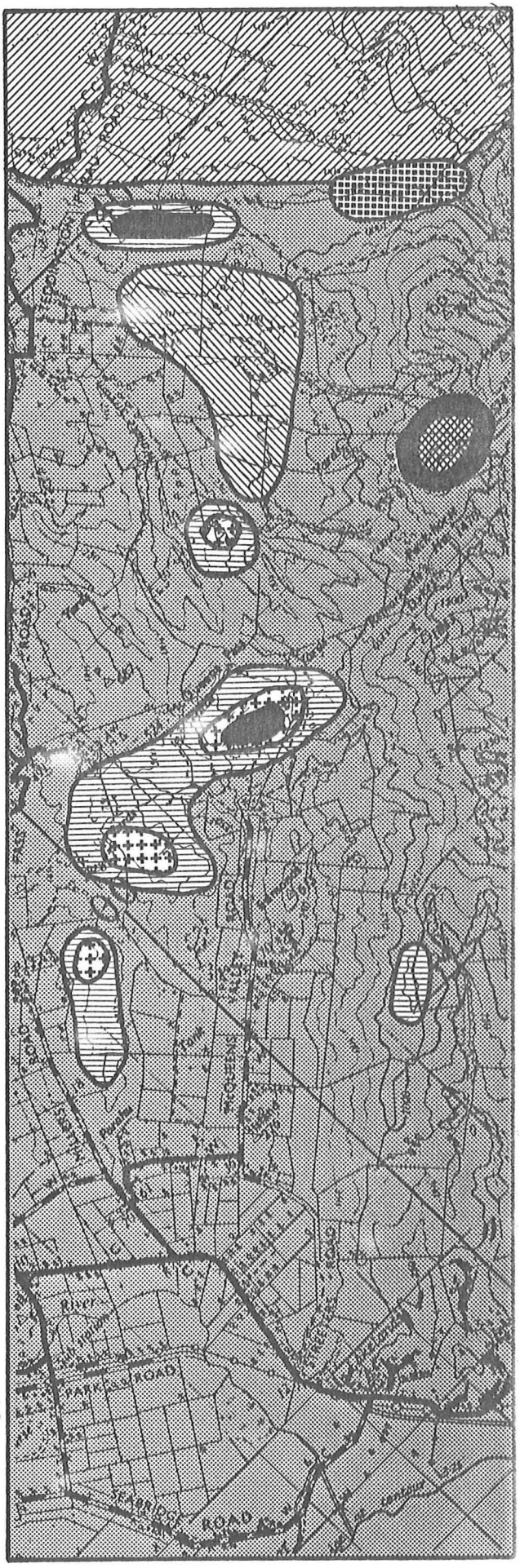

FIG. 9·45 SPEED-UP RATIO AREAS FOR MODEL C ROUGHNESS ADDED, $Z_p = 40m$.

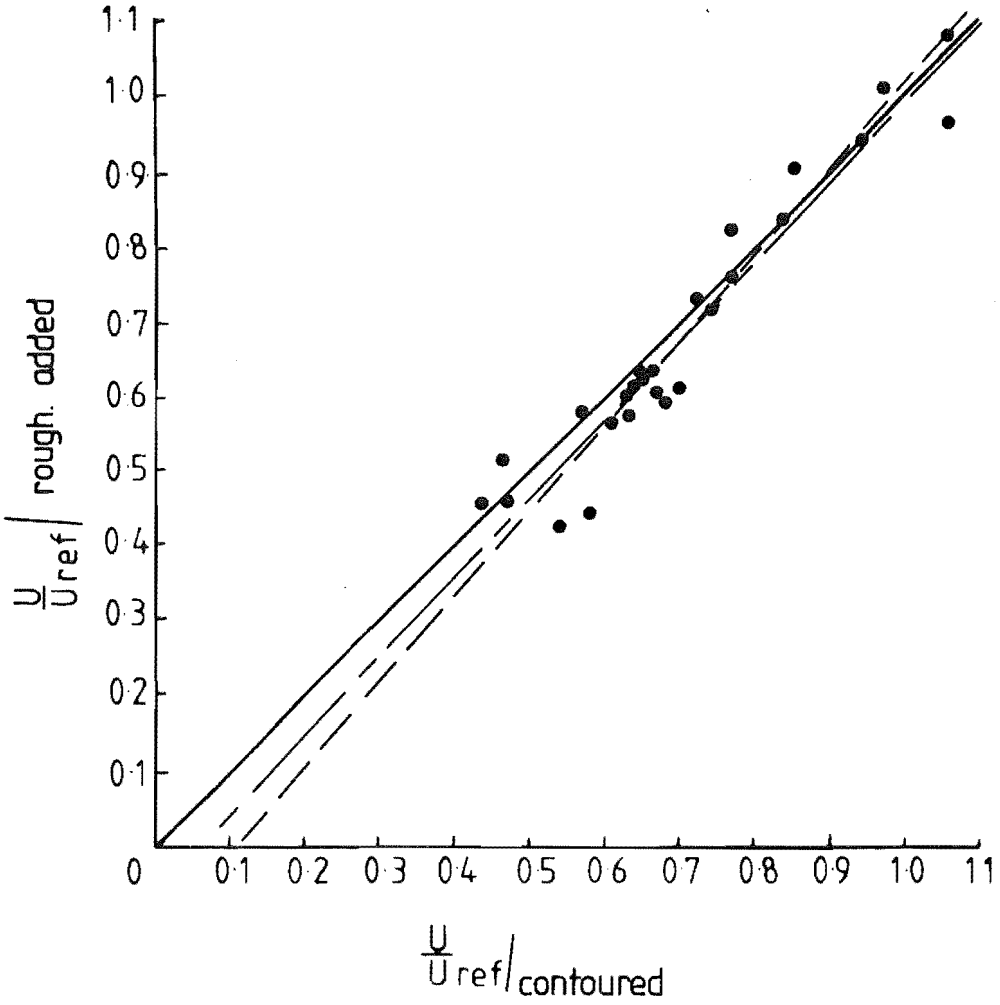

Regression lines

$$- - - - \quad \frac{U}{U_{ref}}\Big|_{contoured} = 0 \cdot 87 \frac{U}{U_{ref}}\Big|_{rough.\ added} + 0 \cdot 111$$

$$- \text{——} - - \quad \frac{U}{U_{ref}}\Big|_{rough.\ added} = 1 \cdot 05 \frac{U}{U_{ref}}\Big|_{contoured} - 0 \cdot 663$$

Correlation coefficient $r = 0 \cdot 96$

FIG. 9·46 SCATTER DIAGRAM FOR MODEL C AT Z = 5 mm.

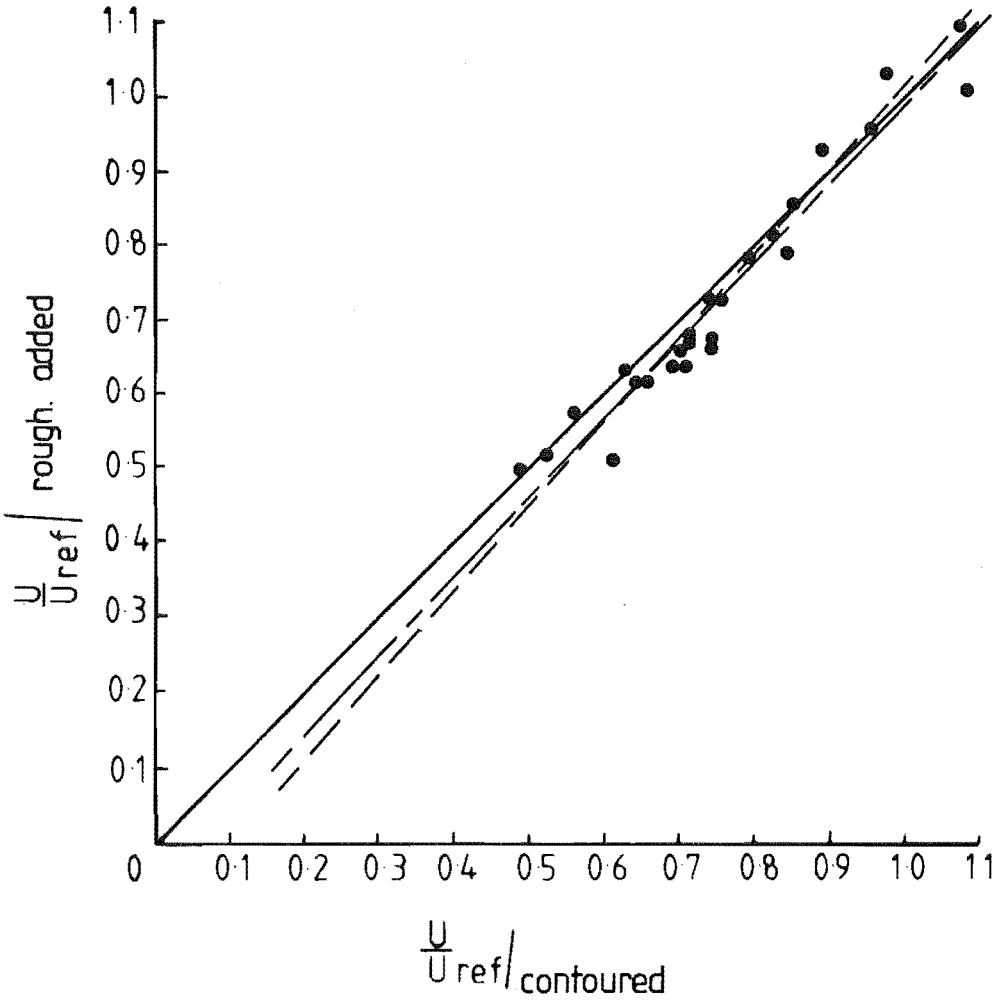

Regression lines

$$\text{- - - -}\quad \frac{U}{U_{ref}}\Big|_{contoured} = 0\cdot 89\ \frac{U}{U_{ref}}\Big|_{rough.\ added} + 0\cdot 104$$

$$\text{- — - —}\quad \frac{U}{U_{ref}}\Big|_{rough.\ added} = 1\cdot 05\ \frac{U}{U_{ref}}\Big|_{contoured} - 0\cdot 070$$

Correlation coefficient $r = 0\cdot 97$

FIG. 9·47 SCATTER DIAGRAM FOR MODEL C AT Z = 10 mm.

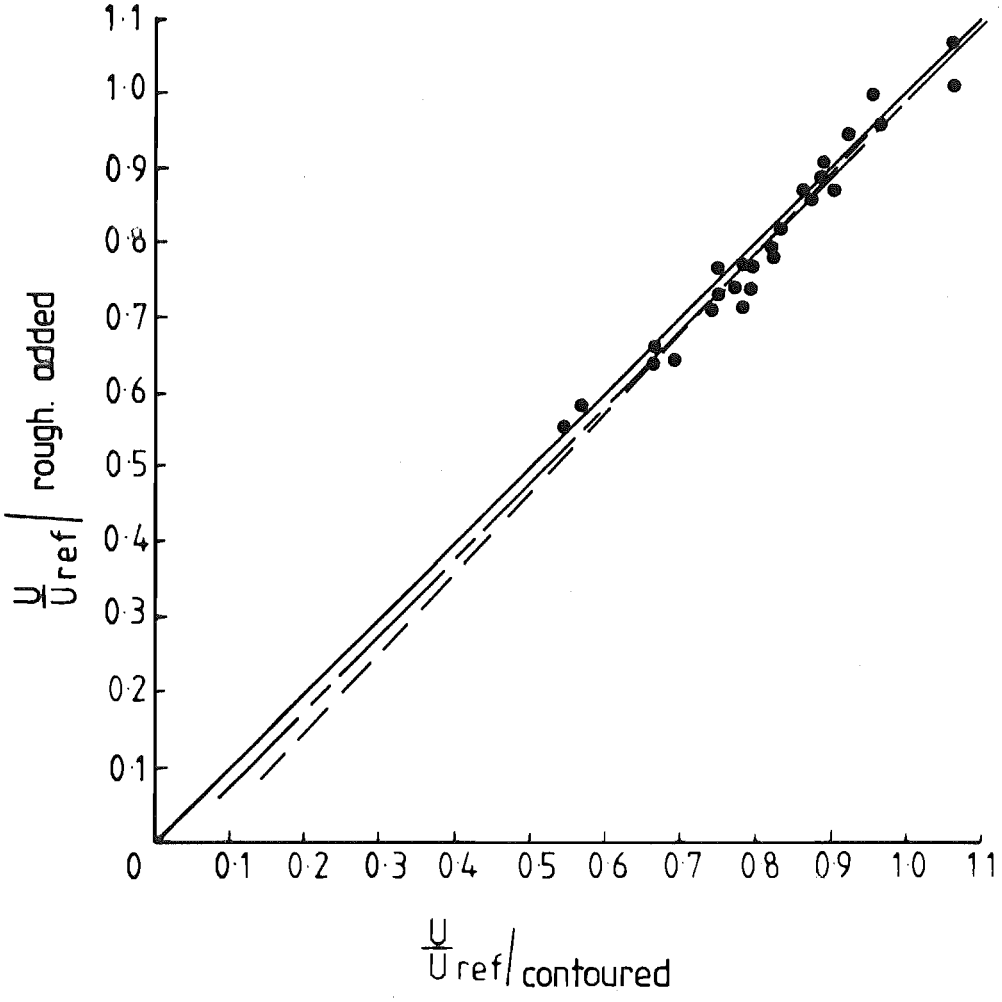

Regression lines

$$\text{- - - -}\quad \frac{U}{U_{ref}}\Big|_{contoured} = 0.95\,\frac{U}{U_{ref}}\Big|_{rough.\ added} + 0.061$$

$$\text{- — - —}\quad \frac{U}{U_{ref}}\Big|_{rough.\ added} = 1.00\,\frac{U}{U_{ref}}\Big|_{contoured} - 0.025$$

Correlation coefficient $r = 0.97$

FIG. 9·48 SCATTER DIAGRAM FOR MODEL C AT Z = 20 mm.

Z (mm)	n_1	r_1	n_2	r_2
5	28	0.64	26	0.96
10	28	0.81	26	0.97
20	28	0.77	26	0.98

r - Correlation coefficient

TABLE 9.2: Variation of Correlation Coefficient with height and sample size.

high data. This was lower than one would expect, especially after the high correlations obtained between these forms of construction for the other models. To narrow down the cause, a correlation was obtained using 16 points located on the southern half of the model. This yielded a correlation of 0.94 for the 5mm data. The remaining 12 points produced a correlation of 0.61. Further observation of these points resulted in points 71 and 72 being omitted. A correlation of the remaining 10 points produced a coefficient of 0.97. Points 71 and 72 are situated directly behind a shelterbelt which resulted in the velocity at these points being drastically reduced - in the case of point 71 from 1.02 to 0.19. The point gained from this exercise is an appreciation of how only 2 points in 28 could dramatically influence the correlation result. This raises the questions:

1) When is the correlation result being unduly influenced by one, two or more data points?

2) How many data points can be rejected before their rejection unduly influences the result?

These are very awkward questions to answer; the author considers the following factors as a general guide:

i) The cause of the variation resulting in a biased correlation must be defined and understood.

ii) Data should not be removed simply to improve the correlation.

Finally, although this is not a definitive factor, one may need to supplement the above factors with good sense, honesty and experience, and

still regard the results with caution.

Chien *et al* (1979) established criteria for the rejection of data. Their method of putting the results into different categories appeared rather subjective and probably relied heavily on the experience of the researchers. It would be extremely difficult to generate criteria that could be applied to any situation.

9.3.4 Comparisons Between the Two Forms of Construction

To demonstrate the effect of the added roughness elements, several parameters will be compared.

1) Velocity Profiles: The velocity profile for point 39 is presented in Fig. 9.49. The profile for the roughness added model shows a small reduction in velocity between the 8m and 80m heights. Point 39 is on the flat terrain in a shelterbelted region but is not downstream of any added roughness which is capable of producing significant changes.

Point 48 is situated downstream of point 39 and is still on open flat terrain; the velocity profile for this is presented in Fig. 9.50. Point 48 shows the same features as discussed for point 39.

A direct comparison between the profiles for both points shows them to be almost the same.

The velocity profile for point 64 is presented in Fig. 9.51. This point is situated downstream from point 48, see Fig. 9.14, and is on top of a hill situated at the northern end of a long valley. This situation results in high velocities at this point and the vertical nature of the profile also gives an indication of the degree of speed-up close to the surface.

Point 74 is in a valley located between two ridges with a lateral axis. The downstream ridge is located at lateral cross section 4, see Fig. 9.14. The velocity profile for this point is presented in Fig.9.52 and shows significant differences between the two forms of construction. The roughness added profile shows significant velocity reductions in the bottom 20m of the boundary layer. This can be directly attributed to the presence of shelterbelts upstream of this point. Above the influence of this local roughness, the profiles are in good agreement.

The velocity profile for point 76 which is situated on the top of the lateral ridge at cross section 4, is presented in Fig. 9.53. The profile

Symbol	Model C Point 39
×	Contoured
Δ	With roughness

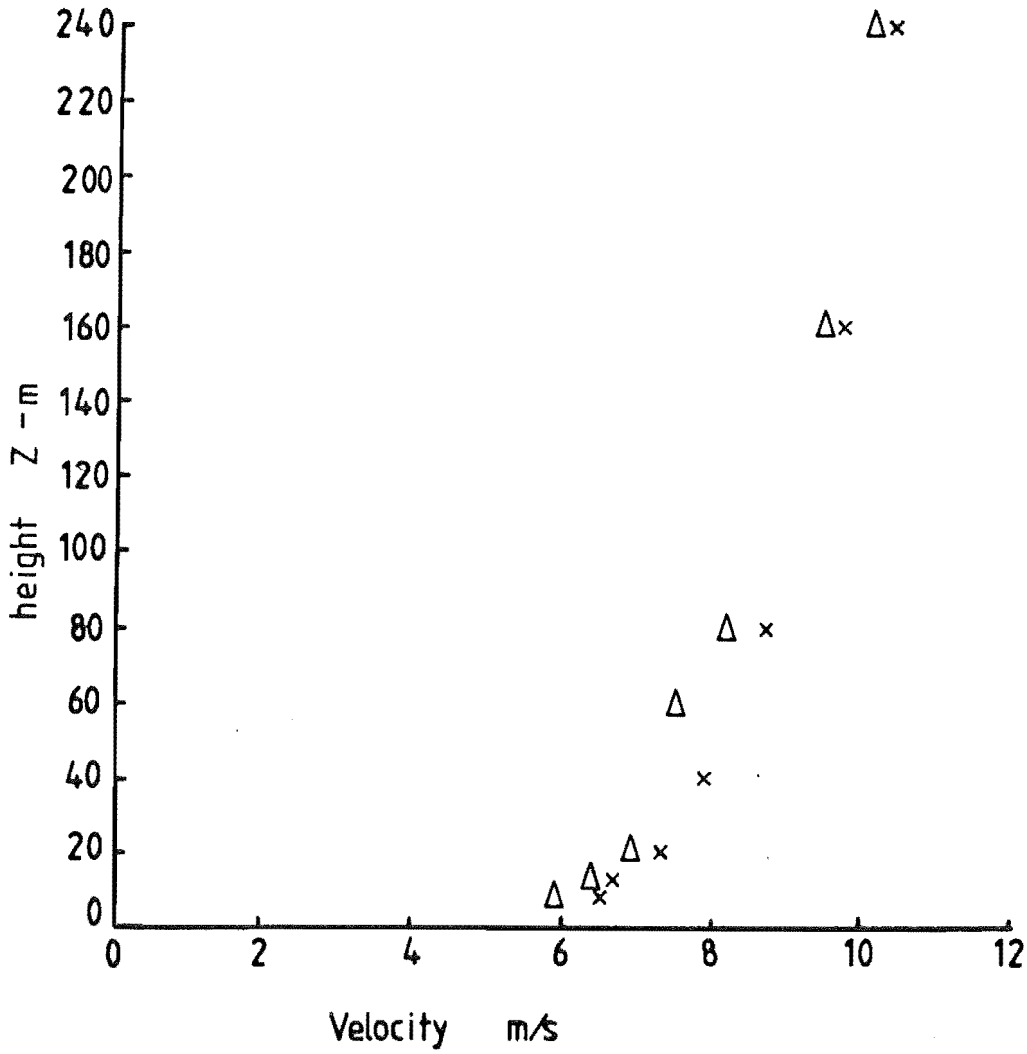

FIG. 9·49 COMPARISON OF VELOCITY PROFILES FOR MODEL C POINT 39

Symbol	Model C Point 48
×	Contoured
Δ	With roughness

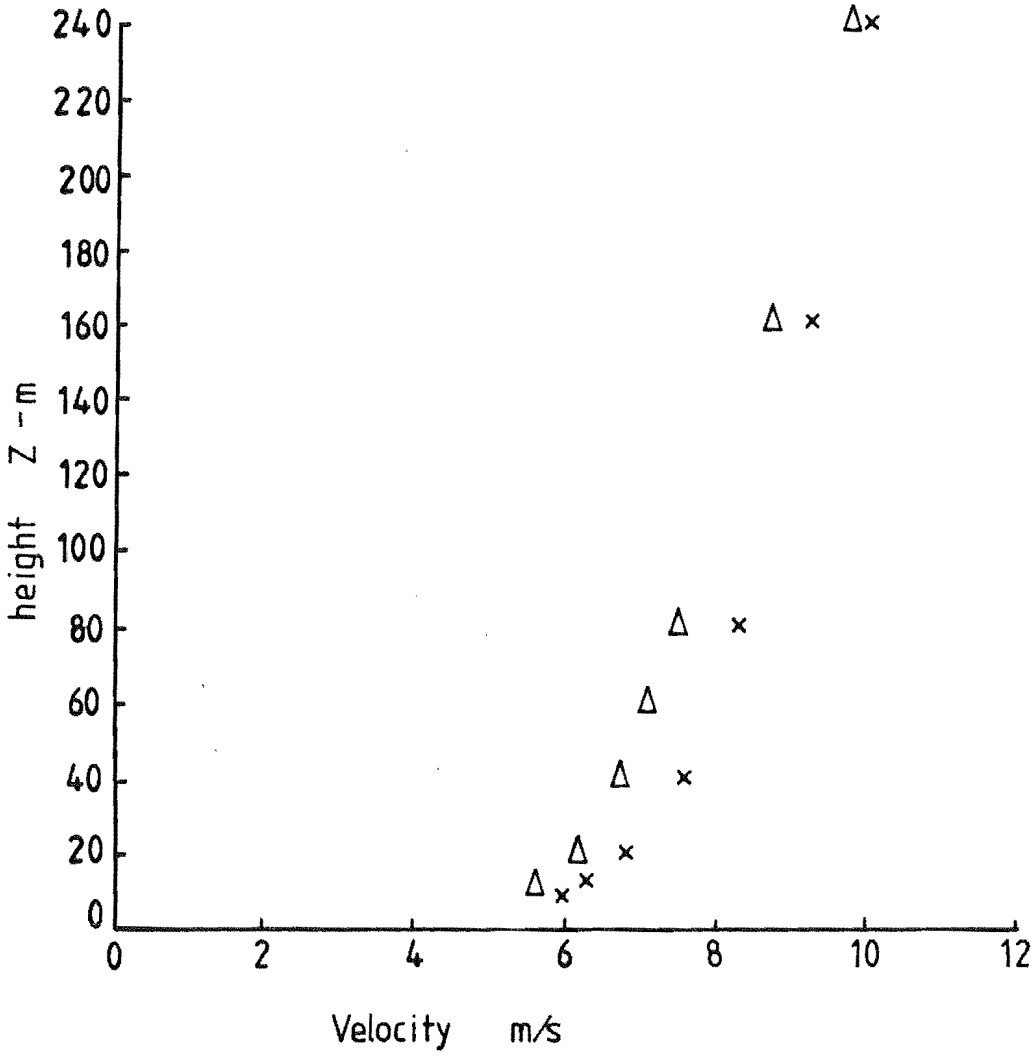

FIG 9·50 COMPARISON OF VELOCITY PROFILES FOR MODEL C POINT 48

Symbol	Model C Point 64
×	Contoured
Δ	With roughness

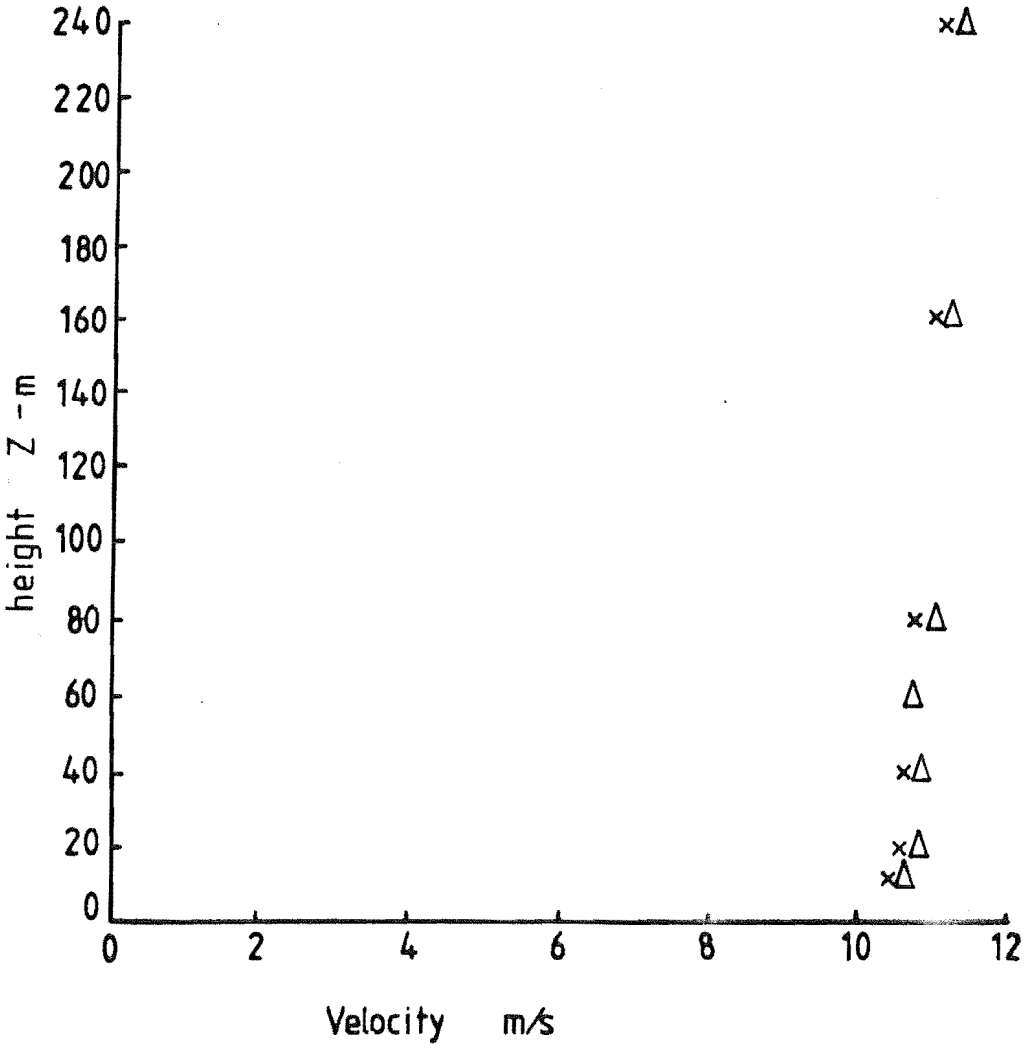

FIG 9·51 COMPARISON OF VELOCITY PROFILES FOR MODEL C POINT 64

Symbol	Model C Point 74
×	Contoured
Δ	With roughness

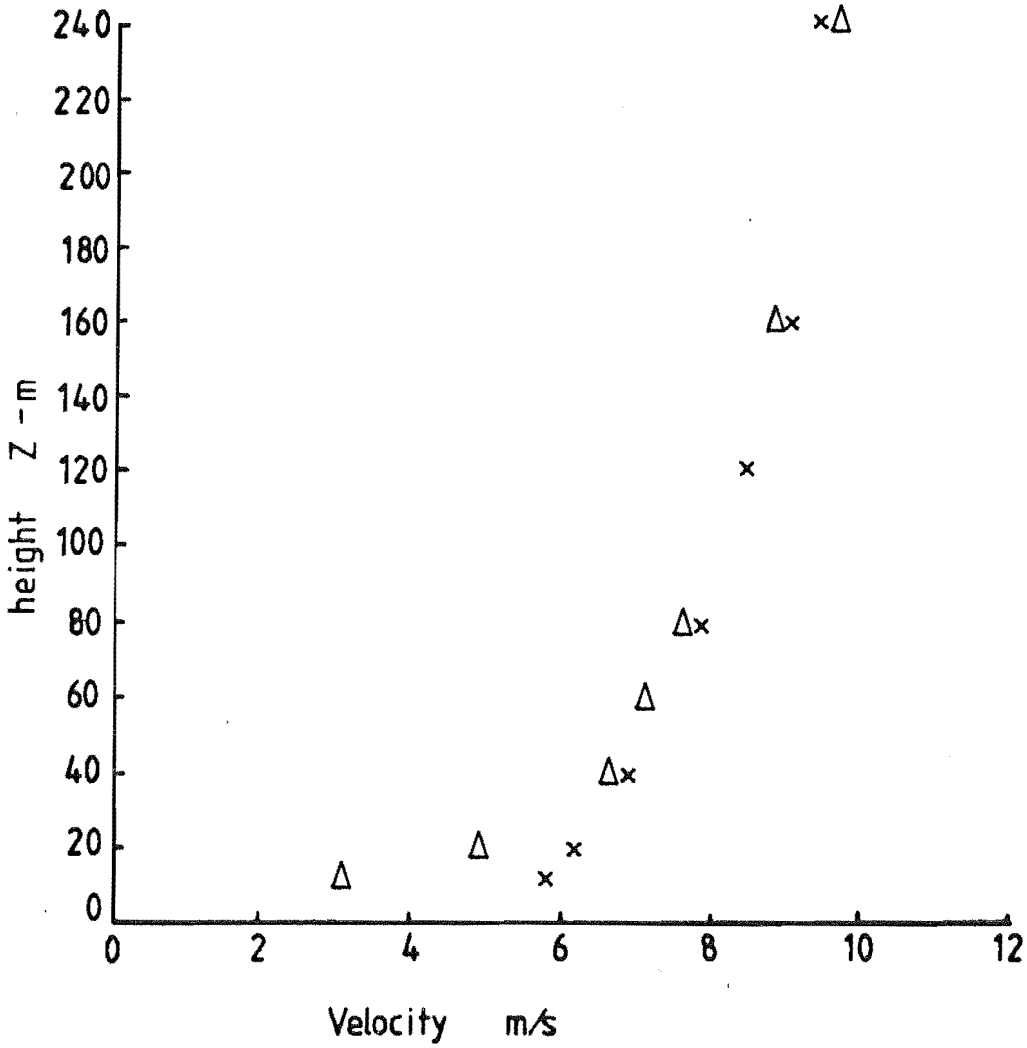

FIG 9·52 COMPARISON OF VELOCITY PROFILES FOR MODEL C POINT 74

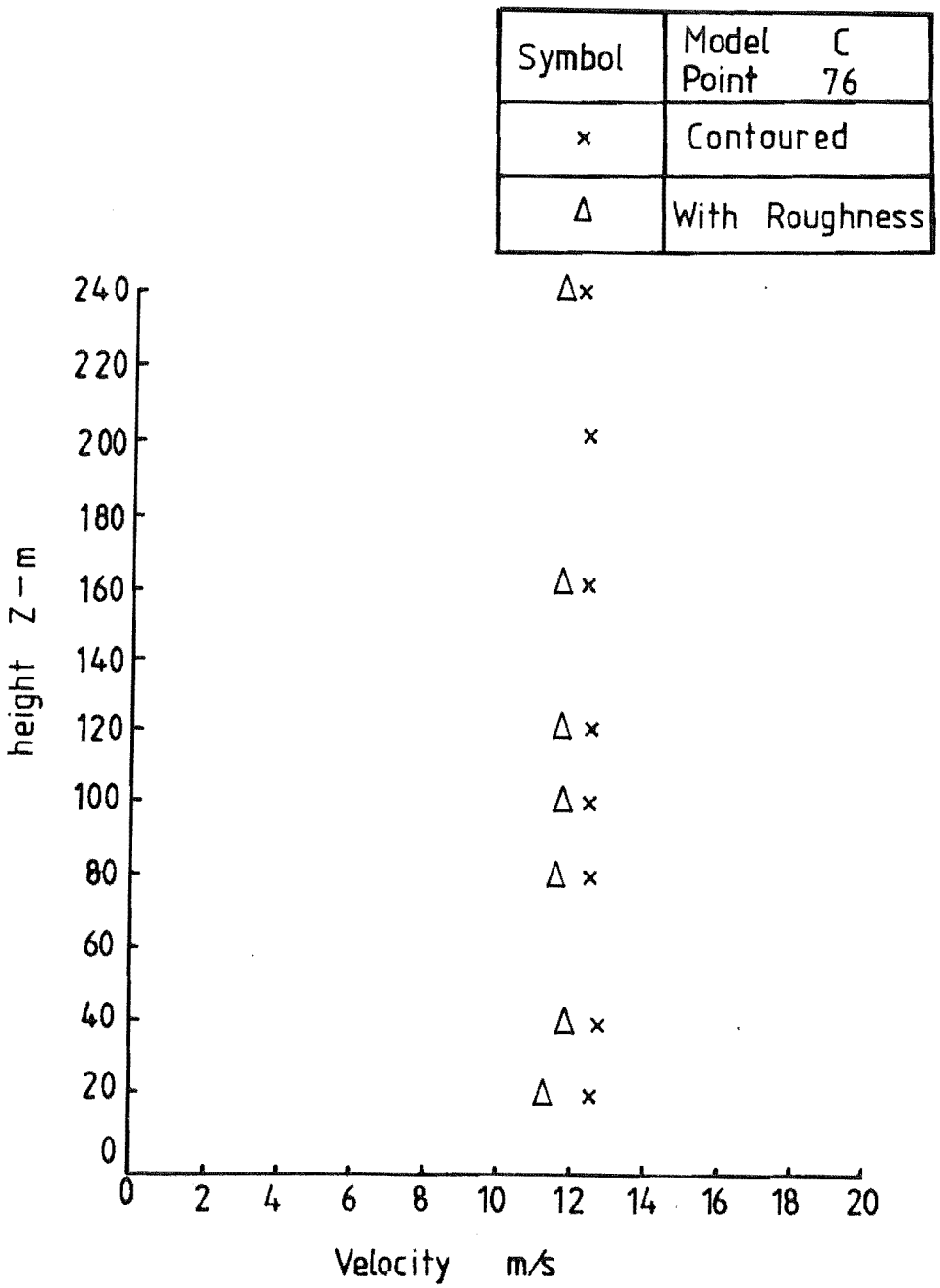

FIG 9·53 COMPARISON OF VELOCITY PROFILES FOR MODEL C POINT 76

indicates high velocities and an almost vertical profile. The roughness added profile is lower than the contoured profile for heights below 160m. This is explained by the shelterbelt and scrub roughness added to the windward face of the ridge. It was noted in the isotach contours that significant flow modification took place on this ridge after the addition of the roughness elements.

2) Turbulence Intensity Profiles: The turbulence intensity profiles for several points approaching the saddle region are presented in Fig. 9.54. These profiles are for the roughness added model and clearly show an increase in turbulence intensity from point 39 to point 48. The location and description of these points were given in subsection (1). The turbulence intensity profile at point 64 shows a marked reduction, due primarily to the increase in velocity at this point.

Turbulence intensity profiles at several points on the ridge at lateral cross section 4 are presented in Fig. 9.55.

Apart from the 12m reading at point 74, the profiles show a generally decreasing trend as the flow increases in speed passing over the ridge. The 12m reading at point 74 is strongly influenced by the presence of the shelterbelt upstream.

3) Energy Spectra: Energy spectra for the longitudinal component will be compared for four points leading up to and over the saddle region.

The spectra for points 44, 39, 64 and 65 at a height of 5mm are presented in Fig. 9.56. Points 44 and 39 have identical high frequency energy levels. The positions of their respective peaks are slightly different and suggest that some of the lower frequency energy has been "broken up" in the case of point 39. This is a reasonable assumption because there are several shelterbelts between points 44 and 39 which would provide the extra mixing to have this effect.

At point 64, the spectrum has moved to the left; this is a function of the higher velocity at this point caused by the flow moving up the face of the saddle. The nett result is an increased length scale value which can be explained by the longitudinal "stretching" of the turbulence as the flow accelerates.

Point 65, located on the leeward side of the saddle, is on the top of a small hill and is subjected to high velocities, as is shown in the speed-up ratio area diagram - see Fig. 9.45. The continuity of the

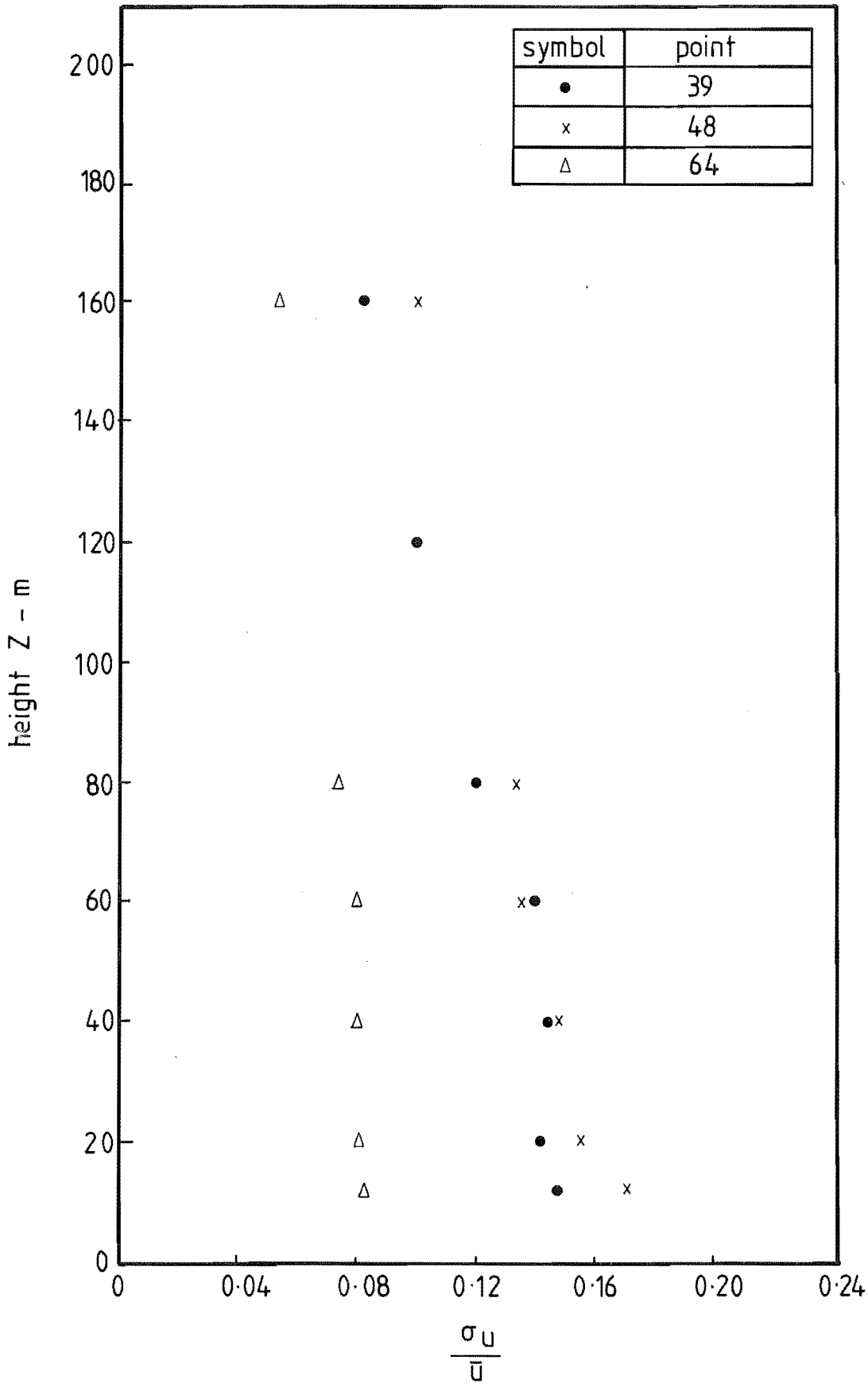

FIG 9·54 VARIATION OF TURBULENCE INTENSITY APPROACHING SADDLE.

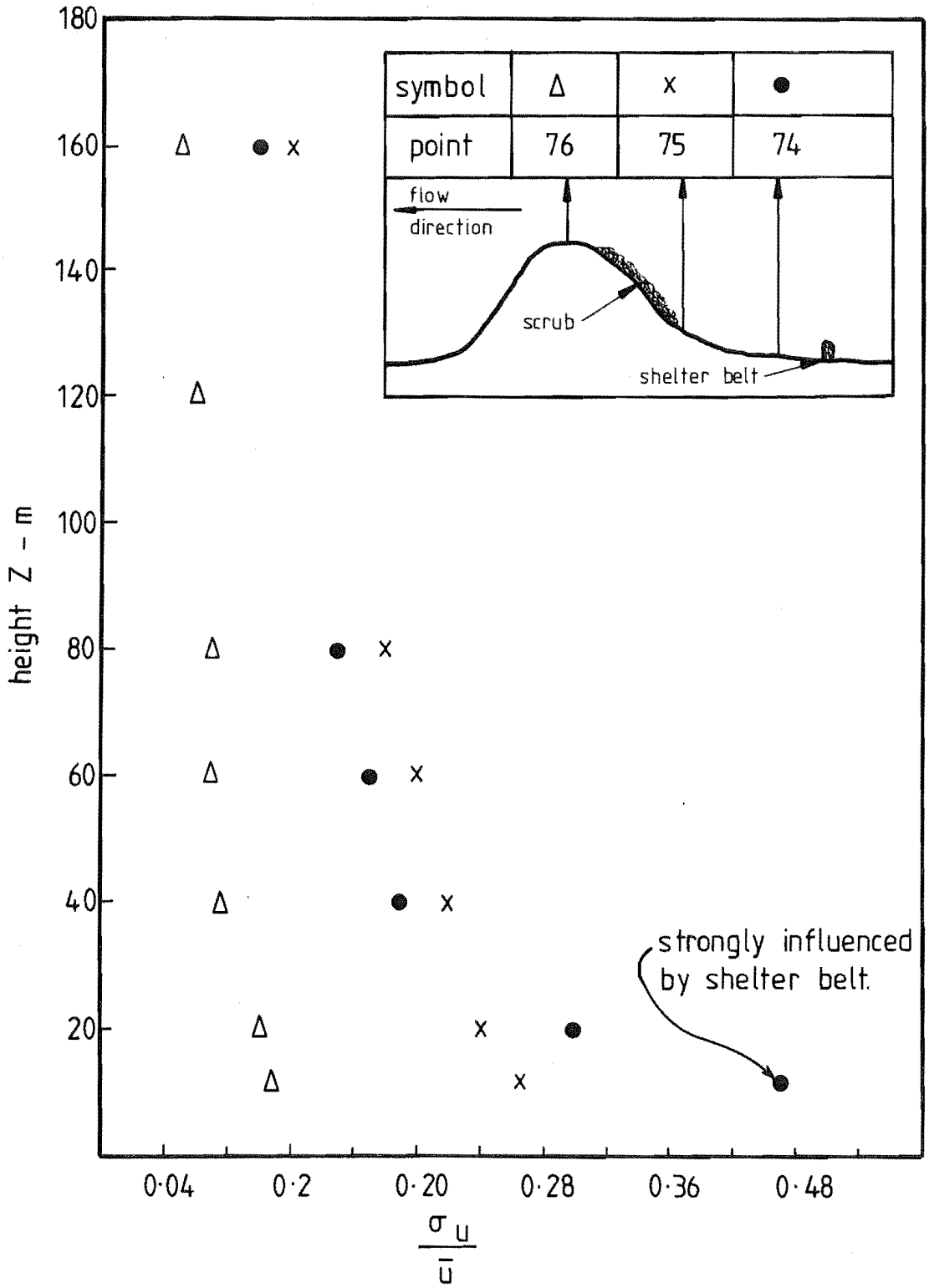

FIG 9·55 VARIATION OF TURBULENCE INTENSITY PROFILES OVER THE RIDGE AT LATERAL CROSS SECTION 4.

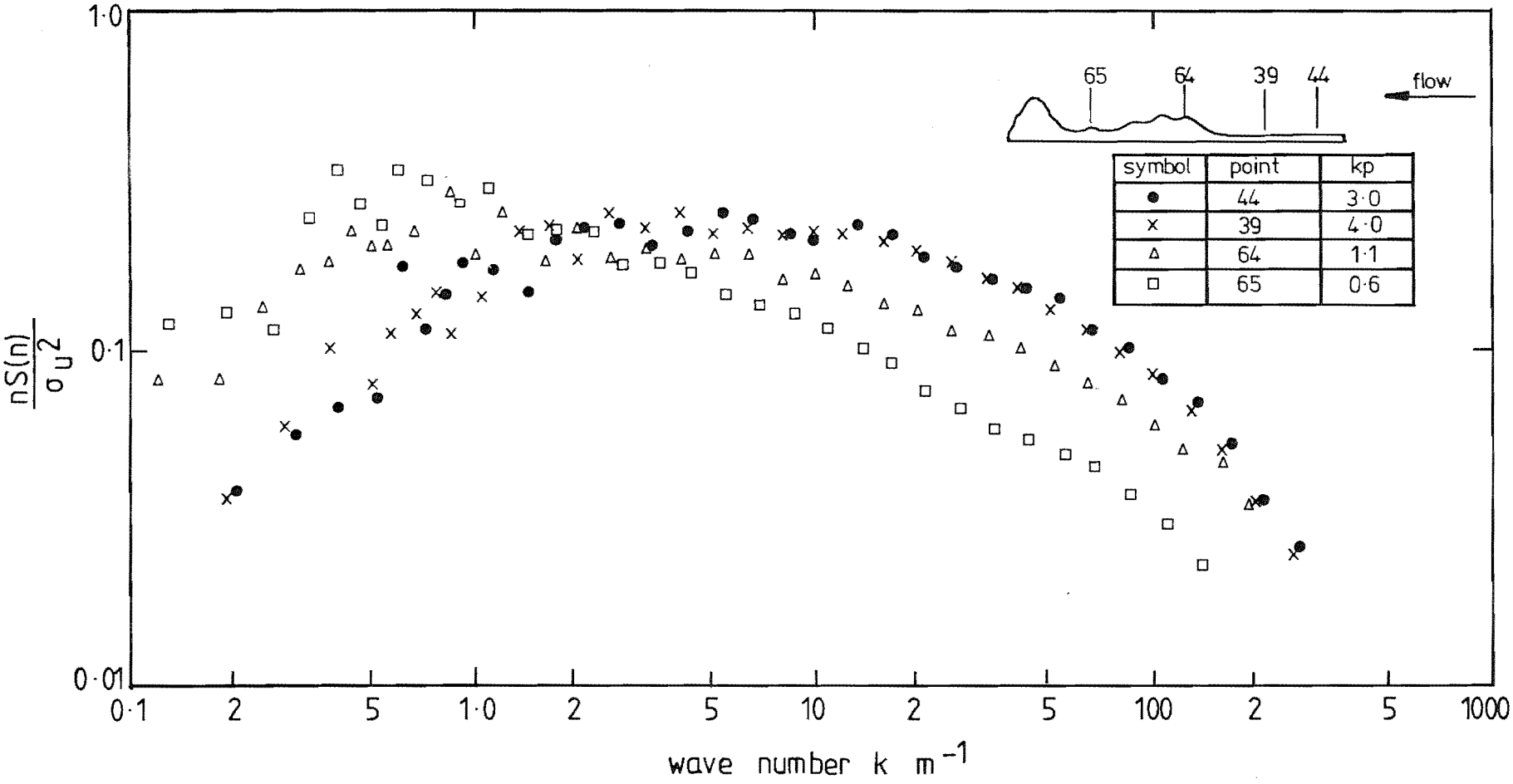

FIG. 9·56 VARIATION OF ENERGY SPECTRA ALONG SECTION YY, Z_p = 20 m

isotach contours suggests that separation is not occurring from the saddle upstream of this point. The length scale, L_{u_x}, calculated from this spectrum, suggests even larger values than were found at point 64. This suggests that the saddle is having a significant effect on the turbulence structure between these two points. This is a reasonable prediction because point 64 is upstream of the saddle crest.

4) Length Scales: The integral length scale, L_{u_x}, was calculated for the points discussed in the previous section, see Table 9.3.

Z_p (mm)	Point	k_p (m^{-1})	L_{u_x} (m)		
			Spectra	Autocorrelation T_i	Autocorrelation T_e
20	44	3.0	195	246	190
20	39	4.0	147	250	167
20	64	1.1	530	756	575
20	65	0.6	1073	950	903

TABLE 9.3: Variation of length scale, L_{u_x}, along cross section YY

Similar trends in length scale variations are found with both methods of calculation. The use of an integral time scale based on an exponential decay ($\frac{1}{e}$), provides a value of L_{u_x} which is closer to those predicted from the spectral peak. This feature has been common throughout the tunnel data comparisons.

9.4 EVALUATION OF FLOW OVER A 2-DIMENSIONAL RIDGE

The ridge at lateral cross section 4 extends from the base of Mt Herbert at right angles to the general flow. The ridgeline is essentially horizontal and extends almost completely across the wind tunnel. This ridge was used as an approximation to a 2-dimensional triangular hill to provide a comparison with 2-dimensional studies conducted by other researchers.

The amplification factor is given by the expression

$$A_i(z) = \bar{U}_i(z)/\bar{U}_o(z) \quad \ldots\ldots\ldots\ldots\ldots\ldots\ldots\ldots\ldots\ldots (9.1)$$

where $\bar{U}_o(z)$ is the mean velocity at height z of a reference velocity

profile, $\bar{U}_i(z)$ is the mean velocity at the same height z at a specific height and $A_i(z)$ is the amplification factor for site i.

Generally, in 2-dimensional studies, required approach flow characteristics are generated over a flat surface by using grids, trip fences and added surface roughness. Therefore, the reference profile to be used in the amplification factor calculations is usually well established and clearly defined.

In the Gebbies Pass situation, the terrain directly upstream of the ridge at lateral cross section 4 is flat for a short distance - approximately three hill heights. Immediately upstream of this area is the Gebbies Pass saddle, which is nearly as high as the ridge and features many valleys, small hills and ridges. Therefore, the profile measured, for reference purposes, upstream of the ridge is not in equilibrium. This means that the amplification contours calculated for the Gebbies Pass model can only provide an indication of the flow régime. The resulting amplification contours presented in Fig. 9.57 are compared with those measured by Pearse (1979) for flow over a smooth triangular hill in a 1:3000 rural simulation. The agreement between the two models is extremely good. Comparisons of velocity and turbulence intensity profiles at the crest are presented in Fig. 9.58. The normalised velocity profiles agree reasonably well. The slowing of velocity on the Gebbies Pass model below 40m is probably caused by the added roughness, due to a large scrub area immediately upstream of this point. This feature also prevails on the turbulence intensity profile with a significant increase in turbulence intensity below 40m. The profiles above this height are in excellent agreement.

9.5 CONCLUSIONS

Model C was shown to have the largest tunnel blockage of all the models tested. The blockages were shown to be most significant towards the NE boundary of the model; therefore, the degree of analysis in that region was reduced.

The poor correlation obtained over models A and B in the terraced form prompted the omission of an analysis of model C terraced.

The contoured and roughness added models showed a good correlation of 0.96, 0.97, 0.98 at the 5mm, 10mm and 20 mm heights respectively. This was comparable with both models A and B.

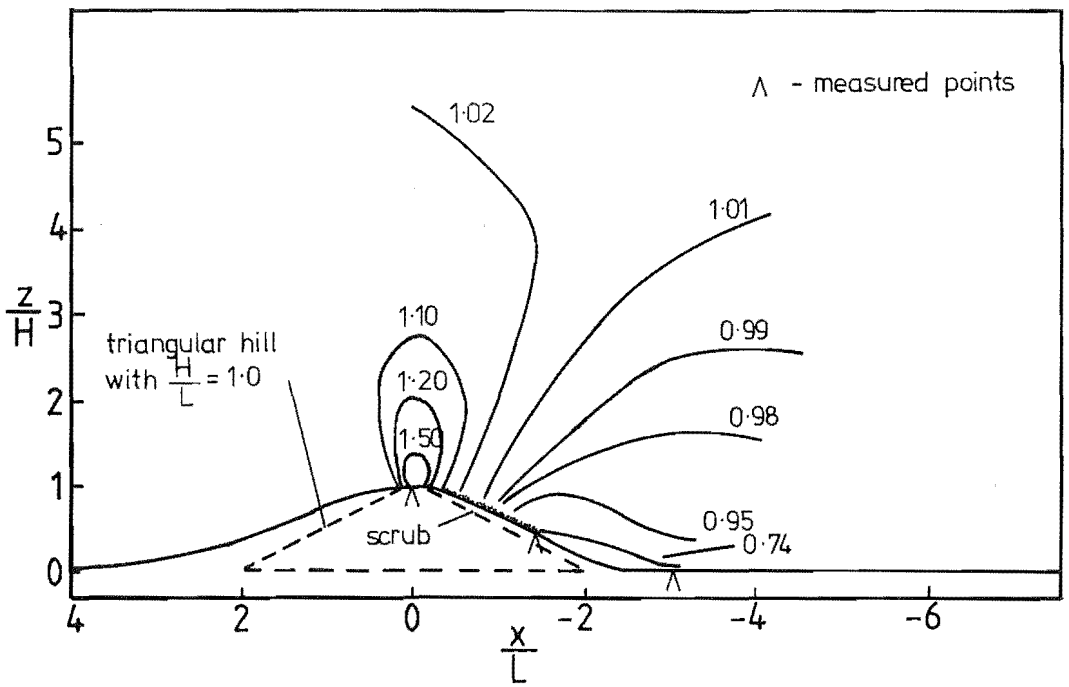

a) Amplification factor contours for Gebbies Pass model

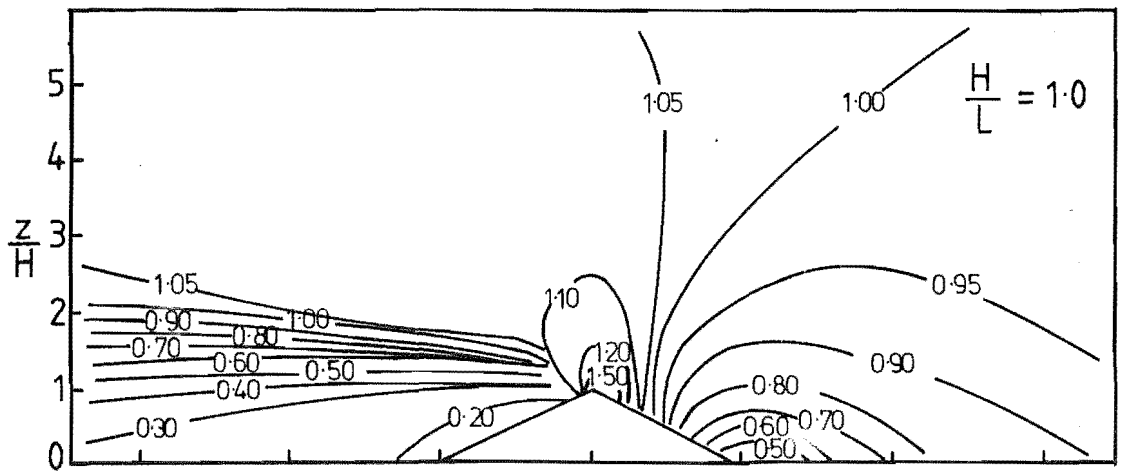

b) Amplification factor contours for a smooth triangular hill (After Pearse 1979)

FIG. 9·57 AMPLIFICATION FACTOR COMPARISONS FOR 2 - D TRIANGULAR HILL AND MODEL C LATERAL CROSS SECTION 4 RIDGE

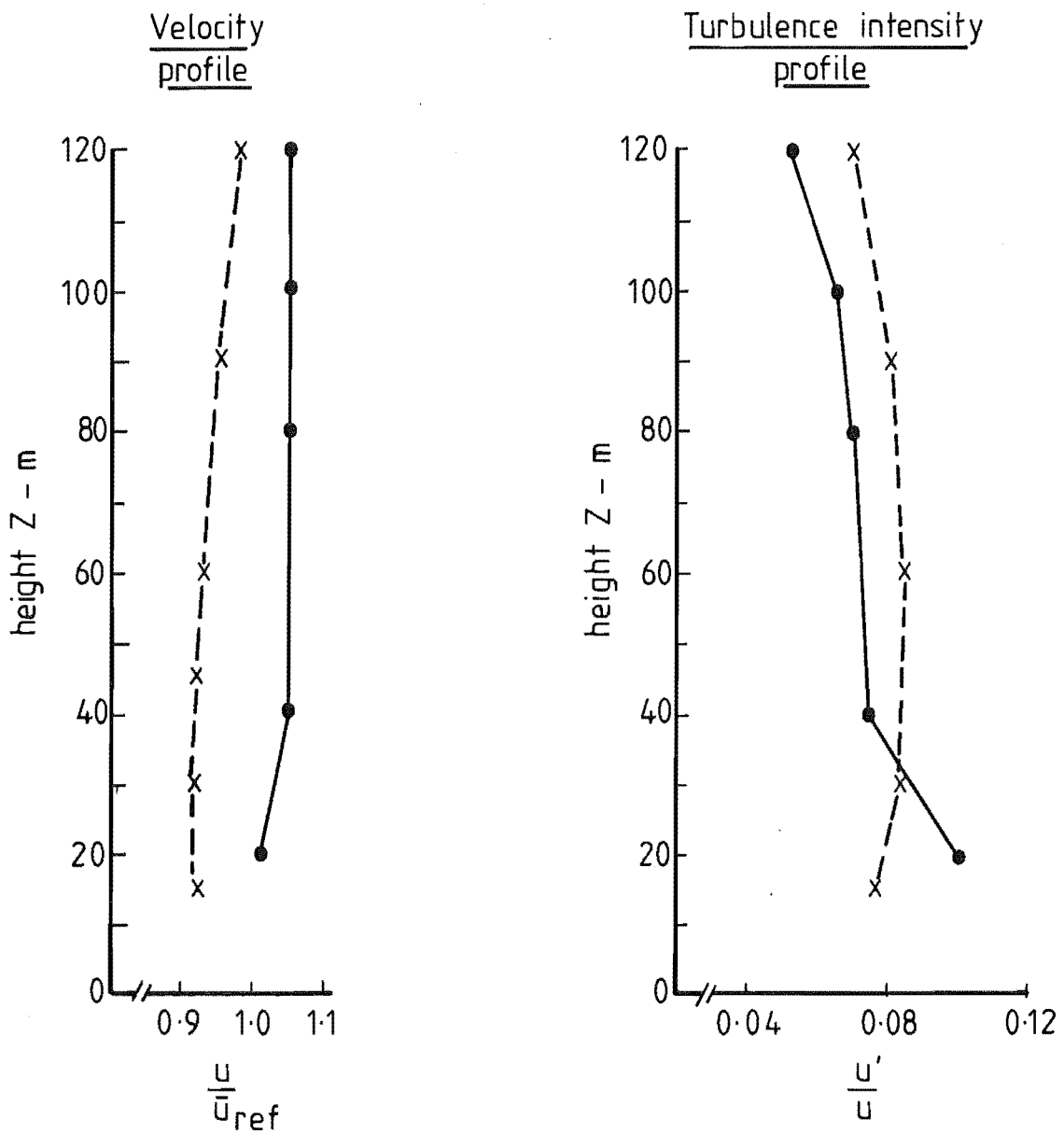

FIG. 9·58 COMPARISONS OF VELOCITY AND TURBULENCE PROFILES AT RIDGE CREST.

The correlations for model C highlighted the sensitivity of the correlation coefficient to large variations in the data. The removal of two data points having large differences due to the added roughness changed the correlation coefficient from 0.64 to 0.96. Criteria were proposed for the removal of data which could result in a biased correlation. The difficulty of establishing and applying such critera was discussed.

Despite the possible blockage effects, a ridge was analysed as an approximation to a 2-dimensional hill and compared with results for flow over triangular hills. Velocity and turbulence profiles at the crest were in excellent agreement, and the amplification factor contours were in reasonable agreement.

9.6 SUMMARY OF CONCLUSIONS FOR THE MODELLING PHASE OF THE RESEARCH

The approach adopted in the generation of a suitable boundary layer in the wind tunnel was to simulate the velocity profile, roughness length and turbulence intensity profile to the measured approach flow conditions, which approximated a flat rural terrain situation.

Spectra and length scales were then measured and found to agree closely to those required.

The ability to reproduce the required characteristics to a high degree was also demonstrated.

The wind tunnel phase of the research has highlighted several areas.

The wind tunnel blockage varied between the three models. Model B, which is the most relevant for comparisons with collected field data, had an acceptable blockage level. The blockage for Models A and C were of some concern; it is therefore recommended that a 1:8000 scale analysis of the area be undertaken. This will have two advantages:

(i) Help show the effect of scale;

(ii) The total area studied will be represented by a model 1.2m x 1.8m which will fit into the wind tunnel Therefore, the validity of splitting an area into sections for analysis will be tested.

The terraced form of construction consistently produced low correlation coefficients. This trend agreed with other research involving this form of topographical modelling. Correlations were shown to be extremely

sensitive to the inclusion of points that are greatly affected by surface features. The problems encountered in the elimination of such data were shown to be severe.

Model A showed small velocity increases after the addition of the roughness elements, most of the points involved exhibiting increases that were within the experimental error of the measuring system. Models B and C showed a slowing of the flow after the addition of the roughness elements.

It is suggested that in the case of model A, the low density of added roughness combined with the significant terrain features, resulted in the flow being influenced by the general terrain rather than the added roughness.

Model B did not present such severe terrain and therefore the added roughness became far more significant. Therefore, it is concluded that each modelling situation must be evaluated on its own merits. If the area of interest is higher than four roughness element heights, it is suggested that there is little to gain by the addition of the roughness elements. In all cases, correlations in excess of 0.96 were obtained at this height.

The $\rho\overline{uw}$ Reynolds stress profiles measured over model B generally behaved predictably, with a decrease at the saddle in a high velocity low turbulence region and an increase in the lee of the saddle where the reverse conditions occurred.

The variation of the spectral peak position at points along the model were explained in terms of the general terrain and roughness upstream of the points.

The length scales derived from both the spectra and the autocorrelation coefficient curves were in good agreement. However, there was a notable lack of values for comparison; this was the case for the following parameters

1) $\rho\overline{uw}$ Reynolds stress;
2) Spectra;
3) Length scales.

Therefore, these were measured, to a limited degree, in the field.

CHAPTER 10

FIELD PROGRAMME

This Chapter presents the field data collection programme which has been under way for approximately two years. The four types of field data collected have been described in Chapter 6, these being:

1) Long Term Data.
2) One-Day Field Data.
3) Tala Kite Data.
4) 20m Tower, Wind Structure, Data.

To achieve compatibility with the wind tunnel tests, field data could only be collected during weather patterns producing south to south-west winds over the South Island of New Zealand. Unfortunately, southerly winds in New Zealand are synonymous with cold, wet weather; these conditions were sometimes so severe they made several of the pre-selected field measurement sites inaccessible. Care was taken during the site selection phase of the programme to reduce this foreseeable problem, but on several occasions, chains were required on all wheels of cross-country vehicles to gain access to the required sites.

A total of 30 field points were measured during the research, these being shown earlier in Chapter 6, Fig. 6.5.

During the period January 1978 to January 1979 there was an unusual dearth of south-west weather patterns, and this was later established as being a 1 in 50 year occurrence.

When southerlies were generated they invariably occurred on weekends, making the necessary organisation of personnel impossible.

The Department's 20m tower was erected in the field during March 1978 so it would be ready for the winter months (June-August), this supposedly being the southerly season. Seven months elapsed before a southerly was actually measured.

10.1 LONG TERM DATA

The data loggers, supplied by the Wind Energy Task Force and described in Section 6.3, were installed at several sites during the research programme. A reference tower was positioned at field point 1 on the southern boundary of

the modelled region and this was monitored by a data logger running from mains power. A second tower was positioned at field point 24 for six months and then moved to field point 15 for a further four months. These sites are presented on the map in Fig. 10.1.

The objective of this part of the field programme was to collect data for extended periods so the velocity ratio between the site tower and the reference tower could be measured. The point of interest was to see how the ratio varied with different approach wind speeds.

Since the data loggers record continuously, a record was kept noting days when strong south-west winds prevailed as only data recorded on these days could be used for analysis in this study.

A great deal of time and effort was devoted to maintaining this equipment. Cattle caused problems with the tower tie wires, but these problems were overcome by invoking the aid of an electric fence. To negate any possible influence from the electric fence and the large amounts of radio frequency in the area (as explained in Section 6.4.4), all the equipment was shielded and earthed. However, despite all these precautions, the results obtained with this equipment suggested almost constant wind velocities during the recording period (28 days).

Unfortunately, this situation could not be detected at the time of recording because the data retrieval hardware was still in the development stages. In fact, it was approximately six months after the recording date before the data retrieval equipment was operational.

In view of the doubt cast on these results, a test programme was established to check the equipment. The anemometers were mounted in the Department's aeronautical wind tunnel and connected to their respective data loggers. The data loggers were powered in the same manner as they had been in the field, one by mains power and one by battery. The wind tunnel was then run at a known speed for 105 minutes, ensuring that one block of data had been collected and transferred to the digital tape. The wind tunnel speed was then changed and the procedure repeated, this continuing until six hours of data had been collected.

The results were subsequently analysed on the data retrieval equipment which produces a velocity output representing the mean wind speed for each minute. The output obtained disagreed with the actual wind tunnel velocities used for the test.

FIG 10·1 SITES FOR DETAILED DATA COLLECTION

At the time of writing the cause of this fault was not positively identified, but a faulty component was suspected. Consequently, all the data collected with this equipment had to be disregarded.

10.2 ONE-DAY FIELD DATA

The rationale and technique adopted for this phase of the research programme has been described in Section 6.2.

10.2.1 December Data

A strong south-westerly wind event occurred in December 1978, lasting from 10th to 15th December. On several of these days - 11th, 13th and 14th - personnel from the Mechanical Engineering Department "took to the hills" to record wind velocities. The weather maps for these days, prepared by the New Zealand Meteorological Service, are presented in Fig. 10.2.

The field points measured during the three days are presented on the map in Fig. 10.3. Several of the points were measured on more than one occasion, thus permitting the calculation of the correlation between one day and another.

The reference tower data for 11th December showed a steady decrease during the day which made some of the results after 2.30 p.m. doubtful. The velocity time graphs for the December data are presented in Fig. 10.4 with a least square regression curve fitted to show any linear trends.

The recorded velocities are presented in Table 10.1, which shows the velocity measured at the various field sites and the velocity ratio obtained by normalising the data to the reference tower velocity.

Based on eight observations recorded on 13th and 14th December, a correlation of 0.89 was calculated; the scatter diagram and regression lines for this data are presented in Fig. 10.5. However, as indicated by Kimble (1976) it can be very dangerous to place too much emphasis on correlation coefficients, especially if they are based on a small number of observations. In this Chapter, scatter diagrams and correlation coefficients will be used extensively as they are the most straightforward approach to presentation of the data. A more detailed statistical analysis of the data will be given in Chapter 11.

10.2.2 May Data

A second suitable wind event occurred during May 1979. Two field trips were conducted during this wind event, one on 16th May and a second

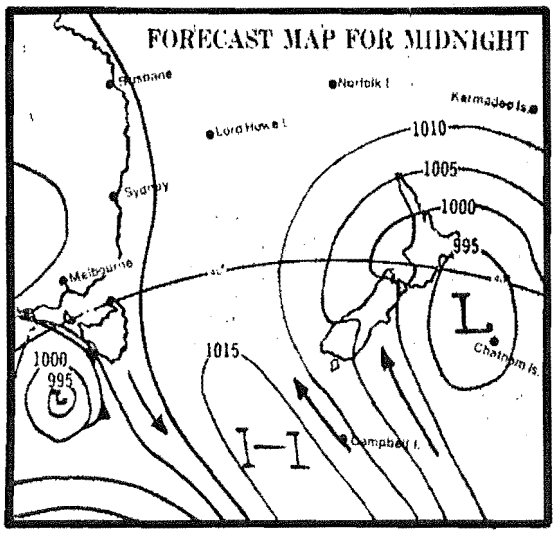

a)

11/12/78

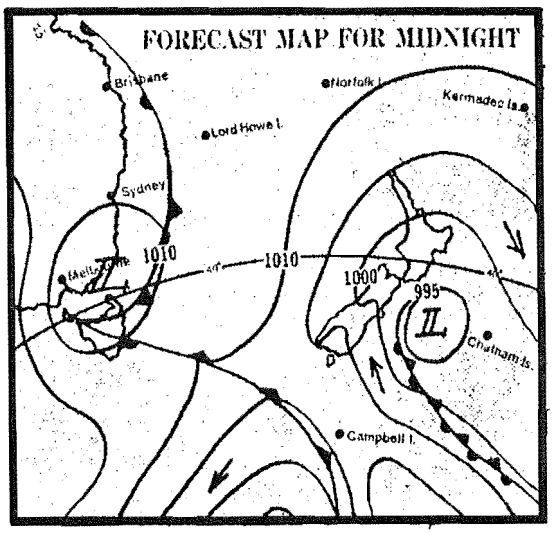

b)

13/12/78

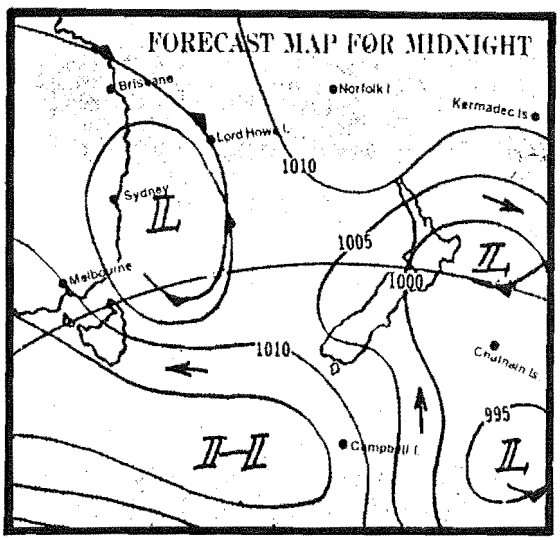

c)

14/12/78

FIG 10·2 METEOROLOGICAL SERVICE FORECAST FOR DECEMBER 1978

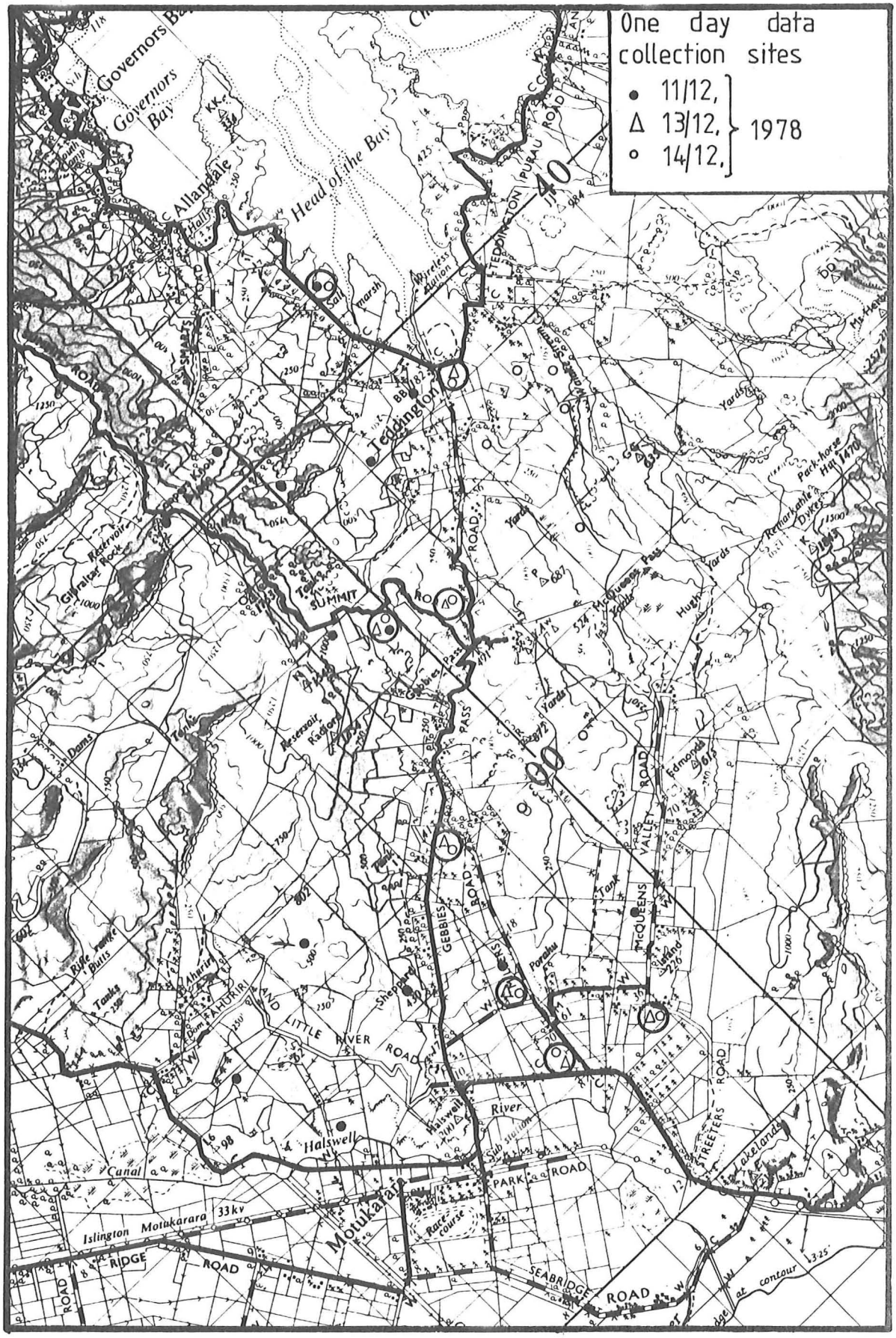

FIG 10·3 ONE DAY FIELD DATA COLLECTION SITES FOR DECEMBER 1978

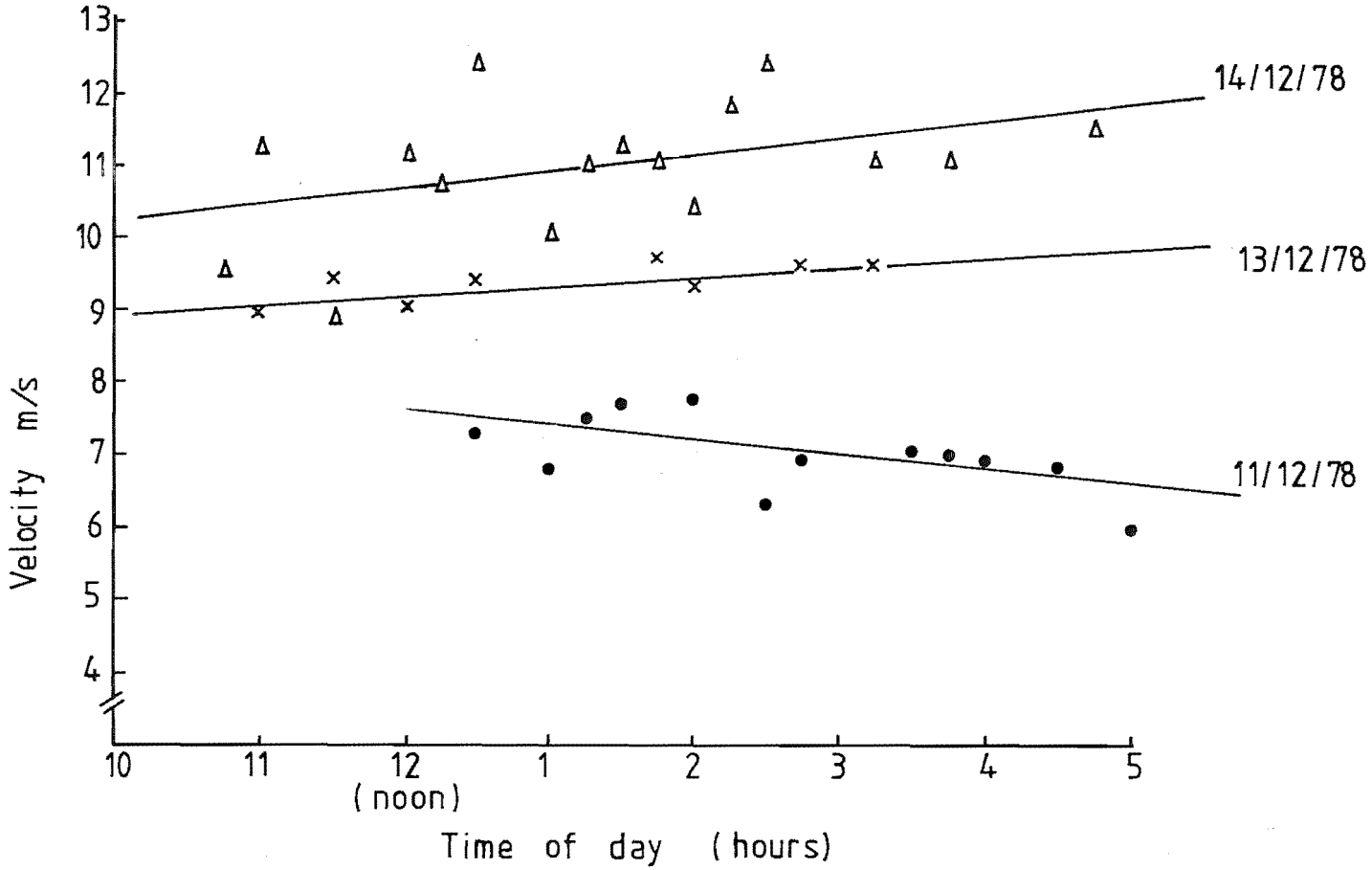

FIG 10·4 VELOCITY TIME GRAPHS FOR THE REFERENCE TOWER DURING THE DECEMBER DATA COLLECTION.

DECEMBER DATA

(Velocities in m/s)

Field Point	11th			13th			14th		
	$\bar{U}_{ref}$	$\bar{U}$	Ratio $\bar{U}/\bar{U}_{ref}$	$\bar{U}_{ref}$	$\bar{U}$	Ratio $\bar{U}/\bar{U}_{ref}$	$\bar{U}_{ref}$	$\bar{U}$	Ratio $\bar{U}/\bar{U}_{ref}$
1*	-	-	-	-	-	-	-	-	-
2	6.85	7.50	1.09						
3	6.00	5.55	0.93				10.95	10.00	0.91
4				9.40	9.45	1.00	11.25	9.75	0.87
5				9.00	8.65	0.96	8.85	7.95	0.89
6	4.40	3.20	0.73						
7	5.25	5.56	1.06	9.40	8.20	0.87	9.60	9.20	0.96
8	6.95	7.60	1.09						
9	7.00	6.50	0.93						
10				8.90	7.90	0.88	11.15	9.75	0.87
11							8.85	10.60	1.19
12							10.70	13.80	1.29
13							11.65	16.80	1.44
14	6.80	10.45	1.54						
15	7.70	11.25	1.46	9.30	15.00	1.61	11.80	18.30	1.55
16				9.75	15.40	1.58	12.40	16.40	1.32
17							11.05	12.25	1.10
18							11.30	14.55	1.28
19							10.95	12.80	1.16
20	7.35	6.00	0.82	9.55	6.25	0.65	10.05	7.70	0.76
21	6.30	9.75	1.55						
22	7.35	11.00	1.50						
23	6.00	10.65	1.77						
24	7.75	8.75	1.13						
25							10.45	18.05	1.72
26							12.40	12.50	1.00
27				9.60	9.95	1.04	11.00	7.80	0.71
28	7.50	9,90	1.32						
29	7.00	7.90	1.13				10.95	8.80	0.80
30	6.95	11.85	1.70						

* - Field Point 1 is the Reference Tower.

TABLE 10.1: Velocities and Velocity Ratios for December Data

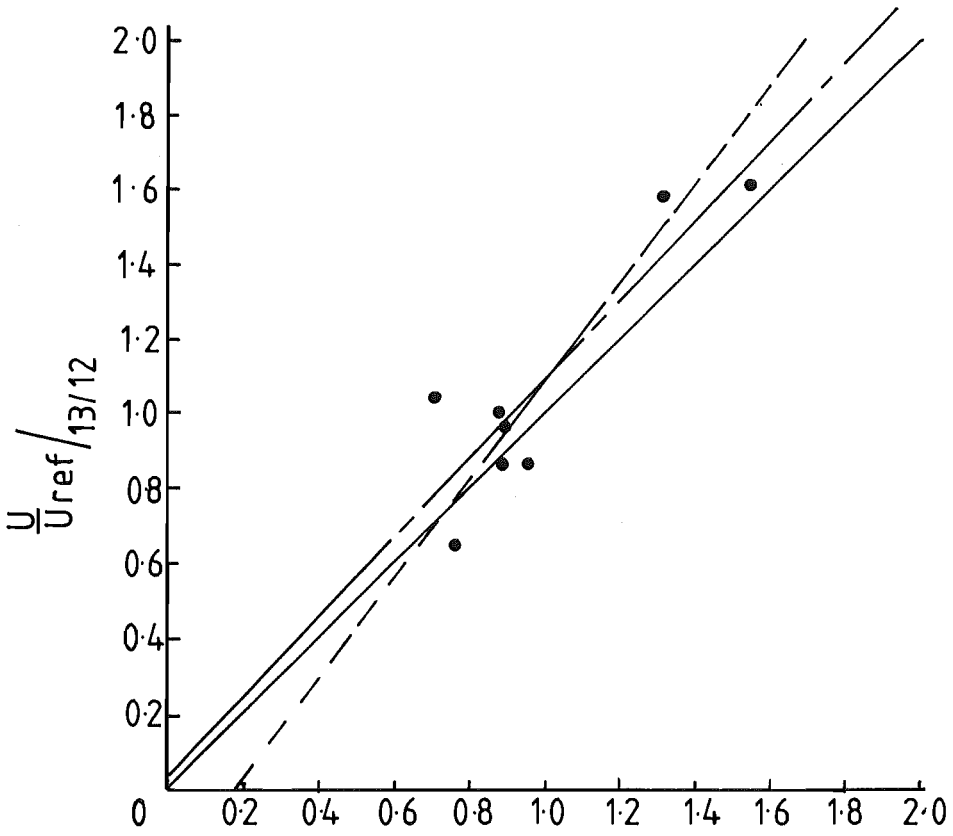

Regression lines

$$\frac{U}{U_{ref}}\Big|_{13/12} = 1{\cdot}05 \ \frac{U}{U_{ref}}\Big|_{14/12} + 0{\cdot}032$$

$$\frac{U}{U_{ref}}\Big|_{14/12} = 0{\cdot}76 \ \frac{U}{U_{ref}}\Big|_{13/12} + 0{\cdot}176$$

Correlation coefficient $r = 0{\cdot}89$

FIG 10·5 SCATTER DIAGRAM FOR FIELD DATA COLLECTED ON 13/12/78 AND 14/12/78

on 17th May. The weather maps for New Zealand on these days are presented in Fig. 10.6.

The points measured are indicated on the map in Fig. 10.7, and the actual velocities recorded are presented in Table 10.2. The velocity time graphs for these days, presented in Fig. 10.8, are very interesting because they show opposite trends. The velocity dropped to 5-6 m/s during the afternoon of 16th May; the significance of this is that below 7 m/s one cannot assume neutral stability. In spite of the marked differences between the two days, a correlation, based on 13 points, of 0.87 was found to exist. This was particularly interesting because it suggests that data collected in wind events having strong trends can, if the normalising procedure is used, still be quite representative of the area.

10.2.3 August Data

Measurements at nine points, shown in Fig. 10.9, were made during south-westerly weather in August 1979. The New Zealand Meteorological Service weather map for this day is presented in Fig. 10.10.

The reference tower velocity time graph, given in Fig. 10.11, shows that the mean wind speed stayed relatively constant all day, and remained in excess of 7 m/s.

Based on eight field points, a correlation of 0.81 was found between data collected on 16th May and the August results. The actual field measurements recorded on 9th August are presented in Table 10.3.

A summary of the various correlations which can be obtained from the six days of data is presented in tabular form in Table 10.4.

The one day field data has been presented in a fairly brief form in this Chapter, and a more detailed statistical analysis of these results will be presented in Chapter 11.

10.2.4 Tala Kite Data

Throughout this study, every effort was made to collect suitable wind data when it occurred. Due to the small number of personnel involved and the compact nature of the equipment, the Tala kites were ideal for obtaining data at short notice. Therefore, during this study, in particular during 1979, a very high percentage of the suitable winds were measured with the kite equipment.

The sites measured with the kites are shown on the map in Fig. 10.1,

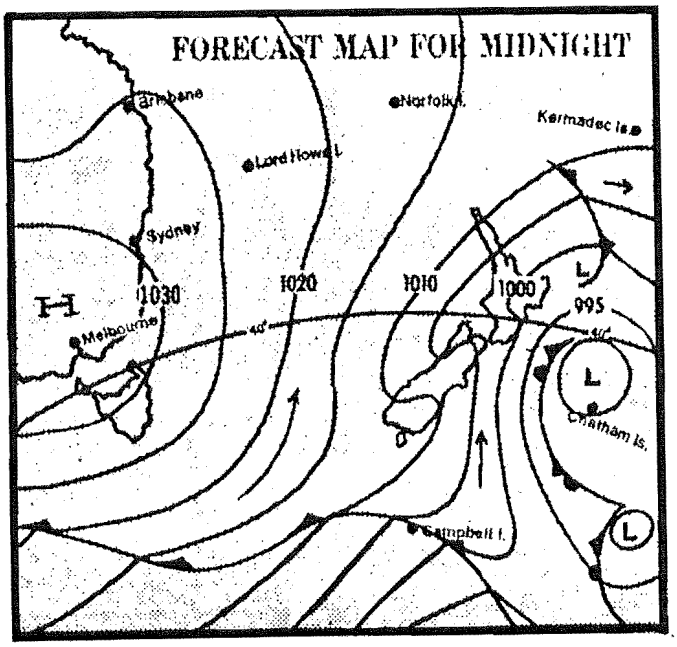

16/5/79

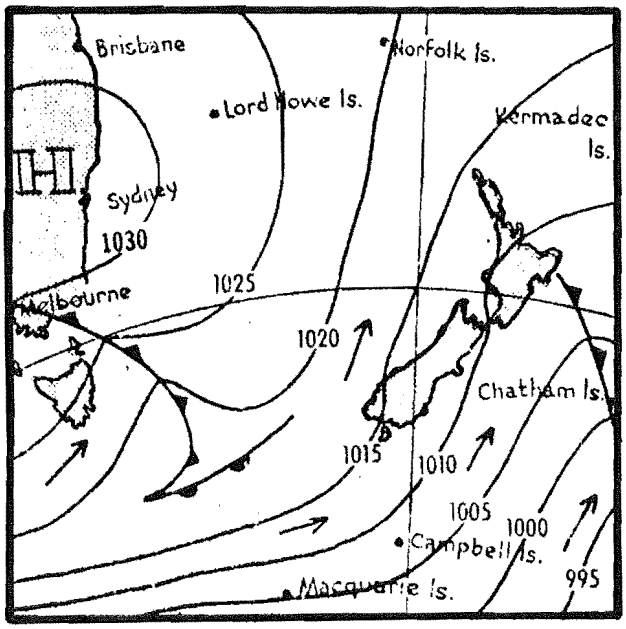

NOON FORECAST

17/5/79

FIG 10·6 METEOROLOGICAL SERVICE FORECAST FOR MAY 1979

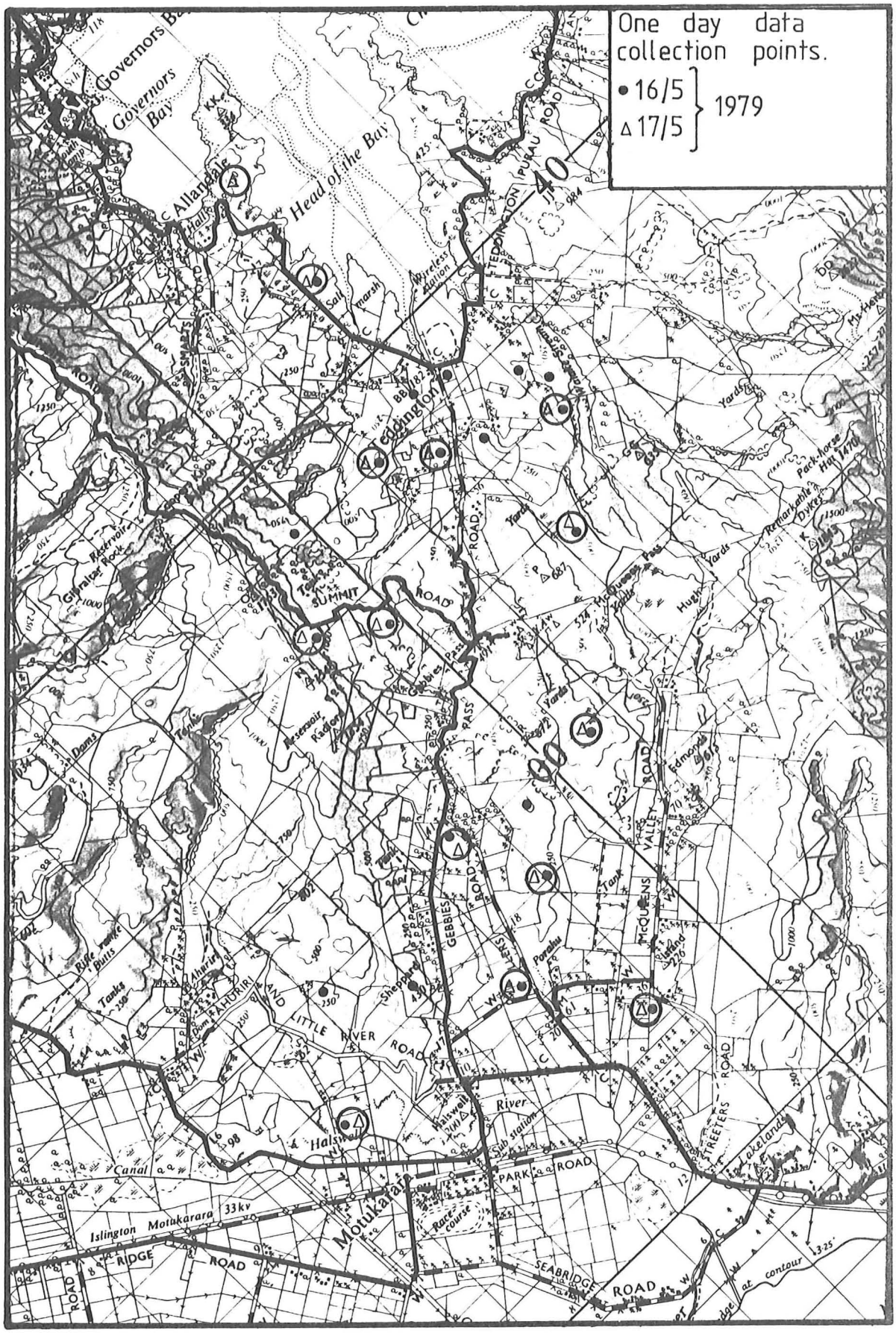

FIG 10·7 ONE DAY FIELD DATA COLLECTION SITES FOR MAY 1979

MAY DATA

(Velocities in m/s)

Field Point	16th			17th		
	$\bar{U}_{ref}$	$\bar{U}$	Ratio $\bar{U}/\bar{U}_{ref}$	$\bar{U}_{ref}$	$\bar{U}$	Ratio $\bar{U}/\bar{U}_{ref}$
1*	-	-	-	-	-	-
2						
3	7.90	6.75	0.85	10.65	10.40	0.97
4						
5	7.20	7.10	0.98	11.15	9.60	0.86
6	6.15	6.10	0.99			
7	8.55	7.35	0.86	13.50	12.00	0.89
8	7.90	10.95	1.38			
9	7.45	9.30	1.25			
10	8.10	5.75	0.71	12.20	12.15	1.00
11	7.45	9.35	1.25	12.90	14.10	1.09
12	7.45	12.30	1.65			
13	7.20	12.25	1.70	13.50	21.65	1.60
14	7.75	10.55	1.36	13.50	16.00	1.18
15	6.90	13.10	1.90	14.15	20.20	1.43
16						
17	5.30	6.35	1.20	12.20	13.80	1.13
18	4.60	7.60	1.65	8.90	17.15	1.92
19	5.30	6.50	1.22			
20	5.70	3.75	0.65	9.00	5.75	0.64
21	5.00	7.45	1.49			
22	5.75	7.20	1.25			
23						
24	5.30	8.85	1.67	12.20	16.65	1.36
25	4.60	6.95	1.51			
26	4.10	4.55	1.11			
27	5.30	4.85	0.91			
28	4.60	5.80	1.26			
29	5.00	3.60	0.72	10.70	8.05	0.75
30				8.90	14.15	1.59

* - Field point 1 is the Reference Tower.

TABLE 10.2: Velocities and Velocity Ratios for May Data

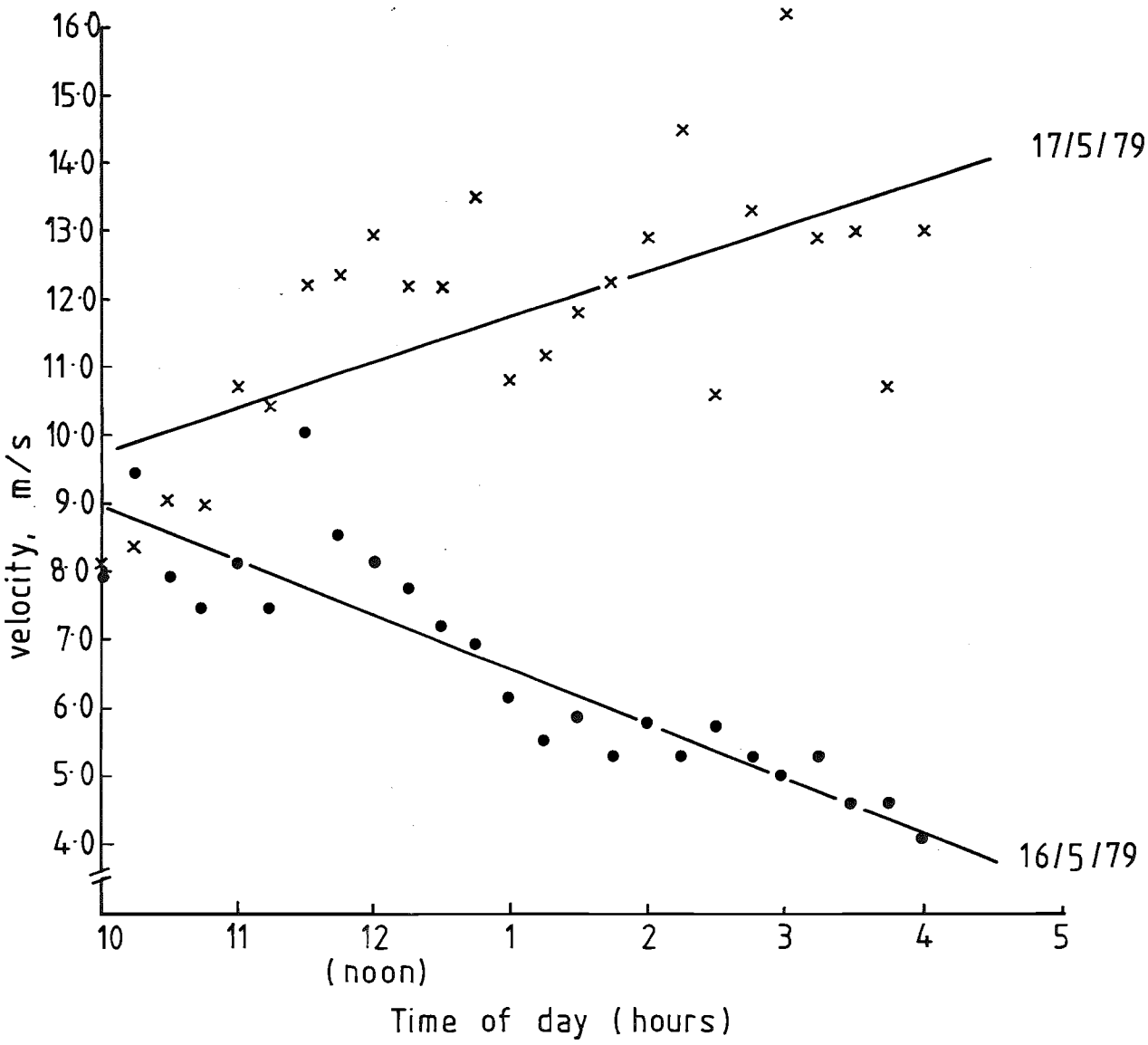

FIG 10·8 VELOCITY TIME GRAPHS FOR THE REFERENCE TOWER DURING THE MAY DATA COLLECTION

FIG 10·9 ONE DAY FIELD DATA COLLECTION SITES FOR AUGUST 1979

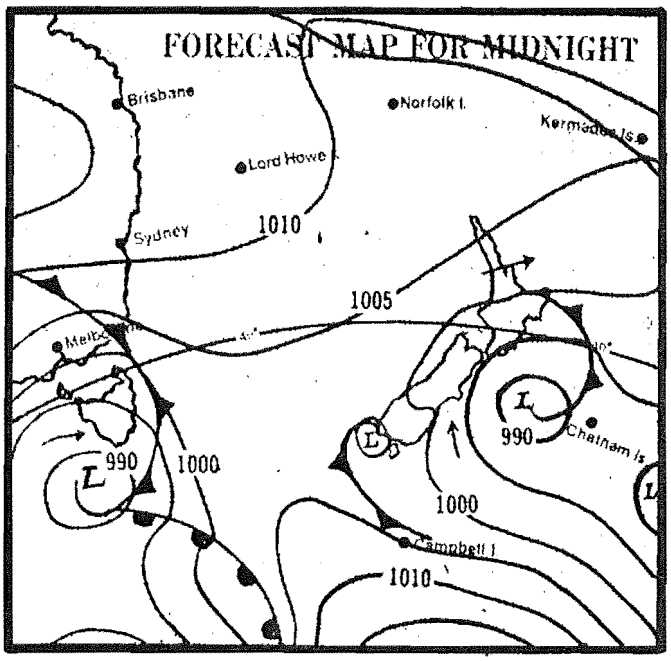

9/8/79

FIG 10·10 METEOROLOGICAL SERVICE FORECAST FOR AUGUST 1979

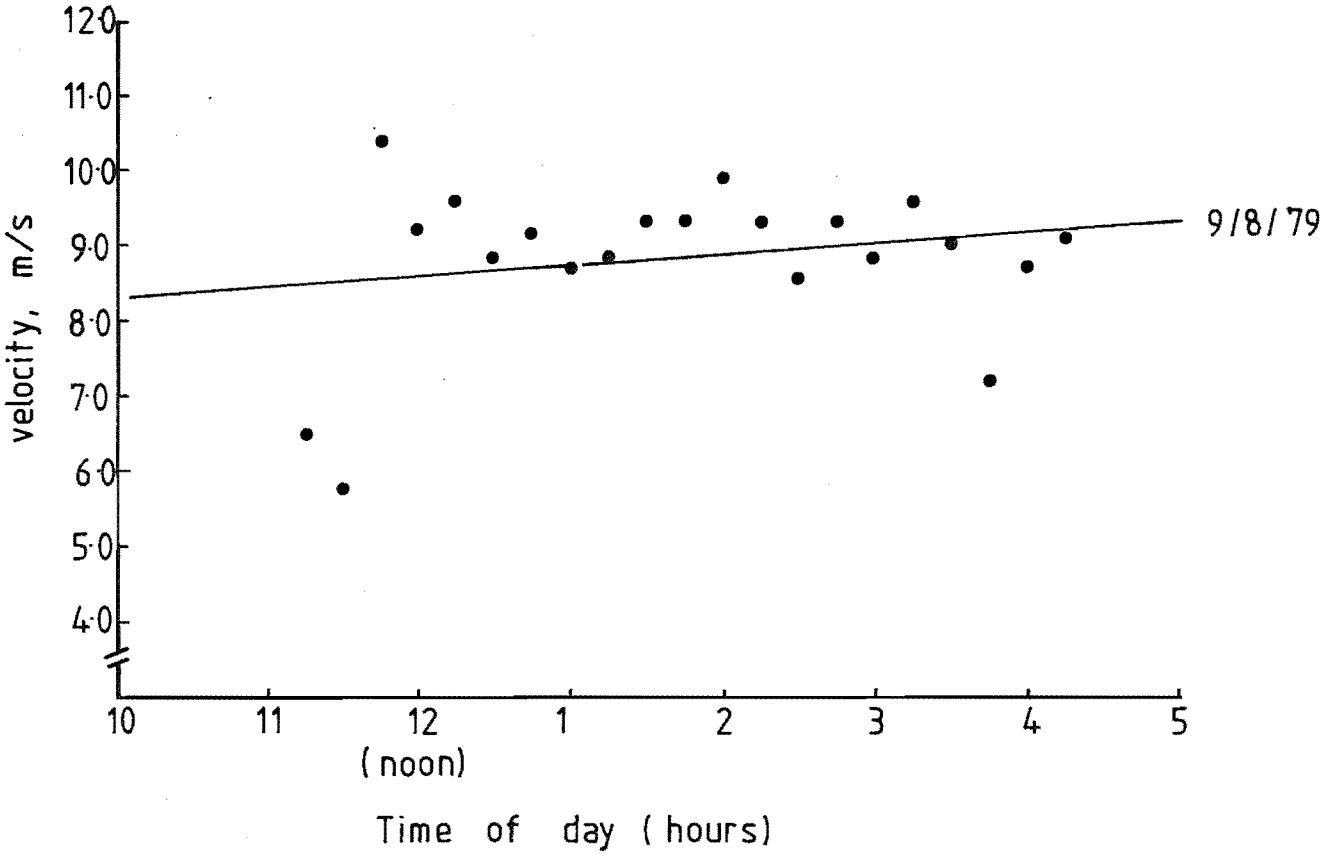

FIG 10·11 VELOCITY TIME GRAPH FOR THE REFERENCE TOWER DURING THE AUGUST DATA COLLECTION

AUGUST DATA

(Velocities in m/s)

Field Point	9th		
	$\bar{U}_{ref}$	$\bar{U}$	Ratio $\bar{U}/\bar{U}_{ref}$
1*	-	-	-
2			
3	9.20	7.30	0.79
4	8.85	8.35	0.94
5	9.30	8.05	0.86
6			
7	8.70	6.75	0.77
8			
9			
10	8.85	8.90	1.00
11			
12			
13			
14			
15	9.00	13.30	1.48
16			
17			
18			
19			
20	8.70	7.50	0.86
21			
22	8.55	11.00	1.28
23			
24			
25			
26			
27	9.10	5.60	0.61
28			
29			
30			

* - Field Point 1 is the Reference Tower

TABLE 10.3: Velocities and velocity ratios for August Data

Date	Number of data pairs	Correlation Coefficient
11/12/78 v 13/12/78	only 3 pts	-
11/12/78 v 14/12/78	5	0.88
13/12/78 v 14/12/78	8	0.89
11/12/78 v 16/5/79	13	0.62
13/12/78 v 16/5/79	6	0.97
14/12/78 v 16/5/79	16	0.89
11/12/78 v 17/5/79	8	0.81
13/12/78 v 17/5/79	5	0.96
14/12/78 v 17/5/79	11	0.84
16/5/79 v 17/5/79	13	0.87
11/12/78 v 9/8/79	5	0.89
13/12/78 v 9/8/79	7	0.75
14/12/78 v 9/8/79	8	0.90
16/5/79 v 9/8/79	8	0.81
17/5/79 v 9/8/79	6	0.86

TABLE 10.4: Correlations between the one-day field data.

many of these being measured on several occasions.

The velocity time graphs shown in the previous section showed trends which existed over a period of 5-7 hours. This situation prompted consideration of the effect of trends over much shorter periods while Tala kite profiles were being measured.

To investigate this, Tala kite profiles were measured at field points 1 and 5 and normalised to the mean velocity measured at the same time with a cup anemometer at a height of 10m. The results of this procedure are given in Fig. 10.12, which clearly show that the corrected profile is changed very little by the normalising procedure. It was very difficult to select a time with either a steadily increasing or decreasing wind régime to show the effect of normalising the data. Unfortunately, the reference tower velocity time graph shows that the mean velocity remained quite steady during the tests.

As an approximation to this normalising procedure, data recorded on 17th May was used. The velocity time graph in Fig. 10.8 showed that a trend of increasing wind velocity occurred on this day. In particular, between 1.00 p.m. and 2.00 p.m., the velocity steadily increased from 10.8 m/s to 13.0 m/s at the reference tower, field point 1.

Fortunately, during this period, a Tala kite profile was being measured at field point 5. This site is approximately 2 km downstream from field point 1. The trend exhibited at the refrence tower was removed from the velocity profile measured with the Tala kite to give some indication of the magnitude of the adjustment. The results are presented graphically in Fig. 10.13 and show a maximum variation of only 4% at the 40m level.

These tests are by no means conclusive, but simply indicate the magnitude of adjustment that can be expected. The fact that a trend can be shown to exist at, say, 10m, does not mean that this can be applied generally to all heights. The severe limitations of this procedure are recognised as is the lack of information on this topic.

Several velocity profiles measured to 180m with the Tala kite at field point 1 are presented in Fig. 10.14. A scaled wind tunnel velocity profile for the equivalent model point is given for comparison. Data collected in the field on 13th April 1979 and 9th August 1979 agree with the modelled velocity profiles very well, particularly in shape.

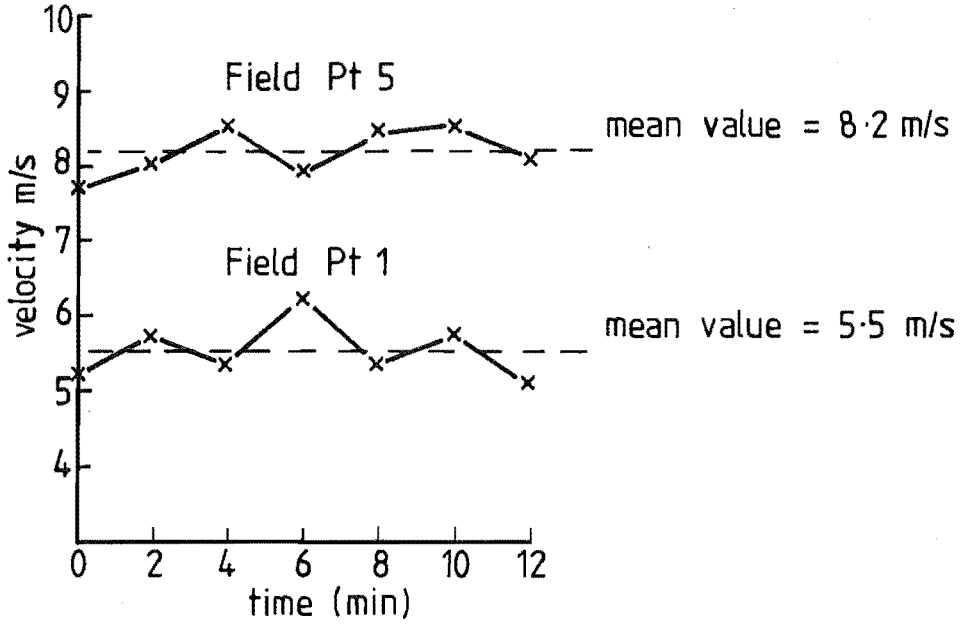

a) Mean wind speeds used for normalizing Tala readings

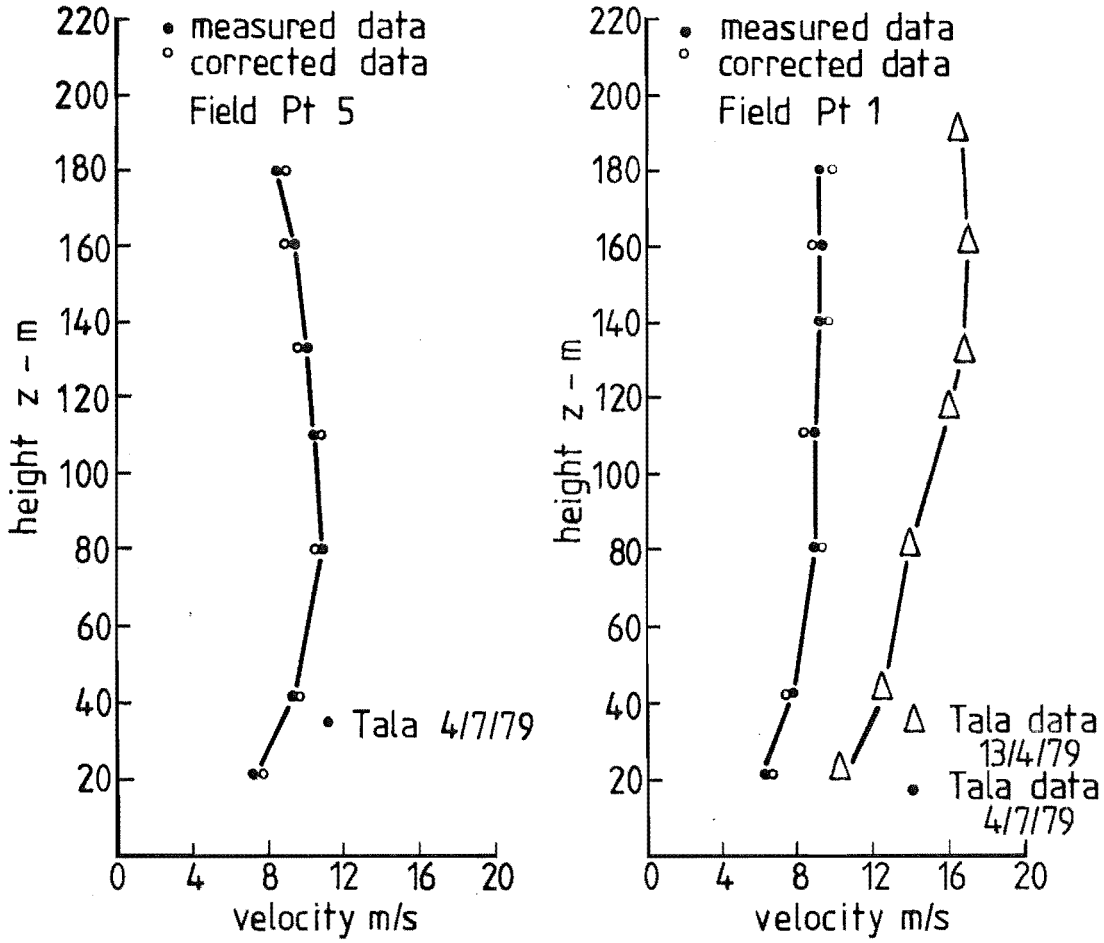

b) Tala velocity profiles with corrected and measured data

FIG 10·12 EFFECTIVENESS OF NORMALISING TALA DATA TO A 10m REFERENCE

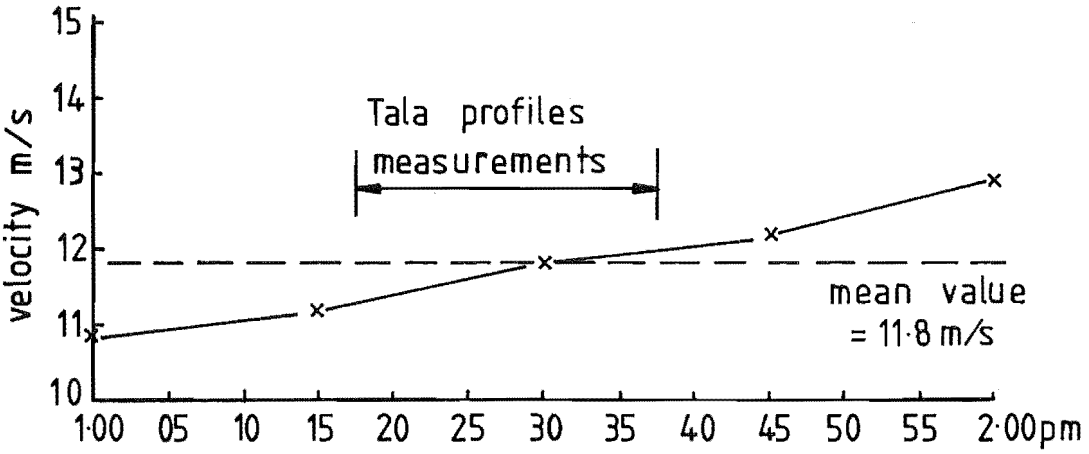

a) Reference tower mean velocity showing trend

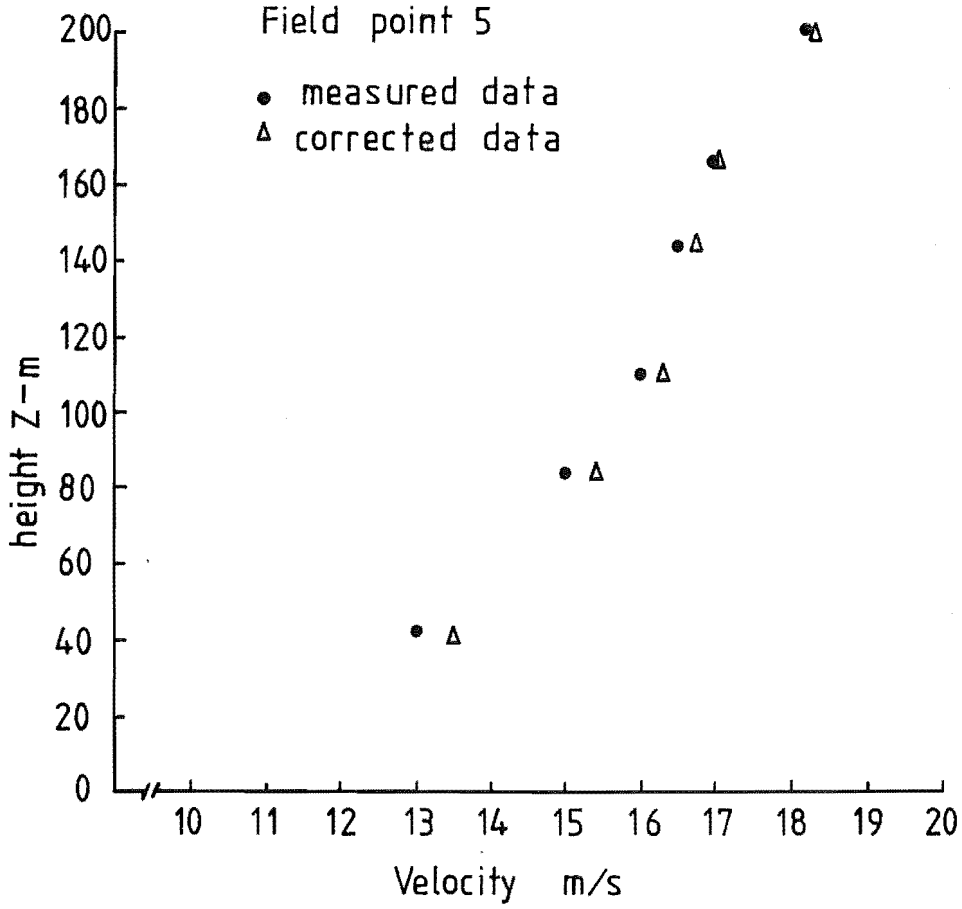

b) Tala velocity profile with measured and corrected data.

FIG 10·13 EFFECT OF NORMALISING ON DATA HAVING A TREND

COMPARISONS FOR FIELD POINT 1 (Reference Point)

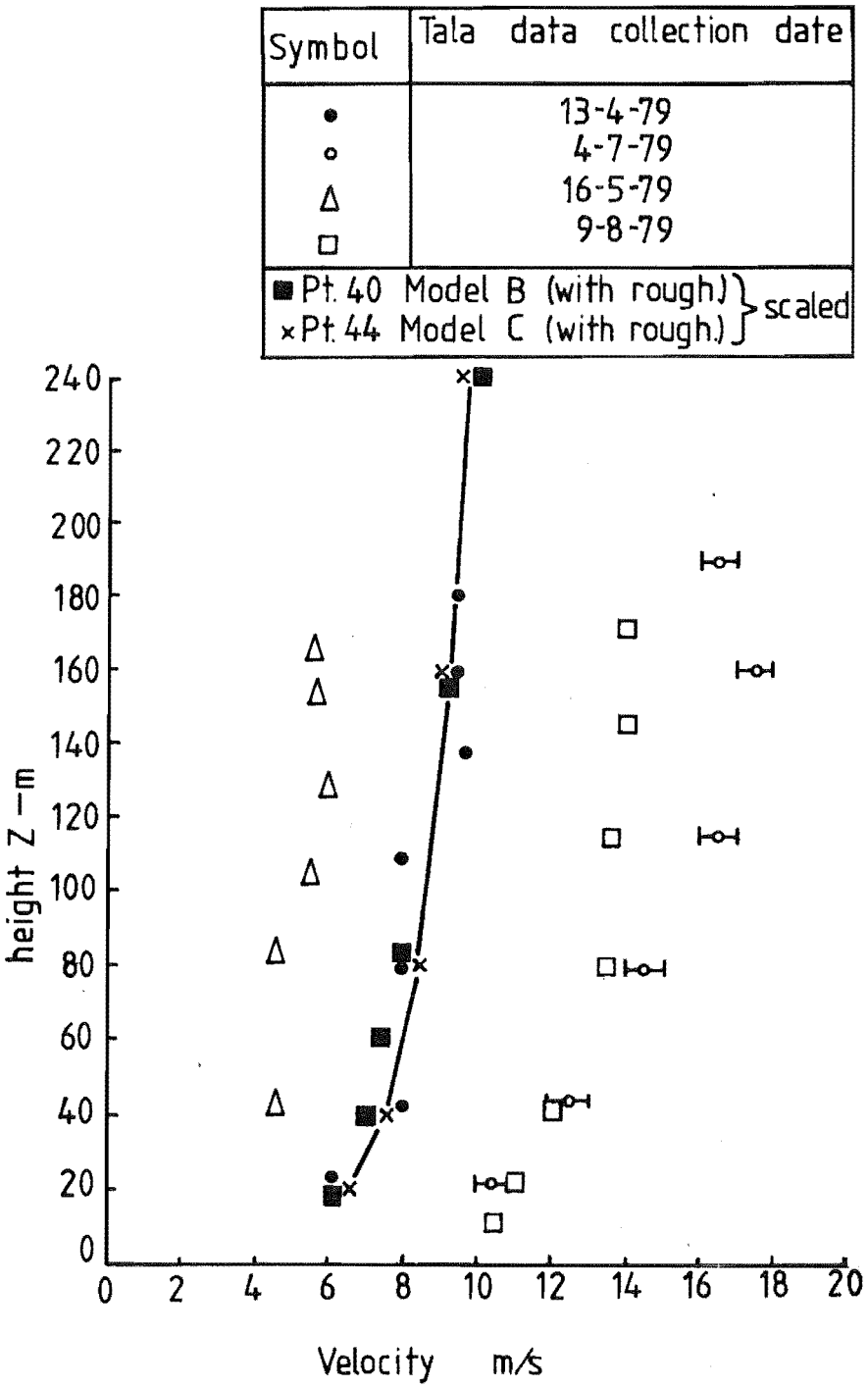

FIG 10·14 FIELD AND WIND TUNNEL VELOCITY PROFILE COMPARISONS

The measured velocity profiles for field point 3 are presented in Fig. 10.15 and compared with modelled velocity profiles. These velocity profiles do not show a good agreement. However, this can be explained in terms of the local terrain features. Field point 3 is on the southern boundary of the modelled region, situated in an area where there are many low cliffs as described in Section 6.1.1. Because many of these cliffs are less than 40m high, they are not represented on the map used for the model construction and therefore it is probable that the results obtained in the field are strongly influenced by these local features. Velocity profiles for field point 5 and field point 7 given in Figs 10.16 and 10.17 respectively show an excellent agreement with the modelled velocity profiles measured at the same site.

The velocity profiles for field point 15 are given in Fig. 10.18, these comparing most favourably with the modelled velocity profiles at the same point. Field point 15 is situated on a hill on the top of the Gebbies Pass Saddle in an area where high velocity speed-up ratios have been observed both in the wind tunnel and on the prototype. Nearly all the data presented in Fig. 10.18 suggests an almost vertical velocity profile. This site will be discussed in more detail in the next section as it was used for detailed wind structure analysis with the Department's instrumented 20m tower.

The measured velocity profiles for field point 29, given in Fig. 10.19, show a very good agreement with each other. However, they do not compare favourably with the modelled velocity profiles. This point is situated north of the Gebbies Pass Saddle, and during the recording of velocities with the Tala kite, the operators reported that the tether line exhibited a pronounced change of direction, i.e., it was passing through an area of high wind shear. The cause of this effect could not be evaluated without an extensive measurement programme around this location, and this was considered to be beyond the scope of the present work and the limitations of the equipment.

10.3 TOWER DATA

The Department's 20m instrumented tower and associated equipment have been described in Chapter 6. The sites at which the tower was set up are shown in Fig. 10.1.

10.3.1 Approach Terrain Site

Some of the information derived from this site is included in Chapter 7

COMPARISONS FOR FIELD POINT 3

Symbol	Tala data collection date
Δ	16-5-79
•	17-5-79
□(1)	9-8-79
◪	corrected data for 9-8-79
∘Pt. 21 Model A (with rough) } scaled	
×Pt. 21 Model B (with rough) } scaled	

(1) The mean wind speed increased during the recording of 9.8.79 TALA data, this is corrected to a mean for the recording period.

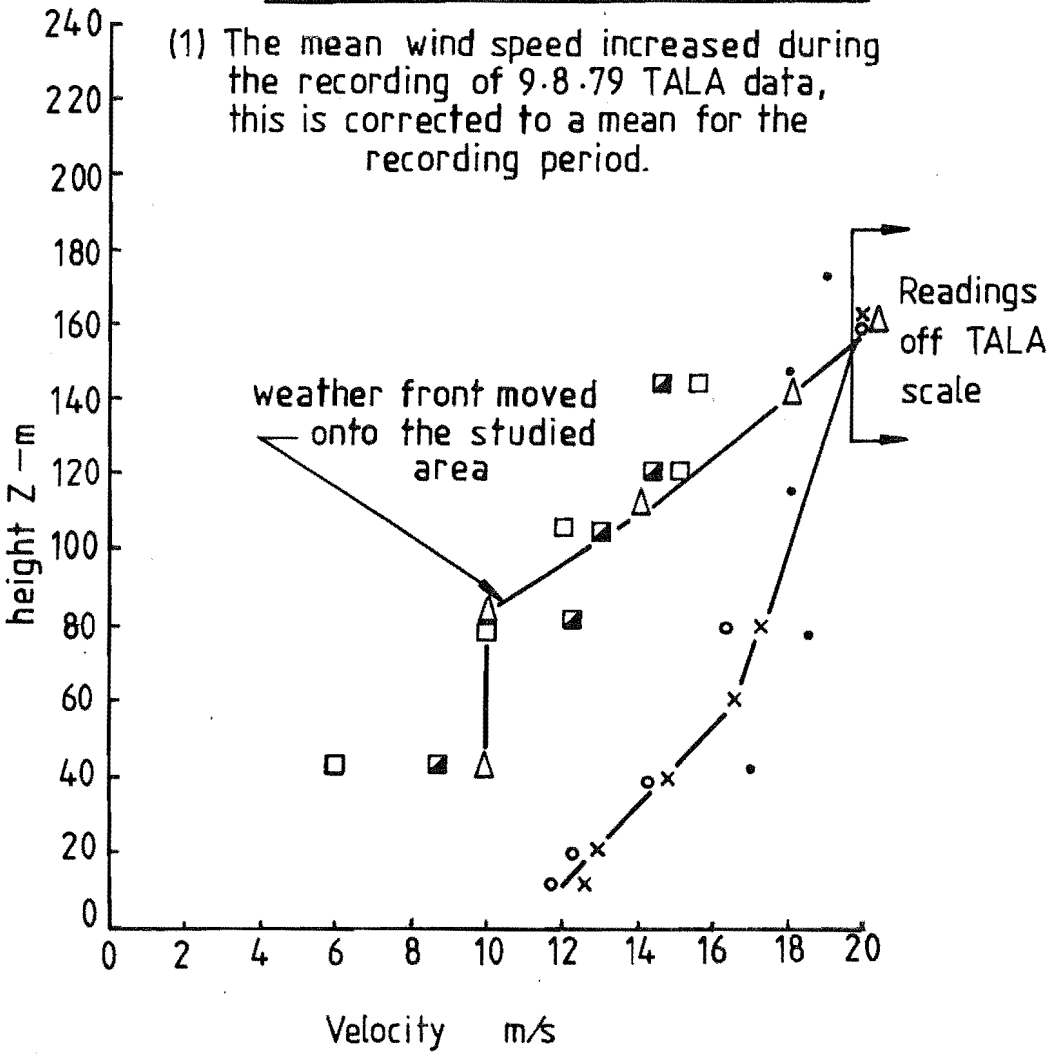

FIG 10·15 FIELD AND WIND TUNNEL VELOCITY PROFILE COMPARISONS

COMPARISONS FOR FIELD POINT 5

Symbol	Tala data collection date
o	4-7-79
Δ	16-5-79
•	17-5-79
□	9-8-79
■ Pt. 39 Model B (with rough.) } scaled	
× Pt. 39 Model C (with rough.) } scaled	

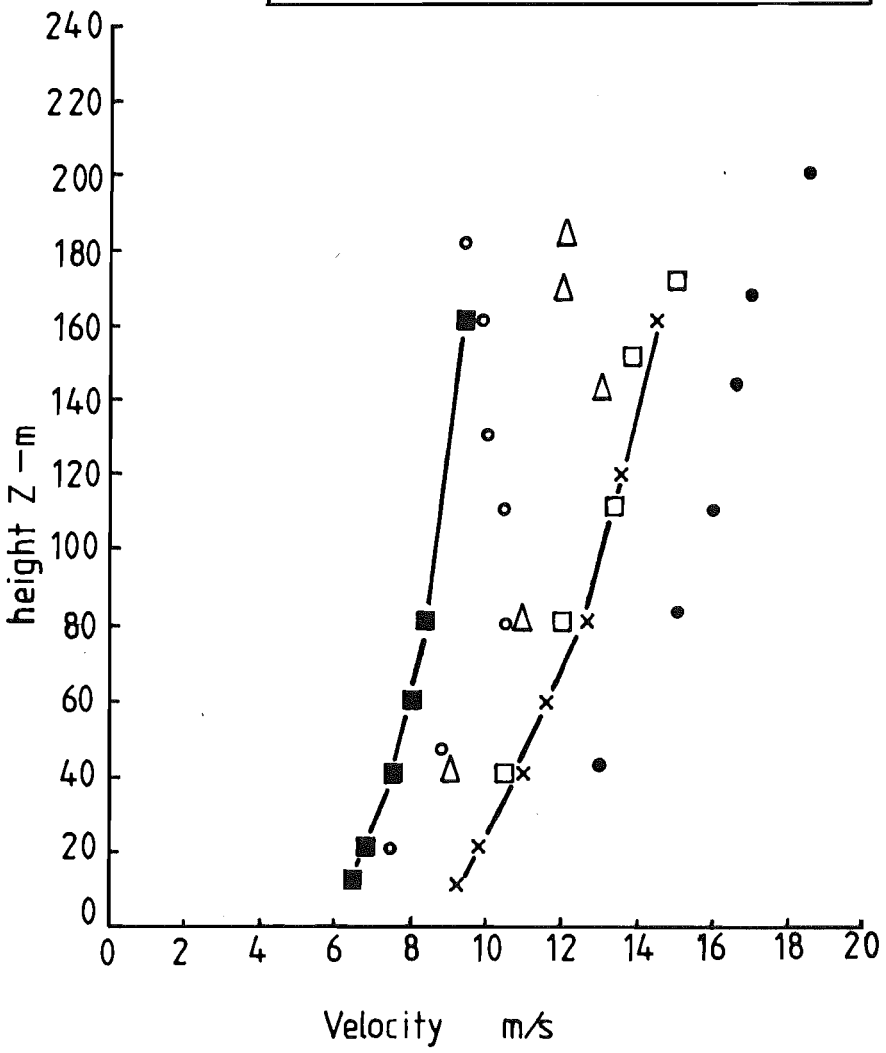

FIG 10·16 FIELD AND WIND TUNNEL VELOCITY PROFILE COMPARISONS

COMPARISONS FOR FIELD POINT 7

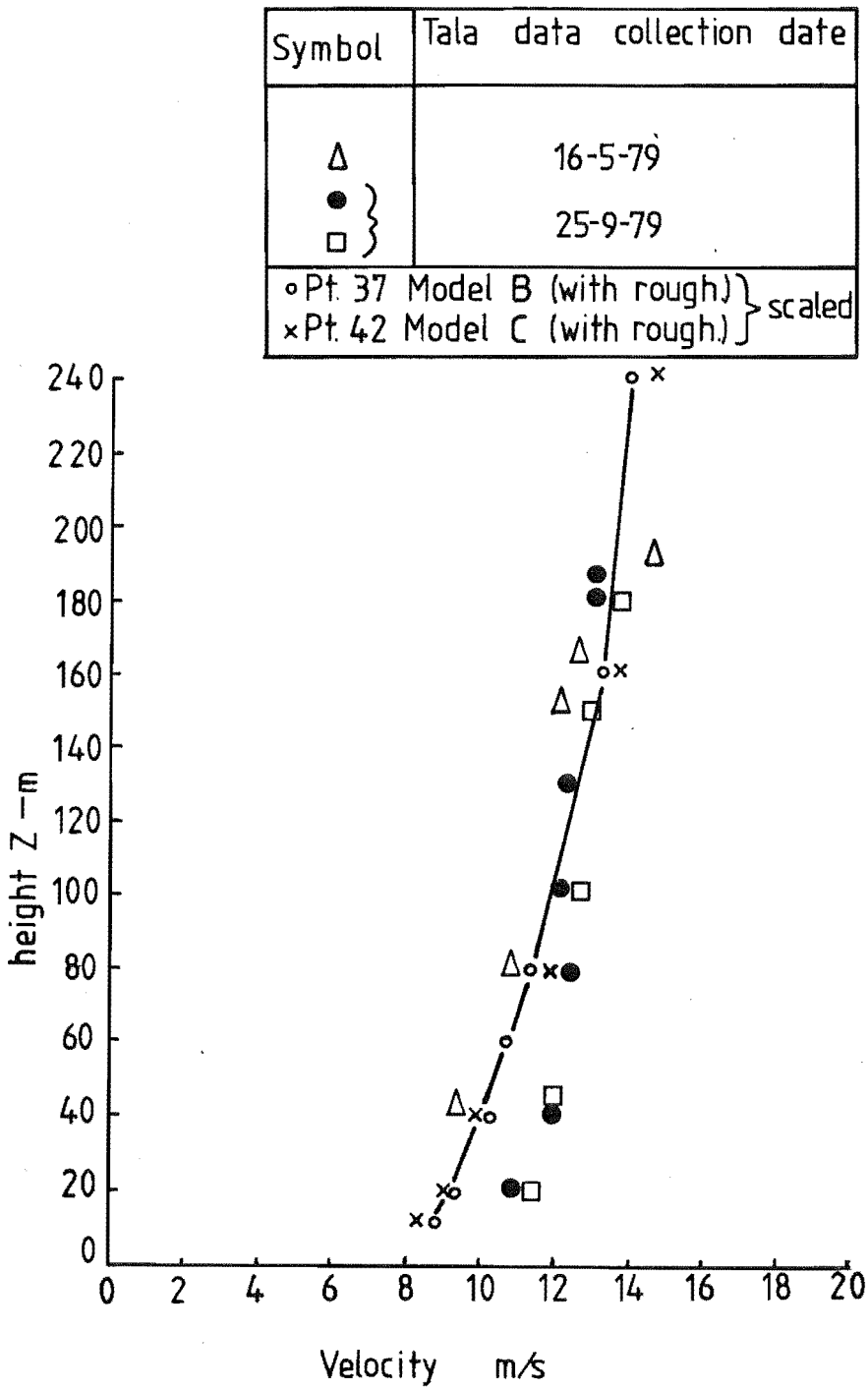

FIG 10·17 FIELD AND WIND TUNNEL VELOCITY PROFILE COMPARISONS

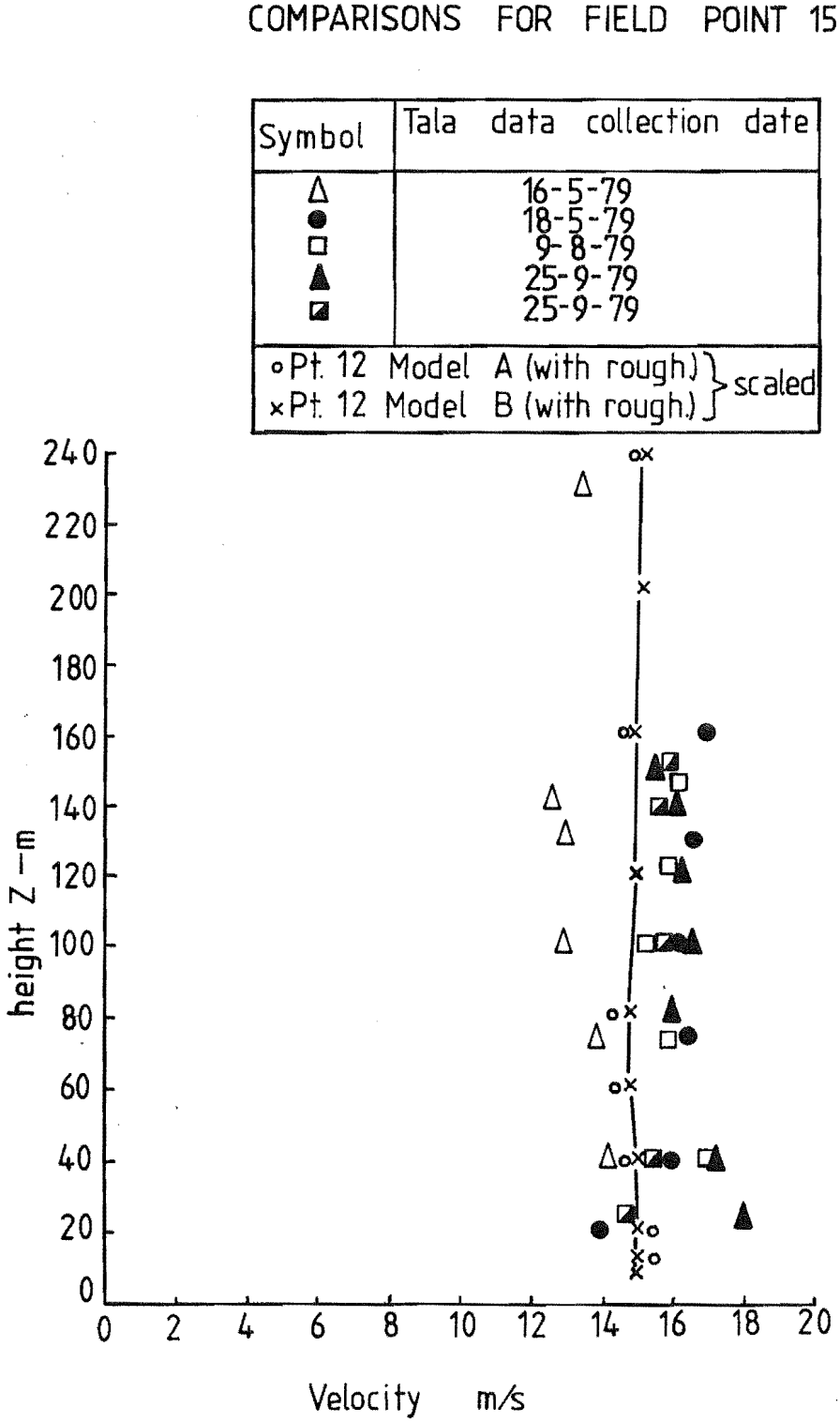

FIG 10·18 FIELD AND WIND TUNNEL VELOCITY PROFILE COMPARISONS

COMPARISONS FOR FIELD POINT 29

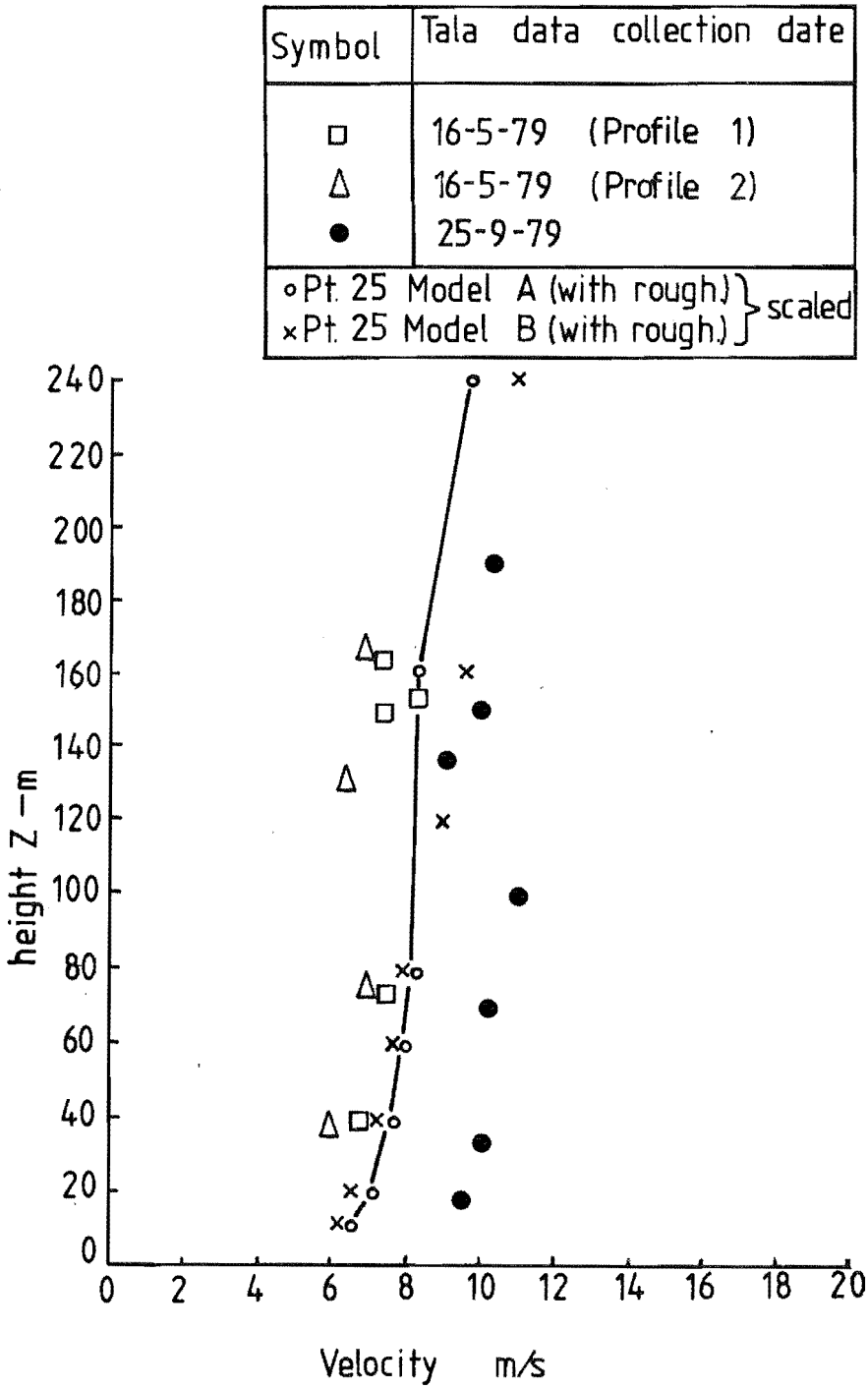

FIG 10·19 FIELD AND WIND TUNNEL VELOCITY PROFILE COMPARISONS

in the description of the modelled approach flow conditions.

A strong south-west wind event occurred on 21st October 1978 and two files were created in measuring this wind event. The first was called SW1 and lasted for 73 minutes; the second was called SW2 and lasted for 37 minutes. Since these files were recorded consecutively with a break of approximately one minute to change tapes, the final 36 minutes of SW1 was added to SW2 to form a file called 'Combined'.

The velocity time graphs for the SW1 and SW2 files are presented in Fig.10.20 to give a visual representation of the steadiness of the wind. However, to assess the stationarity of a wind event, the mean squares over short time intervals of the longitudinal velocity component are calculated. The computer programmes which have been developed to perform this task are discussed in full by Flay (1978). In this case a time interval of 2.28 minutes is used.

An individual time history is stationary if its properties computed over short time intervals do not vary "significantly" from one interval to the next. This means that the observed variations must not be greater than those due to normal sampling variations in order for it to be stationary. The resulting computer output had a parabolic trend removal performed on the data, the significance of trend removal techniques being discussed fully by Flay (1978).

The resulting mean squares were checked using a *Run Test*. This is defined as one plus the number of times a line joining consecutive samples of the sequence of mean squares crosses the line of the average mean squares value for the entire sample record. The number of *Runs* is then tested to see if it is significantly different from that of a random variable.

Bendat and Piersol (1971) have tabulated the number of *Runs* which are acceptable for several levels of significance, and for different numbers of samples in a sequence. The mean squares plots for SW1 and SW2 are given in Fig.10.21(a) and (b) respectively. For the SW1 file there are 32 samples; for a 0.05 level of significance, the number of *Runs* should lie between 11 and 22. The SW1 file has 14 *Runs*. For the SW2 file, the number of *Runs* should lie between 4 and 13 for a 0.05 level of significance. The SW2 file has 5 *Runs*. Therefore, one can say that both files are stationary with a 0.05 level of significance. In other words, there is a 0.05 chance of the number of *Runs* being outside the suggested range and the data still being stationary.

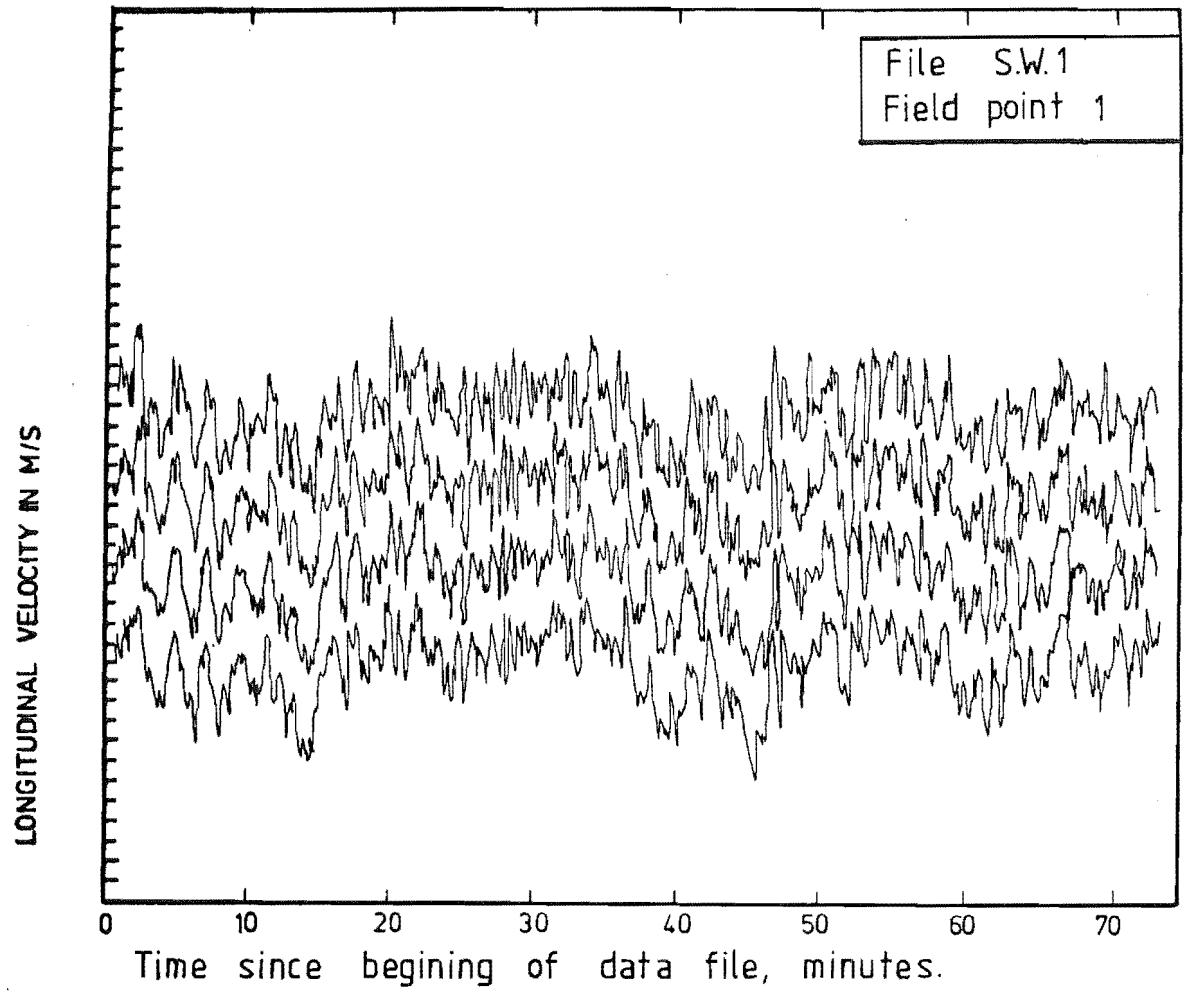

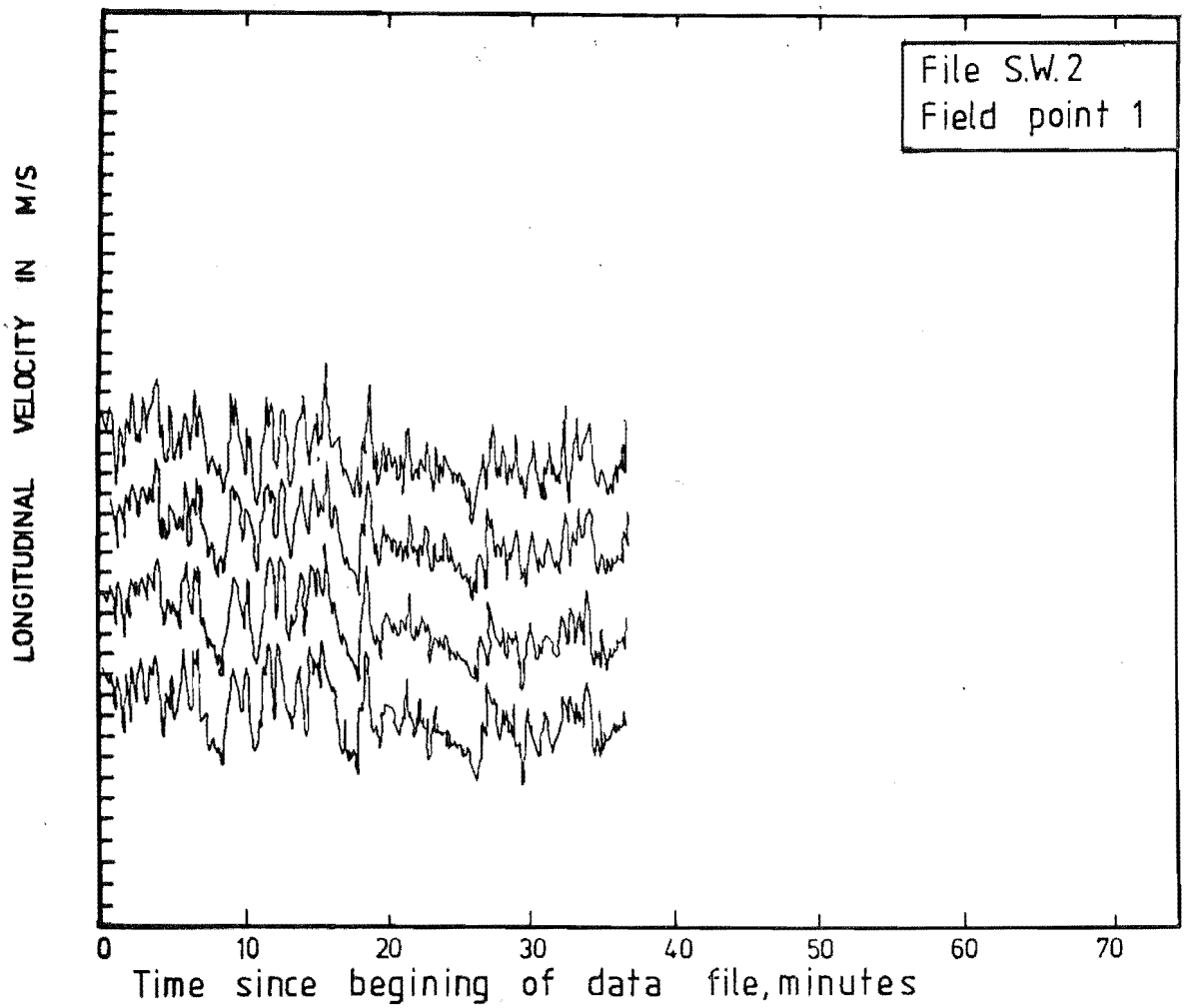

FIG. 10·20 VELOCITY AS A FUNCTION OF TIME OVER MEASURED PERIOD FOR FILES S.W.1 AND S.W.2

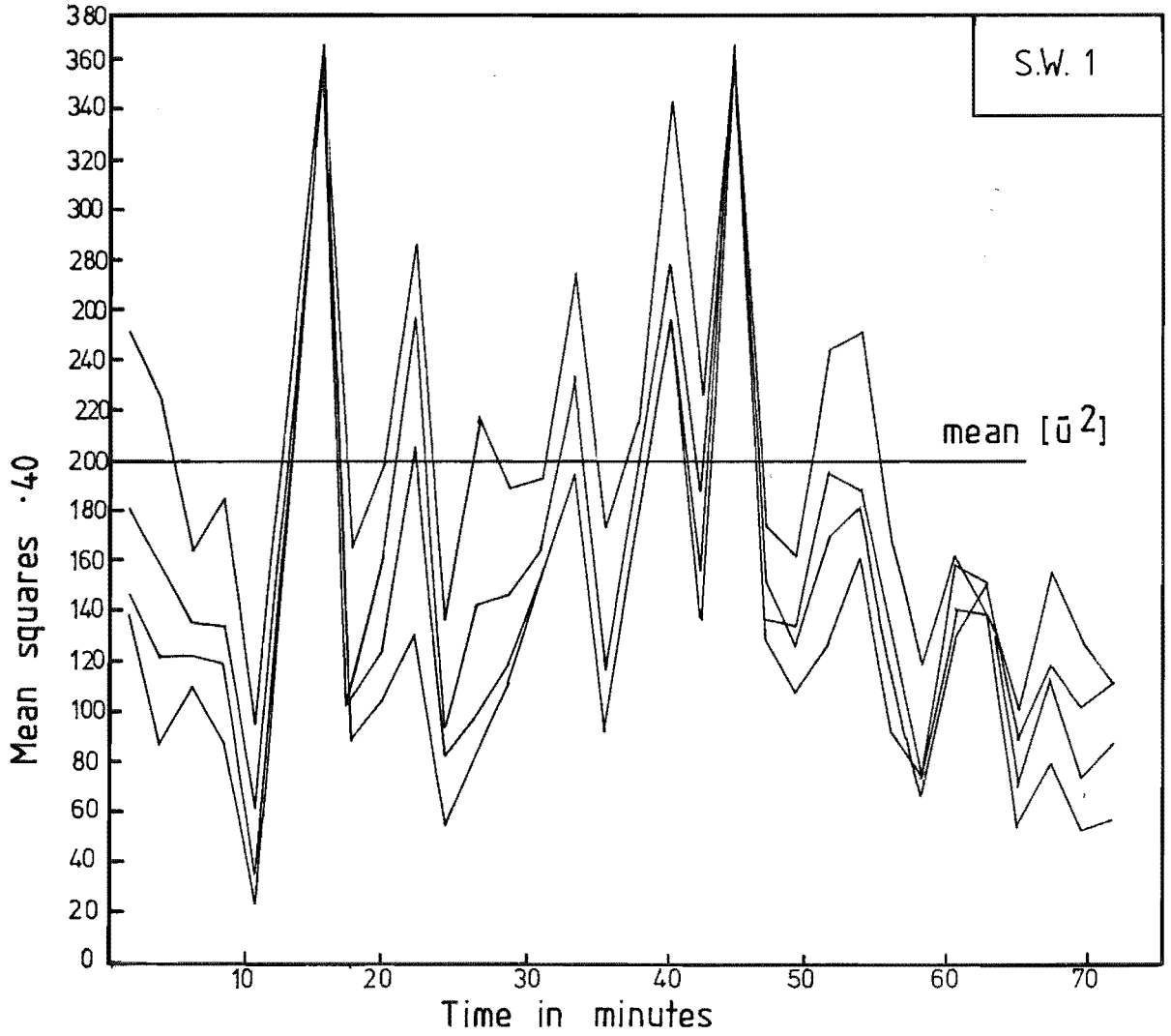

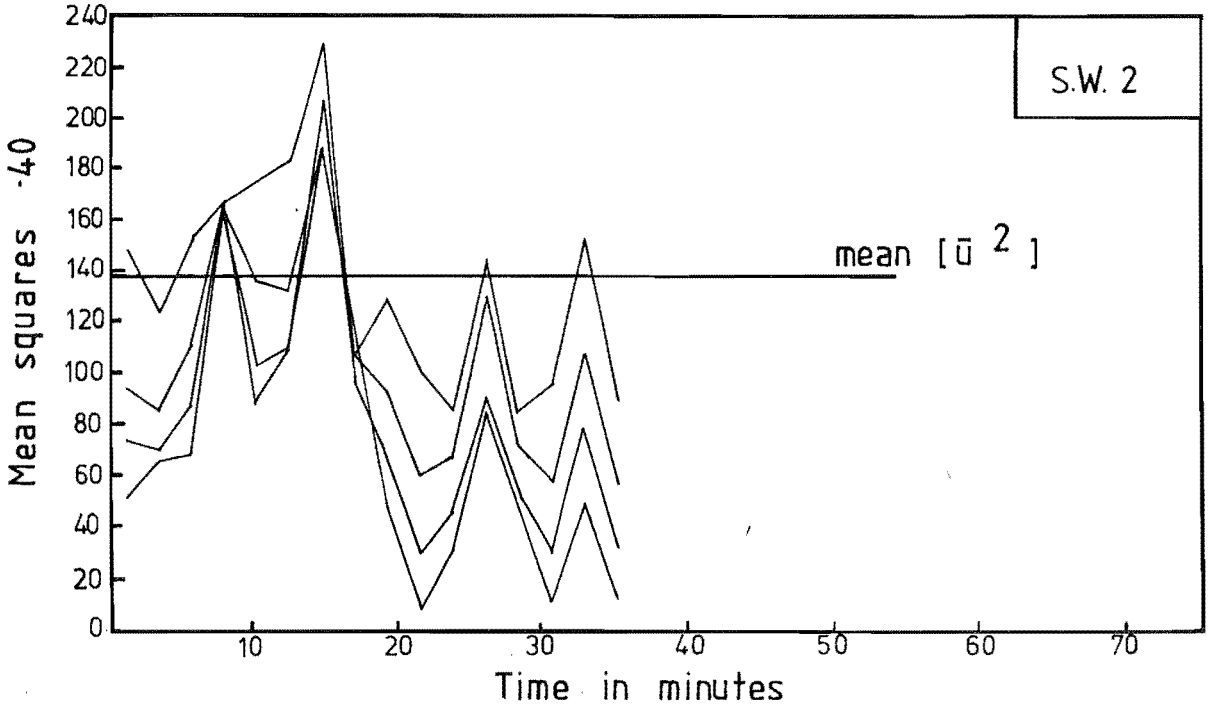

FIG 10·21 VARIATION OF MEAN SQUARES WITH TIME FOR FILES SW1 AND SW2.

Measured values of power law index, roughness length, autocorrelation curves and length scale of turbulence up to a height of 20m have been presented in Chapter 7, the remaining major parameters being presented here.

1) Turbulence Intensity Profiles

Turbulence intensity profiles measured at field point 1 are presented in Fig. 10.22 and compared with theoretical models. The measured profiles are in good agreement with each other and agree particularly well with the theoretical profile proposed by Counihan (1975).

2) $\rho\overline{uw}$ Reynolds Stress

The measured $\rho\overline{uw}$ Reynolds stress is plotted in Fig. 10.23. As the field equipment can only measure to a height of 20m, profiles measured by Flay (1978) have been included as a comparison. The justification for this is that his measurements were carried out on terrain very similar to that at field point 1. Included on Fig. 10.23 are theoretical profiles and the modelled Reynolds stress profile. Unfortunately, the hot wire probe used could only be lowered to an effective height of 5 mm. However, at this height, 20m on prototype, the modelled value of $\frac{\overline{uw}}{U_\infty^2}$ lies between the values actually measured. The modelled profile shows a constant shear stress layer between 20m and 45m, which agrees with Counihan (1975). The value of the Reynolds stress in this region agrees with that proposed by Counihan, which is of the form

$$\frac{\overline{uw}}{U_\infty^2} = 2.75 \times 10^{-3} + 6 \times 10^{-4} \log_{10} z_o \quad \ldots\ldots\ldots\ldots \quad (10.1)$$

which clearly show no variation with height but is only applicable up to approximately 50m.

3) Energy Spectra

Energy spectra for field data files SW1, SW2 and Combined are compared with the modelled spectra for Z_p = 20m in Fig. 10.24. The measured spectra have been scaled to make them compatible with the modelled spectra. The integral length scale was shown (see Section 2.1.5) to be related to the spectral peak wave number by

$$L_{u_x} = \frac{0.146}{k_{p_u}} \quad \ldots\ldots\ldots\ldots\ldots\ldots\ldots\ldots\ldots\ldots \quad (10.2)$$

due to the linear scaling

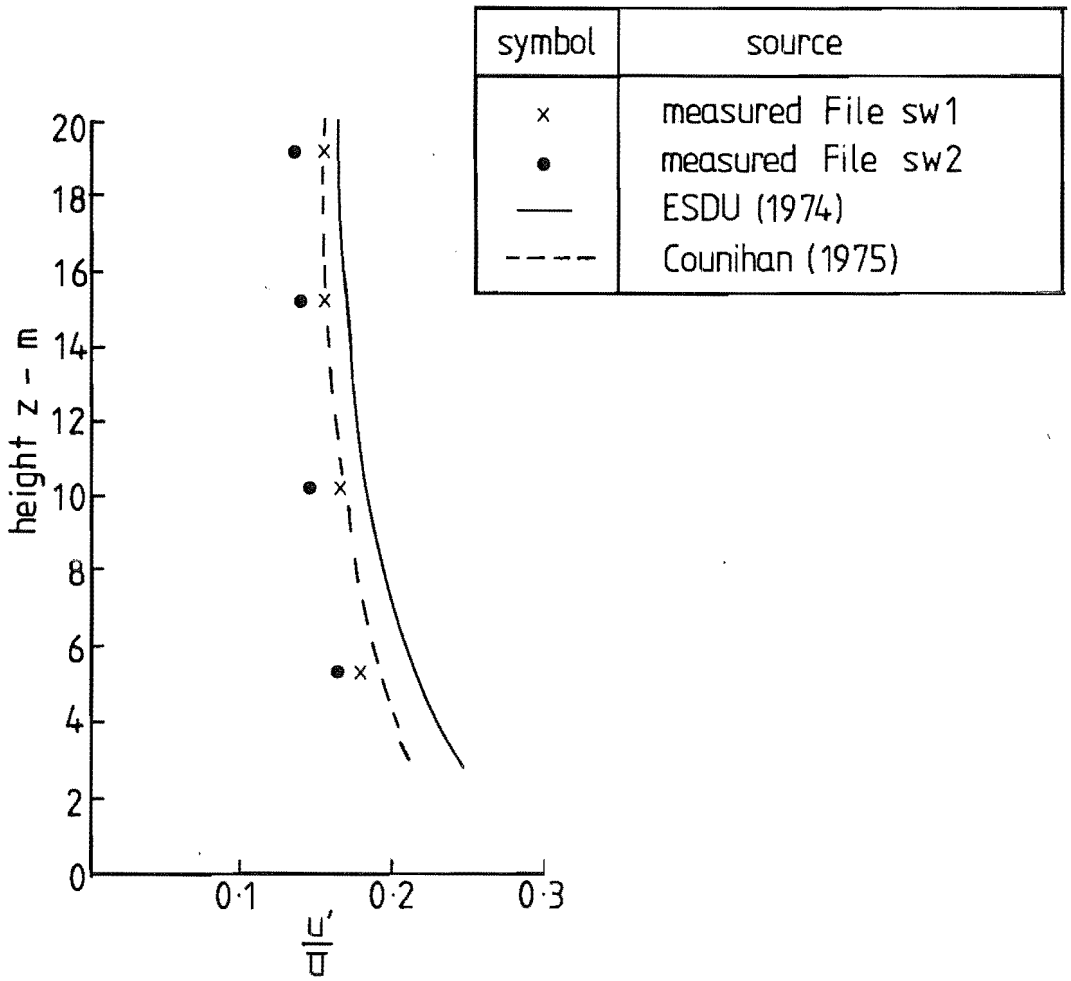

FIG. 10·22 COMPARISON OF TURBULENCE INTENSITY PROFILES FOR FIELD POINT 1.

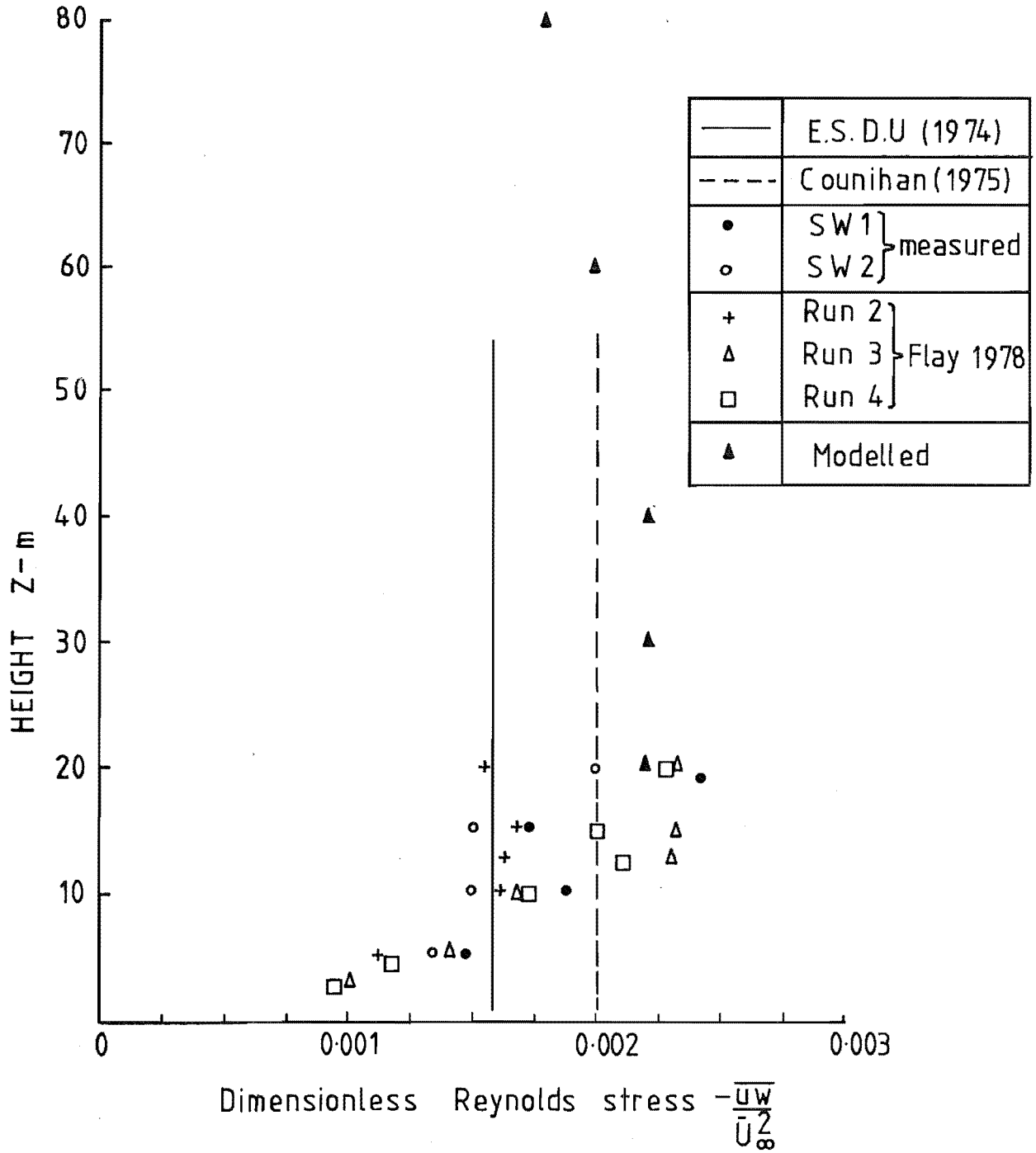

FIG 10·23 REYNOLDS STRESS PROFILES

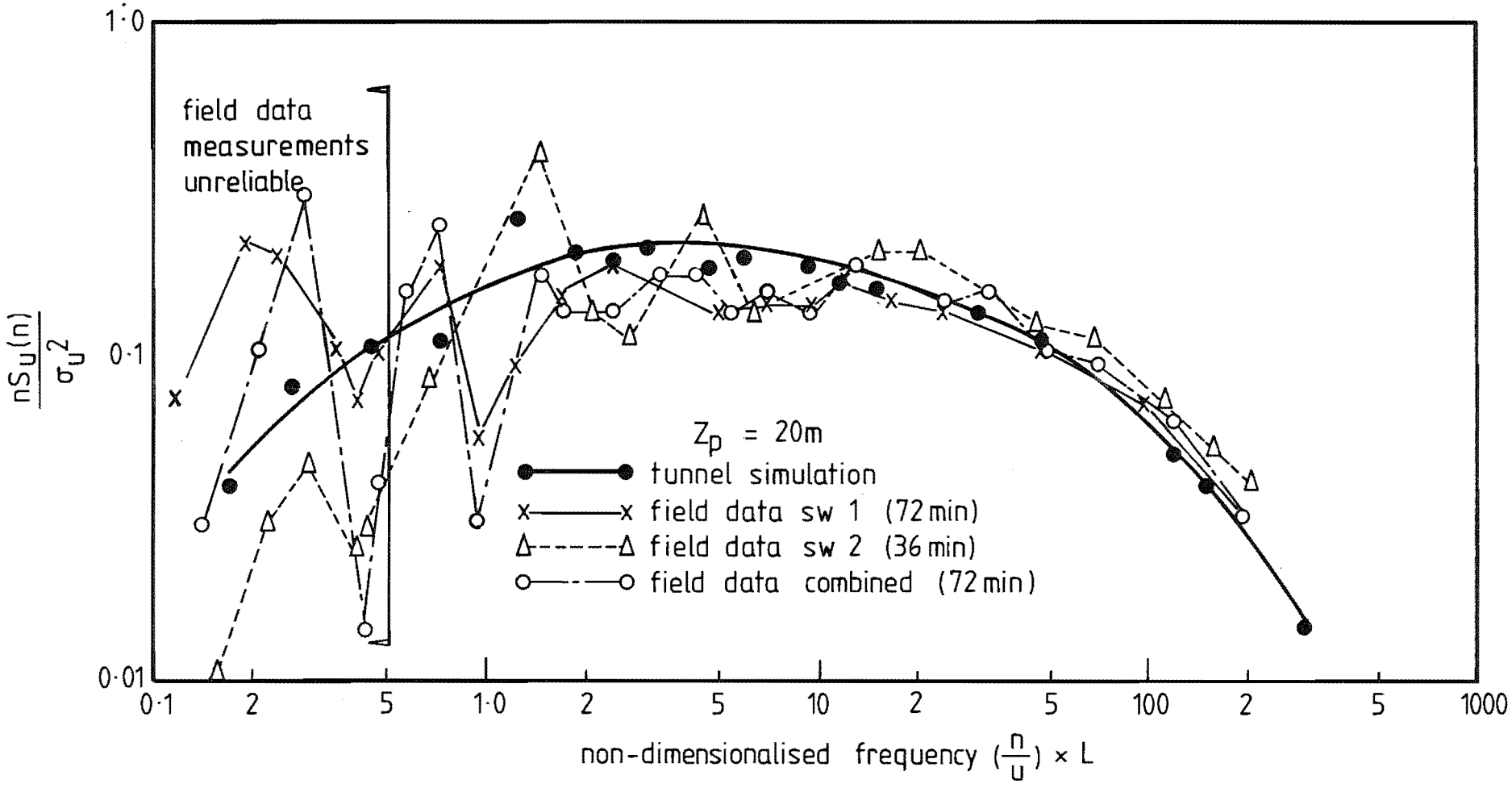

FIG 10·24 COMPARISON OF MEASURED AND MODELLED ENERGY SPECTRA FOR FIELD POINT 1.

$$\frac{L_{u_x(\text{model})}}{L_{u_x(\text{field})}} = \frac{1}{4000}$$

Therefore, it follows that

$$k_{p_{u(\text{model})}} = k_{p_{u(\text{field})}} \times 4000 \quad \ldots\ldots\ldots\ldots \quad (10.3)$$

If the scaling factor is given the units of metres, the base scale expression becomes dimensionless. The shape of the spectra and location of the peaks are in excellent agreement. A vertical line is included on the diagram; measurements to the left of this line are considered unreliable. This is due primarily to the limitations of the equipment and is explained in detail by Flay (1978). This situation is not considered a major drawback because the area of most interest regarding spectra is the location of the spectral peak and the energy distribution in the inertial subrange, which has been discussed in Section 2.1.5.

The longitudinal component of the energy spectrum is presented for four heights in Fig. 10.25. The effect of the non-dimensionalised frequency scale is to collapse the spectra into a small band in the higher frequency range. The data presented from file SW1 clearly demonstrates this effect.

The interesting feature to note is that at the lowest height, 5.3m, the spectrum is significantly flatter than at the 19.2m height. This feature also occurred in the wind tunnel simulation and is clearly shown by Fig. 7.24.

4) Length Scale L_{u_x}

Values of the integral length scale derived from several sources are presented for comparison in Table 10.5.

Model	Field Point	Spectra	Autocorrelation
40*		300	346
-	1(File SW2)	160	166
-	1(File Combined)	365	454

(All measurements at 20m)

* - Model B with roughness added.

TABLE 10.5: Comparison of Length Scales

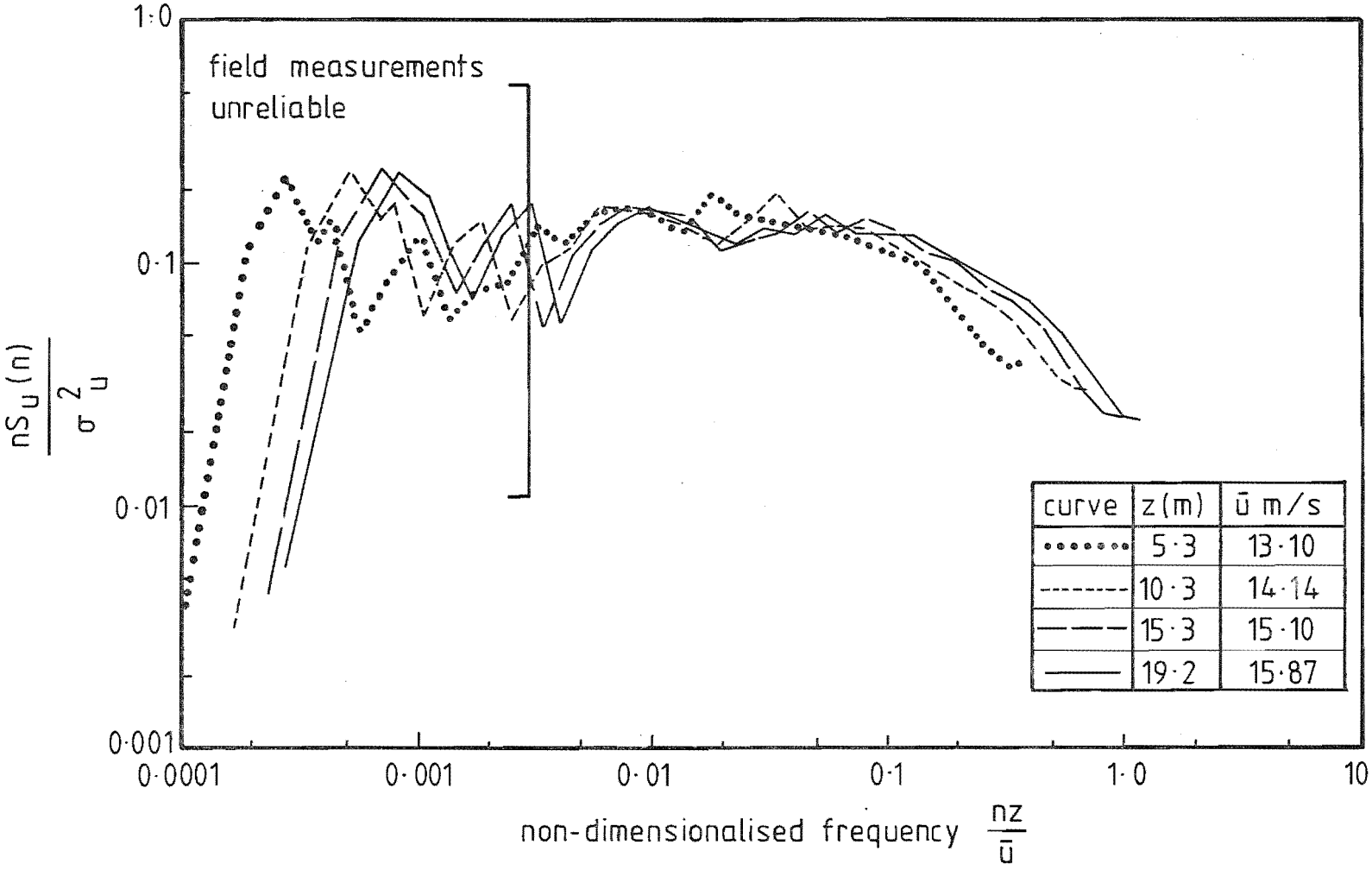

FIG 10·25 VARIATION OF LONGITUDINAL ENERGY SPECTRA WITH HEIGHT AT FIELD POINT 1.

The autocorrelation curves used in Table 10.5 were presented in Fig. 7.15. Counihan (1975) suggests that the variation of length scale with height can be represented by the formula

$$L_{u_x} = C(Z)^{\frac{1}{n}} \quad \ldots\ldots\ldots\ldots\ldots\ldots\ldots\ldots\ldots\ldots (10.4)$$

C and $\frac{1}{n}$ are variables and are obtained from a graph which gives their variation with roughness length Z_o.

For field point 1, a roughness length of 0.025m will be used, yielding the formula

$$L_{u_x} = 95(Z)^{0.20} \quad \ldots\ldots\ldots\ldots\ldots\ldots\ldots\ldots\ldots\ldots (10.5)$$

ESDU (1974) also gives values of L_{u_x} for different values of Z_o and over a range of heights. These values, together with Counihan's predictions, are plotted against the length scales derived from the energy spectra in Fig. 10.26. Considering the difficulty in determining the value of k_p from the energy spectra and the large discrepancy between ESDU and Counihan, it is most encouraging that the measured length scales lie between the theoretical values. The actual shape of the curve for the measured data only indicates the variation, as it is extremely difficult to determine k_p.

10.3.2 Gebbies Pass Site

The 20m tower was moved to field point 15, located on the Gebbies Pass Saddle, see Fig. 10.1. The approach terrain to this point is shown in the photograph in Fig. 10.27. A wide angle lens was used for this photograph resulting in a small amount of distortion.

Several data files were recorded at this site over a period of six months. Equipment malfunctions prevented the use of much of this data and of the files that were selected. In several cases, a portion of the data had to be disregarded. Fortunately the data handling computer software made this task very simple and quick. The data files to be used are given in Table 10.6, together with their scan rate, recorded length and length to be used.

The wind direction during the recording of the files remained fairly constant. Typical wind direction graphs for the periods of recording tapes GP6 and GP7 show the steady nature of the wind. The wind was shown to approach from a SSW direction, see Fig. 10.28, which is the same as that for model B, as described in Chapter 8.

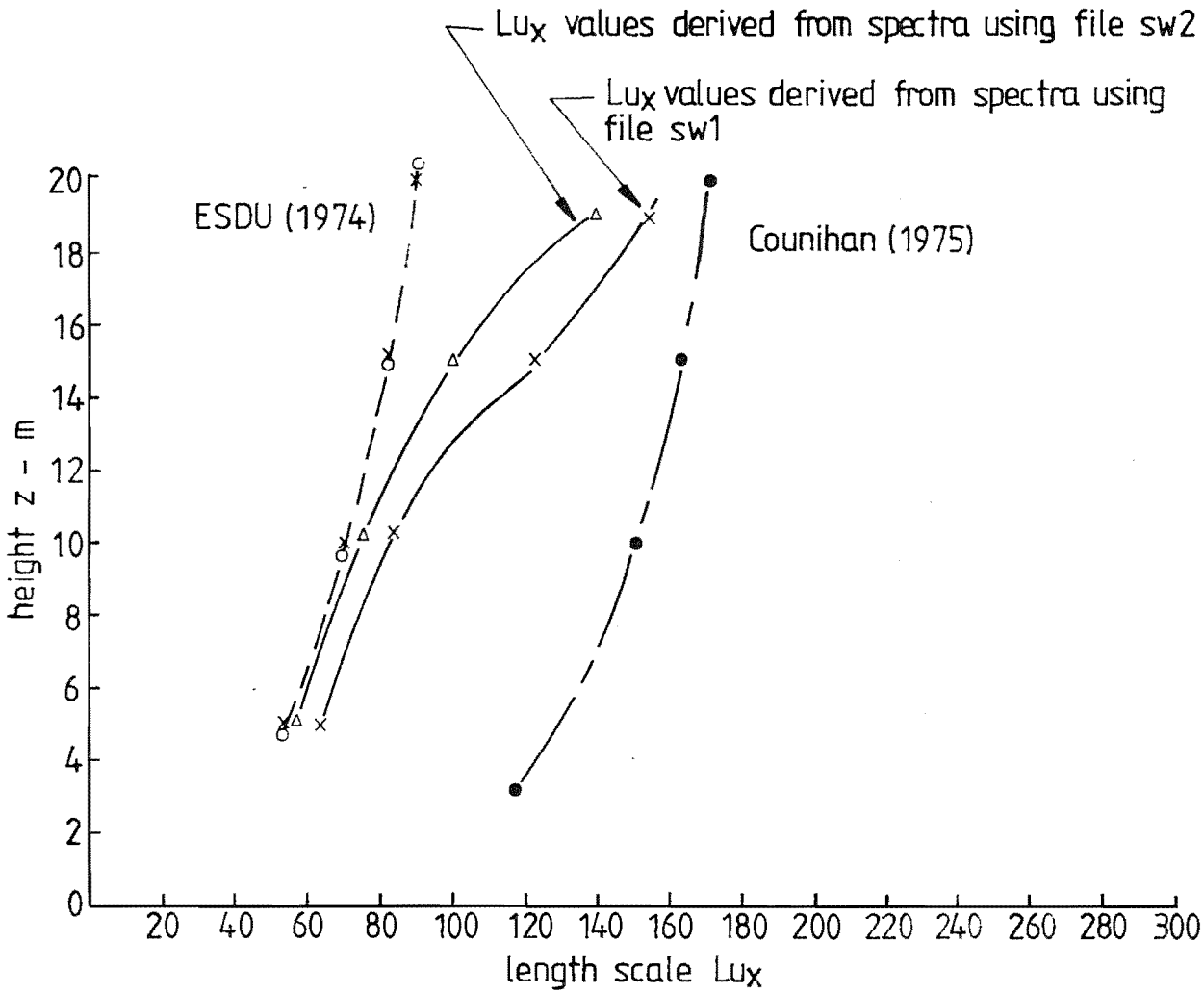

FIG. 10·26 VARIATION OF LENGTH SCALE (L_{ux}) WITH HEIGHT FOR FIELD POINT 1

660/33

FIG 10·27 VIEW LOOKING SW FROM FIELD POINT 15.

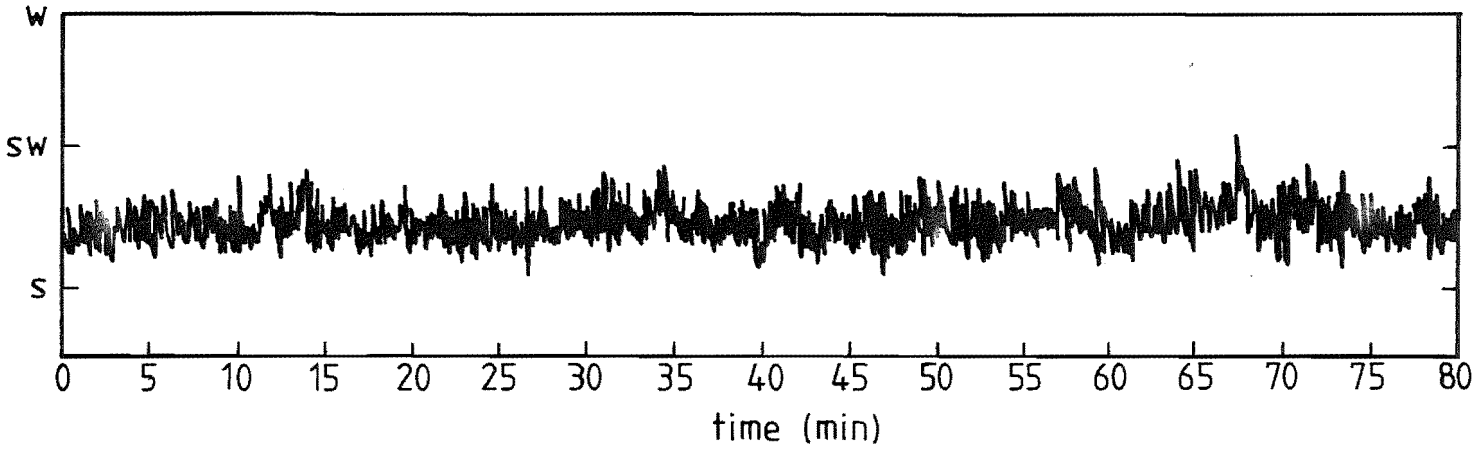

a) wind direction during the recording of tape GP6 on the 5/7/79

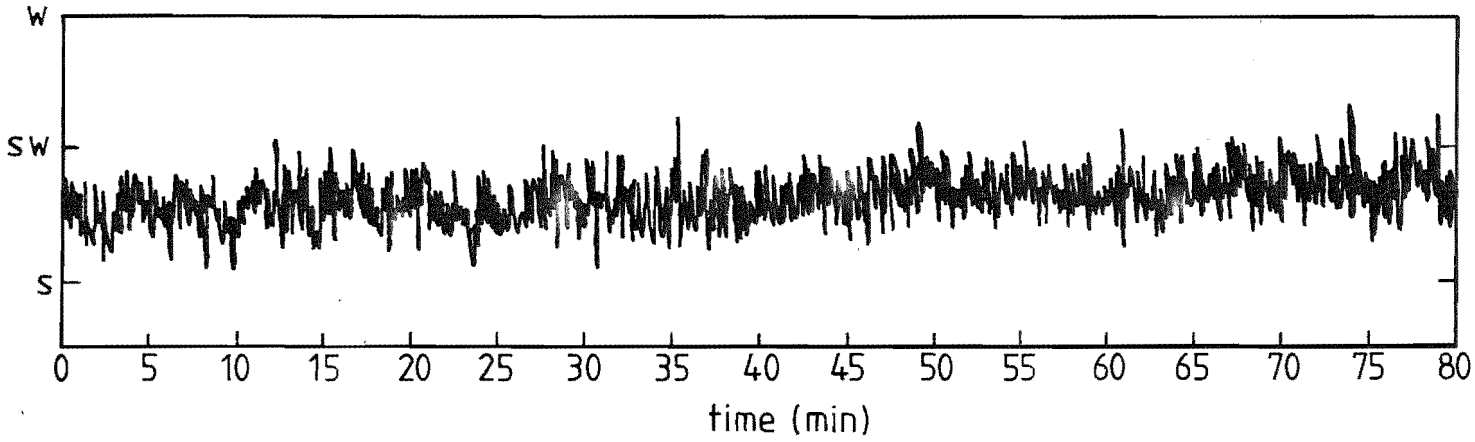

b) wind direction during the recording of tape GP7 on the 15/7/79

FIG 10·28 WIND DIRECTION GRAPHS FOR THE PERIODS DURING THE RECORDING OF FIELD TAPES GP6 AND GP7

File	Scan Rate (Hz)	Recorded Length (min)	Length of data to be used (min)
GP3	32	75	72.8
GP6	16	76	36.4
GP7	16	58	36.4
GP8	16	78	36.4
GP9	16	45	18.2

GP - refers to Gebbies Pass site (field point 15)

TABLE 10.6: Data Files for Field Point 15

Velocity time graphs for all GP files are presented in Figs 10.29 to 10.32. In all cases, the data was found to be stationary.

1) Velocity Profiles

Velocity profiles up to 20m for the five files at field point 15 are presented in Fig. 10.33(a). The profiles for all files are almost identical, showing an increase in velocity from 10-15m and a decrease in velocity from 15-20m heights. The model results for this point suggested that the flow close to the model surface, i.e. Z < 10mm, had a speed-up ratio greater than 1. This means that the velocity at some height Z at the point being considered is greater than the velocity at the same height in the upstream approach flow. Bowen (1979) in his study of flow over an escarpment, found this effect, as did Chien, Meroney and Sandborne (1979) in their study of sites for wind power installations on Hawaii. Although this effect is commonly measured on models and has been predicted with two-dimensional numerical models, there is very little field data which clearly shows the shape of the velocity profile in the speed-up region.

Figure 10.33(a) includes the modelled velocity profile for model B in the roughness added form of construction. The three scaled measurements made closest to the model surface were at 8m, 12m and 20m; the lack of a measurement at a scaled height of 15m made it difficult to determine if the speed-up occurred over the model in a similar way to that measured.

2) Turbulence Intensity Profiles

Turbulence intensity profiles are compared in Fig. 10.33(b). The

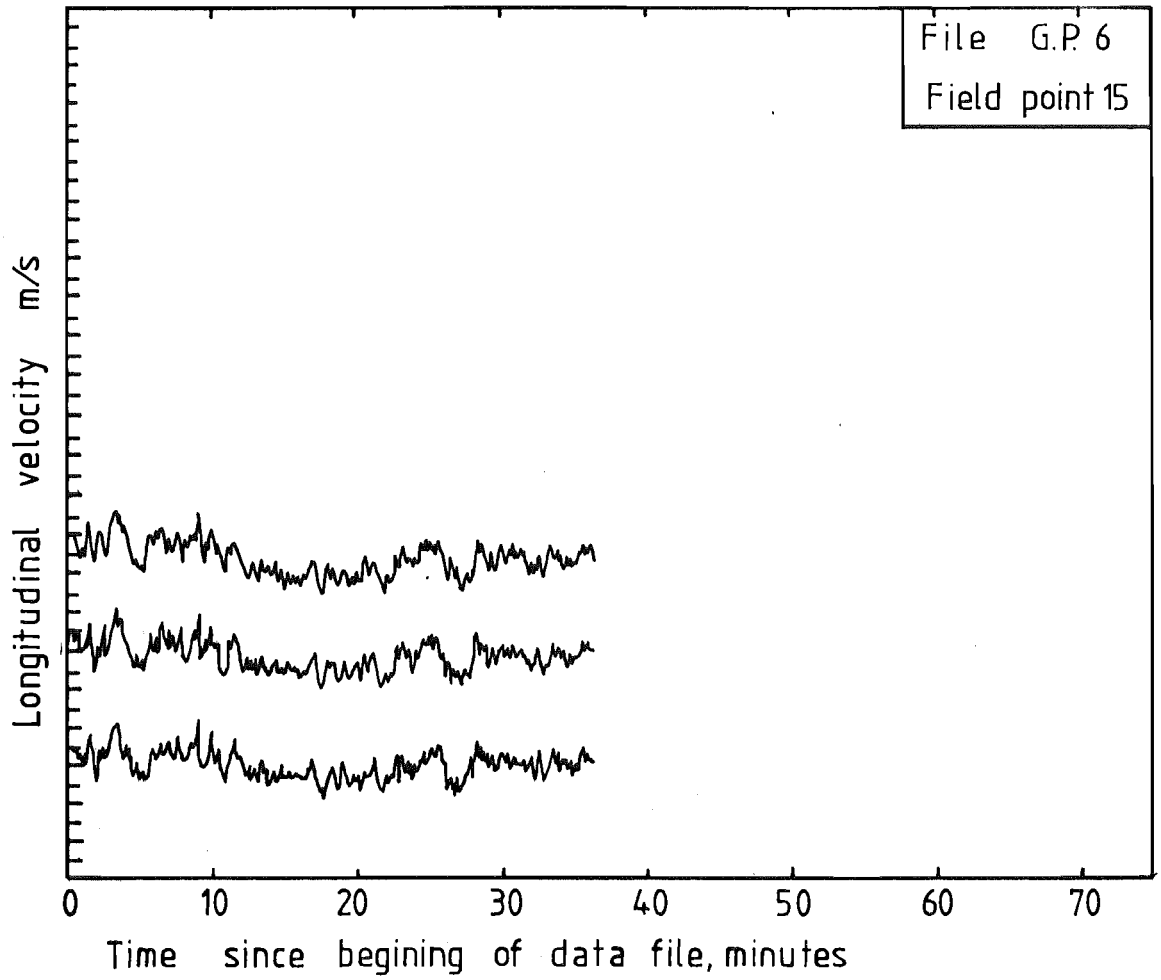

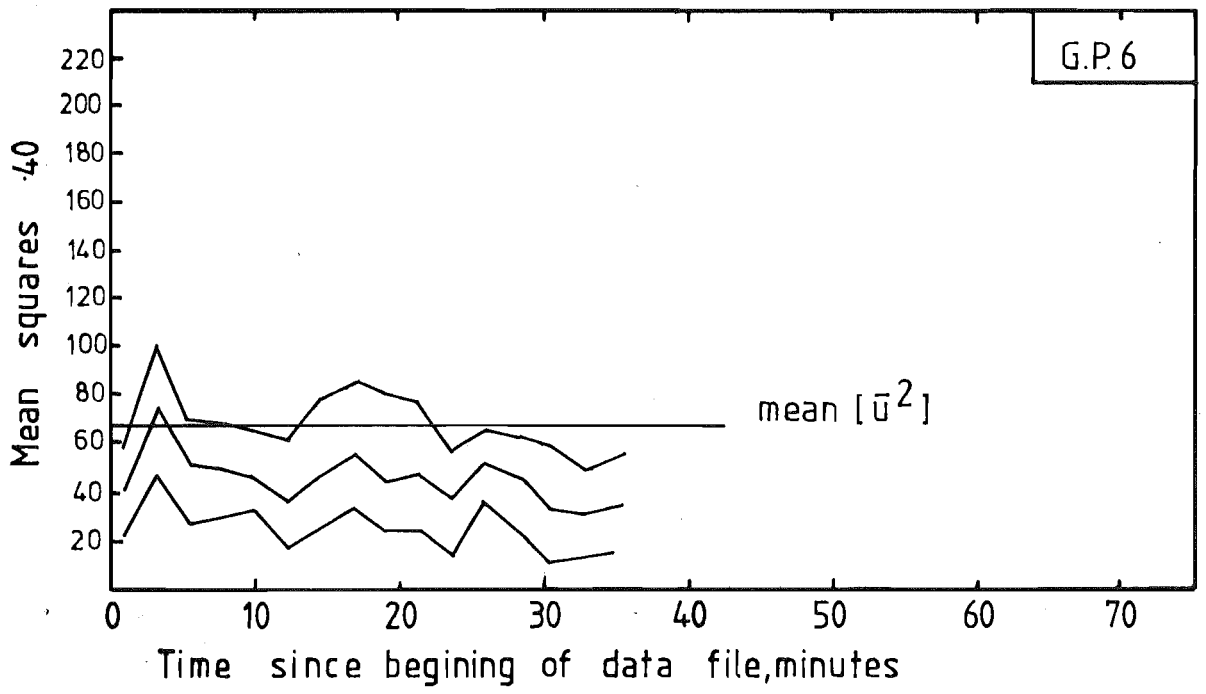

FIG 10·29a VELOCITY TIME GRAPHS FOR FILE G.P. 6.

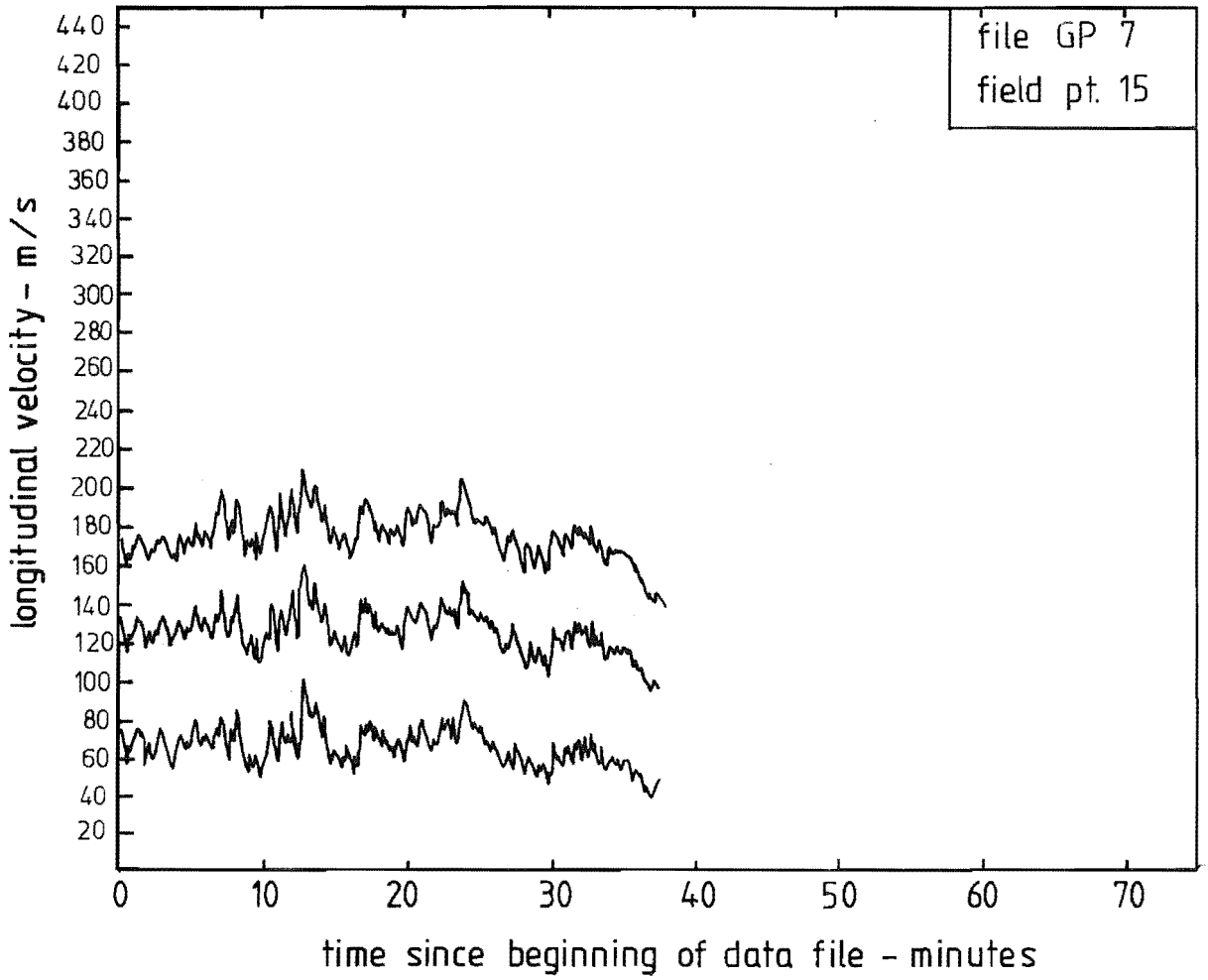

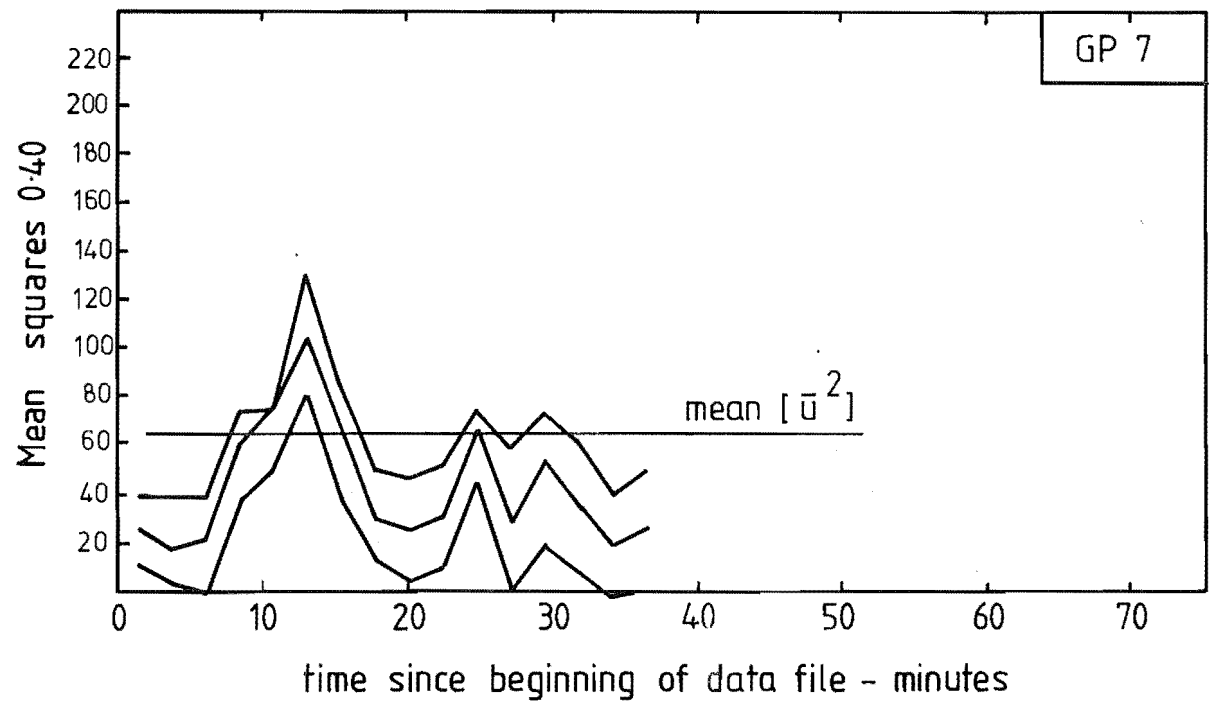

FIG 10·29b VELOCITY TIME GRAPHS FOR FILE G.P.7

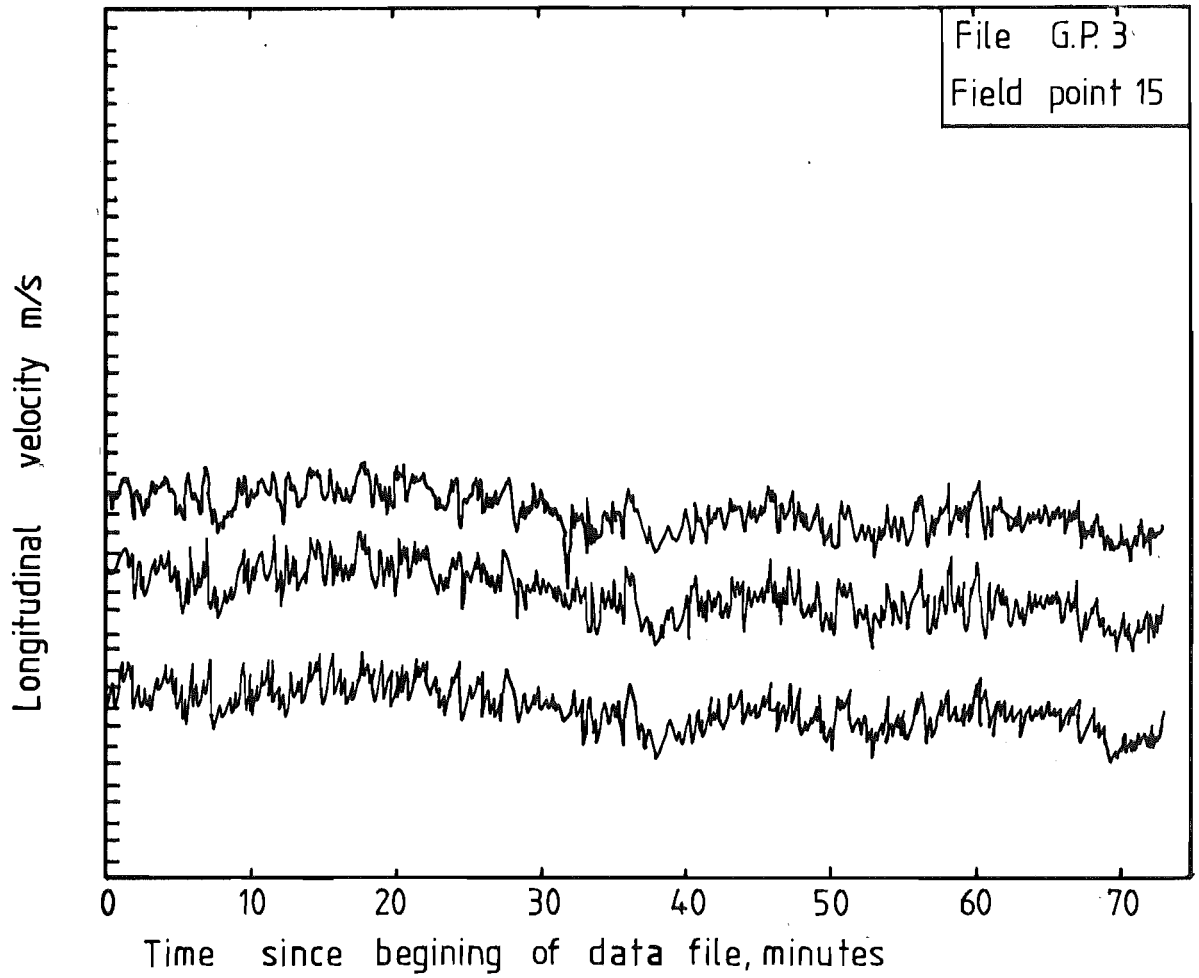

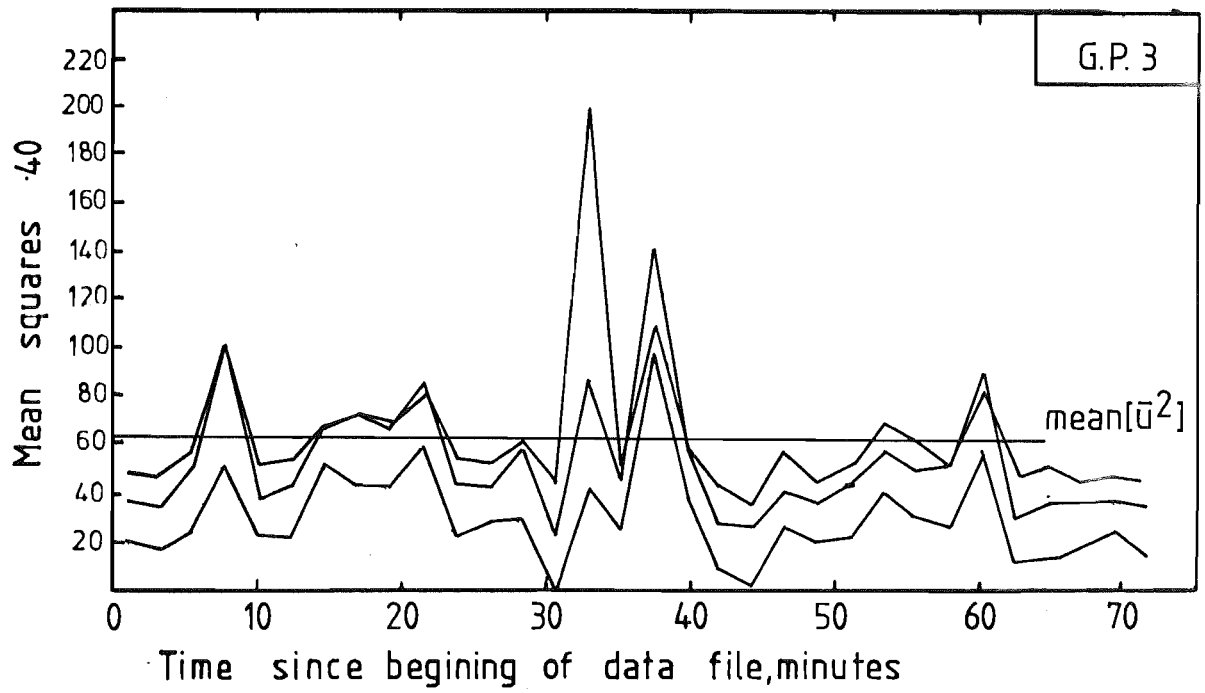

FIG 10·30 VELOCITY TIME GRAPHS FOR FILE G.P 3

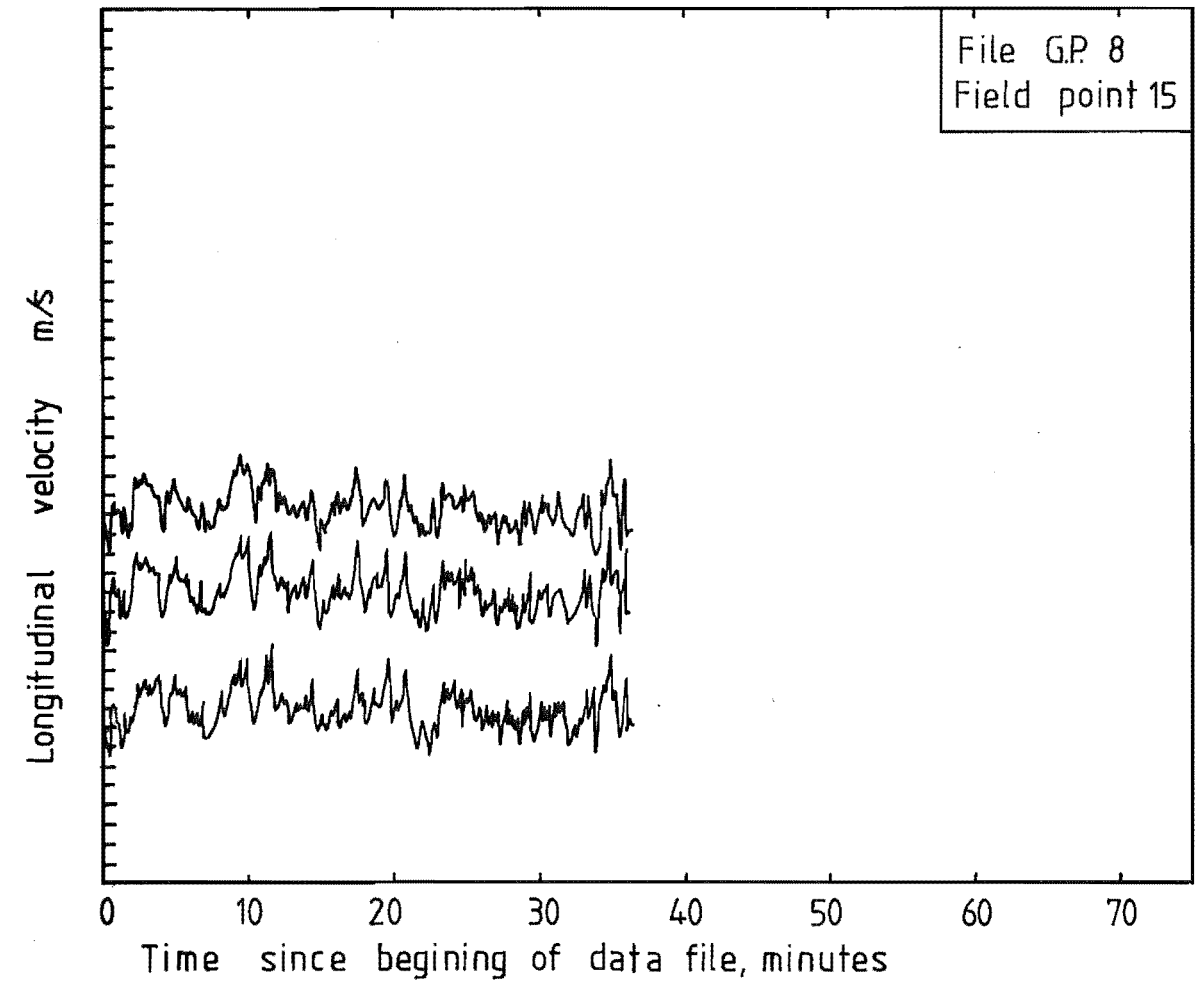

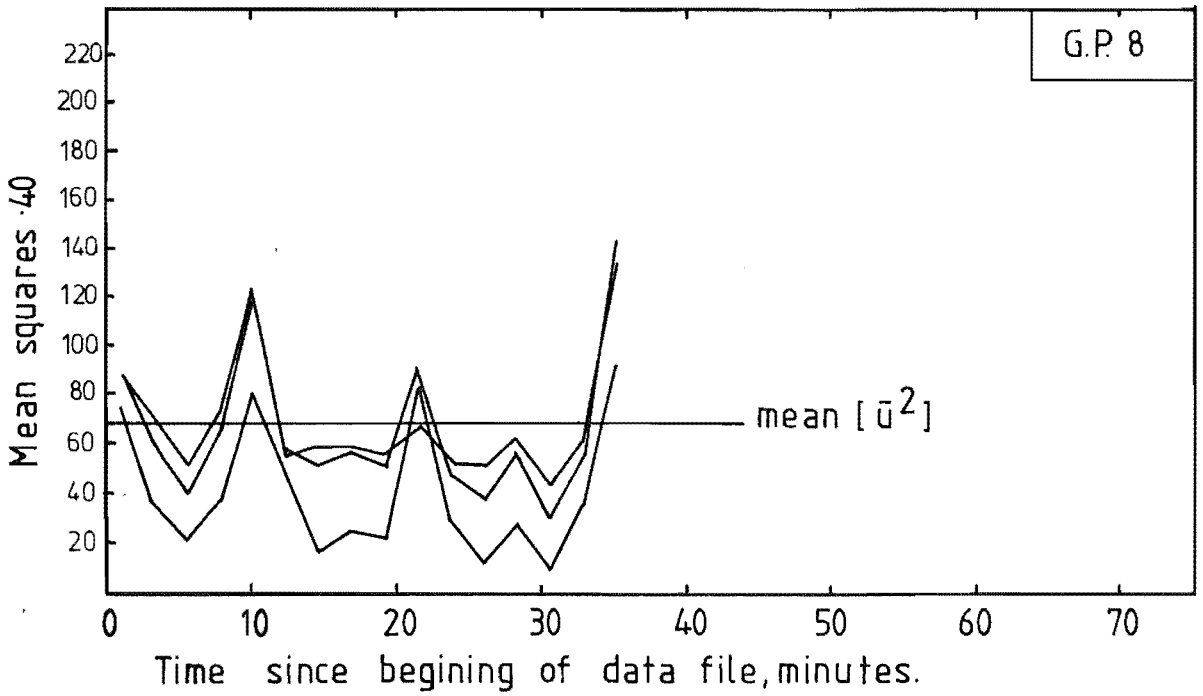

FIG 10·31 VELOCITY TIME GRAPHS FOR FILE GP8.

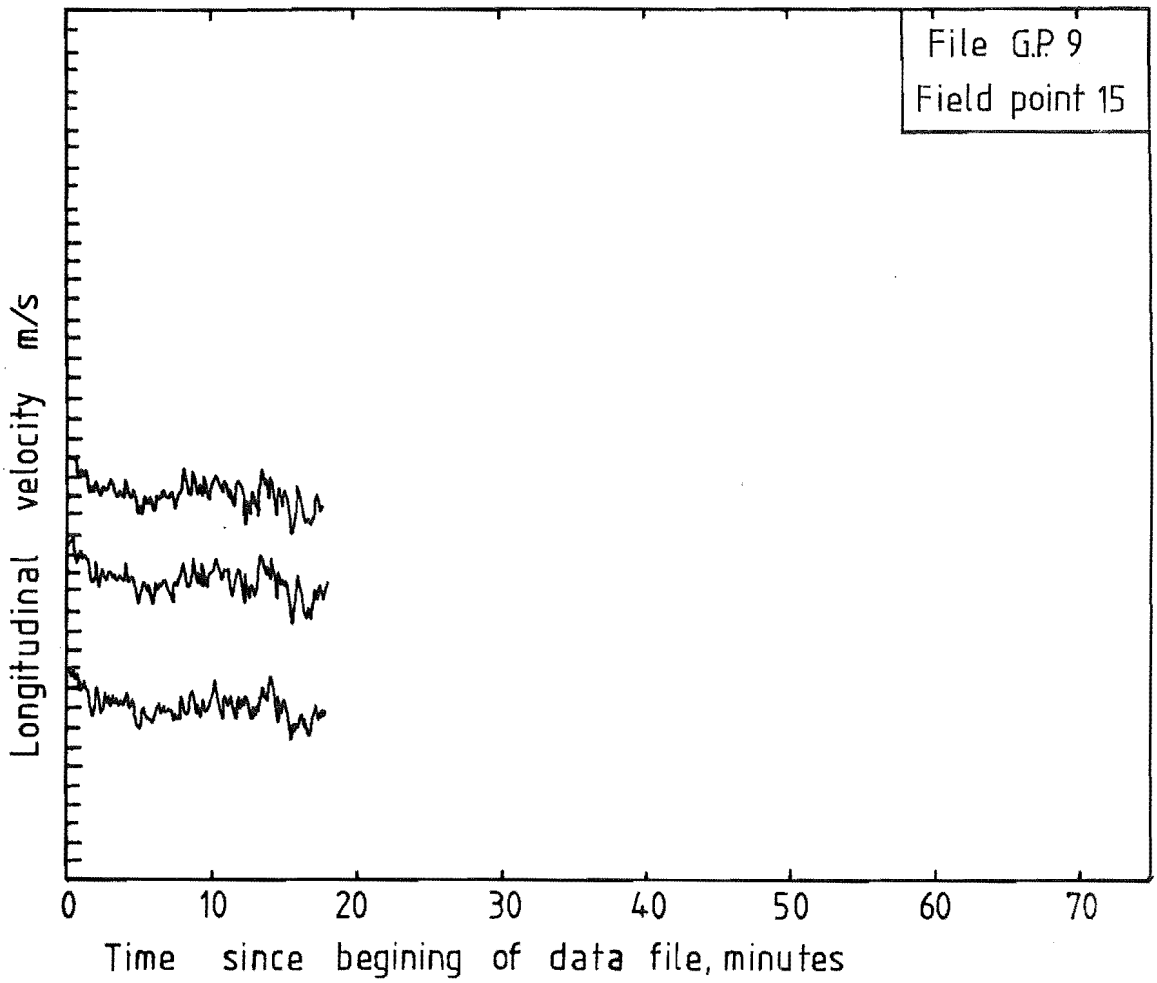

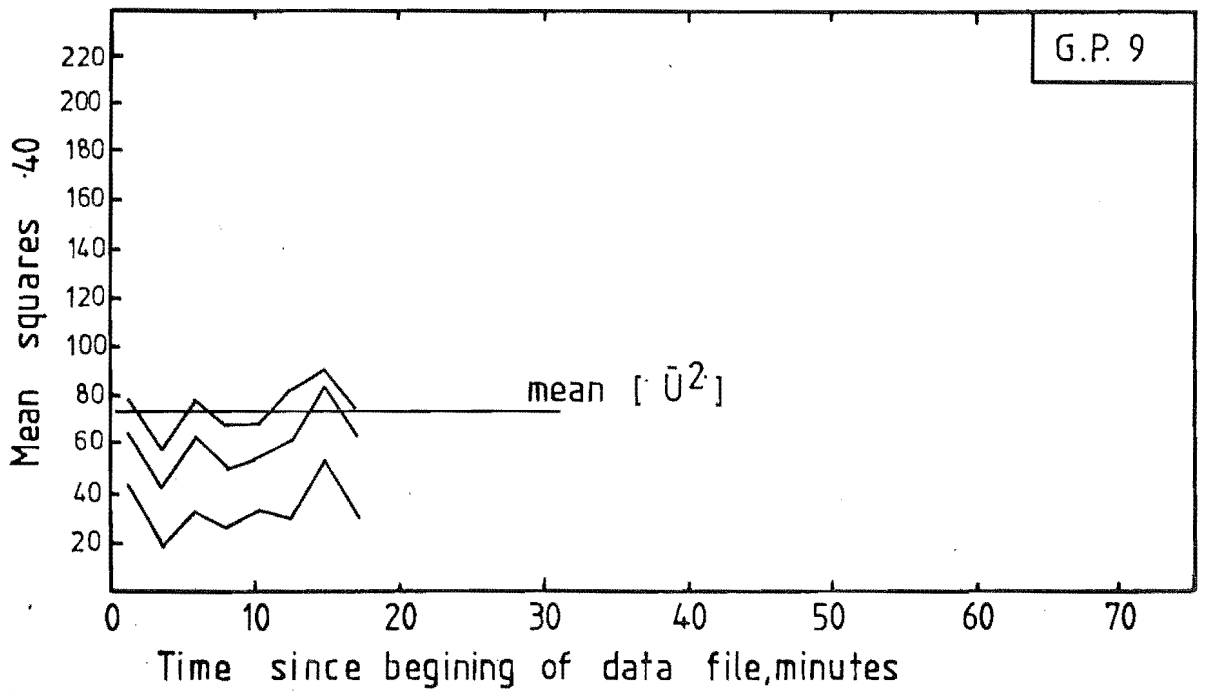

FIG 10·32 VELOCITY TIME GRAPHS FOR FILE G.P.9

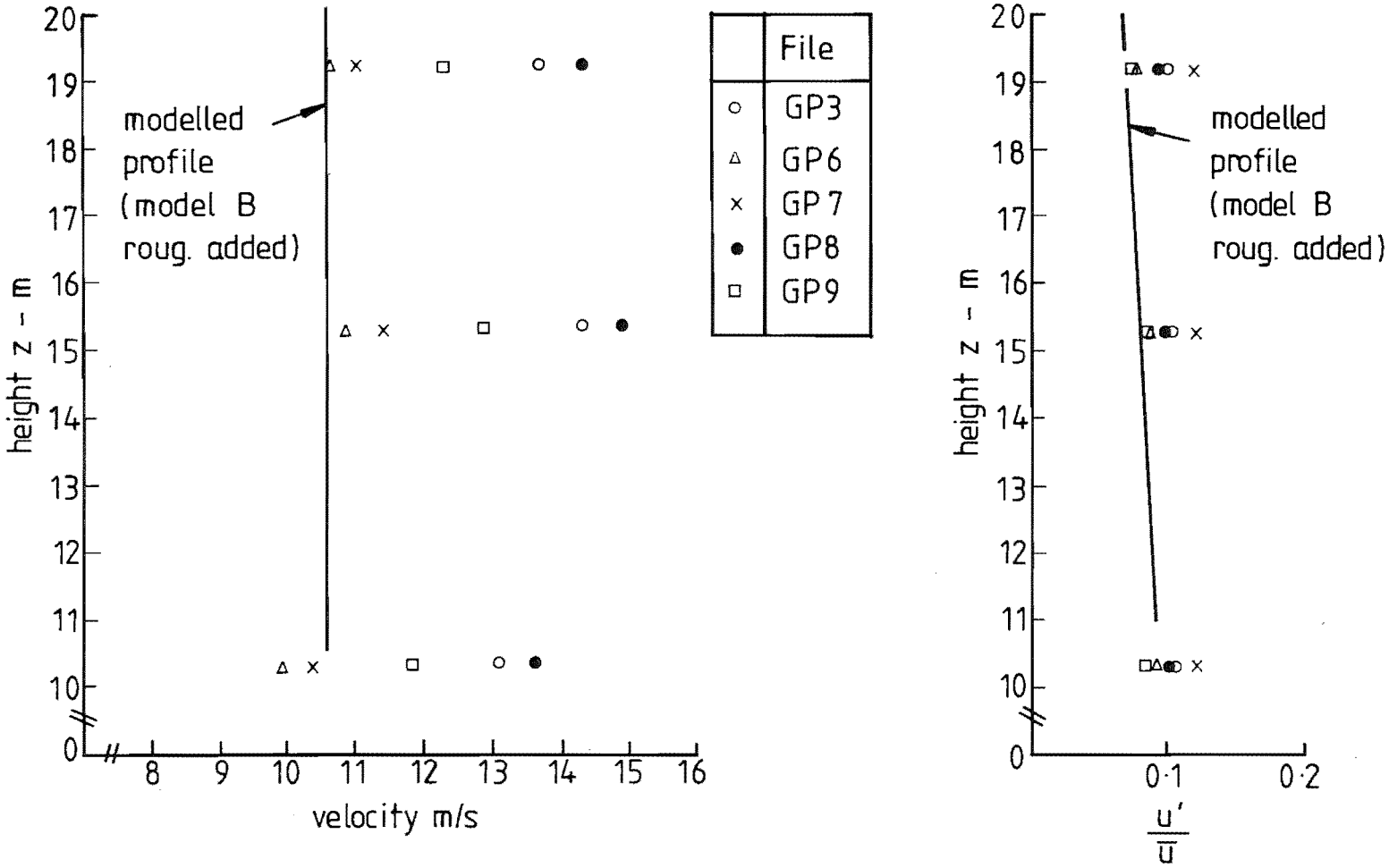

a) Velocity Profiles

b) Turbulence Intensity Profiles

FIG. 10·33 VELOCITY AND TURBULENCE INTENSITY PROFILES FOR FIELD POINT 15

measured and modelled profiles are in good agreement in terms of shape and excellent agreement in terms of magnitude.

3) Roughness Length

Tala kite and model measurements at field point 15 (point 12 on models A and B) showed the velocity profile to be almost vertical up to 240m. The lack of a velocity gradient prevents the use of the log law profile to determine the roughness length, Z_o.

The u component of turbulence intensity can be used to obtain a Z_o value using the relationship proposed by Counihan (1975)

$$\frac{u'}{\bar{U}} = \frac{1}{\text{Log}_e Z/Z_o} \quad \ldots\ldots\ldots\ldots\ldots\ldots\ldots\ldots\ldots\ldots (10.6)$$

Table 10.7 presents the resulting values of Z_o from both the field and the tunnel.

	Z (m)	$\frac{\sigma_u}{\bar{u}}$	Z_o (m)
Point 12 (Model B)	20.0	0.085	0.000155
File GP3	19.2	0.100	0.00091
File GP6	19.2	0.080	0.000074
File GP8	19.2	0.096	0.00057
File GP9	19.2	0.077	0.000044

TABLE 10.7: Roughness Length Values

There is such a large variation of roughness length suggested by the field data that this term cannot be quoted or used with any degree of confidence.

4) $\overline{\rho uw}$ Reynolds Stress Profiles

It is common practice to present the Reynolds stress profile in a non-dimensional form. For field point 1, the Reynolds stress was non-dimensionalised by dividing by the gradient velocity squared. The nature of the velocity profile at point 15 makes it impractical to fit a power law profile to the data, therefore making the calculation of the gradient height wind speed extremely difficult. Hence, the Reynolds stress profiles presented in Fig. 10.34 have been non-dimensionalised by dividing $\overline{uw}$ by rms of the mean velocity for the longitudinal and vertical

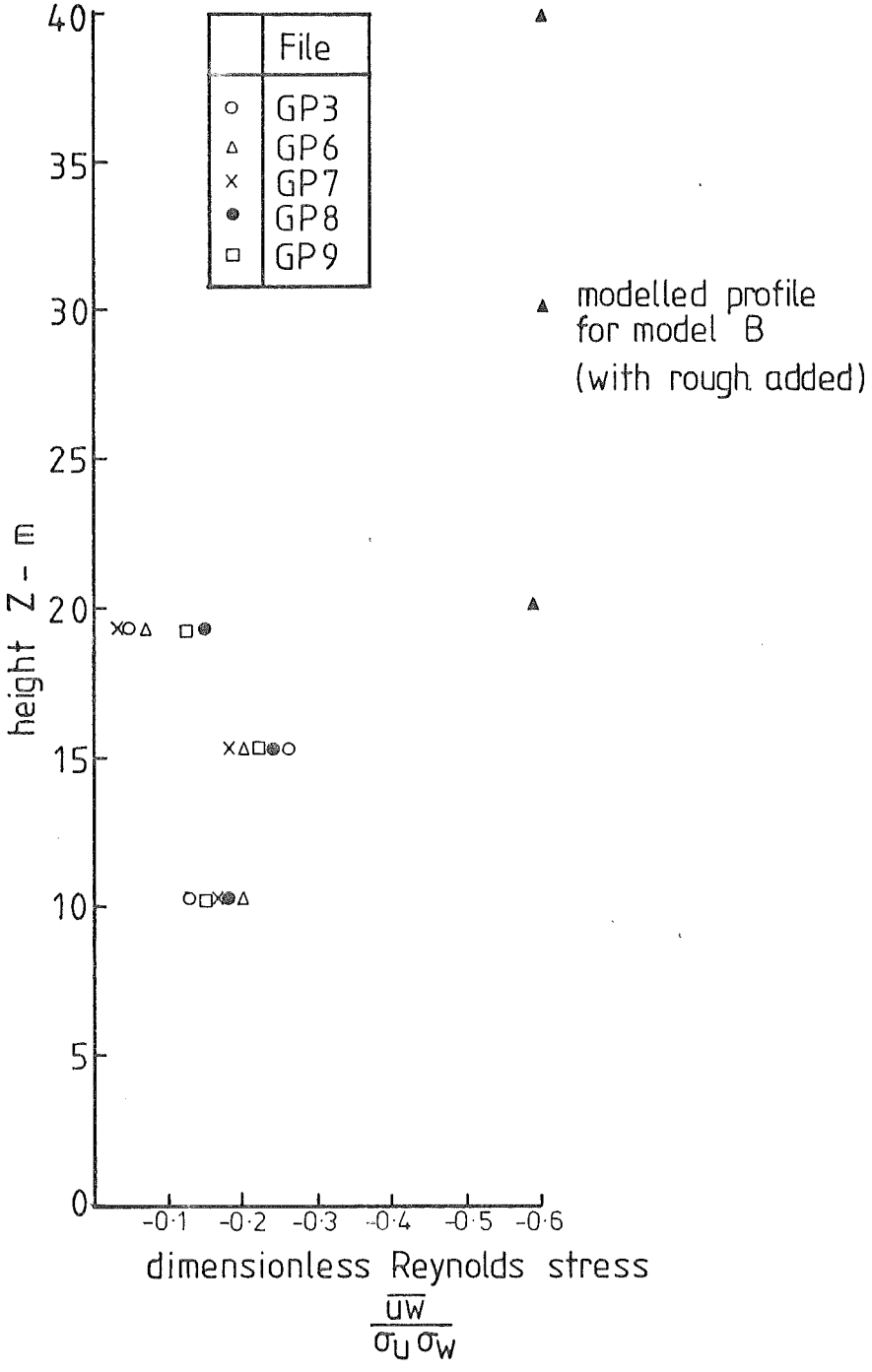

FIG. 10·34 $\rho\overline{uw}$ REYNOLDS STRESS PROFILE AT FIELD POINT 15

components, i.e., σ_u, σ_w. The measurements at the 19.2m level can be seen to fall off to about half the values at the 10.3 and 15.3m levels. This trend is consistent with the velocity profile discussed earlier; however, no major variation was apparent at this height in the turbulence intensity profile. Reynolds stress values predicted by ESDU (1974) and Counihan (1975) are dependent on knowledge of the roughness length which, in this case, cannot be determined from wind velocity measurements due to the nature of the velocity profile.

The modelled Reynolds stress is also presented for comparison, giving values much higher than those measured.

The $\rho\overline{uw}$ values recorded at point 40 on model B (with roughness added) were very close to those recorded at point 15. This is in agreement with field measurements made by Bowen (1979). He compared $\rho\overline{uw}$ values at 10m for two situations

(i) Cliff escarpment;
(ii) 2:1 slope escarpment.

Reynolds stress measurements were found not to differ significantly between the upstream site and the site on top of the escarpment.

The Gebbies Pass field measurements suggest that the $\rho\overline{uw}$ value decreases by a factor of 2 for the site on top of the saddle (field point 15).

In terms of equipment errors, the hot wire $\rho\overline{uw}$ values are far more susceptible to significant error, the major factors being

a) Misalignment to the velocity stream. Raine suggests that an alignment error of 10° can result in $\rho\overline{uw}$ errors of >70%.

b) Averaging effects. The cross probe with its centre at 5mm is effectively averaging over a prototype range of 10m - 30m.

The anemometers used on the 19.2m high array were tested in the laboratory and found to be operating correctly. Misalignment of the arrays to the flow stream are not a significant factor because the computer programmes which analyse the data have a built in correction to reduce this effect.

5) Tubulence Components

The longitudinal and vertical turbulence components are presented in

Fig. 10.35. Due to the difficulty of determining the gradient velocity the rms values have been non-dimensionalised by the velocity at 15m. From this figure the field measurement ratios at 19.2m are

				File
u' : w' =	1.82	:	1.00	GP3
	2.16	:	1.00	GP6
	2.55	:	1.00	GP7
	1.80	:	1.00	GP8
	1.88	:	1.00	GP9

From modelled results

u' : w' = 1.66 : 1.00

The field results show a large variation. File GP7 appears much higher than the other files; if this is removed and the remaining files averaged,

u' : w' = 1.90 : 1.00

This shows reasonable agreement with the modelled value and excellent agreement with Teunissen (1970) who predicts that for flat rural terrain

u' : w' = 1.92 : 1.00

6) Autocorrelations

The longitudinal component autocorrelation functions showed a high degree of similarity, the one exception being file GP3, which suggested that a trend still existed in the data. The autocorrelation curves (with GP3 omitted) showed a small change with increasing height. This effect is seen in the resulting length scale values which were based on the time for the autocorrelation coefficient to drop to $\frac{1}{e}$ (0.368).

Lateral component autocorrelation curves for files GP3, GP6 and GP7 showed that a strong trend still existed in the data, preventing their use in calculating length scales.

This factor was discussed by Flay (1978), who suggested that in some cases, the parabolic trend removal was not severe enough. The data appeared to be stationary as determined by the *Run Test* on the longitudinal component data. Flay suggested that the stationarity test should also be applied to the lateral component.

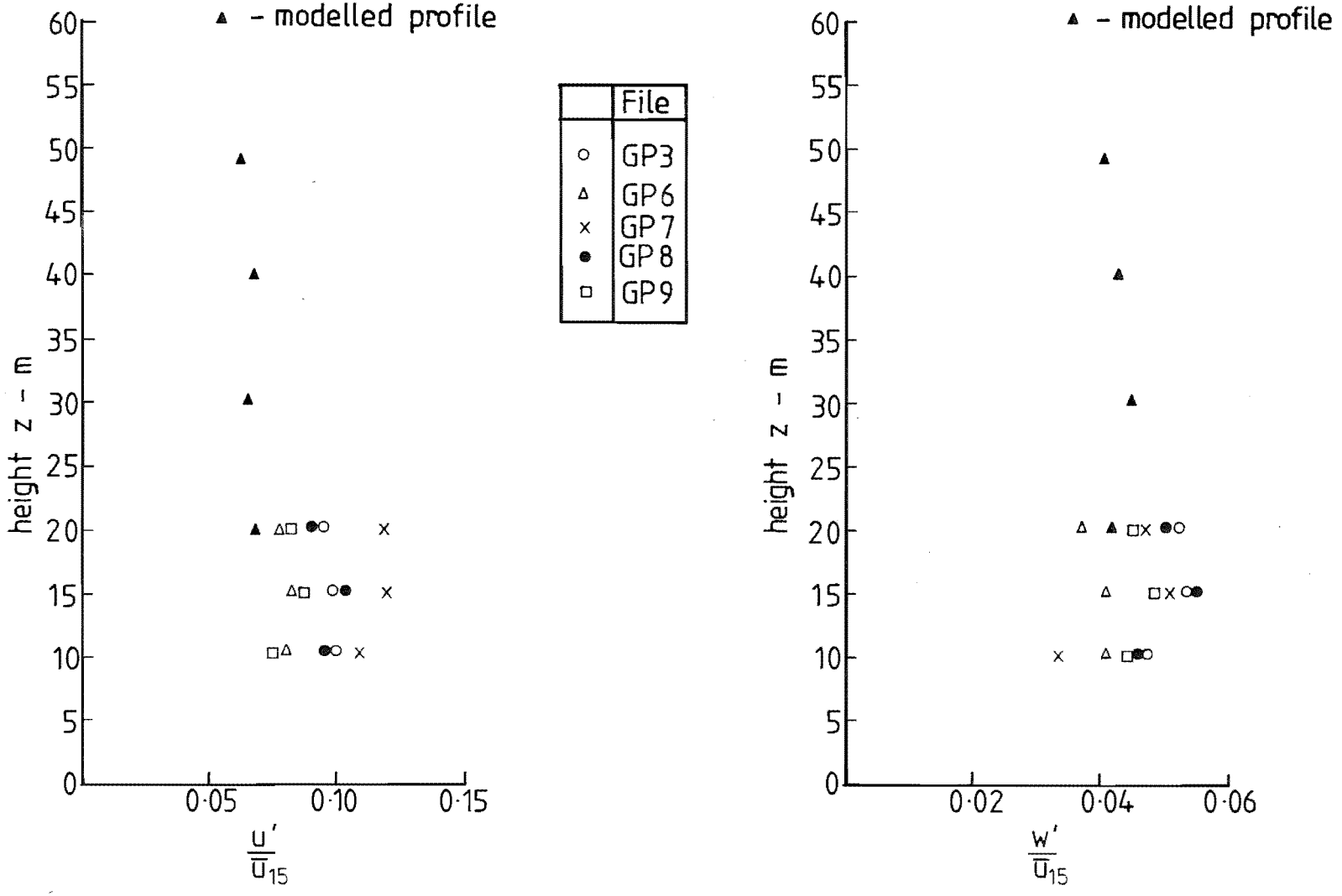

FIG. 10·35 TURBULENCE INTENSITY PROFILES

The autocorrelation curves do not suggest a definite variation with height. The resulting length scales L_{u_x} confirmed this.

The vertical component autocorrelation functions obtained from all files were very close. In all cases, the correlation fell to zero at at time lag between 10-20 seconds, and the curves were identical for all files in the region between an autocorrelation coefficient of 1 to $\frac{1}{e}$. The vertical component propeller anemometer is rather insensitive to small vertical velocity fluctuations. The major factor causing this is the flow generally being horizontal and often lying within the propellers stalled region. This problem is discussed in detail by Flay (1978), but he did not suggest any modifications to improve this situation. An obvious method of improving the response of the vertical anemometer is to mount it at, say, 45° from the vertical and use vector analysis to determine the vertical velocity component. This should result in the anemometer spending less time in its stalled region. However, Horst (1973) carried out tests comparing the results from one such arrangement with an orthogonal array, as used here, and a sonic anemometer. He concluded that, although this system was an improvement on the orthogonal arrangement, the extra computation required to handle the data made it a marginal improvement and only advantageous for the calculation of a few parameters.

7) Longitudinal Spectra

The longitudinal component of the energy spectrum for the five data files at heights of 10.3m, 15.3m and 19.2m, are presented and compared in Figs 10.36 to 10.38.

The spectra from all runs agrees very well in shape and spectral peak. The effect of the non-dimensional frequency scale, $\frac{nz}{u}$, is to collapse spectra from any height on to one curve. Comparisons between the spectra at the three measured heights show this to be the case, even in a situation where the velocity profile is almost constant.

Teunissen (1979) measured, amongst other parameters, the three components of the energy spectrum over rural terrain. He suggested a modified form of the theoretical spectra curve proposed by Kaimal *et al* (1972). The form suggested by Teunissen was

$$\frac{n\, S_u(n)}{u^{*2}} = \frac{415\, f}{(1+75\, f)^{5/3}} \qquad \ldots\ldots\ldots\ldots\ldots\ldots (10.7)$$

where all terms have their usual meanings.

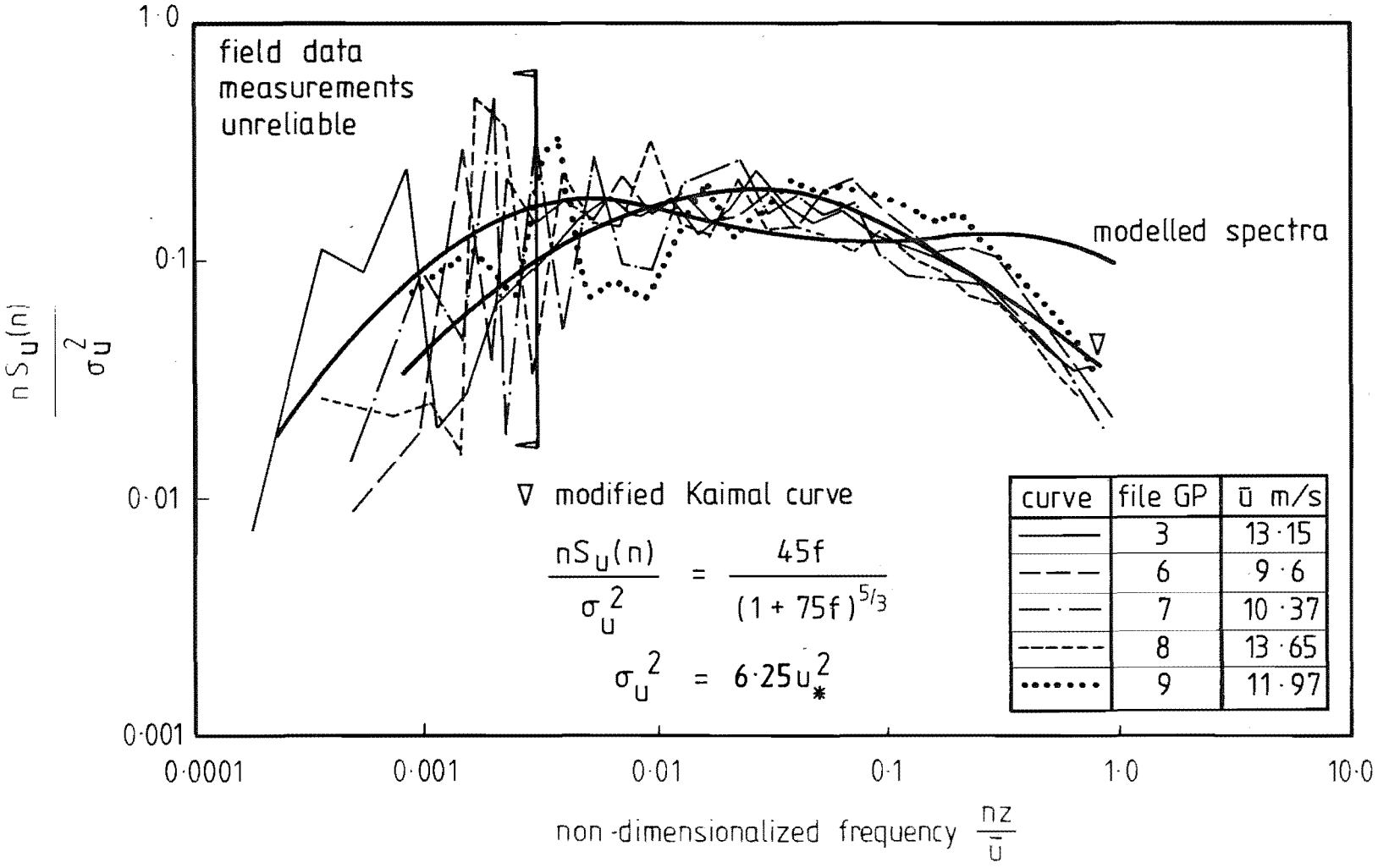

FIG 10·36 LONGITUDINAL COMPONENT OF ENERGY SPECTRA AT Z_p = 10·3m FOR FIELD Pt 15

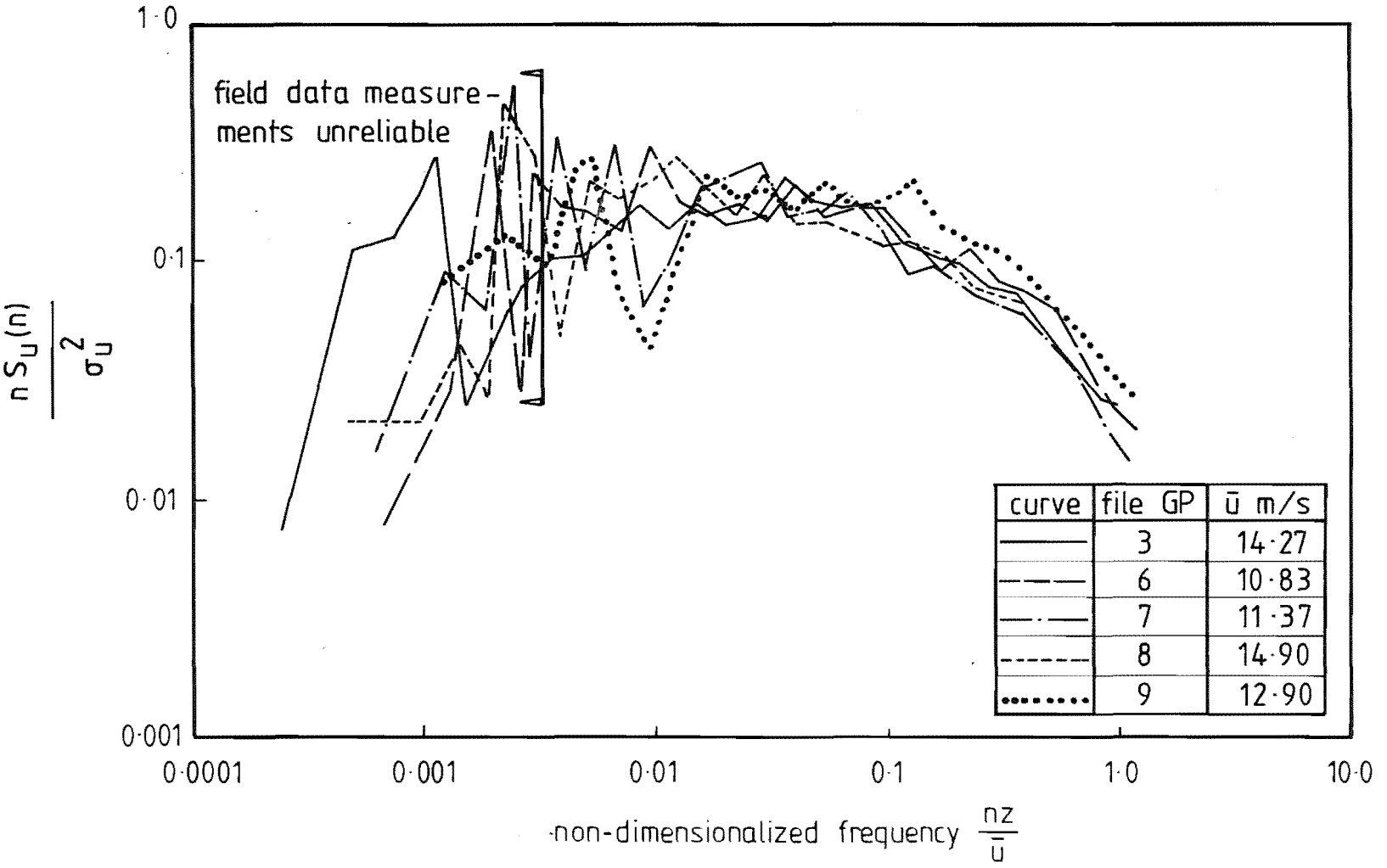

FIG 10·37 LONGITUDINAL COMPONENT OF ENERGY SPECTRA AT Z_p = 15·3m FOR FIELD Pt 15

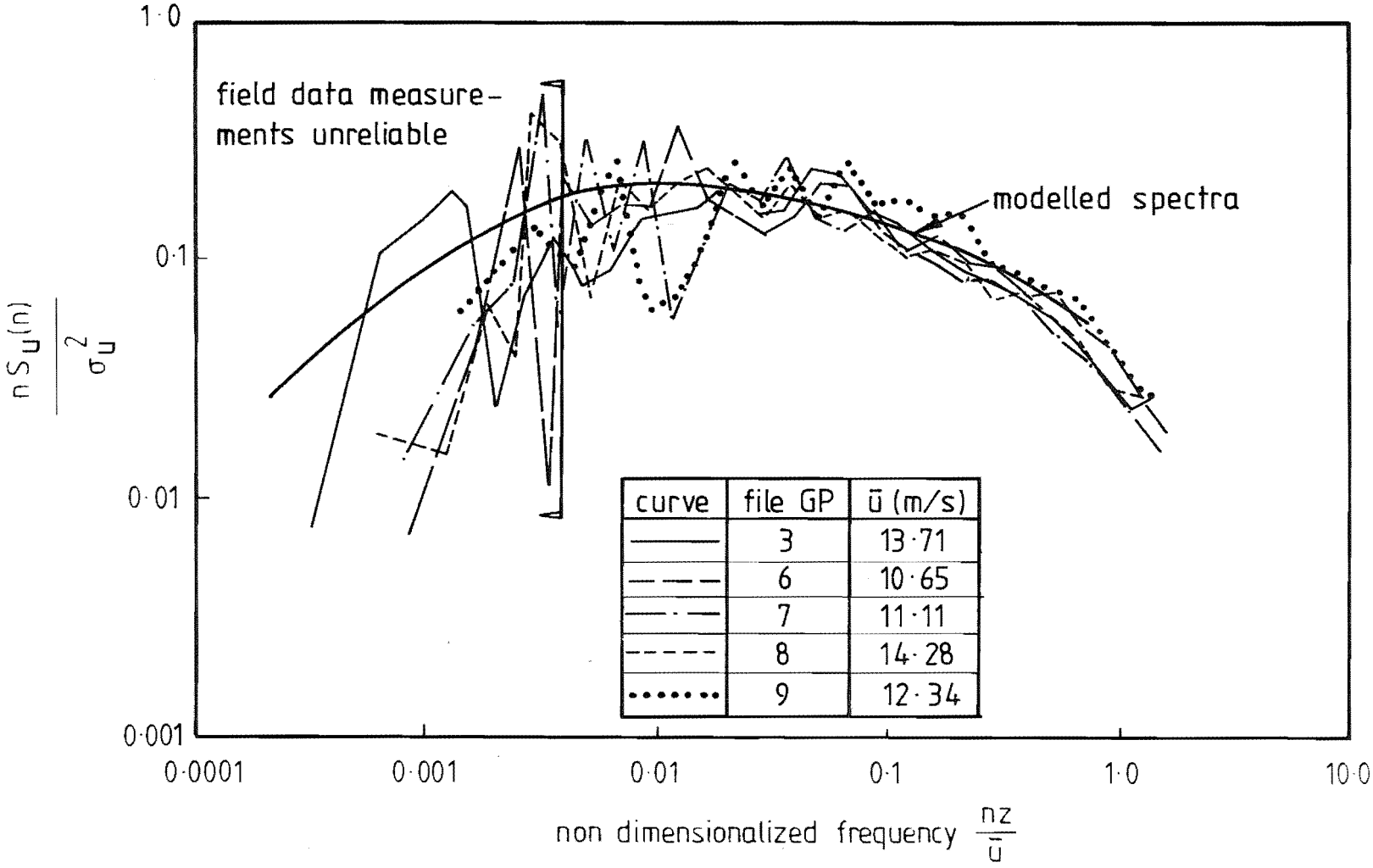

FIG 10·38 LONGITUDINAL COMPONENT OF ENERGY SPECTRA AT Z_p = 19·2m FOR FIELD Pt 15

To make the left hand side compatible with the present work, the accepted relationship between the rms and friction velocity was used,

$$\sigma_u = 2.5\, u_* \quad \ldots\ldots\ldots\ldots\ldots\ldots\ldots\ldots\ldots\ldots (10.8)$$

From this, equation 10.7 becomes

$$\frac{n\, S_u(n)}{\sigma_u^2} = \frac{66.5\, f}{(1+75\, f)^{5/3}} \quad \ldots\ldots\ldots\ldots\ldots\ldots (10.9)$$

This curve was found to be generally higher than the measured curves. A further modification was made to the constant in the numerator thus producing

$$\frac{n\, S_u(n)}{\sigma_u^2} = \frac{45\, f}{(1+75\, f)^{5/3}} \quad \ldots\ldots\ldots\ldots\ldots\ldots (10.10)$$

This modification was achieved by introducing a further scaling factor which could be considered as a terrain factor. The values used in equation (10.8) could not incorporate the rms and u_* values measured in the field because normally the friction velocity is only applicable where a log-law relationship exists. It was shown earlier that no such relationship existed on the ridge top at field point 15.

The initial spectral curve suggested by Kaimal *et al* (1972) and further modified by Teunissen (1979) was for flat homogeneous terrain. The situation at field point 15 is far from this classification, and it is possible that a terrain factor should be included in the theoretical curve. If the ratio of σ_u^2/u_*^2 is to be used, it would suggest a terrain factor of approximately 0.68, thus resulting in the following expression:

$$\frac{n\, S_u(n)}{\sigma_u^2} = \beta \frac{u_*^2}{\sigma_u^2} \frac{415\, f}{(1+75\, f)^{5/3}} \quad \ldots\ldots\ldots\ldots\ldots\ldots (10.11)$$

where β is a terrain factor.

It would be convenient to tie this factor to some parameter which can easily be measured in the field and varies directly with the terrain roughness. The roughness length would be the most obvious choice, but as shown with field point 15, local velocity increases can make this a difficult term to determine. The solution to this situation requires analysis over many more types of terrain before a general solution can be shown

to exist, if at all.

8) Lateral Spectra

The lateral spectra for heights of 10.3m, 15.3m and 19.2m are presented in Figs 10.39 to 10.41. The most significant feature of the spectra is the degree of variation exhibited by the different data files. This is explained by the trends in the lateral data, which were discussed in the sub-section on autocorrelations.

From the lateral component autocorrelations, it was concluded that data files GP8 and GP9 were not significantly affected by trends in the data. These files will be used as a basis for comparison with the modified Kaimal spectrum, as proposed by Teunissen (1979).

The accepted relationship between the lateral rms value and the friction velocity was used

$$\sigma_v = 1.875\ u_* \quad \ldots\ldots\ldots\ldots\ldots\ldots\ldots\ldots\ldots (10.12)$$

The spectral curve proposed by Teunissen (1979) is of the form

$$\frac{n\ S_v(n)}{u_*^2} = \frac{87\ f}{(1+25\ f)^{5/3}} \quad \ldots\ldots\ldots\ldots\ldots\ldots (10.13)$$

Therefore, introducing equation (10.12) and the topography factor, this becomes

$$\frac{n\ S_v(n)}{\sigma_v^2} = \beta\ \frac{u_*^2}{\sigma_v^2}\ \frac{87\ f}{(1+25\ f)^{5/3}} \quad \ldots\ldots\ldots\ldots\ldots\ldots (10.14)$$

The resulting form of the theoretical curve is

$$\frac{n\ S_v(n)}{\sigma_v^2} = \frac{0.68 \times 0.28 \times 87\ f}{(1+25\ f)^{5/3}} = \frac{17\ f}{(1+25\ f)^{5/3}} \quad \ldots\ldots (10.15)$$

This curve fits the spread of the data from all data files at all heights reasonably well. The degree of variability of the lateral spectra makes it difficult to be confident about the accuracy of the fitted curve.

9) Vertical Spectra

The vertical component of the energy spectrum is presented in Figs 10.42 to 10.44. The vertical spectra showed very little difference between the various five data files and showed no significant variation with increasing

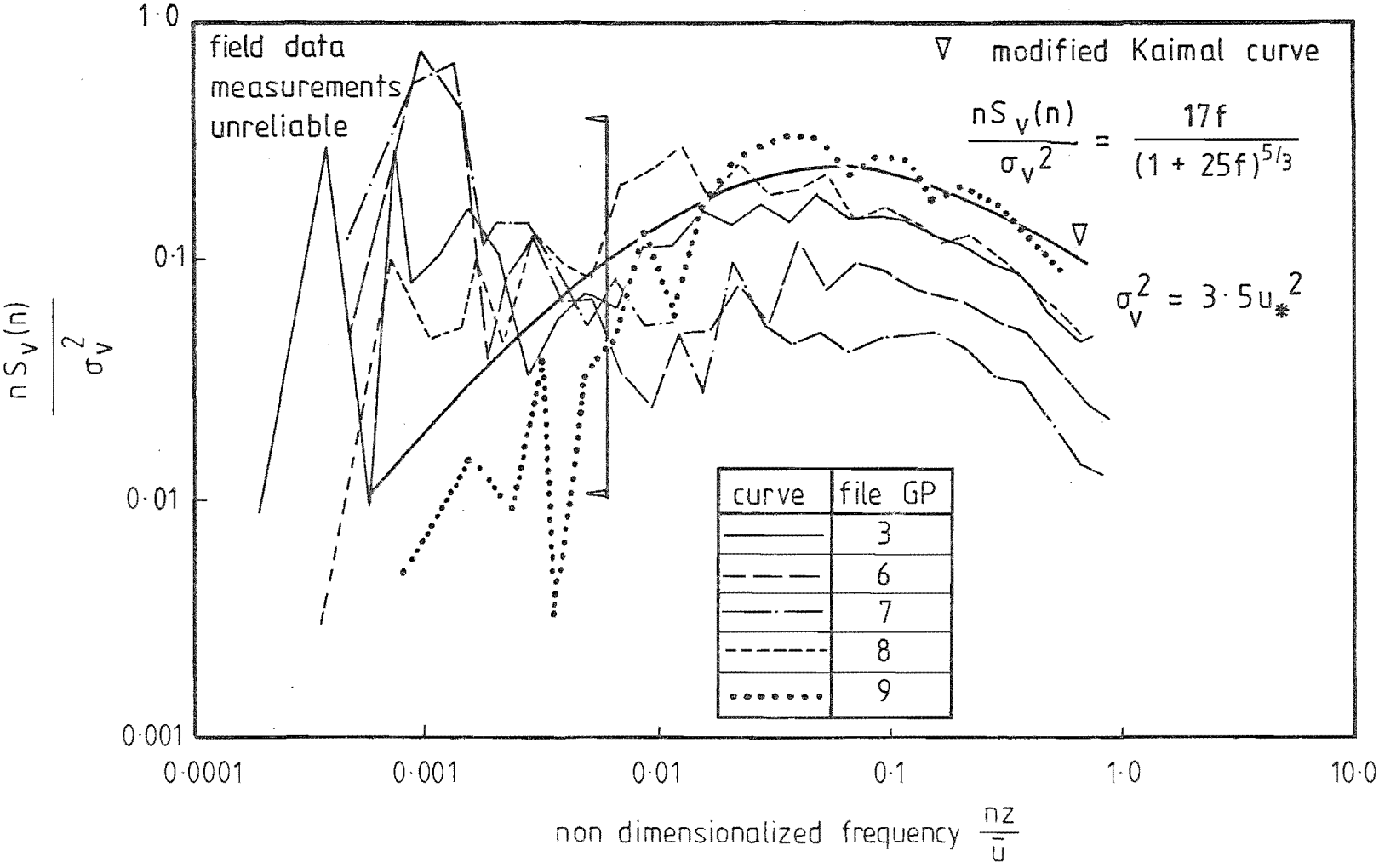

FIG 10·39 LATERAL COMPONENT OF ENERGY SPECTRA AT Z_p = 10·3m FOR FIELD Pt 15

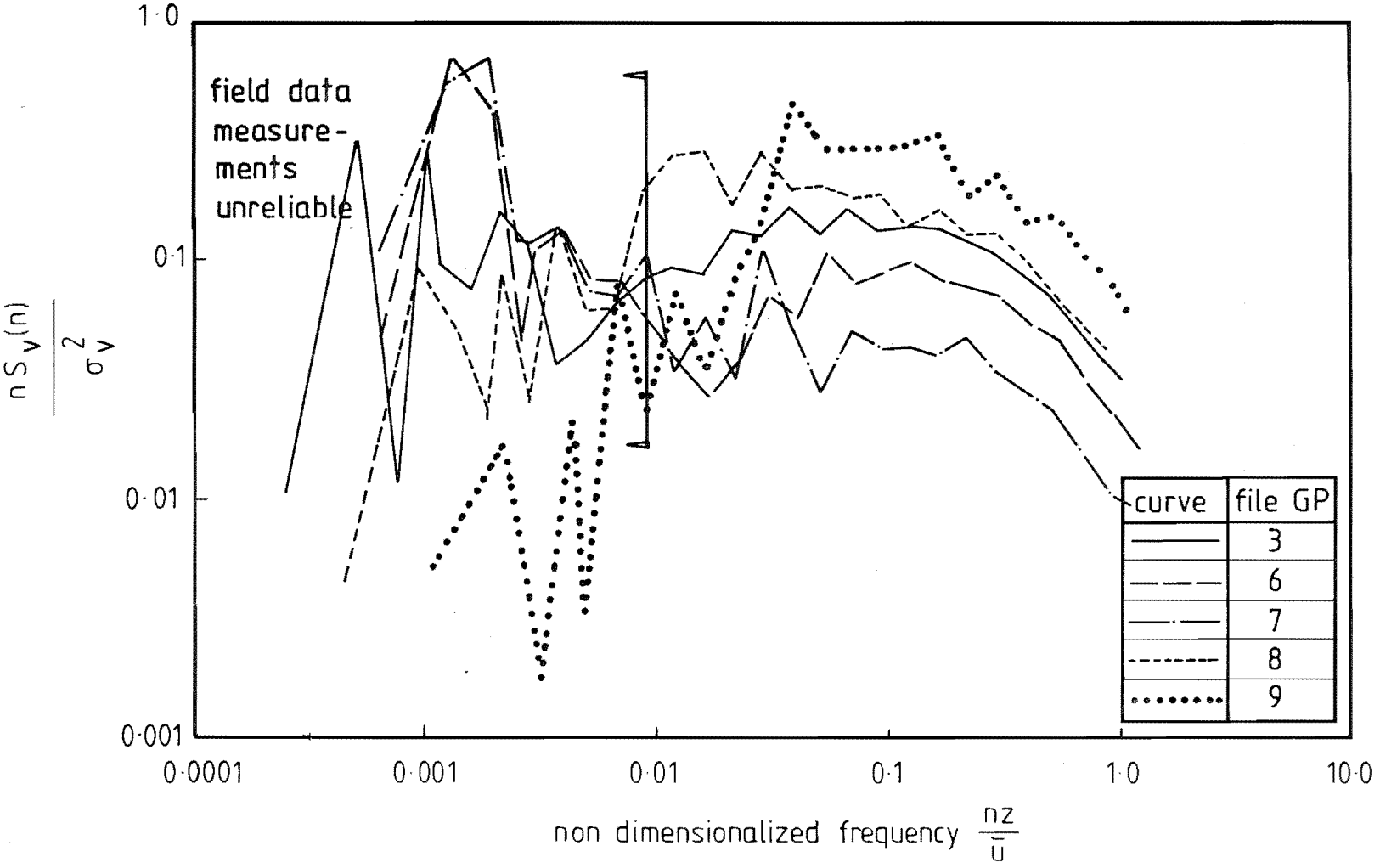

FIG 10·40 LATERAL COMPONENT OF ENERGY SPECTRA AT Z_p = 15·3m FOR FIELD Pt. 15

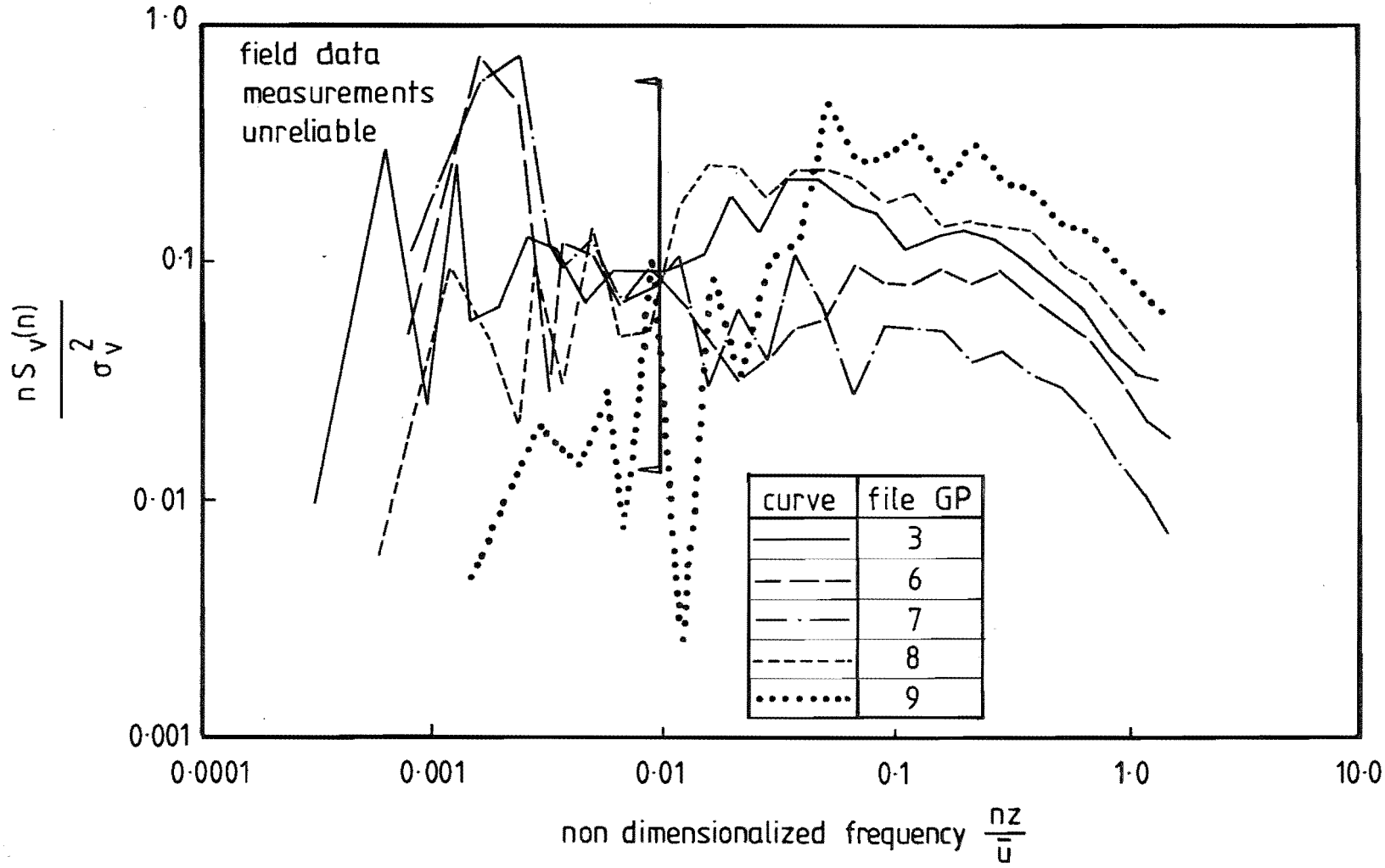

FIG 10·41 LATERAL COMPONENT OF ENERGY SPECTRA AT Z_p = 19·2m FOR FIELD Pt. 15

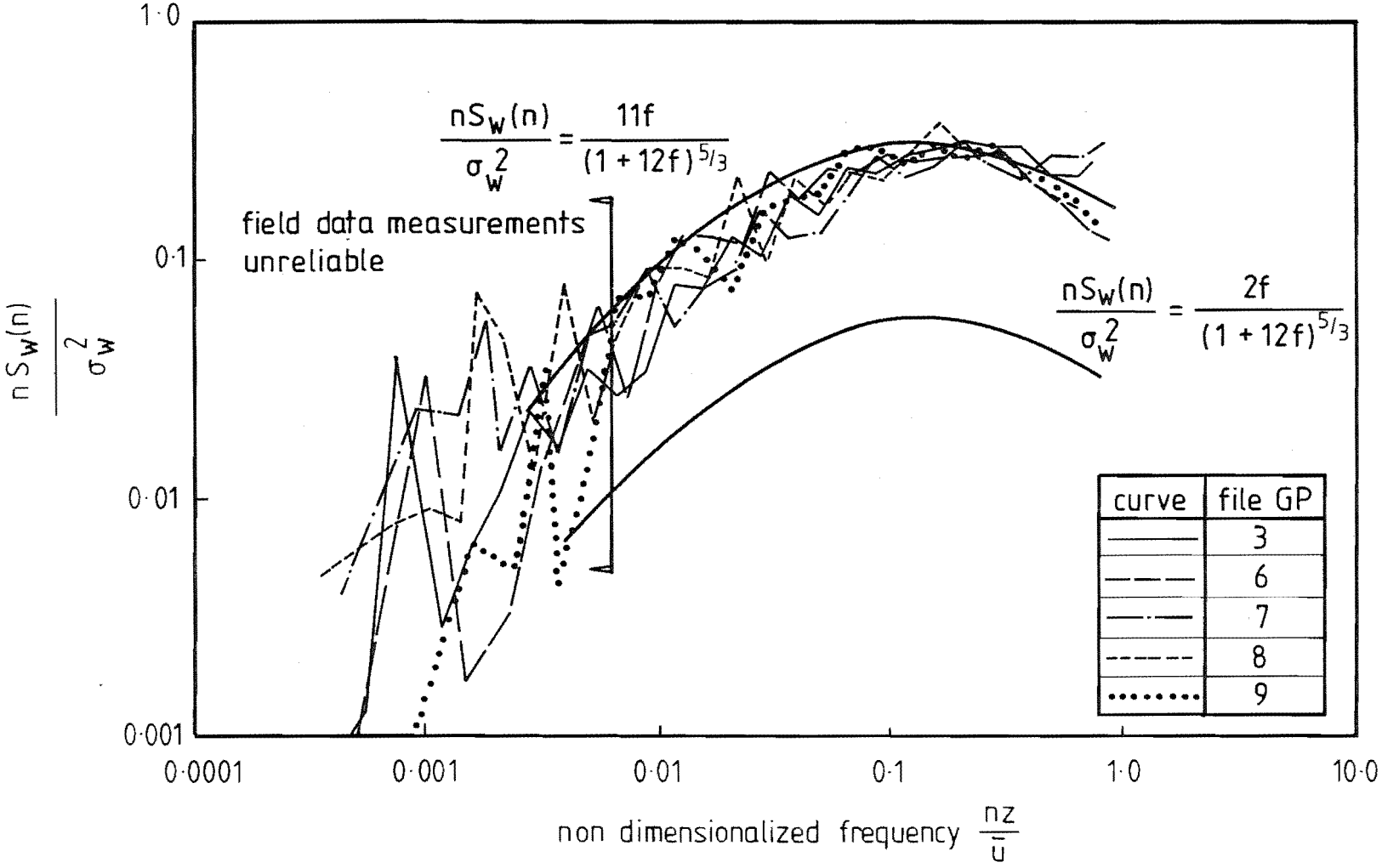

FIG 10·42 VERTICAL COMPONENT OF ENERGY SPECTRA AT Z_p = 10·3m FOR FIELD Pt 15

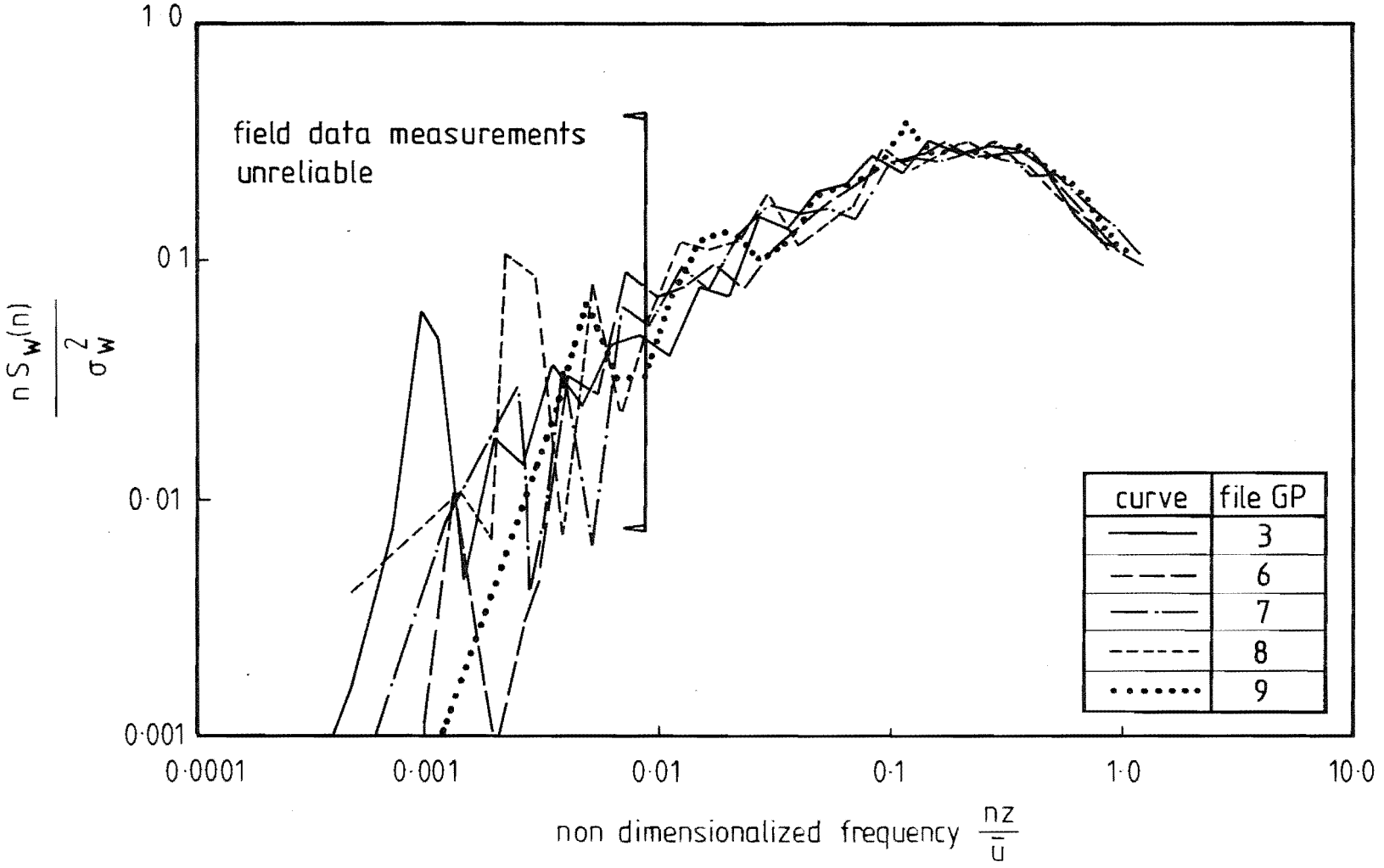

FIG 10·43 VERTICAL COMPONENT OF ENERGY SPECTRA AT Z_p = 15·3m FOR FIELD Pt 15

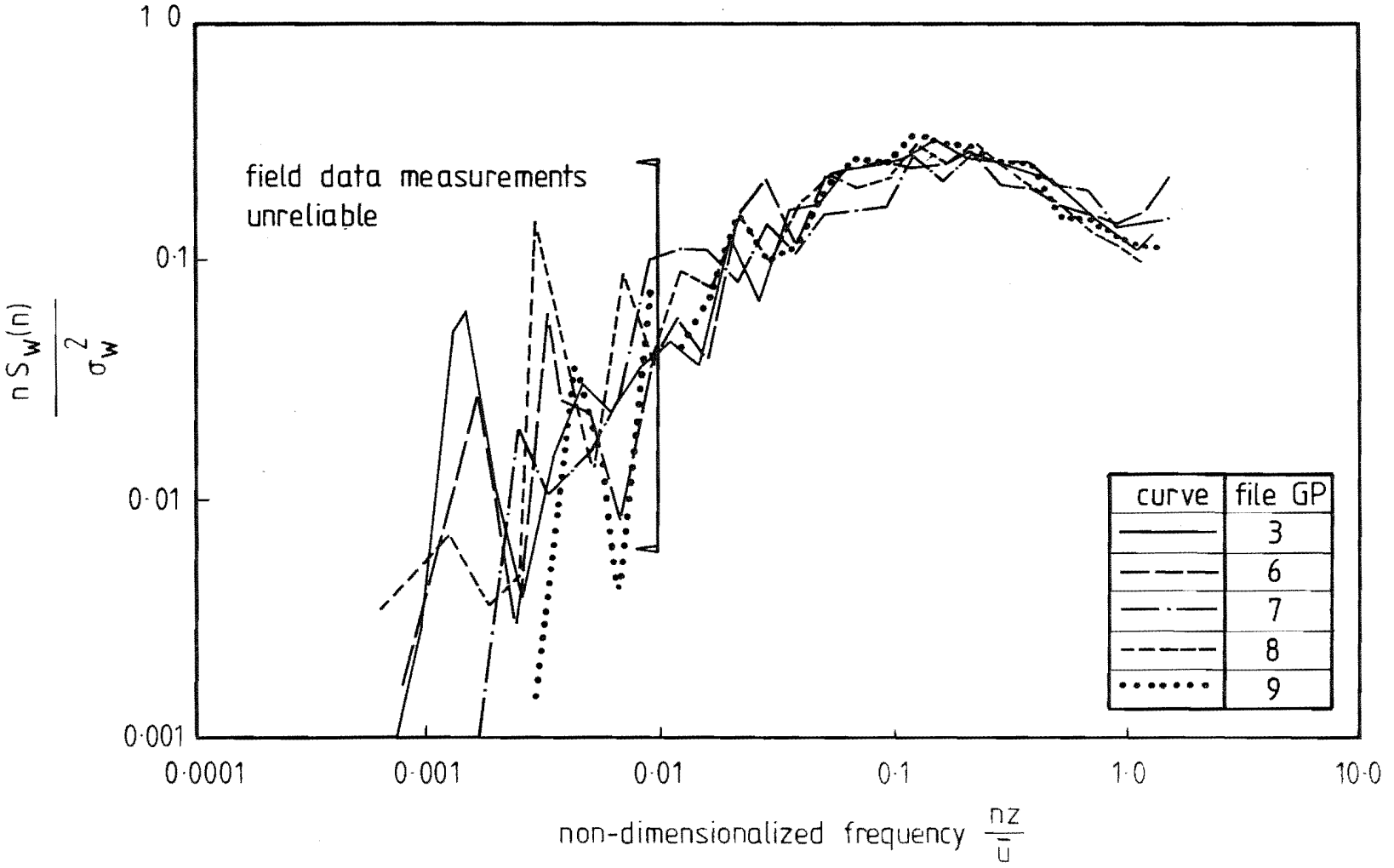

FIG 10·44 VERTICAL COMPONENT OF ENERGY SPECTRA AT Z_p = 19·2m FOR FIELD Pt. 15

height. This is to be expected because of the non-dimensionalised frequency scale. The spectral curve suggested by Teunissen (1979) is given by

$$\frac{n\,S_w(n)}{u_*^2} = \frac{4.5\,f}{(1+12\,f)^{5/3}} \quad \ldots\ldots\ldots\ldots\ldots\ldots \quad (10.16)$$

For the vertical component the accepted relationship suggests

$$\sigma_w = 1.25\,u_* \quad \ldots\ldots\ldots\ldots\ldots\ldots\ldots\ldots \quad (10.17)$$

Therefore, introducing equation (10.17) and the topography factor into equation (10.16) yields

$$\frac{n\,S_w(n)}{\sigma_w^2} = \frac{2\,f}{(1+12\,f)^{5/3}} \quad \ldots\ldots\ldots\ldots\ldots\ldots \quad (10.18)$$

This form of the spectral curve generally understimated the measured spectra; however, it did show a very similar shape to that of the measured data. Equation (10.18) was multiplied by a factor of 5.5 to produce a good match to the measured data.

The adjustments made to the Kaimal theoretical spectral curves were intended to be used to provide a comparison of shape when compared with the measured results. Other theoretical curves could have been used but the Kaimal curves were chosen because Teunissen (1979) found these to have a favourable shape and to be particularly suited to applying scale adjustments. Care must be taken in commenting on the position of the relative curves because the modified curve is no longer normalised to make the area unity. Therefore, the only valid comments are those restricted to a comparison of the shape of the various curves.

10) Length Scales

Length scales predicted by ESDU (1974) and Counihan (1975) require a knowledge of the roughness length Z_o. This parameter has been discussed and shown not to be reliable for the point 15 site. Therefore, comparisons of length scales will be limited to the values presented in Table 10.8.

All length scales calculated from autocorrelation curves are based on the time taken for the autocorrelation coefficient to drop to a value of e^{-1}. This is converted to a length scale using Taylor's hypothesis

$$L_{i_x} = \bar{u} \times T_{e^{-1}} \quad \ldots\ldots\ldots\ldots\ldots\ldots\ldots \quad (10.19)$$

Length scales calculated from spectra use the following relationship

$$L_{u_x} = \frac{0.146}{k_p} \quad \ldots\ldots\ldots\ldots\ldots\ldots\ldots\ldots \quad (10.20)$$

$$L_{v_x} = \frac{0.106}{k_p} \quad \ldots\ldots\ldots\ldots\ldots\ldots\ldots\ldots \quad (10.21)$$

$$L_{w_x} = \frac{0.106}{k_p} \quad \ldots\ldots\ldots\ldots\ldots\ldots\ldots\ldots \quad (10.22)$$

where k_p is the wave number at the spectral peak.

Model B (rough added)	Field File GP	L_{u_x}		L_{v_x}		L_{w_x}	
		Spectra	Auto	Spectra	Auto	Spectra	Auto
12	-	400	335	-	-	-	-
-	3	190	*	40	*	13	20
-	6	280	200	17	*	14	25
-	7	160	210	50	*	10	20
-	8	175	190	55	75	14	26
-	9	140	130	20	35	12	23

All field measurements at 19.2m
Tunnel measurement at Z_p = 20m
* Data exhibited a strong trend.

TABLE 10.8: u, v, w Component Length Scales.

In the absence of other sources of length scales for hill sites, the comparisons are limited to the data in Table 10.8. The longitudinal length scales calculated from the spectral peak and autocorrelation curves are in good agreement. The model suggests a generally higher value of length scale than those measured at field point 15. This is possibly the result of less surface roughness on the model than on the prototype. The model can only be as accurate as the maps from which it was constructed and therefore features less than 75m high were not added unless the author had noted them as being particularly significant. It is suggested that it is this limitation that is causing the difference between the modelled and measured length scales.

The lateral length scales are very limited by the high degree of trend evident in the data. The vertical length scales show very good agreement.

This can reasonably be expected since the flow being accelerated over field point 15 will tend to stretch the turbulence, therefore increasing the longitudinal and reducing the vertical - and probably lateral - length scales.

10.4 CONCLUSIONS

The one-day field data was shown to correlate extremely well, this being the case for data collected over a period of days or data collected months apart.

The TALA kite was shown to be an extremely valuable tool for wind studies. It was considered that in reasonably steady conditions, it could be read to ±0.5 m/s. However, it provided velocity profiles up to 240m which were invaluable in establishing the correct wind tunnel simulation of this parameter. One of the major advantages of this equipment was the speed and ease of measurement; however, knowledge of the standard deviation would have been very useful.

Measurements made with the Department's instrumented 20m tower provided a comparison between the model simulation, theoretical predictions and measured data. The parameters measured included $\rho\overline{uw}$ Reynolds stress, turbulence intensity values, integral length scales and the u,v and w components of energy spectra. These parameters, with the exception of the v and w component spectra, were shown to have been modelled in the wind tunnel to a satisfactory degree in establishing the approach flow characteristics for the study.

The tower was sited at field point 15, which is on top of the Gebbies Pass saddle in a very exposed position. The velocities measured showed an increase up to the 15m height and decreased to the 20m height. This could have been the result of the development of an internal boundary layer. Before this could be established with any certainty, measurements would be required above this height and to a greater level of accuracy than provided by the TALA kite.

The $\rho\overline{uw}$ Reynolds stress profiles measured at field point 15 were shown to be significantly smaller than those recorded on the model. This situation was probably caused by the response characteristcs of the vertical anemometer, combined with alignment errors in the modelled values, described in Section10.3.2.

Strong trends were apparent in the lateral component data; this restricted the use of this data and limited the confidence with which it could be applied particulary in the lateral component spectra and integral length scales L_{v_x}.

As suggested by Flay (1978), the lateral component of the data should have a trend removal applied. In the GP3 data file, the parabolic trend removal was not severe enough to remove the trend suggesting that a higher order trend removal should be used. It was noted however, that great care should be taken in the removal of trends because, at some stage, the results become representative of the trend removal rather than the original data.

A modified form of the Kaimal *et al* (1972) theoretical spectral curves was presented which also introduced a topography factor. However, even without this factor, which raised or lowered the whole spectrum, the measured spectra fitted the theoretical spectra extremely well.

CHAPTER 11

STATISTICAL ANALYSIS

This Chapter presents the statistical analysis of the field and model data. Correlations and null hypothesis tests will be used to show the relationship between the field and model data.

If physical modelling is to be a useful means of predicting wind speed and therefore wind power, there should be a high linear causal relationship between measurements in the laboratory and field.

11.1 STATISTICAL THEORY

The starting point in all statistical tests is the statement of one or more hypotheses. The type of hypothesis used is called the null hypothesis. Such an hypothesis is a statement of no difference which can be made at any level of confidence. The level of confidence, known as the alpha (α) level, is selected by the researcher in advance of the test. Care has to be exercised in selecting the alpha level because it can, if set too high, generate its own errors.

If the null hypothesis is rejected at the 5% level, there are 5 chances in 100 that the rejection was wrong and that the null hypothesis was, in fact, true. This is known as a type I error. Errors of this type may be reduced by making a more rigorous test such as putting the alpha value at the 1% level. Then there would be only 1 chance in 100 of being wrong. However, as the chances of making a type I error are reduced so the chances of making a type II error are increased. This error consists of *not* rejecting the null hypothesis when it should be rejected. Generally, in statistical analysis the possibility of making a type I error is reduced by adopting a relatively high confidence level.

In this study α values of 5% and 2% will be used throughout. These levels are considered satisfactory by Meroney *et al* (1978), and Holmes, Walker and Steen (1979) used an alpha of 10% in comparisons between field and model for flow over an isolated hill.

Where two variables are involved, say x and y, the sample correlation coefficient r between a set (x,y) is calculated using the relationship

$$r = \frac{n\Sigma xy - \Sigma x \Sigma y}{\left[[n\Sigma x^2 - (\Sigma x)^2] \, [n\Sigma y^2 - (\Sigma y)^2] \right]^{\frac{1}{2}}} \qquad \ldots\ldots\ldots\ldots\ldots\ldots \quad (11.1)$$

where n is the total number of data pairs used.

The correlation coefficient always lies between -1 and +1. If, and only if, all points lie on the regression line, then $r = \pm 1$. If $r = 0$, the regression does not explain anything about the variation of y and the regression line is horizontal.

The equation of the sample regression line of y on x is

$$y' = a_o + b_o x \quad \ldots\ldots\ldots\ldots\ldots\ldots\ldots\ldots\ldots\ldots \quad (11.2)$$

The prime (y') distinguishes a predicted value from an observed value. The regression coefficient, the slope of the regression line, is given by

$$b_o = \frac{\Sigma(x-\bar{x})(y-\bar{y})}{\Sigma(x-\bar{x})^2}$$

$$= \frac{n\Sigma xy - \Sigma x \Sigma y}{n\Sigma x^2 - (\Sigma x)^2} \quad \ldots\ldots\ldots\ldots\ldots\ldots\ldots\ldots\ldots \quad (11.3)$$

and the y intercept is

$$a_o = \frac{\Sigma y - b_o \Sigma x}{n} \quad \ldots\ldots\ldots\ldots\ldots\ldots\ldots\ldots\ldots \quad (11.4)$$

Where observations of x also involve measurement error in addition to inherent variability, it is also useful to construct the equation of the sample regression line for x on y

$$x' = a_1 + b_1 y \quad \ldots\ldots\ldots\ldots\ldots\ldots\ldots\ldots\ldots\ldots \quad (11.5)$$

The relationships for the regression coefficient and the intercept become

$$b_1 = \frac{n\Sigma xy - x\Sigma y}{n\Sigma y^2 - (\Sigma y)^2} \quad \ldots\ldots\ldots\ldots\ldots\ldots\ldots\ldots\ldots \quad (11.6)$$

$$a_1 = \frac{\Sigma x - b_1 \Sigma y}{n} \quad \ldots\ldots\ldots\ldots\ldots\ldots\ldots\ldots\ldots \quad (11.7)$$

The scatter, in the vertical direction, of the observed points about the regression line is measured by $s_{y/x}$ where

$$s_{y/x}^2 = \frac{n-1}{n-2}\left[s_y^2 - b^2 s_x^2\right] \quad \ldots\ldots\ldots\ldots\ldots\ldots\ldots \quad (11.8)$$

The quantity $s^2_{y/x}$ estimates that part of the variance of y left unexplained by the regression of y on x. It is defined with n-2 in the denominator rather than n-1 because two degrees of freedom are absorbed by the estimates a_o and b_o.

The standard error of the regression coefficient is denoted by s_b which is determined by the expression

$$s_b = \frac{s_{y/x}}{s_x\sqrt{n-1}} \quad \ldots\ldots\ldots\ldots\ldots\ldots\ldots\ldots\ldots\ldots \quad (11.9)$$

Knowledge of this term allows a null hypothesis test about the regression coefficient. To test the null hypothesis that the slope of the regression line has a value of 1.0, i.e., perfect correlation exists, the relationship

$$t = \frac{b - B}{s_b} \quad \ldots\ldots\ldots\ldots\ldots\ldots\ldots\ldots\ldots\ldots \quad (11.10)$$

is used where B = 1.0.

The null hypothesis can be rejected at a significance level α if $|t|$ exceeds the critical value $t_{\alpha/2,\ n-2}$ found in the students t distribution tables.

If wind tunnel modelling of complex terrain is to be a useful tool for WECS site selection, it must provide accurate predictions of wind speeds at any site.

The individual value of y corresponding to a given x=X for a $100(1-\alpha)\%$ prediction interval for y is given by

$$y' \pm t_{\alpha/2,\ n-2}\, s_{y/x} \sqrt{1 + \frac{1}{n} + \frac{(X-\bar{x})^2}{(n-1)s_x^2}} \quad \ldots\ldots\ldots \quad (11.11)$$

11.2 CORRELATIONS BETWEEN FIELD DAYS

The fifteen possible correlation combinations resulting from six separate field days were presented in Table 10.4.

The resulting correlation coefficients ranged from 0.62 to 0.97, the average of 0.85 was considered most encouraging and suggests that data collected on any of the field days can be used confidently for comparison with modelled results. The lowest value, 0.62, occurred for data pairs from 11/12/78 and 16/5/79. Of the thirteen data pairs

Field Point	Velocity Ratios					
	December			May		August
	11th	13th	14th	16th	17th	9th
1*	-	-	-	-	-	-
2						
3	0.93		0.91	0.85	0.97	0.79
4		1.00	0.87			0.94
5		0.96	0.89	0.98	0.86	0.86
6	0.73			0.99		
7	1.06	0.87	0.96	0.86	0.89	0.77
8	1.09			1.38		
9	0.93			1.25		
10		0.88	0.87	0.71	1.00	1.00
11			1.19	1.25	1.09	
12			1.29	1.65		
13			1.44	1.70	1.60	
14	1.54			1.36	1.18	
15	1.46	1.61	1.55	1.90	1.43	1.48
16		1.58	1.32			
17			1.10	1.20	1.13	
18			1.28	1.65	1.92	
19			1.16	1.22		
20	0.82	0.65	0.76	0.65	0.64	0.86
21	1.55			1.49		
22	1.50			1.25		1.28
23						
24	1.13			1.67	1.36	
25			1.72	1.51		
26			1.00	1.11		
27		1.04	0.71	0.91		0.61
28	1.32			1.26		
29	1.13		0.80	0.72	0.75	
30	1.70				1.59	

* Field point 1 is the Reference Tower

TABLE 11.1: Velocity ratios for points measured on several field days.

four showed very large discrepancies, but with these removed, the correlation improved to 0.80. There is very limited field data of this type available for comparison. The values of the correlation coefficients obtained during this study are generally much higher than those of Meroney *et al* (1978), who found a correlation of 0.68 between two field days.

The velocity ratios for points measured on several occasions are presented in Table 11.1. Field points 3, 5 and 7, which are situated on flat terrain approaching the Gebbies Pass saddle, see Fig. 6.5, show a high level of repeatability.

More interesting are the values for field point 15, which is located on top of a hill on the Gebbies Pass saddle and measured on all field days. Apart from the particularly high value obtained on 16/5/79 which cannot readily be explained, the remaining ratios are in good agreement.

Field point 20 is on the leeward side of the Gebbies Pass saddle and was measured on all field days. The resulting velocity ratios are in excellent agreement.

11.3 CORRELATIONS BETWEEN FIELD AND WIND TUNNEL MODEL

The points common to both the field and model will be correlated and compared statistically in this section. All measurements will be compared for a height of Z_p = 10m.

11.3.1 Field Data vs Model A

The results of the correlation analysis for model A are presented in Table 11.2.

No. of Data Pairs n	Field Data Date	Correlation Coefficients		
		Terraced	Contoured	Roughness Added
11	11/12/78	-0.16	0.37	0.51
10*	11/12/78	-	0.61 *	0.73 *
9	16/5/79	0.12	0.82	0.80
5	17/5/79	0.25	0.94	0.91

* Correlation with field point 23 removed

TABLE 11.2: Correlations between field and Model A

Generally, the terraced model does not correlate favourable with the field data. The contoured and roughness added models produce correlations that are very close to each other and are generally high, $r > 0.80$. The correlations for data collected on 11/12/79 were very low for all forms of model construction. The sites measured on 11/12/78 included field point 23, see Fig.6.5, which is situated on the top of a ridge on the leeward side of the Port Hills range. On the one-day data collection trips, speed was an important factor; the time and effort required in reaching field point 23 in poor weather conditions precluded its inclusion in other field days. It follows that this point could not be included in the correlations between the various field days. These features, position and single measurement, make the result for this point suspect. It was therefore considered justifiable to remove this point from the correlation calculations. This was seen to have a significant effect and increased the correlation coefficient for the contoured model by 60% and for the roughness added model by 42%. The results of correlations using data collected on three field days and model A in the various forms of construction are presented in Table 11.3. Regression lines for y on x (field on tunnel) and x on y have been calculated. The (1) subscript refers to the result when y is the dependent variable and the (2) subscript is for x as the dependent variable. The Table also contains the results of several null hypothesis tests;

1) That the true correlation coefficient is zero at the 5% significance level.
2) That the true regression coefficient is 1.0 at the 2% significance level.
3) The variance values for the variables.
4) The standard error of estimate.
5) The standard error of regression.

The results showed that in all cases, the null hypothesis test that $r = 0$ could be rejected for the contoured and roughness added models. It is interesting to note that the inclusion of the data for field point 23 changes the result of this null hypothesis test.

The terraced model shows variability in the null hypothesis test that the true regression coefficient is 1.0. However, the contoured and roughness added models show that this hypothesis cannot be rejected in all cases.

The resulting scatter diagrams for the roughness added model vs field

Data Correlated		n	a_1	b_1	r	$r_{critical}$ @ 5%	Reject r=0 95% Conf.	s_x^2	s_y^2	$(s_{x/y})^2$	s_{b_1}	$\|t\|_1$	s_{b_2}	$\|t\|_2$	$t_{0.01}$ n-2	Reject with 98% Conf.	
Field Day	Model A															$B_1=1.0$	$B_2=1.0$
11.12.78	Terraced	11	1.450	-0.193	-0.168	0.602	No	0.062	0.082	0.298	0.378	3.15	0.286	4.00	2.82	Yes	Yes
	Contoured	11	0.848	0.361	0.376 0.610*	0.602	No Yes*	0.089	0.082	0.280	0.296	2.15	0.322	1.88	2.82	No	No
	Rough.added	11	0.687	0.473	0.513 0.732*	0.062	No Yes*	0.097	0.082	0.260	0.263	2.00	0.311	1.42	2.82	No	No
16.5.78	Terraced	9	1.135	0.206	0.124	0.666	No	0.047	0.131	0.384	0.621	1.27	0.226	4.08	3.00	No	Yes
	Contoured	9	0.141	0.943	0.823	0.666	Yes	0.100	0.131	0.220	0.246	0.23	0.187	1.50	3.00	No	No
	Rough.added	9	0.167	0.883	0.802	0.666	Yes	0.108	0.131	0.231	0.249	0.47	0.205	1.32	3.00	No	No
17.5.79	Terraced	5	0.771	0.420	0.252	0.878	No	0.028	0.078	0.313	0.929	0.62	0.335	2.52	4.54	No	No
	Contoured	5	0.314	0.716	0.940	0.878	Yes	0.135	0.078	0.110	0.151	1.88	0.259	0.89	4.54	No	No
	Rough.added	5	0.281	0.692	0.915	0.878	Yes	0.140	0.078	0.130	0.175	1.76	0.307	0.68	4.54	No	No

Subscript (1) - refers to value when field data is the dependent variable
Subscript (2) - refers to value when model result is the dependent variable
* - result with field point 23 data removed

TABLE 11.3: Values of Statistical Parameters for Field Data and Model A

data are presented in Figs 11.1 to 11.3.

11.3.2 Field Data vs model B

Model B has the largest number of points common to both the field and the model. The resulting correlation coefficients are presented in Table 11.4.

The high correlation coefficients obtained for 13/12/78 can be explained in terms of the location of the points used.

No. of Data Pairs n	Field Data Date	Correlation Coefficients		
		Terraced	Contoured	Roughness Added
11	11/12/78	-0.13	0.75	0.53
10	11/12/78	-	-	0.73*
6	13/12/78	0.89	0.98	0.97
8	14/12/78	0.71	-	-
10	14/12/78	-	0.87	0.90
11	16/5/79	0.37	0.72	0.73
9	17/5/79	0.25	-	-
10	17/5/79	-	0.87	0.71
8	9/8/79	0.49	0.90	0.88

* Correlation with field point 23 removed.

TABLE 11.4: Correlations between field and Model B

Of the six data points used, four were located on the flat approach terrain which is not affected by the form of construction. However, the remaining two points have a significant effect on the correlation value when a comparison between the terraced and other forms of construction is considered.

The results of the statistical analysis for the field data vs model B are presented in Table 11.5. The omission of data for field point 23 was again seen to be significant and made the difference between rejecting and accepting the null hypothesis that the true value of the correlation coefficient is zero.

The results suggest that the terraced model is not representative of the field situation. Generally, the contoured and roughness added models

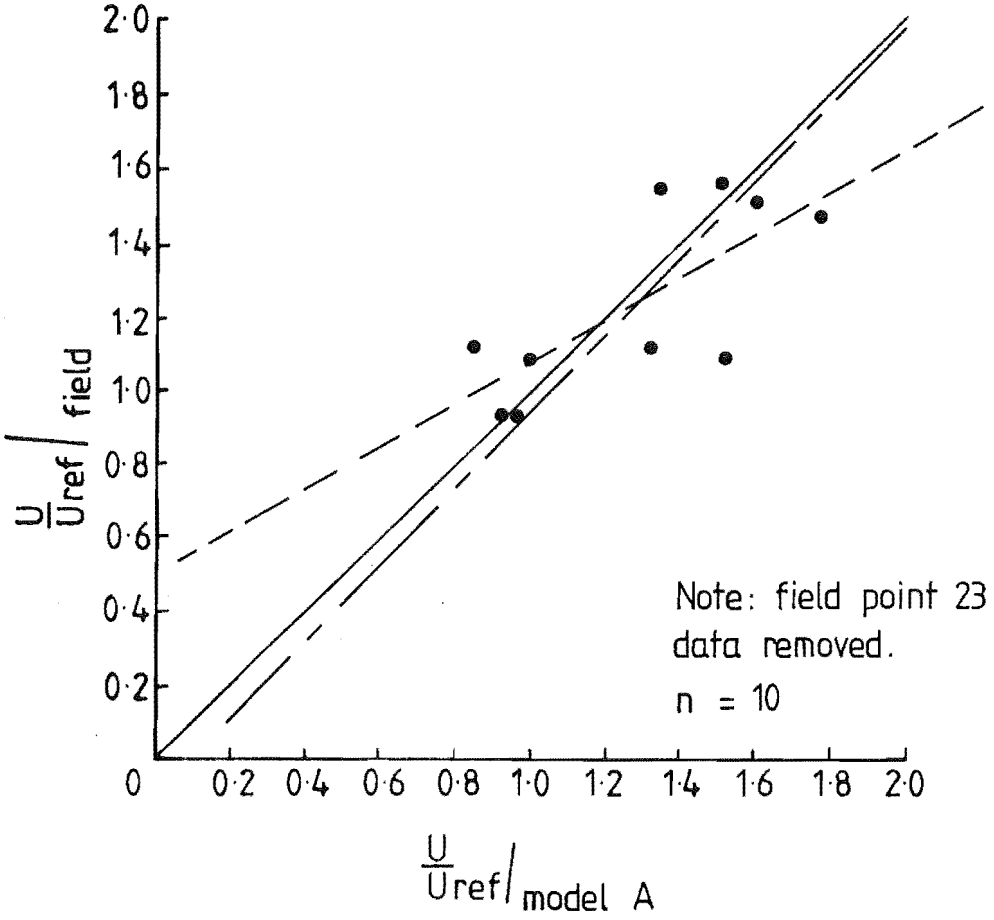

Regression lines

$$\frac{U}{U_{ref}}\Big|_{field} = 0 \cdot 56 \; \frac{U}{U_{ref}}\Big|_{model\ A} + 0 \cdot 51$$

$$\frac{U}{U_{ref}}\Big|_{model\ A} = 0 \cdot 95 \; \frac{U}{U_{ref}}\Big|_{field} + 0 \cdot 10$$

Correlation coefficient $r = 0 \cdot 73$

FIG. 11 · 1 SCATTER DIAGRAM FOR FIELD DATA COLLECTED ON 11/12/78 AND MODEL A IN THE ROUGHNESS ADDED FORM OF CONSTRUCTION. Z_p = 10m

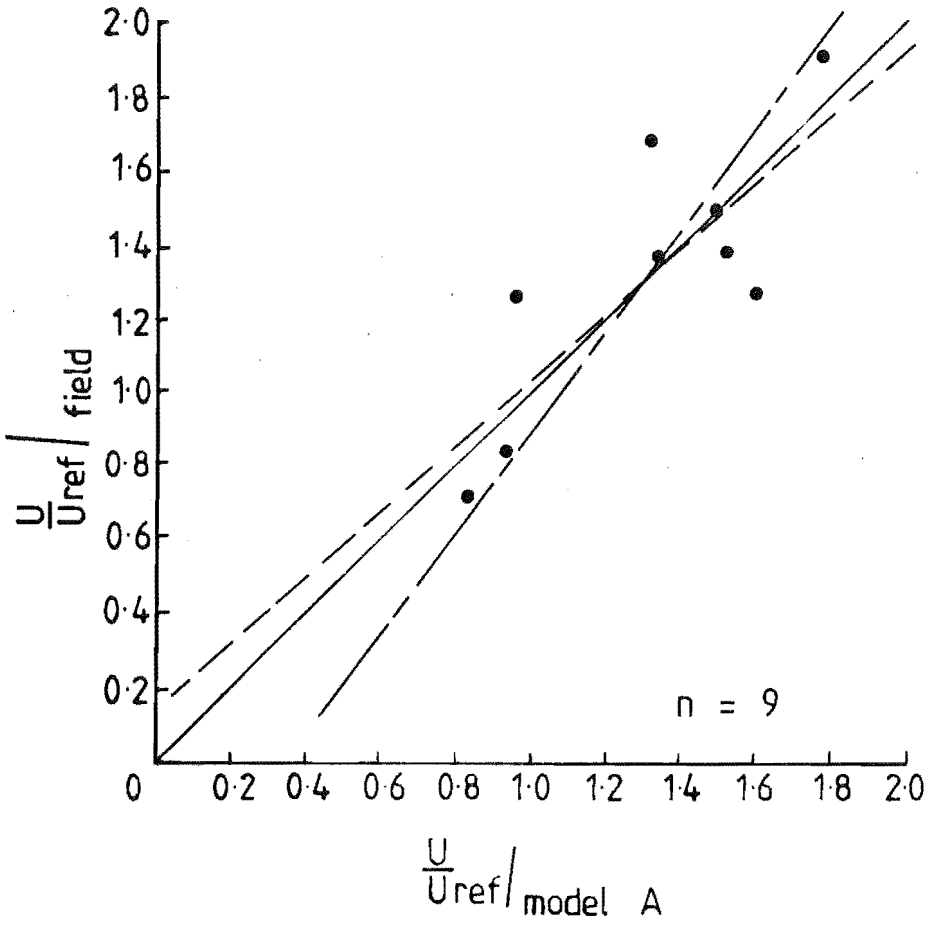

Regression lines

$$\text{- - - -}\quad \frac{U}{U_{ref}}\Big|_{field} = 0 \cdot 88 \frac{U}{U_{ref}}\Big|_{model\ A} + 0 \cdot 16$$

$$\text{- ——- —}\quad \frac{U}{U_{ref}}\Big|_{model\ A} = 0 \cdot 73 \frac{U}{U_{ref}}\Big|_{field} + 0 \cdot 34$$

Correlation coefficient $r = 0 \cdot 80$

FIG. 11 · 2 SCATTER DIAGRAM FOR FIELD DATA COLLECTED ON 16/5/79 AND MODEL A IN THE ROUGHNESS ADDED FORM OF CONSTRUCTION

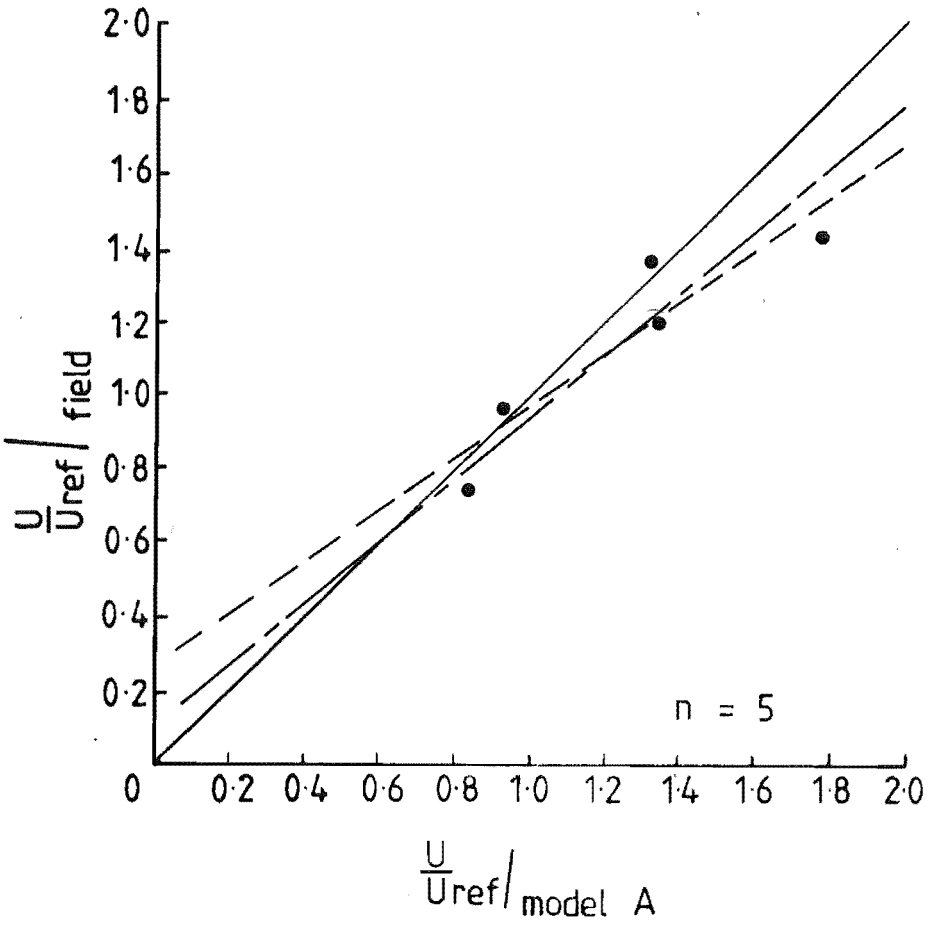

Regression lines

$$\frac{U}{U_{ref}}\Big|_{field} = 0 \cdot 69 \; \frac{U}{U_{ref}}\Big|_{model\ A} + 0 \cdot 28$$

$$\frac{U}{U_{ref}}\Big|_{model\ A} = 1 \cdot 21 \; \frac{U}{U_{ref}}\Big|_{field} - 0 \cdot 14$$

Correlation coefficient $r = 0 \cdot 91$

FIG. 11 · 3 SCATTER DIAGRAM FOR FIELD DATA COLLECTED ON 17/5/79 AND MODEL A IN THE ROUGHNESS ADDED FORM OF CONSTRUCTION

Data Correlated								Reject r=0 with 95% conf.								Reject 98% Conf.	
Field Day	Model B	n	a_1	b_1	r	$r_{critical}$ @ 5%		S_x^2	S_y^2	$(S_{x/y})_1$	S_{b_1}	$\|t\|_1$	S_{b_2}	$\|t\|_2$	$t_{0.01, n-2}$	B_1= 1.0	B_2= 1.0
11.12.78	Terraced	11	1.440	-0.254	-0.13	0.602	No	0.029	0.105	0.340	0.624	2.00	0.175	6.12	2.82	No	Yes
	Contoured	11	0.453	0.638	0.75	0.602	Yes	0.147	0.105	0.224	0.184	1.96	0.258	0.42	2.82	No	No
	Rough.added	11	0.690	0.454	0.53 0.73*	0.602	No Yes*	0.141	0.105	0.291	0.245	2.22	0.328	1.20	2.82	No	No
Δ 13.12.78	Terraced	6	-1.627	2.62	0.89	0.811	Yes	0.012	0.105	0.166	0.675	2.41	0.077	9.00	3.75	No	Yes
	Contoured	6	0.003	0.906	0.98	0.811	Yes	0.125	0.105	0.059	0.076	1.24	0.089	0.82	3.75	No	No
	Rough.added	6	-0.125	1.021	0.97	0.811	Yes	0.095	0.105	0.090	0.130	0.16	0.117	0.69	3.75	No	No
14.12.78	Terraced	8	-0.316	1.323	0.71	0.707	Yes	0.018	0.062	0.189	0.530	0.61	0.154	3.99	3.14	No	Yes
	Contoured	10	0.150	0.810	0.87	0.632	Yes	0.074	0.064	0.132	0.162	1.22	0.187	0.34	2.89	No	No
	Rough.added	10	0.050	0.905	0.90	0.632	Yes	0.064	0.064	0.115	0.151	0.63	0.151	0.64	2.89	No	No
16.5.79	Terraced	11	0.156	1.041	0.37	0.602	No	0.022	0.172	0.406	0.868	0.048	0.110	7.88	2.83	No	Yes
	Contoured	11	0.206	0.792	0.72	0.602	Yes	0.142	0.172	0.303	0.254	0.820	0.210	1.64	2.82	No	No
	Rough.added	11	0.192	0.794	0.73	0.602	Yes	0.145	0.172	0.300	0.248	0.830	0.209	1.57	2.82	No	No
17.5.79	Terraced	9	0.513	0.580	0.25	0.666	No	0.019	0.107	0.340	0.864	0.486	0.155	5.77	3.00	No	Yes
	Contoured	10	0.044	0.905	0.87	0.632	Yes	0.089	0.096	0.160	0.178	0.531	0.165	0.94	2.89	No	No
	Rough.added	10	0.184	0.787	0.71	0.632	Yes	0.079	0.096	0.230	0.273	0.780	0.273	0.78	2.89	No	No
9.8.79	Terraced	8	-0.280	1.296	0.49	0.707	No	0.009	0.064	0.237	0.925	0.320	0.136	5.96	3.14	No	Yes
	Contoured	8	0.311	0.595	0.90	0.707	Yes	0.146	0.064	0.119	0.117	3.46	0.269	1.35	3.14	Yes	No
	Rough.added	8	0.292	0.605	0.88	0.707	Yes	0.136	0.064	0.129	0.132	3.00	0.281	1.00	3.14	No	No

Subscript (1) - refers to value when field data is the dependent variable

Subscript (2) - refers to value when model data is the dependent variable

* - result with field point 23 removed

Δ - 4 of the 6 data pairs are situated on flat approach terrain

TABLE 11.5: Values of Statistical Parameters for Field Data and Model B

reject the null hypothesis that $r = 0$ and cannot reject the null hypothesis that the regression coefficient is 1.0. In this respect the results for both models A and B show the same trends. The scatter diagrams and regression curves for model B vs field data are presented in Figs 11.4 to 11.9; these are for the roughness added form of construction only.

Correlations have shown the degree of similarity between the field and tunnel results; however, it can be more useful to know how closely a particular tunnel result represents the true field situation. The formula used to calculate the prediction interval at a particular confidence level was given in Equation 11.11. Predicted limits have been calculated at 80% and 90% confidence limits and are compared with the field data in Table 11.6. The results are for model B in the roughness added form of construction. There are numerous combinations of field data dates, points, models and forms of construction. Therefore, the data in Table 11.6 was produced to give an indication of the effects of different sample sizes, data collection dates and the magnitude of the confidence levels used.

Date of Field Data Collection used in analysis	Field Point	Confidence Limits		C	Measured Data Spread
		90%	80%		
14/12/78	7	0.78 - 1.23	0.84 - 1.17	6	0.77 - 1.06
	11	0.90 - 1.35	0.96 - 1.29	3	1.09 - 1.25
	15	1.30 - 1.87	1.37 - 1.80	5	1.43 - 1.90
16/5/79	7	0.47 - 1.60	0.61 - 1.45	6	0.77 - 1.06
	11	0.58 - 1.70	0.72 - 1.55	3	1.09 - 1.25
	15	0.93 - 2.13	1.07 - 2.00	6	1.43 - 1.90
17/5/79	7	0.42 - 1.34	0.53 - 1.22	6	0.77 - 1.06
	11	0.67 - 1.57	0.78 - 1.45	3	1.09 - 1.25
	15	0.98 - 2.06	1.12 - 1.92	6	1.43 - 1.90

C - Number of measurements made at the field point

TABLE 11.6: Prediction intervals for field speed-up ratios based on model B tunnel data

Generally, the modelled results predict the actual field measurements quite well. The aim of modelling is not to determine absolute values in terms of say, available energy but to locate the most likely sites so that detailed field measurements can be undertaken on a relatively small scale.

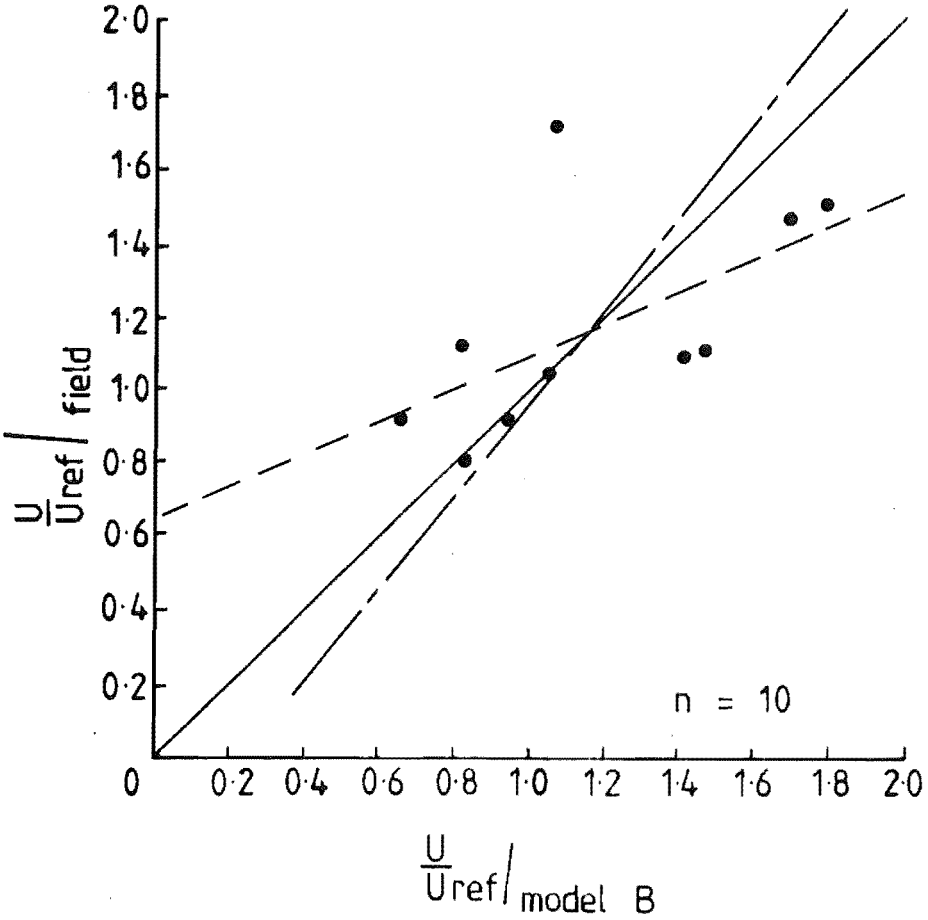

Regression lines

$$\frac{U}{U_{ref}}\Big|_{field} = 0 \cdot 42 \; \frac{U}{U_{ref}}\Big|_{model\ B} + 0 \cdot 67$$

$$\frac{U}{U_{ref}}\Big|_{model\ B} = 0 \cdot 81 \; \frac{U}{U_{ref}}\Big|_{field} + 0 \cdot 22$$

Correlation coefficient $r = 0 \cdot 59$

FIG. 11 · 4 SCATTER DIAGRAM FOR FIELD DATA COLLECTED ON 11/12/78 AND MODEL B IN THE ROUGHNESS ADDED FORM OF CONSTRUCTION

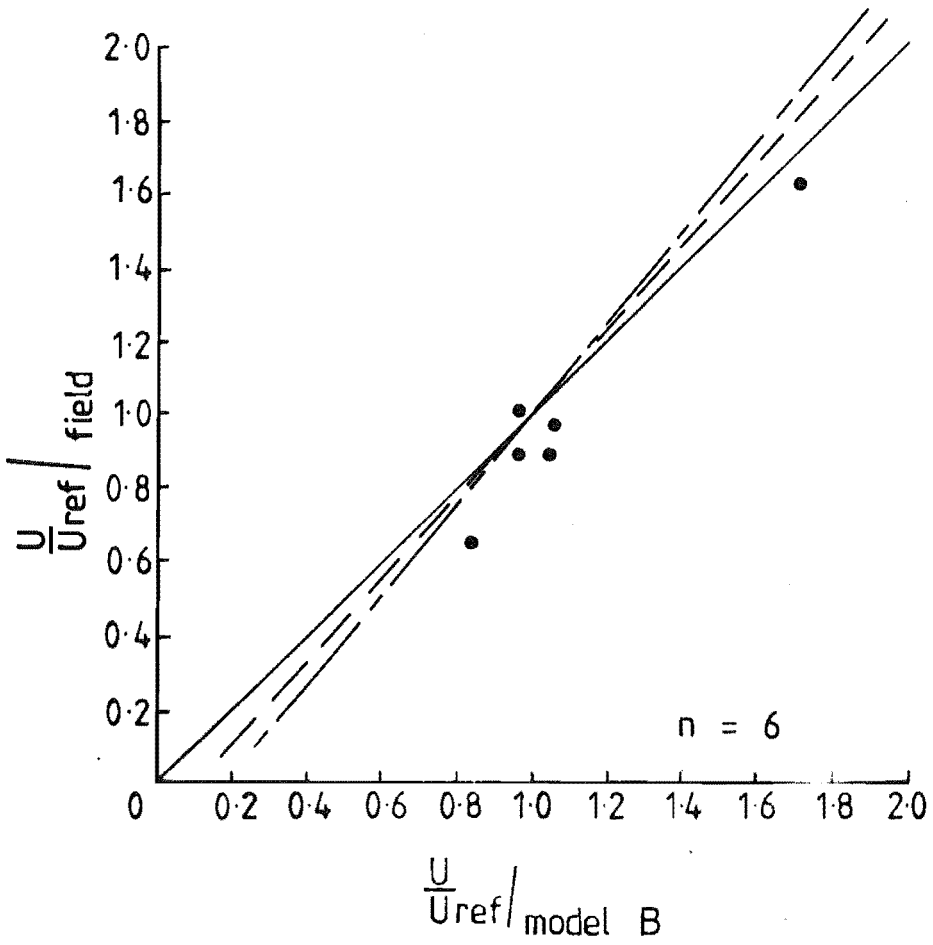

Regression lines

$$\frac{U}{U_{ref}}_{field} = 1 \cdot 02 \; \frac{U}{U_{ref}}_{model\ B} - 0 \cdot 12$$

$$\frac{U}{U_{ref}}_{model\ B} = 0 \cdot 92 \; \frac{U}{U_{ref}}_{field} + 0 \cdot 18$$

Correlation coefficient r = 0·97

FIG. 11 · 5 SCATTER DIAGRAM FOR FIELD DATA COLLECTED ON 13/12/78 AND MODEL B IN THE ROUGHNESS ADDED FORM OF CONSTRUCTION

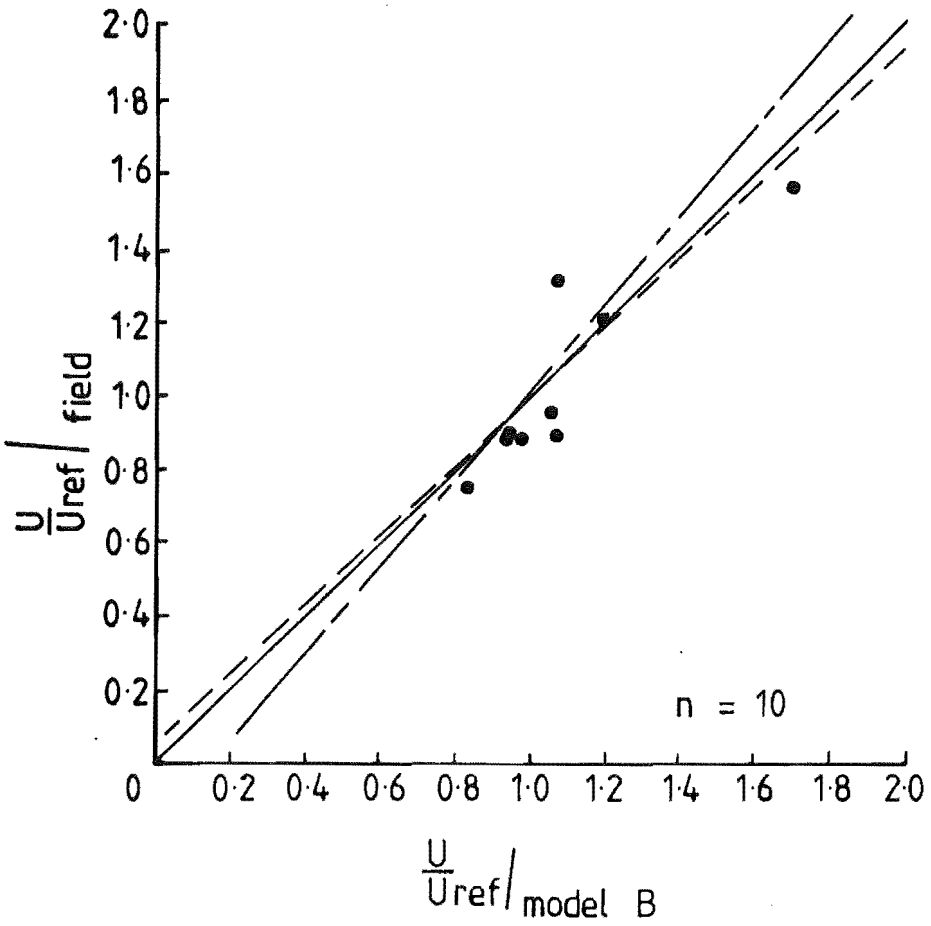

Regression lines

$$\frac{U}{U_{ref}}\Big|_{field} = 0 \cdot 90 \; \frac{U}{U_{ref}}\Big|_{model\ B} + 0 \cdot 05$$

$$\frac{U}{U_{ref}}\Big|_{model\ B} = 0 \cdot 90 \; \frac{U}{U_{ref}}\Big|_{field} + 0 \cdot 15$$

Correlation coefficient $r = 0 \cdot 90$

FIG. 11 · 6 SCATTER DIAGRAM FOR FIELD DATA COLLECTED ON 14/12/78 AND MODEL B IN THE ROUGHNESS ADDED FORM OF CONSTRUCTION

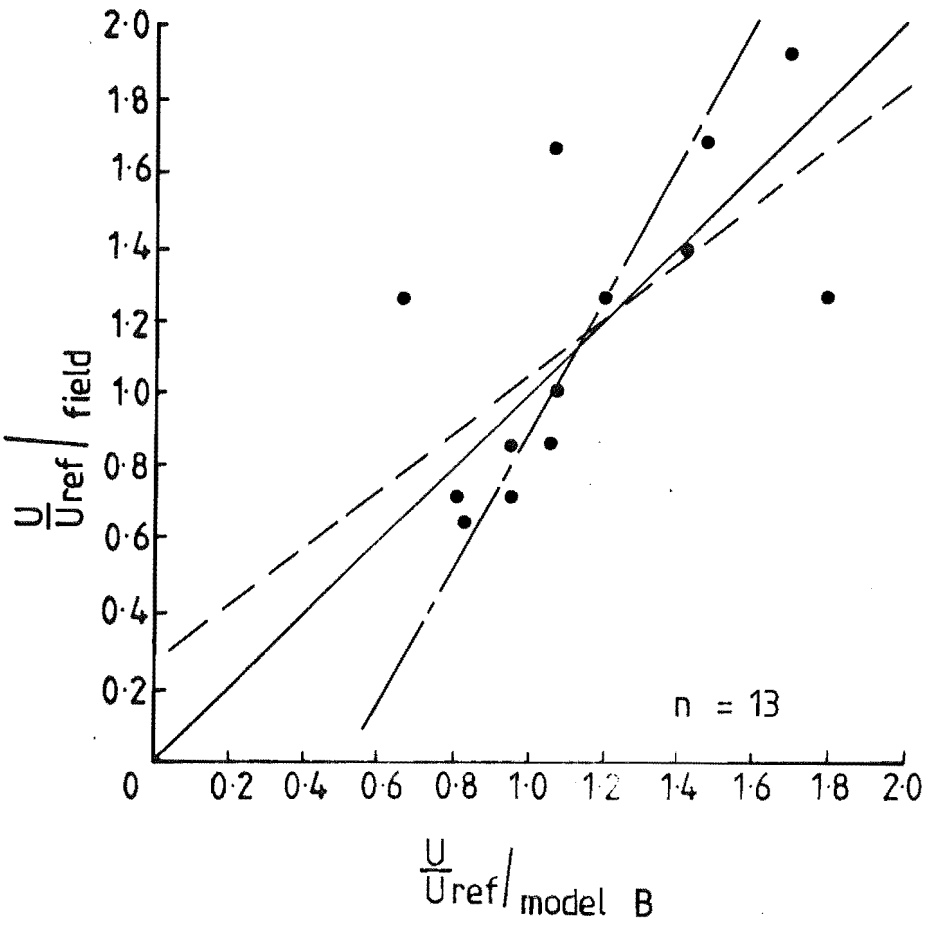

Regression lines

$$\frac{U}{U_{ref}}_{field} = 0 \cdot 76 \frac{U}{U_{ref}}_{model\ B} + 0 \cdot 28$$

$$\frac{U}{U_{ref}}_{model\ B} = 0 \cdot 56 \frac{U}{U_{ref}}_{field} + 0 \cdot 50$$

Correlation coefficient $r = 0 \cdot 65$

FIG. 11·7 SCATTER DIAGRAM FOR FIELD DATA COLLECTED ON 16/5/79 AND MODEL B IN THE ROUGHNESS ADDED FORM OF CONSTRUCTION

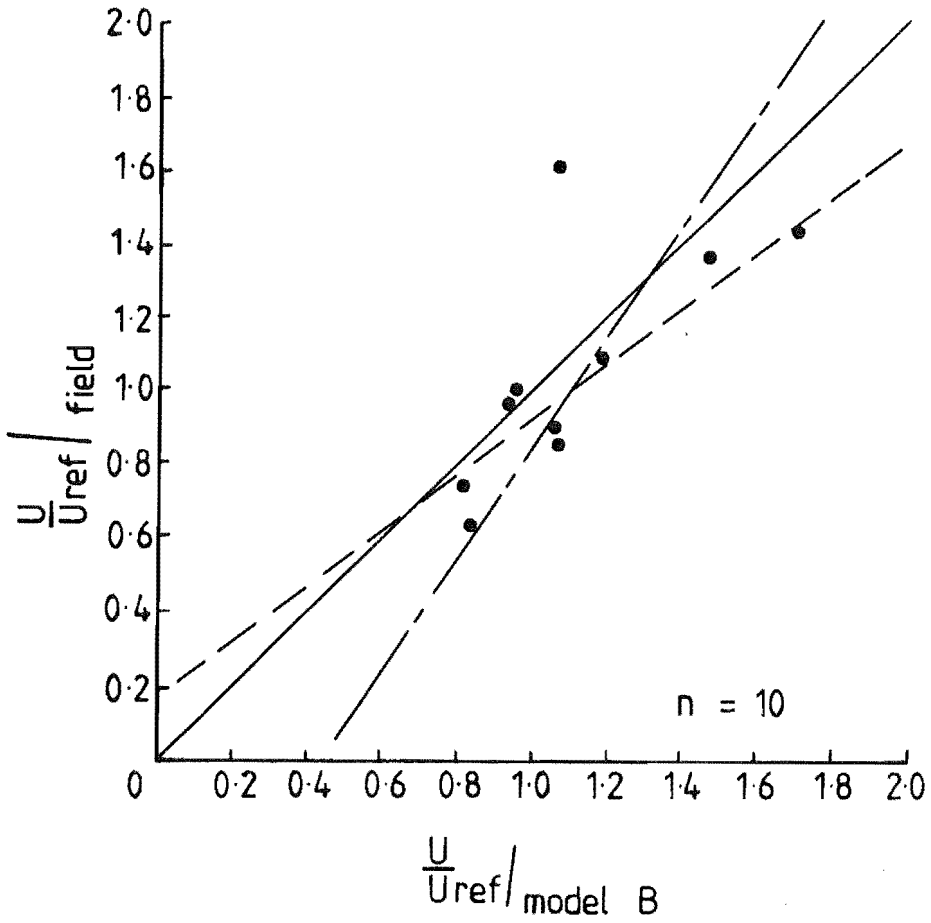

Regression lines

$$\frac{U}{U_{ref}}\Big|_{field} = 0 \cdot 79 \; \frac{U}{U_{ref}}\Big|_{model\ B} + 0 \cdot 18$$

$$\frac{U}{U_{ref}}\Big|_{model\ B} = 0 \cdot 65 \; \frac{U}{U_{ref}}\Big|_{field} + 0 \cdot 42$$

Correlation coefficient $r = 0 \cdot 71$

FIG. 11 · 8 SCATTER DIAGRAM FOR FIELD DATA COLLECTED ON 17/5/79 AND MODEL B IN THE ROUGHNESS ADDED FORM OF CONSTRUCTION

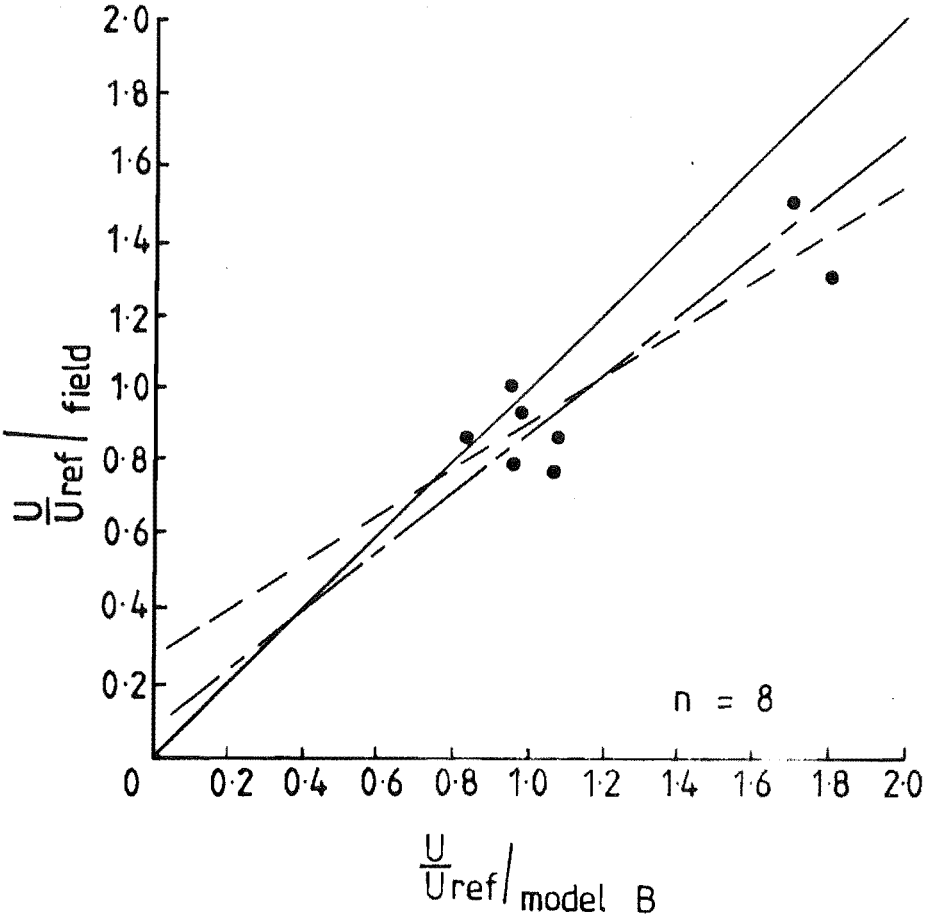

Regression lines

$$\frac{U}{U_{ref}}\Big|_{field} = 0 \cdot 60 \; \frac{U}{U_{ref}}\Big|_{model\ B} + 0 \cdot 29$$

$$\frac{U}{U_{ref}}\Big|_{model\ B} = 1 \cdot 28 \; \frac{U}{U_{ref}}\Big|_{field} - 0 \cdot 11$$

Correlation coefficient $r = 0 \cdot 88$

FIG. 11 · 9 SCATTER DIAGRAM FOR FIELD DATA COLLECTED ON 9/8/79 AND MODEL B IN THE ROUGHNESS ADDED FORM OF CONSTRUCTION

The results suggest that such an approach is feasible and that 80% confidence limits, in this study, produce results which agree with the field data very well.

11.3.3 Field Data vs Model C

Model C has the smallest number of points common to both the field data collection programme and the model. Correlation coefficients for two field days vs model C in the contoured and roughness added forms of construction are presented in Table 11.7.

No. of Data Points	Field Data Date	Correlation Coefficient	
		Contoured	Roughness Added
7	14/12/78	0.73	0.67
8	16/5/79	0.91	0.94

TABLE 11.7: Correlations between field and model C

No explanation can be given for the significant variation in correlation coefficients between the two days or for the significant reduction for 14/12/79 and the roughness added model. The results of the statistical analysis for the field data vs model C are presented in Table 11.8.

The null hypothesis tests for model C show that the correlation with field data for 14/12/78 is not reliable. The null hypothesis that $r = 0$ cannot be rejected, which means that the correlation obtained could be due purely to chance. The results for 16/5/79 are favourable and suggest this to be useful data.

Prediction intervals at 80% and 90% confidence levels are presented for field points 5, 7 and 11, Table 11.9. These are based on the regression curves for 16/5/79 data vs model C with roughness added.

The calculated confidence limits fit the measured results very well and are better than those between the same field data and model B. This can be explained by the higher correlation which was found between 16/5/79 and model C.

Data Correlated																Reject 98% Conf.	
Field Day	Model C	n	a_1	b_1	r	$r_{critical}$ @ 5%	Reject r=0 with 95% Conf.	s_x^2	s_y^2	$(s_{x/y})_1$	s_{b_1}	$\|t\|_1$	s_{b_2}	$\|t\|_2$	$t_{0.01, n-2}$	B_1= 1.0	B_2= 1.0
14.12.78	Contoured	7	-0.486	1.49	0.73	0.754	No	0.021	0.088	0.220	0.615	0.79	0.149	4.30	3.36	No	Yes
	Rough.added	7	0.148	0.95	0.67	0.754	No	0.043	0.088	0.241	0.471	0.10	0.233	2.46	3.36	No	No
16.5.79	Contoured	8	-0.896	1.94	0.91	0.707	Yes	0.023	0.106	0.142	0.348	2.70	0.078	7.28	3.14	No	Yes
	Rough.added	8	-0.291	1.43	0.94	0.707	Yes	0.046	0.106	0.115	0.203	2.12	0.089	4.22	3.14	No	Yes

Subscript (1) - refers to value when field data is the dependent variable
Subscript (2) - refers to value when model data is the dependent variable

TABLE 11.8: Values of Statistical Parameters for Field Data and Model C

Date of Field Data Collection used in Analysis	Field Point	Confidence Limits		C	Measured Data Spread
		90%	80%		
16/5/79	5	0.76 - 1.25	0.83 - 1.19	5	0.86 - 0.98
	7	0.75 - 1.24	0.81 - 1.18	6	0.77 - 1.06
	11	1.13 - 1.60	1.19 - 1.54	3	1.09 - 1.25

C - Number of measurements at the field point

TABLE 11.9: Prediction intervals for field result based on Model C tunnel data

The scatter diagrams and regression curves for the field vs model C in the roughness added form of construction are presented in Figs 11.10 and 11.11.

An indication of the modelling accuracy can be obtained by using the modelled speed-up ratio value to predict the velocity at a point on the terrain given the velocity at a reference site upstream of the complex terrain. This is expressed by, $\bar{U}'_f$

$$\bar{U}'_f = \bar{U}_{ref} \left|_{field} \times \frac{\bar{U}_{2.5}}{\bar{U}_\delta} \right|_{pt} \times \frac{\bar{U}_\delta}{\bar{U}_{2.5}} \Bigg|_{ref\ pt} \quad \ldots\ (11.12)$$

where $\bar{U}'_f$ is the predicted velocity for a particular field point.

Model B was analysed in this way and the results are presented in Table 11.10.

Reference Tower Velocity m/s	Field Data Date	No. of points in comparison	% of predicted results within ±1m/s	±2m/s
See Fig. 10.4	11/12/78	10	30	50
	13/12/78	6	66	100
	14/12/78	9	66	89
See Fig. 10.8	16/5/79	13	46	77
	17/5/79	10	30	60
See Fig. 10.11	9/8/79	8	38	75

TABLE 11.10: Predicted velocities within ±1 m/s and ±2 m/s of measured values

Field point 15, situated on the top of the Gebbies Pass saddle, was measured on all six field days. It is included in the predicted values for all field days excepting 17/5/79. This is encouraging because it

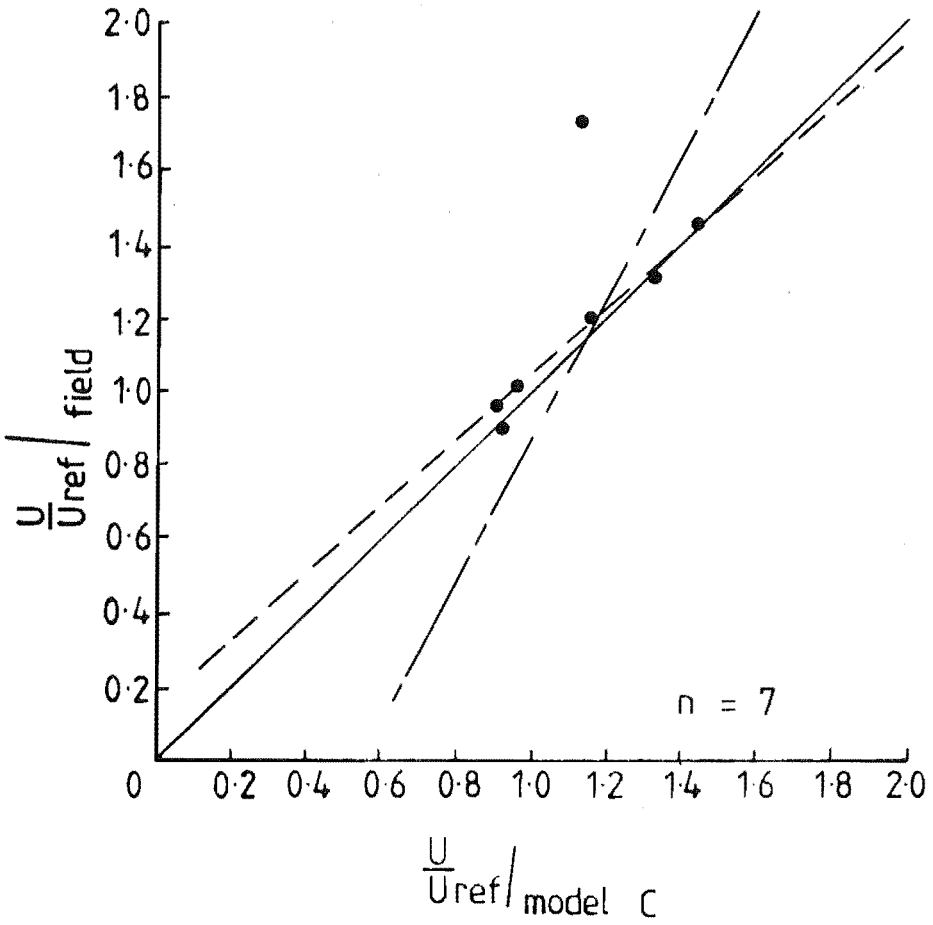

Regression lines

$$\text{- - - -}\quad \frac{U}{U_{ref}}\Big|_{field} = 0\cdot95\ \frac{U}{U_{ref}}\Big|_{model\ C} + 0\cdot15$$

$$\text{- — - —}\quad \frac{U}{U_{ref}}\Big|_{model\ C} = 0\cdot47\ \frac{U}{U_{ref}}\Big|_{field} + 0\cdot54$$

Correlation coefficient $r = 0\cdot67$

FIG. 11·10 SCATTER DIAGRAM FOR FIELD DATA COLLECTED ON 14/12/78 AND MODEL C IN THE ROUGHNESS ADDED FORM OF CONSTRUCTION

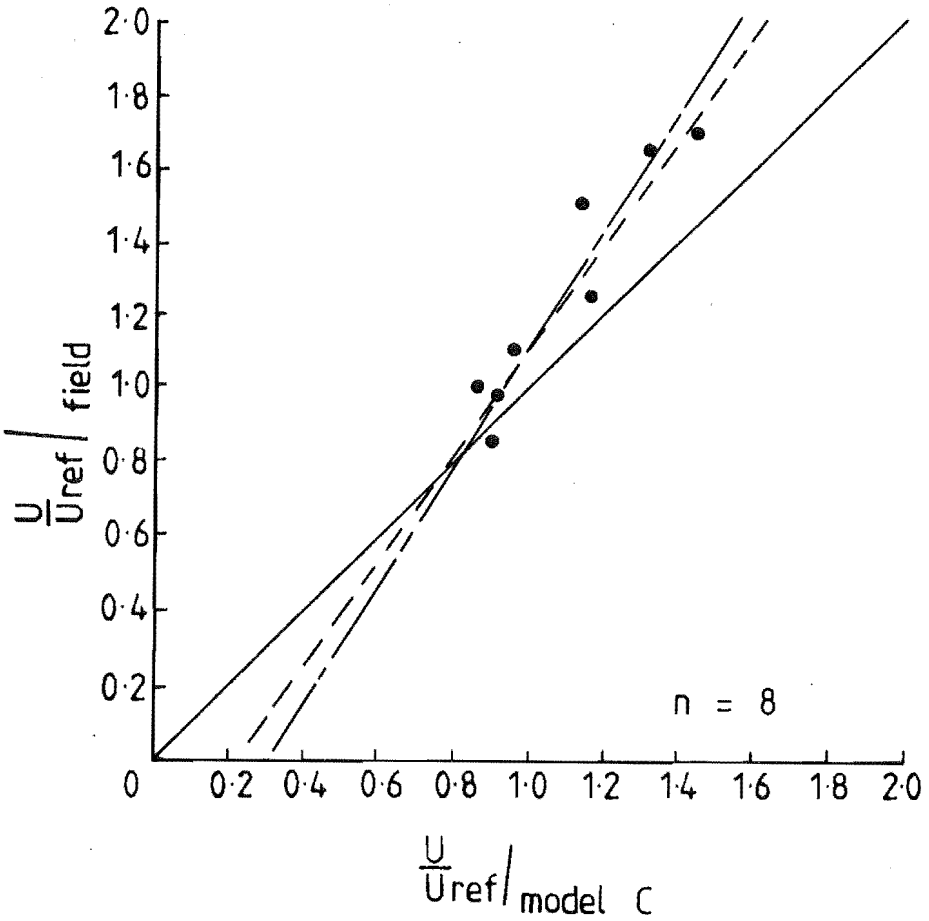

Regression lines

$$\text{- - - -}\quad \frac{U}{U_{ref}}\Big|_{field} = 1 \cdot 43 \frac{U}{U_{ref}}\Big|_{model\ C} - 0 \cdot 29$$

$$\text{- — - —}\quad \frac{U}{U_{ref}}\Big|_{model\ C} = 0 \cdot 62 \frac{U}{U_{ref}}\Big|_{field} + 0 \cdot 30$$

Correlation coefficient $r = 0 \cdot 94$

FIG. 11·11 SCATTER DIAGRAM FOR FIELD DATA COLLECTED ON 16/5/79 AND MODEL C IN THE ROUGHNESS ADDED FORM OF CONSTRUCTION

suggests that wind speeds on the top of a hill can be predicted to a high degree of accuracy.

Similarly, field point 20, situated on flat terrain on the leeward side of the Gebbies Pass saddle, was measured on all field days. It is included in the predicted values for all field days.

Even at the ±2 m/s level, a very high percentage of the field points can be predicted repeatedly. In terms of using models as a tool for investigating complex terrain, this is extremely encouraging.

11.4 CONCLUSIONS

The statistical analysis was carried out with α levels of 0.02, 0.10 and 0.20 for the null hypothesis test that the true regression coefficient $b = 1.0$, and confidence limits for prediction of field results respectively. These confidence levels were considered consistent with those used by other researchers involved in comparisons between field and model.

The sample correlation coefficient was used and shown to be very sensitive to small changes in the data analysed. This result suggested that caution should be observed when commenting on the degree of relationship based on sample correlation coefficients.

Linear regression curves were fitted to the data and from these a null hypothesis test and prediction intervals were calculated It was shown that the terraced form of construction compared very poorly with the field situation. There was very little difference in the results obtained from the models in the contoured and roughness added forms of construction. Modelling of surface roughness such as shelterbelts and scrub was shown to be significant in terms of point analysis where a knowledge of the wind structure is of importance. Therefore, the detailed statistical analysis was confined to the models in the roughness added form of construction. Model B contained the largest number of points common to both the model and field, and it was therefore analysed in more detail than the other models.

Confidence limits of 90% and 80% were used to predict field values from the modelled results, which were then compared with the spread of values obtained during the field surveys. The maximum number of field measurements used for this comparison was limited to six; however, there was little difference in the results when only three or four values were used

The model speed-up ratios were used to predict the actual velocities at the field points to within ±1 m/s and ±2 m/s. The percentage of points that met this criterion were very high and were shown to be applicable to field points in a variety of situations. In particular, field point 15, located on the top of the Gebbies Pass saddle, and field point 20, located in the lee of the Gebbies Pass saddle, generally produced predicted velocity values that were within the ±1 m/s range.

CHAPTER 12

CONCLUSIONS

12.1 SUMMARY OF CONCLUSIONS

The objectives of this research were outlined in Section 1.2, the major objective being to determine whether a complex terrain situation could be modelled in a wind tunnel with sufficient accuracy to make the results directly applicable to the prototype situation.

A. The Modelling Phase of the Study

1) A boundary layer generating system consisting of a honeycomb section, coarse grid and uniform roughness was used to generate a simulated atmosphere boundary layer. The parameters considered during the simulation included velocity and turbulence profiles, integral length scale L_{u_x}, and the longitudinal component of the energy spectrum. These parameters compared most favourably with measured and theoretically predicted values.

2) Due to the lack of information regarding the effects of wind tunnel blockage in complex separated three-dimensional flows, the tunnel blockage was generally kept below 5%. However, in two instances, this increased to slightly over 6%.

Wall effects can produce very complex flow situations which do not exist in the atmosphere. Therefore, the measurements were restricted to the central region of the wind tunnel, and the region within 200mm from the side walls was neglected.

3) For heights less than 20mm (two terrace heights), the terraced model gave lower velocities and higher turbulence intensity values. This result was consistent with other modelling studies of this type. For heights greater than two terrace heights, a reasonable correlation was found between the three forms of construction - terraced, contoured and roughness added.

4) The contoured and roughness added models correlated extremely well in all cases. In this study, the addition of roughness elements was not particularly significant since they were not extensive, although for points immediately downstream from the shelterbelts or scrub, there were significant effects. Meroney *et al* (1978) found that the addition of roughness elements did have a significant overall effect. The general conclusion from this study is that roughness elements should be added where possible.

The models showed that the tops of hills and ridges produced the most

significant velocity increases; however, this feature was shown to be accentuated above the Gebbies Pass saddle. The results suggested that there is a funnelling of the flow over Gebbies Pass saddle, which resulted in a constant velocity profile up to 200m. This feature is desirable for WECS because it provides less cyclic stressing of the structure whilst giving a high energy output without requiring an excessively high structure.

B. The Field Data Collection

1) The six one-day field data collection programmes were shown to correlate *inter se* extremely well, even where data had been collected months apart.

2) The TALA kite was shown to be an extremely useful tool. In reasonably steady wind conditions, it facilitated the recording of velocities with an accuracy of ±0.5 m/s, up to a height of 300m.

3) Detailed wind structure measurements made on the flat approach terrain with the 20m tower were shown to agree very closely with those predicted by other researchers and ESDU (1974). The measurements of velocity, turbulence intensity, autocorrelation function, $\rho\overline{uw}$ Reynolds stress and energy spectra, made in the complex terrain at field point 15 on the Gebbies Pass saddle, were shown to agree with the wind tunnel simulation.

4) The results from the simulation and field were compared statistically by means of the sample correlation coefficient. This was shown to be extremely sensitive to the inclusion or omission of data points.

Generally, the results indicated a very poor correlation between the field and terraced models and high correlations between the field and the models in the other forms of construction. Linear regression curves were fitted to the data. These were used to predict field values, based on the model regression curve, which were found to be in close agreement with the actual field measurements.

The study has shown that the complex terrain situation, as at Gebbies Pass, can satisfactorily be simulated in a wind tunnel to provide information regarding the flow régime and wind structure.

12.2 EQUIPMENT DEVELOPMENTS AND ADDITIONS

The field programme pursued in this study prompted several suggestions which would result in the ability to measure wind parameters with a higher degree of confidence.

1) The results obtained in the present study are only valid for neutral conditions. If temperature measuring sensors were incorporated on the instrumented tower, it would make this a more versatile piece of equipment.

2) The anchors used with the tower guy wires should be improved. In strong winds and on light soil the present system was found unsatisfactory and required constant attention.

3) In complex terrain situations, the bottom 5 - 10m of the boundary layer can be significantly affected by the terrain immediately upstream of the point. It is therefore desirable to be able to measure the wind to heights greater than 20m so that more general flow patterns can be observed. This would also make wind tunnel comparisons easier, especially at scales as large as 1:4000 where 20m in the field is only 5mm above the model. It is suggested that a tower 50m high would be a definite enhancement to the existing system.

4) The w component anemometer spends much of its time in its stalled region. An improvement would involve the development of a smaller, lighter propeller to be used on this anemometer, thus improving its response and allowing greater confidence in the results obtained for this component.

5) The TALA kite proved to be an extremely useful piece of equipment and warrants consideration of additional units being acquired. A TALA system is available that provides the rms component of velocity in the longitudinal direction. One such unit would be extremely valuable in providing turbulence information for heights up to 300m.

12.3 RECOMMENDATIONS FOR FUTURE WORK

1) 1:8000 scale survey of the Gebbies Pass area is suggested. This will provide information on the following:

i) effects of model scale;
ii) show the extent of the wall effects;
iii) test the validity of splitting an area for study and testing the sections separately;
iv) show the effects of tunnel blockage.

2) Additional field measurements should be made on the Gebbies Pass saddle, preferably to heights greater than 20m. This will provide much needed information about the existence of the internal boundary layer.

3) Consideration should be given to the development of a better statistical model to show the relationship between field and wind tunnel measurements with a greater confidence level.

REFERENCES

ASTLEY, R.J., (1977), A finite element frozen vorticity solution for two-dimensional wind flow over hills. 6th Australasian Hydraulics and Fluid Mechanics Conference, University of Adelaide, South Australia; 443-446.

BATCHELOR, G.K. (1953), The theory of homogeneous turbulence. Cambridge University Press.

BENDAT, J.S. and PIERSOL, A.G. (1971), Random data: Analysis and measurement procedures. Wiley Interscience: 407 p.

BJERKNESS, V., BJERKNESS, J., SOLBERG, H., and BERGERON, T. (1933), Physikalische Hydrodynamik, Berlin, 1933.

BRADSHAW, P., (1971), An introduction to turbulence and its measurement. Pergamon Press, London.

BRYER, D.W. and PANKHURST, R.C., (1971), Pressure probe methods for determining wind speed and flow direction. N.P.L., Her Majesty's Stationery Office, London: 120 p.

B.S.C.P.3 (1972), Code of basic data for the design of buildings, Chapter V, part 2, Windloads.

BOWEN, A.J. (1979), Some effects of escarpments on the atmospheric boundary layer. Thesis presented for degree of Ph.D. in Mechanical Engineering, University of Canterbury, Christchurch, New Zealand, 1979.

BOUWMEESTER. R.J.B., MERONEY, R.N., SANDBORN, V.A., and RICER, M.A. (1977), The influence of hill shape on wind characteristics over two-dimensional hills. 3rd Wind Energy Workshop, Washington, D.C. Vol.2; 646-652.

BUSCH, N.E. and PANOFSKY, H.A., (1968), Recent spectra of atmospheric turbulence. Q.J.R. Met. Soc., 94: 132-148.

CALDER, K.L. (1939), A note on the constancy of horizontal turbulent shearing stress in the lowest layers of the atmosphere. Q.J.R. Met. Soc., 65: 537-541.

CARRUTHERS, N.B. and HOUGHTON, E.L., (1976), Wind forces on buildings and structures; an introduction. Publ. Arnold, 243 p.

CERMAK, J.E. and ARYA, S.P. (1970), Problems of atmospheric shear flows and their laboratory simulation. Boundary Layer Meteorology, 1, 1970: 40.60.

CHANGERY, M.J. (1975), Initial wind energy data assessment study. NSF-RA-N-75-020.

CHERRY, N.J. (1976), Wind energy resources survey of New Zealand - Preliminary analysis of meteorological data. N.Z.E.R.D.C. Report No.8.

CHIEN, MERONEY, SANDBORNE (1977), Sites for wind power installations: Physical modelling of the wind field over Kanuku Point, Oahu, Hawaii. DOE Contract No. DE-AS06-77ET20292, A004. Draft.

COOK,N.J. (1973), On simulating the lower third of the urban adiabatic boundary layer in a wind tunnel. Atmos. Environment, 3: 197-214, 1973.

COOK, N.J. (1977), Determination of the model scale factor in the wind tunnel simulations of the adiabatic atmospheric boundary layer. Jour. of Industrial Aerodynamics, 2: 311-321.

COROTIS, R.B. (1977), Stochastic modelling site wind characteristics. Dept of Civil Engineering, Final Report, ERDA/PLO/2342-77/2. Northwestern University, 143 p.

COROTIS, R.B. (1976), Stochastic modelling site wind characteristics. Dept of Civil Engineering, Final Report, ERDA/NSF/00357-76/1, Northwestern University, 297 p.

COUNIHAN, J. (1973), Simulation of an adiabatic urban boundary layer in a wind tunnel. Atmos. Environment, 7: 673-689, 1973.

COUNIHAN, J. (1975), Adiabatic atmospheric boundary layers: A review and analysis of data from the period 1880 to 1972. Atmospheric Environment, vol.9: 871-905.

CROW, E.L., DAVIS, F.A., and MAXFIELD, M.W. (1960), Statistics Manual, Dover Publications, New York. 288 p.

DAVENPORT, A.G.(1960), Rationale for determining design wind velocities. Proc. Am. Soc. Civ.Eng - J.Struct. Div. (May 1960), 86, (No. ST5): 39-68.

DAVENPORT, A.G. (1961a), Application of statistical concepts to the wind-loading of structures. Proc. Inst. Civ. Engrs, 19: 449-472.

DAVENPORT, A.G. (1961b), The spectrum of horizontal gustiness near the ground in high winds. Q.J.R. Met. Soc., 87: 194-211.

DAVENPORT, A.G. (1963), The relationship of wind structure to wind loading. Paper 2, Sump. 16, Proc. of Conf. on Wind Effects on Buildings and Structures at N.P.L.

DAVENPORT, A.G. (1964), The buffeting of large superficial structures by atmospheric turbulence. Reprinted from Ann. N.Y. Acad. Sci., 116: 1350159.

DAVENPORT, A.G. (1967), The dependence of wind loads on meteorological parameters. Paper 2, Conf. on Wind Loads on Buildings, Univ. of Toronto Press, Toronto.

DEACON, E.L., (1957), Wind profiles and the shearing stress - an anomaly resolved. Q.J.R. Met. Soc., 83: 537-541.

DEAVES, D.M. (1956/76), Wind over hills: A numerical approach. J.Industrial Aerodynamics, 1: 371-391.

ELDERKIN, C.E., (1967), Comparison of turbulence spectra from Hanford, Washington and Liberal, Kansas, U.S.A.E.C. Met. Info. Meeting, Chalk River, Ont., Canada (Cont AT(45-1)-1830).

ELLISON, T.J. (1956), Atmospheric Turbulence. Surveys in Mechanics (edited by Batchelor and Davies), Camb. Univ. Press, London.

ESDU 72026, (1972), Characteristics of wind speed in the lower layers of the atmosphere near the ground: Strong winds (neutral atmosphere), ESDU, London.

ESDU 74030 (1974), Characteristics of atmospheric turbulence near the ground: Part I, definitions and general information. ESDU, London.

ESDU 74031, (1974), Characteristics of atmospheric turbulence near the ground: Part II, Single point data for strong winds (neutral atmosphere), ESDU, London.

ESDU 75001 (1975), Characteristics of atmospheric turbulence near the ground: Part III, Variations in space and time for strong winds (neutral atmosphere), ESDU, London.

FLAY, R.G.J. (1978), Structure of a rural atmospheric boundary layer near the ground. Dept of Mechanical Engineering, University of Canterbury, Christchurch, New Zealand. Ph.D. Thesis, 400 p and Appendices.

FREEMAN, B.E. and TAFT, J.R. (1976), Mathematical modelling of topographical effects on wind energy systems. Paper A3, Int. Symp. on Wind Energy Systems, Cambridge, Sept 7-9: 39-51.

GILL, G.C. (1966), Temperature and wind measuring systems - basic principles and dynamic response. Seminar Series at White Sands Missle Range, Oct. 24-28.

GILL, G.C., OLSSON, L.E., SELA, J., and SUDA, M., (1967), Accuracy of wind measurements on towers and stacks. Bulletin Americal Meteorological Society, 48; No.9: 665-674.

GOLDING, E.W. (1949), Large-scale generation of electricity by wind power - preliminary Report, E.R.A. TEchnical Report C/T 101.

GOLDING, E.W. and STODHARD, A.H. (1952), The selection and characteristics of wind-power sites. E.R.A. TEchnical Report C/T 108.

HARDY, D.M. (1977), Wind studies in compex terrain. Lawrence Livermore Laboratories Report, University of California.

HARRIS, R.I. (1968), Measurements of wind structure at heights up to 598 ft above ground level. Conf. on Wind Loads on Buildings, Loughborough University.

HARRIS, R.I. (1970), The nature of the wind. Paper 3, presented at the Construction Industry Research and Information Assoc. Seminar on the Modern Design of Wind-Sensitive Structures, London, England, June 18.

HENNESSEY, Jr, J.P., (1977), Some aspects of wind power statistics. Journ. of App. Meteorology, vol.16, No.2.

HINZE, H.O. (1959), Turbulence. McGraw-Hill.

HOLMES, J.D., WALKER, G.R., and STEEN, W.E. (1979), The effect of an isolated hill on wind velocities near ground level - initial measurements. Wind Engineering Report 3/79, James Cook University of North Queensland, Queensland, Australia.

HORST, T.W. (1973), Corrections for response errors in a three-component propellor anemometer. J. Appl. Meteorology, 12: 716-725.

JONES, P.M., DE LARRINGA, M.A., and WILSON, L.B. (1971), The urban wind velocity profile. Atmos. Environ., vol.5: 89-102.

JUUL, J. (1949), Investigation of the possibilities of utilisation of wind power. Elektroteknikeren, vol.45, No.20, October 22: 607-635.

KAIMAL, J.C. (1973), Turbulence spectra, length scales, and structure parameters in the stable stuface layer. B.L.Met., vol.4: 289-309.

KAIMAL, J.C., WYNGAARD, J.C., IZUMI, Y., and COTE. P.R. (1972), Spectral characteristics of surface layer turbulence. Q.J.R.Meteor.Soc., 98: 563-588.

KIMBLE, G.A. (1978), How to use (and misuse) statistics. Prentice Hall, Englewood Cliffs, New Jersey: 290 p.

LAPPE, U.O. (1965), A low altitude gust model for estimating gust loads on aircraft. A.I.A.A., Paper 65 - 14.

LINDLEY, D., ISAACS, N., TOLLERTON, D., STUDT, F., BARR, H., AND LUMB, T., (1978), Data appendix of New Zealand for an initial multi-national study of future energy systems and impacts of some evolving technologies. Unpublished, N.Z.E.R.D.C. Contract 3097.

MAHRER, Y., and PIELKE, R.A. (1975), A numerical study of the air flow over mountains using the two-dimensional version of the University of Virginia Mesoscale Model. J. of Atmos. Sciences, 32: 2144-2155.

MARRS, R.W., and MARWITZ., J. (1977), Locating areas of high wind energy potential by remote observation of Eolian geomorphology and topography. Wind Energy Workshop, vol.1: 307-311.

MERONEY, R.N. (1976), Battelle Contract EY-76-S-06-2438. Semi-annual Report.

MERONEY, R.N., SANDBORN, V.A., BOUWMEESTER, R., and RIDER, M. (1976), Wind tunnel simulation of the influence of two-dimensional ridges on wind speed and turbulence. International Symposium on Wind Energy Systems, Cambridge, England.

MERONEY, R.N., BOWEN, A.J., LINDLEY, D., and PEARSE, J. (1978), Wind characteristics over complex terrain: Laboratory simulation and field measurements at Rakaia Gorge, New Zealand. Report No. TH/FL.102/78, Dept of Mechanical Engineering, University of Canterbury, Christchurch, New Zealand,

NEAL, D., and STEVENSON, D.C. (1980), Gebbies Pass model results - Raw data, Report No. 100/80, Dept of Mechanical Engineering, University of Canterbury, Christchurch, New Zealand.

NEMOTO, S. (1961), Similarity between natural wind in the atmosphere and model wind in a wind tunnel. Papers in Meteorology and Geophysics, Tokyo. Vol.12, No.1: 3052. Vol.12, No.2: 117-128. Vol.12, No.2: 129-154.

NZS 4203, (1976), New Zealand Standard code of practice for general design and design loadings for buildings.

ORGILL, M.M., CERMAK, J.E., GRANT, L.O. (1971), Research and development technique for estimating airflow and diffusion parameters related to the atmospheric water resources program. Final Report, Bureau of Reclaimation Contract No. 14-06-D-6842, Colorado State Univ., CER71-72 MMO-JEC-LOG-20: 111 p.

ORLANSKI, I., (1975), A rational sub-division of scales for atmospheric processes. Bull. Am. Meteoro. Soc. 56(5): 527-530.

PANOFSKY, H.A., BLACKADAR, A.K., McVEHIL, G.E. (1960), The diabatic wind profile. Q.J.R. Met. Soc. 86: 390.

PANOFSKY, H.A. and VAN DER HOVEN, I., (1955), Spectra and cross-spectra of velocity components of the micro-meteorological range. Q.J.R. Met. Soc., 81: 350.

PASQUILL, F. (1950), The aerodynamic drag of grassland. Proc. Roy. Soc. Atmos. 202: 143-151

PASQUILL, F. (1961), The statistics of turbulence in the lower part of the atmosphere. Paper 4, Sump. on Atmos. Turbulence and its relation to Aircraft, RAE, Farnborough.

PASQUILL, F. (1970), Wind structure in the atmospheric boundary layer. Discus. on Archit. Aero. Phil. Trans. Roy. Soc. A.269: 321-554.

PEARSE, J.R., (1978), A data acquisition system for an atmospheric boundary layer wind tunnel, based on the use of a Hewlett-Packard 2100A Digital Computer. Report No. TH/FL 101/78, Dept of Mechanical Engineering, University of Canterbury, Christchurch, New Zealand.

PEARSE, J.R. (1979), The influence of two-dimensional hills on simulated atmospheric boundary layers: Thesis presented for degree of Ph.D. in Mechanical Engineering, University of Canterbury, Christchurch, New Zealand 1979.

PENWARDEN, A.D. and WISE, A.F.E. (1975), Wind environment around buildings. Building Research Establishment Report: 52p.

POPE, A. and HARPER, J.J. (1966), Low speed wind tunnel testing. J. Wiley and Sons: 457 p.

PRANDTL, L. (1932), Meteorologische Anwerdung der Strömungslahre, Buträge Fur Physik der Freuen Atmosphäre, vol.19: 188.

PUTNAM, P.C. (1948), Power from the wind. D. Van Nostrand Co. Inc.

RAINE, J.R. (1974), Modelling the natural wind: Wind protection by Fences. Thesis presented for degree of Ph.D., in Mechanical Engineering, University of Canterbury, Christchurch, New Zealand.

RAINE, J.K. and STEVENSON, D.C., (1977), Wind protection by model fences in a simulated atmospheric boundary layer. Journal of Industrial Aerodynamics, vol.2: 159-180.

REED, J.W. (1974), Wind power climatology. Westerwise, Dec. 1974: 237-242.

RICHARDSON, L.F. (1920), The supply of energy from and to atmospheric eddies. Proc. Roy. Soc. of London, vol.97: 354 p.

RIDER, N.E. (1954), Eddy diffusion of momentum, water vapour and heat near the ground. Phil. Trans. Roy. Soc. Atmos., 246: 481-501.

SHEPPARD,P.A., (1951), Atmospheric turbulence. Weatherwise, vol.5: 42p.

SHIEH, C.F. and FROST, W., (1976), Tether analysis for a kite anemometer. Contract No. AC06-76ET20242.

SLADE, D.H. (1969), Wind measurements on a tall tower in rough and inhomogeneous terrain. J. of App. Met.: 293-297.

SMITH, S.D. (1970), Thrust anemometer measurements on wind turbulence, Reynolds stresses and drag coefficient over the sea. J. Geophys. Res. 75: 6758-6770.

SNYDER, W.E, BRITTER, R., and HUNT, J.C.R. (1979), A fluid modelling study of the flow structure and plume impingement on a three-dimensional hill in stably stratified flow. 5th International Conf. on Wind Engineering Colorado State University, Fort Collins, 8-13 July 1979.

STEEL, L.P. (1976) A study of the relation between the surface wind at Trawsfynydd Power Station and nearby topography. B.L.Met, 10, 381-392.

SUMNER, C.J. (1968), A low torque cup anemometer. Australian Journal of Instrumentation and Control, October 1968: 39-40.

SUTTON, O.G. (1949), Atmospheric turbulence. Methven Monograph.

SUTTON, O.G. (1953), Micrometeorology. McGraw-Hill, New York.

TAYLOR, G.I. (1927), Turbulence. Q.J.R. Met. Soc., vol.53: 201.

TAYLOR, P.A.(1977b), Numerical studies of neutrally stratified planetary boundary layer flow above gentle topography. I. Two-Dimensional cases. Boundary Layer Meteorology, 12: 37-60.

TEUNISSEN H.W. (1970), Characteristics of the mean wind and turbulence in the planetary boundary layer. UTIAS Review No.32.

TEUNISSEN, H.W. (1979), Structure of mean winds and turbulence in the planetary boundary layer over rural terrain. Internal Report No. MSRB 79-1, Atmospheric Environment.

TYSON, P.D. and PRESTON-WHYTE, R.A., (1972), Observations of regional topographically induced wind systems in Natal; Journ. of Appl.Met., 11, 643-650.

VAN DER HOVEN, I., (1957), Power spectrum of horizontal wind speed in the frequency range from 0.0007 to 700 Hz/hr. J. Met. 14: 160.

VON KÁRMÁN, T., (1948), Progress in the statistical theory of turbulence. Proc. Nat. Acad. Sci., Wash., 34: 530-539.

VICKERY, B.J. (1965), A model of atmospheric turbulence for studies of wind loadings on buildings. Paper presented at 2nd Aust. Conf. on Hydraulic and Fluid Mechanics, Nov. 1965.

WARD, G.T., KADIVAR, S., and BROUGHTON, R.S., (1974), Wind power potential in Southern Quebec. Annual Meeting, Canadian Soc. of Agric. Eng., Laval University, Quebec.

WARDS, I. ed. (1976), New Zealand Atlas. A.R.Shearer, Govt. Printer, Wellington: 292 p.

WAX, M.P.,. (1956), An experimental study of wind structure. ERA Technical Report C/T 114.

WINTERMITZ, F.A.L. (1956), Probe measurements in three-dimensional flow. Airc. Eng, vol.28, No.330: 273-278.

YAMAMOTO, G., and SHIMANUKI, A. (1964) Profiles of Wind. Rep. Tohuku Univ., 5th Series Geophysics 15(3).

YOSHIMO, M.M. (1973), Studies of wind-shaped trees: Their classification, districtuion and significance as a climatic indicator. Climatological Notes 12, Dept of Geog., Hosei University, Tokyo, Japan: 52 p.

APPENDIX I

REVIEW OF SIMILITUDE CRITERIA

(Orgill, Cermak, & Grant (1971b))

Basic Equations

The basic equations necessary for considering atmospheric motions and dispersion are the following:

Equations of motion,
Continuity equation,
Equation of state,
Poisson's equation,
Equation of turbulent heat transfer,
Equation of heat transfer from the surface boundary, and
Parabolic diffusion equation.

In this study the continuity equation and equation of state are of little importance to the similarity analysis and will be omitted from further discussion. Therefore, the principal equations to be considered in determining similarity criteria for air motion and dispersion are:

1. Equation of Motion

$$\frac{\partial \bar{U}_i}{\partial t} + \bar{U}_j \frac{\partial \bar{U}_i}{\partial x_j} + 2\varepsilon_{ijk}\Omega_j \bar{U}_k = -\frac{1}{\rho}\frac{\partial \bar{p}}{\partial x_i} + \frac{1}{\rho}\frac{\partial \sigma_{ij}}{\partial x_j} + \frac{1}{\rho}\frac{\partial \sigma_{ij}}{\partial x_j} - \frac{\Delta \bar{T}}{\bar{T}} g\delta_{i3} \qquad \text{A-1}$$

2. Equation of Poisson

$$\theta = T\left(\frac{1000}{p}\right)^{R_d/C_{p_d}} \qquad \text{A-2}$$

3. Equation of Turbulent Heat Transfer

$$\rho C_p\left(\frac{\partial \bar{T}}{\partial t} + \bar{U}_j \frac{\partial \bar{T}}{\partial x_j}\right) - \frac{\partial \bar{p}}{\partial t} - \bar{U}_j \frac{\partial \bar{p}}{\partial x_j} - \overline{\bar{U}_j' \frac{\partial p'}{\partial x_j}}$$

$$= \frac{\partial}{\partial x_j}\left(k \frac{\partial \bar{T}}{\partial x_j}\right) - C_p \rho \frac{\partial}{\partial x_j}\left(\overline{T'u_j'}\right) + \bar{\phi} \qquad \text{A-3}$$

4. Equation of Heat Transfer from the Surface Boundary

$$Q_T - Q_R + Q_{L\downarrow} - Q_{L\uparrow} = \pm Q_G \pm Q_H \pm Q_E \qquad \text{A-4}$$

5. Parabolic Diffusion Equation

$$\frac{\partial \bar{C}}{\partial t} = \frac{\partial}{\partial x_i}(\bar{C}\,\bar{U}_i) = \frac{\partial}{\partial x_i} K_{ii} \frac{\partial \bar{C}}{\partial x_i} + k_m \frac{\partial^2 \bar{C}}{\partial x_i \partial x_i} \qquad \text{A-5}$$

This set of equations may be simplified further depending upon the type of airflow under investigation and the boundary conditions. The fourth equation, the equation of heat transfer from the surface boundary has not been used in deriving similarity criteria before and, because of the similarity difficulties this equation presented to the study, it was neglected except as a general tool for analysing the similarity problem in depth.

For the set of equations to be complete, equations dealing with the physics of clouds should be included, but this aspect of the study cannot be considered in a laboratory physical model at the present time.

Boundary Conditions

The general boundary conditions for a study of air motion and dispersion over irregular terrain can be expressed mathematically as the following (see Fig. 2-1 also):

1. $\lim_{z \to z_o} \vec{U} = 0$

2. $\lim_{z \to H} \vec{U} = \vec{U}_g$

3. $\lim_{z \to z_o} \vec{T} = \vec{T}_o$ A-6

4. $\lim_{z \to H} \vec{T} \to \vec{T}_{min}$

5. $\lim_{x,y,z \to \infty} C \to 0$

6. $\lim_{x,y,z \to 0} C \to \infty$

The continuity condition

$$\int_{-\infty}^{\infty} \int_{0}^{\infty} \bar{U}\, C(x,y,z)\,dz\,dy = Q \quad \text{for all} \quad x>0 \qquad \text{A-7}$$

will not be satisfied in the field because of the action of deposition and depletion variables.

Similitude Criteria

The similitude parameters governing the airflow and dispersion patterns may be derived by dimensional analysis, similarity theory and inspectional analysis. The purpose of this section is to give a review of the similarity criteria that several authors have derived that pertain to this particular problem and not to discuss the relative advantages and disadvantages of the similarity methods.

Sundaram (1976) derived the similitude requirements for the atmospheric boundary layer by applying similarity techniques to the differential equations governing the relevant flow processes. The following mathematical expressions summarises part of the similarity criteria derived by Sundaram for different airflow conditions:

1. Steady, turbulent, incompressible and neutral airflow:

$$\frac{u}{U_\infty} = f\left(\frac{z}{L_o}, \frac{U_\infty L_o}{\nu}, \frac{U_\infty L_o}{K_M}\right) \qquad \text{A-8}$$

2. Steady, uniform, turbulent flow (aerodynamically rough):

$$\frac{u}{U_\infty} = f\left(\frac{z}{z_o}, \frac{U_\infty z_o}{K_{M_o}}\right) \qquad \text{A-9}$$

3. Turbulent flow with temperature gradient (temperature gradient is sufficiently small so that deviation from neutral conditions are small; vertical gradients are more important than horizontal ones):

$$\left(\frac{u}{U_\infty}, \frac{\delta T}{\Delta T}\right) = f\left(\frac{z}{L_o}, \frac{U_\infty L_o}{\nu}, \frac{U_\infty L_o}{K_m}, \frac{U_\infty L_o}{K}, \frac{U_\infty L_o}{K_H}, g\frac{L_o}{U_\infty^2}\frac{\Delta T}{T_o}\right) \qquad \text{A-10}$$

with modifications

$$\left(\frac{u}{U_\infty}, \frac{\delta T}{\Delta T} = f\left(\frac{z}{z_o}, Pr_t, Re_t, B\right) \text{ where } B = g\frac{z_o}{U_\infty^2}\frac{\Delta T}{T_o}\right) \qquad \text{A-11}$$

4. Turbulent flow with temperature gradient (fractional changes in potential temperatures are not small):

$$\left(\frac{u}{U_\infty}\ ,\ \frac{\delta T}{\Delta T}\right) = f\left(\frac{z}{z_o}\ ,\ Pr_t,\ Re_t,\ B,\ \frac{\Delta T}{T_o}\right) \qquad \text{A-12}$$

5. Unsteady flows

$$\left(\frac{u}{U_\infty}\ ,\ \frac{\delta T}{\Delta T}\right) = f\left(\frac{z}{L_o}\ ,\ \frac{t}{t_o}\ ,\ \frac{U_\infty t_o}{L_o}\ ,\ \frac{U_\infty L_o}{\nu}\ ,\ \frac{U_\infty L_o}{KM}\ ,\ \frac{U_\infty L_o}{K}\ ,\ \frac{U_\infty L_o}{K_H}\right.$$

$$\left. g\frac{L_o}{U_\infty^2}\frac{\Delta T}{T_o}\ ,\ \frac{u^*}{U_\infty}\ ,\ -\frac{1}{ku^*}\frac{Q}{\rho C_p}\frac{1}{\Delta T}\ ,\ \frac{\theta_o}{\Delta T}\right) \qquad \text{A-13}$$

6. Similarity of turbulent fluctuations:

$$\frac{u_o}{\sqrt{u_o'^2}}\ ,\ \frac{(\Delta T)_o}{\sqrt{T_o'^2}}\ \ \frac{L_o}{z_o}\ ,\ \frac{U_o z_o}{K_{M_o}}\ ,\ \frac{K_{M_o}}{K_{H_o}}\ ,\ g\frac{z_o}{U_o^2}\frac{(\Delta T)_o}{T_o} \qquad \text{A-14}$$

Nemoto (1961, 1962), derived the similitude requirements for the atmospheric boundary layer by using inspectional analysis and turbulence theory. A summary of his criteria are:

1. Turbulent and incompressible flow (neutral conditions)

$$\left[\frac{K_i}{L_o U_\infty}\right]_F \quad \left[\frac{K_i}{L_o U_\infty}\right]_M \quad \left[\frac{u_i'^2}{U_\infty^2}\right]_F \quad \left[\frac{u_i'^2}{U_\infty^2}\right]_M \qquad \text{A-15}$$

Nemoto modifies the eddy Reynolds number requirement by considering local isotropic turbulence theory and derives the following:

$$\frac{U_{\infty_M}}{U_{\infty_F}} = \left(\frac{\varepsilon_M}{\varepsilon_F}\right)^{1/3} \left(\frac{L_{M_o}}{L_{F_o}}\right)^{1/3} \qquad \text{A-16}$$

2. Thermal stratification-similarity based on equation of turbulent energy change:

$$\frac{U_{\infty_F}}{U_{\infty_M}} = \left(\frac{L_{o_F}}{L_{o_M}}\right)^{1/2} \left(\frac{\theta_M}{\Delta\theta_M}\Big/\frac{\theta_F}{\Delta\theta_F}\right)^{1/2} \qquad \text{A-17}$$

3. Turbulent flow field with thermal stratification:

$$\left[\frac{K_i}{L_o U_\infty}\right]_F \equiv \left[\frac{K_i}{L_o U_\infty}\right]_M \quad \left[\frac{\overline{u_1'^2}}{U_\infty^2}\right]_F \equiv \left[\frac{\overline{u_i'^2}}{U_\infty^2}\right]_M \quad \left[g\frac{L_o}{U_\infty^2}\right]_M \equiv \left[g\frac{L_o}{U_\infty^2}\right]_F \qquad \text{A-18}$$

Nemoto indicates that the above three conditions can be simultaneously satisfied if the following relation holds among the sizes and velocities of the apparent mean eddies in the i-direction of model and prototype flows:

$$\frac{U_{miM}}{U_{miF}} = \left(\frac{L_{M_o}}{L_{F_o}}\right)^{3/2} \left(\frac{\Lambda_{miM}}{\Lambda_{miF}}\right)^{-1} \qquad \text{A-19}$$

Bernstein (1965) used the ordinary dimensional method and a generalised dimensional analysis to derive the similarity criteria for the atmospheric planetary layer. On the basis of the equations of motion and boundary conditions he indicates that the variables relevant to flow in the atmospheric planetary layer are $\vec{U}$, $\vec{U}_g$, ρ, f, $\vec{\tau}$, $\vec{\tau}_o$, z, H and z_o. In this analysis he represents vectors as complex variables and assumes that relevant vectors lie in the horizontal plane and, therefore, are two-dimensional.

Bernstein used ordinary dimensional analysis to find the following functional relationship for neutral conditions,

$$\frac{\vec{U}}{\vec{U}_*} = f\left(\frac{\vec{U}_{*o}}{\vec{U}_g}, \frac{\vec{U}_g}{fz_o}, \frac{H}{z_o}, \frac{z}{z_o}, \frac{\vec{U}_*}{\vec{U}_{*o}}\right) \qquad \text{A-20}$$

and from his generalised dimensional analysis:

$$\frac{\vec{U}}{\vec{U}_g} = f\left(\frac{\vec{U}_{*o}^2}{fz_o\vec{U}_g}, \frac{H}{z_o}, \frac{z}{z_o}, \frac{\vec{U}_*}{\vec{U}_{*o}}\right) \qquad \text{A-21}$$

Cermak et al (1966) have used the inspectional method for deriving similarity criteria for atmospheric flows. These criteria are:

1. Turbulent and neutral airflow

$$\tau_{o_F} \equiv \tau_{o_M} \qquad \text{A-22}$$

$$C_{D_M}\rho_M\bar{U}_M^2 \equiv C_{D_F}\rho_F\bar{U}_F^2$$

2. Turbulent flow with thermal stratification:

$$Re = \frac{U_o L_o}{\nu_o}$$

$$Ri = \frac{\Delta T_o}{\bar{T}_o} \frac{L_o}{U_o^2} g_o$$

$$R_o = \frac{U_o}{L_o \Omega_o}$$

$$Pr = \frac{\nu_o}{k_o / \rho_o C_{p_o}} \qquad \text{A-23}$$

$$Ek = \frac{U_o^2}{C_{p_o} \Delta \bar{T}_o}$$

3. Comparison on laminar laboratory airflow model to a turbulent atmospheric prototype airflow:

Model		Field
$Re = \frac{U_o L_o}{\nu}$	$\equiv R_{c_t}$	$= \frac{U_o L_o}{K_i}$
$Pr = \frac{\mu C_p}{k}$	$\equiv P_{r_t}$	$= \frac{K_M}{K_H}$

$$Ri \equiv \frac{g_o}{T_o} \frac{\Delta T_o L_o}{U_o^2} \qquad \text{A-24}$$

$$E_u = \frac{\Delta p_o}{\rho U_o^2}$$

$$Ek = \frac{U_o^2}{C_p \Delta T_o}$$

For dispersion similarity,

$$Pe = \frac{U_o O_o}{k_m} \equiv Pe_t = \frac{U_o L_o}{K_c}$$

Partial Simulation

One of the most important practical problems that arises in laboratory simulation is the effect of not satisfying exactly all the similarity requirements. The situation in which the modeling criteria are not completely fulfilled is called partial simulation. In practice partial simulation is unavoidable since many similarity criteria impose diametrically opposing requirements on the scaling parameters. Thus, it is well known that in fluids with the same kinematic viscosity, simultaneous modeling of both Reynolds and Froude number is nearly impossible.

Unfortunately, it is clear that in the flow problems of the type discussed above, all the similarity criteria cannot be satisfied simultaneously and that partial simulation becomes unavoidable. When dealing with the simulation of the above class of flow problems on a different scale one has to decide which of the similarity parameters are more important for a satisfactory description of the physical processes governing the problems.

Sundaram (1967) listed the various questions that arise in connection with the practical application of laboratory modeling techniques. The ones important are:

1. "Of all the various similitude parameters occurring in a given problem, which ones are the most important?

2. "How accurately should the similarity parameters be reproduced in the laboratory and what are the effects of relaxing them?

3. "What range of values of these similarity parameters should any facility be capable of reproducing?

4. "How accurately should quantities be measured in a facility?"

The area of modeling in which the greatest amount of experience is available and in which there is abundant evidence of successful partial simulation is in the modeling of flow about objects, buildings and prominant features of terrain. The principal concern in these problems has been in the simulation of the streamlines of mean flow and the location of wakes and eddies.

In simulating the flow around sharp-edged terrain features, since Reynolds number is not expected to influence the gross flow features it has been possible to duplicate the mean streamline, the regions of turbulent eddies, and probably even the coarse structure of the turbulence by providing geometrical similarity in the models. Examples of successful modeling in this type of flow problem have been conducted by Field and Warden (1929), Garrison and Cermak (1968) and Halitsky et al. (1965).

In the case of terrain features, such as hills and valleys, viscous effects may become important for gross flow features in a model and it is necessary to consider Reynolds number effects. In this case, the procedure in model experiments has been to match a model Reynolds number to a "turbulent" Reynolds number for the atmosphere, a number obtained by using a representative value of eddy viscosity. Studies in which this type of reasoning has been applied are Abe (1941) and Cermak and Peterka (1966).

Scale Distortion

Distorted geometric models are common in hydraulics and ocean engineering laboratory studies, but have not been used to any great extent in wind-tunnel modeling. A recent study by Chaudhry and Cermak (1971) has examined the problem in relation to modeling urban areas. A complete examination of the distorted similarity problem has not been considered, however, Nemoto (1961) has analysed some aspects of the problem.

Nemoto examined the equations of motion of a turbulent atmosphere and found that in case of vertical exaggeration the degree of distortion is related to K_x and K_z, the eddy-diffusion (viscosity) coefficients in the longitudinal and vertical directions. He found that the relation

$$\alpha = \left[\frac{\left(\frac{K_x}{K_z} \right)_F}{\left(\frac{K_x}{K_z} \right)_M} \right]^{1/2} \qquad \text{A-25}$$

should be satisfied between α and the eddy diffusion coefficients for the mean flow patterns to be similar for prototype and model. At the present time the difficulty of obtaining measurements of the eddy-diffusion coefficients in the field and model have hindered efforts to check this

relation. However, the recent urban area study by Chaudhry and Cermak (1971) was an attempt to examine this relation in terms of a fully-rough flow in the wind tunnel.

GLOSSARY OF TERMS

Eckert No.	$Ek = \frac{U_o^2}{C_{P_o} (\Delta T)_o}$ $Ek = (\gamma-1) M^2$ $\gamma = C_p / C_u$	Nondimensional ratio between inertia force and a compression force. Equivalent to the Mach number.
Euler No.	$Eu = \frac{\Delta P_o}{\rho_o U_o^2}$	Nondimensional ratio between the pressure force and the inertia force.
Froude No.	$Fr = \frac{U_o}{\sqrt{g_o L_o}}$	Nondimensional ratio between the inertia force and force of gravity.
Peclet No.	$Pe = \frac{U_o L_o}{K_c}$	Nondimensional ratio between inertial force and mass diffusivity.
Prandtl No.	$Pr = \frac{C_p \mu}{k}$ $Pr_t = \frac{K_M}{K_H}$	Nondimensional ratio between the product of heat advection and viscous forces and the product of heat diffusion and inertia forces.
Reynolds No.	$Re = \frac{U_o}{L_o \nu_o}$ $Re_t = \frac{U_o}{L_o K_{M_o}}$	Nondimensional ratio of the inertial force to the viscous force.
Richardson No.	$Ri - g_o \frac{1}{\theta_o} \frac{(\partial\theta/\partial z)_o}{(\partial U/\partial z)_o^2}$	Nondimensional number arising in the study of shearing flows of a stratified fluid. Number expresses a characteristic ratio of work done against gravitational stability to energy transferred from mean to turbulent motion.

Rossby No.	$Ro = \frac{U_o}{f_o L_o}$	Nondimensional ratio of the inertial force to the Coriolis force.

APPENDIX II

DIMENSIONS FOR WIND TUNNEL SIMULATION

A.2.1 GRID, MODEL AND ROOF POSITIONS

The positions of the vertical and horizontal bars used in the 1:4000 scale simulation are presented in Fig.A2.1. To ensure that the bars were set with the correct dimensions, spacer blocks were machined to fit between the bars during setting up. All bars were checked to be horizontal or vertical with a spirit level.

The positions and dimensions of the approach flow polystyrene and battens are presented in Fig. A2.2. The polystyrene sheet was of a medium density and left unpainted.

The roof position, as measured above the traverser support rail, is presented in Fig. A2.3.

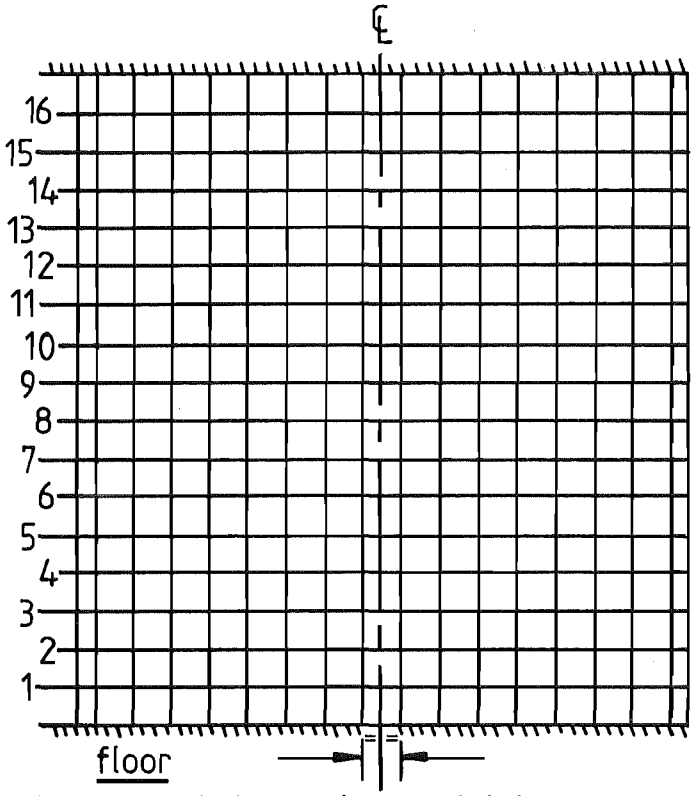

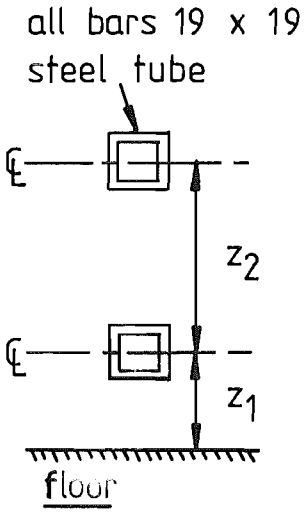

distances between horizontal bars

z_1	floor - 1	58·5
z_2	1 - 2	68·5
"	2 - 3	71
"	3 - 4	67
"	4 - 5	70
"	5 - 6	70
"	6 - 7	71
"	7 - 8	70
"	8 - 9	68·5
"	9 - 10	70
"	10 - 11	70
"	11 - 12	70
"	12 - 13	66
"	13 - 14	76
"	14 - 15	74
"	15 - 16	96

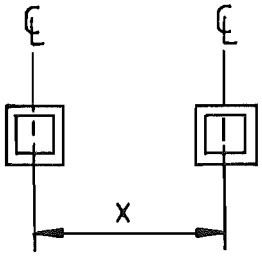

distances between the 16 vertical bars are equal at x = 89 mm.

all dimensions in mm.

FIG. A 2·1 POSITIONS OF BARS FOR INFLOW GRID

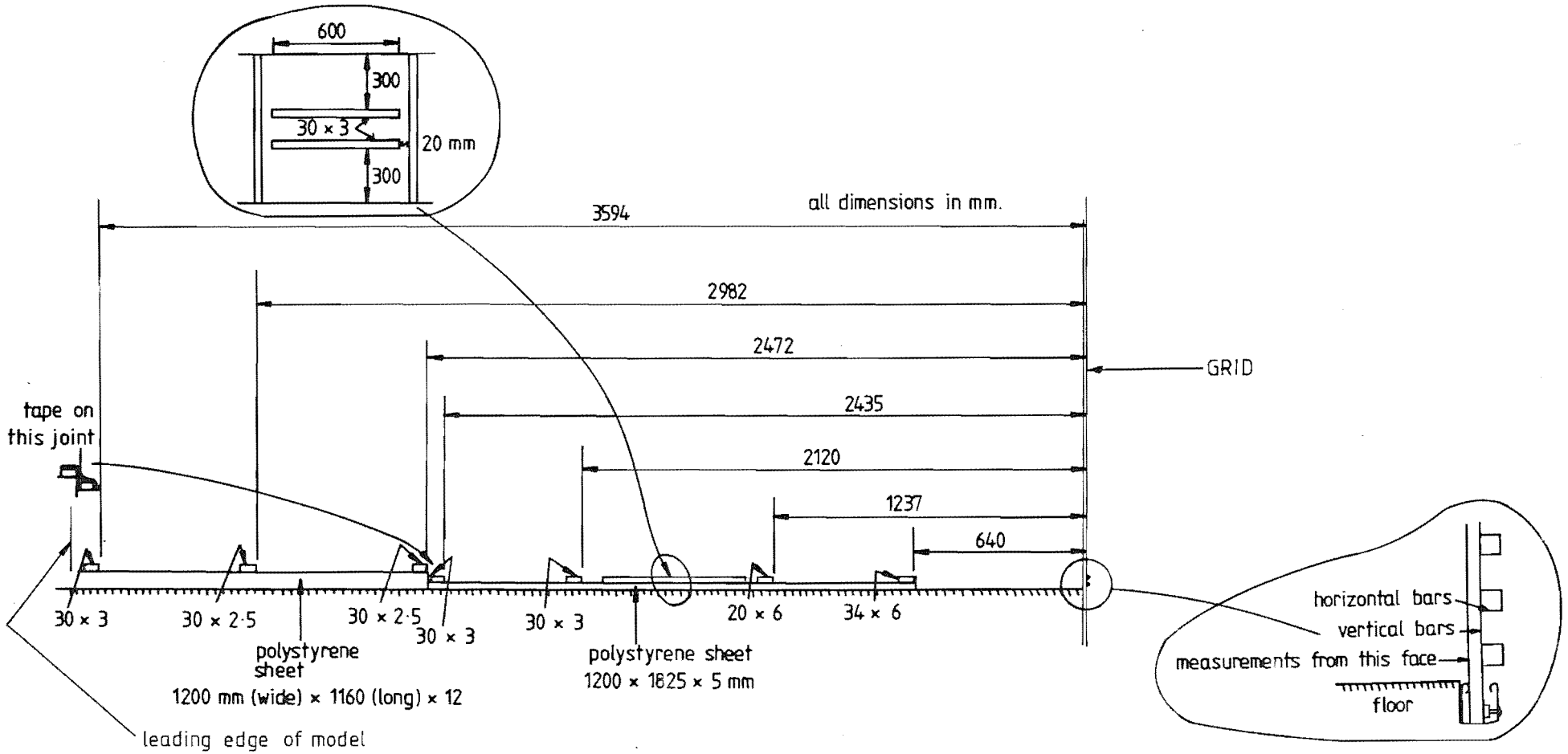

FIG. A2·2 POSITIONS AND DIMENSIONS OF THE SIMULATION APPROACH MATERIALS.

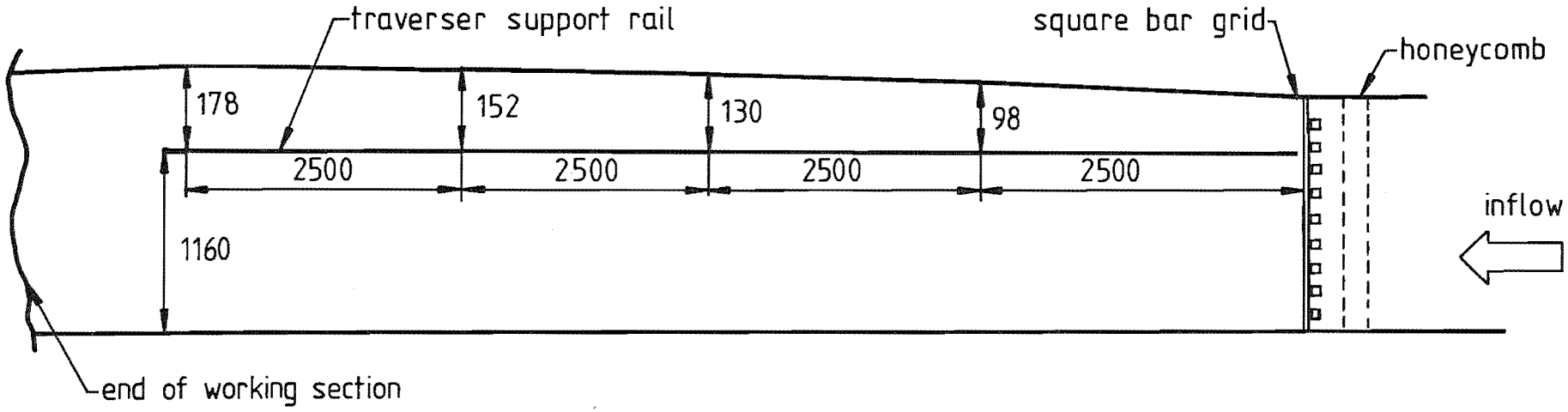

FIG. A2·3 POSITION OF WIND TUNNEL ROOF